Interpreting Excavation-Induced Displacements around a Tunnel in Highly Stressed Granite

By

Rodney Stewart Read

A Thesis
Submitted to the Faculty of Graduate Studies
in Partial Fulfillment of the Requirements
for the Degree of

Doctor of Philosophy

Department of Civil and Geological Engineering
University of Manitoba
Winnipeg, Manitoba

ISBN 0-315-99059-7

Name Rodney Stewart Read

Dissertation Abstracts International is arranged by broad, general subject categories. Please select the one subject which most nearly describes the content of your dissertation. Enter the corresponding four-digit code in the spaces provided.

Engineering - Civil
SUBJECT TERM

0543
SUBJECT CODE

UMI

Subject Categories

THE HUMANITIES AND SOCIAL SCIENCES

COMMUNICATIONS AND THE ARTS
Architecture 0729
Art History 0377
Cinema 0900
Dance 0378
Fine Arts 0357
Information Science 0723
Journalism 0391
Library Science 0399
Mass Communications 0708
Music 0413
Speech Communication 0459
Theater 0465

EDUCATION
General 0515
Administration 0514
Adult and Continuing 0516
Agricultural 0517
Art 0273
Bilingual and Multicultural 0282
Business 0688
Community College 0275
Curriculum and Instruction 0727
Early Childhood 0518
Elementary 0524
Finance 0277
Guidance and Counseling 0519
Health 0680
Higher 0745
History of 0520
Home Economics 0278
Industrial 0521
Language and Literature 0279
Mathematics 0280
Music 0522
Philosophy of 0998
Physical 0523
Psychology 0525
Reading 0535
Religious 0527
Sciences 0714
Secondary 0533
Social Sciences 0534
Sociology of 0340
Special 0529
Teacher Training 0530
Technology 0710
Tests and Measurements 0288
Vocational 0747

LANGUAGE, LITERATURE AND LINGUISTICS
Language
- General 0679
- Ancient 0289
- Linguistics 0290
- Modern 0291

Literature
- General 0401
- Classical 0294
- Comparative 0295
- Medieval 0297
- Modern 0298
- African 0316
- American 0591
- Asian 0305
- Canadian (English) 0352
- Canadian (French) 0355
- English 0593
- Germanic 0311
- Latin American 0312
- Middle Eastern 0315
- Romance 0313
- Slavic and East European 0314

PHILOSOPHY, RELIGION AND THEOLOGY
Philosophy 0422
Religion
- General 0318
- Biblical Studies 0321
- Clergy 0319
- History of 0320
- Philosophy of 0322

Theology 0469

SOCIAL SCIENCES
American Studies 0323
Anthropology
- Archaeology 0324
- Cultural 0326
- Physical 0327

Business Administration
- General 0310
- Accounting 0272
- Banking 0770
- Management 0454
- Marketing 0338

Canadian Studies 0385
Economics
- General 0501
- Agricultural 0503
- Commerce-Business 0505
- Finance 0508
- History 0509
- Labor 0510
- Theory 0511

Folklore 0358
Geography 0366
Gerontology 0351
History
- General 0578
- Ancient 0579
- Medieval 0581
- Modern 0582
- Black 0328
- African 0331
- Asia, Australia and Oceania 0332
- Canadian 0334
- European 0335
- Latin American 0336
- Middle Eastern 0333
- United States 0337

History of Science 0585
Law 0398
Political Science
- General 0615
- International Law and Relations 0616
- Public Administration 0617

Recreation 0814
Social Work 0452
Sociology
- General 0626
- Criminology and Penology ... 0627
- Demography 0938
- Ethnic and Racial Studies 0631
- Individual and Family Studies 0628
- Industrial and Labor Relations 0629
- Public and Social Welfare 0630
- Social Structure and Development 0700
- Theory and Methods 0344

Transportation 0709
Urban and Regional Planning 0999
Women's Studies 0453

THE SCIENCES AND ENGINEERING

BIOLOGICAL SCIENCES
Agriculture
- General 0473
- Agronomy 0285
- Animal Culture and Nutrition 0475
- Animal Pathology 0476
- Food Science and Technology 0359
- Forestry and Wildlife 0478
- Plant Culture 0479
- Plant Pathology 0480
- Plant Physiology 0817
- Range Management 0777
- Wood Technology 0746

Biology
- General 0306
- Anatomy 0287
- Biostatistics 0308
- Botany 0309
- Cell 0379
- Ecology 0329
- Entomology 0353
- Genetics 0369
- Limnology 0793
- Microbiology 0410
- Molecular 0307
- Neuroscience 0317
- Oceanography 0416
- Physiology 0433
- Radiation 0821
- Veterinary Science 0778
- Zoology 0472

Biophysics
- General 0786
- Medical 0760

EARTH SCIENCES
Biogeochemistry 0425
Geochemistry 0996
Geodesy 0370
Geology 0372
Geophysics 0373
Hydrology 0388
Mineralogy 0411
Paleobotany 0345
Paleoecology 0426
Paleontology 0418
Paleozoology 0985
Palynology 0427
Physical Geography 0368
Physical Oceanography 0415

HEALTH AND ENVIRONMENTAL SCIENCES
Environmental Sciences 0768
Health Sciences
- General 0566
- Audiology 0300
- Chemotherapy 0992
- Dentistry 0567
- Education 0350
- Hospital Management 0769
- Human Development 0758
- Immunology 0982
- Medicine and Surgery 0564
- Mental Health 0347
- Nursing 0569
- Nutrition 0570
- Obstetrics and Gynecology .. 0380
- Occupational Health and Therapy 0354
- Ophthalmology 0381
- Pathology 0571
- Pharmacology 0419
- Pharmacy 0572
- Physical Therapy 0382
- Public Health 0573
- Radiology 0574
- Recreation 0575
- Speech Pathology 0460
- Toxicology 0383

Home Economics 0386

PHYSICAL SCIENCES
Pure Sciences
Chemistry
- General 0485
- Agricultural 0749
- Analytical 0486
- Biochemistry 0487
- Inorganic 0488
- Nuclear 0738
- Organic 0490
- Pharmaceutical 0491
- Physical 0494
- Polymer 0495
- Radiation 0754

Mathematics 0405
Physics
- General 0605
- Acoustics 0986
- Astronomy and Astrophysics 0606
- Atmospheric Science 0608
- Atomic 0748
- Electronics and Electricity 0607
- Elementary Particles and High Energy 0798
- Fluid and Plasma 0759
- Molecular 0609
- Nuclear 0610
- Optics 0752
- Radiation 0756
- Solid State 0611

Statistics 0463

Applied Sciences
Applied Mechanics 0346
Computer Science 0984
Engineering
- General 0537
- Aerospace 0538
- Agricultural 0539
- Automotive 0540
- Biomedical 0541
- Chemical 0542
- Civil 0543
- Electronics and Electrical 0544
- Heat and Thermodynamics ... 0348
- Hydraulic 0545
- Industrial 0546
- Marine 0547
- Materials Science 0794
- Mechanical 0548
- Metallurgy 0743
- Mining 0551
- Nuclear 0552
- Packaging 0549
- Petroleum 0765
- Sanitary and Municipal 0554
- System Science 0790

Geotechnology 0428
Operations Research 0796
Plastics Technology 0795
Textile Technology 0994

PSYCHOLOGY
General 0621
Behavioral 0384
Clinical 0622
Developmental 0620
Experimental 0623
Industrial 0624
Personality 0625
Physiological 0989
Psychobiology 0349
Psychometrics 0632
Social 0451

INTERPRETING EXCAVATION-INDUCED DISPLACEMENTS AROUND A TUNNEL IN HIGHLY STRESSED GRANITE

BY

RODNEY STEWART READ

A Thesis submitted to the Faculty of Graduate Studies of the University of Manitoba in partial fulfillment of the requirements for the degree of

DOCTOR OF PHILOSOPHY

Abstract

In concepts for the underground storage of nuclear fuel waste, the primary rock mechanics concern is the development of damage around excavations. By controlling the extent of the excavation damage zone, the potential for transport of radionuclides, either by diffusion or by groundwater flow within this zone, can be controlled. To this end, it is first necessary to demonstrate that the fundamental behaviour of the rock mass around underground openings is understood. The measurement and interpretation of excavation-induced displacements around openings plays a key role in this respect. For example, in the absence of appreciable excavation-induced damage, displacements have been used extensively to back calculate *in situ* stresses. In rock damaged during excavation, displacement measurements, in combination with numerical models and *in situ* characterization, are also important as a means of determining the extent and characteristics of the damaged zone, and the processes responsible for its development. These two applications tend to be mutually exclusive.

Using AECL's Mine-by Experiment as the field study, this thesis considers the problems associated with analysis and interpretation of displacement measurements taken during excavation of a cylindrical tunnel in a massive, highly stressed, brittle rock mass. A technique using the radial displacement response from within one diameter of the tunnel face is developed to back analyze the *in situ* stress tensor in conditions where extensive excavation damage is evident in parts of the tunnel. The estimated stress tensor is, in turn, used in conjunction with observations and results from field characterization, and numerical modeling, to determine the extent and characteristics of excavation damage around the tunnel. The

relationship between displacement, stress and excavation damage is also explored through comparison of results from numerical modeling and field characterization.

The main contributions represented by this thesis are:

- An *in situ* stress back analysis technique based on radial displacement measurements taken within one tunnel diameter of the face.
- General approximating functions to describe the relationship between radial displacement and tunnel face position (i.e., the *spliced logistic function*), and between radial displacement and radial distance for positions within one diameter of the tunnel face.
- Parametric functions describing the *characteristic radial displacement surfaces* associated with components of a partitioned unit stress tensor.
- An interpretative methodology for displacement measurements in highly stressed brittle rock, including a correction methodology for face curvature and stepped longitudinal tunnel geometry.
- An assessment of the limitations of posterior-type displacement monitoring instruments, such as convergence arrays, and the assumptions inherent in interpreting results from them.
- An estimate of *in situ* stress conditions and material properties at the 420 Level of AECL's Underground Research Laboratory.
- An interpretation of the extent and characteristics of the damaged zone around the Mine-by Experiment test tunnel, and the processes responsible for its development.

Acknowledgements

I would first like to thank my wife, Angel, for her tireless support and encouragement through a very hectic period of our lives involving the births of our two sons, Joshua and Kieran. Without her and our shared faith, this work would not have come to fruition.

This thesis represents a culmination of ideas and experiences from what can only be described as a remarkable research environment in which to work. I am indebted to AECL Research for the financial support provided to pursue graduate studies at the University of Manitoba, and to Gary Simmons and Derek Martin for the opportunity to serve as Principal Investigator for the Mine-by Experiment. I would also like to express sincere thanks to Neil Chandler for many interesting and insightful conversations.

I am grateful to my parents for their support in this and all of my academic pursuits. Their long-distance interest helped motivate me when the task of putting pen to paper seemed too daunting to undertake. My sister, Linda, also provided incentive to complete this project.

Finally, I would like to thank my advisor, Brian Stimpson, and examination committee for their guidance and recommendations that have helped steer this thesis in its evolution. Their comments and criticism provided impetus when the creative wheels sometimes needed greasing.

Contents

List of Figures

List of Tables

Symbols and Notation

x, y, z	Rectangular cartesian coordinates
r, θ, z	Standard cylindrical coordinates with z parallel to the tunnel axis
r, θ, x	Cylindrical coordinates with x parallel to the tunnel axis
a	Tunnel radius
a_{eff}	Effective tunnel radius
a_{max}	Maximum tunnel radius within a stepped excavation round
Δa	Difference between the maximum and minimum tunnel radii
D	Tunnel diameter
r	Radial distance from the tunnel centre
R	Normalized radial distance r/a
x_{face}	Axial position of the tunnel face
$x_{instrument}$	Axial position of the instrument
X	Difference between the face and instrument locations $(x_{face} - x_{instrument})$
x_{zero}	True axial position of a curved tunnel face
$x_{deepest}$	Axial position of the deepest point on the face
d	Maximum deviation between the axial position of the edge and centre of the tunnel
θ	Rotation angle measured counterclockwise, looking into the tunnel, from the point of intersection of a horizontal line through the tunnel centre with the right tunnel wall
E	Young's modulus
G	Shear modulus
ν	Poisson's ratio
σ	Field stress under axisymmetric conditions
σ_1	Maximum principal stress component
σ_2	Intermediate principal stress component
σ_3	Minimum principal stress component
σ_{11}	Plane normal component of stress tensor
σ_{33}	Plane normal component of stress tensor

σ_{13}	Plane shear component of stress tensor
σ_{22}	Antiplane normal component of stress tensor
σ_{12}	Antiplane shear component of stress tensor
σ_{23}	Antiplane shear component of stress tensor
σ_{rr}	Radial stress component
$\sigma_{\theta\theta}$	Tangential stress component
σ_{zz}	Axial stress component
σ_{rz}	Shear stress component in the $r-z$ plane
$\sigma_{\theta z}$	Shear stress component in the $\theta-z$ plane
$\sigma_{r\theta}$	Shear stress component in the $r-\theta$ plane
σ_p	Maximum plane stress component
σ_q	Minimum plane stress component
σ_x	Normal component of stress in the x-direction
σ_y	Normal component of stress in the y-direction
τ_{xy}	Shear component of stress in the xy plane
K	Stress ratio relative to σ_3
K_{max}	Ratio of maximum to minimum plane stress
K_{axial}	Ratio of axial to minimum plane stress
K_{min}	Ratio of minimum to minimum plane stress (unity)
I_1	First stress invariant
I_2	Second stress invariant
I_3	Third stress invariant
$\overline{\sigma}$	Mean stress tensor
$S_{\overline{\sigma}}$	Standard deviation tensor
σ_c	Uniaxial compressive strength
σ_t	Tensile strength
σ_{ci}	Crack initiation stress
σ_{cd}	Crack damage stress (start of unstable crack growth)
m	Hoek-Brown shape parameter
s	Hoek-Brown scaling factor to account for *in situ* discontinuities
U	Displacement
U_r	Radial displacement
U_a or U_z	Axial displacement
U_θ	Tangential displacement
U_{tot}	Total displacement
$U_{r_{max}}$	Maximum radial displacement in the plane orthogonal to the tunnel axis
$U_{r_{min}}$	Minimum radial displacement in the plane orthogonal to the tunnel axis
A	Abscissa of pivot point controlling the shape of the curve in the *spliced logistic function*
B	Slope parameter in the *spliced logistic function*
D_l	Radial displacement at $X = 0$ in the *spliced logistic function*

E_l	Radial displacement at $X = +\infty$ in the posterior domain and at $X = -\infty$ in the anterior domain in the *spliced logistic function*
F	$(E_l - D_l)$ in the posterior domain and $(D_l - E_l)$ in the anterior domain in the *spliced logistic function*
λ	Scaling factor in the *spliced logistic function*
α	Mean displacement response in parametric functions
β	Amplitude of the harmonic component of the displacement response in parametric functions
ψ	Phase constant in parametric functions
A_i	Scalar coefficients in the inverse polynomial series function
r^2	Coefficient of determination
C_f	Ratio of the normalizing factor used in the partitioned stress tensor models and $U_{r_{max}}$ used to normalize the measured response
c_1	Magnitude of σ_{11} multiplied by C_f
c_2	Magnitude of σ_{33} multiplied by C_f
c_3	Magnitude of σ_{13} multiplied by C_f
c_4	Magnitude of σ_{22} multiplied by C_f
c_5	Magnitude of σ_{12} multiplied by C_f
c_6	Magnitude of σ_{23} multiplied by C_f
f_{1-6}	Parametric functions describing the *characteristic radial displacement surfaces* for the partitioned stress tensor components
$f_{1_e-6_e}$	Modified parametric functions for posterior extensometers
$f_{1_c-6_c}$	Modified parametric functions for convergence arrays
C	Number of constraint equations used in back analysis
$\mathbf{U}$	Strain energy
σ_{ij}	Stress tensor
ϵ_{ij}	Strain tensor
dV	Differential volume
P	Ratio used to correct for missed displacement in the axial direction
κ	Curvature function

Chapter 1

Introduction

Excavation-induced displacements in a rock mass figure prominently in many current rock mechanics problems, ranging from practical tunneling issues, such as support design, to more research-oriented topics, such as the design of effective sealing systems for a nuclear fuel waste disposal vault. The level of knowledge required about the displacement field around an excavation is dependent largely on the proposed application for the underground opening. For instance, the resolution of displacement measurements in a mining situation may only be required to a few centimetres to establish the safety of an opening, whereas displacements in the order of micrometres may be of interest in a vault sealing application to assess the potential for groundwater migration. Regardless of the end use of the excavation, the displacement field around an underground opening is influenced by many factors, including tunnel shape, *in situ* stresses, material properties of the rock mass, and progressive failure.

1.1 Problem Statement

Correct interpretation of an excavation-induced mechanical response has important implications in terms of nuclear fuel waste disposal. As described by Read and Martin [157], the specific rock mechanics issues associated with the underground disposal of nuclear wastes are related primarily to the complex coupling of groundwater flow with thermal, mechanical, and geochemical effects. Stress redistribution around the opening and the subsequent

heating due to the waste emplacement, for instance, can alter the porosity and hydraulic conductivity around an excavation, both through the creation of new fractures and through opening or closing of existing fractures. By controlling the extent of the excavation damage zone, the potential for transport of radionuclides, either by diffusion or by groundwater flow within this zone, can be controlled. Interpretation of the extent and characteristics of this zone by means of displacement measurements is therefore of primary concern in vault design. The reliability of such an interpretation is, however, dependent on an understanding of the *in situ* stress conditions.

In linear elastic ground, standard techniques for interpreting tunnel wall displacements can be used to estimate the far-field *in situ* stress tensor from the measured rock mass response [117, 74]. These types of approaches are generally acceptable in low to moderate stress regimes in granite or other brittle rocks, where excavation-induced damage is not an issue. However, in high stress regimes where stress concentrations are sufficient to damage the rock immediately around the underground opening, the interpretation of these types of displacement measurements using linear elasticity may result in unrealistic estimates of *in situ* stresses. Consequently, for openings with appreciable damage zone development, it is necessary to recognize departure from linear elastic material behaviour in order to properly assess *in situ* stress conditions.

Routine measurements of tunnel convergence or closure typify large-scale displacement monitoring programs in many mines and tunneling operations. Convergence arrays are commonly used for this purpose because of the relatively low cost of the instrumentation and the ease and speed with which measurements can be taken. Multi-anchor extensometers are also used to determine the radial displacement profile away from an opening, but these are more costly than convergence arrays, and are only used where detailed information is required. The interpretation of the mechanical response measured by these instruments is complicated by the fact that, with the exception of specific mining applications like that detailed by Atkins and Keen [2], or rock mechanics research experiments such as that

described by Heuzé [73], displacement monitoring generally involves installing instruments some distance behind the advancing tunnel face (Figure 1.1). Consequently, only a portion of the total displacement response is typically measured.

To account for the *posterior* nature of the installation of these instruments, i.e., installation behind the advancing face, general rules of thumb are usually applied to the interpretation of radial displacement data. For example, Panet and Guenot [147] have reported that, in the case of a cylindrical flat-faced tunnel under hydrostatic stress conditions, approximately 27% of the total displacement at the tunnel wall occurs ahead of the tunnel face, and is therefore not picked up by posterior-type instruments. However, because of large displacement gradients near the tunnel face, and dependence of the response on more factors than just the distance of the measurement point from the advancing face, indiscriminate application of such general rules to displacement measurements can lead to large

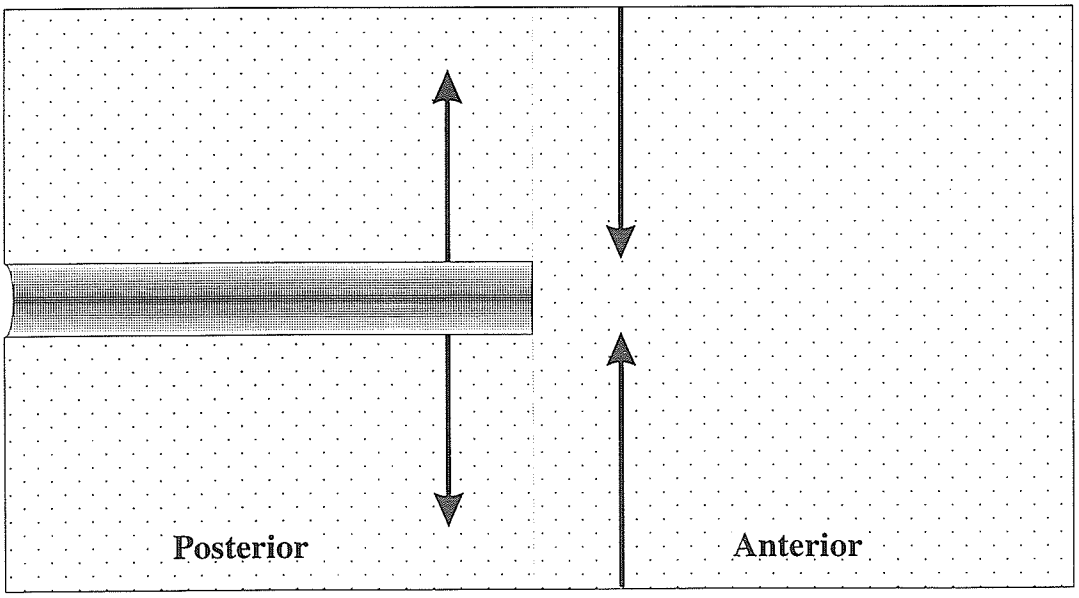

Figure 1.1: Definition of the posterior and anterior domains for an idealized cylindrical tunnel. The positions of arrows represent typical locations of instruments in each domain, and the direction of the arrow indicates the typical direction of installation: for the posterior domain, from the tunnel outwards; and for the anterior domain, from an external opening inwards.

interpretative errors.

The posterior installation of instruments is just one of the problems faced when interpreting measured displacements. In a more general sense, interpretation of displacement measurements suffers in most instances from a lack of characterization data about the rock mass around the tunnel, and poorly defined boundary conditions, such as the *in situ* stress state, and material properties. Many authors have suggested that the effort required to develop a refined interpretative methodology for posterior displacement measurements is not warranted given the large degree of uncertainty associated with selecting appropriate values of parameters describing the rock mass and its mechanical behaviour. To date, there is little or no experience with controlled *in situ* experiments, incorporating both posterior and anterior instruments, in a well-characterized rock mass with known boundary conditions.

The difficulties associated with the interpretation of displacement measurements have relegated their use to only a handful of rudimentary cases where elasticity theory can be applied. The work undertaken in this thesis attempts to extend the use of such measurements to cases involving the development of an excavation damage zone in a non-hydrostatic stress field. Simply stated, the working hypothesis for this thesis is that, in unjointed, highly stressed, brittle rock that has sustained significant damage through excavation-induced stress redistribution, displacements measured near the face of a cylindrical tunnel can be used to interpret both the far-field *in situ* stress tensor, and the extent and characteristics of the excavation-induced damage zone around the tunnel as long as the rock mass, prior to excavation, can be considered a homogeneous, isotropic continuum.

1.2 Scope of Work

AECL's Underground Research Laboratory (URL), located approximately 120 km northeast of Winnipeg, Manitoba in the Lac du Bonnet granite batholith (Figure 1.2), provided the field study location for this thesis. The URL constitutes a well-characterized *in situ* environment in a previously undisturbed volume of rock for experiments that address issues of

importance in assessing the Canadian disposal concept, and/or that demonstrate elements of the proposed disposal technology. In particular, the Mine-by Experiment [155] at the 420 Level of the URL, designed to investigate the excavation-induced rock mass response around underground openings, incorporated both anterior-type instruments (multi-anchor extensometers, triaxial strain cells, and an acoustic emission/microseismic system), and posterior-type instruments (convergence arrays and miniaturized multi-anchor extensometers) to measure the excavation-induced rock mass response, and consequently presents a unique opportunity to assess the factors that influence the measurement of displacements.

The author's involvement in the Mine-by Experiment as Principal Investigator included design, project management, numerical modeling and analysis. The work described in this thesis is an extension of that involvement to subjects that would not otherwise be

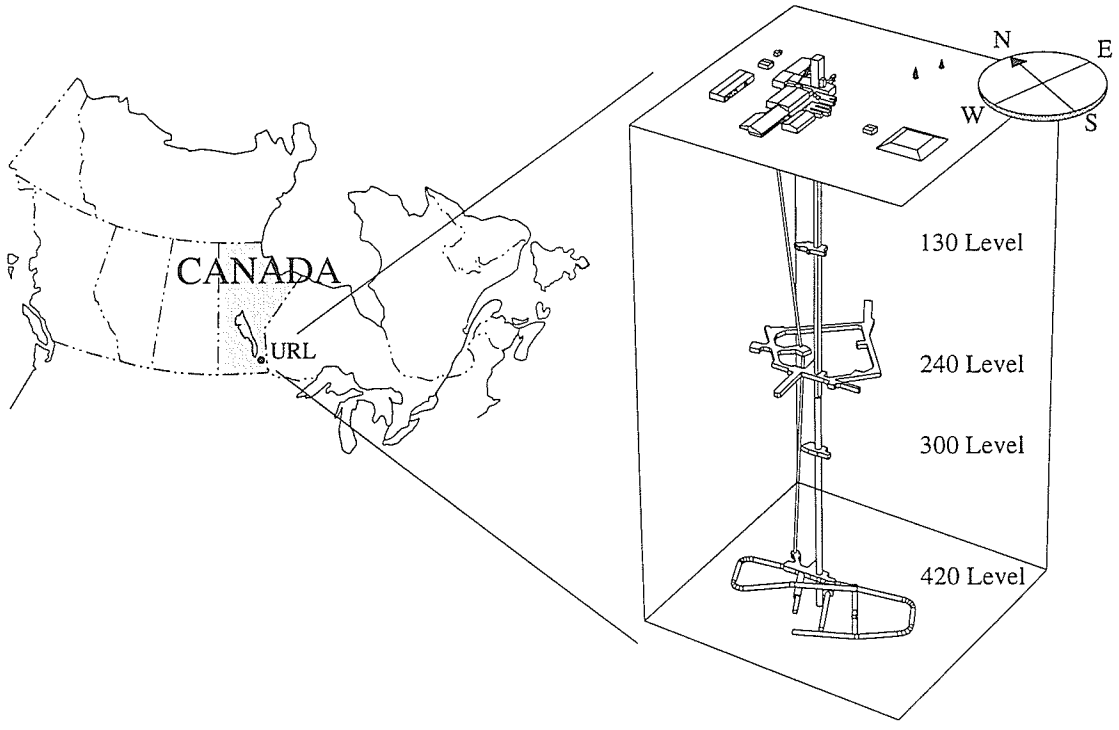

Figure 1.2: Location and arrangement of AECL's Underground Research Laboratory showing the main working levels.

considered in depth in the course of analyzing the experimental data. Results from AECL's Mine-by Experiment are used to identify and quantify the factors influencing the measured displacement field; to compare anterior- and posterior-type displacement measurements; and in combination with numerical modeling, to test the working hypothesis for this thesis.

As part of the Mine-by Experiment, the philosophy adopted for numerical modeling was that a staged approach, ranging from the use of closed-form solutions to three-dimensional damage mechanics models, was necessary to assess the level of complexity required to accurately simulate the *in situ* rock mass behaviour. It was demonstrated that relatively simple models incorporating linear elasticity were illustrative of many aspects of the observed behaviour [154, 125]. The numerical modeling undertaken in this thesis uses both two- and three-dimensional numerical codes, and focuses on elastic material behaviour.

The thesis is arranged in seven chapters. Chapter 1 introduces the topic of displacement interpretation and establishes the working hypothesis and framework for the thesis. Chapter 2 is a review of literature concerning the relationship between excavation-induced displacements around tunnels, far-field *in situ* stresses and the nature of the damage zone, focusing particularly on cylindrical tunnels in brittle rock. Chapter 3 provides background of the field study area, and summarizes the pre-excavation characterization results upon which initial predictions of the *in situ* stress tensor and the excavation-induced displacement response were made. Chapter 4 describes the development of a technique to back analyze *in situ* stresses from radial displacements measured within one diameter of the face of a cylindrical tunnel, and summarizes a series of numerical modeling studies conducted to investigate the effects of face shape and stepped longitudinal geometry on the measured radial displacement response. An interpretative methodology is developed and applied to displacement measurements from the field study in Chapter 5. In this chapter, results from anterior- and posterior-type displacement monitoring instruments are compared, and the *in situ* stress tensor is estimated through incremental analysis of radial displacement measurements from both instrument types. Chapter 6 explores the relationship between

displacement, stress and excavation damage, and presents results of post-excavation characterization of the Mine-by Experiment test tunnel emphasizing the shape and extent of the visible damage zone around the tunnel. Incorporating the visible damage into a numerical model, different material behaviour in the posterior domain is investigated to account for the difference between the predicted linear elastic displacement response and that measured. Finally, Chapter 7 summarizes the interpretation of excavation-induced displacement measurements in terms of the back analysis of *in situ* stresses and characterization of excavation damage in highly stressed brittle rock masses, with specific reference to results from the field study.

Several appendices are included to accommodate data and figures from numerical modeling, mathematical derivations, and results from field monitoring. Only figures and tables required to illustrate pertinent concepts or to support conclusions are included in the body of the thesis. Additional tabular data for some figures are not included but are available from the author.

Chapter 2

Literature Review

Under low to moderate stress conditions, brittle crystalline rocks such as granite are generally assumed to behave like the ideal linear elastic material in their intact, unweathered states. However, under highly stressed conditions in which damage can develop around an underground opening, the interpretation of displacement measurements in terms of *in situ* stresses and material behaviour in the damage zone can be complex. With particular emphasis on cylindrical tunnels in highly stressed brittle rock masses, the literature was reviewed for studies that considered the relationship between excavation-induced displacements around tunnels, far-field *in situ* stresses and nature of the damage zone.

2.1 Displacements around an Idealized Cylindrical Tunnel

2.1.1 Elastic cases without excavation damage

Only a few closed-form solutions exist for displacements and stresses around underground openings in linear elastic, isotropic media. Kirsch [99] first published the solution for stresses around a circular hole in an infinite plate subjected to a uniaxial stress. Mindlin [131] presented an elegant treatment of stresses around a horizontal cylindrical hole in a semi-infinite elastic solid under the action of gravity. Terzaghi and Richart [181] considered stresses around openings of different shape including spheroidal cavities, and summarized the major contributions on stress redistribution around discontinuities in stressed elastic media.

Of the more recent rock mechanics publications, Goodman [59] provides the equations for stresses and displacements around a circular opening in a useful form, whereas those presented in the first edition of Brady and Brown [8] are incorrect. Based on the general solutions, Leeman [117], Hiramatsu and Oka [74] and others developed techniques to back calculate far-field *in situ* stresses from tunnel (or borehole) wall displacements induced by stress relief methods. When applied to single tunnels, these techniques provide an estimate of the stress components in the plane orthogonal to the tunnel axis. The maximum and minimum stresses in this plane correspond to principal stresses only if the tunnel axis is parallel to a principal stress direction.

The analytical solutions for the circular tunnel relating excavation-induced displacements and far-field *in situ* stresses implicitly assume plane strain conditions at the measurement point both before and after stress relief. In practice, displacement measurements taken from within tunnels violate this assumption. Heuzé [72] wrote:

> *The fact is that all deformations measured inside rock masses are residual in nature. No matter how close to the openings or how soon the instrument or station was emplaced, some deformation has already taken place that could not be measured. If absolute deformations as well as absolute stresses are needed to compare model predictions to prototype reactions, one will have to infer the absolute deformations from the residual ones measured.*

Field studies designed to measure the total excavation-induced displacement response [40, 119, 42, 100, 78], including that portion occurring ahead of the advancing face, have generally been inconclusive owing to inhomogeneity of the rock mass.

To further complicate the interpretation of measured displacements, deviations from linear elasticity can result in stress and displacement patterns significantly different from those predicted by isotropic elasticity. Kawamoto [94], for example, considered the state of stress and deformation around a tunnel in orthotropic elastic ground. He found that

orthotropy resulting from stratification, structure, mineral differences, or discontinuities, had a marked effect on displacement patterns, illustrating that characterization of the rock mass is an important precursor to interpretation of displacement measurements. The effect of non-linearity was considered by Santarelli et al. [169] and Santarelli and Brown [168], who explained anomalously high strength around boreholes in hydrostatically loaded sandstone samples using a radial-stress-dependent elastic modulus. Ewy and Cook [48, 49] showed that an analytical solution with the elastic modulus dependent on radial distance gave a better representation of observed non-linear behaviour. Several other authors [37, 162, 31] have developed equations describing non-linear stress-strain relationships which can be extended to cover the case of a pressure- or mean stress-dependent modulus. In each of these cases, the effect of non-linearity is to reduce the elastic modulus near the opening, resulting in a decrease in stress concentrations, and an increase in radial displacement, at the tunnel (or borehole) wall.

Recognizing the limitations of analytical solutions for infinitely long circular tunnels, and the fact that a closed-form solution for stresses and displacements near the face of a cylindrical tunnel does not exist, attention focused on relating residual or posterior displacement and strain measurements to *in situ* stresses through physical and numerical model studies. Galle and Wilhoit [56] used a photoelastic technique to measure stresses around a borehole, and showed that, through superposition of results from various loading configurations, any combination of geostatic stresses could be considered. Hoskins [79] conducted full-scale laboratory tests using doorstopper stress measurements. Stress concentration factors at various points on the tunnel face were also investigated using numerical models [19, 76]. In an attempt to improve the doorstopper technique, Hoskins [80] and later van Heerden [185] conducted tests with flat and hemispherically-ended boreholes to determine if a non-planar face was effective in reducing stress concentrations and potential fracture zones near measurement gauges. Sugawara and Obara [175] and Kobayashi et al. [101] also considered the hemispherically-ended borehole. The borehole deepening method of stress measurement,

studied by de la Cruz and Goodman [30], used the finite element method to relate the residual deformation close to the bottom of the borehole to the initial stresses and elastic constants. These techniques have proven satisfactory in conditions where the rock mass around the tunnel or borehole can be considered an isotropic, linear elastic continuum, but are susceptible to misinterpretation if stresses are high enough to cause non-elastic behaviour near the measurement gauges.

Other numerical modeling studies were conducted to determine the effects of various factors on the excavation-induced displacement response. Kulhawy [103, 104, 105] used a two-dimensional finite element model to look at the effects of E, ν, gravity, initial stress magnitude and orientation, opening shape, and non-linear stress-dependent material properties in continuous and discontinuous media. His studies highlighted the fact that, even under ideal conditions, the displacement response can be complicated by tunnel geometry and material properties. Niwa et al. [135] used the integral equation method to examine the effects of individual unit stress components on the displacement field around a cylindrical tunnel. However, the use of quarter symmetry in the three-dimensional model misrepresented the effects of antiplane components of the stress tensor. The study did, however, demonstrate that the relationship between far-field *in situ* stresses and displacements can be complex near the tunnel face.

2.1.2 Cases involving plastic zone development

In conjunction with the observational approach, e.g., Rabcewicz [153], prediction of tunnel convergence is an integral part of the characteristic line method described originally by Fenner [52], and later improved by such workers as Morrison and Coates [132]. Although the focus of this thesis is not tunnel supports per se, the many efforts to predict convergence for support design are relevant because they consider the effects of different material behaviour near the tunnel wall on the radial displacement response. A detailed review of the characteristic line method is given in Hoek and Brown [78].

As described by Brown et al. [12], the stresses and displacements in the rock surrounding a tunnel and in the tunnel support system depend on the rock mass properties, the *in situ* stresses, the type and stiffness of the support system, and the timing of its installation. The interaction of these various elements can be represented on a ground-support interaction diagram (Figure 2.1) by a characteristic line and a support reaction line. The characteristic line represents the relationship between tunnel convergence and support pressure. The choice of rock mass failure criteria, stress-strain model, and treatment of plastic volumetric strains markedly affects the extent and dilational characteristics of the plastic zone, and, consequently, the characteristic line and maximum radial displacement. According to Duddeck [36], prediction of the characteristic line analytically is restricted to one-dimension, i.e., the axisymmetric case (Figure 2.1). This limitation implies a circular cross section; plane strain; hydrostatic *in situ* stresses; a homogeneous, isotropic continuum; uniform radial support pressure; and a uniformly thick plastic zone. Derivation of the equations describing the characteristic line for a typical axisymmetric case, assuming an elastic-perfectly plastic material governed by the Hoek-Brown failure criterion, is demonstrated in Hoek and Brown [78]. Brown et al. [12] summarized other solutions up to 1983 (Appendix A).

Most solutions to the axisymmetric tunnel problem have used the Mohr-Coulomb failure criterion. However, uses of Fairhurst's non-linear criterion based on Griffith crack theory [107], Mohr-Coulomb based on long-term strength parameters [107], piece-wise linear approximations to non-linear Mohr envelopes [98, 102], and the Hoek-Brown failure criterion [12] have also been documented. More recently, Panet and Guenot [147] used a von Mises and a Drucker criterion for different materials. Likewise, the use of elastic-plastic or elastic-brittle-plastic stress-strain relationships was prevalent in most studies, although strain-softening behaviour of the rock mass, represented by a trilinear stress-strain law, has also been considered [39, 40, 134, 144].

Plastic volumetric strains have been represented in a number of ways. Most of the

earlier solutions assumed that the rock in the plastic zone would deform at a constant volume [52, 93, 132, 9]. The concept of an average plastic dilation in the rock mass, introduced by Labasse [106], was used by several other authors [28, 1, 121, 122], but Ladanyi [107] showed that plastic dilation varies with radius and location within the plastic zone. Parameters defining the post-peak volumetric strain have been determined directly for intact rock material [25, 38, 108], but other authors have used the associated flow rule to estimate them [167, 107, 54, 78]. Schwartz and Einstein [170] used a non-associated flow rule to simulate zero total volume change in the yielded zone.

Characteristics of the plastic zone have also been treated differently by various authors.

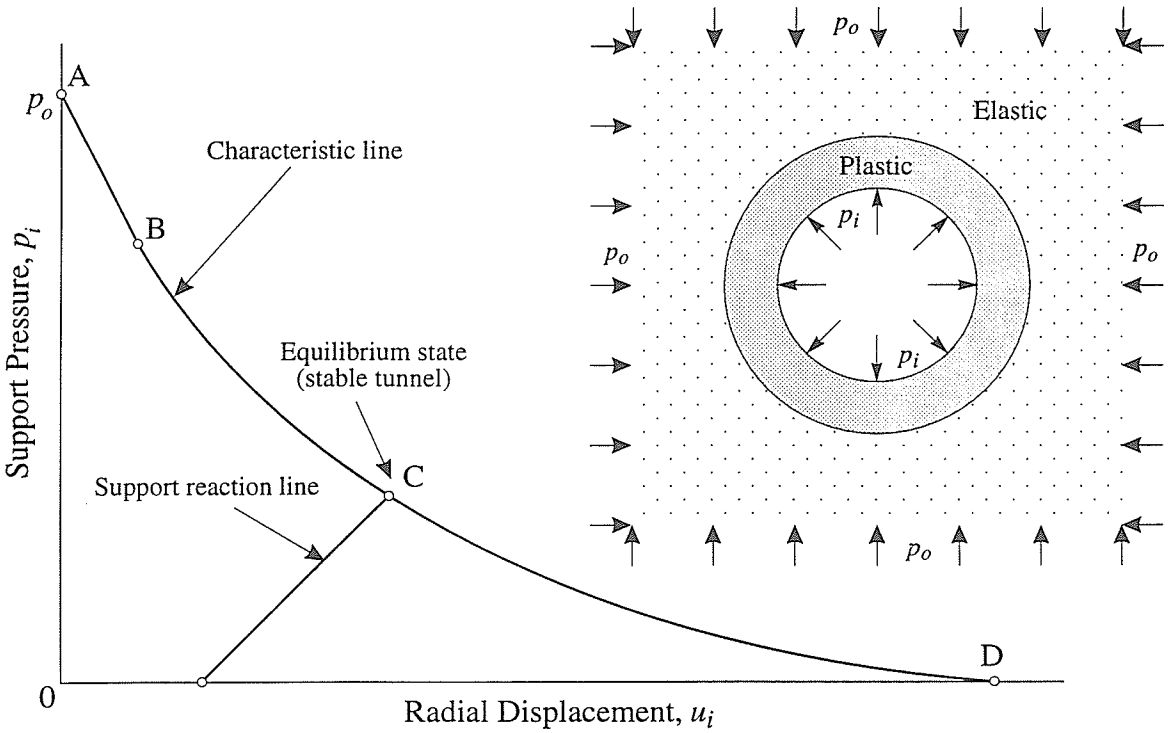

Figure 2.1: Typical ground-support interaction diagram showing the characteristic line for an axisymmetric tunnel in an elastic-perfectly plastic medium governed by the Hoek-Brown failure criterion. Reference points on the characteristic line are: (A) far-field hydrostatic stress, (B) transition from elastic to plastic response, (C) equilibrium state, and (D) maximum convergence for the unsupported case. The axisymmetric tunnel problem is illustrated in the upper right diagram.

Lombardi [122] showed that variations in cohesion and friction angle within the plastic zone could be represented by annular regions with different characteristic lines. Florence and Schwer [54] demonstrated that three different plastic zones could develop around a tunnel under axisymmetric load depending on the values of Poisson's ratio and the friction angle. Other authors [67, 75, 84] have postulated solutions based on different values of the elastic constants in the elastic and plastic zones. Kaiser [83] concluded that tunnel wall displacements were affected by the history-dependent post-peak behaviour of the rock mass, and that the extent and shape of the plastic zone were rate-dependent and could vary within a wide range.

There have also been many recent publications concerning the visco-elastic axisymmetric tunnel problem. Sulem et al. [176], for example, developed an analytical solution assuming a linear creep law, constant volume creep, a Mohr-Coulomb failure criterion, and constant volume plastic strain. Others [172, 141] have formulated the visco-elastic equations for various rheological models from Laplace transformation of the elastic plane strain solution for displacements around a circular tunnel.

While the large number of solutions to the axisymmetric tunnel problem is impressive, the basic assumption of a hydrostatic stress field limits the usefulness of these solutions for most *in situ* conditions. In addition, because *in situ* material behaviour may differ from that observed in laboratory samples, the determination of failure criteria and post-peak material behaviour is not straightforward. In most cases, it is possible to use several different models to match an observed displacement response. However, unless the model reflects the actual physics of the observed behaviour around the tunnel, it is of limited use in characterizing the behaviour in the plastic zone. In emphasizing this point, Gesta et al. [57] stated that *in situ* measurements could only be satisfactorily interpreted within the framework of a correct mechanical model.

To overcome the limitation of hydrostatic stress conditions in the axisymmetric tunnel problem, Detournay and Fairhurst [32] considered non-hydrostatic loading using a linear elastic, perfectly plastic isotropic material characterized by a cohesive-frictional yield strength and by dilatant behaviour during yield. The yield function and non-associated plastic potential were represented by Mohr-Coulomb criteria, and excavation was simulated by monotonically decreasing the internal pressure in the tunnel. The authors found that the obliquity m, defined as the ratio of the far-field stress deviator to the yield limit, was important in defining deviation from hydrostatic conditions, and in particular, controlled the shape of the failed zone, the ellipticity of the cavity caused by non-uniform closure, and static determinacy. Based on this work, Detournay and St. John [33] developed design charts to predict the size and shape of the failed rock regions and induced closure for cases of non-uniform *in situ* stress fields. In related work, Pan and Chen [143] considered displacement behaviour and plastic-zone development around tunnels of different cross-section under plane strain conditions, and developed families of characteristic lines for various non-hydrostatic *in situ* stress conditions.

Although solutions to the axisymmetric tunnel problem predict radial displacement at the tunnel wall under different internal radial pressures, Lombardi [122] and Eisenstein et al. [41] pointed out that the two-dimensional nature of the solutions precludes consideration of the complex stress redistribution associated with the advancing face of the tunnel. To overcome this limitation, several extensions to the plane strain solution were proposed. Pan and Hudson [140] applied a correction function to results from the plane strain analysis to approximate the three-dimensional case. Gesta et al. [57] cited examples that used a fictitious radial support pressure to account for the support provided by the face. Using this approach, Panet and Guellec [146] found that results from locations further than one-half the tunnel radius from the face compared favourably with those from a three-dimensional analysis. Schwartz and Einstein [170] demonstrated the "core modulus reduction" scheme to account for the face effects in a similar manner. Amberg and Lombardi [1] used body

forces directed outwards into the rock mass. The use of a fictitious radial support pressure, or other "internal" boundary condition, however, improperly represents *in situ* conditions because, although the deviatoric stresses near the tunnel wall are preserved, the confining stresses at which they act are not. Consequently, the ability to predict material instability at the tunnel wall with any of the accepted failure criteria is adversely affected.

Perhaps the most significant advancement to the characteristic line method was made by Panet and Guenot [147], who developed equations relating wall convergence to the position of the advancing tunnel face. Based on finite element model studies for different materials and earlier work by Panet [145], the tunnel convergence function was given by

$$C_1(x) = C_\infty \left[1 - \left(\frac{1}{1 + \frac{x}{0.84 r_p}}\right)^2\right] \tag{2.1}$$

where $C_1(x)$ is the convergence at distance x from the tunnel face, C_∞ is the convergence far from the face, and r_p is the plastic radius.

Equation 2.1 agreed well with the modeling results in the region further than one-half radius from the tunnel face. For non-viscous ground, the authors showed that measurement of convergence or convergence rate at two points was sufficient to determine the plastic radius and the final convergence. In ground with time-dependent properties, the authors suggested that the equation for convergence is a function of both distance from the face and time. Using the Fréjus and Las-Planas tunnels as case studies, Guenot et al. [61] further modified the equation describing convergence to

$$C(x,t) = C_1(x)\left\{1 + m\left[1 - \left(\frac{T}{t+T}\right)^n\right]\right\} \tag{2.2}$$

where $C_1(x)$ is given by Equation 2.1, and T is the relaxation time of the rheological model. The curve-fit parameters m and n were found to be independent of the tunnel lining stiffness. Application of the method was described in more detail in Sulem et al. [177].

The analytical solution presented in Equation 2.2 is appealing in that the relationship between displacement and support pressure is implicit in the plastic radius parameter in

the denominator, the relationship is independent of material type, and the equation parameters have physical meaning and therefore can be verified *in situ*. However, the underlying assumptions in applying the equation, i.e., that the tunnel is of circular cross-section (not true of the Fréjus or Las Planas tunnels) and that the initial stresses in the ground are hydrostatic, limit the applicability of the approach. In addition, the relatively poor fit between measured and predicted data within one-half radius of the face brings into question the choice of function used to represent the time-independent displacement response.

Barlow [4] and Barlow and Kaiser [5] extended the solution to account for the effects of support/ground interaction, and for tunnel excavation sequence (e.g., heading and bench) by describing the anterior and posterior domains with different displacement functions. The tunnel convergence in the anterior domain was given as

$$C(x,t) = Q_1 \left[\frac{1}{1 + \left(\frac{x_f - x}{0.84 r_p} \right)} \right]^{1.2} [C_{x\infty} + AC_2(t)] \tag{2.3}$$

where Q_1 is the proportion of the total stress change associated with excavation that occurs ahead of the face, x_f is the value of x at the tunnel face, r_p is the plastic radius, $C_{x\infty}$ is the ultimate time-independent tunnel convergence, A is the ultimate time-dependent convergence, and $C_2(t)$ is the time-dependent convergence distribution given by Equation 2.2. For the posterior domain, the convergence function was given as

$$C(x,t) = [Q_1 + Q_2 C_1(x)][C_{x\infty} + AC_2(t)] \tag{2.4}$$

where Q_2 is the proportion of the total stress change associated with excavation that occurs after the face, and $C_1(x)$ is given by Equation 2.1. This work suggests that construction methods/sequences and tunnel support could influence the measured convergence, particularly if the ground response has a large time-dependent component. It also shows that the convergence response is best described by a piece-wise continuous function.

Extensive numerical model studies have been conducted to consider factors related to rheological behaviour, and their impact on the excavation-induced displacement response.

Many authors [58, 164, 142] have found that the advance rate of the tunnel and the timing of the lining installation are important factors in squeezing or swelling ground where time-dependent behaviour is a concern. Panet [145] developed an empirical relationship for time-dependent tunnel convergence to account for these and other effects. Based on published data, Kaiser and Morgenstern [87] developed a phenomenological three component model to explain their observation that the strength of rock consists of a time-dependent and time-independent resistance to deformation. Field studies where rheological models have been applied have generally involved weak or fractured rock, e.g., [121, 138, 61, 189], and have been largely phenomenological in nature. Lombardi [121] stressed that the actual cause of the rheologic behaviour in the rock mass, e.g., true viscous behaviour or progressive failure, was of subordinate importance in support design. However, in characterizing the excavation-induced damage zone, the cause of the observed behaviour is the important issue, and therefore phenomenological models are of limited use in this regard.

Findings from other three-dimensional parametric studies of stresses and displacements around underground openings are also applicable to displacement interpretation in hard brittle rock. Hanafy and Emery [64, 65] evaluated the effects of stress ratios on tunnel wall convergence in squeezing ground using a rheological axisymmetric finite element model with non-axisymmetric loading represented by Fourier series. Results of the study showed that radial displacement increased with increasing longitudinal stress ratio (i.e., ratio of axial to vertical stress), decreased in the crown and increased at the springline with increasing transverse stress ratio (i.e., ratio of lateral to vertical stress), decreased with increasing advancement rate, and increased with increasing time delays.

Pelli [148] and Pelli et al. [149] used a three-dimensional finite element model, with non-associated flow plasticity and incremental excavation, to investigate the effects of the virgin stress field (for stress ratios $K \leq 2$), zero reading delay, rock mass anisotropy, non-linear ground behaviour, and tunnel support on convergence and extensometer readings. They found that zero reading delay significantly impacted the amount of displacement missed

by posterior-type instruments, and that high values of the axial stress component, i.e., the normal antiplane component of the stress tensor, affected the displacement patterns significantly. They further showed that plots of radial displacement versus radial distance and versus excavation advance could be used to estimate the elastic modulus near the tunnel, and identify zones of non-linearity. Application of the findings to the Donkin-Morien tunnel in Nova Scotia [150] illustrated the problems introduced in displacement interpretation by a poorly-defined stress state, heterogeneity of the rock mass and inadequate instrumentation.

2.1.3 Cases involving brittle failure

Numerous laboratory studies have been conducted to simulate the behaviour observed around tunnels, and have generally used materials with pre-drilled holes to represent typical underground openings [125]. Kaiser and Morgenstern [88, 89, 90] performed a particularly illustrative study of displacements using continuously datalogged extensometers and convergence arrays to examine the deformation of small tunnels in weak or jointed, brittle rock represented by a large block of coal. They found that local geological features affected the final pattern of convergence, and that global or local softening near the opening, rather than strain weakening behaviour, could account for displacements in excess of linear elastic predictions. Results from this study also showed that, for orthotropic compressible material like coal, convergence measurements reflect the global response of the rock mass and the general stress redistribution caused by the development of local yield or fracture zones, whereas extensometer measurements provide a much more detailed local record of deformation. Similar conclusions were reported for a tunnel in fractured dolerite [195]. Kaiser et al. [86] concluded that analytical solutions cannot be used to predict behaviour if rupture occurs.

Many numerical modeling studies of damage zone development have been conducted, but have generally not been related to displacement interpretation. Barla [3] used an iterative two-dimensional finite element approach to analyze stresses in brittle rock. Kelsall

et al. [97] developed an equivalent porous medium based on stress-hydraulic conductivity relationships obtained in the laboratory to study damage development. Zheng et al. [196] used an iterative elastic two-dimensional finite element model to demonstrate that, by simulating progressive failure through element removal, the final stable shape of a borehole breakout could be determined. Borehole breakouts and their formation were also considered by other authors, e.g., [63, 197, 139]. Most of these studies, while claiming the ability to predict the final breakout geometry, do not attempt to match observed processes involved in the development of progressive failure. Kaiser [83] emphasized that deformation processes in model predictions must be compared with *in situ* processes to validate numerical models. Recent work by Read [154] and Martin [125] suggests that, in order to properly capture the development of progressive failure, the three-dimensional effects caused by the advancing face of the tunnel must be taken into consideration.

2.2 Field Studies of Excavation-Induced Displacements

2.2.1 Deep hard rock mining experience in South Africa

The control of displacements to limit instability was a prevalent theme in many of the early publications regarding South African mining practices, and the problems faced in brittle quartzite at great depth. In considering rockbursts, Cook [20] and others [22, 165] concluded that behaviour around underground excavations in hard rock is largely elastic, except near the opening where the rock is generally fractured. Using an elastic analysis technique based on Muskhelishvili [133], Ortlepp and Cook [137] predicted displacements around longwall excavations by measuring E and ν from small laboratory samples, and by assuming a lithostatic vertical stress component and horizontal to vertical stress ratio between $\frac{1}{3}$ and $\frac{1}{2}$. Hoek and Brown [78] pointed out that this was a common assumption in the 1950's and early 1960's. *In situ* monitoring was carried out using stainless steel links, and crude wire extensometers, and it was concluded that two-dimensional elastic models were adequate to predict displacements around deep hard rock excavations, albeit, at some

distance from the tunnel wall. Ryder and Officer [163], using an extension of the theory for an inclined excavation [166], reached the same conclusion.

Even in hard brittle rock, displacements were found to be fairly complex in nature. Field work by Walsh [188, 187] showed that deformation around deep hard rock excavations occurs in two parts, the first immediately after blasting, and the second gradually within a day. It was also noted that convergence near the working face was generally larger than predicted due to cracking where shear stresses were sufficiently high to cause slip. Atkins and Keen [2] described displacements about excavations in a typical South African gold mine as a complicated interaction of elastic deformation, sliding on parting and shear planes, extensional movement due to bed separation, and displacement due to dilation associated with extensive fracturing ahead of the advancing face. They measured displacements normal to the direction of mining ahead of the advancing face by installing extensometers from an adjacent opening, and found that much of the deformation occurred coseismically. They further noted that discontinuities could effect excessive "ride" displacement, and that *in situ* and laboratory-derived material properties for fractured rock masses could differ significantly.

Pierce and Ryder [151] described a two-dimensional plane strain boundary element technique capable of incorporating inelastic behaviour to account for the skin of fractured material surrounding deep-level excavations. They modeled a case history of fracture development around a square opening, and showed that the resulting fracture zone significantly exceeded that predicted by simple linear elastic theory, in keeping with field observations.

The South African hard rock mining experience is significant with regards to this thesis in several ways. First, in highly stressed brittle rock, the rock mass was shown to behave essentially in a linear elastic fashion, with the exception of zones close to the excavation which were fractured as a result of stress concentration. Second, the experience with instrumentation and analytical tools has shown that, with a prudent choice of instruments, installation locations and numerical modeling techniques, the understanding of material

behaviour can be improved. Third, problems in determining the *in situ* stress tensor and representative material properties increase the uncertainty in the interpretation of near-field behaviour. Stress conditions, particularly at depth in hard rock, are generally not hydrostatic [11, 68, 69, 71], and can vary significantly from the assumed condition of a horizontal to vertical stress ratio between $\frac{1}{3}$ and $\frac{1}{2}$. Finally, in an environment with a lithostatic stress of 70 MPa, the tabular shape of openings in South African mines can create stress concentrations in confined areas near the face in the order of 900 MPa [20]. These stress magnitudes are well beyond the realm of those in rock considered highly stressed in this thesis, and, consequently, the South African experience must be considered in this light.

2.2.2 Climax Spent Fuel test

Heuzé et al. [73] described an excavation response experiment conducted at 420-m depth in the Climax granite pluton in Nevada. The experiment comprised two parallel drifts from which two arrays of extensometers and vibrating wire stressmeters were installed. A central horse-shoe-shaped drift was excavated between, and parallel to, the instrumentation drifts in heading-and-bench fashion using a drill-and-blast method. The rock mass comprised quartz monzonite and granodiorite, with a number of shear zones intersecting the tunnels, and three near orthogonal joint sets. Results from finite element modeling of the excavation sequence, using a laboratory-determined elastic modulus and ignoring the discontinuities, showed poor agreement with the measured response. Consequently, a detailed site characterization program was undertaken to establish better estimates of material properties and *in situ* stresses. Assuming that the rock mass was initially unstressed, calculation of Poisson's ratio was based on the relative magnitudes of the vertical and horizontal stresses. Results from a second finite element simulation, using a Mohr-Coulomb failure criterion based on published data for the strength of granite, and incorporating joint elements to represent discontinuities, showed better agreement with measured results.

The Climax experiment has many similarities to AECL's Mine-by Experiment. Both

experiments are in granitic plutons at 420-m depth, similar instrumentation was used, and the experiment arrangements are similar. The main difference between the experiments is the complexity of the rock mass and the resulting difficulties in characterization, monitoring, and back analysis. The Climax test demonstrated that discontinuities and a relatively poorly characterized rock mass complicate the back analysis of material behaviour. It also showed that it is difficult to characterize a fractured rock mass, and that numerical models must include key elements, e.g., discontinuities, blast damage, or strain-softening, that govern the rock mass behaviour. However, the level of complexity in the numerical model in this case outweighed the level of understanding of the rock mass characteristics.

2.2.3 Colorado School of Mines test

The Colorado School of Mines (CSM) test was conducted approximately 100 m below surface in fractured granitic gneiss near Idaho Springs, Colorado, to study the development, and means of characterizing, excavation-induced damage. As part of the instrumentation, posterior extensometers were installed to monitor displacements as the tunnel was advanced using a carefully-designed drill-and-blast technique. Following excavation, characterization of the damage zone, created by a combination of stress redistribution and blasting effects, was conducted using a variety of techniques. The excavation damage zone was found to extend between 0.5 and 1.0 m into the rock mass. An important finding from this study was that the posterior extensometers provided very little information because the majority of the rock mass response occurred ahead of the face, prior to installation of the instruments.

2.2.4 Geomechanics studies at the URL

During the construction phase of the URL, a series of multi-anchor extensometers and convergence arrays were installed to monitor the excavation-induced displacement response in the URL shaft, and at the 240 and 420-m Levels. In each of these studies, displacements measured by the extensometers and convergence arrays were posterior in nature, and

therefore subject to the same problem as other posterior-type measurements. A detailed summary of the studies is given in Read and Martin [157].

Instrument arrays were installed during excavation of the rectangular (upper) shaft at 15-, 62-, 185-, and 218-m depth in fractured granite containing three near-orthogonal joint sets [116]. The results of this initial study showed that the mechanical response of the rock near the shaft wall was quite variable and was controlled to a large extent by subvertical joints [171]. Numerical models based on linear elastic continuum behaviour did not predict the mechanical response very well near the excavation boundary, but showed better agreement 1.5 m and further from the shaft wall. A discontinuum approach was more successful in modeling the fractured rock mass response [171], although the rectangular geometry of the shaft complicated the analysis. Chan et al. [15] showed that, in order to match the measured response in the 15-m Array, an elastic modulus increasing linearly from about 10 to 40 GPa over 1.5 m near the opening was required.

An excavation response experiment was conducted in Room 209 at the 240 Level in 1986 [115]. This experiment was designed around a 3.5-m-wide horseshoe-shaped tunnel excavated through a near-vertical water-bearing fracture oriented almost perpendicular to the tunnel axis. Three different groups performed numerical model predictions of the excavation-induced response. Kaiser et al. [85] found that predicted displacements and stress changes agreed reasonably well with the measured response using an elastic modulus of 50 GPa for the rock mass. However, better agreement was achieved in the back analysis if the damage around the excavation was simulated by zones of different moduli. Chan et al. [14] showed that the modulus next to the opening could be as low as 10 GPa, but that one diameter from the opening it was about 60 GPa, similar to that obtained on intact laboratory samples.

Instrument arrays were installed at 324-, and 384-m depth in the circular (lower) shaft in massive, unjointed granite [128, 130]. Displacement results generally showed that the rock mass behaves as a linear elastic, isotropic continuum except for a small region near

the shaft wall (Figure 2.2). Convergence measurements were also carried out at twenty-six instrumented arrays in the lower shaft during excavation [128] using an ISETH distometer [183]. It was assumed, based on results from one anterior extensometer in the Room 209 experiment, that only 40% of the total displacement response was recorded by the posterior convergence measurements. Back analysis of *in situ* stresses from measured displacements gave consistently higher results than from other methods, suggesting that the various factors affecting near-field displacements around the shaft were not properly considered in the initial interpretation and back analysis. In particular, the face shape deviated significantly from the assumed planar condition.

The rock mass response was monitored during the excavation of the 420 Level station and access tunnels using seven convergence arrays. Results from preliminary analysis of three of these arrays demonstrated that an analytical approach was not appropriate for a non-circular tunnel with a damage zone in an anisotropic stress field. Given the lack of an

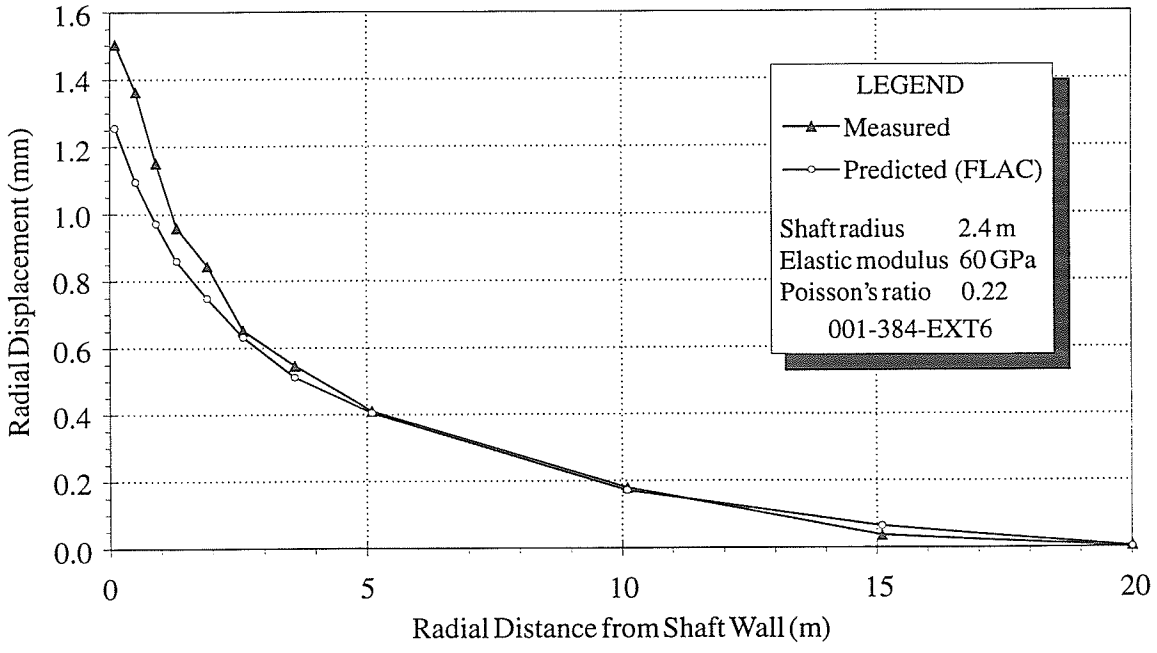

Figure 2.2: Comparison of measured and predicted displacements at the 384 Array. Note that the measured response exceeds the predicted response near the shaft wall.

alternative approach, no further analysis was attempted for these arrays.

2.3 Summary

The review of the literature considered the relationship between excavation-induced displacements, *in situ* stresses and the nature of the damage zone, and identified several deficient areas that are addressed by this thesis.

In purely elastic conditions, techniques to back analyze *in situ* stresses from displacement measurements rely on the plane strain solution for an infinitely long circular tunnel. This solution, however, requires an estimate of absolute displacements from the residual ones measured, and produces an estimate of only the stresses acting in the plane orthogonal to the tunnel axis. The determination of absolute displacements is complicated by zero reading delay in posterior instruments, and the effect of the axial stress component on the radial displacement response. In conditions where rupture occurs, closed form solutions cannot be used to back calculate *in situ* stresses. Methods that use measured strains to calculate stresses through relationships based on linear elasticity are also susceptible to problems associated with anisotropy, non-linearity and non-elastic behaviour near the measurement gauges. This thesis describes the development and implementation of a technique to back analyze the complete *in situ* stress tensor from a single arbitrarily-oriented cylindrical tunnel using the radial displacement response measured within one diameter of the tunnel face. The technique is particularly useful in ground showing excavation damage in the posterior domain.

By far the most work with regards to material behaviour around underground openings has focused on the axisymmetric tunnel problem, primarily for the purpose of tunnel support design. However, the underlying assumption of a hydrostatic stress field, and the two-dimensional nature of the problem, preclude the application of the analytical solutions under most *in situ* conditions. The work by Detournay and Fairhurst [32] in the case of non-hydrostatic loading, and Panet and Guenot [147] in accounting for the effect of

the tunnel face, represent important advances in the applicability of such solutions to real situations. Nevertheless, both of these solutions are subject to one or more of the limitations of the axisymmetric tunnel problem. A functional relationship between face position and the radial displacement response for the case of non-hydrostatic stress conditions has not been reported in the literature, and, with the exception of hemispherically-shaped tunnel faces, the effect of a non-planar tunnel face on the displacement response has not been considered. This thesis presents general approximating functions to describe the relationship between radial displacement and tunnel face position (i.e., the *spliced logistic function*), and between radial displacement and radial distance from the tunnel centre. These relationships are, in turn, used to develop parametric functions describing the *characteristic radial displacement surfaces* associated with components of a partitioned unit stress tensor.

Numerical modeling studies related to excavation-induced displacements have been, for the most part, phenomenological in nature, and incorporate a large number of parameters. Simple linear elastic models have been more successful in illustrating important aspects related to the development of excavation damage. In addition, previous parametric studies have considered the effects of material properties, constitutive behaviour, tunnel geometry and stress ratios up to $K = 2$ for tunnels oriented parallel to a principal stress direction, i.e., no antiplane shear stresses [53]. The effect of antiplane shear stresses on displacements around underground openings has not been widely considered. This thesis uses relatively simple two- and three-dimensional numerical models to assess the relationship between components of a partitioned unit stress tensor, including the antiplane stress components, and the displacement response around a cylindrical tunnel. The material behaviour around a tunnel in highly stressed rock is also investigated, and the effects of face shape and longitudinal geometry are considered up to stress ratios of $K = 4$.

The laboratory studies by Kaiser and Morgenstern [88, 89, 90] suggest that displacement

measurements can be used to determine the nature of excavation damage, and that convergence arrays and extensometers compliment one another in this regard. However, an understanding of the characteristics and boundary conditions of the rock mass is an essential precursor to the interpretation of material behaviour. Many case studies of excavation-induced displacements around tunnels have considered weak or fractured rock, where displacements are large, and the failure zone around the tunnel is extensive. In these conditions, characteristics of the rock mass and boundary conditions are often poorly understood. Other field studies in highly stressed brittle rock have shown that the rock mass behaves essentially elastically, except for zones near the opening which show non-linear or non-elastic behaviour. In addition, *in situ* monitoring around tunnels often suffers from inadequate instrumentation and, with the exception of a few studies conducted with extensometers installed ahead of the advancing face, most studies have used posterior-type measurements. This thesis considers a well-characterized, homogeneous, unjointed granitic rock mass, with well-defined material properties, in which displacements are small, and large-scale failure around the tunnel is limited to localized areas of high stress concentrations. The field study incorporates state-of-the-art anterior- and posterior-type instruments around a cylindrical tunnel excavated using a non-explosive technique, thus permitting direct comparison of the results from the two instrument types without the added complication of blast-induced damage.

Chapter 3

Geotechnical Aspects of the Field Study

The Mine-by Experiment arrangement was based, in part, on *in situ* characterization of the URL shaft and 420 Level station conducted prior to extensive development of the 420 Level. The geotechnical aspects of the field investigation and subsequent laboratory testing include geology, *in situ* stress conditions and rock properties. As background for the field study, the results from the initial characterization phase, and a synopsis of the experiment arrangement including elements of construction, instrumentation and monitoring associated with the Mine-by Experiment, are summarized.

3.1 AECL's Underground Research Laboratory

3.1.1 Excavation sequence

The underground workings at the URL consist of a shaft, ventilation raise, small shaft stations at 130- and 300-m depth, and major developments at the 240 and 420 Levels. The URL shaft was constructed in two stages. The upper shaft (Stage 1) was excavated from the surface to a depth of 255 m between March 1983 and April 1985 as a nominal 2.8- by 4.9-m-rectangular shaft by the traditional drill-and-blast benching method. Benches were drilled 1.5 m, giving an average 0.75 m advance for each blast. Timber sets spaced 2.5 m were installed to within 15 m of the face during sinking. Development of the 240

Level, using several drill-and-blast variations, followed completion of the upper shaft. The lower shaft (Stage 2) was excavated as a 4.6-m-diameter circular shaft between July 1987 and November 1988 using a full-face drill-and-blast technique. Each blast round used a specially-designed blast pattern with a central burn cut to minimize shaft wall damage. The rounds ranged from 1.0 to 3.4 m in length. Following completion of the lower shaft, the 420 Level was developed for use in several Operating Phase experiments [173], including the Mine-by Experiment.

3.1.2 Geology

The URL is located in the Lac du Bonnet batholith, which is considered to be typical of many granitic intrusions of the Precambrian Canadian Shield [29]. The batholith is an elongated body about 75 by 25 km in surface area and about 10 km in depth, and has an ENE-WSW trend. It lies in the Winnipeg River plutonic complex of the western Superior Province, and has been dated as Late Kenoran in age (2680 ± 81 Ma).

The geology of the URL has been characterized from detailed logging of drill-core from boreholes, and geological mapping of surface and subsurface exposures. From these investigations, it has been concluded that, near the URL, the batholith is made up of five main rock units: the pink (altered) or grey (unaltered) granite groundmass of the batholith, xenolithic inclusions of various compositions, leucocratic granitic segregations, and subvertical granodiorite and pegmatite dykes. This classification scheme is based primarily on age relationships between the various rock units [43].

During excavation of the URL shaft, two major thrust faults (Fracture Zones 3 and 2) and their associated splays (Fracture Zones 2.5 and 1.9) were intersected (Figure 3.1). These faults dip to the southeast at between 20 and 30° and typically contain low-dipping fractures, secondary alteration products such as clay, hematite and chlorite, zones of cataclasite, gouge and rubble, and regions of moderate-to-high groundwater flows.

Above Fracture Zone 2.5, the rock mass comprises mainly pink granite. In this region,

two subvertical joint sets have been identified: a prominent set striking about 020 to 040° , and a less prominent, intermittent set striking about 150 to 180°. Below Fracture Zone 2.5, the rock mass is essentially unfractured, with the exception of Fracture Zone 2 and its associated splays 1.9 and 1.5.

According to Everitt et al. [47], the rock mass at the 420 Level is composed of three major litho-structural domains: a gneissic grey granite, a leucocratic granite, and a xenolithic-leucocratic granite. A major subvertical granodiorite dyke swarm, approximately 100 m thick and striking NNW, crosscuts these domains and is present throughout the 420 Level. From earlier work by Brown et al. [10] at the other levels at the URL, the granodiorite

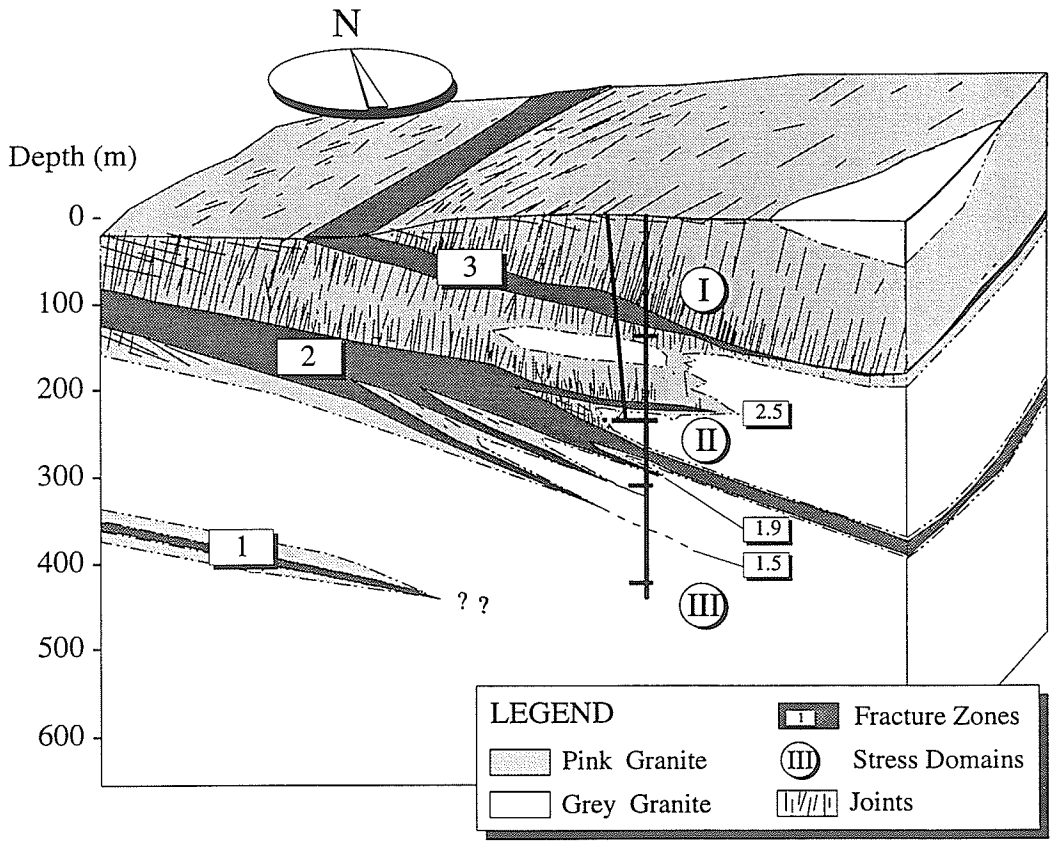

Figure 3.1: General geological setting of the Underground Research Laboratory showing the major Fracture Zones and stress domains (after Everitt et al. [44]).

is poorer in alkali feldspar and richer in plagioclase than the grey granite, although the transition between the two units is diffuse (Figure 3.2). Thin pegmatite dykes crosscut all other rock types, but are mostly confined to the larger granodiorite dykes at this level. Detailed petrographic analysis was not conducted on rock types from the 420 Level prior to the Mine-by Experiment because of wide mineralogic variations within each unit.

A few minor closed fractures, associated with the granodiorite dyke swarm to the west of the station, were identified in drill core from exploratory boreholes for the Mine-by

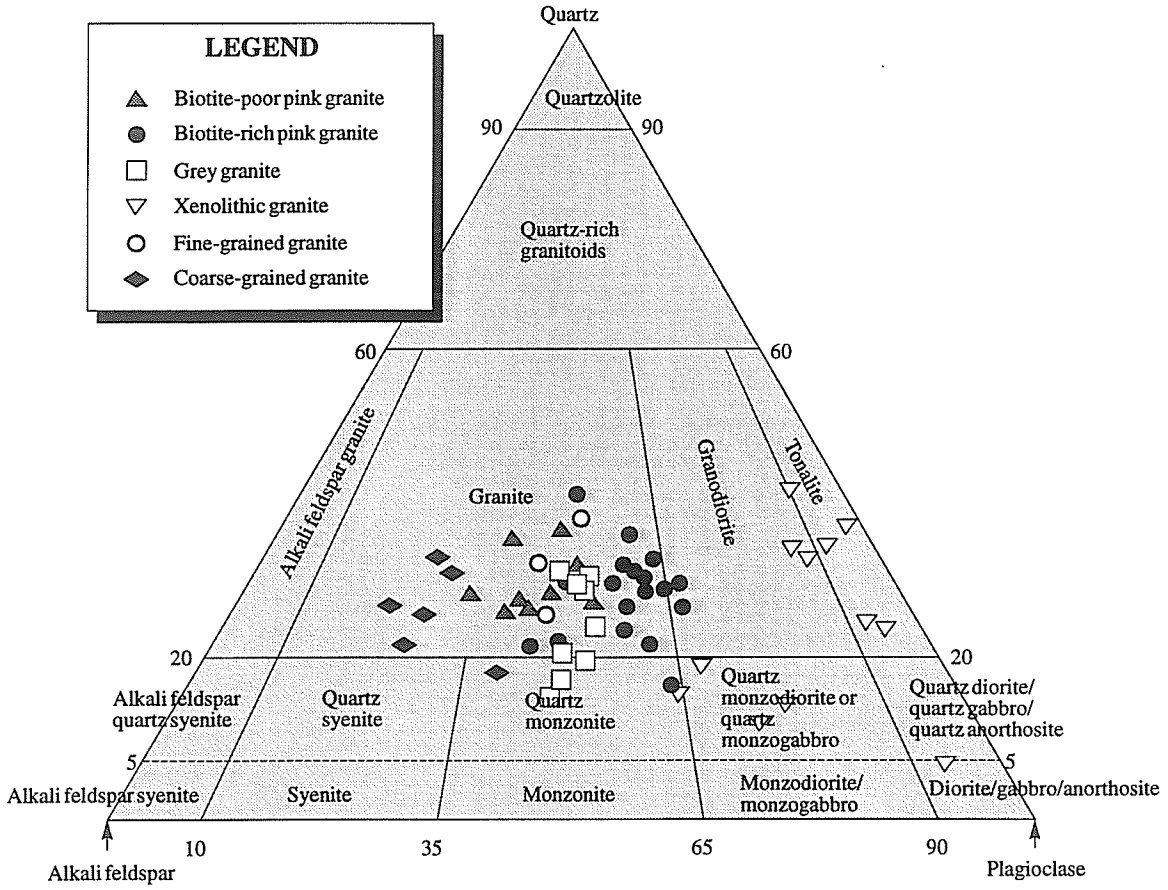

Figure 3.2: Ternary diagram showing the composition of granite and granodiorite for the URL (after Brown et al. [10]). Note that in this classification no distinction was made between the granite and granodiorite, the latter being grouped with biotite-rich granite. The inverted triangles represent xenolith compositions.

Experiment. However, because these fractures were not detected in the tunnel wall following room excavation, their areal extent is small. This appears to be the only fracture type in the immediate vicinity of the 420 Level. In the absence of fracturing, the *in situ* hydraulic conductivity of the rock mass is very low (10^{-13} m/s).

3.1.3 *In situ* stress

In 1982, AECL Research carried out the first *in situ* stress measurements at the proposed site for the URL. These hydraulic fracturing measurements were taken between the 12- and 540-m depth in the general area of the proposed access shaft to the URL. During the nine years following, seven different classes of *in situ* stress measurement methods were used: five methods of overcore testing, the Bock borehole slotter method, under-excavation (i.e., large-scale undercoring), hydraulic fracturing, source location of microseismic events, convergence measurements and observations. Martin et al. [127] concluded from these investigations that large-scale techniques, such as convergence measurements, are less sensitive to the effects of processes like microcracking, and that the use of a larger rock volume in the measurement tends to reduce the inherent variability associated with small-scale measurement techniques.

An extensive *in situ* stress research program, started in 1985 after completion of the rectangular shaft, was conducted to characterize the *in situ* stress state around the URL access shaft and the main development levels. This work continued with the extension of the shaft, completed in 1988. The existence of major thrust faults and subvertical joint sets in the upper 275 m of the URL complicated the interpretation of *in situ* stress measurements and observations. Martin [124] concluded that the stress conditions at the URL can best be described as a series of stress domains separated by the major thrust faults, Fracture Zones 2.5 and 2 (Figure 3.1).

Stress Domain I, above Fracture Zone 2.5, is a region of relatively low stresses due to stress relief associated with the extensional joint sets. The orientation of the maximum horizontal stress in this region is 040°, parallel to the major extensional joint set. In

comparison to stress measurements at other sites in the Canadian Shield [71], this direction differs by about 90° from the average NW-SE direction. Martin [124] suggested that, because the mass of rock above Fracture Zone 2 has undergone reverse thrusting of about 7.3 m, the upper portion of the rock mass is analogous to a brittle beam in bending, resulting in extensional cracking perpendicular to the direction of thrusting and stress relief perpendicular to the extensional joints. As a result of this process, the stress component parallel to the extensional joints is now the maximum horizontal stress. In terms of stress magnitude, Stress Domain I is considered "normal" for the Canadian Shield. The minimum stress is vertical and very close to lithostatic; the maximum horizontal stress increases from about 8 to 15 MPa with depth; and the horizontal stress ratio increases from about 1.6 to 2.4.

Stress Domain II, between Fracture Zones 2.5 and 2, is a transitional zone with moderate stresses. The stress orientations within this domain are the same as in Domain I, primarily because of the existence of the same subvertical joints. The stress magnitudes, however, are quite different. The vertical stress shows a large perturbation near Fracture Zone 2 related to local high contact stresses between the upper and lower surfaces of the shear zone [124], increasing from about 12 to 26 MPa with depth. The maximum horizontal stress shows a similar jump in values, increasing from 24 to 32 MPa with depth. The horizontal stress ratio in this region shows a corresponding increase from 1.2 to 2.0. Extensive stress measurements were carried out at the 240 Level excavated in this stress domain.

Stress Domain III, below Fracture Zone 2, is a highly stressed region where the rock mass is unfractured with the exception of Fracture Zones 1.9 (a splay of Fracture Zone 2) and 1.5, a relatively narrow zone of shallow-dipping fractures. The maximum horizontal stress direction in this region, estimated at azimuth 135°, is very similar to the average NW-SE trend measured elsewhere in the Canadian Shield. However, because of the absence of fracturing, the *in situ* stress magnitudes are higher than those measured at similar depths in other parts of the Shield [71]. The vertical stress is perturbed in the vicinity of Fracture

Zone 2, reaching 25 MPa, but approaches the calculated lithostatic stress near 420 m depth. The estimated maximum horizontal stress is between 50 and 60 MPa. Estimates of the horizontal stress ratio range from 1.05 to 1.25.

The highly stressed condition of this domain posed a problem for stress measurements at the 420 Level. A variety of techniques were tried during level development, with limited success. Overcoring provided unreliable results because of exaggerated axial straining (incipient discing). Hydraulic fracturing produced subhorizontal fractures in horizontal and vertical boreholes, from which the vertical stress was estimated [35]. A large-scale undercoring (under-excavation) test in the 420 to 240 Level vent raise using triaxial strain cells provided estimates of both the magnitude and orientation of the maximum and intermediate stresses, but produced unrealistic results for the minimum principal stress [92, 190]. Results from an acoustic emission/microseismic array installed in four inclined boreholes around the URL shaft [179] provided estimates of the maximum and minimum horizontal stress directions, which were supported by observations of breakouts in the shaft, but provided no estimates of magnitudes. Doorstopper tests performed in boreholes drilled for the Mine-by Experiment at the 420 Level [23] produced an estimate of the stress tensor for the area, but the results for stress magnitudes did not correlate with results from other tests or observed behaviour around excavations at the 420 Level. A composite stress tensor for the 420 Level (Table 3.1) was compiled from the best evidence for principal stress magnitudes and directions from the various testing methods, and from observations of breakouts in the shaft and in tunnels at the 420 Level. The composite nature of the tensor, however, precluded the use of rigorous statistical methods in determining the mean value and confidence intervals of each of the stress components, and their respective orientations. Nevertheless, this composite tensor was sufficient for designing the Mine-by Experiment arrangement.

Table 3.1: Estimated *in situ* stresses and 90% confidence intervals for the 420 Level (after Read and Martin [155]).

Stress Components	σ_1	σ_2	σ_3
Magnitude (MPa)	55 ± 5	48 ± 5	14 ± 1
Trend (°)	135 ± 10	044 ± 10	290 ± 25
Plunge (°)	10 ± 5	05 ± 5	79 ± 5
Stress Ratios	σ_1/σ_2	σ_1/σ_3	σ_2/σ_3
	1.15 ± 0.1	3.93 ± 0.5	3.43 ± 0.5

3.1.4 Geotechnical properties

The geotechnical properties of the Lac du Bonnet granite have been determined from extensive laboratory testing, e.g., Lajtai [112, 113], Lajtai and Bielus [109], Lajtai and Schmidtke [111], Jackson et al. [81], Stimpson and Chen [174]. However, extrapolation of these results to the *in situ* material properties of the rock mass is not straightforward, even in situations where the rock mass has no joints to account for *in situ* strength reduction. The difficulty lies in the fact that the boundary conditions and stress history of a sample of rock differ from the field to the laboratory, i.e., a laboratory specimen must go through a complete unloading cycle prior to being tested. If the stresses relieved during drilling are high, the resulting laboratory sample may contain significant damage that is not present in the field. Conversely, if samples are selected from a low stress regime, the amount of sample disturbance is reduced, and results are more representative of the *in situ* rock mass properties. Martin [125] illustrated the importance in recognizing sample disturbance when interpreting the results of laboratory testing on Lac du Bonnet granite.

The geotechnical properties of rock in the field study area (Table 3.2) were estimated from laboratory tests performed by the Canada Centre for Mineral and Energy Technology (CANMET) on representative rock samples from the 420 Level, and on samples of granite from the upper 275 m of the batholith. Results from samples taken from the high stress domain at the 420 Level showed a marked decrease in peak strength from those taken at

Table 3.2: Estimated geotechnical properties for granite and granodiorite in the field study area (after Read and Martin [157]).

Rock Type	Granite	Granodiorite
Density (kg/m^3)	2630 ± 10	2660 ± 20
Uniaxial Compressive Strength (MPa)	213 ± 20	228 ± 20
Tangent Young's Modulus (GPa)	65 ± 5	66 ± 5
Poisson's Ratio	0.25 ± 0.05	0.25 ± 0.05

the 240 Level and above, suggesting a substantial amount of sample disturbance caused by induced microfracturing. Read and Martin [157] concluded that results from samples of granite from lower stress domains nearer surface were likely most representative of the undamaged *in situ* rock mass properties at the 420 Level. Martin [125] also showed that samples of Lac du Bonnet granite taken from Cold Spring Quarry, near Seven Sisters, Manitoba, had similar properties to those taken from the upper 275 m of the batholith at the URL.

Triaxial compression tests were conducted on samples from the 420 Level, and from the upper 275 m of the batholith to determine a Hoek-Brown failure envelope representative of the *in situ* rock strength. The Hoek-Brown failure criterion [78] is given by

$$\sigma_1 = \sigma_3 + \sqrt{m\sigma_c\sigma_3 + s{\sigma_c}^2} \tag{3.1}$$

where σ_1 and σ_3 are the maximum and minimum principal stresses, respectively, σ_c is the uniaxial compressive strength of an intact laboratory sample, m is a shape parameter, and s is a scaling factor to account for the presence of joints or discontinuities *in situ*. The tensile strength associated with the Hoek-Brown criterion is given by

$$\sigma_t = \frac{\sigma_c}{2}\left[m - \left(m^2 + 4s\right)^{\frac{1}{2}}\right] \tag{3.2}$$

By definition, Equation 3.1 is a peak strength criterion, and in the unconfined case, reduces to

$$\sigma_1 = \sqrt{s}\sigma_c \tag{3.3}$$

In cases where s is equal to 1, i.e., no *in situ* joints or discontinuities , Equation 3.3 implies that the uniaxial stress required to cause failure *in situ* is equivalent to the laboratory-derived uniaxial compressive strength of a cylindrical sample. Martin [125], however, showed that the peak strength measured in the laboratory is influenced by a number of factors, including sample size, loading rate and stress history of the sample, and can therefore not be considered a true material property. Consequently, three key stress levels [6, 113], corresponding to: 1) the start of crack initiation σ_{ci}, 2) the start of unstable crack growth σ_{cd}, and 3) the short-term peak strength σ_c, were determined from the triaxial tests. The Hoek-Brown envelopes associated with each of these stress levels for grey and pink granite, and granodiorite, are shown in Figure 3.3.

Numerical modeling simulations were conducted for two orthogonal excavations at the 420 Level [126] using the average stresses given in Table 3.1. Employing the Hoek-Brown envelopes defined by the peak strength results for the three rock types, the stresses at no point around either opening exceeded the rock strength, even when σ_c from the damaged 420 Level samples was used. These findings were at odds with observations of breakout notch development in the roof of Room 405, excavated orthogonal to the $\sigma_1 - \sigma_3$ plane (Figure 3.4). Because there are no natural fractures in the rock mass at this level to account for an *in situ* strength reduction, i.e., $s = 1$, Martin and Read [126] concluded that traditional peak strength results from laboratory samples overestimate the *in situ* rock strength, especially near the tunnel boundary. This observation is consistent with experience elsewhere [70, 150].

Implementation of the other Hoek-Brown envelopes shown in Figure 3.3 into the boundary element model of orthogonal rooms at the 420 Level showed that the best agreement with observed behaviour was achieved when the envelope representing crack initiation for pink granite was used in the analysis. However, Martin [125] and Read [154] showed that the use of such an envelope underestimates the strength of the rock mass away from the opening, and that a more complex failure envelope is required to properly represent both confined and unconfined conditions. Studies on very small tunnels in laboratory tests have

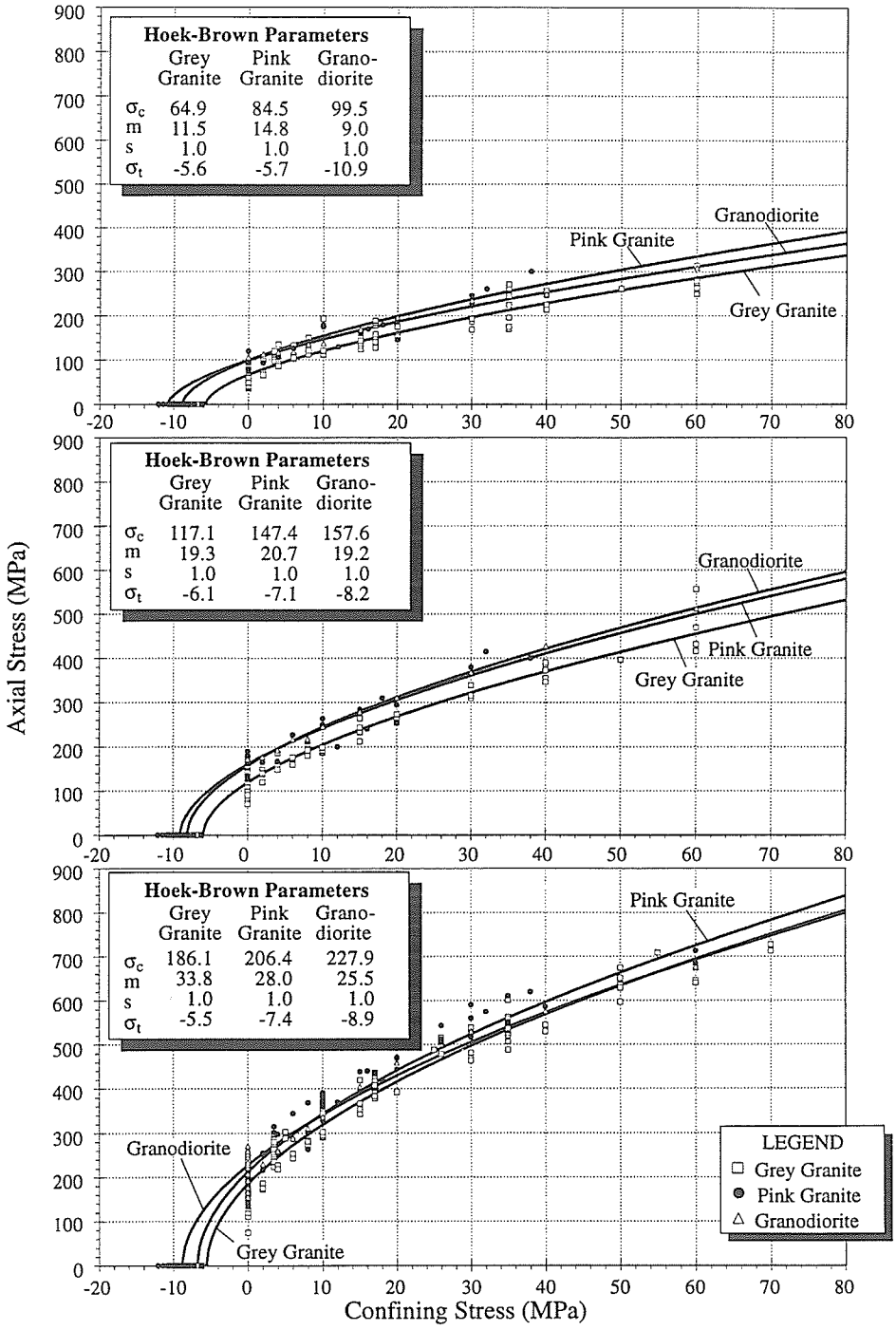

Figure 3.3: Results from uniaxial and triaxial tests on grey granite, pink granite and granodiorite. The Hoek-Brown failure envelopes are based on: 1) crack initiation stress σ_{ci} (upper), 2) unstable crack growth initiation stress σ_{cd} (middle), and 3) short-term peak strength σ_c (bottom).

shown that the strength of the rock at the tunnel wall can exceed the uniaxial compressive strength [168, 48], but that the effect diminishes with increasing tunnel dimensions. The initial modeling results from the 420 Level of the URL suggest that failure at the periphery of a 3.5-m-diameter tunnel occurs at less than 50% of the laboratory-measured uniaxial compressive strength of the rock [125]. Consequently, *in situ* rock strength can be a complex issue even in situations where the rock mass contains no joints or discontinuities.

Mapping of excavation-induced damage during construction of the 300 Level suggested that damage zone development was more pronounced in granite than in granodiorite [45]. During development of access tunnels at the 420 Level, similar observations were made near discrete granodiorite dykes. However, the difference in excavation-induced damage between the massive granite and the outer margin of a large granodiorite dyke was less pronounced in a drill-and-blast excavation (Room 405) driven orthogonal to the $\sigma_1 - \sigma_3$ plane. Although laboratory testing suggests that the mechanical properties of the two rock types are similar,

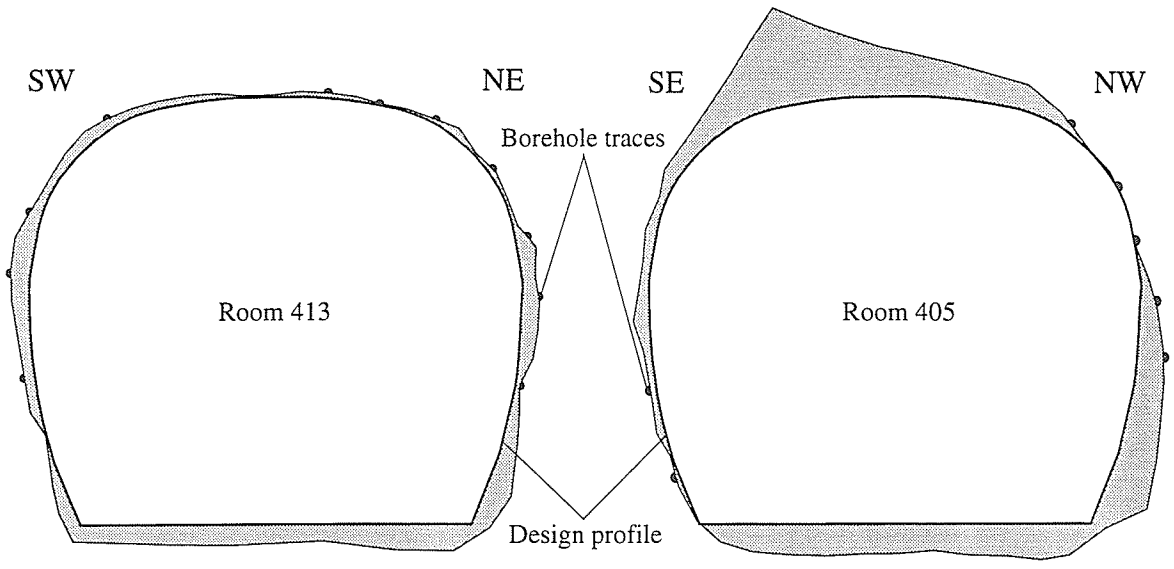

Figure 3.4: Comparison of breakout notch development in two orthogonal rooms at the 420 Level illustrating the effect of orientation relative to the plane of maximum deviatoric stress on the development of excavation-induced damage. Room 405 is aligned with σ_2, and Room 413 is aligned with σ_1.

the field observations imply that there are differences in their fracturing characteristics, i.e., the growth and interaction of cracks. This difference is noticeable upon stress relief during sampling.

3.2 The Mine-by Experiment

The premise for the Mine-by Experiment was to locate a volume of rock typical in terms of geology and stress conditions of potential disposal sites elsewhere in the Canadian Shield, to characterize the rock mass volume and instrument it with state-of-the-art instrumentation, then to excavate a test tunnel through the instrumented volume to measure the excavation-induced response. As discovered during the characterization of the URL, it seemed possible to meet the experiment's objectives by locating the Mine-by Experiment at the 420 Level in Stress Domain III, where the stress conditions are similar to those at a depth of about 1000 m in other parts of the Shield. A complete description of the final detailed design of the Mine-by Experiment is given in Read and Martin [155].

3.2.1 Experiment arrangement

The arrangement of the Mine-by Experiment (Figure 3.5) was the result of an optimization process drawing upon a variety of technical proposals for instrumentation layouts and monitoring methods, evaluation of the practicality and safety of the operations associated with implementation, and evaluation of the most effective use of available resources in conjunction with the overall URL experimental program. The azimuth of the test tunnel (225°) was chosen so as to maximize the stress ratio in the plane orthogonal to the tunnel axis in order to promote excavation-induced damage development.

Access for instrumentation installation was provided by a series of drill-and-blast excavations. An incline and a decline were excavated at 20% grade on tangent, and 10% grade through the curves to develop an upper and lower instrument gallery, Rooms 409 and 413 respectively, orthogonal to the planned test tunnel. A vertical raise (Room 004)

was excavated to connect the upper and lower galleries for ventilation purposes, and a drill station (Room 416) was excavated at mid-height in the raise for instrumentation borehole drilling. A third instrument gallery (Room 405), parallel to the proposed test tunnel, was extended off the existing 420 Level for additional drilling access. All access tunnels were initially 3.4 m wide by 2.9 m high and horseshoe-shaped, but the first 30 m of Room 405 was slashed to 5.0 m wide by 3.5 m high to accommodate additional testing. The vent raise drill station (Room 416) was excavated as a 3.5 m wide by 2.7 m high opening.

Following excavation of the access tunnels and installation of the instrumentation for the experiment, the 3.5-m-diameter circular test tunnel (Room 415) was excavated at 0.5% grade to 46 m in length from an assembly chamber (Room 414). The wall-to-wall spacing between the instrument galleries and the test tunnel was approximately 18.5 m.

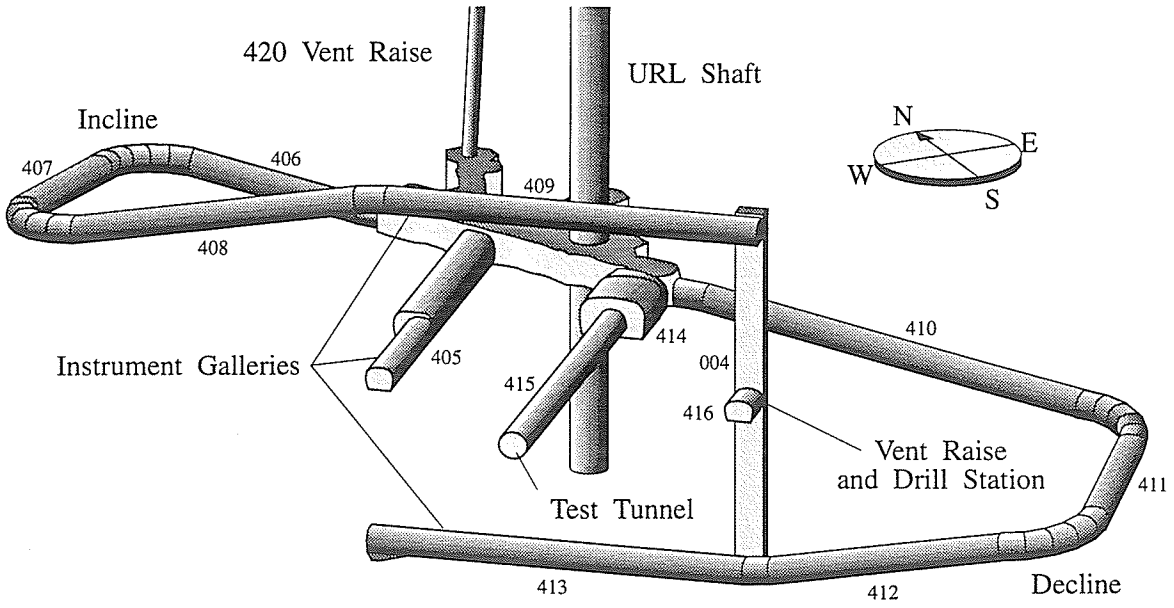

Figure 3.5: Arrangement of the Mine-by Experiment at the 420 Level of the URL.

3.2.2 Excavation technique and equipment

From previous experience in Room 209 and the URL shaft with the drill-and-blast excavation method, the damage zone near the tunnel wall results from a combination of stress redistribution and blast effects. Similar observations in granite have been reported by Pusch and Stanfors [152]. Because the intent of the Mine-by Experiment was to study the damage resulting from stress redistribution, the test tunnel was designed as a full-face machine-excavated opening to avoid the undesirable percussive effects of blasting. Initially, a tunnel boring machine (TBM) was considered the best technical option [156], but the costs associated with excavating such a short section of tunnel, including equipment preparation and mobilization, were prohibitive. Consequently, an alternative method was devised.

The excavation method (Figure 3.6) involved line-drilling and reaming a series of 1-m-deep perimeter holes around the design diameter of the tunnel, and then progressively breaking out the interior of the round using hydraulic rock splitters in a series of production holes [95, 136]. Although the test tunnel was initially designed as a 3.5-m-diameter cylindrical opening with a flat face, the excavation method necessitated a stepped longitudinal profile to accommodate drilling of each round, with a maximum diameter of 3.5 m in each

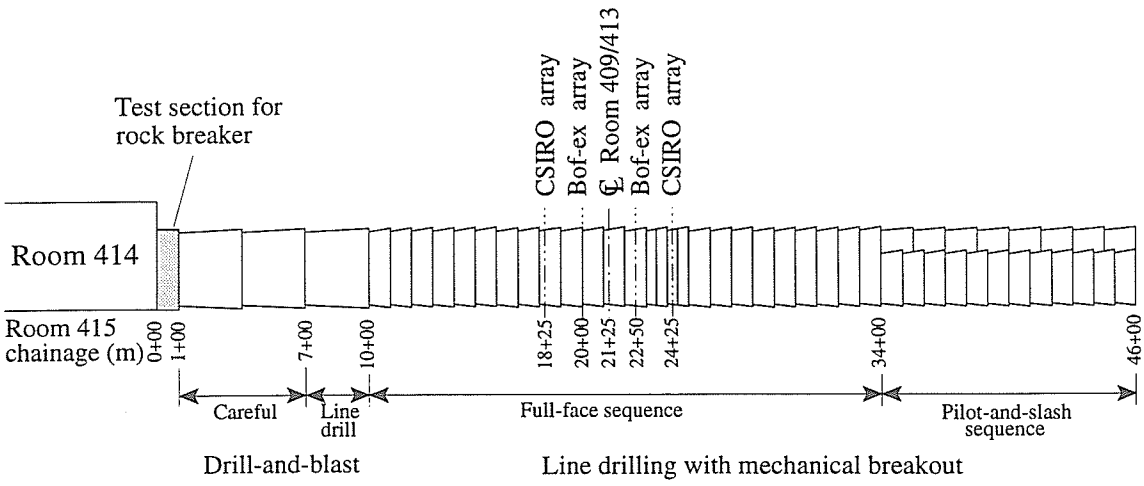

Figure 3.6: Excavation method and sequence used for the Mine-by Experiment.

round. Based on previous excavations at the URL, some deviation from planarity was also expected in the shape of the face.

The excavation sequence for the test tunnel incorporated several rounds of careful drill-and-blast for the first 10 m of the tunnel, followed by 36 m excavated by line-drilling and rock breaking in 1-m rounds. The first 34 m of Room 415 were excavated as full-face rounds, and the final 12 m of the test tunnel used a pilot-and-slash sequence. In total, 50 excavation rounds were required to complete the test tunnel.

3.2.3 Enthalpy control

Enthalpy control (i.e., the control of temperature and humidity) was considered important in terms of limiting the number of variables in the interpretation of the measured responses. A 75 kW capacity system comprising an air handling unit, a blast cooler, and two compressor/condensor units was installed at the 420 Level to maintain as close as possible the ambient rock conditions, i.e., 10.5° C, > 90% RH, in the test tunnel as excavation proceeded. Although some short-term spikes were recorded in the air temperature during peak excavation activities, the overall rock temperature was maintained within about 1.5° C of ambient temperature. Relative humidity was consistently above 90%.

3.2.4 Instrumentation

The Mine-by Experiment incorporated two tiers of instruments. The first was selected on the basis of previous excavation response tests at the URL, and included extensometers and convergence arrays to measure displacements, triaxial strain cells to measure induced strains, and thermistors to measure temperature. A second tier of instrumentation based on acoustic emission/microseismic (AE/MS) technology was used to study the development of the damage zone around the Mine-by Experiment test tunnel [178]. In keeping with the scope of this thesis, only the results from the convergence arrays and the twelve radial extensometers are considered in detail. Results from the other instruments are used in a

qualitative fashion for the interpretation of *in situ* behaviour. Monitoring data from the instruments are discussed later in this thesis.

Extensometers

Borehole fracture extensometers (Bof-exs) have been used successfully in other major experiments at the URL to monitor very small displacements [182], and formed the majority of the displacement-monitoring system for the Mine-by Experiment (Figure 3.7). The Bof-ex is an incremental-type extensometer, i.e., it measures relative displacement between anchors. Each extensometer string incorporated ten direct current linear variable differential transformer (DC-LVDT) displacement transducers, eleven mechanical screw-type anchors, Invar or stainless-steel rods, and centralizers. The repeatability of each transducer is $\pm 0.6\mu$m, and the range is ± 6 mm. Seven thermistors were also included in each extensometer string.

The radial Bof-ex strings were installed in 75.7-mm-diameter (NQ-3 size) boreholes.

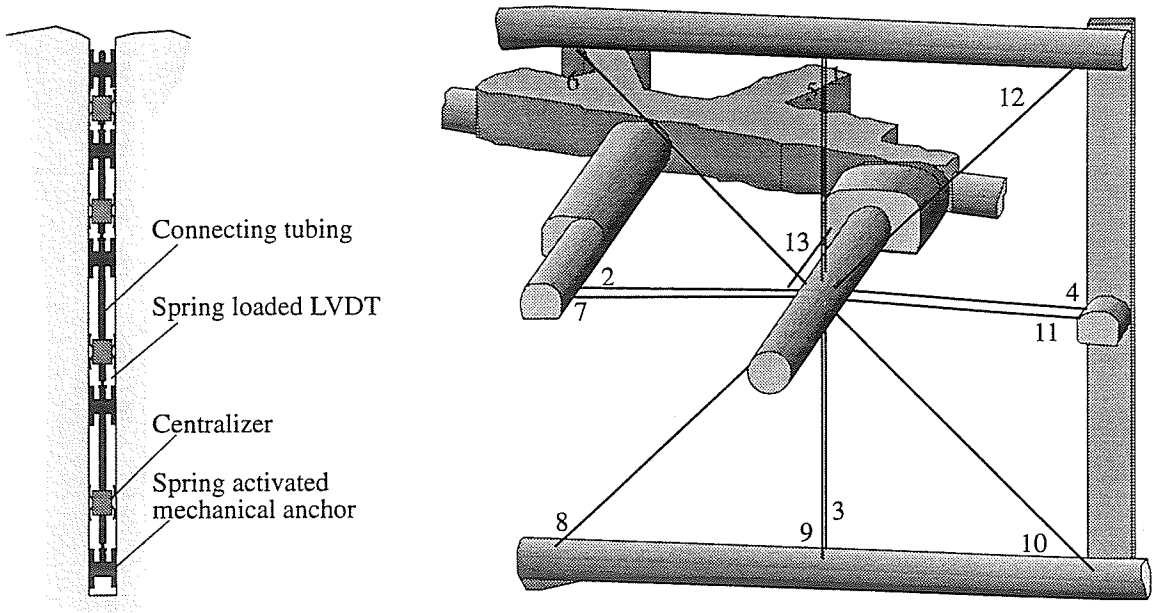

Figure 3.7: Arrangement of Bof-ex boreholes for the Mine-by Experiment and details of a typical extensometer installation.

These holes penetrated the design section of the test tunnel by 200 mm so that the ends of the boreholes could be located once Room 415 was excavated. Accurate collar surveys and downhole laser surveys were conducted for each borehole to determine the exact collar location and alignment deviation [158]. The deviation in alignment was less than 0.5°, which introduced negligible error in the measured radial displacements. Anchors were spaced as close as 340 mm near the tunnel wall in the boreholes, and less closely further from the tunnel. The innermost anchor was approximately 100 mm outside the design perimeter of the test tunnel in each string.

A total of 12 radial Bof-ex strings were installed for the Mine-by Experiment in two instrument arrays at chainages 20+00 and 22+50 in Room 415. The first array comprised two vertical and two horizontal extensometers, and the second array contained two vertical, two horizontal, and four extensometers inclined at ±45° from horizontal. The boreholes for the instruments in these arrays were drilled from the instrument galleries (Rooms 405, 409, 413, and 416) towards the planned location of the test tunnel. Because they were installed prior to the start of excavation, the response measured by the extensometers represents the total displacement induced by the excavation of Room 415 within the radial coverage area of the extensometers. These extensometers are typical of anterior-type instruments.

Convergence arrays

Convergence arrays were installed in Room 415 at eight locations between chainages 10+20 and 31+96 (Table 3.3). Details of a typical convergence array installation are given in Figure 3.8. Convergence arrays in the field study comprised 12 pins installed as close to the tunnel face as possible in a vertical measuring plane orthogonal to the tunnel axis. Specially cut lengths of Invar wire were used in combination with a Kern distometer [128] to measure the distance between opposing pins along six diametral measurement lines. Changes in tunnel diameter were recorded following each excavation round, providing a record of tunnel wall convergence versus excavation advance. Additional readings were also

Table 3.3: Location of convergence arrays in the Mine-by Experiment.

Array	Chainage (m)	Excavation Round
415-1	10.204	5
415-2	12.531	7
415-3	15.380	10
415-4	18.485	13
415-5	22.565	17
415-6	26.062	22
415-7	28.924	25
415-8	31.964	28

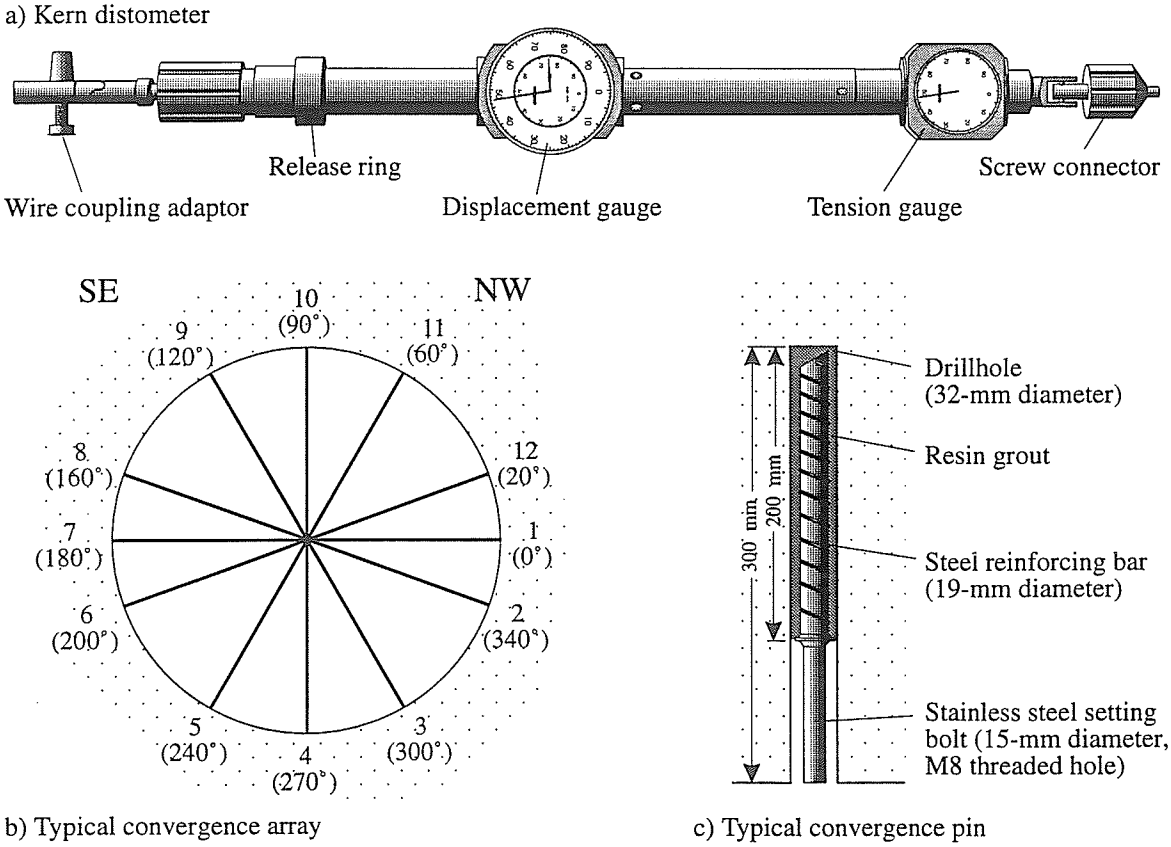

Figure 3.8: Details of the instruments and arrangement of a typical convergence array from the Mine-by Experiment.

taken within each round to determine the tunnel convergence with respect to time. A summary of the convergence data from the Mine-by Experiment is presented in Read et al. [159].

Previous experience with the Kern distometer at the URL has shown a repeatability of ±0.1 mm [128]. Careful calibration of the instrument and Invar wires was performed underground before and after each use with a standard calibration apparatus. In this way, corrections for temperature were incorporated automatically into each reading. The same operator was also used as much as possible to reduce operator bias in the measurements. A standardized reading procedure, repeating each measurement four times, was followed during the Mine-by Experiment.

The convergence pins consisted of 19-mm-diameter steel rebar, 200 mm long, with a 100-mm-long stainless steel setting bolt welded to the end to attach the distometer connector. The convergence pins in each array were installed in 32-mm-diameter percussion drill holes, 300 mm deep, an average of 80 mm from the tunnel face. There was, however, some variation in chainage across the face, as shown in face contours for each round [161]. The floor pins were set in slightly deeper holes, countersunk about 50 mm to protect them from construction equipment. All pins were fixed in place with resin grout. Each array, with the exception of array 415-5, was designed to have convergence pins at 0, 20, 60, 90, 120, 160, 180, 200, 240, 270, 300, and 340° counterclockwise from a NW horizontal line. Array 415-5 had two measurement lines rotated 10° clockwise to avoid interfering with previously installed extensometers.

Other instruments

In addition to the Bof-exs, a series of eight excavation damage extensometers (Ed-exs) were installed at approximately chainage 22+50. These instruments are a miniaturized version of the Bof-ex, approximately 1 m in length, comprising ten ACDT transducers and eleven anchors. The Ed-exs were installed radially outward behind the advancing face in a

posterior fashion to provide detailed displacement measurements within 1 m of the tunnel wall. A complete description of the instrument and an example of its application is given in Thompson et al. [184]. Results from the Ed-exs are used qualitatively in this thesis.

The CSIRO Hollow Inclusion (HI) triaxial strain cell [193] has been used almost exclusively at the URL to measure incremental strains due to excavation. Information gained from these instruments has been used to calculate changes in the *in situ* stress field and to validate results from computer modeling [190, 191, 192]. A total of twelve CSIRO HI cells were installed in two arrays for the Mine-by Experiment at chainages 18+25 and 24+25. Results are summarized in Read et al. [160].

The results from an AE/MS system, installed to monitor excavation-induced seismicity in the rock mass during extension of the URL shaft, were used to design a more elaborate system for the Mine-by Experiment to evaluate the physics of fracturing associated with development of a damage zone around the test tunnel [178]. Two of the objectives of this design were to improve the accuracy of source location determinations and to develop more rigorous source mechanism analysis procedures. The AE/MS system comprised 16 three-component accelerometers coupled to the rock with grout. The pattern of 16 sensors optimized the measured response; in the centre of the array source location accuracy was better than 0.25 m. This number of sensors also allowed the use of a moment tensor inversion scheme to perform source mechanism analysis [51]. A summary of AE/MS results for the Mine-by Experiment is given in Martino et al. [129].

Ultrasonic tomography and acoustic emission (AE) data obtained during laboratory hydraulic fracturing tests on two 600-mm-diameter samples of URL granite [18] showed that the development of microcracks could be monitored with high-frequency sensors acoustically coupled to the rock surface, and that source locations and mechanisms could be determined on a small scale. This approach was applied to the *in situ* rock mass in the NW sidewall of the test tunnel in conjunction with the Ed-exs to determine the level of activity at various distances away from the tunnel wall. From these data, the distribution of acoustic emissions

with location and orientation relative to the excavation were determined [13].

Information on the P and S wave velocities in the rock mass was obtained through several tomographic surveys carried out with AECL's miniCHARTS system between the various excavated openings prior to excavation of the test tunnel (Hayles, pers. comm.). This study required two 40- and twenty 1.5-m-long vertical boreholes in the floor of Room 409 and roof of Room 413. Other cross-hole tomographic studies were conducted in the Bof-ex instrument boreholes before and after excavation of the test tunnel to detect changes in the rock mass resulting from excavation-induced damage [66].

3.3 Summary

The initial characterization of the field study area was conducted prior to the large-scale development of the 420 Level, and excavations related to the Mine-by Experiment. However, the information gained from the various investigations was sufficient to design the Mine-by Experiment arrangement, and to conduct preliminary numerical modeling related to failure around some of the underground openings at the 420 Level.

Based on the initial characterization of the 420 Level, the geology in the field study area was expected to be a mixture of granite and granodiorite. From laboratory studies, the effect of lithological variations within the field study area was assumed to be negligible because of the similarity in the elastic properties of the two rock types. However, field observations suggested that the failure characteristics of the two rock types were different. Nevertheless, in comparison with granitic rock masses in other excavation response experiments [73], the rock mass in the field study area was considered homogeneous and isotropic, and contained no significant discontinuities.

A number of different stress determination techniques were tried at the 420 Level, but none of them produced a satisfactory estimate of the complete *in situ* stress tensor. Consequently, individual components of the tensor were estimated by different means. Because

of the composite nature of the estimated tensor, it was not possible to apply rigorous statistical methods to determine the mean value and confidence intervals of each of the stress components. The estimate was, however, considered sufficient to lay out the excavations for the Mine-by Experiment and to perform preliminary numerical modeling. The maximum principal stress component was estimated to plunge at about 10° to the SE, and the intermediate principal stress was thought to be near-horizontal. The test tunnel was designed to be parallel to the σ_2 direction.

The properties of Lac du Bonnet granite have been well-characterized in a variety of laboratory testing programs. Based on the results of uniaxial and triaxial tests on undamaged samples of Lac du Bonnet granite, the rock mass at the 420 Level was expected to behave in a linear elastic fashion. However, progressive failure, resulting in pronounced breakout notches in some of the excavations, was noted at this level. Numerical modeling undertaken to explain these observations of *in situ* failure suggested that a Hoek-Brown failure criterion based on the crack initiation stress, rather than the peak strength, from laboratory tests was a better indicator of rock strength at the tunnel wall. From numerical model studies, the rock at the tunnel wall was estimated to have a strength less than 50% of the unconfined compressive strength obtained from intact laboratory samples.

The test tunnel was initially designed to be cylindrical with a diameter of 3.5 m and a flat face. The excavation method, however, necessitated a stepped longitudinal profile to accommodate drilling of each round, with a maximum diameter of 3.5 m in each round. Based on previous excavations at the URL, some deviation from planarity was also expected in the shape of the face. Precise survey control was maintained during the excavation, drilling and instrument installation activities to ensure the exact location of the instruments relative to the test tunnel was known.

Twelve radial extensometers and eight convergence arrays were installed as part of the monitoring instrumentation for the Mine-by Experiment. The innermost extensometer anchor was placed within 100 mm of the design perimeter of the test tunnel. Other types

of instruments were also installed for the experiment, but results from them are considered only qualitatively in this thesis. In particular, an AE/MS system and a series of tomographic surveys were included to assess damage induced by the excavation of Room 415. Results from the instrumentation and monitoring studies are discussed in later parts of this thesis.

Chapter 4

Parametric Study of Linear Elastic Displacements

As shown in Chapters 2 and 3, most stress determination techniques are limited to conditions of low to moderate *in situ* stresses. To develop a technique applicable to highly stressed rock masses, where excavation damage may develop within the tunnel, parametric studies of displacements around a cylindrical tunnel in a continuous, homogeneous, isotropic, linear elastic medium were conducted. The studies assessed the effects of stress components, face shape and tunnel perimeter geometry on the measured displacement response using two-dimensional, axisymmetric and three-dimensional numerical models.

4.1 Description of Numerical Codes and Conventions

A comparison of displacement results from different codes for a cylindrical tunnel in a linear elastic medium under hydrostatic stress conditions illustrated that FLAC [26] and EXAMINE^{3D} [27] gave results within 2% of the closed-form plane strain solution far from the tunnel face. Near the face, the displacement responses produced by the two codes were comparable. Based on these findings, FLAC was used on a 486-50 MHz personal computer for two-dimensional and axisymmetric analysis, and EXAMINE^{3D} was used on a Silicon Graphics Personal Iris computer for three-dimensional analysis.

During the course of the parametric study, a number of different coordinate systems,

involving both rectangular and cylindrical conventions, were used to illustrate different aspects of the work. The conventions are described within each section. Unless otherwise specified, the material properties used in the analyses were Young's modulus (65 GPa) and Poisson's ratio (0.25). In all cases, standard SI units were adopted.

4.1.1 Two-dimensional and axisymmetric studies

FLAC is a two-dimensional explicit finite difference code, with axisymmetric capabilities, primarily intended for geotechnical engineering applications. Its finite difference formulation differs from the finite element method in that it uses a mixed discretization scheme [123], full dynamic equations of motion, and an explicit solution scheme capable of handling arbitrary non-linear stress-strain laws. The resulting matrix equations are identical to those for the finite element method using constant strain triangles. Code verification and validation have been extensively documented [26].

The conventions used in FLAC follow traditional mechanical engineering practice. Tensile stresses are considered positive, and forces and displacements are positive if directed in the positive coordinate direction in the two-dimensional case, or radially outward in the axisymmetric case. To be consistent with geotechnical engineering conventions, results from FLAC were converted to follow the convention of compressive stress and inward radial displacement positive. In this way, *convergence* is defined as positive displacement of the rock mass directed towards the tunnel centre, while *divergence* is negative displacement directed away from the tunnel centre.

Results from the numerical models for locations far from the face were compared to the analytical plane strain solution [59]. The radial and tangential displacements around a circular hole in an infinite medium are given, respectively, by

$$U_r = \frac{a^2}{4Gr}\left\{(\sigma_1+\sigma_2)+(\sigma_1-\sigma_2)\left[4(1-\nu)-\frac{a^2}{r^2}\right]\cos 2\theta\right\} \tag{4.1}$$

and

$$U_\theta = -\frac{a^2}{4Gr}\left\{(\sigma_1 - \sigma_2)\left[2(1-2\nu) + \frac{a^2}{r^2}\right]\sin 2\theta\right\} \tag{4.2}$$

where a is the tunnel radius, G is the shear modulus, r is the radial distance from the tunnel centre, σ_1 and σ_2 are the principal stresses in the plane orthogonal to the tunnel axis, ν is Poisson's ratio, and θ is the rotation angle measured counterclockwise from the σ_1 direction (after Goodman [59]).

Plots of radial displacement versus face position were generated using dimensionless coordinate variables. Normalized face position X/D was used as the abscissa, where X is the difference in axial location of the tunnel face and instrument given by

$$X = x_{face} - x_{instrument} \tag{4.3}$$

and D is the tunnel diameter. Normalized radial displacement $U_r/U_{r_{max}}$ was used as the ordinate.

For the axisymmetric case, $U_{r_{max}}$ is the maximum radial displacement induced by a field stress of 1 MPa, and is given by

$$U_{r_{max}} = \frac{a}{2G} \tag{4.4}$$

For a general axisymmetric plane strain case with field stress σ, the tangential displacement around the tunnel is zero, and the normalized radial displacement is given by

$$\frac{U_r}{U_{r_{max}}} = \frac{\sigma a}{r} \tag{4.5}$$

Stress ratios for the axisymmetric studies are presented as the maximum plane, axial, and minimum plane stresses normalized to the minimum plane stress, e.g., $K = 1,2,1$ means that the ratios of maximum plane and axial stress to the minimum plane stress are 1:1 and 2:1, respectively. The individual normalized stress ratios are referred to as K_{max}, K_{axial} and K_{min}. For the condition of axial symmetry, the maximum to minimum plane stress ratio is always unity.

4.1.2 Three-dimensional studies

EXAMINE^{3D} and its companion programs are designed for modeling and visualizing three-dimensional geometry and data, and for analyzing stresses and displacements. The codes are based on the boundary element method, and incorporate, among other features, automatic mesh generation and a mixed integration scheme to accurately calculate stresses and displacements at field points. Validation of the code, conducted in part by comparing results to those from ANSYS, a commercial finite element code, showed negligible difference between results from the boundary element and the finite element codes for a cylindrical tunnel under non-axisymmetric loading [60].

In EXAMINE^{3D}, compressive stresses are considered positive. The convention for positive normal and shear stresses is illustrated in Figure 4.1 for a general x, y, z coordinate system. The same definitions for convergence and divergence used for the axisymmetric cases also apply to these studies. For special cases where one of the principal stress directions coincides with the tunnel axis, the definitions of stress ratios also apply.

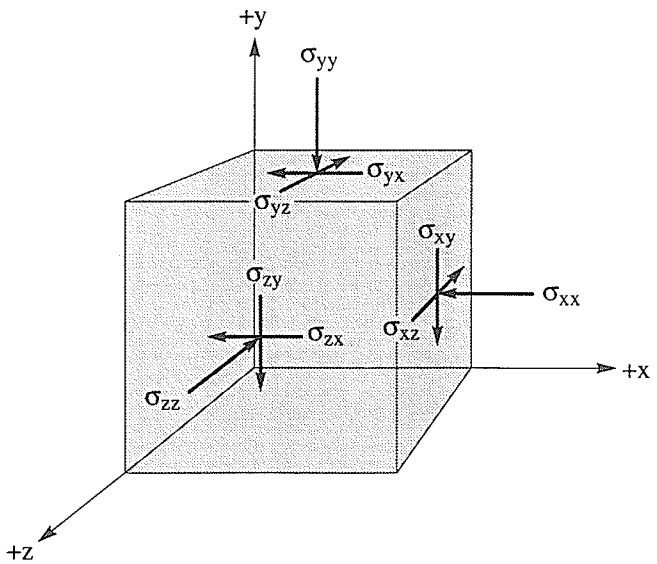

Figure 4.1: Convention for positive stresses in EXAMINE^{3D}.

Results from the studies are presented as *characteristic radial displacement surfaces*, an adaptation of the characteristic line concept. The x, y and z axes correspond to normalized face position X/D, rotation angle θ and normalized radial displacement $U_r/U_{r_{max}}$, respectively. Looking towards the tunnel face, rotation angle is measured counter-clockwise from a point on the right sidewall at the height of the centreline. A constant normalizing factor $U_{r_{max}}$, in this case equivalent to the maximum radial displacement induced by applying a uniaxial far-field stress of 1 MPa orthogonal to the tunnel axis, was used to avoid dependence of the results on the shear modulus G and tunnel radius a. For the three-dimensional studies, $U_{r_{max}}$ is given by

$$U_{r_{max}} = \frac{a\,(1-\nu)}{G} \tag{4.6}$$

and the normalized radial and tangential displacements far from the face are given respectively by

$$\frac{U_r}{U_{r_{max}}} = \frac{a}{4r\,(1-\nu)} \left\{ (\sigma_1+\sigma_2) + (\sigma_1-\sigma_2) \left[4\,(1-\nu) - \frac{a^2}{r^2} \right] \cos 2\theta \right\} \tag{4.7}$$

and

$$\frac{U_\theta}{U_{r_{max}}} = -\frac{a}{4r\,(1-\nu)} \left\{ (\sigma_1-\sigma_2) \left[2\,(1-2\nu) + \frac{a^2}{r^2} \right] \sin 2\theta \right\} \tag{4.8}$$

The three-dimensional *characteristic radial displacement surfaces* can be represented in two-dimensions by considering the radial displacement response versus either face position for a fixed rotation angle, or rotation angle for a fixed face position. The studies also considered, in a qualitative manner, the tangential and axial components of displacement. Positive normalized axial displacement is interpreted as movement of a point at the tunnel perimeter towards the start of the tunnel, and positive normalized tangential movement is clockwise looking towards the tunnel face.

4.2 Effect of Stress Components on Displacements

The relationship between stresses and displacements can be complex depending on the geometry of the problem under consideration. In linear elasticity, stresses are related directly to strains, which are, in turn, related to the partial derivatives of displacement, i.e., the displacement gradient. Displacements are therefore described by an integral function of stress or strain. For simple geometries, such as a circular hole in an infinitely thick plate, the solution for stresses within the plate may be obtained by introducing an Airy's stress function, then solving the biharmonic equation for a given set of boundary conditions [55]. For more complex three-dimensional geometries, there is generally no analytical solution describing the stress distribution. In the absence of a closed-form solution, a three-dimensional boundary element modeling study was conducted to investigate the effect of stress components on the displacement response at the wall of a cylindrical tunnel.

4.2.1 Model description

The model used in the three-dimensional study is shown in Figure 4.2. The closed cylinder

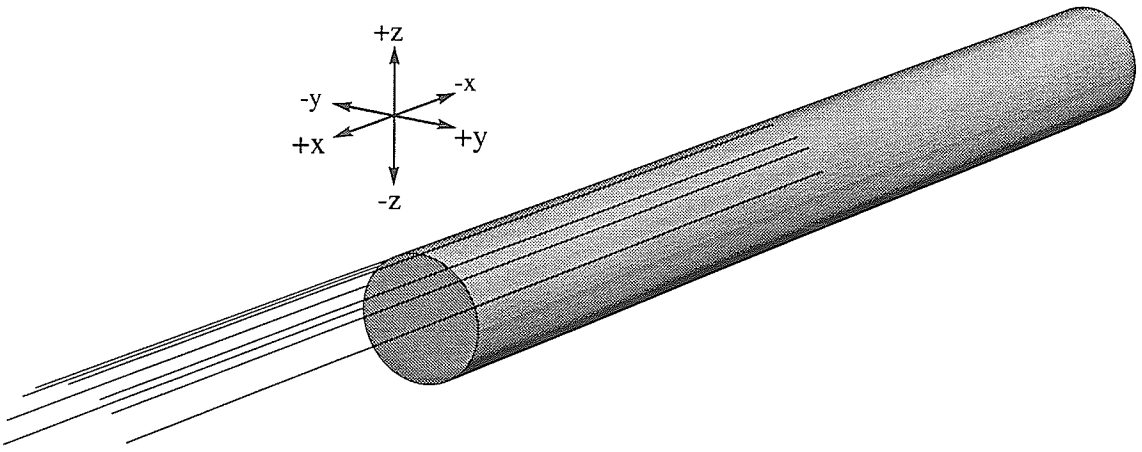

Figure 4.2: Model geometry used in EXAMINE^{3D} to analyze effects of stress components on tunnel wall displacements. Grid lines are located at θ = 0, 20, 45, 60, 90, 120, 135, and 160° and extend five tunnel diameters either side of the face.

representing the tunnel is 3.5 m in diameter, with a length to diameter ratio of ten to minimize end effects. Rather than simulating the complete displacement response at a fixed instrument location by iteratively advancing the tunnel face, a gradual face advance of ten tunnel diameters was simulated in one step by using a series of field grid points, representing different relative distances between the instrument and face locations, arranged in eight axial lines. The grid lines extend five tunnel diameters either side of the face with field points spaced 10 mm within 1 m of the face, and 100 mm outside this region. Field grid points were located 5 mm outside the design perimeter of the tunnel, i.e., 1.755 m from the tunnel centreline. The boundary element mesh on the cylinder surface is not shown in Figure 4.2, but contained 3772 linear elements. A total of 4284 field grid points were used, 531 points per gridline.

The method of simulation, i.e., maintaining a fixed face position and considering instruments at various axial locations, is at odds with the field condition where the instruments are fixed and the face position changes. To reconcile the two approaches, a cartesian coordinate system was chosen for the model such that the tunnel axis was coincident with the x axis. In this way, the definition of face position X is consistent with the field definition given by Equation 4.3. The region where $X > 0$ represents the posterior domain and the area where $X < 0$ is the anterior domain. To maintain a right-handed convention, the positive y direction is horizontal to the left looking in the positive x direction, and the positive z direction is up.

4.2.2 The partitioned stress tensor

Most previous studies involving displacements around a cylindrical tunnel have considered special stress states involving axial symmetry or zero antiplane shear stresses [12, 148], i.e, the tunnel axis coincides with a principal stress direction. To assess a general elastic case where the far-field stress components are unequal, and the tunnel axis does not coincide with any of the principal stress directions, the principle of superposition can be used to partition

a unit stress tensor into a set of three normal stress and three shear stress tensors [135], i.e.,

$$\underbrace{\begin{bmatrix} 1 & 1 & 1 \\ 1 & 1 & 1 \\ 1 & 1 & 1 \end{bmatrix}}_{\sigma} = \underbrace{\begin{bmatrix} 1 & 0 & 0 \\ 0 & 0 & 0 \\ 0 & 0 & 0 \end{bmatrix}}_{\sigma_{11}} + \underbrace{\begin{bmatrix} 0 & 0 & 0 \\ 0 & 1 & 0 \\ 0 & 0 & 0 \end{bmatrix}}_{\sigma_{22}} + \underbrace{\begin{bmatrix} 0 & 0 & 0 \\ 0 & 0 & 0 \\ 0 & 0 & 1 \end{bmatrix}}_{\sigma_{33}} + \underbrace{\begin{bmatrix} 0 & 1 & 0 \\ 1 & 0 & 0 \\ 0 & 0 & 0 \end{bmatrix}}_{\sigma_{12}} + \underbrace{\begin{bmatrix} 0 & 0 & 0 \\ 0 & 0 & 1 \\ 0 & 1 & 0 \end{bmatrix}}_{\sigma_{23}} + \underbrace{\begin{bmatrix} 0 & 0 & 1 \\ 0 & 0 & 0 \\ 1 & 0 & 0 \end{bmatrix}}_{\sigma_{13}} \tag{4.9}$$

By applying scalar multipliers to the six partitioned tensors, any general stress tensor can be described. Hence, by describing the displacement responses for the six base cases, the response for any combination of the six tensors can be found by adding the individual displacement responses. Of the six partitioned tensors, σ_{11}, σ_{33} and σ_{13} represent plane components of stress, i.e, oriented in the cross-sectional plane orthogonal to the tunnel axis, while σ_{22}, σ_{12} and σ_{23} are antiplane components [53]. In terms of the coordinate system used for the model (Figure 4.2), σ_{11} is coincident with the y-axis, σ_{22} with the x-axis, and σ_{33} with the z-axis.

4.2.3 Displacements related to plane components of stress

The plane components of the partitioned stress tensor are illustrated in Figure 4.3. The displacement responses produced by the σ_{11} tensor are shown in Figure 4.4 versus face position, and are characteristic of the harmonic responses associated with these components, i.e., sinusoidal in terms of displacement versus rotation angle. The difference between the displacement responses related to the various plane components is characterized by a phase shift in the harmonic response. As shown in the plots of displacement response versus rotation angle (Appendix B; Figures B.1 to B.6), the responses for the radial, axial and tangential displacement components have a periodicity of 180° for all three of the plane tensor components, but differ in the positions and magnitudes of their respective maxima and minima.

The radial displacement response produced by σ_{11} has a sigmoidal shape in the axial direction, and shows convergence for the quadrants where $-60° < \theta < 60°$ and $120° < \theta < 240°$, and divergence for the quadrants where $60° < \theta < 120°$ and $240° < \theta < 300°$. The response is, therefore, asymmetric with respect to zero displacement, with the transition between convergence and divergence occurring at $\theta = 60, 120, 240$ and $300°$ for $X/D = +\infty$. Near the face, the rotation angle at which this transition occurs varies slightly, as shown in the plot of displacement versus face position. The maximum normalized radial displacement is 1 and occurs at $\theta = 0$ and $180°$ for $X/D = +\infty$. The minimum is -0.333 and occurs at $\theta = 90$ and $270°$ for $X/D = +\infty$. The proportion of the radial displacement occurring in the anterior domain, i.e., the amount missed by posterior-type instruments, was consistently 31% of the plane strain solution for displacement at the tunnel wall given by Equation 4.2.

The axial displacement response versus face position for σ_{11} has a complicated asymmetric shape. The displacement near $X/D = 0$ is directed in the positive axial direction into the rock mass ahead of the tunnel, resulting in axial compression of the rock in the anterior domain, and extension in the posterior domain. Some variation in the response with rotation angle was noted near $X/D = 0$, and two crossover points were apparent in the posterior domain at $X/D = 0.086$ and 0.486. The maximum normalized axial displacement

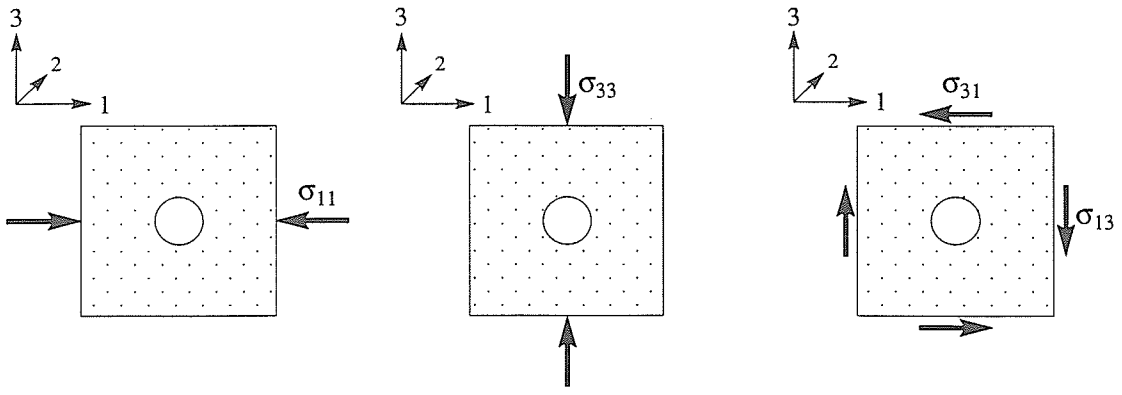

Figure 4.3: Plane components of the partitioned stress tensor. All stress components have a magnitude of 1 MPa.

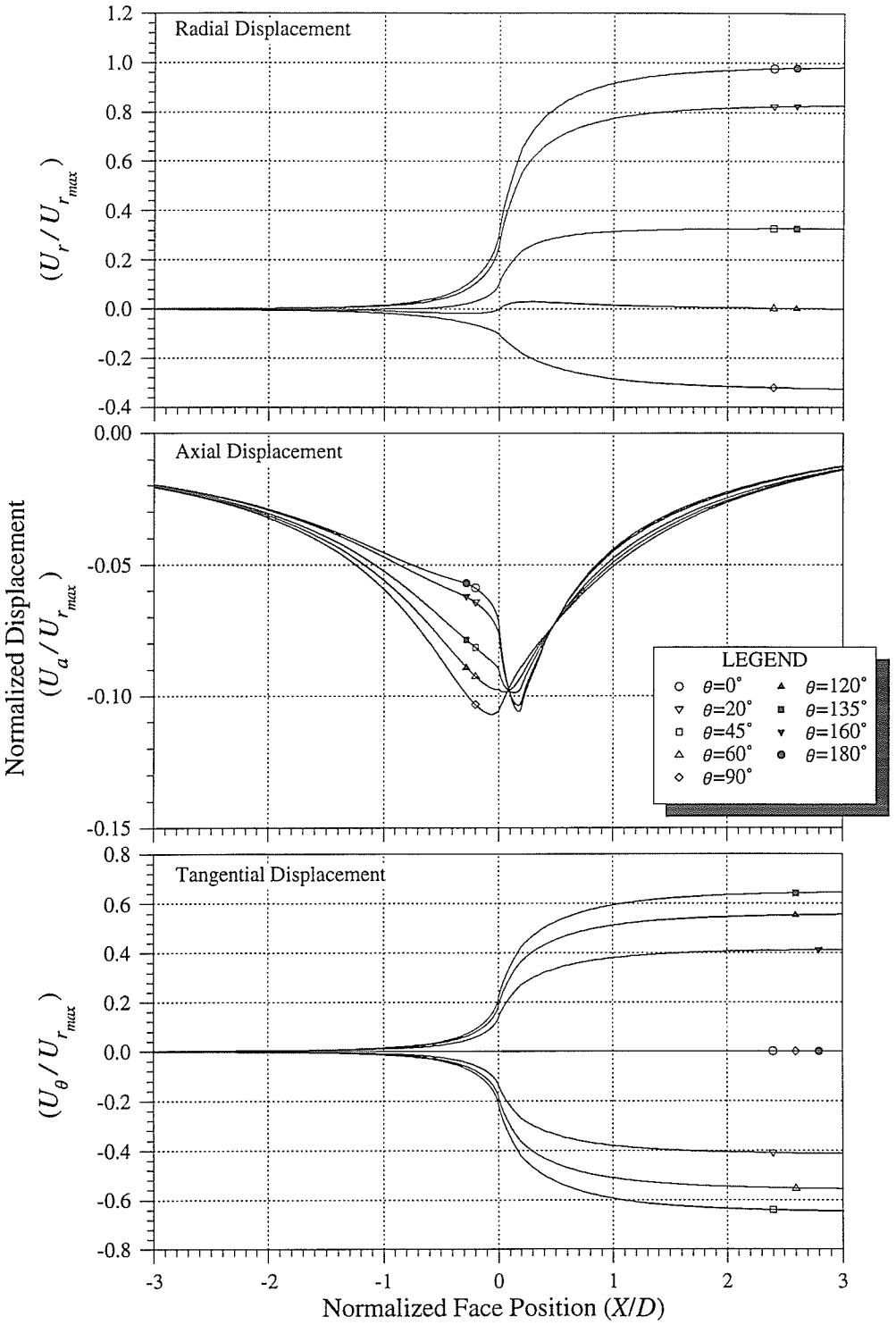

Figure 4.4: Displacement responses versus face position for σ_{11} tensor.

is 0 and occurs at $X/D = \pm\infty$ for all θ. The minimum has two peaks, -0.106 and -0.107, at $X/D = 0.174$ for $\theta = 0$ and 180°, and $X/D = -0.060$ for $\theta = 90$ and 270°, respectively.

The tangential displacement response associated with σ_{11} is sigmoidal in the axial direction, and symmetric about $U_\theta/U_{r_{max}} = 0$. The maximum displacement is 0.667 and occurs at $X/D = +\infty$ for $\theta = 135$ and 315°. The minimum is -0.667 and occurs at $X/D = +\infty$ for $\theta = 45$ and 225°. The transition between positive and negative tangential displacement occurs at $\theta = 0$, 90, 180 and 270°.

The displacement responses produced by the σ_{33} tensor are identical to those for the σ_{11} tensor, with the exception of a phase shift of 90° in the rotation angle. Consequently, the various maxima, minima and transition points are located 90° clockwise from those for the σ_{11} tensor, with the maximum radial displacement occurring at $\theta = 90$ and 270°.

The σ_{13} tensor represents pure plane shear. Through simple transformation, the same stress state can be produced by combining a unit compressive normal stress component oriented at $\theta = 45/225°$ and a unit tensile normal stress component oriented at $\theta = 135/315°$. Therefore, the displacement responses can be determined by subtracting the σ_{33} response from the σ_{11} response, and adding a phase shift of 45°. The resulting displacement responses have a periodicity of 180° and are all symmetric about $U/U_{r_{max}} = 0$ in the axial direction.

The radial and tangential displacement responses for σ_{13} are both sigmoidal in the axial direction, with maximum and minimum normalized displacement of ± 1.333, respectively, at $X/D = +\infty$. For the radial response, the maximum displacement occurs at $\theta = 45$ and 225°, the minimum is at $\theta = 135$ and 315°, and the transition from convergence to divergence occurs at $\theta = 0$, 90, 180 and 270°. For the tangential response, the maximum displacement occurs at $\theta = 0$ and 180°, the minimum is at $\theta = 90$ and 270°, and the transition occurs at $\theta = 45$, 135, 225 and 315°.

The axial displacement response associated with σ_{13} is relatively complex, although the maximum absolute magnitude is only 0.045 at $X/D = -0.174$. A smaller peak is also evident at $X/D = 0.174$. As in the case of σ_{11}, the axial displacement response has two

neutral points in the posterior domain: one at $X/D = 0.086$, the other at $X/D = 0.486$. Positive axial displacement is associated with zones of radial convergence, while negative axial displacement is related to zones of radial divergence. The axial displacement far from $X/D = 0$ in both the anterior and posterior domains is zero for all rotation angles.

4.2.4 Displacements related to antiplane components of stress

The antiplane components of the partitioned stress tensor are illustrated in Figure 4.5. As shown in Appendix B (Figures B.7 to B.11), the displacement responses produced by the antiplane stress components are more complex than those for the plane components, particularly near the tunnel face. The antiplane shear components produce harmonic displacement responses, while the antiplane normal component produces an axisymmetric response, as shown in Figure 4.6.

The radial displacement response produced by the σ_{22} tensor rises in the axial direction for all θ from zero at $X/D = -\infty$ to a peak of 0.049 at $X/D = -0.343$, then declines through a neutral point at $X/D = -0.063$, dropping to -0.050 at $X/D = 0$. In the posterior domain, the response shows a sharp transition, rising towards zero at $X/D = +\infty$. Likewise, the axial displacement response rises from zero at $X/D = -\infty$ to a peak of 0.309 at $X/D = -0.066$, then gradually declines to zero again at $X/D = +\infty$. Because of the axisymmetric nature of the response, there is no tangential displacement produced by the axial stress component.

The σ_{12} and σ_{23} tensors produce displacement responses with a periodicity of 360°. Consequently, near the tunnel face, the displacement pattern produced by the antiplane shear components is antisymmetric with respect to the tunnel axis. The displacement responses versus face position associated with σ_{12} are shown in Figure 4.7. As illustrated in Appendix B (Figure B.9), the displacement response for σ_{23} is 90° out of phase with the σ_{12} response.

In the axial direction, the radial displacement response rises from zero at $X/D = -\infty$

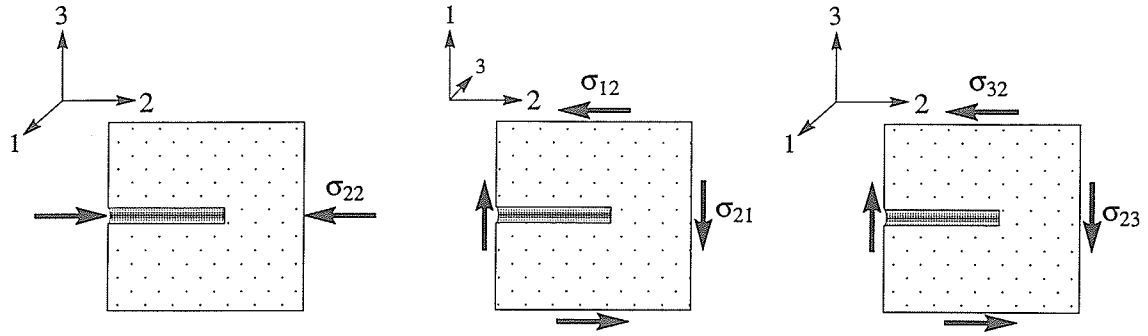

Figure 4.5: Antiplane components of the partitioned stress tensor. All stress components have a magnitude of 1 MPa.

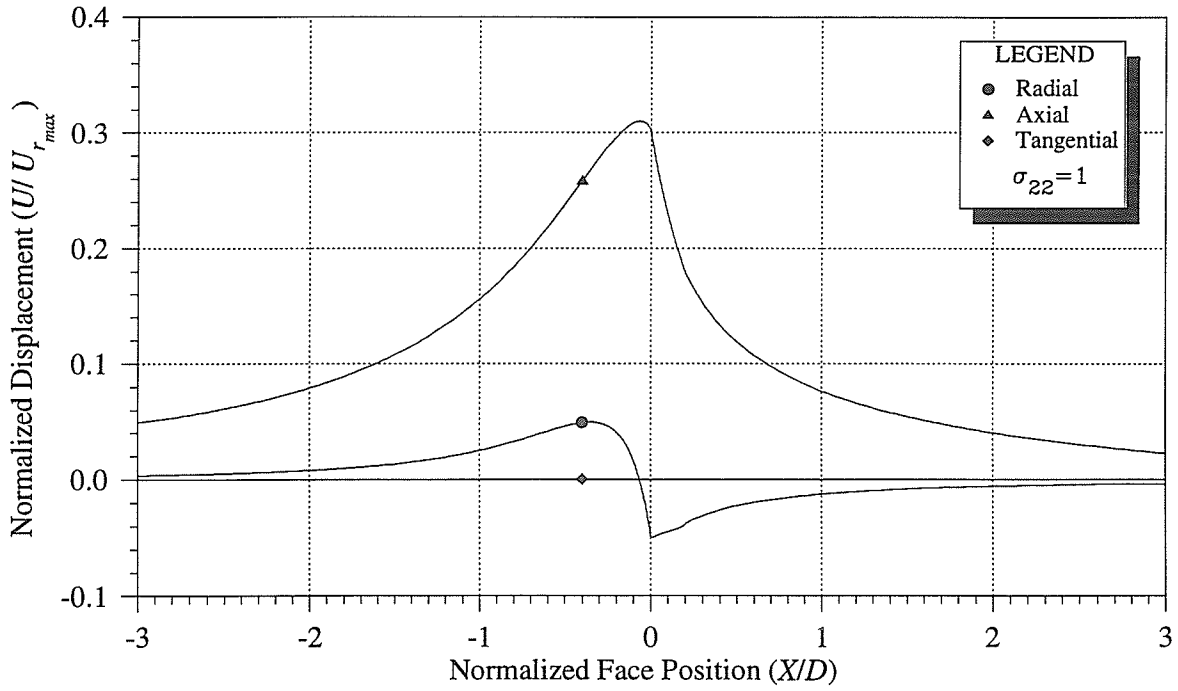

Figure 4.6: Displacement responses versus face position for σ_{22} tensor. Note that, because of the axial symmetry of the applied field stress, the responses for the radial and axial components are axisymmetric, and the response for the tangential component is zero.

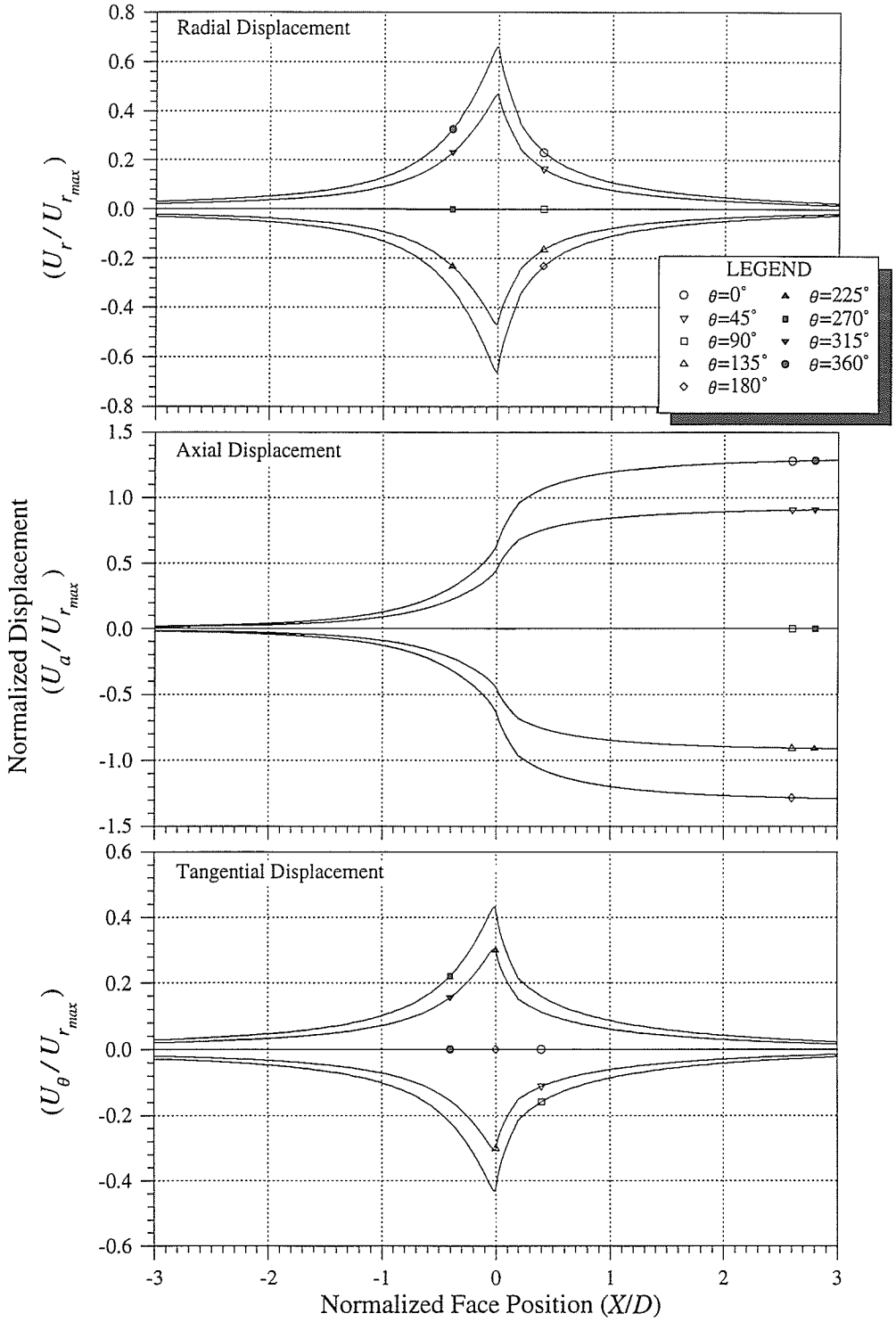

Figure 4.7: Displacement responses versus face position for σ_{12} tensor.

to a sharp peak of 0.654 at $X/D = 0$, then declines back to zero at $X/D = +\infty$. For the σ_{12} tensor, the maximum positive peak occurs at $\theta = 0°$, whereas for the σ_{23} tensor, the maximum peak is at $\theta = 90°$. The responses are neutral at $\theta = 90$ and 270° for σ_{12}, and at $\theta = 0$ and 180° for σ_{23}.

The axial displacement response for the antiplane shear components has a sigmoidal shape in the axial direction, rising from zero at $X/D = -\infty$ to a maximum of 1.300 at $X/D = +\infty$ and $\theta = 0°$ for σ_{12}, and $\theta = 90°$ for σ_{23}. The response is symmetric about $U_a/U_{r_{max}} = 0$, which means that the minimum axial displacement is equal in magnitude, but opposite in sign, to the maximum displacement. Moreover, the maximum and minimum are antisymmetric, i.e., 180° out of phase, resulting in relative axial displacement between opposite walls of the tunnel. This type of movement is termed "ride" displacement in the literature [187], and can affect convergence measurements if the magnitudes are significant. The response is neutral at $\theta = 90$ and 270° for σ_{12}, and at $\theta = 0$ and 180° for σ_{23}.

The tangential displacement responses for the antiplane shear components are symmetric about $U_\theta/U_{r_{max}} = 0$ and have the same shape as the radial displacement responses except for a 90° phase shift. The peak magnitude is 0.422 and occurs at $\theta = 270°$ for σ_{12}, and at $\theta = 0°$ for σ_{23}.

4.2.5 Axisymmetric cases

The axisymmetric case is typified by equal plane normal stresses, and zero plane and antiplane shear stresses. Seven such cases with different normal antiplane stress components were considered: $K_{axial} = 0$, $\frac{1}{4}$, $\frac{1}{2}$, 1, 2, 3 and 4. Owing to the rotational invariance of the applied stress field, the radial displacement response versus face position is also independent of rotation angle θ. Typical responses for five of the cases, shown in Figure 4.8, illustrate the effect of the axial stress component on the radial displacement response. As the axial stress ratio increases, the radial displacement response in the anterior domain changes from a monotonically increasing response with positive gradient to one with a smooth reversal in

gradient for $X/D < 0$ and a second sharp reversal at $X/D = 0$. In addition, the y-intercept of the response, corresponding to the proportion of the total radial displacement response occurring in the anterior domain, decreases dramatically (Table 4.1). As illustrated in Figure 4.8, the radial displacement response for the axisymmetric cases is also characterized by a neutral point in the anterior domain that is independent of axial stress ratio. This point corresponds to the neutral point in the σ_{22} radial displacement response.

The other displacement components were also considered (Appendix B: Figures B.12 to B.15). In all cases, the tangential displacement component is zero because of the axial symmetry of the model. However, the axial displacement response for a fixed point on the tunnel perimeter varies considerably with axial stress ratio. For cases of $K_{axial} < 1$, the axial displacement at the tunnel perimeter near $X/D = 0$ is directed into the rock mass away from the tunnel, resulting in axial compression in the anterior domain, and extension in the posterior domain. Far from the face, the axial displacement approaches zero in both domains. For the case of $K_{axial} = 1$, the axial displacement at the perimeter near $X/D = 0$ is positive, directed towards the start of the tunnel. The response illustrates extension in the anterior domain, compression in the posterior domain between $0 < X/D \leq 0.4$, and extension for $X/D > 0.4$. For higher values of axial stress, the axial displacement at the perimeter near $X/D = 0$ is positive, resulting in axial extension in the anterior domain, and compression in the posterior domain (Figure 4.9). The axial displacement is zero far from the face.

The total displacement response also illustrates the effect of axial stress ratio. For $K_{axial} < 1$, the axial displacement component accounts almost entirely for the total displacement response in the anterior domain, but has relatively little influence in the posterior domain. For $K_{axial} = 1$, the contribution of the axial displacement component is localized to the region around $X/D = 0$. For larger axial stress ratios, the axial displacement component produces a pronounced perturbation in the total displacement response in the anterior region close to $X/D = 0$. As shown in Figure 4.9, this perturbation is very significant for

Table 4.1: Proportion of the radial displacement response occurring in the anterior domain for seven different axisymmetric stress conditions. Results are based on a three-dimensional boundary element model.

Face Shape	Proportion of Total Radial Displacement in Anterior Domain (%)						
	K=1,0,1	1,$\frac{1}{4}$,1	1,$\frac{1}{2}$,1	1,1,1	1,2,1	1,3,1	1,4,1
Flat	31.0	29.4	27.5	23.9	16.5	9.2	1.7

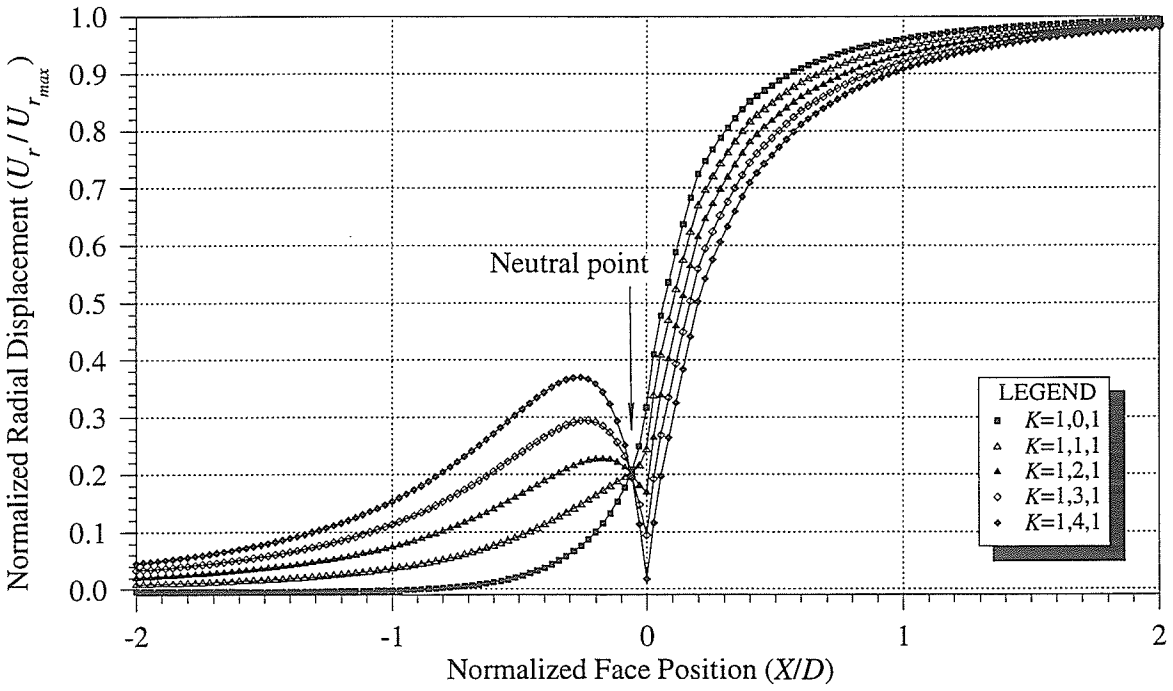

Figure 4.8: Radial displacement response versus face position for five axisymmetric cases. Note that the neutral point is independent of the axial stress component.

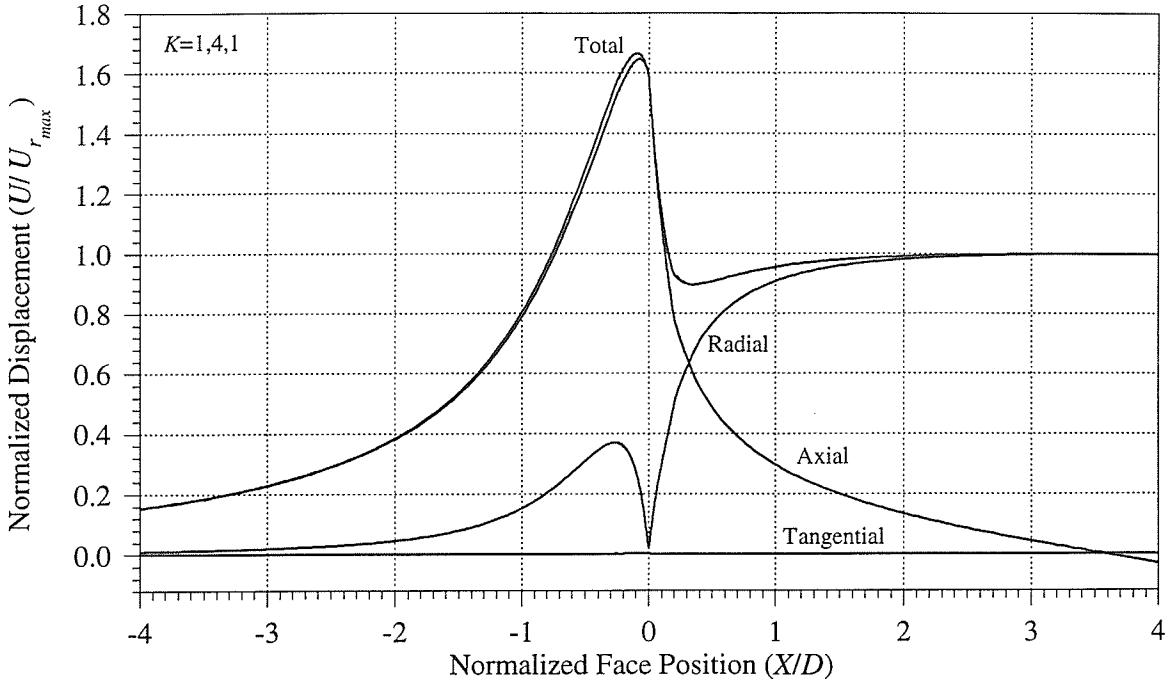

Figure 4.9: Components of displacement for $K = 1, 4, 1$.

the case of $K_{axial} = 4$, with the peak total displacement occurring at $X/D = -0.1$ instead of in the plane strain condition far from the tunnel face. In all cases, the contribution of the axial displacement component to the total displacement response is negligible for $X/D > 2$.

4.2.6 Non-axisymmetric cases with zero antiplane shear

The general non-axisymmetric case with zero antiplane shear differs from the axisymmetric case only in the fact that the plane normal stress components are not equal, and the plane shear component can be non-zero if the principal stresses are not aligned with the coordinate axes. In total, 21 different combinations of stress ratios were considered, with $K_{max} = 2$, 3 and 4, and $K_{axial} = 0$, $\frac{1}{4}$, $\frac{1}{2}$, 1, 2, 3 and 4. A typical plot (Figure B.16) is contained in Appendix B. In addition, a numerical simulation using the estimated stress tensor for the 420 Level of the URL was conducted.

The radial displacement responses for non-axisymmetric cases are considerably more

complex than for the axisymmetric cases owing to the introduction of rotational dependency in the response. For example, Figure 4.10 illustrates the radial displacement response versus face position for nine rotation angles under stress conditions of $K = 3.93, 3.43, 1$ with σ_1 at $\theta = 14.5°$. The normalizing factor $U_{r_{max}}$ for this case was the maximum radial displacement produced by K_{max} in the plane strain solution. The responses from this case represent a forward prediction of displacements around the Mine-by Experiment test tunnel. Note that for $\theta = 90$ and 120°, the response shows negative radial displacement (i.e., divergence) far from the face. This effect is characteristic of $K_{max} > 3$.

As shown in Figure 4.10, for rotation angles not coincident with the maximum principal stress direction, the tangential displacement component contributes significantly to the total displacement response. In addition, the axial displacement response appears to be largely independent of rotation angle, suggesting that the antiplane normal stress component controls the axial displacement response.

4.3 Functional Relationships for Radial Displacement

Functional relationships can be of two general types [82]. An *approximating function* is an equation that represents x, y, z data which can be used for interpolation. What is important in this type of function is seldom the coefficient values derived from the fit or the number of coefficients, but rather the effectiveness of the fit itself. A *parametric function*, on the other hand, relates the dependent variable z to the independent variables x and y via a postulated physical relationship between them. In this case, the coefficients may be related to physically or theoretically real quantities. Both types are useful in analyzing displacement responses; the approximating function for representing and interpolating individual measured data sets, and the parametric function for establishing a general relationship between stresses, face position, rotation angle, and displacements at the tunnel wall.

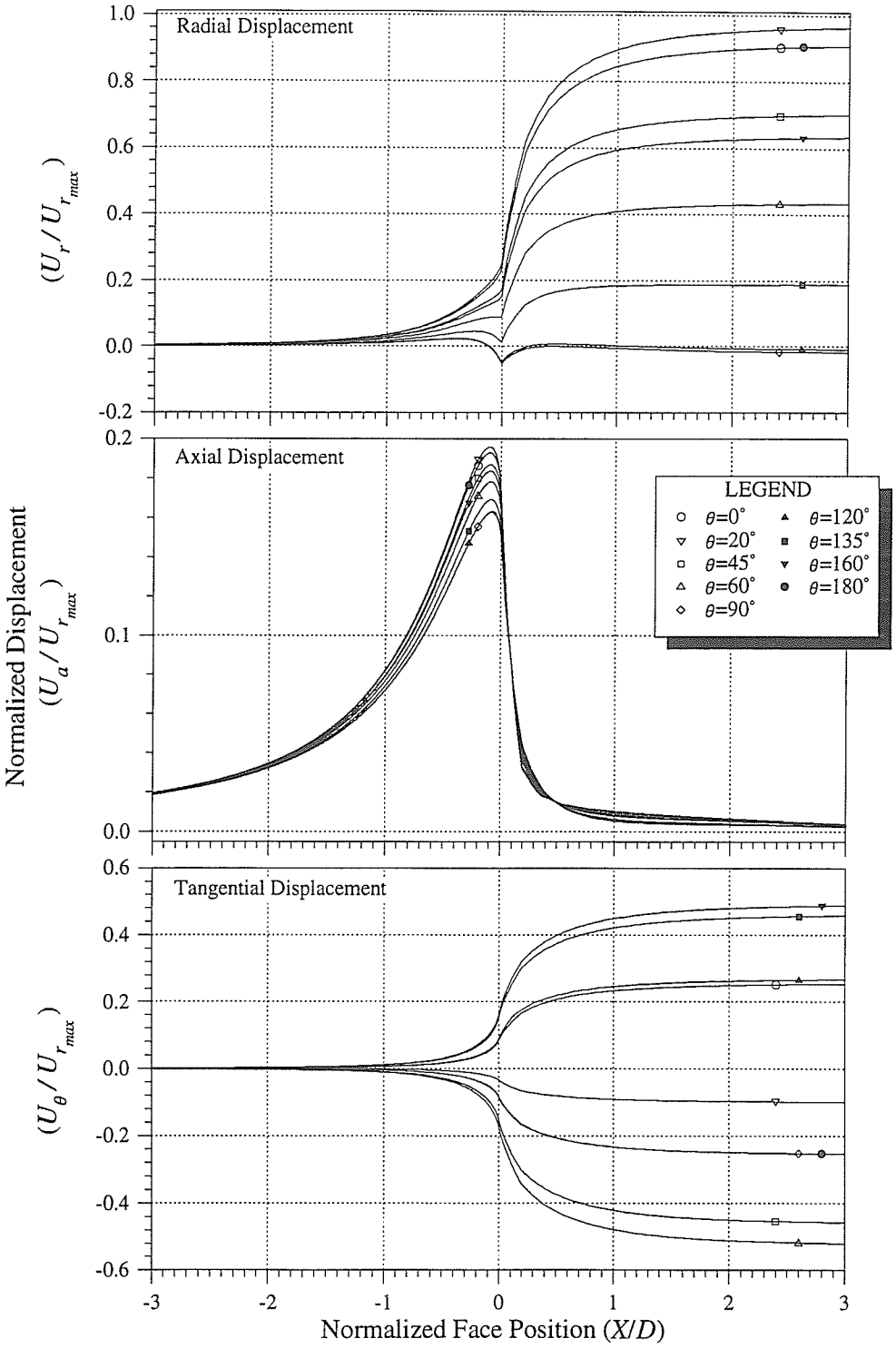

Figure 4.10: Displacement responses versus face position for $K = 3.93, 3.43, 1$ with σ_1 at $\theta = 14.5°$, representing an elastic forward prediction for the Mine-by Experiment.

4.3.1 Approximating functions

Functional relationships to describe radial displacement at the tunnel wall have focused on the special case of axisymmetric stresses, i.e., the antiplane normal stress is parallel to the tunnel axis, and the plane principal stresses are equal [147, 4, 148]. As discussed in Chapter 2, the solution by Panet and Guenot [147] is attractive in that each parameter in the equation is related to physical properties measurable in the field. It suffers, however from inaccuracy within one-half tunnel radius from the face, the area of particular interest in interpreting posterior-type measurements such as convergence readings. Barlow's extension of the solution [4] covers both the anterior and posterior domains, but is also inaccurate near the tunnel face. The Ramberg-Osgood function suggested by Pelli [148] for interpreting convergence measurements tends to show a better fit to measured data, but is unsuitable for defining the complex radial displacement response associated with non-axisymmetric cases or axisymmetric cases with a significant axial stress component. The Ramberg-Osgood function is given by

$$U_r(x) = \frac{(S_i - S_f)\,x}{\left[1 + \left|\frac{(S_i - S_f)x}{U_{r_o}}\right|^n\right]^{\left(\frac{1}{n}\right)}} + S_f x \tag{4.10}$$

where S_i and S_f are the initial and final slope of the curve, respectively; U_{r_o} is the y intercept of the asymptote with slope S_f; n is a shape parameter; and x is the face position. Among the other solutions, the sigmoid function has the desired transitional form of the radial displacement response, but has a significantly different curvature. The sigmoid function is given by

$$U_r(x) = \frac{[U_{r_{max}} - U_{r_{min}}]}{\left[1 + e^{(B_s x)}\right]^{C_s}} \tag{4.11}$$

where B_s and C_s are slope and symmetry parameters, respectively, $U_{r_{max}}$ is the radial displacement far from the face in the posterior domain, and $U_{r_{min}}$ is the radial displacement far from the face in the anterior domain.

From the results of numerical modeling and the earlier work by Barlow [4], it is clear that radial displacement at the tunnel wall cannot be described by a single continuous approximating function for all values of face position. For the general case of non-axisymmetric stress ratios and/or a significant axial stress component, the radial displacement response is best described by a piece-wise function comprising an anterior and a posterior component. The derivation of a general approximating function, capable of describing the complex radial displacement response associated with non-axisymmetric stress ratios, is given in Appendix C. The function, composed of two modified five-parameter logistic functions [82] and their second derivatives, is referred to as the *spliced logistic function*, and is given by

$$U_r(x) = y + \lambda \frac{d^2y}{dx^2} \tag{4.12}$$

where

$$y = D_l + sign(x)\, F \left[1 + \left|\frac{x}{A}\right|^B\right]^{\frac{1}{B}} \tag{4.13}$$

$$\frac{d^2y}{dx^2} = sign(x)\, \frac{F(B-1)}{|A|^B} \left\{ \left[1 + \left|\frac{x}{A}\right|^B\right]^{\left(\frac{1}{B}-1\right)} |x|^{(B-2)} \right\} - sign(x)\, \frac{F(B-1)}{|A|^{2B}} \left\{ \left[1 + \left|\frac{x}{A}\right|^B\right]^{\left(\frac{1}{B}-2\right)} |x|^{2(B-1)} \right\} \tag{4.14}$$

and

$$sign(x) = \begin{cases} 1 & x > 0 \\ 0 & x = 0 \\ -1 & x < 0 \end{cases}$$

Using X for the x-variable in the above equations, D_l is the radial displacement at $X = 0$, λ is a scaling factor, and $F = (E_l - D_l)$ in the posterior domain and $(D_l - E_l)$ in the anterior domain. The parameter E_l is defined as the radial displacement at $X = +\infty$ in the posterior domain, and at $X = -\infty$ in the anterior domain. Likewise, the parameters A and B, where A is the abscissa of a pivot point controlling the shape of the curve, and B is a slope parameter, have different values in the posterior and anterior domains. To make the function dimensionless, $U_r(x)$, D_l, and F can be normalized with respect to the maximum

radial displacement far from the face, $U_{r_{max}}$, and X can be expressed as X/D. For cases with no significant axial stress component, the scaling factor λ on the second derivative becomes zero.

This approximating function is suitable for representing displacement responses versus face position measured for a particular rotation angle, and is especially useful for interpolating sparse data sets as described by Read et al. [159]. However, it does not provide a means of describing the entire radial displacement field at the tunnel wall. In order to develop a general parametric function, the relationship between radial displacement at the tunnel wall and rotation angle θ was considered.

4.3.2 Parametric functions

Parametric functions describing *characteristic radial displacement surfaces* were derived by first considering the relationship between the radial displacement response and rotation angle for the six base cases, then examining the relationship between the function parameters and the tunnel face position. As shown in Appendix B (Section B.1), the radial displacement response versus rotation angle is harmonic with a periodicity of 180° for the plane components of stress, and 360° for the antiplane shear components. The antiplane normal stress component produces an axisymmetric response. The normalizing factor $U_{r_{max}}$ in this section is given by Equation 4.6.

Plane components

The parametric function between normalized radial displacement and rotation angle for the plane components of stress is given by

$$\frac{U_r}{U_{r_{max}}} = \alpha + \beta \cos\left[2\left(\theta - \psi\right)\right] \tag{4.15}$$

where α is the mean displacement response, β is the amplitude about the mean of the harmonic component of the displacement response, ψ is the phase constant, and θ is the rotation angle.

Based on the results from Section 4.2.3, the displacement response for the σ_{11} tensor can be used to determine the equation parameters. As shown in Appendix B (Figure B.1), the mean displacement response for the σ_{11} tensor occurs at $\theta = 45°$. Therefore, the relationship between the parameter α in Equation 4.15 and face position can be determined by finding a suitable function to describe the radial displacement response versus face position for $\theta = 45°$. The *spliced logistic function* given by Equation 4.12, with the scaling parameter $\lambda = 0$, accurately describes this relationship. Likewise, the amplitude β of the harmonic component of the displacement response is the difference between the peak radial displacement response at $\theta = 0°$ and the mean response at $\theta = 45°$. The relationship between β and face position can also be described accurately by a *spliced logistic function* with $\lambda = 0$.

The resulting parametric equation for the *characteristic radial displacement surface* produced by the σ_{11} tensor is given by

$$\frac{U_{r_{11}}}{U_{r_{max}}} = \alpha_{11} + \beta_{11} \cos\left[2\left(\theta - \psi\right)\right] \tag{4.16}$$

where

$$\alpha_{11} = D_\alpha + sign\left(x\right) F_\alpha \left[1 + \left|\frac{x}{A_\alpha}\right|^{B_\alpha}\right]^{\frac{1}{B_\alpha}} \tag{4.17}$$

$$\beta_{11} = D_\beta + sign\left(x\right) F_\beta \left[1 + \left|\frac{x}{A_\beta}\right|^{B_\beta}\right]^{\frac{1}{B_\beta}} \tag{4.18}$$

$$\psi = 0$$

and

$$sign\left(x\right) = \begin{cases} 1 & x > 0 \\ 0 & x = 0 \\ -1 & x < 0 \end{cases}$$

The parameter values in the above equations are given in Table 4.2. The associated *characteristic radial displacement surface* is shown in Figure 4.11.

As noted in Section 4.2.3, except for a 90° phase shift, the σ_{33} and σ_{11} tensors produce identical radial displacement responses. Therefore, the parametric function described by

Table 4.2: Coefficients for parametric equation describing the *characteristic radial displacement surface* produced by the σ_{11} tensor. Note that for the σ_{11} tensor, the phase shift $\psi = 0$. The coefficient of determination $r^2 = 0.9999$.

Mean Radial Displacement Component α			Harmonic Radial Displacement Component β		
Parameter	Anterior Domain	Posterior Domain	Parameter	Anterior Domain	Posterior Domain
A_α	0.1615	0.2182	A_β	0.2494	0.3241
B_α	-1.5602	-1.3371	B_β	-1.4120	-1.3072
D_α	0.1037	0.1037	D_β	0.2063	0.2063
E_α	0.0	0.3333	E_β	0.0	0.6667
F_α	0.1037	0.2296	F_β	0.2063	0.4603

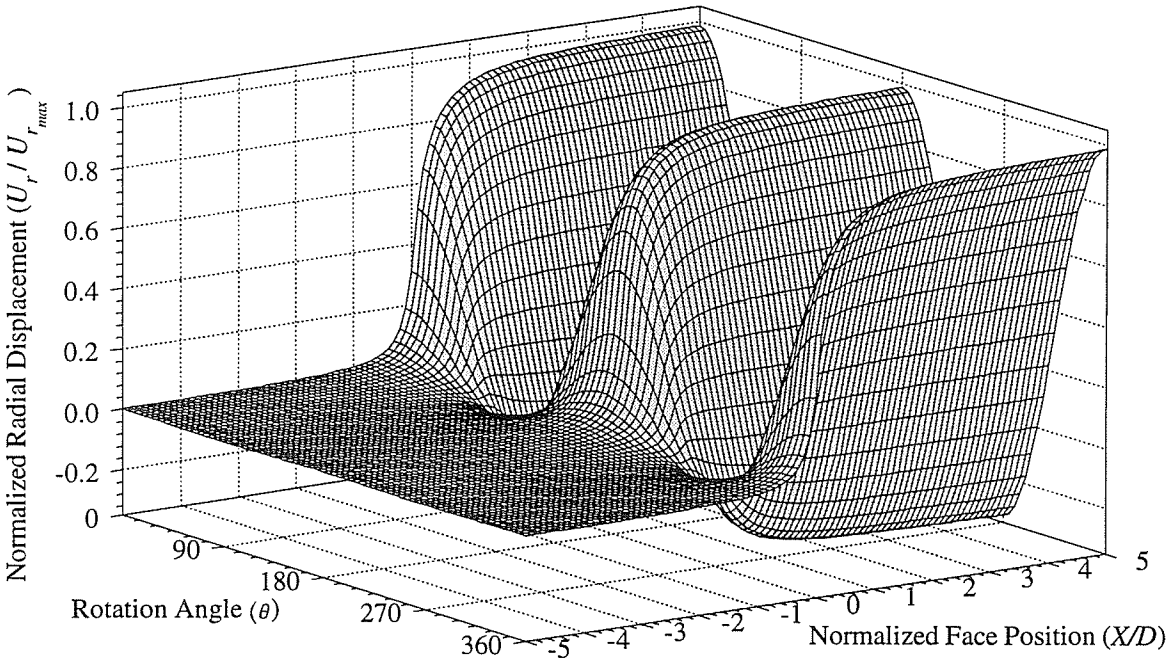

Figure 4.11: *Characteristic radial displacement surface* for σ_{11} tensor.

Equations 4.16, 4.17 and 4.18 can also be used to describe the characteristic radial displacement surface for σ_{33} if a phase shift $\psi = 90°$ is included in Equation 4.16. Likewise, the parametric function describing the radial displacement response produced by the σ_{13} tensor can be derived from Equations 4.16, 4.17 and 4.18 as

$$\frac{U_{r_{13}}}{U_{r_{max}}} = 2\beta_{11} \sin(2\theta) \tag{4.19}$$

Antiplane normal component

The radial displacement response associated with the σ_{22} tensor is unique in that it is independent of rotation angle. However, the complex shape of the response suggests that a combination of functions is required to accurately describe it. The parametric function describing the response was found to be of the form

$$\frac{U_{r_{22}}}{U_{r_{max}}} = \alpha_1 + \alpha_2 + \alpha_3 \tag{4.20}$$

where α_1, α_2 and α_3 are logistic-type functions. In this case, α_1 is restricted to the posterior domain, while α_2 and α_3 are restricted to the anterior domain. To maintain continuity in the displacement response, the y-intercepts of the three functions are related. The logistic functions are given by

$$\alpha_1 = D_{\alpha_1} + sign(x)\, F_{\alpha_1} \left[1 + \left| \frac{x}{A_{\alpha_1}} \right|^{B_{\alpha_1}} \right]^{\frac{1}{B_{\alpha_1}}} \tag{4.21}$$

$$\alpha_2 = D_{\alpha_2} + sign(x)\, F_{\alpha_2} \left[1 + \left| \frac{x}{A_{\alpha_2}} \right|^{B_{\alpha_2}} \right]^{\frac{1}{B_{\alpha_2}}} \tag{4.22}$$

$$\alpha_3 = D_{\alpha_3} + sign(x)\, F_{\alpha_3} \left[1 + \left| \frac{x}{A_{\alpha_3}} \right|^{B_{\alpha_3}} \right]^{\frac{1}{B_{\alpha_3}}} \tag{4.23}$$

and

$$sign(x) = \begin{cases} 1 & x > 0 \\ 0 & x = 0 \\ -1 & x < 0 \end{cases}$$

The parameter values for the logistic functions are given in Table 4.3. Note that the parameter $D_{\alpha_3} = D_{\alpha_1} - D_{\alpha_2}$. The associated *characteristic radial displacement surface* is shown in Figure 4.12.

Antiplane shear components

The parametric function between normalized radial displacement and rotation angle for the antiplane shear components of stress is given by

$$\frac{U_r}{U_{r_{max}}} = \beta \cos(\theta - \psi) \tag{4.24}$$

where β is the amplitude about the mean response, ψ is the phase constant, and θ is the rotation angle. Note that this equation is similar to Equation 4.15, except that the mean response is zero and the periodicity of the function is 360° rather than 180°.

Using the same approach as was used for the plane components, the radial displacement response for the σ_{12} tensor can be used to determine the equation parameters. For this case, the mean displacement response is zero and occurs at $\theta = 90°$. The amplitude β is therefore described by the radial displacement response for $\theta = 0°$. The relationship between β and face position can again be described by a *spliced logistic function* with $\lambda = 0$, given by

$$\frac{U_{r_{12}}}{U_{r_{max}}} = \beta_{12} \cos(\theta - \psi) \tag{4.25}$$

where

$$\beta_{12} = D_\beta + sign(x)\, F_\beta \left[1 + \left|\frac{x}{A_\beta}\right|^{B_\beta}\right]^{\frac{1}{B_\beta}} \tag{4.26}$$

$$\psi = 0$$

and

$$sign(x) = \begin{cases} 1 & x > 0 \\ 0 & x = 0 \\ -1 & x < 0 \end{cases}$$

The parameter values for the *spliced logistic function* are given in Table 4.4. The associated *characteristic radial displacement surface* is shown in Figure 4.13. The same function

Table 4.3: Coefficients for parametric equation describing the *characteristic radial displacement surface* produced by the σ_{22} tensor. The coefficient of determination $r^2 = 0.9993$.

Parameter	Radial Displacement Component		
	α_1	α_2	α_3
	$X/D > 0$	$X/D < 0$	$X/D < 0$
A_α	0.7032	0.9592	0.1622
B_α	-1.5660	-1.9329	-1.2281
D_α	-0.0507	0.1417	-0.1924
E_α	0.0	0.0	0.0
F_α	0.0507	0.1417	-0.1924

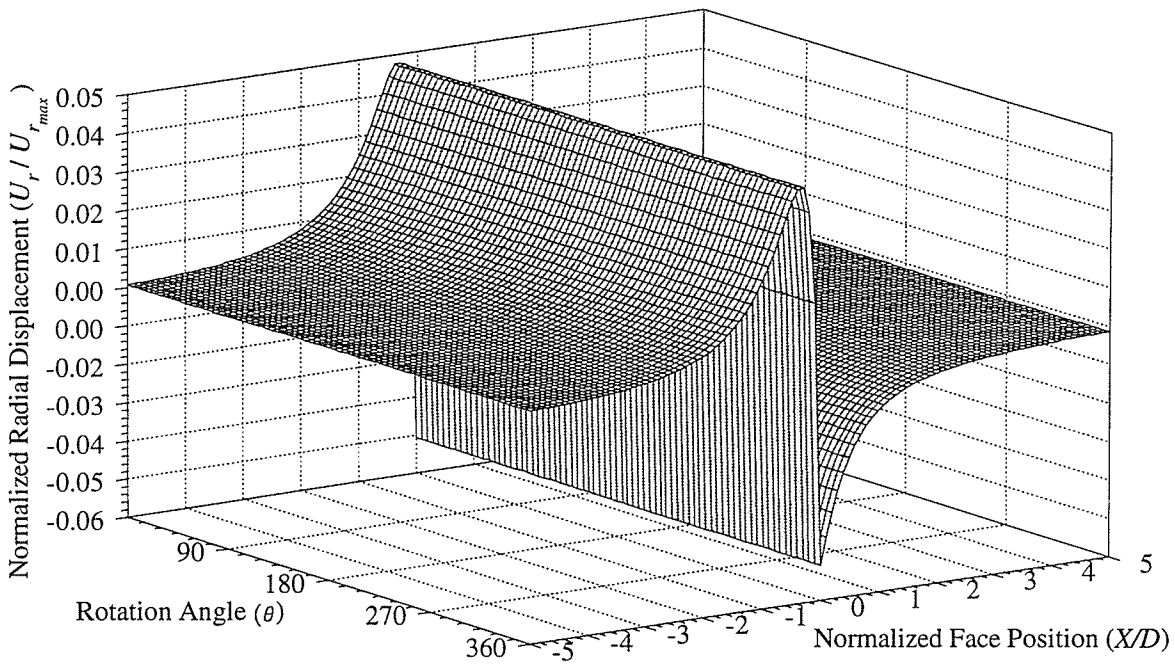

Figure 4.12: *Characteristic radial displacement surface* for σ_{22} tensor.

given by Equation 4.24 can be used with a phase shift of $\psi = 90°$ to describe the radial displacement response produced by the σ_{23} tensor.

4.3.3 Application to axisymmetric cases

The *characteristic radial displacement surfaces* for axisymmetric cases can be considered a combination of the three surfaces corresponding to the σ_{11}, σ_{33}, and σ_{22} tensors. In terms of the parametric functions associated with these surfaces, the *characteristic radial displacement surface* for the general axisymmetric case is given by

$$\frac{U_r}{U_{r_{max}}} = \underbrace{c_1\left(2\alpha_{11}\right)}_{\sigma_{11}+\sigma_{33}} + \underbrace{c_2\left(\alpha_1+\alpha_2+\alpha_3\right)}_{\sigma_{22}} \tag{4.27}$$

where the coefficients c_1 and c_2 are the stress magnitudes of σ_{11} and σ_{22} (in MPa) , respectively, multiplied by a conversion factor C_f. The conversion factor C_f in these cases is the ratio of the normalizing factor used in the partitioned stress tensor models (Equation 4.6) and $U_{r_{max}}$ used to normalize the combined axisymmetric response. The *characteristic radial displacement surface* for the case $K = 1, 4, 1$, based on results from EXAMINE^{3D}, is shown in Figure 4.14. The parametric function given by Equation 4.27 was compared to results for this case, and the coefficient of determination r^2 was found to be 0.9992.

4.3.4 Application to non-axisymmetric cases with zero antiplane shear

The *characteristic radial displacement surface* for cases where the plane stress components are unequal and the antiplane shear stress is zero, can be considered a combination of the surfaces produced by the σ_{11}, σ_{33}, σ_{13}, and σ_{22}. In terms of the parametric functions associated with these surfaces, the *characteristic radial displacement surface* for the general non-axisymmetric case with zero antiplane shear is given by

$$\begin{aligned}\frac{U_r}{U_{r_{max}}} = &\underbrace{c_1\left[\alpha_{11}+\beta_{11}\cos\left(2\theta\right)\right]}_{\sigma_{11}} + \underbrace{c_2\left[\alpha_{11}-\beta_{11}\cos\left(2\theta\right)\right]}_{\sigma_{33}} \\ &+ \underbrace{c_3\left[2\beta_{11}\sin\left(2\theta\right)\right]}_{\sigma_{13}} + \underbrace{c_4\left(\alpha_1+\alpha_2+\alpha_3\right)}_{\sigma_{22}}\end{aligned} \tag{4.28}$$

Table 4.4: Coefficients for parametric equation describing the *characteristic radial displacement surface* produced by the σ_{12} tensor. Note that for the σ_{12} tensor, the phase shift $\psi = 0$. The coefficient of determination $r^2 = 0.9996$.

Harmonic Radial Displacement Component β		
Parameter	Anterior Domain	Posterior Domain
A_β	0.6855	0.2846
B_β	-1.7715	-1.1961
D_β	0.6542	0.6542
E_β	0.0	0.0
F_β	0.6542	-0.6542

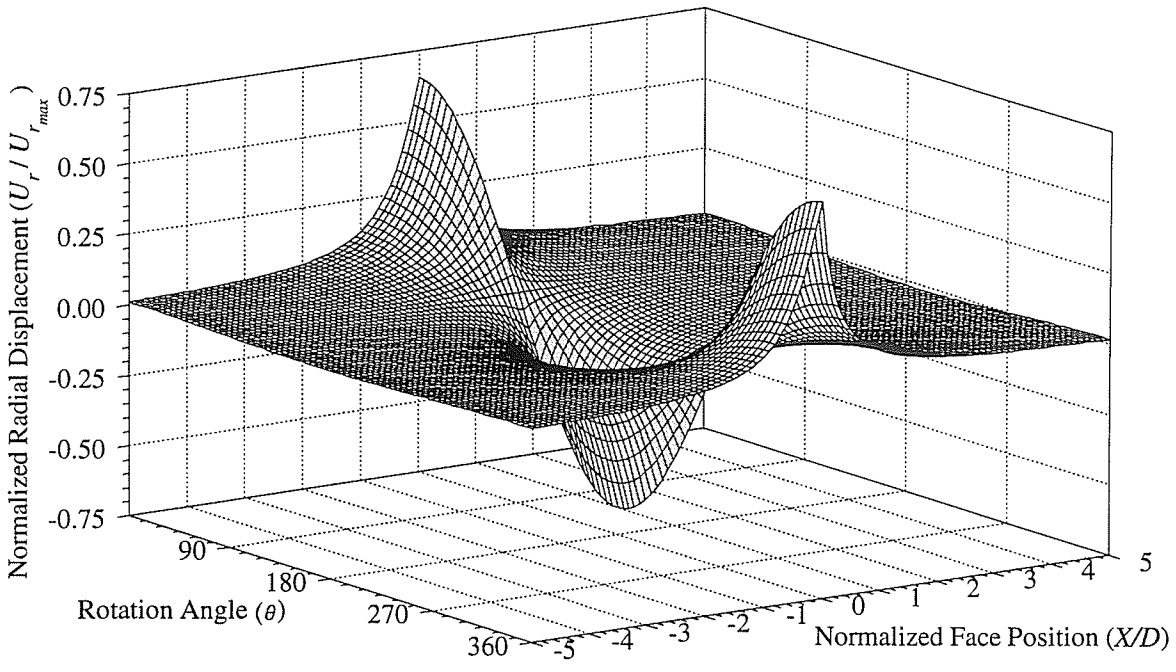

Figure 4.13: *Characteristic radial displacement surface* for σ_{12} tensor.

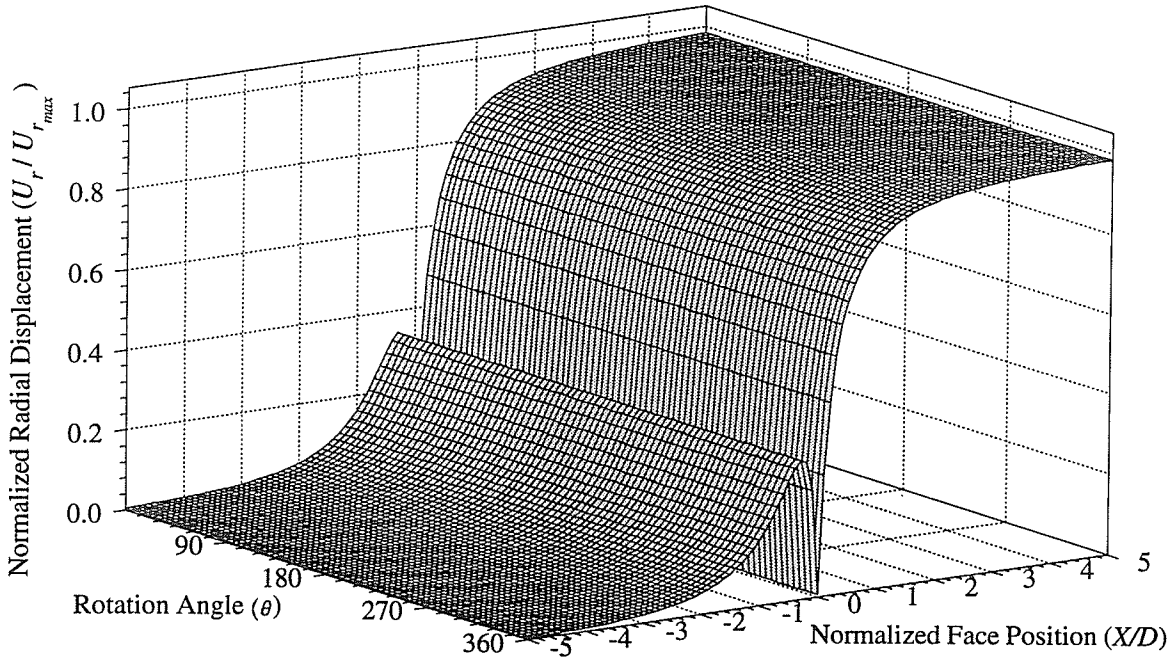

Figure 4.14: *Characteristic radial displacement surface* for $K = 1, 4, 1$.

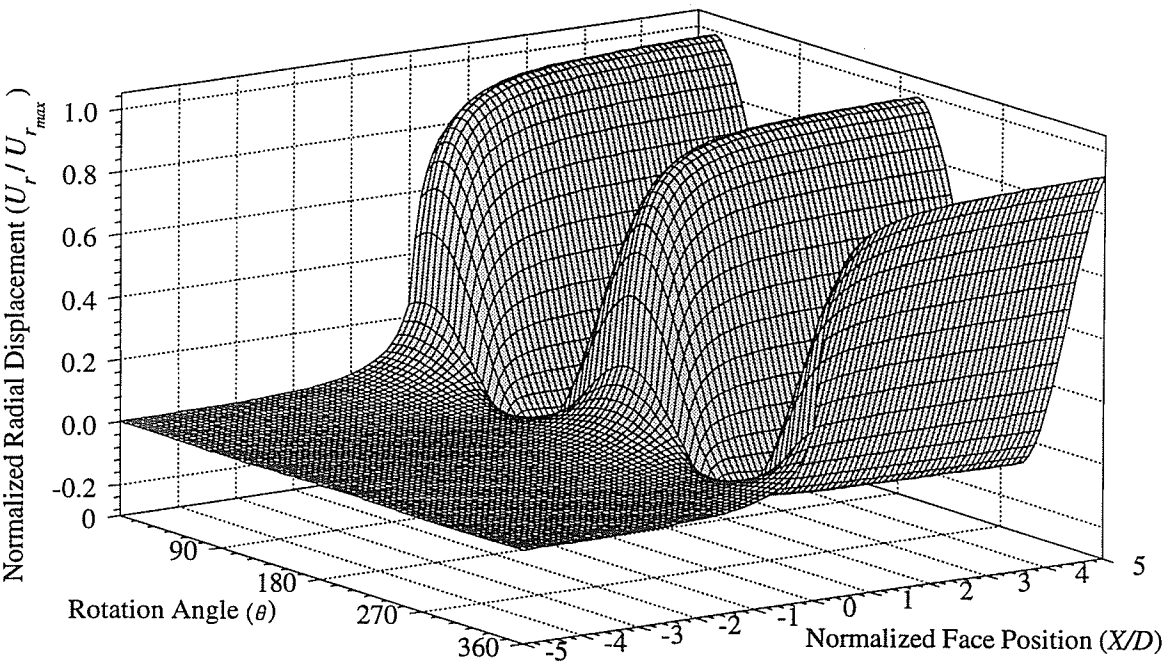

Figure 4.15: *Characteristic radial displacement surface* for $K = 3.93, 3.43, 1$ with σ_1 at $\theta = 14.5°$.

In Equation 4.28, the coefficients c_1, c_2, c_3 and c_4 are equal to the stress magnitude (in MPa) of σ_{11}, σ_{33}, σ_{13} and σ_{22}, respectively, multiplied by the conversion factor C_f. The conversion factor C_f in these cases is the ratio of the normalizing factor used in the partitioned stress tensor models (Equation 4.6) and $U_{r_{max}}$ used to normalize the combined non-axisymmetric response. The *characteristic radial displacement surface* for the case $K = 3.93, 3.43, 1$ with σ_1 at $\theta = 14.5°$, based on results from EXAMINE^{3D}, is shown in Figure 4.15. The parametric function given by Equation 4.28 was compared to results for this case, and the coefficient of determination r^2 was found to be 0.9998.

4.3.5 Application to general cases

The *characteristic radial displacement surface* for general stress cases can be considered a combination of the surfaces produced by the σ_{11}, σ_{33}, σ_{13}, σ_{22}, σ_{12}, and σ_{23} tensors. In terms of the parametric functions associated with these surfaces, the *characteristic radial displacement surface* for the general case is given by

$$\begin{aligned}\frac{U_r}{U_{r_{max}}} = &\underbrace{c_1\left[\alpha_{11} + \beta_{11}\cos(2\theta)\right]}_{\sigma_{11}} + \underbrace{c_2\left[\alpha_{11} - \beta_{11}\cos(2\theta)\right]}_{\sigma_{33}} \\ &+ \underbrace{c_3\left[2\beta_{11}\sin(2\theta)\right]}_{\sigma_{13}} + \underbrace{c_4\left(\alpha_1 + \alpha_2 + \alpha_3\right)}_{\sigma_{22}} \\ &+ \underbrace{c_5\left[\beta_{12}\cos(\theta)\right]}_{\sigma_{12}} + \underbrace{c_6\left[\beta_{12}\sin(\theta)\right]}_{\sigma_{23}}\end{aligned} \tag{4.29}$$

In Equation 4.29, the coefficients c_1, c_2, c_3, c_4, c_5 and c_6 are equal to the stress magnitude (in MPa) of σ_{11}, σ_{33}, σ_{13}, σ_{22}, σ_{12}, and σ_{23}, respectively, multiplied by the conversion factor C_f. The conversion factor C_f in these cases is the ratio of the normalizing factor used in the partitioned stress tensor models (Equation 4.6) and $U_{r_{max}}$ used to normalize the general combined response.

4.3.6 Back analysis of stresses using tunnel wall displacements

Traditionally, back analysis of stresses from tunnel wall displacements has involved using the radial displacements measured in the posterior domain in combination with the plane strain

solution given by Equation 4.2, or a transformed expression in terms of x, y, z components (Chandler, pers. comm.) given by

$$U_r = \frac{a}{4G}\left\{\left[1 + (3 - 4\nu)\cos 2\theta\right]\sigma_x + \left[1 - (3 - 4\nu)\cos 2\theta\right]\sigma_y + \left[2\,(3 - 4\nu)\sin 2\theta\right]\tau_{xy}\right\} \quad (4.30)$$

Equation 4.30 represents a linear combination of three unknowns corresponding to σ_x, σ_y and τ_{xy}, and is of the general form

$$U_r = \sigma_x f_1(\theta) + \sigma_y f_2(\theta) + \tau_{xy} f_3(\theta) \quad (4.31)$$

Using a least-squares approach [118] (Appendix D), the values of the stress components can be estimated from a minimum of three measurements of the total radial displacement induced by excavating the tunnel, taken at different rotation angles. However, a better estimate can be obtained if the system of equations is overdetermined.

This methodology has several limitations. First, it assumes that the tunnel wall in the posterior domain deforms elastically, implying no excavation damage development. It is therefore only applicable to circular tunnels in elastic ground. Second, it assumes that absolute displacements are either measured by anterior instruments, or estimated from the residual displacements recorded by posterior instruments. However, as shown in Section 4.2.5, the proportion of the absolute displacement occurring in the anterior domain (and therefore missed by posterior instruments) is a function of the axial stress component. For non-axisymmetric cases, the proportion is also a function of rotation angle. Consequently, a conundrum exists where knowledge of the anterior proportion of the radial displacement response is required to estimate the *in situ* stresses, and knowledge of the *in situ* stresses is needed to estimate the anterior proportion of the radial displacement response. Therefore, adjustment of residual or partial displacement measurements from posterior-type instruments to absolute displacements cannot be accomplished by simply assuming a constant proportion of the response is missed ahead of the face for all rotation angles. Finally, the approach only measures the plane components of the stress tensor, and assumes that the

tunnel is parallel to one of the principal stress directions. If this condition does not apply, multiple orthogonal tunnels are required to estimate the complete stress tensor [74].

An alternative methodology is to use the expression given by Equation 4.29 and the least-squares method to estimate all six components of the *in situ* stress tensor from tunnel wall displacements taken near the tunnel face. Equation 4.29 represents a linear combination of six unknowns of the form

$$\frac{U_r}{U_{r_{max}}} = c_1 f_1(x,\theta) + c_2 f_2(x,\theta) + c_3 f_3(x,\theta) + c_4 f_4(x) + c_5 f_5(x,\theta) + c_6 f_6(x,\theta) \quad (4.32)$$

where functions f_{1-6} are described by the *characteristic radial displacement surfaces* for the partitioned stress tensor components. If $U_{r_{max}}$ is described by Equation 4.6, then the coefficients c_{1-6} correspond directly to the stress components (in MPa) σ_{11}, σ_{33}, σ_{13}, σ_{22}, σ_{12}, and σ_{23}, respectively. By using m radial displacement measurements at various values of x and θ, a system of m equations can be defined, and used with the least-squares technique to determine the complete stress tensor.

Because the maxima and minima of the radial displacement responses for the antiplane components occur near the tunnel face, back analysis of the antiplane stress components is only possible if measurements from the region $-1 \leq X/D \leq 1$ account for a large proportion of the data set. Measurements outside this region in the posterior domain will help establish the plane components, but will not constrain the estimates of antiplane components. Supplemental equations relating the various stress components can also be added to the analysis to provide additional constraint on the estimated tensor. Weighting of a particular measurement or constraint can be accomplished by repeating the equation associated with the measurement within the system of equations.

Wall displacements from anterior instruments

In highly stressed ground, measurements from anterior instruments are least likely to be affected by large-scale excavation damage development in the posterior domain because of

the restraint provided by the unexcavated rock mass ahead of the face. The assumption that the rock mass behaves essentially elastically in this area is explored further in Chapter 6. Radial displacement measurements at the design perimeter in this region, therefore, represent the best data for use with the back analysis method. In addition, by choosing values of x corresponding approximately to the maximum, neutral and minimum points on the radial displacement response associated with the normal antiplane stress component, the estimate of σ_{22} can be constrained. The *spliced logistic function* is useful in this respect for interpolating displacement values from the measured radial displacement response versus face position.

NEARFACE, a spreadsheet of the least-squares matrix operations (Appendix D), was developed and tested using displacement results from an EXAMINE^{3D} model of the estimated stress conditions at the 420 Level of the URL. A total of 238 radial displacement measurements at the tunnel wall from $-1 \leq X/D \leq 1$ were generated. Two back analyses of the far-field *in situ* stress tensor were conducted, one using all of the data, the other using just the subset for $-1 \leq X/D \leq 0$. As shown in Table 4.5, the estimated far-field *in situ* stress tensor compares very closely to the tensor used in the model in both cases. The coefficient of determination was further improved by constraining the σ_1/σ_2 ratio to 1.146, and giving the constraint equation a weight of 10, i.e., it was repeated ten times. The use of this particular constraint assumes a knowledge of the orientation of the maximum principal stress.

Wall displacements from posterior instruments

The radial displacement response measured by posterior extensometers can be considered a partial *characteristic radial displacement surface.* The functions given in Equation 4.29 can be modified to reflect this fact. In the α and β expressions described by *spliced logistic functions* for each component of the partitioned stress tensor, the y-intercept parameter D_l is set to zero. This change results in new functions $f_{1_e-6_e}$. For convergence measurements,

Table 4.5: Results from stress back analyses using 238 wall displacement measurements from anterior extensometers, showing a comparison with the actual stress tensor used in the model. The number of constraint equations added to each analysis is given as C.

Stress Component	Stress Magnitude (MPa)				
	Actual Values	Estimated Values			
		$-1 \leq X/D \leq 1$		$-1 \leq X/D \leq 0$	
		$(C = 0)$	$(C = 10)$	$(C = 0)$	$(C = 10)$
σ_{11}	52.43	52.36	52.42	52.05	51.84
σ_{33}	16.57	16.65	16.72	16.63	16.57
σ_{13}	9.94	9.86	9.86	9.83	9.78
σ_{22}	48.00	46.23	47.94	45.20	47.42
σ_{12}	0.00	-0.01	-0.01	0.00	0.01
σ_{23}	0.00	0.00	0.00	0.00	0.00
r^2		0.9988	1.0000	0.9969	0.9997

the functions $f_{1_e-6_e}$ require a further modification to account for the relative nature of the measurement, i.e., the relative displacement between pins on opposite sides of the tunnel is measured rather than the absolute displacement of individual convergence pins. To this end, the functions $f_{1_e-6_e}$ for posterior extensometers on opposite sides of the tunnel are added to define new functions $f_{1_c-6_c}$. A direct consequence of this modification is that the new functions $f_{5_c-6_c}$ associated with the antiplane shear components of the stress tensor are zero because of the antisymmetric nature of the radial displacement responses produced by these components. In other words, convergence measurements are unaffected by antiplane shear stresses, and therefore cannot be used to back calculate these components of the tensor.

Although measurements of radial displacement at the tunnel wall taken with posterior instruments can be used in a similar fashion as anterior measurements, there are some limitations in back analyzing the *in situ* stress tensor. Most notably, if excavation damage occurs in the tunnel, the material behaviour in the damage zone may be non-linear and/or non-elastic. Consequently, only the segment of tunnel between the face and the start of the excavation damage can be used in the stress determination. However, there are no

Table 4.6: Results from stress back analysis using 102 posterior wall displacement measurements, showing a comparison with the actual stress tensor used in the model. The number of constraint equations added to each analysis is given as C.

Stress Component	Stress Magnitude (MPa)		
	Actual Values	Estimated Values $0 \leq X/D \leq 1$	
		$(C = 0)$	$(C = 10)$
σ_{11}	52.43	50.99	52.18
σ_{33}	16.57	15.40	16.58
σ_{13}	9.94	9.81	9.82
σ_{22}	48.00	63.11	47.74
σ_{12}	0.00	-0.01	-0.01
σ_{23}	0.00	0.00	0.00
r^2		0.9375	1.0000

characteristic points in the posterior domain for the radial displacement response associated with the antiplane normal stress component that allow its independent determination, i.e, its shape is similar to that for σ_{11} and σ_{33}. Therefore, additional information from other orthogonal tunnels must be used to develop supplemental equations that constrain the value of c_4 relative to c_1 and c_3.

Using the EXAMINE^{3D} model described in the previous section, 102 posterior radial displacement data, typical of measurements taken with extensometers installed from within the tunnel, were generated for the region $0 \leq X/D \leq 1$. Results of the stress back analysis using the data with no constraints, and with a constraint on the σ_1/σ_2 ratio, are shown in Table 4.6. Clearly, without the additional constraint on σ_2, the estimate of the antiplane normal stress component is relatively poor compared to that for the anterior instruments.

4.4 Displacement as a Function of Radial Distance

As shown in the previous section, back analysis of the *in situ* stress tensor can be improved when anterior extensometers are used to measure displacement at the tunnel wall. Further improvement in the method can be achieved if the radial displacement responses versus

radial distance measured by the extensometers are also considered. The effect of radial distance from the tunnel centre on the measured displacement response was studied using a three-dimensional boundary element model. Tangential and axial displacement responses were also considered in a qualitative manner. Employing the concept of the partitioned stress tensor, the displacement responses versus radial distance were determined for the six base cases. Results of the investigation are contained in Appendix B (Section B.4).

4.4.1 Model description

The three-dimensional model used in the investigation is shown in Figure 4.16. The closed cylinder representing the tunnel is the same as in the previous study, 3.5 m in diameter,

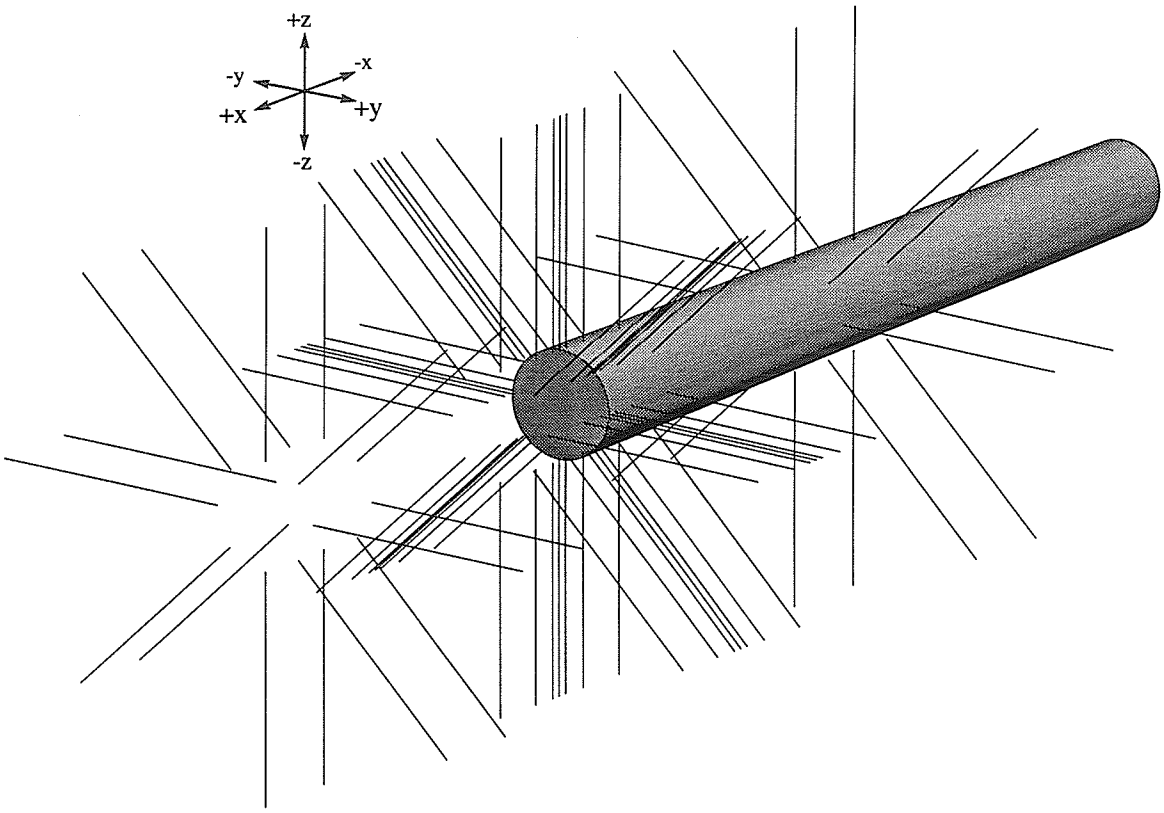

Figure 4.16: Model geometry used in EXAMINE^{3D} to study the effects of radial distance on the displacement response. Grid lines are located at θ = 0, 45, 90, 135, 180, 225, 270 and 335°.

with a length to diameter ratio of ten to minimize end effects. The radial grid lines are located within five tunnel diameters of the face at $X/D = -5$, -4, -1, -0.4, -0.1, 0, 0.1, 0.4, 1, 4, and 5. Field points in each radial gridline were located at r/a = 1.005, 1.075, 1.275, 1.50, 1.75, 2.00, 2.25, 2.75, 3.50, 5.00, 7.50 and 10.75. A total of 1056 field grid points were used. The boundary element mesh on the cylinder surface is not shown in Figure 4.16, but contained 3772 linear elements. The conventions used in the study were the same as those described in Section 4.2.1.

4.4.2 Displacement responses versus radial distance

With reference to the results in Appendix B (Section B.4), the displacement response versus radial distance plots related to the σ_{11}, σ_{13}, σ_{22} and σ_{12} tensors typify the responses for the plane and antiplane components of the partitioned stress tensor. For the σ_{11} tensor, the radial displacement response for $\theta = 0°$ (Figure 4.17) shows that the radial displacement gradient near the design perimeter of the tunnel is positive, i.e., compressive, in the anterior domain, becoming negative, i.e., extensional, in the posterior domain. The axial displacement response indicates that the maximum axial displacement occurs approximately one tunnel radius from the wall at $X/D = 0.0$, with opposite sign to the axial displacement occurring at the wall. The tangential response is zero. For $\theta = 45$ and 135°, the radial displacement responses are similar in shape to those for $\theta = 0°$, but the magnitudes are reduced. The axial response, however, shows that the peak displacement occurs at the tunnel wall, approaching zero with increasing radial distance. The tangential displacement response also has a similar shape to the radial displacement response, except for a sign reversal for $\theta = 45°$. For $\theta = 90°$, the radial and axial responses have similar shapes, showing the peak displacement occurring at about 0.25 tunnel radii from the tunnel wall. This result implies a zone of radial extension near the tunnel wall, changing to radial compression for $r/a \geq 0.25$. The tangential displacement for $\theta = 90°$ is zero. Plots for σ_{33} are identical to those for σ_{11}, but with a phase shift of 90°.

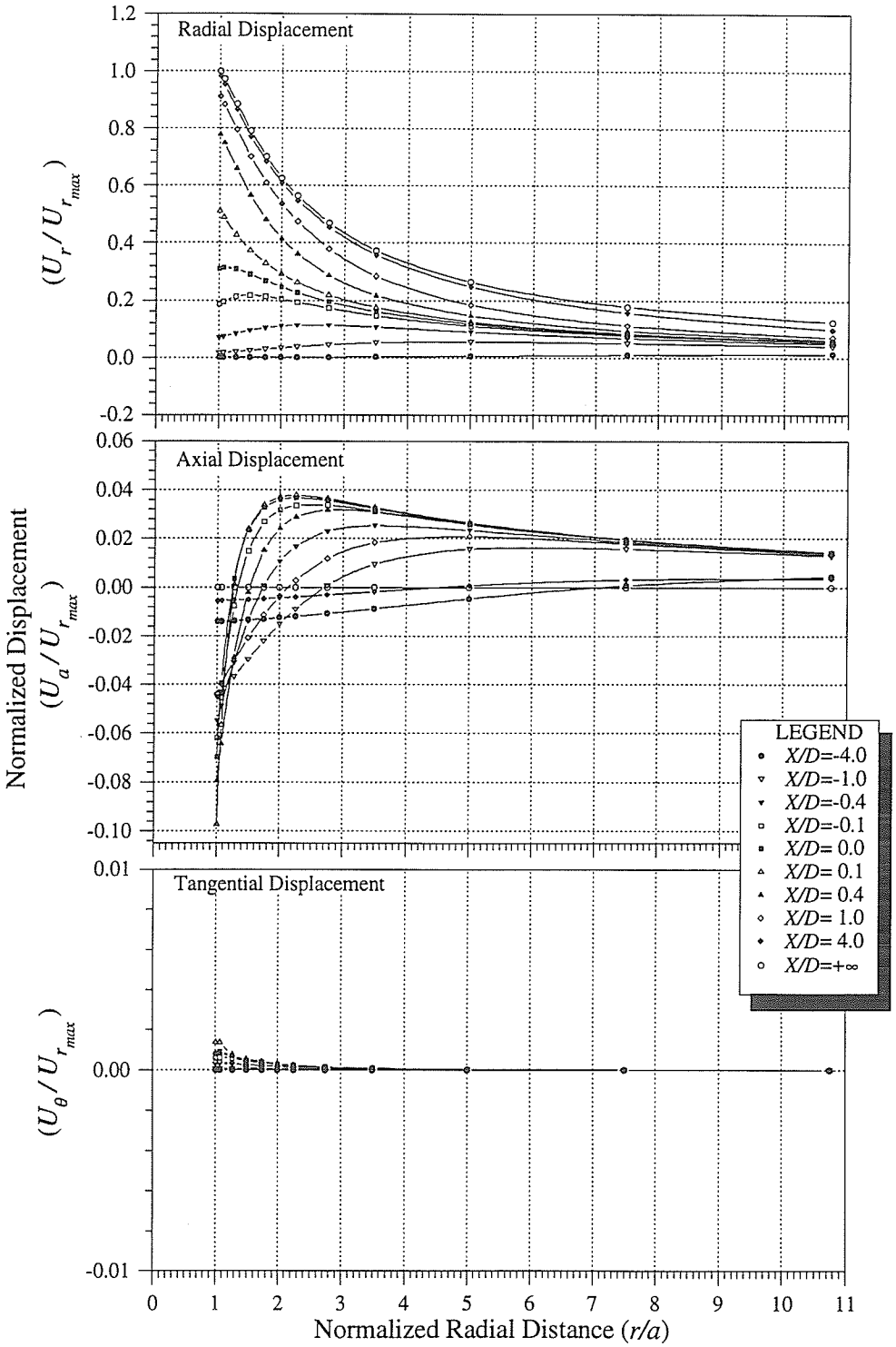

Figure 4.17: Displacement response versus radial distance for σ_{11} tensor, $\theta = 0°$.

For the σ_{13} tensor, the plane shear case, the plots for $\theta = 0$ and 90° are identical except for a sign reversal. The same is true for the plots for $\theta = 45$ and 135°. No radial or axial displacement responses were generated at $\theta = 0$ and 90°. The tangential displacement response shows a decrease in tangential displacement with increasing radial distance from the tunnel wall. For $\theta = 45$ and 135°, the tangential displacement is zero. For $\theta = 45°$, the radial displacement response is similar to that for the σ_{11} tensor, with radial compression near the design perimeter in the anterior domain, changing to radial extension in the posterior domain. The axial displacement shows a peak at about 0.5 radii from the tunnel wall for $X/D = 0.0$. The opposite radial and axial displacement responses occurs at $\theta = 135°$.

The axisymmetric displacement responses for the σ_{22} tensor are somewhat more complicated than those for the plane components. The radial displacement response shows that the peak displacement occurs at, or within 0.5 tunnel radii of, the tunnel wall, decreasing with increasing radial distance. The axial displacement response generally shows peak displacement at the tunnel wall. There is no tangential displacement associated with the σ_{22} tensor.

The σ_{12} tensor produces displacement responses similar in shape to the radial displacement response produced by the σ_{11} tensor. In contrast, though, the responses for $\theta = 0$ and 180° are identical except for a sign reversal, both producing zero tangential displacement. Likewise, the responses for $\theta = 90$ and 270° are identical except for a sign reversal, with zero radial and axial displacement responses. The responses for the σ_{23} tensor are identical, but with a phase shift of 90°.

4.4.3 Approximating functions

In the plane strain condition far from the tunnel face, the equation relating radial displacement and radial distance is of the general form

$$\frac{U_r}{U_{r_{max}}} = \frac{A}{R} + \frac{B}{R^3} \tag{4.33}$$

where A and B can be obtained from Equation 4.2, and R is the radial distance from the tunnel centre r normalized to the tunnel radius a. However, from the modeling study, it was found that, within the region $-5 \leq X/D \leq 5$, Equation 4.33 cannot be used to describe the radial displacement response versus radial distance. The complicated induced stresses within this region necessitate a function with more degrees of freedom to closely approximate the displacement response. By considering Equation 4.33 as part of an inverse polynomial series of the form

$$\frac{U_r}{U_{r_{max}}} = \sum_{i=1}^{n} \frac{A_i}{R^i} \tag{4.34}$$

where A_i are scalar coefficients, it was determined that $n = 5$ was sufficient to match the various radial displacement responses around a cylindrical tunnel. In the region $-0.4 \leq X/D \leq 0.4$, the number of terms n can be reduced to 3 with no appreciable decrease in the goodness-of-fit. The unique property of this type of function is that at $R = 1$ the normalized radial displacement is equal to the sum of the coefficients A_i.

4.4.4 Parametric functions

Parametric functions describing the radial displacement versus radial distance were developed in similar fashion to those describing the tunnel wall displacement with face position, by investigating the displacement responses associated with individual components of the partitioned stress tensor. From the investigation, it was found that the radial displacement resulting from the six partitioned tensors at a particular position X/D relative to the tunnel face can be described by

$$\begin{aligned}\frac{U_r}{U_{r_{max}}} = &\underbrace{c_1\left[\alpha_{11} + \beta_{11}\cos(2\theta)\right]}_{\sigma_{11}} + \underbrace{c_2\left[\alpha_{11} - \beta_{11}\cos(2\theta)\right]}_{\sigma_{33}} \\ &+ \underbrace{c_3\left[2\beta_{11}\sin(2\theta)\right]}_{\sigma_{13}} + \underbrace{c_4\left(\alpha_{22}\right)}_{\sigma_{22}} \\ &+ \underbrace{c_5\left[\beta_{12}\cos(\theta)\right]}_{\sigma_{12}} + \underbrace{c_6\left[\beta_{12}\sin(\theta)\right]}_{\sigma_{23}}\end{aligned} \tag{4.35}$$

In Equation 4.35, α_{11}, β_{11}, α_{22} and β_{12} are all of the form given by Equation 4.34

with $n = 3$ within the region $-0.4 \leq X/D \leq 0.4$. Therefore, there are 12 coefficients to determine at each face position X/D to describe the complete radial displacement response versus radial distance. The coefficients related to the σ_{11} tensor were found by recognizing that α_{11} is given by the response at $\theta = 45°$, and that β_{11} is the difference in the responses for $\theta = 0°$ and $\theta = 45°$. Likewise, α_{22} was determined by curve-fitting the axisymmetric radial displacement response produced by the σ_{22} tensor, and β_{12} was found from the difference between the responses for $\theta = 0°$ and $\theta = 90°$ related to the σ_{12} tensor. The six unknowns c_{1-6} have the same definition as in Section 4.3.

4.4.5 Back analysis of stresses using radial extensometer data

An attempt was made to relate the 12 coefficients at several face positions X/D, but it was not possible to develop a general four-dimensional function relating radial displacement, rotation angle, face position and radial distance. As an alternative, the 12 coefficients for the six functions in Equation 4.35 were determined at five face positions: $X/D = -0.4$, -0.1, 0, 0.1 and 0.4 (Table 4.7).

Using these coefficients and their related functions, the least-squares matrix operation can be applied to anterior extensometer measurements. These displacement measurements can be treated in two ways: either by using individual data points to evaluate the six functions in Equation 4.35 at specific values of r and θ, or by fitting a three-component approximating function of the form given by Equation 4.34 to the radial displacement response versus radial distance for each extensometer string. The first approach generates the same number of equations as there are data points, and weights each equation equally. The individual data points within each extensometer can be given different weights, however, by duplicating the equation associated with a given point in the least-squares operations. The second approach generates three equations per extensometer by equating the coefficients for like values of i, and therefore weights each extensometer equally. In this approach, data points can be weighted differently in the curve-fitting process to reflect the degree of

Table 4.7: Coefficients for radial displacement versus radial distance relationship at five face positions.

X/D	Stress Component	Coefficient					
		A_{1_α}	A_{2_α}	A_{3_α}	A_{1_β}	A_{2_β}	A_{3_β}
-0.4	σ_{11}	0.16398	-0.31322	0.16253	0.47221	- 0.78082	0.36698
	σ_{22}	-0.03828	0.20895	-0.12166	-	-	-
	σ_{12}	-	-	-	0.62975	-0.13572	-0.17374
-0.1	σ_{11}	0.16940	-0.13616	0.01981	0.48948	- 0.40147	0.04170
	σ_{22}	-0.00979	-0.02801	0.05548	-	-	-
	σ_{12}	-	-	-	0.51860	0.38300	-0.32683
0.0	σ_{11}	0.16343	-0.05508	-0.00394	0.47141	- 0.18398	-0.08200
	σ_{22}	-0.02103	0.01009	-0.03731	-	-	-
	σ_{12}	-	-	-	0.57078	0.12493	-0.04398
0.1	σ_{11}	0.17067	-0.04119	0.05548	0.47115	- 0.06017	-0.08213
	σ_{22}	0.00722	-0.14289	0.08844	-	-	-
	σ_{12}	-	-	-	0.50707	0.43688	-0.47057
0.4	σ_{11}	0.15446	0.22335	-0.09864	0.43503	0.55103	-0.48399
	σ_{22}	-0.02745	-0.09091	0.09422	-	-	-
	σ_{12}	-	-	-	0.67066	-0.42177	-0.02677

confidence in the measurement, and equations for individual extensometers can be repeated to weight them more heavily in the best-fit determination.

Using the EXAMINE^{3D} model of the estimated stress conditions at the 420 Level of the URL, 120 typical anterior extensometer measurements were generated for the region $-1 \leq X/D \leq 1$. Two back analyses of the far-field *in situ* stress tensor were conducted, one using all the data, the other using just the subset for $-1 \leq X/D \leq 0$. As shown in Table 4.8, the estimated far-field *in situ* stress tensor compares very closely to the tensor used in the model in both cases. The use of a constraint on the σ_1/σ_2 ratio further improved the estimate of σ_{22}, although only marginally when the entire region $-1 \leq X/D \leq 1$ was considered. A combined back analysis was also conducted using the measurements from simulated anterior extensometers and posterior convergence arrays. The results from this study are contained in Table 4.9.

Table 4.8: Results from stress back analyses using 120 radial displacement measurements from anterior extensometers, showing a comparison with the actual stress tensor used in the model. The number of constraint equations added to each analysis is given as C.

Stress Component	Stress Magnitude (MPa)				
	Actual Values	Estimated Values			
		$-1 \leq X/D \leq 1$		$-1 \leq X/D \leq 0$	
		$(C = 0)$	$(C = 10)$	$(C = 0)$	$(C = 10)$
σ_{11}	52.43	52.16	52.52	52.40	52.50
σ_{33}	16.57	16.37	16.77	16.56	16.67
σ_{13}	9.94	9.96	9.95	9.92	9.91
σ_{22}	48.00	45.78	48.04	47.05	48.00
σ_{12}	0.00	0.02	0.02	0.00	0.00
σ_{23}	0.00	0.03	0.03	0.02	0.02
r^2		0.9981	1.0000	0.9997	1.0000

4.5 Effect of Face Shape

Most tunnel faces show some amount of curvature intermediate between the flat and hemispherical cases, which can affect both the displacement response near the tunnel face through stress redistribution, and the definition of face position relative to the fixed instrument locations. Aside from a few studies looking at hemispherically-ended boreholes, e.g., [80, 185, 175, 101], most studies related to displacements and stresses around the tunnel face have assumed the face to be perfectly planar. An axisymmetric numerical modeling study was undertaken to assess the significance of a non-planar face in the context of conducting stress back analysis near the tunnel face.

4.5.1 Model geometry

The study considered four face shapes (flat, filleted, curved and hemispherical) under seven different axial stress ratios ($K_{axial} = 0, \frac{1}{4}, \frac{1}{2}, 1, 2, 3$ and 4). The face shapes were chosen to cover a broad range, with the flat and hemispherical faces representing the two bounding cases for the study. The filleted case is a slight modification to the flat face, replacing the sharp transition at the face edge with a curved transition of normalized radius $r/a = 0.143$.

Table 4.9: Results from stress back analyses using 460 radial displacement measurements from anterior extensometers and convergence arrays, showing a comparison with the actual stress tensor used in the model. The number of constraint equations added to each analysis is given as C.

Stress Component	Stress Magnitude (MPa)		
	Actual Values	Estimated Values $0 \leq X/D \leq 1$	
		$(C = 0)$	$(C = 10)$
σ_{11}	52.43	52.36	52.38
σ_{33}	16.57	16.62	16.65
σ_{13}	9.94	9.87	9.87
σ_{22}	48.00	46.85	47.85
σ_{12}	0.00	0.00	0.00
σ_{23}	0.00	0.01	0.01
r^2		0.9995	1.0000

The curved shape, by contrast, is characterized by a circular arc with a radius greater than that of the tunnel, centred on the tunnel axis. Two curved faces were considered for the study, one with a maximum normalized deviation between the axial position of the edge and centre of the tunnel $d/D = 0.143$ (representative of typical faces in the URL shaft excavation), the second with $d/D = 0.071$ (representative of the maximum deviation noted in the Mine-by Experiment test tunnel excavation). To maintain clarity in the plots, only displacement responses from the second curved case are shown.

Typical meshes used in the study, shown in Figure 4.18, were more dense near the tunnel face to provide better resolution in the region of large displacement gradients. Quadrilateral and triangular elements with constant elastic properties and a linear stress-strain relationship were used in all cases. To minimize boundary effects, the horizontal and vertical dimensions of the mesh were greater than eight tunnel diameters.

4.5.2 Boundary conditions and material properties

The boundary conditions were imposed by first initializing the stresses in the original mesh elements to the specific stress state under investigation, then applying a constant stress

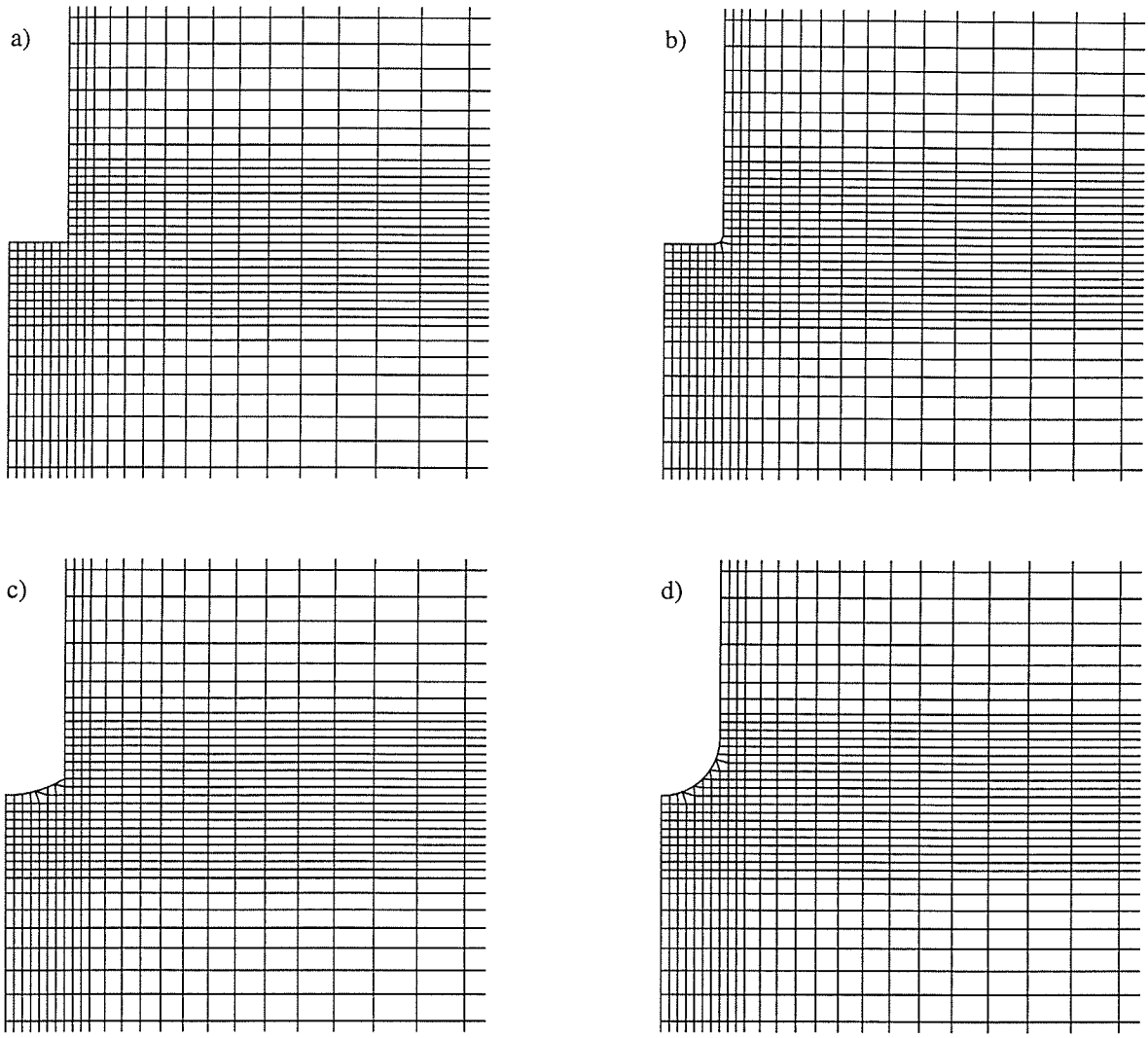

Figure 4.18: Mesh geometries used in axisymmetric studies with FLAC to analyze effects of face shape and axial stress ratio on the radial displacement response. Note that only a portion of the entire mesh is shown in each case, and that the left edge of each mesh is an axis of rotational symmetry. The cases shown are for a) flat, b) filleted, c) curved and d) hemispherical faces.

boundary at the vertical edge opposite the symmetry axis, and along the upper and lower edges of the mesh. Excavation was simulated by removing the elements within the design perimeter of the opening, and then allowing the stresses and displacements to equilibrate through approximately 500 time steps. The material properties specified in the analyses were bulk modulus (33 GPa), shear modulus (25 GPa) and density (2650 kg/m^3).

4.5.3 Displacement responses for different face shapes

Results from the study for each face shape under three of the stress conditions considered are shown in Figure 4.19 plotted as normalized radial displacement $U_r/U_{r_{max}}$ versus normalized face position X/D. In these cases, the deepest point on the tunnel face was used as the reference position of the face to determine X/D.

Referring to Figure 4.19, the responses for the flat and hemispherical faces can be considered representative of the upper and lower geometrical bounds for the problem. For the flat shape, the radial displacement response is focused closer to the face, and has a larger gradient in the posterior region, than the hemispherical shape. The filleted and curved faces represent intermediate cases, with the response for the filleted face closely resembling that for the flat face, and the curved face response approximating the average response of the flat and hemispherical faces.

The effect of axial stress ratio is also evident in Figure 4.19. For the case of zero axial stress ratio ($K = 1, 0, 1$), all four face shapes produce a similar response, but with a shift to the right with more pronounced face curvature. The possibility that this shift is an artifact of the choice of reference point for face position is considered in the next section. As the axial stress ratio increases, the shapes of the different displacement responses vary. In all cases, the gradient of the response in the near-face regime decreases with increasing axial stress ratio, resulting in a reversal in gradient in the anterior domain close to $X/D = 0$ above $K = 1, 1, 1$. The reversal is most pronounced for the flat, filleted and curved faces, with the effect decreasing as the face shape approaches hemispherical. The effect becomes

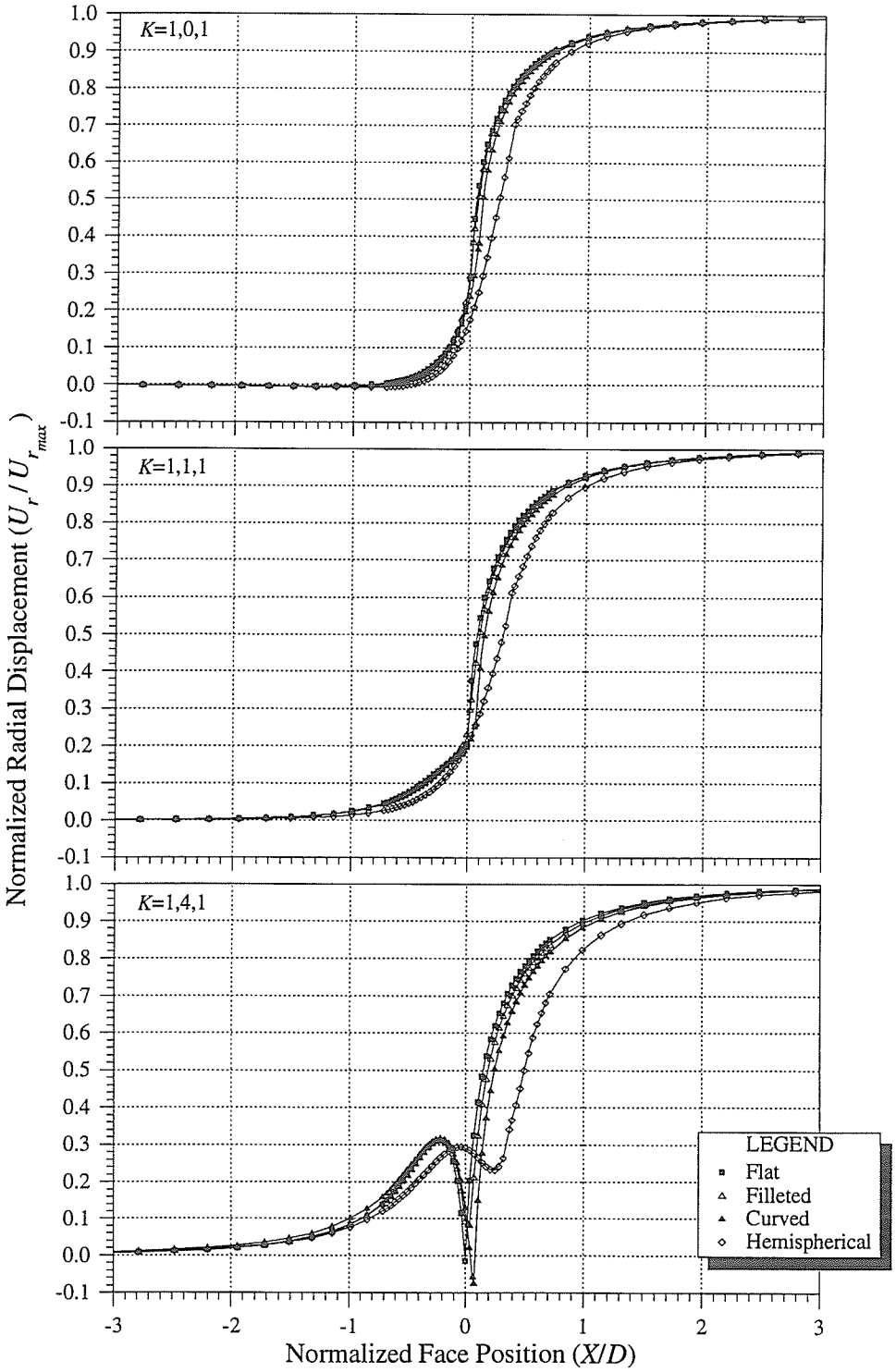

Figure 4.19: Radial displacement responses for different face shapes under axisymmetric far-field stress conditions. In all cases, the deepest point on the face was used to determine X/D.

Table 4.10: Proportion of radial displacement response occurring in the anterior domain for five different face shapes under seven different axisymmetric stress conditions. Note that $X/D = 0$ was determined relative to the deepest point on the tunnel face. Results are from a finite difference approach and differ slightly from results from the boundary element study. The value in parentheses is d/D for the curved faces.

Face Shape	Proportion of Total Radial Displacement in Anterior Domain (%)						
	K=1,0,1	1,$\frac{1}{4}$,1	1,$\frac{1}{2}$,1	1,1,1	1,2,1	1,3,1	1,4,1
Flat	28.6	26.0	23.7	19.9	12.8	5.6	-1.4
Filleted	29.4	27.3	25.6	23.1	18.6	13.8	9.3
Curved (0.071)	23.9	22.9	22.1	20.6	18.6	15.9	13.1
Curved (0.143)	22.1	21.9	22.0	22.0	21.7	21.6	22.1
Hemispherical	17.5	18.3	19.0	20.5	23.3	26.2	29.2

more exaggerated for all face shapes as the axial stress ratio increases.

The other major effect evident in Figure 4.19 is the variation in the proportion of the total displacement response occurring in the anterior domain (Table 4.10), which appears to be related to a combination of face shape and axial stress ratio . For the flat and filleted faces, as well as the curved face with $d/D = 0.071$, the proportion of anterior displacement decreases with increasing axial stress ratio. The converse is true for the hemispherical face. The curved face with $d/D = 0.143$ shows a relatively constant proportion of the total radial displacement occurring in the anterior domain.

These results imply that, in conditions where the axial stress ratio is less than unity, posterior-type instruments installed in a plane at the deepest point on the face would record more of the total displacement response for a hemispherical face than for faces with less curvature. For cases where the axial stress ratio is greater than unity, the trend is reversed. In reality, however, posterior-type instruments would, by necessity, be installed near the shallowest point on a curved or hemispherical face. Thus less of the total displacement response would be recorded for the curved and hemispherical shapes under all axial stress conditions.

4.5.4 Zero reference position for different face shapes

The choice of an appropriate zero reference point for a non-planar face, defining the boundary between the anterior and posterior domains, is important in applying the approximating and parametric functions to a radial displacement response. In the cases considered in the previous section, the reference point for face position was chosen to be the deepest point on the face, i.e., maximum chainage for a horizontal tunnel. However, this choice was arbitrary. To standardize the definition of face position, a characteristic reference point, corresponding to the sharp transition in the displacement gradient near the face, was identified for each of the displacement responses. From the results described in Section 4.2.4, the characteristic point is controlled by the minimum of the radial displacement response versus face position produced by the antiplane normal stress component.

For the flat face, the characteristic point is at $X/D = 0$. The results from the study of different face shapes suggest that the characteristic point shifts to the right with increasing face curvature when results are plotted relative to the deepest point on the face. This effect is particularly apparent in the case of large axial stress ratio, for example $K = 1, 4, 1$, where the sharp increase in displacement gradient for the curved and hemispherical faces occurs at $X/D = 0.125$ and 0.210, respectively. As shown in Figure 4.20, by translating the displacement response for the curved and hemispherical faces to the left such that the characteristic point coincides with $X/D = 0$, the responses in the regions $X/D < -1$ and $X/D > 1$ overlay one another, i.e., they are independent of face shape.

A numerical modeling study was undertaken to determine a physical explanation for the observation that, for the curved and hemispherical faces, the true zero position of the face, defined by the characteristic point, falls some distance inside the tunnel. An attempt to correlate the centroid of the excavated volume represented by the curved face with the characteristic point was unsuccessful, but suggested that the position of the characteristic point and the strain energy associated with excavating different shaped faces might be

related. Strain energy is given by

$$\mathbf{U} = \frac{1}{2}\int_V \sigma_{ij}\epsilon_{ij}dV \tag{4.36}$$

where σ_{ij} and ϵ_{ij} are the stress and strain tensor, respectively, and dV is the differential volume.

A routine was written for FLAC to determine the strain energy density as the dot product of the stress and strain tensors. The strain energy distribution ahead of a flat face in the axisymmetric model was then determined by multiplying the strain energy density for each element by half its volume of revolution. Having established the strain energy distribution ahead of a flat face, faces of different curvature were then superimposed to determine the amount of strain energy contained within the volume bounded by the curved face. In this way, the amount of strain energy U associated with excavating 26 different

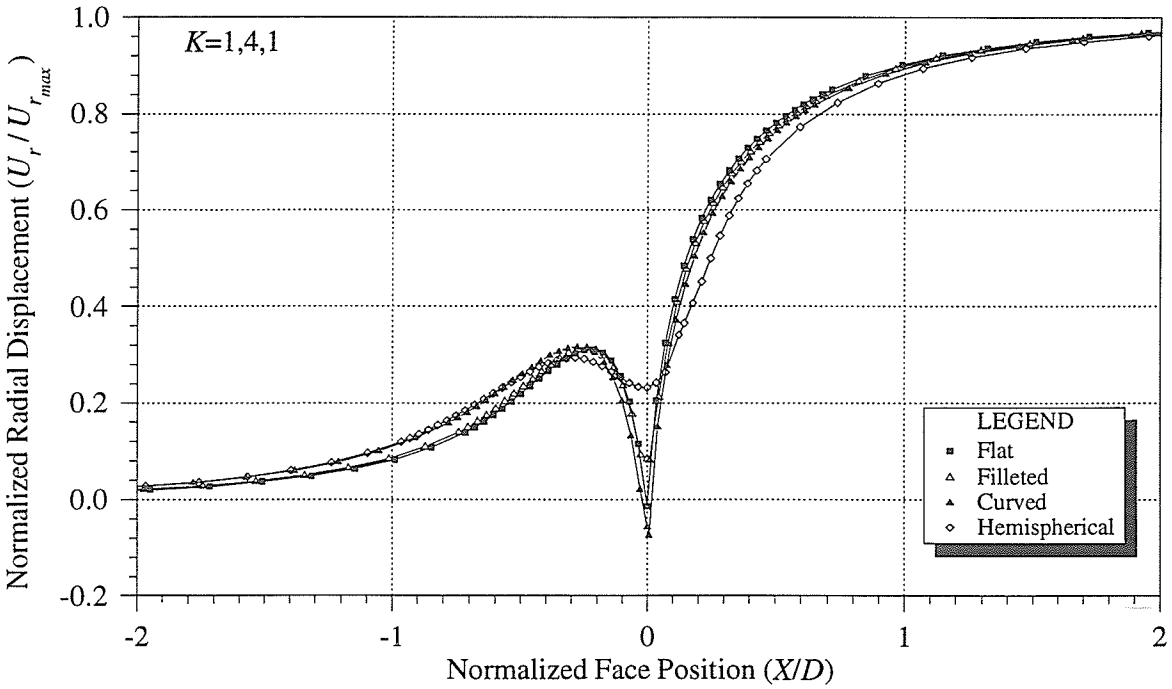

Figure 4.20: Radial displacement responses adjusted for face position for different face shapes under axisymmetric far-field stress conditions of $K = 1, 4, 1$. Note that for regions $X/D < -1$ and $X/D > 1$ the displacement responses are independent of face shape.

faces with shapes ranging from flat to hemispherical was determined. In each case, the edges of the curved face remained coincident with the initial flat face position. In addition, the strain energy associated with advancing a flat-faced cylinder different distances was determined. The results from the two investigations were then compared on the basis of equivalent strain energy to match each curved face with an equivalent flat face advance. The equivalent flat face position was taken as the true zero position of the curved face.

Figure 4.21 shows the relationship between face curvature, expressed as the variation in axial position across the tunnel face d normalized to the tunnel diameter D, and the normalized difference between the true zero face position and the deepest point on the face, $\Delta x/D$. Note that the difference is always negative, meaning that the true zero position of the face is some distance inside the tunnel, i.e., behind the advancing face. For faces with

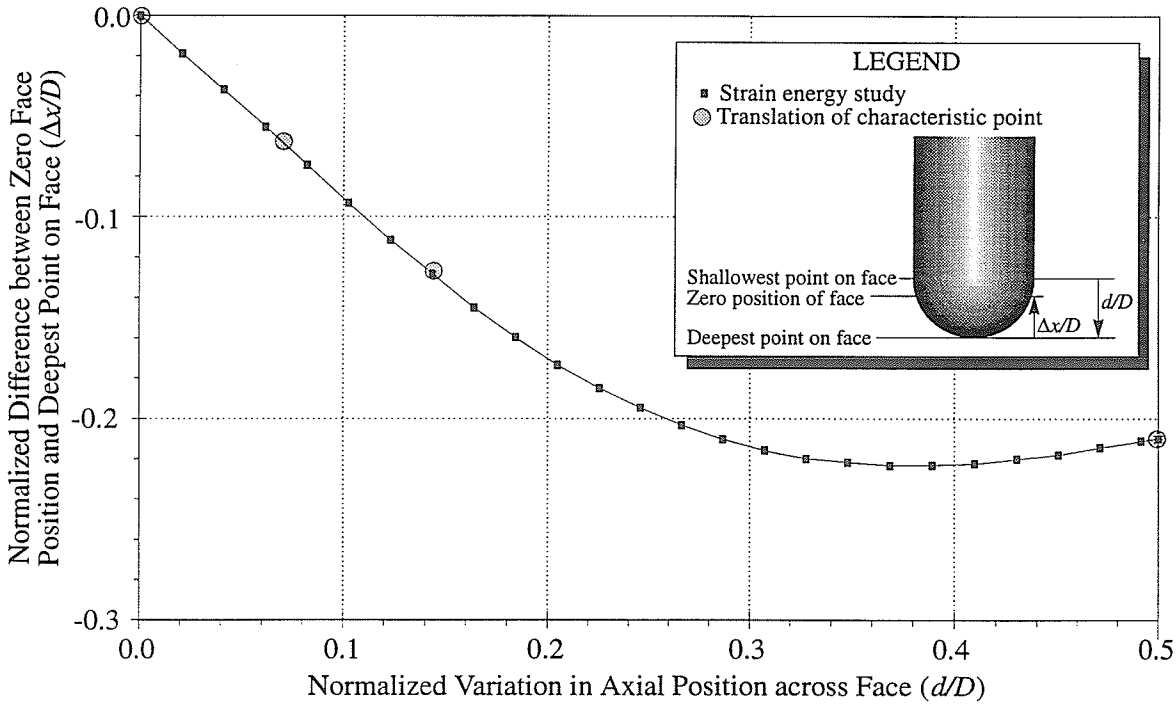

Figure 4.21: Relationship between face curvature and the zero position of the tunnel face based on the concept of equivalent strain energy. Terms are defined in the inset. Note that for small amounts of curvature, the relationship is linear.

curvature $d/D < 0.12$, the relationship between face curvature and true zero position is linear and can be written as

$$x_{zero} = x_{deepest} - 0.91d \tag{4.37}$$

where x_{zero} is the true face position along the tunnel axis, and $x_{deepest}$ is the position of the deepest point on the face. Results from translating the displacement curves to match responses in the regions $X/D < -1$ and $X/D > 1$ agree well with this relationship.

Using this definition of zero face position, results for the proportion of the total displacement response occurring in the anterior domain were adjusted for the curved and hemispherical faces (Table 4.11). The results show that a much larger proportion of the response occurs in the adjusted anterior domain, and also that the proportion decreases with increasing axial stress ratio. This result is significant, for example, in applications where posterior-type measurements are extrapolated to the zero reference point to estimate total displacements. Owing to the large displacement gradient near the tunnel face, an incorrect assumption about the true zero reference point can result in a poor estimate of the total response.

The position of the neutral point described in Section 4.2.5 was also found to depend on the shape of the face, as shown in Table 4.12. An increase in face curvature results in a shift of the neutral point to the left relative to the true reference position of the face, i.e., the characteristic point. Note that the value associated with the flat face is identical to the result obtained using the boundary element approach described in Section 4.2.4. In conjunction with the adjusted results for the proportion of the radial displacement response occurring in the anterior domain, the results for the position of the neutral point show that, as the face curvature increases, the shape of the radial displacement response changes. Both sets of results suggest that the radial displacement response associated with the antiplane normal stress component, which determines the location of the neutral point and affects the value of the y-intercept, is sensitive to face shape. These findings suggest that, for

Table 4.11: Adjusted proportion of the radial displacement response occurring in the anterior domain for five different face shapes under seven different axisymmetric stress conditions. Note that the reference point for face position has been adjusted for face curvature to match the characteristic point with $X/D = 0$. The value in parentheses is d/D for the curved faces.

Face Shape	Proportion of Total Radial Displacement in Anterior Domain (%)						
	K=1,0,1	1,$\frac{1}{4}$,1	1,$\frac{1}{2}$,1	1,1,1	1,2,1	1,3,1	1,4,1
Flat	28.6	26.0	23.7	19.9	12.8	5.6	-1.4
Filleted	38.3	35.6	33.4	29.7	22.7	15.5	8.5
Curved (0.071)	36.6	33.5	30.7	25.2	15.5	4.9	-5.8
Curved (0.143)	42.7	39.4	36.5	30.7	18.7	6.9	-4.1
Hemispherical	50.5	49.0	47.1	43.6	36.6	29.9	23.2

Table 4.12: Position of the neutral point for various face shapes.

Face Shape	Position relative to Deepest Point on Face (X/D)	Position relative to True Face Position (X/D)
Flat	-0.063	-0.063
Filleted	-0.049	-0.074
Curved ($d/D = 0.071$)	-0.033	-0.098
Curved ($d/D = 0.143$)	0.000	-0.125
Hemispherical	0.089	-0.161

cases where curvature $d/D > 0.1$, the coefficient values determined for the parametric functions describing the radial displacement response for an ideal cylindrical tunnel may not be applicable.

4.6 Effect of Tunnel Perimeter Geometry

Although most studies looking at stresses and displacements around underground openings have idealized the tunnel geometry as perfectly cylindrical in longitudinal profile, most tunnels excavated by traditional drill-and-blast techniques have a stepped profile owing to the necessity to "look-out" each round to permit drilling [95]. The effect of this departure from a smooth tunnel profile on the displacement field around a tunnel was considered in an axisymmetric model simulation using FLAC.

4.6.1 Mesh geometry

Two meshes were used for the study. The first was constructed to simulate a tunnel with a longitudinal geometry comprising 1-m-long rounds with a look-out of 150 mm per round. The minimum tunnel diameter in a given round was 3.2 m, expanding linearly to 3.5 m at the round end. The second mesh was constructed with the same far-field element configuration, but with a smooth 3.5-m-diameter tunnel. The mesh geometries used for the investigation are shown in Figure 4.22. Quadrilateral and triangular elements with constant elastic properties and a linear stress-strain relationship were used in all cases. To minimize boundary effects, the horizontal and vertical dimensions of the mesh were greater than ten tunnel diameters.

4.6.2 Boundary conditions and material properties

The boundary conditions and material properties were the same as those used in Section 4.5. The far-field stress ratios were $K = 1, 2, 1$. Each of the two simulations required between 2500 and 3000 time steps to equilibrate.

4.6.3 Comparison of results for stepped and smooth profiles

The results of the study are shown as contour plots of normalized radial displacement $U_r/U_{r_{max}}$ (Figure 4.23). It is obvious from the plots that the radial displacement fields around the two tunnels are similar but not identical. In particular, the displacement contours very near the stepped tunnel wall show a perturbation associated with the variation in tunnel diameter over a given round. This perturbation is evident as far out as the 0.6 contour. In addition, at three tunnel diameters from the face, the normalized radial displacement exceeds 0.9 only over a small portion of the round. In contrast, the contours for the smooth tunnel profile are very uniform, and the normalized displacement at $X/D = 3$ approaches 1.0 at the tunnel wall.

To illustrate the differences in the model results, the normalized radial displacement responses versus radial distance for points 10 tunnel diameters from the face were compared. Figure 4.24 shows five responses: the response for the smooth cylinder, and the responses

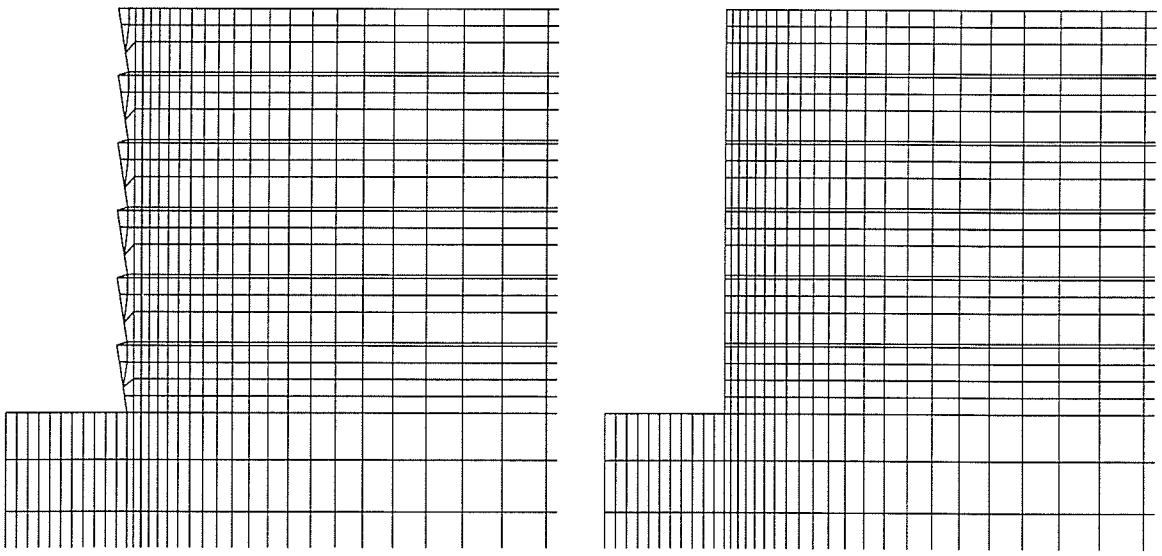

Figure 4.22: Mesh geometries used in axisymmetric studies with FLAC to analyze effects of tunnel perimeter geometry. Note that only a portion of the entire mesh is shown in each case, and that the left edge of each mesh is an axis of rotational symmetry. The left mesh is for a stepped profile, and the right is for a smooth profile.

associated with four positions within a given round for a stepped tunnel. From the plane strain solution, the normalized radial displacement response for the axisymmetric case of $K = 1, 2, 1$ is described simply by

$$\frac{U_r}{U_{r_{max}}} = \frac{a}{r} \tag{4.38}$$

where a is the tunnel radius and r is the radial distance from the tunnel centre. A comparison of the model results for the smooth cylindrical tunnel and Equation 4.38 gave a coefficient of determination of $r^2 = 0.9998$.

The responses for the stepped profile fall below that for the smooth cylinder, which suggests that the stepped tunnel induces less radial displacement, and therefore has an effective radius smaller than that for the smooth tunnel. The effective radius was determined

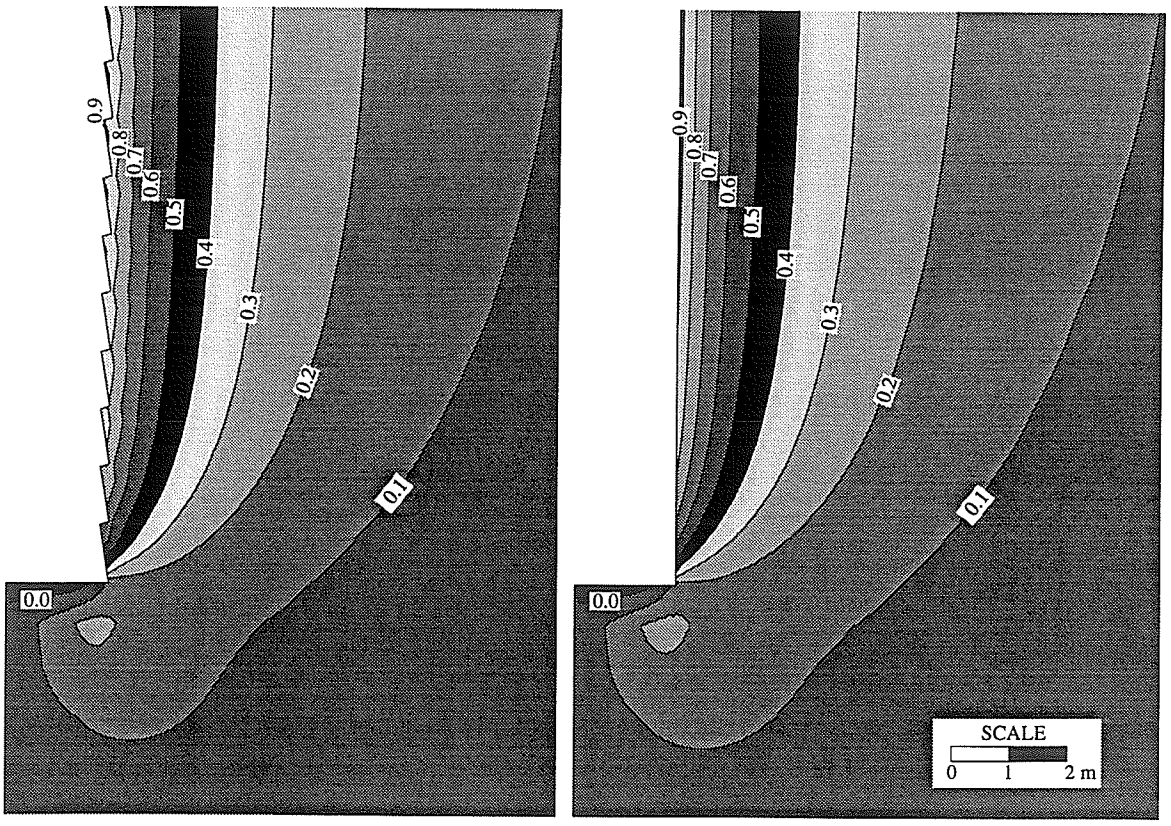

Figure 4.23: Contours of normalized radial displacement for stepped and smooth perimeter geometry. Note the perturbations near the tunnel wall for the stepped profile.

by translating the response for the stepped profile to minimize the sum of squared residuals between it and the response for the smooth profile. From this approach, the effective radius, a_{eff}, was found to be 1.605 m. This finding suggests that the effective radius is described by

$$a_{eff} = a_{max} - 0.9643\Delta a \tag{4.39}$$

where a_{max} is the maximum radius within a round, and Δa is the difference between the maximum and minimum radii.

Another important effect of the stepped profile, illustrated in Figure 4.25, is the variation in radial displacement response within a stepped round. In the region $1 \leq r/a < 1.5$, the radial displacement responses for the points within a round corresponding to the maximum and minimum radii fall below that for the smooth cylinder when normalized to the effective

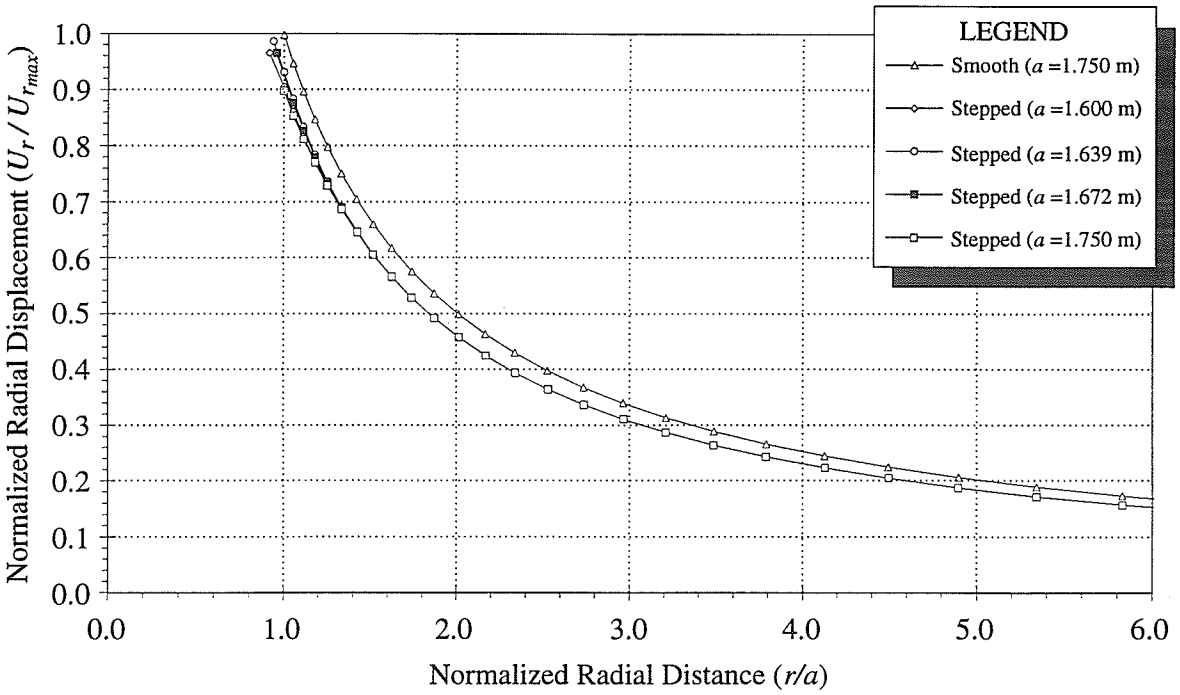

Figure 4.24: Comparison of radial displacement responses far from the face for tunnels with stepped and smooth perimeter geometries. Note that the stepped responses correspond to the points at different positions within an excavation round.

radius. However, the responses associated with points from the central portion of the round are much closer to the smooth cylinder response using the same normalizing factor. Therefore, unless instruments are located exactly at the end points of the round, the effective radius concept can be used to standardize the radial displacement response in the region $1 \leq r/a < 1.5$ for a stepped profile to that for a smooth cylinder with a radius a_{max}. For the region $r/a \geq 1.5$, the variation in the responses from different locations within the round is negligible, as is the difference between the response for the smooth tunnel normalized to its radius and the response for the stepped tunnel normalized to its effective radius.

Results from two axisymmetric stepped models with different stress ratios ($K = 1, 2, 1$ and $K = 1, 0, 1$) were also compared to the smooth tunnel model to assess the effect of the stepped geometry on the radial displacement response versus face position. The comparison

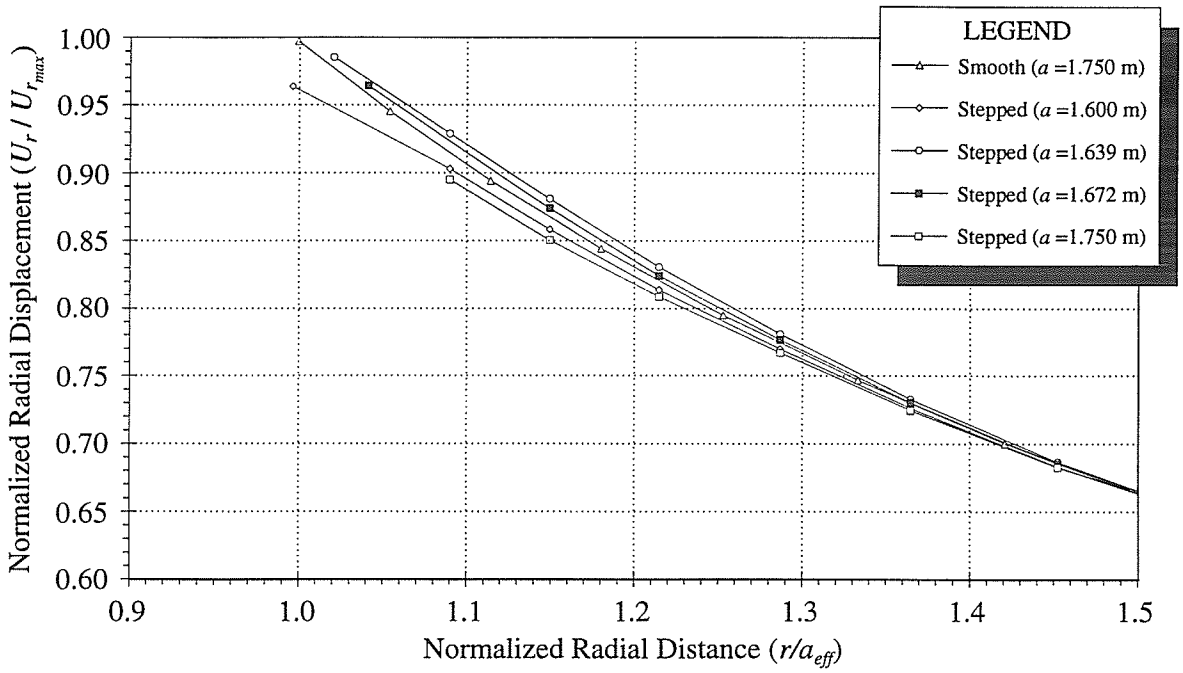

Figure 4.25: Comparison of radial displacement responses near the tunnel wall for tunnels with stepped and smooth perimeter geometries. Note the variation in the stepped responses within an excavation round. The stepped response is normalized to the effective radius, $a_{eff} = 1.605$ m.

showed virtually no difference in the position of the neutral point for the stepped and smooth geometries, and only about 2% difference in the value of $U_r/U_{r_{max}}$ at $X/D = 0$, suggesting that the radial displacement response ahead of the tunnel face is relatively independent of the longitudinal geometry.

4.7 Summary

The numerical modeling studies described in this chapter considered, in part, the fundamental relationships between stresses and displacements around a cylindrical tunnel in a linear elastic medium. The effects of individual components of stress on displacement responses were determined by partitioning a unit stress tensor into a set of three plane and three antiplane components, and applying the principle of superposition. The resulting displacement responses showed that the plane components of stress produce harmonic radial displacement responses with a periodicity of 180°. In contrast, the antiplane normal stress component produces an axisymmetric response, and the antiplane shear components produce harmonic responses with a periodicity of 360°.

For combined cases with zero antiplane shear stress, i.e., the tunnel is coincident with a principal stress direction, the antiplane normal stress component was found to significantly affect the proportion of the radial displacement response occurring in the anterior domain, depending on the axial stress ratio. For axisymmetric cases, this effect is rotationally invariant, but for non-axisymmetric cases, the effect is a function of rotation angle θ. Therefore, the estimation of absolute radial displacements from residual measurements taken with posterior-type instruments requires à priori knowledge of the *in situ* stress tensor.

Antiplane shear stresses were found to affect the radial displacement response measured by extensometers in an antisymmetric manner, but had no effect on convergence measurements. As a result, convergence measurements cannot be used on their own to back calculate the complete stress tensor. It was further shown that the maxima and minima in the radial displacement responses associated with these stress components occur at the

tunnel face, and that the radial displacements approach zero away from the face in both domains. The same is true of the antiplane normal stress component. Consequently, radial displacements from within the region $-1 \leq X/D \leq 1$ are required in order to back analyze these components.

As an initial step in developing a back analysis technique, the *spliced logistic function* was developed as an approximating function for radial displacement responses versus face position. This function is also a key element of the parametric functions developed to describe the *characteristic radial displacement surface* associated with a general stress tensor. Likewise, an inverse polynomial series function was developed as both an approximating function, and as part of the parametric functions describing the radial displacement response versus radial distance.

Based on a least-squares technique in combination with the parametric functions describing the radial displacement response versus face position, and versus radial distance, a stress back analysis technique was developed. Using displacements generated from a numerical model, it was demonstrated that it is possible to back analyze the complete *in situ* stress tensor using radial displacement measurements from within the region $-1 \leq X/D \leq 1$ around a single cylindrical tunnel. Measurements typical of both anterior and posterior extensometers, and posterior convergence arrays, were incorporated into the back analysis. It was also shown that additional constraints can be stipulated in the form of equations relating the different stress components.

The effects of typical deviations from an ideal cylindrical geometry on displacement responses were also investigated. It was determined that the shape of the tunnel face affects the shape of the radial displacement response, and, in particular, the position of the characteristic and neutral points associated with the antiplane normal stress component. Using the principle of equivalent strain energy, a relationship between face curvature and position of the characteristic point was developed. It was found that, for faces with curvature $d/D \leq 0.1$, the parametric functions for the flat-faced cylinder can be used to back analyze

the *in situ* stress tensor. However, for faces with curvature $d/D > 0.1$, the parametric functions must be adjusted to reflect the face shape.

In terms of the longitudinal geometry of the tunnel, a stepped perimeter geometry reduces the effective tunnel radius, thus reducing the magnitude of induced radial displacements. From numerical modeling, a relationship between the maximum and minimum tunnel radii, and the effective radius, was developed. The stepped profile also causes perturbations to the displacement field within the region $1 \leq r/a_{eff} < 1.5$, varying with position within the stepped excavation round. Outside this region, the radial displacement response for a stepped tunnel, normalized to its effective radius, is virtually identical to that for a smooth tunnel normalized to its radius. Ahead of the tunnel face, the radial displacement response is relatively independent of the longitudinal geometry of the tunnel.

Chapter 5

Analysis of Displacements from the Field Study

As detailed in Chapter 3, the displacements measured during the monitoring phase of the Mine-by Experiment represent a unique data set in that they include measurements both from anterior extensometers and from posterior convergence arrays. An overview of the measurements from the field study is presented, and the anterior and posterior displacement measurements are compared. As demonstrated in Chapter 4, the combination of these types of measurements can be used to back analyze the *in situ* stress tensor. In this chapter, a back analysis methodology based on the findings from the parametric study in Chapter 4 is described, and applied to the measurements from the field study to estimate the *in situ* stress tensor at the 420 Level of the URL. The twelve radial extensometers of particular interest to this thesis are referred to as EXT1 to EXT12, and the eight convergence arrays as Array 415-1 to 415-8.

5.1 Methodology

The methodology for applying the back analysis technique involves seven steps, as outlined in Figure 5.1. The first step is to establish the key parameters related to the tunnel geometry. These parameters are the tunnel diameter D, the effective radius a_{eff} for a stepped tunnel profile, and the curvature of each face described by the deviation d in face chainage between

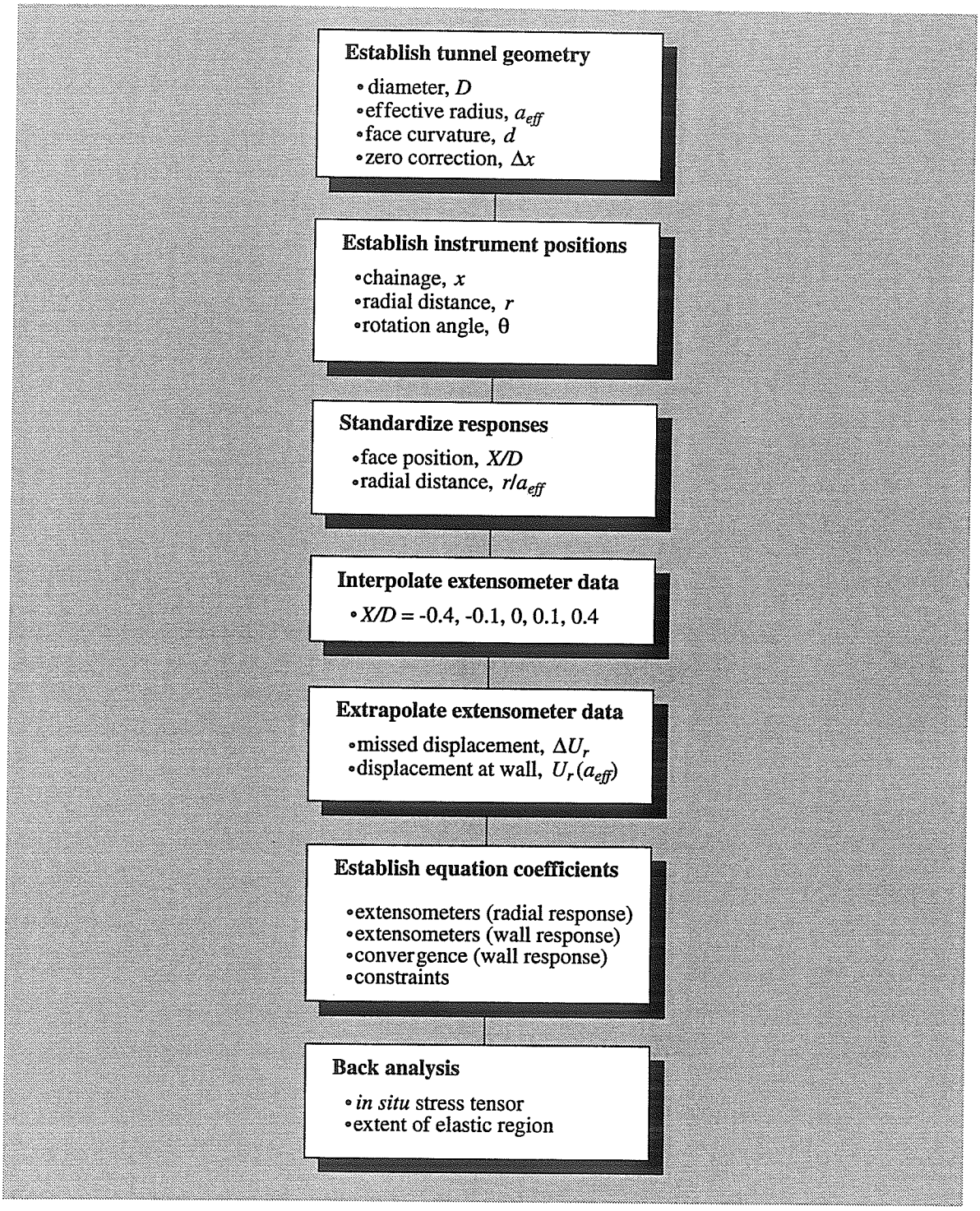

Figure 5.1: Flowchart of the various steps involved in the near-face back analysis methodology.

the sidewall and tunnel centre. For the field study, this last parameter was obtained from a contour plot of the face for each excavation round, generated from carefully controlled survey data. A typical face contour plot is shown in Figure 5.2. The parameter d is calculated as the difference of the chainage at the tunnel centre and the average chainage of the edge points of the face. Provided that the face curvature d/D does not exceed 0.1, the correction to the face chainage can be determined using Equation 4.37. To illustrate the relatively small amount of face curvature associated with the excavation rounds in Room 415, corrected chainages for the first 30 faces are contained in Appendix E (Table E.1).

The second step in the methodology is to establish the position of the extensometer anchors and convergence pins in standard cylindrical coordinates r, θ, x, where x is coincident with the tunnel axis. For the field study, rotation angle θ for each extensometer was based

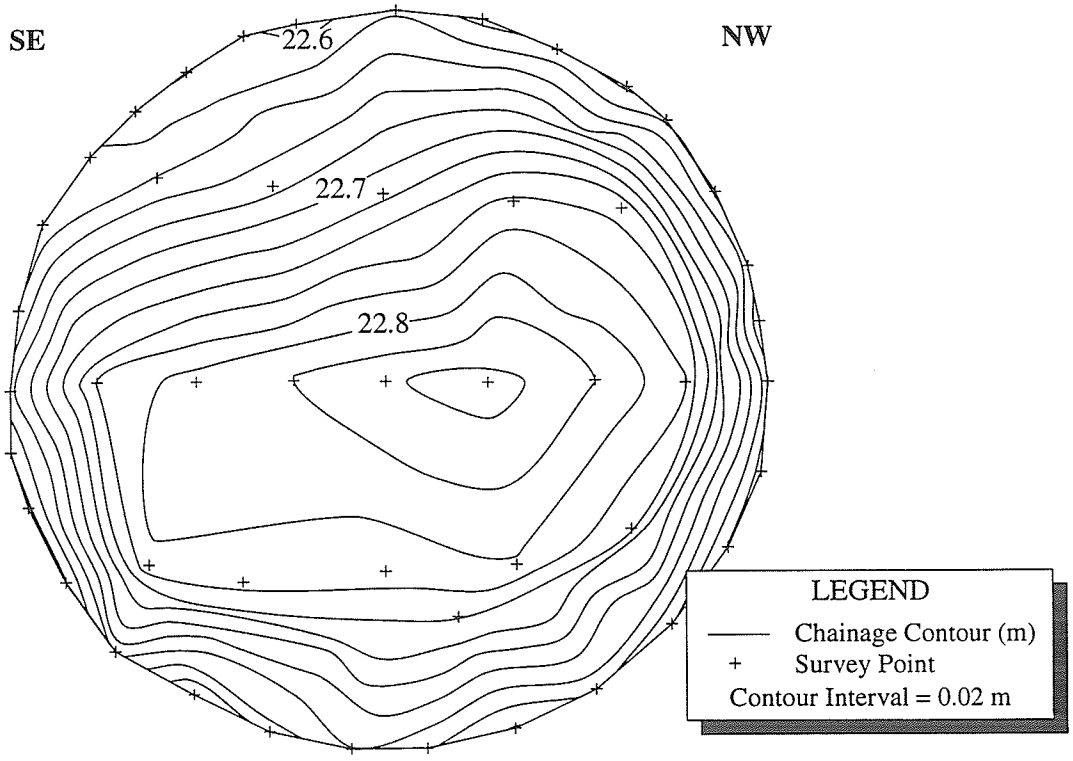

Figure 5.2: Typical face contour plot for the Mine-by Experiment (Face 17).

on the position of the innermost anchor.

Having determined the appropriate normalizing factors for a given tunnel, the third step in the methodology is to create a data set in which the face position and radial distance from the tunnel are described in dimensionless form. Face positions in Room 415 were normalized to a tunnel diameter D of 3.5 m. The effective radius in areas that did not exhibit large-scale excavation damage was taken as 1.605 m as defined in Chapter 4 for a stepped tunnel in a purely elastic medium. For areas where extensive damage had removed significant segments of the stepped profile, the effective radius was taken as 1.75 m.

Knowing the normalized face position X/D for each excavation round, the *spliced logistic function* is then used to interpolate the radial displacement response versus face position at $X/D = -0.4$, -0.1, 0, 0.1 and 0.4 for each extensometer anchor position. For the field study, this fourth step in the methodology required 120 separate interpolations, eleven per extensometer. It was found that a combination of two *spliced logistic functions* in each domain produced near perfect fits to the measured data. An example is shown in Figure 5.3.

The curve-fitting procedure involved first matching the response in the anterior domain and extrapolating to $X/D = 0$, then fixing the parameters for the anterior domain and repeating the curve-fit for the combined data from both domains. In this way, the residuals between the actual data and the interpolation function were on the order of 1 μm in the anterior domain. Residuals in the posterior domain were typically larger near the tunnel, evidence of some degree of excavation damage near both extensometer arrays. In most cases, a significant increase in residuals was apparent near $0.1 < X/D < 0.4$, suggesting that past this point, the effect of excavation damage on the radial displacement response was significant. For the vertical extensometers, extrapolation to $X/D = 0$ was difficult in most instances owing to the steep radial displacement gradient in the posterior domain near $X/D = 0$. Therefore, extrapolated values near the zero face position in these instruments have more uncertainty associated with them than other measurements.

The fifth step in the methodology is to extrapolate the extensometer data to determine

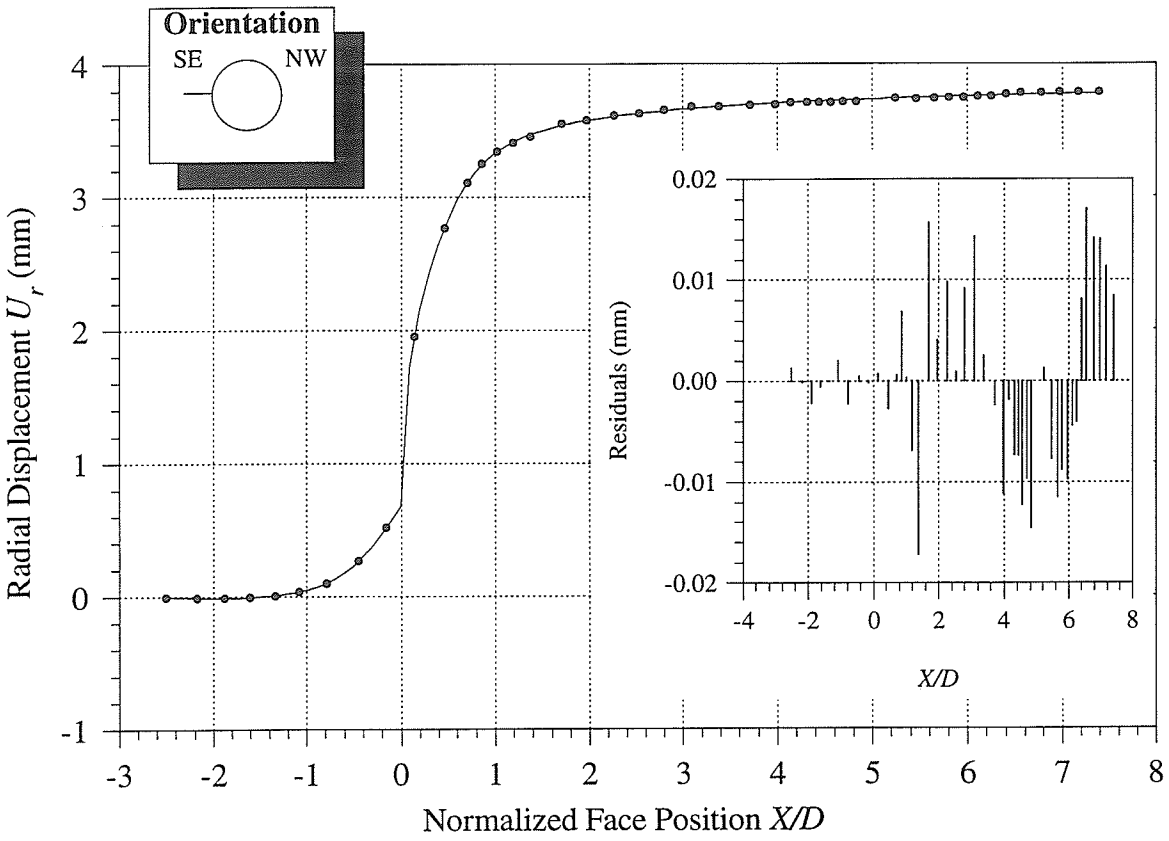

Figure 5.3: Typical results from interpolation of the displacement response for anchor 1 of EXT4. The residuals between the measured data and the fitted curve are shown in the inset. Note the increase in the value of the residuals in the posterior domain, indicating increased variability in the measured response.

three values: the displacement at $r = +\infty$, at $r = a_{eff}$, and at $X/D = -\infty$ for each extensometer. Because extensometer measurements are zeroed to the outermost anchor, the displacement occurring beyond the last measurement point is not picked up. Likewise, by taking the first measurement of radial displacement with the tunnel face at a finite distance from the instrument, a small amount of the displacement response is missed. Estimating the missed displacement in the radial direction is problematic in that the three-parameter inverse polynomial series function used to interpolate values from the measured response is generally not well-constrained as R goes to $+\infty$ unless measurements well beyond the outer extensometer anchors are included in the data set. The same is true of the combined *spliced logistic functions* used to interpolate the response versus face position.

To overcome the first of these difficulties, a procedure was developed whereby an inverse polynomial function of the form

$$\frac{U_r}{U_{r_{max}}} = \frac{A}{R} + \frac{B}{R^3} - \Delta y_1 \tag{5.1}$$

was fitted to the radial displacement response versus radial distance for each extensometer. Using model results from Chapter 4, Δy_1 provided a good estimate of the displacement missed between the second outermost anchor and $R = +\infty$ when the function given by Equation 5.1 was fitted to the measurements from the six outermost anchors, i.e., $R > 2$, excluding the anchor furthest from the test tunnel. Except for EXT8, the outermost anchor was excluded because its performance was influenced by its proximity to the instrumentation galleries. For EXT8, the second outermost anchor showed signs of slippage and was excluded from the analysis. However, because the outermost anchor in this extensometer was not close to the instrumentation galleries, and was therefore not influenced substantially by them, it was included. The study also showed that, if measurements from anchors closer to the tunnel were included in the data set, the coefficient of determination between the function and the measured data was reduced. The displacement at $r = a_{eff}$ was estimated by linearly extrapolating from the innermost two extensometer anchors to the tunnel wall.

In order to estimate the missed displacement between $X/D = -\infty$ and the first measurement position, results from the model studies in Chapter 4 were reviewed. It was determined that the ratio P of displacements measured at the first measurement point and at $X/D = -1$ was relatively constant. For instruments in the first extensometer array with the first measurement at $X/D = -2.8$, the ratio P for instruments at $\theta = 0$, 45, 90 and 135° was 0.131, 0.130, 0.118 and 0.114, respectively. For instruments in the second extensometer array with the first measurement at $X/D = -3.4$, the ratio P for instruments at $\theta = 0$, 45, 90 and 135° was 0.086, 0.084, 0.070 and 0.074, respectively. Based on these findings, the amount of missed displacement in the field measurements between $X/D = -\infty$ and the first measurement point was calculated by

$$\Delta y_2 = \left(U_{r_{X/D=-1}} - U_{r_{first}}\right)\left(\frac{P}{1-P}\right) \tag{5.2}$$

The resulting adjustments applied to the field data were an order of magnitude less than those related to the radial distance response.

With respect to the field study, the final two steps in the methodology involved setting up and solving a series of equations based on the parametric functions developed for anterior and posterior radial displacement measurements at $R \geq 1$, and posterior convergence measurements, to estimate the *in situ* stress tensor (Section 5.3). Results from the stress back analysis for the field study were then used, in combination with *in situ* characterization and numerical modeling, to establish the extent of damage around the test tunnel (Chapter 6).

5.1.1 Estimation of mean values and variability

As pointed out by Costantino [24], useful information about the physics of the rock response may be lost by ignoring systematic deviations from a fitted curve. Scatter in measured data can result from instrument or operator error, or, in the case of redundant instruments, it can be the result of *in situ* variability in the rock mass properties or stress state. Plots of residuals are useful to determine if this scatter represents systematic variability between

the measured response and the fitted curve. TableCurve [82], a commercial curve-fitting software package, was used to fit user-defined functions to the displacement results from the Mine-by Experiment, to determine 95 and 99% confidence intervals on the data sets, and to create plots of residuals. The mean displacement response represented by the best-fit function was then used in the incremental back analysis of stresses.

Estimating the mean value and variability of predictions of the *in situ* stress tensor is complicated when independent estimates are based on different numbers of measurements from varying locations around the tunnel. The approach taken to estimate the *in situ* stress tensor was to consider the three types of radial displacement measurements (convergence, radial displacement at $R = 1$, and radial displacement at $R > 1$) separately, then to combine the most reliable measurements of each type into a final data set. The three stress invariants, I_1, I_2 and I_3, were used as indicators of the variability in incremental predictions [17]. Where the incremental stress predictions were consistent, the stress invariants were stable, i.e., the gradient in plots of stress invariant versus number of measurements approached zero. Where stress predictions were variable, the variability was reflected by a large degree of scatter in the stress invariants. Those sets of data producing stable stress invariant plots were considered reliable, while those that produced scattered invariant plots were considered questionable. The final data set was compiled from those measurements that produced stable invariant plots. Various combinations of the measurements in the final data set were then used to estimate the mean and standard deviation of the *in situ* stress tensor.

For second order tensors, the mean and standard deviation are determined by considering the six independent components of each measured tensor. According to Walker et al. [186], the mean tensor of n stress measurements in a specific reference frame is given by

$$\overline{\sigma} = \begin{bmatrix} \frac{1}{n}\sum_{i=1}^{n}\sigma_{11_i} & \frac{1}{n}\sum_{i=1}^{n}\sigma_{12_i} & \frac{1}{n}\sum_{i=1}^{n}\sigma_{13_i} \\ \frac{1}{n}\sum_{i=1}^{n}\sigma_{21_i} & \frac{1}{n}\sum_{i=1}^{n}\sigma_{22_i} & \frac{1}{n}\sum_{i=1}^{n}\sigma_{23_i} \\ \frac{1}{n}\sum_{i=1}^{n}\sigma_{31_i} & \frac{1}{n}\sum_{i=1}^{n}\sigma_{32_i} & \frac{1}{n}\sum_{i=1}^{n}\sigma_{33_i} \end{bmatrix} \tag{5.3}$$

The eigenvalues and eigenvectors of this tensor represent the mean principal stress magnitudes and directions, respectively. Knowing the mean stress tensor, the standard deviation of the tensor can be determined by first transforming all stress measurements to a common reference frame, then calculating the standard deviation tensor as

$$S_{\overline{\sigma}} = \begin{bmatrix} \sqrt{\frac{1}{n-1}\sum_{i=1}^{n}(\sigma_{11_i} - \overline{\sigma}_{11})^2} & \sqrt{\frac{1}{n-1}\sum_{i=1}^{n}(\sigma_{12_i} - \overline{\sigma}_{12})^2} & \sqrt{\frac{1}{n-1}\sum_{i=1}^{n}(\sigma_{13_i} - \overline{\sigma}_{13})^2} \\ \sqrt{\frac{1}{n-1}\sum_{i=1}^{n}(\sigma_{21_i} - \overline{\sigma}_{21})^2} & \sqrt{\frac{1}{n-1}\sum_{i=1}^{n}(\sigma_{22_i} - \overline{\sigma}_{22})^2} & \sqrt{\frac{1}{n-1}\sum_{i=1}^{n}(\sigma_{23_i} - \overline{\sigma}_{23})^2} \\ \sqrt{\frac{1}{n-1}\sum_{i=1}^{n}(\sigma_{31_i} - \overline{\sigma}_{31})^2} & \sqrt{\frac{1}{n-1}\sum_{i=1}^{n}(\sigma_{32_i} - \overline{\sigma}_{32})^2} & \sqrt{\frac{1}{n-1}\sum_{i=1}^{n}(\sigma_{33_i} - \overline{\sigma}_{33})^2} \end{bmatrix} \tag{5.4}$$

If the standard deviation in the principal stress tensor is required, the n measurements are first transformed to the reference frame described by the principal stress directions before applying Equation 5.4.

5.2 Displacement results from the Mine-by Experiment

The displacement results from the Mine-by Experiment have been documented in detail by Read et al. [161, 159]. An overview of the results is presented in the following sections.

5.2.1 Extensometer results

Displacement measurements from extensometers are presented graphically in three ways: versus time to provide a visual history of the response measured by each instrument, and illustrate any time-dependent effects, or anomalous behaviour over the monitoring period; versus face position to show the relationship between excavation advance and the mean measured response at each excavation step; and versus radial distance to illustrate the effect of distance from the tunnel wall on the measured response. The conventions used in plotting the data follow geotechnical engineering practice. For radial extensometers, positive displacement means movement of the tunnel wall towards the tunnel centre, or overall extension of the extensometer string. All displacement values are cumulative results of individual readings along the instrument string. For the time history plots, measurements have not been adjusted for missed displacement, and are plotted relative to the outermost anchor. For the other types of plot, the adjustments for missed displacement have been applied, so all measurements are relative to points at $R = +\infty$ and $X/D = -\infty$.

As suggested in guidelines prepared for presentation of measured field data [91], estimation of error should be given in the form of error bars or confidence intervals on the measured data. For non-redundant instruments (i.e., no duplication in terms of position relative to the tunnel), the confidence intervals at best represent the measurement error in the instrument and datalogging system, and do not reflect the *in situ* variability in the response being measured. Although the initial design for the instrumentation was such that several of the extensometers would be redundant by virtue of symmetry, slight variations in the as-built locations between instruments were noted. The extensometers were therefore considered individually as non-redundant instruments.

For each excavation round, the measurements taken between completion of excavation and the start of drilling for the next round were statistically sufficient to calculate a mean

value and standard deviation. In all cases, the error bars representing one standard deviation were too small to be plotted, suggesting very little variability attributable to measurement error at each excavation step [161]. Consequently, the plotted results are considered representative of the true behaviour of the rock mass at the instrument locations.

Radial displacement versus time

Typical plots for a vertical and a horizontal extensometer are shown in Figures 5.4 and 5.5. Additional plots for inclined extensometers are contained in Appendix E (Figures E.1 and E.2).

The plots indicate key dates in the excavation schedule for each array. The first Bof-ex array, located at chainage 20+00 in Room 415, was exposed during excavation of round 415-15. The excavation was considered to have passed the instruments once perimeter drilling

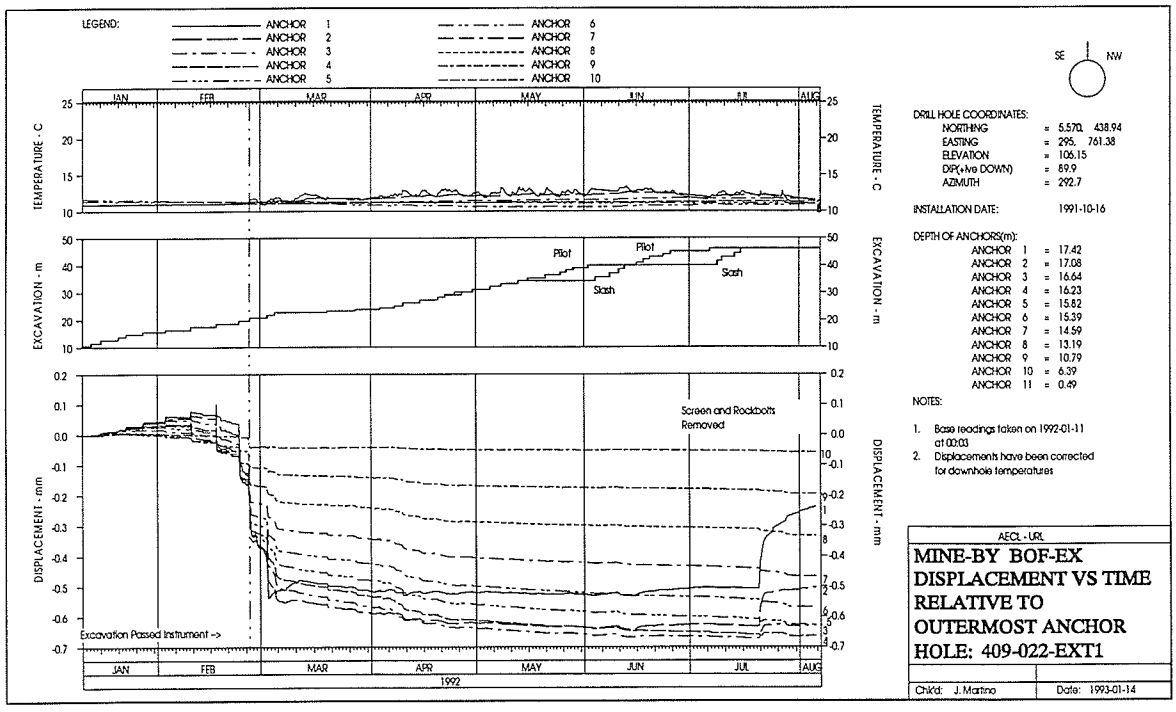

Figure 5.4: Radial displacement response versus time for a typical vertical extensometer (409-022-EXT1).

was complete on February 26, 1992. The second Bof-ex array, located at chainage 22+50, was exposed during excavation of round 415-17. Upon completion of perimeter drilling on March 5, 1992, the excavation was considered to have passed the instruments in this array.

Progressive failure was observed in the upper SE and lower NW quadrants of the test tunnel as excavation progressed. Extensometer anchors located within the zone of damage showed exaggerated convergence once the face passed the instrument location. The performance of anchor 1 in Figure 5.4 typifies this behaviour. As shown by the depth to which individual extensometers were affected, the damage zone produced by progressive failure near the extensometers was more extensive in the roof than in the floor. For instance, the plot for EXT12 in Appendix E (Figure E.2) illustrates damage development in the posterior domain to the depth of the fourth anchor. In addition, horizontal extensometers on the SE side of the tunnel closer to the damage zone in the upper SE quadrant measured larger

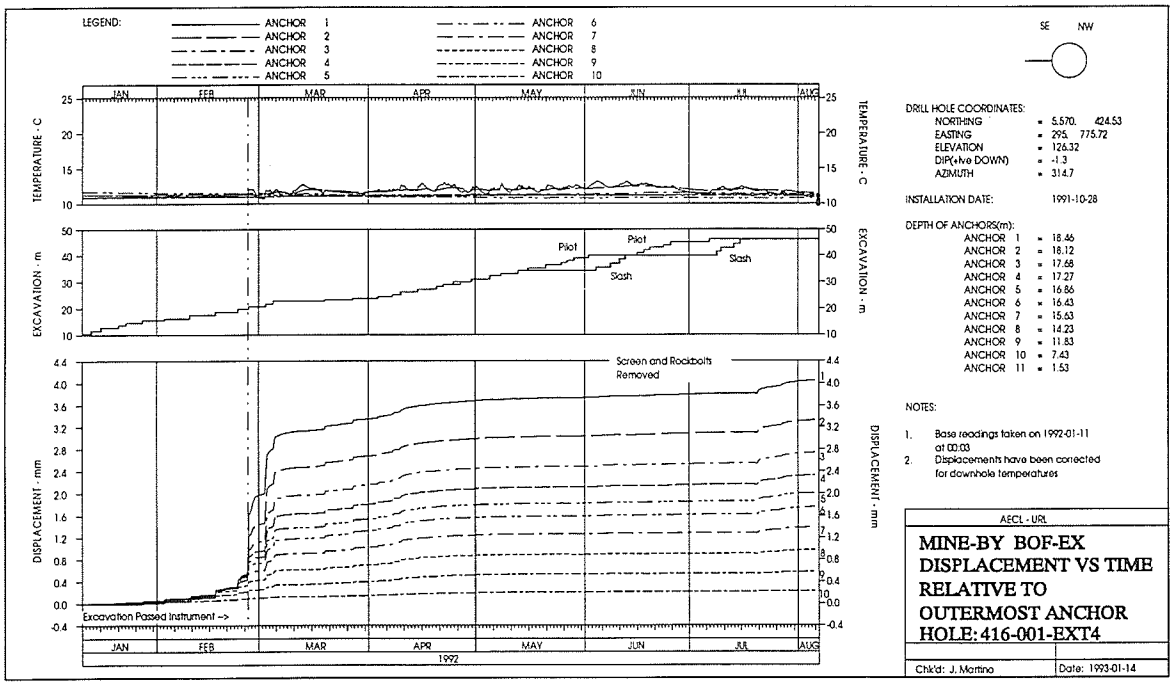

Figure 5.5: Radial displacement response versus time for a typical horizontal extensometer (416-001-EXT4).

total displacements than those on the NW side closer to the damage zone in the lower NW quadrant of the tunnel. However, variations in lithology may have also contributed to the difference in final displacement values between the SE and NW walls. This possibility is explored in Chapter 6.

Artificial support also affected the measured displacement response. For example, the removal of rock bolts and screen, followed by scaling, resulted in convergence of the anchors within the damaged zone of rock, and additional convergence in horizontal and inclined extensometers. The effect of removing support was less pronounced in the floor extensometers, producing slight additional divergence.

Radial displacement versus face position

Figures 5.6, 5.7, 5.8 and 5.9 are typical corrected plots of radial displacement versus face position for vertical, horizontal and inclined extensometers. The displacement response induced by Room 415 is characterized by general convergence (extension) measured in the horizontal extensometers and the inclined extensometers in the upper NW and lower SE quadrants, and overall divergence (contraction) in the vertical extensometers. The inclined extensometers in the lower NW and upper SE quadrants showed a relatively neutral response, but were affected by progressive failure in these regions. This pattern of displacements suggests that the initial stress ratio K_{max} acting in the plane orthogonal to the tunnel axis is greater than 3:1. The orientation of the apex of the progressive failure zone and the final displacement distribution from the extensometers indicate that the maximum stress direction in this plane is oriented at about $10 \pm 5°$ from horizontal, plunging SE.

Results from both vertical extensometers in the first Bof-ex array (EXT1 and 3) indicate convergence (extension) as the tunnel face approached the instrument location, then divergence (contraction) from the point at which the face was within 1 m of the instruments to the end of the excavation. The final radial displacement near the tunnel wall was approximately -0.88 mm in both cases. Progressive failure in the upper SE quadrant

of the tunnel produced sudden convergence of the two innermost anchors in EXT1 to a depth of approximately 0.68 m, beginning once the tunnel face had advanced 1 m past the instrument location. Although the innermost anchor in EXT3 was slightly damaged during drilling, convergence of the floor associated with progressive failure in the lower NW quadrant was still evident for the two innermost anchors to a depth of 0.34 m. The behaviour of the vertical extensometers in the second Bof-ex array was similar to those from the first. Convergence (extension) was recorded until the tunnel face was within 1 m of the instrument location, then increasing divergence (contraction) was noted to the end of tunnel excavation. Convergence related to progressive failure was not apparent until the excavation had advanced about 5 m past the instrument location, at which point the roof extensometer showed extension to about 0.47 m into the rock mass. The floor extensometer

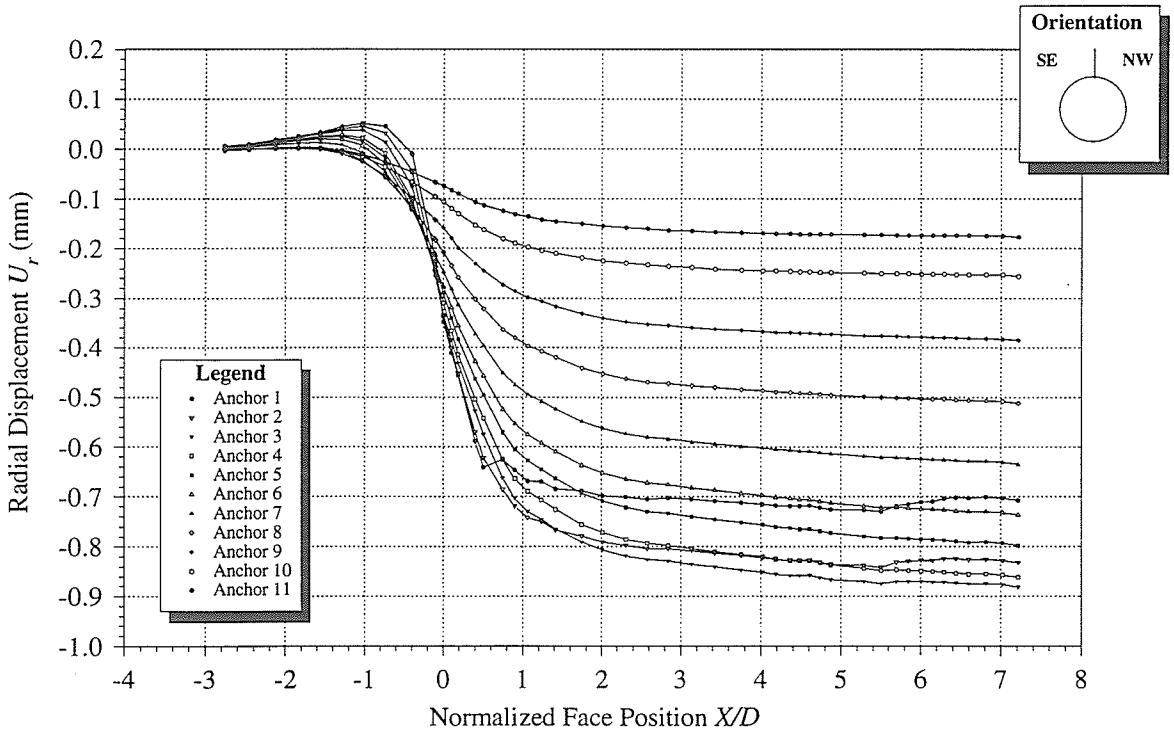

Figure 5.6: Radial displacement response versus face position for a typical vertical extensometer (409-022-EXT1).

showed some convergence of the first two anchors immediately after the face passed the instrument location. The final radial displacement at the innermost anchor in the roof extensometer (EXT5) was -0.67 mm, whereas the floor extensometer (EXT9) measured a value of -0.76 mm. Removal of screen and rock bolts in the roof, and ballast in the floor increased the innermost anchor displacement to about -0.8 mm in EXT9.

Results from the horizontal extensometers in the first Bof-ex array (EXT2 and 4) showed increasing convergence (extension) as the tunnel face approached, and passed, the instrument location. Radial displacement at the innermost anchor ranged from about 3.3 to 4.2 mm for the NW and SE sides of the tunnel, respectively. Removal of screen and rock bolts produced an increase in radial displacement of about 0.2 mm at the SE tunnel wall. This effect was noticeable to a depth of about 3.0 m in EXT4. A typical plot of radial displacement versus face position for a horizontal extensometer is shown in Figure 5.7.

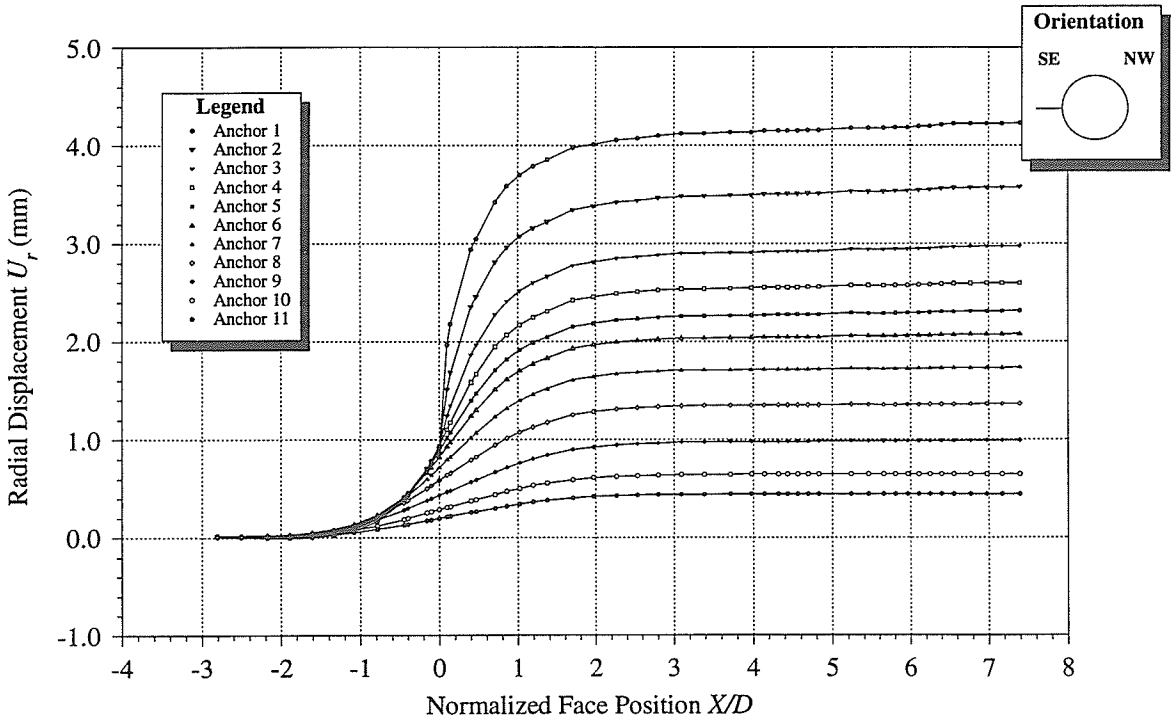

Figure 5.7: Radial displacement response versus face position for a typical horizontal extensometer (416-001-EXT4).

Results from the horizontal extensometers in the second Bof-ex array (EXT7A and 11) were very similar to those from the first array, although the displacement magnitudes varied somewhat, ranging from about 2.9 to 3.8 mm for the NW and SE sides of the tunnel, respectively. Removal of screen and rock bolts produced an increase in convergence of about 0.2 mm at the SE tunnel wall. This effect was noticeable to a depth of about 4.4 m from the wall in EXT11.

In the second Bof-ex array, inclined extensometers EXT6 and 10 in the upper NW and lower SE quadrants measured responses similar to those in the horizontal instruments, but with reduced magnitudes. Prior to the removal of rock bolts and screen, the final radial displacements were 2.2 and 2.0 mm for EXT6 and 10, respectively. An additional 0.2 and 0.1 mm, respectively, were recorded upon removal of the screen and rock bolts. The radial

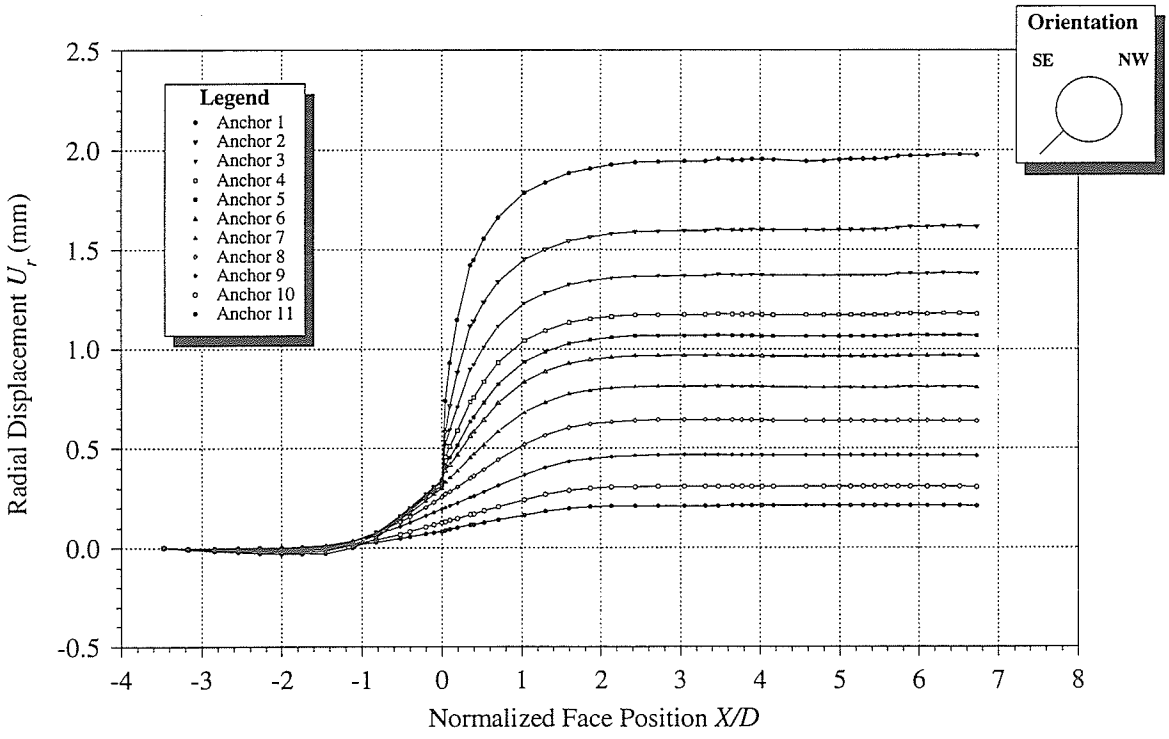

Figure 5.8: Radial displacement response versus face position for a typical 45-225° inclined extensometer (413-001-EXT10).

displacement response versus face position for EXT10 is shown in Figure 5.8.

Extensometers EXT8 and 12, installed at $\theta = 315°$ and 135°, respectively, in the second Bof-ex array, illustrate the difference in the effect of progressive failure on the measured response in the floor and roof. Both extensometers showed convergence (extension) as the tunnel face approached to within 1 m of the instrument location, then divergence (contraction) once the face passed the instruments. Final displacement near the tunnel was only 0.002 mm for EXT8. However, owing to damage development near EXT12, the final radial displacement at the tunnel wall near this extensometer was 1.1 mm, and an additional 0.3 mm was recorded upon removal of the screen and rock bolts (Figure 5.9). The effect of support removal and scaling was apparent to 1.3 m into the rock mass.

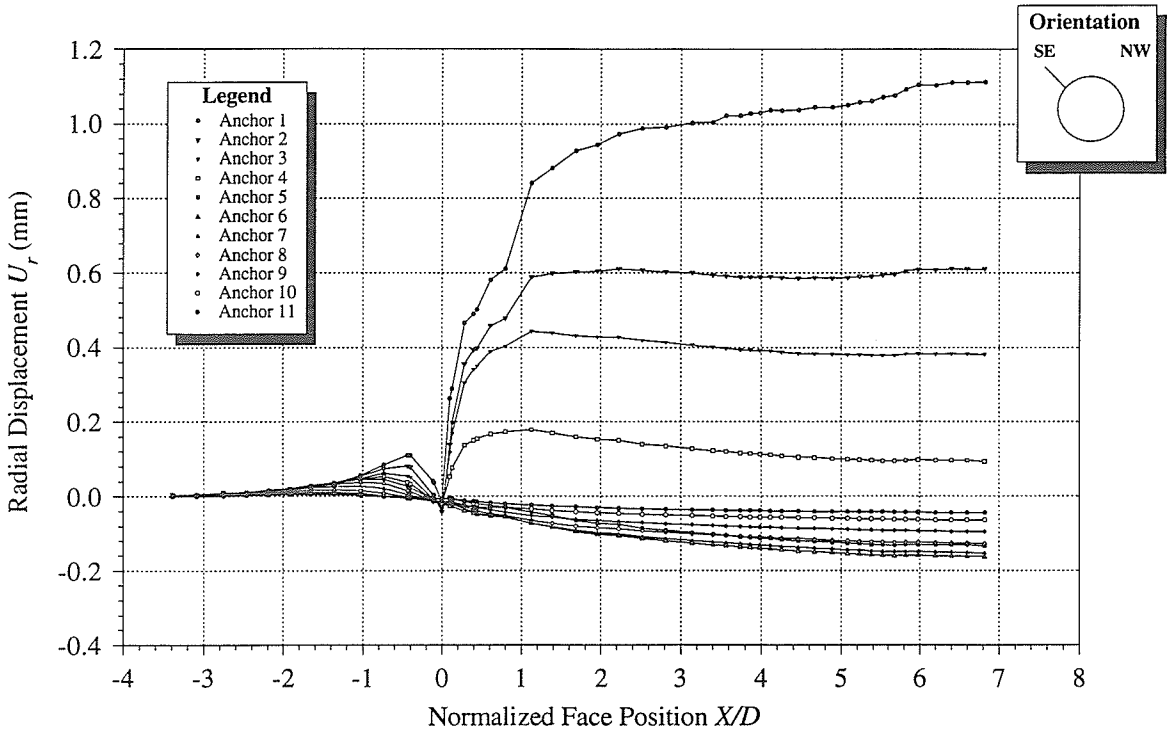

Figure 5.9: Radial displacement response versus face position for a typical 135-315° inclined extensometer (409-042-EXT12).

Radial displacement versus radial distance

Typical corrected plots of radial displacement versus radial distance for vertical, horizontal and inclined extensometers are shown in Figures 5.10, 5.11, 5.12 and 5.13. These plots illustrate the complex transient displacement response associated with tunnel advance, and the diminishing response with increasing radial distance from the tunnel.

The responses from the two vertical extensometers in the first Bof-ex array (EXT1 and 3) are very similar in appearance. In the anterior domain, they initially show convergence (extension) near the tunnel wall with a transition to overall divergence (contraction) as the tunnel face passed the instrument location. The most notable feature of these responses is the development of a zone of radial extension to a depth of 1.12 m in the roof and 0.78 m in the floor, characterized by a negative gradient, and a sharp transition to radial contraction

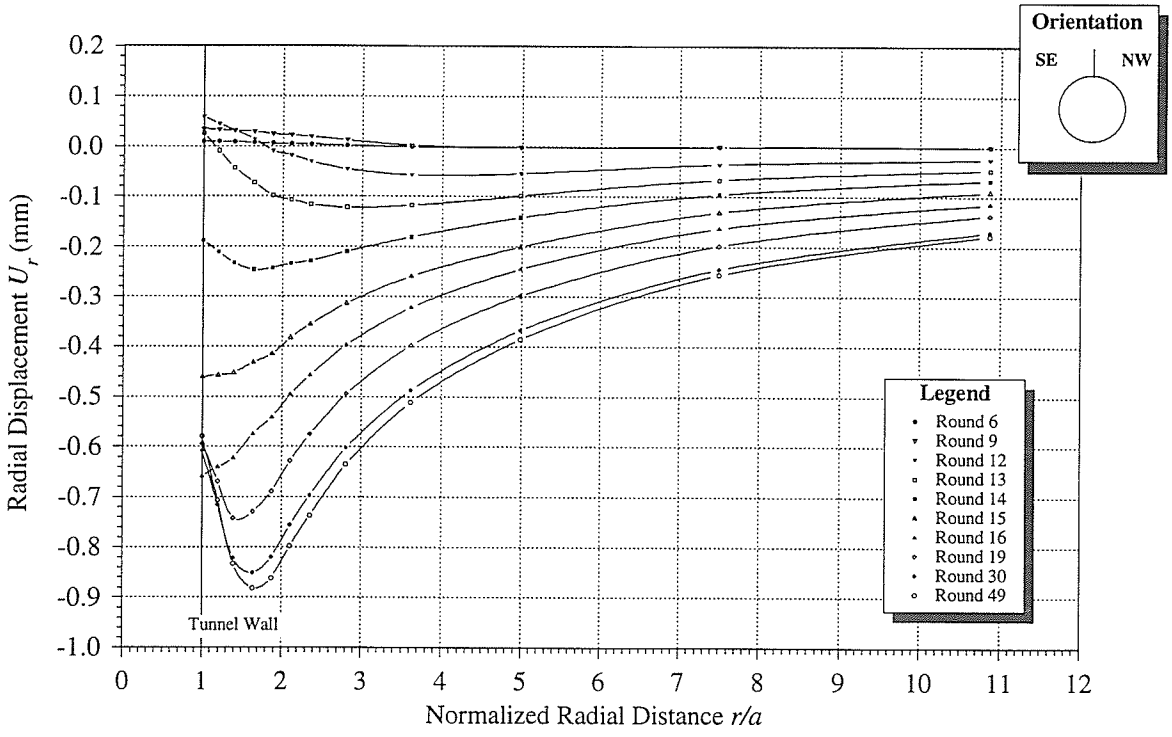

Figure 5.10: Radial displacement response versus radial distance for a typical vertical extensometer (409-022-EXT1).

at the outer zone boundary. The responses from the vertical extensometers in the second array (EXT5 and 9) are similar to those from the first, although not as smooth. They indicate a zone of radial extension to a depth of 1.33 m in the roof, and 0.54 m in the floor.

Aside from the final magnitude of the displacement at the tunnel wall, the two horizontal extensometers in the first Bof-ex array (EXT2 and 4) also measured similar responses. In the anterior domain, the gradient of the response was quite flat near the tunnel wall, with the peak occurring some distance into the rock mass. Once the face was past the array location, very smooth convergence (extension) was recorded, increasing with face advance and decreasing with radial distance from the tunnel. The two horizontal extensometers in the second array (EXT7A and 11) recorded displacement responses very similar to those in the first array.

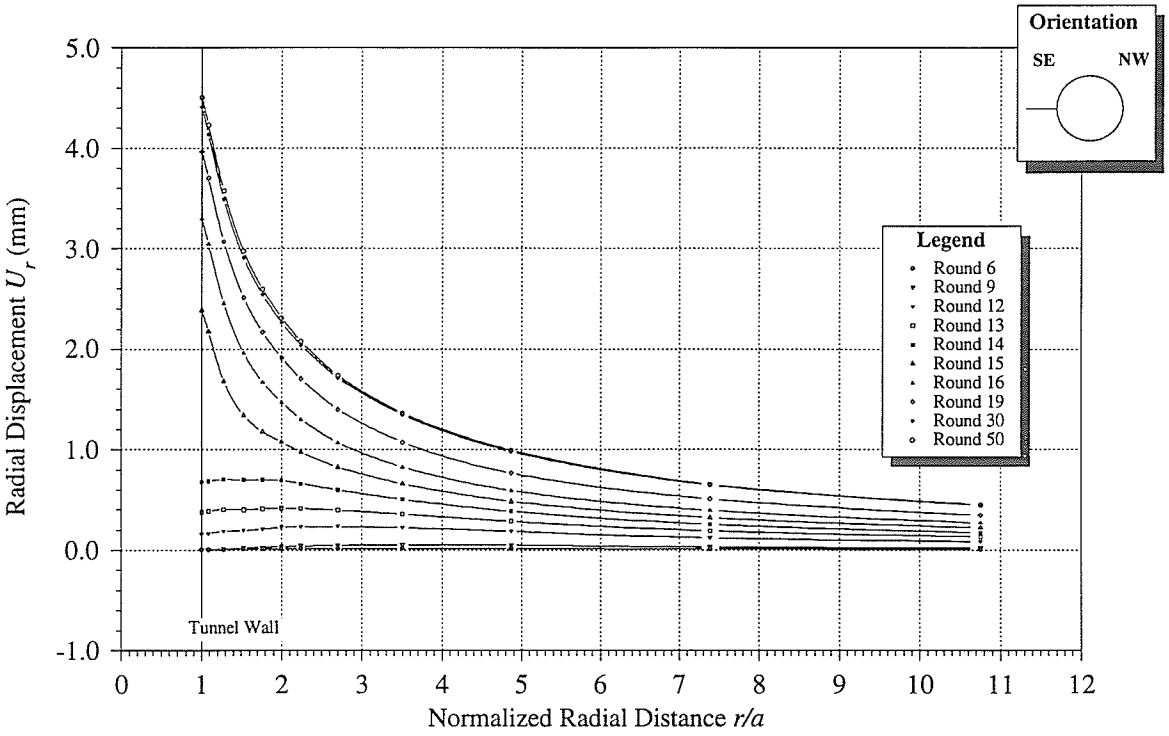

Figure 5.11: Radial displacement response versus radial distance for a typical horizontal extensometer (416-001-EXT4).

The responses for the extensometers in the upper NW and lower SE quadrants of the second Bof-ex array (EXT6 and 10), inclined at $\theta = 45°$ and 225° respectively, have similar characteristics to those from the horizontal extensometers. However, the final displacement magnitudes are less. The radial displacement response for EXT10 is illustrated in Figure 5.12.

The extensometers in the lower NW and upper SE quadrants of the second Bof-ex array (EXT8 and 12), inclined at $\theta = 315°$ and 135°, respectively, recorded complicated responses related to progressive failure near the instruments. EXT8 showed slight convergence (extension) in the posterior domain, then multiple reversals in gradient within 2.65 m of the tunnel wall, and general divergence (contraction) further into the rock mass, once the tunnel face advanced past the array location. EXT12 showed convergence (extension) in the

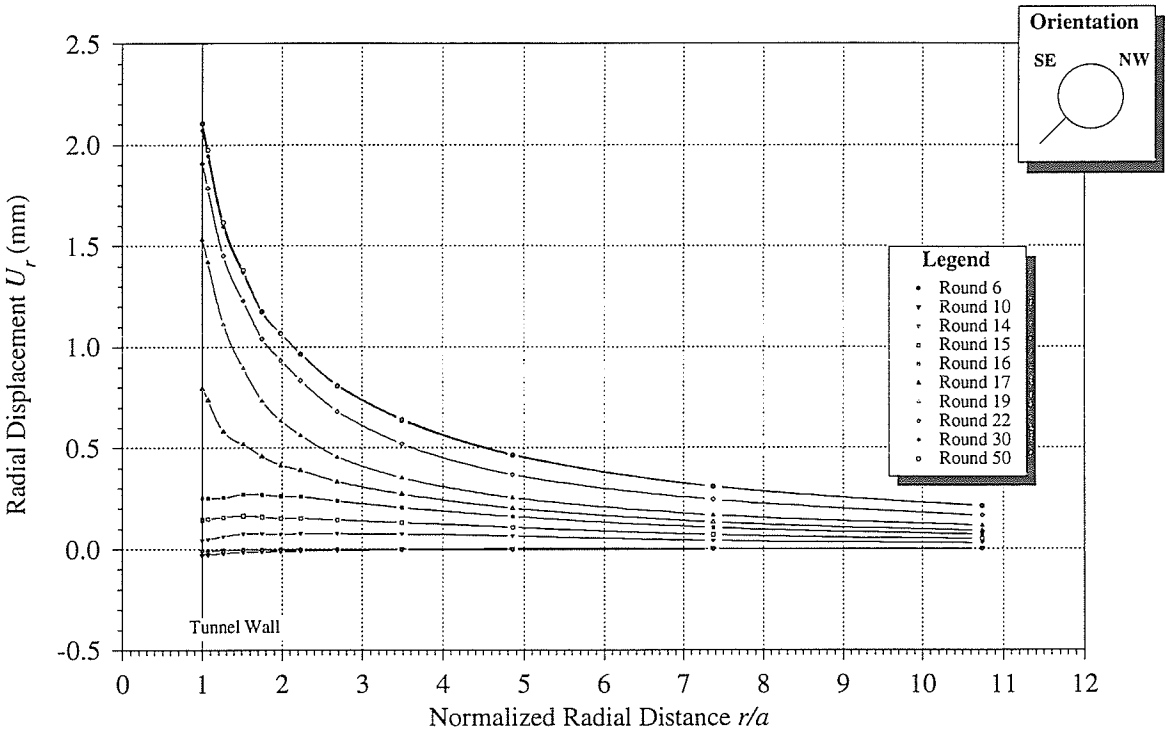

Figure 5.12: Radial displacement response versus radial distance for a typical 45-225° inclined extensometer (413-001-EXT10).

anterior domain, changing to divergence (contraction) with increasing face advance and damage development (Figure 5.13). The effects of progressive failure are obvious to a depth of 1.76 m into the rock mass in the posterior domain near EXT12.

Progressive failure also contributed to the time-dependent displacement response measured during a 319 h quiet period (Figure 5.14). The shapes of the individual responses measured by the Bof-exs over this period are similar to the displacement responses measured during advancement of the test tunnel, showing an increase in divergence in the vertical extensometers, and an increase in convergence in the other extensometers. For example, an increase in radial displacement of 0.095 and 0.126 mm was measured at the innermost anchors of EXT2 and 4, respectively. These findings suggest that the time-dependent change in tunnel geometry associated with progressive failure tends to intensify the difference in

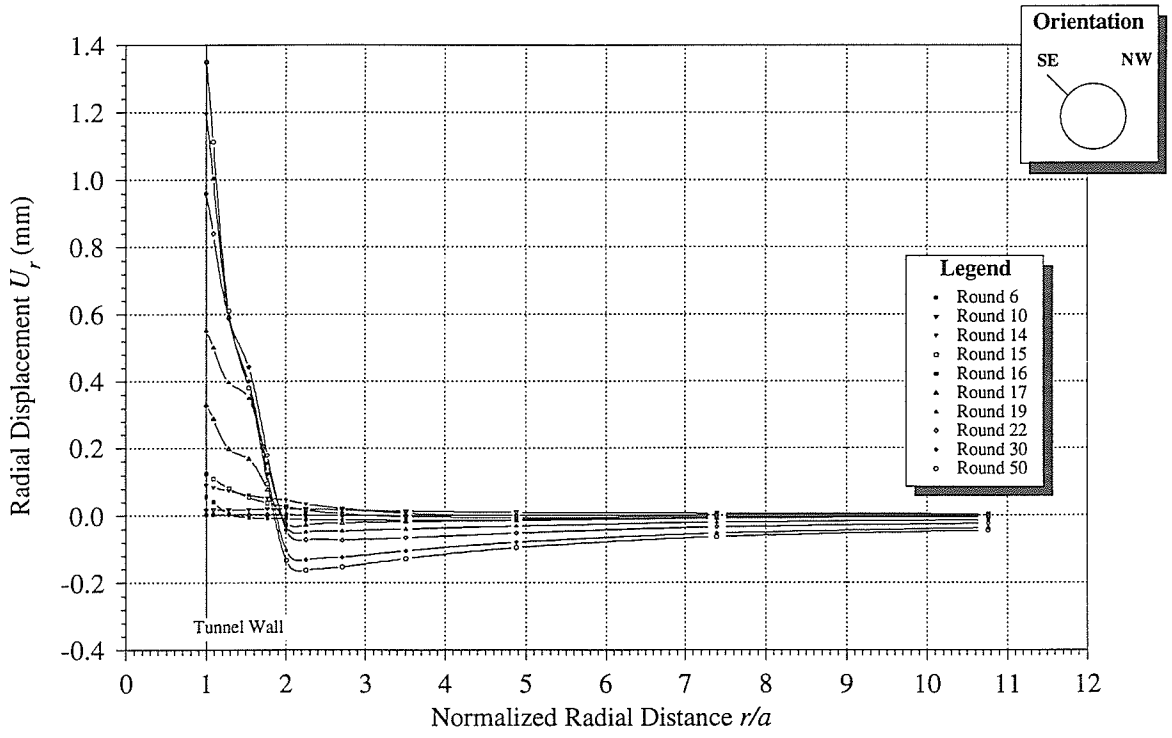

Figure 5.13: Radial displacement response versus radial distance for a typical 135-315° inclined extensometer (409-042-EXT12).

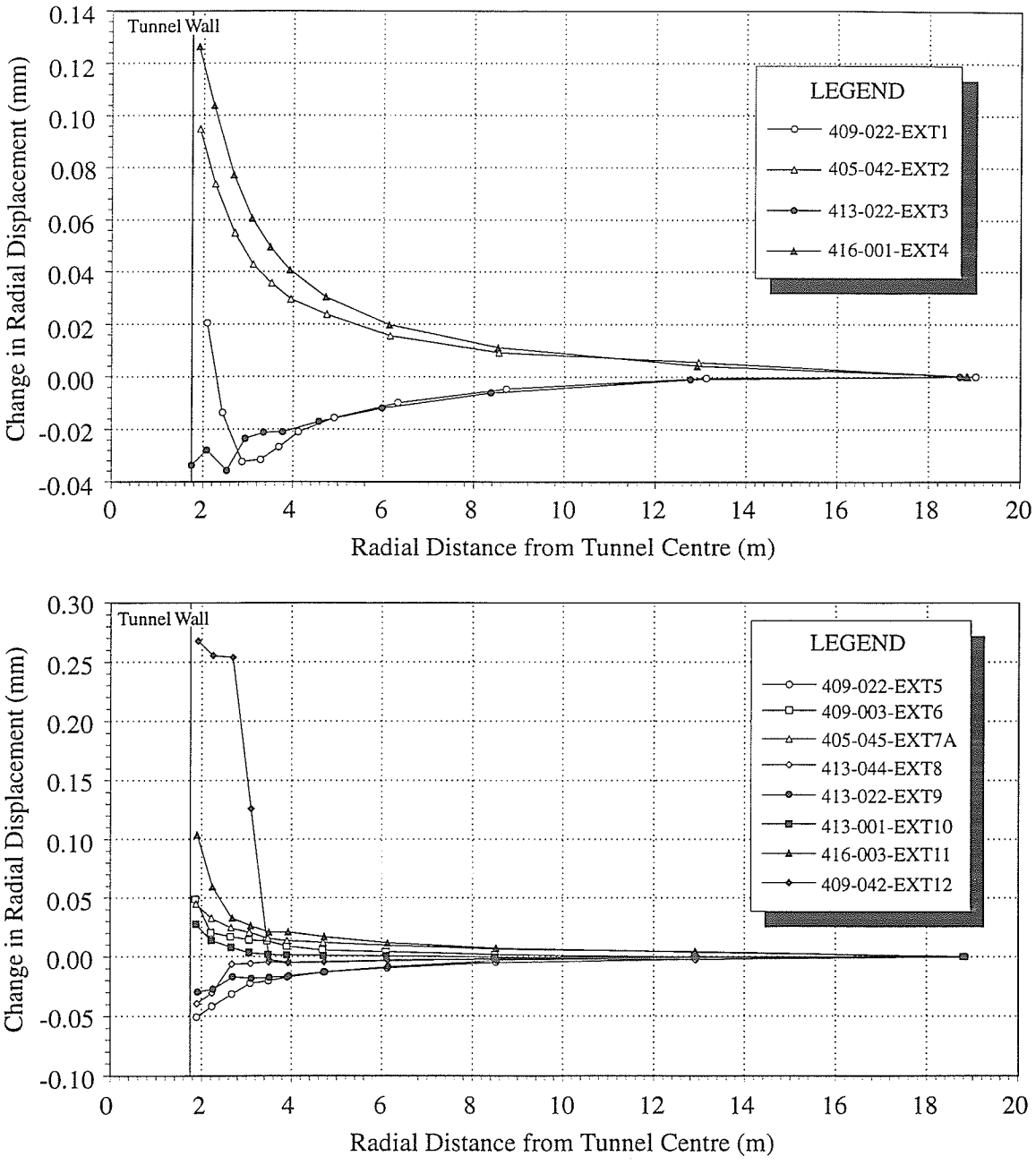

Figure 5.14: Time-dependent behaviour represented by a change in radial displacement in Bof-ex arrays 1 (top) and 2 (bottom) during a 319 h quiet period from March 6 to 19, 1992 for a fixed face position.

displacement behaviour between the maximum and minimum displacement directions.

5.2.2 Convergence results

Convergence measurements are presented versus time to document the history of the instrument array and any time-dependent effects in the response; versus face position to show the relationship between excavation advance and the measured response; and versus rotation angle to illustrate the rotational dependency of the measured response. Each of these plots represents the cumulative change in tunnel diameter relative to a baseline reading taken immediately following array installation. In all cases, positive convergence means a decrease in the relative distance between opposite sides of the tunnel.

Given that all but one of the convergence arrays were arranged in the same pattern relative to the tunnel axis, the data from the arrays can be considered redundant measurements of displacement at various rotation angles around the tunnel. The variation in these measurements reflects the *in situ* variability in the rock mass, e.g., geology, material properties, and *in situ* stresses, as well as instrumentation/operator error. Estimates of error based on the variation in measurements, however, are biased somewhat by the development of large-scale geometry changes in the tunnel section associated with progressive failure (Figure 5.15) and the variation in the time-dependent nature of physical processes associated with these changes. For example, these processes tend to increase the scatter in measurements taken close to the face during the active phase of progressive failure, but are less prevalent once the tunnel geometry stabilizes [159]. Therefore, the confidence limits established for the data account for the combined effect of error and variability of *in situ* conditions and material behaviour.

The number of readings collected for each convergence array was relatively small compared with the number of data from the electronically data-logged extensometers. As detailed in Read et al. [159], the *spliced logisitic function* was applied to the 48 measurement lines from the eight arrays to determine the mean response and confidence intervals. The

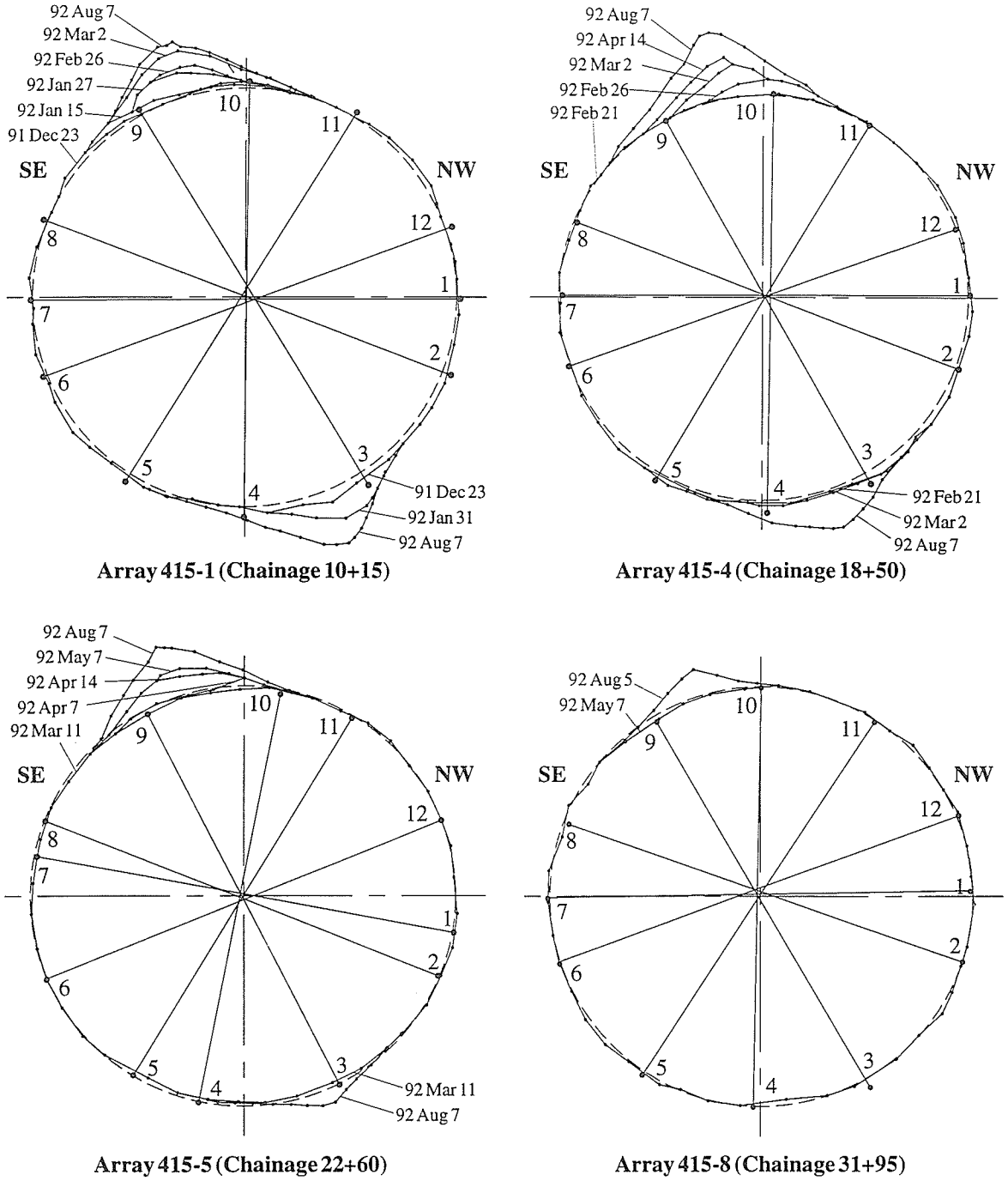

Figure 5.15: Comparison of tunnel profiles at convergence Arrays 415-1, 4, 5 and 8. These profiles represent a progression from a predominantly granite to a predominantly granodiorite region. Note that the extent of large-scale notch development is much less pronounced for Array 415-8 located completely in granodiorite.

exercise was repeated for combined data sets. The final convergence values following tunnel excavation predicted with the approximating function were used to develop plots of final convergence versus rotation angle, including confidence intervals.

Convergence versus time

Typical plots of convergence versus time for two arrays are shown in Figures 5.16 and 5.17. The plots show six data series associated with the diametral measurement lines for an array, as well as the temperature variation and excavation advance, versus time. In all cases except Array 415-8, one or more convergence pins were damaged or loosened during the course of the excavation, owing largely to progressive failure.

The plots in Figures 5.16 and 5.17 highlight the differences between responses from the first and last four arrays. The first four arrays show maximum convergence on lines 1-7 and 6-12 of between 6 and 8 mm. In contrast, the last four arrays show maximum convergence on the same lines of between 4 and 6 mm. The results from both arrays suggest that the maximum principal stress is oriented at approximately $10 \pm 5°$ from horizontal, plunging to the SE. They also suggest that, in comparison with tunnel profiles at the various arrays, the extent of progressive failure (i.e., cross-sectional shape) influences the convergence response. As illustrated in Figure 5.15, the extent of progressive failure appears to be dependent to some extent on geology, with less severe development in areas of predominantly granodiorite material as opposed to areas of grey granite. Similar observations have been made elsewhere at the URL by Everitt et al. [45]. Consequently, the measured response is related to geology. This relationship is explored further in Chapter 6.

Early parts of the curves illustrate time-dependent behaviour related to the gradual development of excavation damage. This phenomenon is represented by a changing response in periods where no excavation occurred, for example, in the period from March 6 to 19, 1992. It is also clear from the time history plots that the variability, either due to *in situ* processes and properties or operator/instrument error, is relatively high for this type

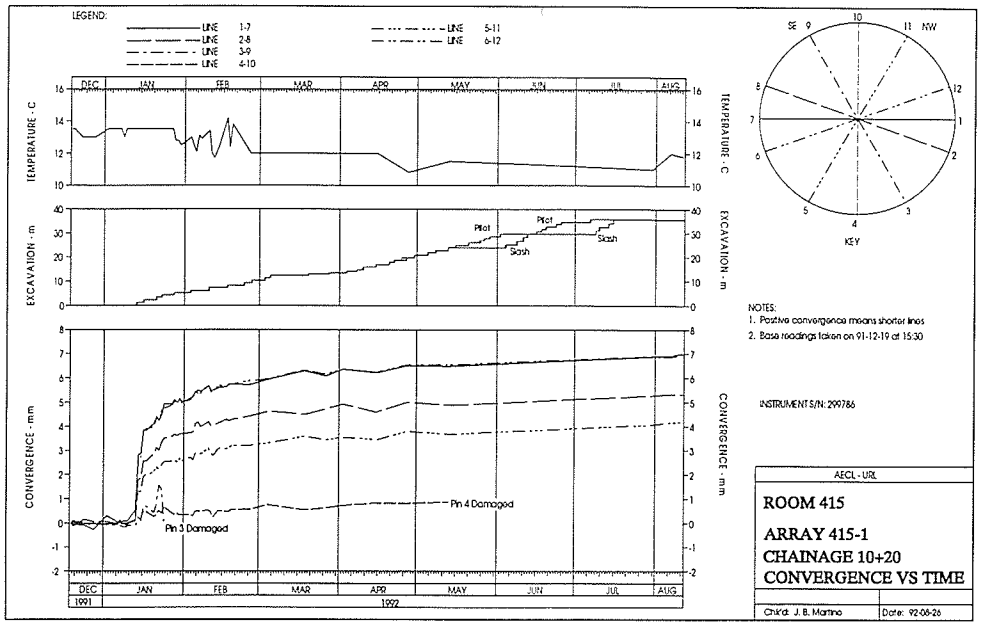

Figure 5.16: Radial convergence response versus time for a typical convergence array (Array 415-1) located in an area of predominantly granite.

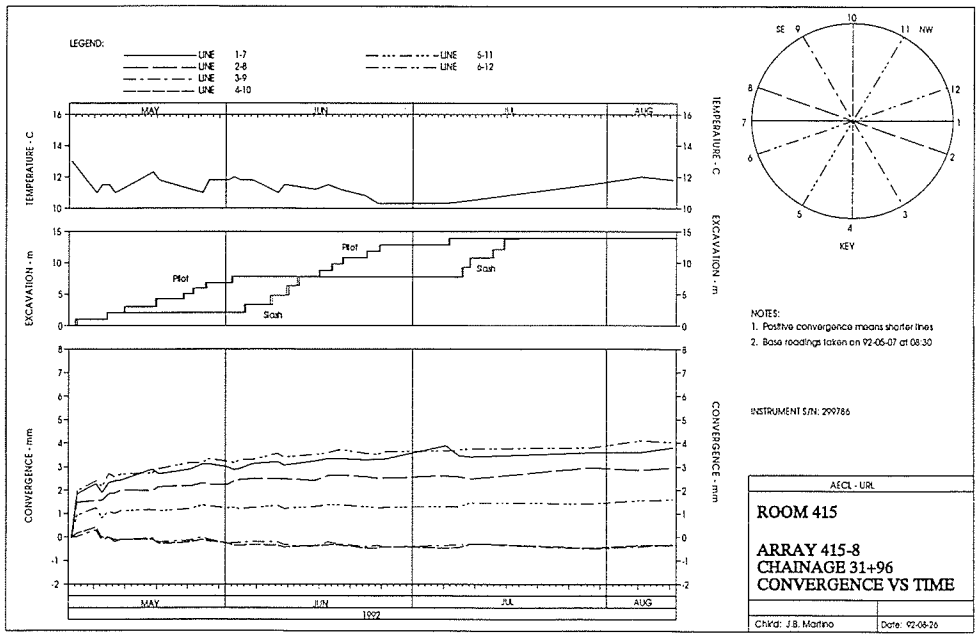

Figure 5.17: Radial convergence response versus time for a typical convergence array (Array 415-8) located in an area of predominantly granodiorite.

of instrument, but tends to decrease with time. Assuming operator/instrument error and property variability to be fairly constant with time, the results suggest that the *in situ* processes responsible for the progressive failure of the tunnel account for a large proportion of the measured variability [159].

Convergence versus face position

Plots of convergence versus face position were produced for each of the 48 measurement lines associated with the Mine-by Experiment [159]. Each plot comprised two parts: 1) a graph of convergence versus face position, showing the actual data used in the curve fit, the mean predicted response, and the 95 and 99% confidence (prediction) intervals on the data; and 2) a graph of residuals versus face position, illustrating the difference between the actual and predicted values. An example is shown in Figure 5.18. Of the 48 plots, 13 were for lines that were either damaged or produced suspect data and, consequently, were not considered representative of the true rock mass response. These 13 plots represent measurement lines 3-9 and 4-10 for Arrays 415-1, 2, 3, 4, 5, and 7, and measurement line 2-8 for Array 415-7. The measurements from the remaining 35 diametral lines typify the rock mass response as measured by convergence arrays.

The best-fit values for the parameters associated with the approximating function for the 35 individual lines are presented in Table E.2 of Appendix E. The values of parameter A in this table have been adjusted from those reported by Read et al. [159] so as to express the face position in dimensionless form, i.e., X/D rather than X. Of particular interest in this table are the values for parameter F, representing the total convergence in the posterior domain, i.e., $E_l - D_l$. The values of F are used in Section 5.2.2 to estimate the final displacement response as a function of rotation angle. The approximating function was simplified in most cases by the fact that $\lambda = 0$ for all except three special cases involving near-zero final convergence (transition from convergence to divergence). It appears that only in such cases is the second-order term necessary in the *spliced logistic function*. The

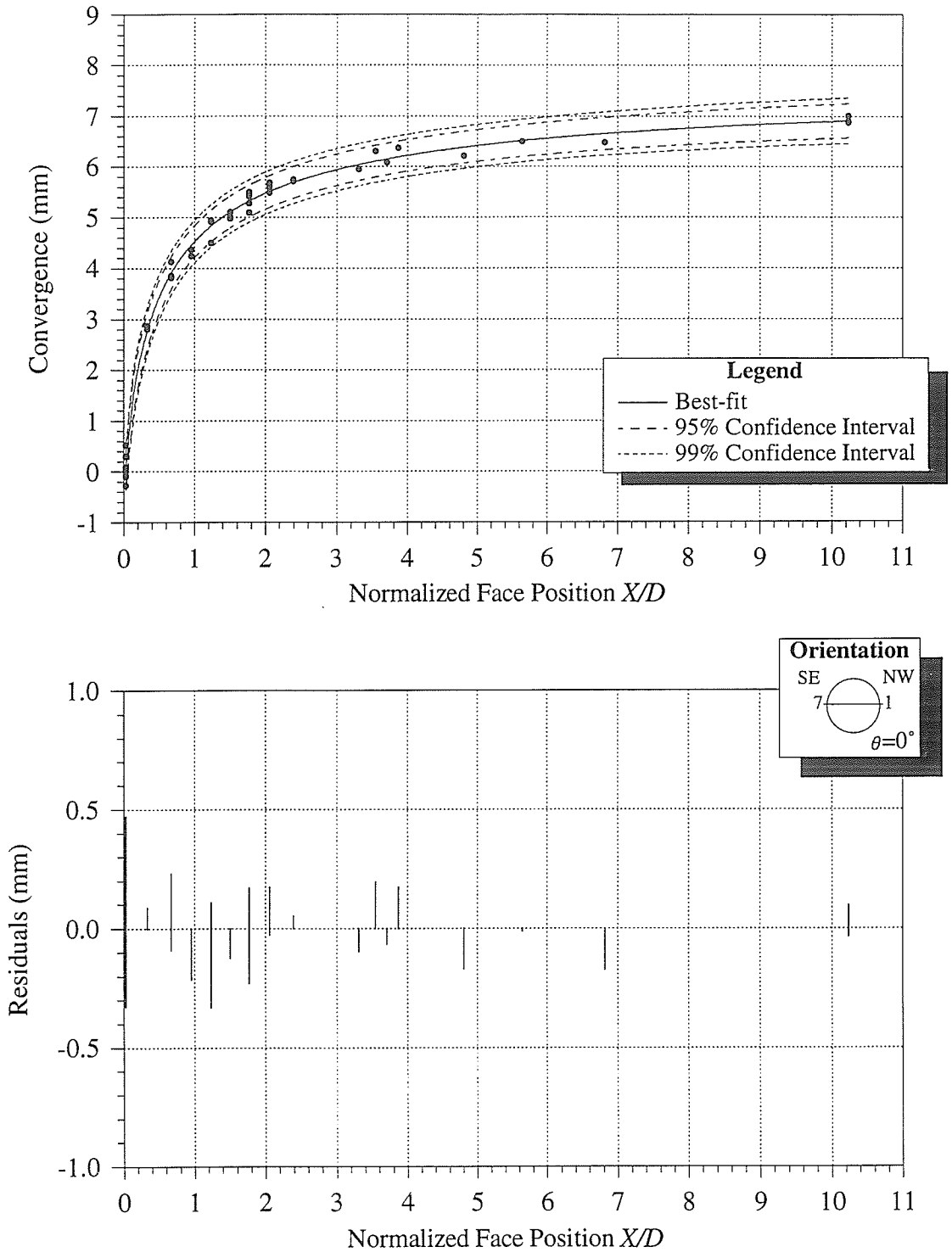

Figure 5.18: Typical plot of convergence versus face position for a horizontal measurement line (Array 415-1).

Table 5.1: Parameter values for convergence versus face position (combined measurement lines).

Array	Line	A	B	E_l	λ	r^2
415-1	1-7	0.294	-0.745	8.201	0.000	0.975
to	2-8	0.419	-0.770	5.825	0.000	0.947
415-4	5-11	0.449	-0.772	5.290	0.000	0.963
	6-12	0.355	-0.849	8.007	0.000	0.987
415-5	1-7	0.208	-0.632	5.544	0.000	0.926
to	2-8	0.092	-0.446	4.885	0.000	0.864
415-8	3-9	1.667	-1.605	-0.426	13.189	0.716
	4-10	2.225	-0.969	-0.478	-3.457	0.336
	5-11	0.007	-0.317	4.018	0.000	0.818
	6-12	0.124	-0.521	6.684	0.000	0.868

coefficient of variation was generally > 0.9 for cases other than the three specified, often approaching 0.99 or better.

Combined data sets were generated by first zeroing the individual responses, then partitioning data from the first four and last four arrays into two groups. The distinction was made on the basis of geology and extent of progressive failure, with those arrays in predominantly grey granite (extensive failure development) selected for the first group, and those in mainly granodiorite (minor failure development) in the second group. As shown in Table 5.1, the data sets for the combined diametral measurement lines showed more variability than the corresponding data sets for individual arrays, but generally agreed well with the approximating function. An example of combined data from measurement line 1-7 for the first four arrays is shown in Figure 5.19. Note that, because the responses were zeroed to a common face position, the parameter D_l is zero in all cases. Therefore, the parameters E_l and F are identical. Owing to irregularities in the convergence pin performance for measurement lines 3-9 and 4-10 in the first four arrays, it was not possible to obtain meaningful estimates of the approximating function parameters for these lines.

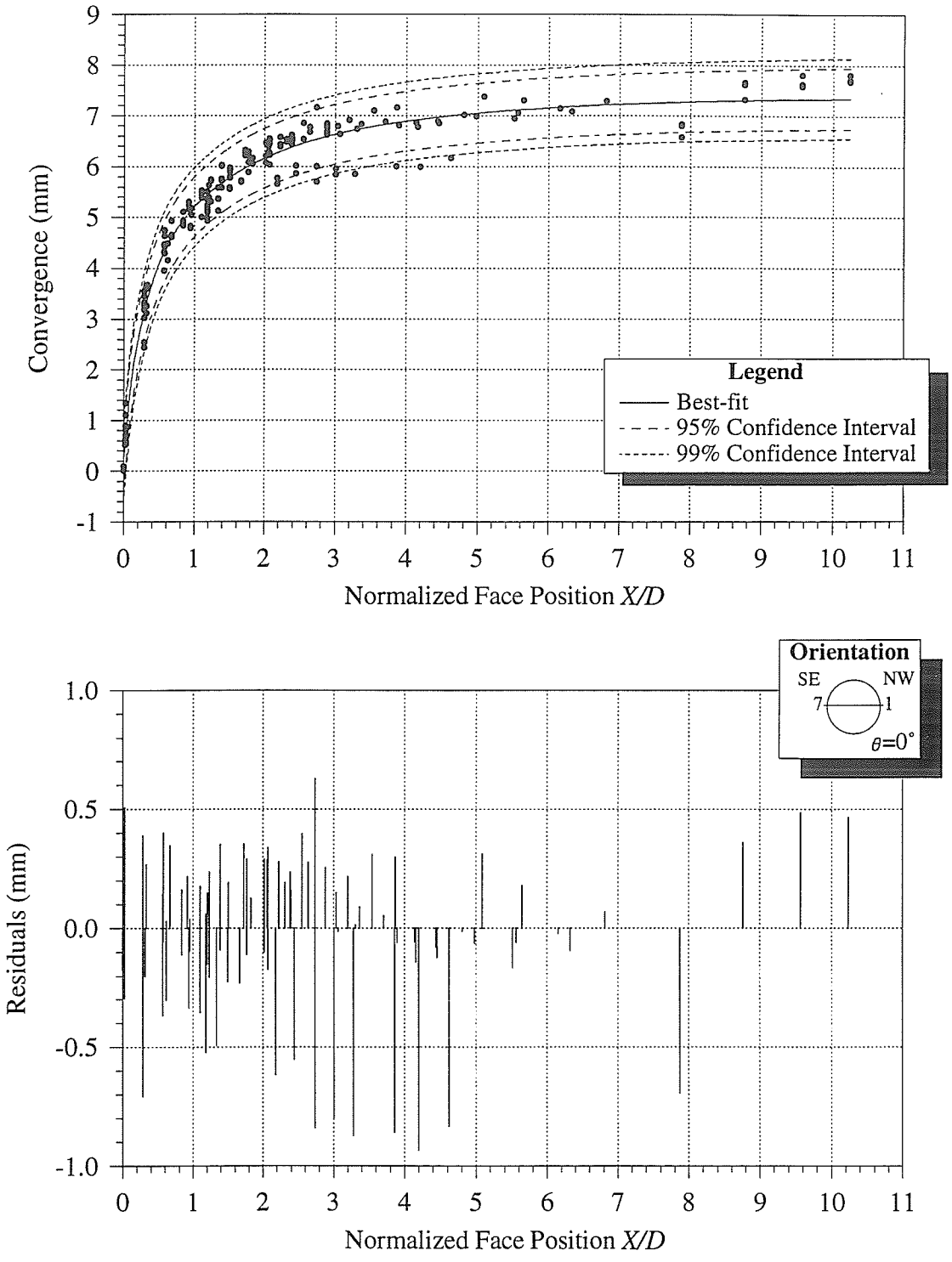

Figure 5.19: Typical plot of convergence versus face position for combined horizontal measurement lines (Arrays 415-1 to 4). Note the increase in variability compared to the individual data for Array 415-1.

Convergence versus rotation angle

Three plots of total convergence in the posterior domain versus rotation angle were compiled from the estimates of F in Table 5.1: two showing responses for the combined data from Arrays 415-1 to 4 (Figure 5.20), and Arrays 415-5 to 8 (Figure 5.21), respectively; the other showing the combined response from all arrays (Figure 5.22). The approximating function used in the plots of convergence versus rotation angle is given by

$$2U_r = \alpha + \beta \cos\left[2\left(\theta - \psi\right)\right] \tag{5.5}$$

where $2U_r$ is the tunnel convergence, α is the mean value of the response, β is the amplitude of the harmonic response about the mean, and ψ is a phase constant. Equation 5.5 is of the same form as the parametric functions associated with the plane components of the partitioned stress tensor (Chapter 4). Because convergence measurements represent the relative displacement between opposite walls of the tunnel, they are affected only by stress components producing either an axisymmetric radial displacement response, or those that have a periodicity of $\theta = 180°$. The antiplane shear stress components produce radial displacement responses with a periodicity of $\theta = 360°$ which show no relative displacement between opposite sides of the tunnel despite significant absolute displacement of each wall near $X/D = 0$. Consequently, the harmonic component of Equation 5.5 is a function of $\cos\left(2\theta\right)$ alone.

As shown in Table 5.2, the combined data from all arrays show more scatter about the mean response than the two separate groups representing regions of different geology and tunnel profile. The mean response α and amplitude β of the response for the arrays in granite are both greater than those for the arrays in granodiorite. In addition, the phase constant ψ varies somewhat between the two groups, although the relatively sparse data in the separate groups used to estimate ψ, and in particular the lack of measurements for lines 3-9 and 4-10 in the first group, increased the uncertainty in the estimated value. The phase constant associated with the data set of all the arrays provides the best estimate of

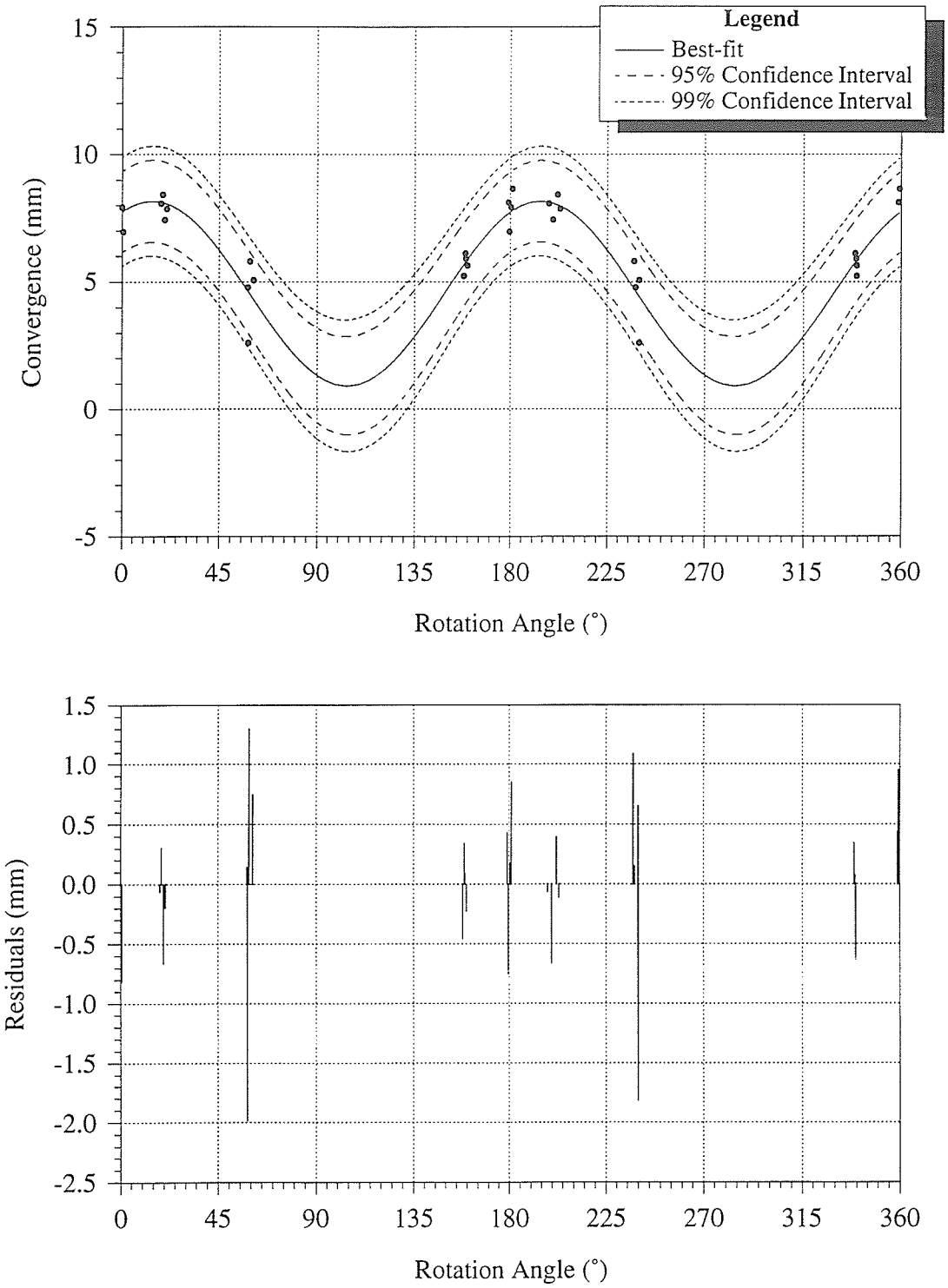

Figure 5.20: Combined final convergence results versus rotation angle for convergence arrays in granite (Arrays 415-1 to 4).

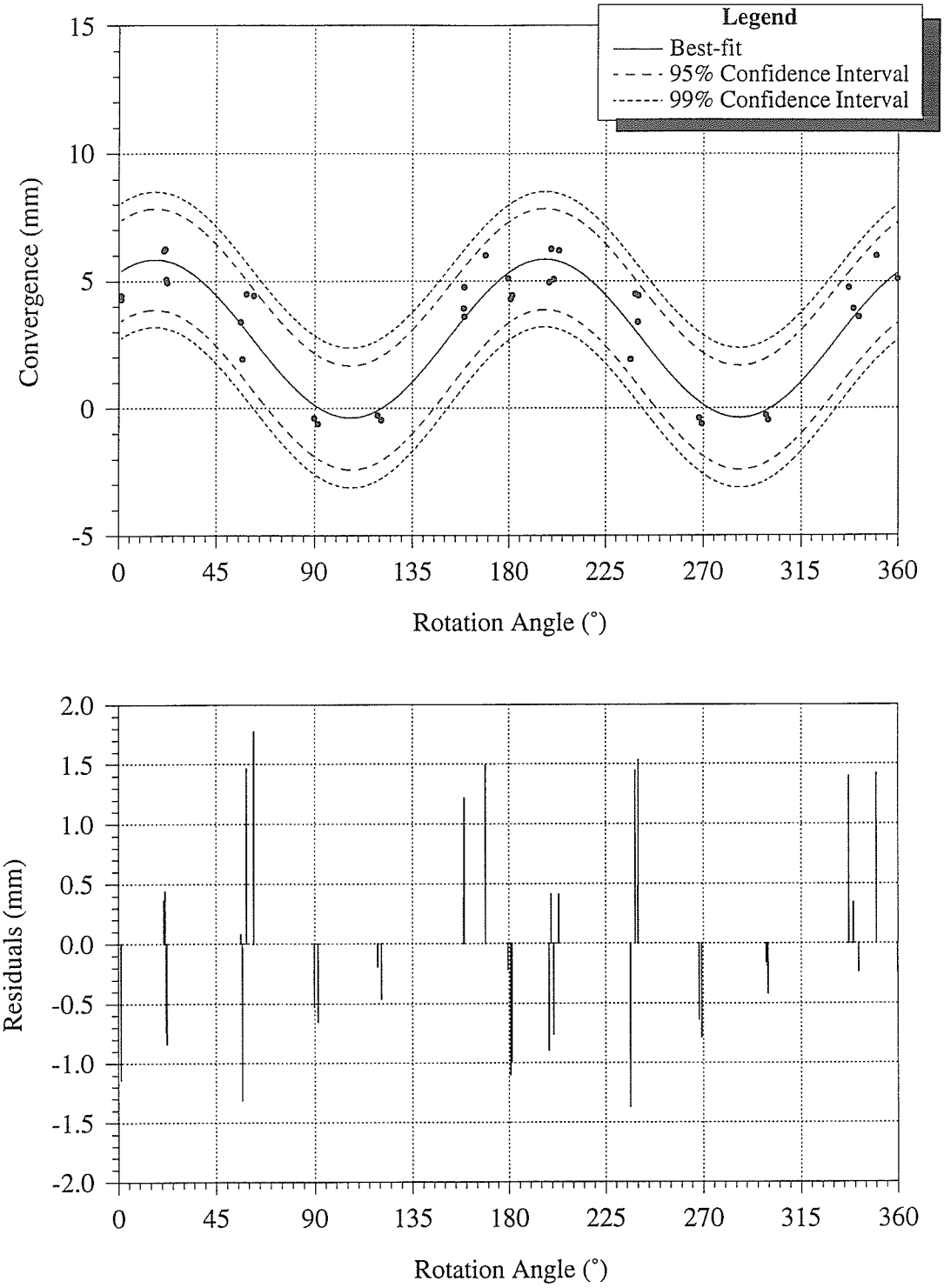

Figure 5.21: Combined final convergence results versus rotation angle for convergence arrays in granodiorite (Arrays 415-5 to 8).

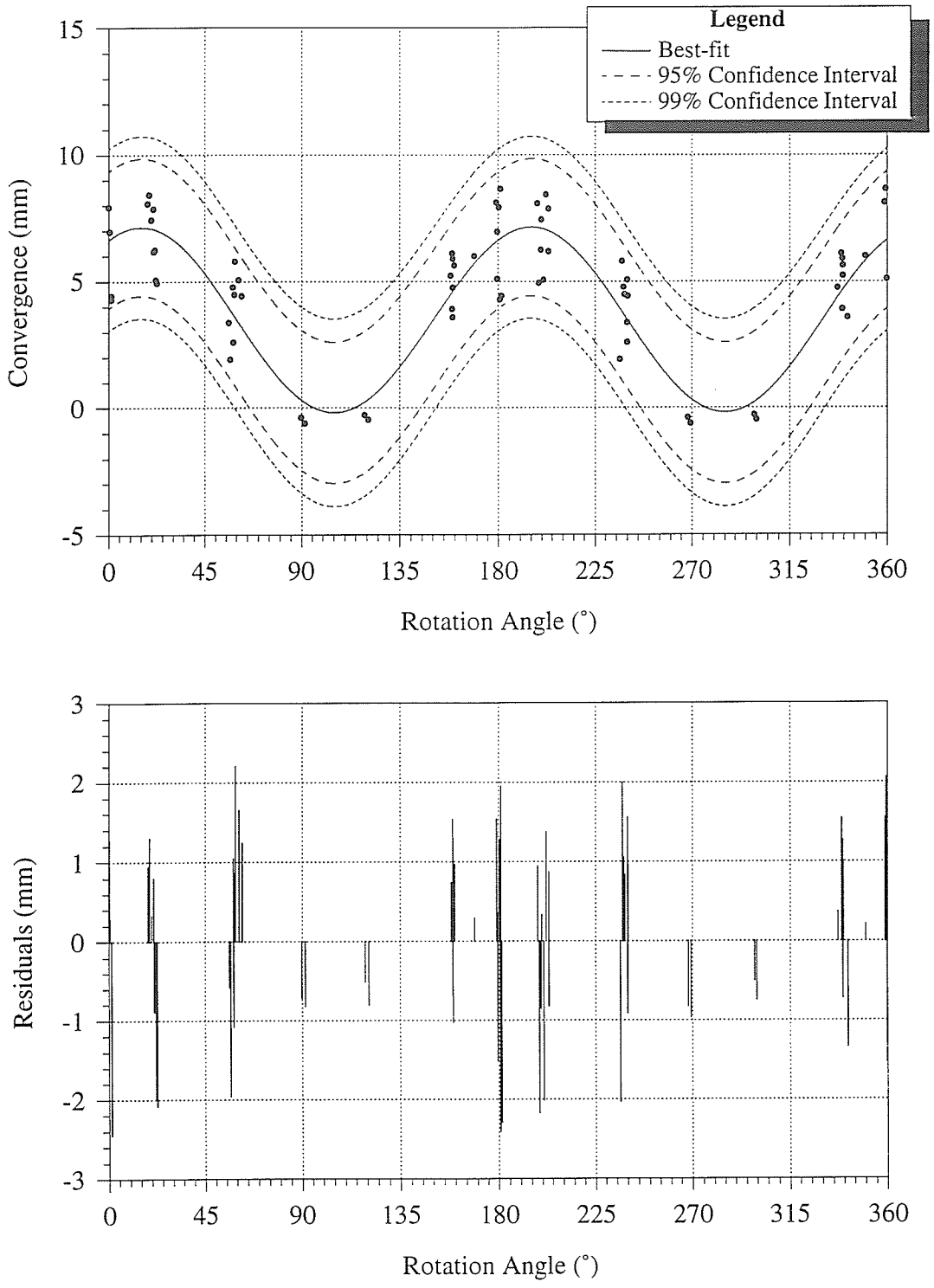

Figure 5.22: Combined final convergence results versus rotation angle for all convergence arrays (Arrays 415-1 to 8).

Table 5.2: Parameter values for convergence versus rotation angle (combined measurement lines). Arrays 415-1 to 4 are in predominantly grey granite, while Arrays 415-5 to 8 are in predominantly granodiorite. Note the similarity in the phase constant ψ between the various groups.

Array	α	β	ψ	r^2
415-1 to 415-4	4.534	3.626	13.948	0.803
415-5 to 415-8	2.735	3.111	16.621	0.838
All	3.475	3.665	15.181	0.726

ψ, suggesting that the maximum radial displacement direction for the excavation-damaged tunnel is oriented at $15 \pm 2°$ from horizontal, plunging to the SE. The fact that the phase constants for the various groups are similar indicates little significant influence of geological variability on the orientation of the maximum radial displacement direction.

5.2.3 Comparison of convergence and extensometer results

As shown in Equation 5.5, tunnel convergence is expressed as the relative radial displacement of opposite walls of the tunnel, and, consequently, the radial displacement of each wall contributes equally to the overall convergence response. From the study in Chapter 4, this condition is valid even in the presence of significant antiplane stresses. As mentioned in Chapter 4, a consequence of the relative, rather than absolute, nature of convergence measurements is that they are unaffected by antiplane shear stresses, and therefore cannot be used to back analyze the complete stress tensor.

In comparing responses from extensometers and convergence arrays, two approaches were explored. In the first, the convergence response was divided in half to approximate the response that would be measured by each of two opposing posterior extensometers. In the second, the measurements from opposing extensometers were added and compared to the convergence response. The first approach permits an assessment of the influence of antiplane shear stresses on the extensometer results, and overcomes the difficulty posed by a lack of perfect symmetry in the extensometers. The second approach provides a direct comparison

of relative displacements without the bias introduced by antiplane shear stresses, but is susceptible to errors associated with misalignment of opposing extensometers.

The first step in comparing responses from the two types of instruments involved approximating the corrected radial displacement response versus face position from each of the twelve extensometers using the *spliced logistic function.* The two-step interpolation technique employed for the initial interpolation of the unadjusted data set was used. In the anterior domain, the best approximating function was a combination of two *spliced logistic functions* with the parameter λ set to zero. In the posterior domain, a single *spliced logistic function* with $\lambda = 0$ was used to match the measured response, except for EXT8 which required a combination of two *spliced logistic functions* in the posterior domain. Although the single approximating function in the posterior domain produced slightly decreased coefficients of determination compared to the initial interpolation where a combination of two functions was used, the reduction in the number of coefficients in the best-fit function facilitated direct comparison of results from different instruments. The parameters associated with the approximating functions for each extensometer are shown in Table E.3 of Appendix E.

From the results in Table E.3, a summary of the radial displacement occurring in the anterior domain (D_l), the total radial displacement (E_l), the radial displacement occurring in the posterior domain (F), and the proportion of the measured radial displacement response occurring in the anterior and posterior domains (D_l/E_l and F/E_l), respectively, was compiled (Table 5.3). It is clear from this table that both the anterior proportion of the total radial displacement response D_l/E_l, and the posterior proportion F/E_l, vary with rotation angle. Because the proportion is not constant, these results imply that the antiplane normal component of stress contributes significantly to the measured response, affecting the amount of radial displacement missed by posterior-type instruments. In addition, the development of excavation damage within the tunnel affects the values of E_l, exaggerating the radial displacement in areas both of convergence and divergence. Back analysis approaches

Table 5.3: Anterior proportion and total radial displacement for the field study extensometers. Note that the radial displacement at $X = -\infty$ is taken as zero instead of extrapolating the combined anterior approximating functions. E_l represents the total radial displacement at $X = +\infty$, D_l/E_l is the anterior proportion of the total radial displacement response, and F/E_l is the posterior proportion.

Instrument	θ	D_l	E_l	F	D_l/E_l	F/E_l
EXT1	88.44	-0.348	-0.716	-0.368	0.49	0.51
EXT2	4.17	0.642	3.452	2.810	0.19	0.81
EXT3	278.59	-0.211	-0.651	-0.441	0.32	0.68
EXT4	184.81	0.880	4.318	3.438	0.20	0.80
EXT5	88.88	-0.235	-0.382	-0.147	0.62	0.38
EXT6	58.11	0.318	2.243	1.925	0.14	0.86
EXT7A	1.26	0.541	3.000	2.458	0.18	0.82
EXT8	313.52	-0.099	0.001	0.100	-91.40	92.40
EXT9	272.63	-0.332	-0.726	-0.394	0.46	0.54
EXT10	228.16	0.313	2.040	1.726	0.15	0.85
EXT11	184.64	0.674	3.989	3.314	0.17	0.83
EXT12	129.78	-0.013	1.226	1.239	-0.01	1.01

that assume a constant missed proportion of the total radial displacement response are, therefore, not applicable to the field study.

To compare the extensometer and convergence measurements, the results for F in Table 5.3 were plotted against rotation angle θ, and the convergence results for all eight arrays were divided in half and overlain (Figure 5.23). Because extensometer measurements are taken relative to a distant fixed reference, they are susceptible to the influence of antiplane shear stresses near the tunnel face. Consequently, based on the results from the parametric study in Chapter 4, the correct approximating function for the radial displacement response versus rotation angle is given by

$$U_r = \alpha + \beta_1 \cos(2\theta) + \beta_2 \sin(2\theta) + \beta_3 \cos(\theta) + \beta_4 \sin(\theta) \tag{5.6}$$

where α is related to a combination of the three normal stress components, β_1 is related to the combined plane normal stress components, β_2 is related to the plane shear stress component, and β_3 and β_4 are related to the antiplane shear stress components. The function

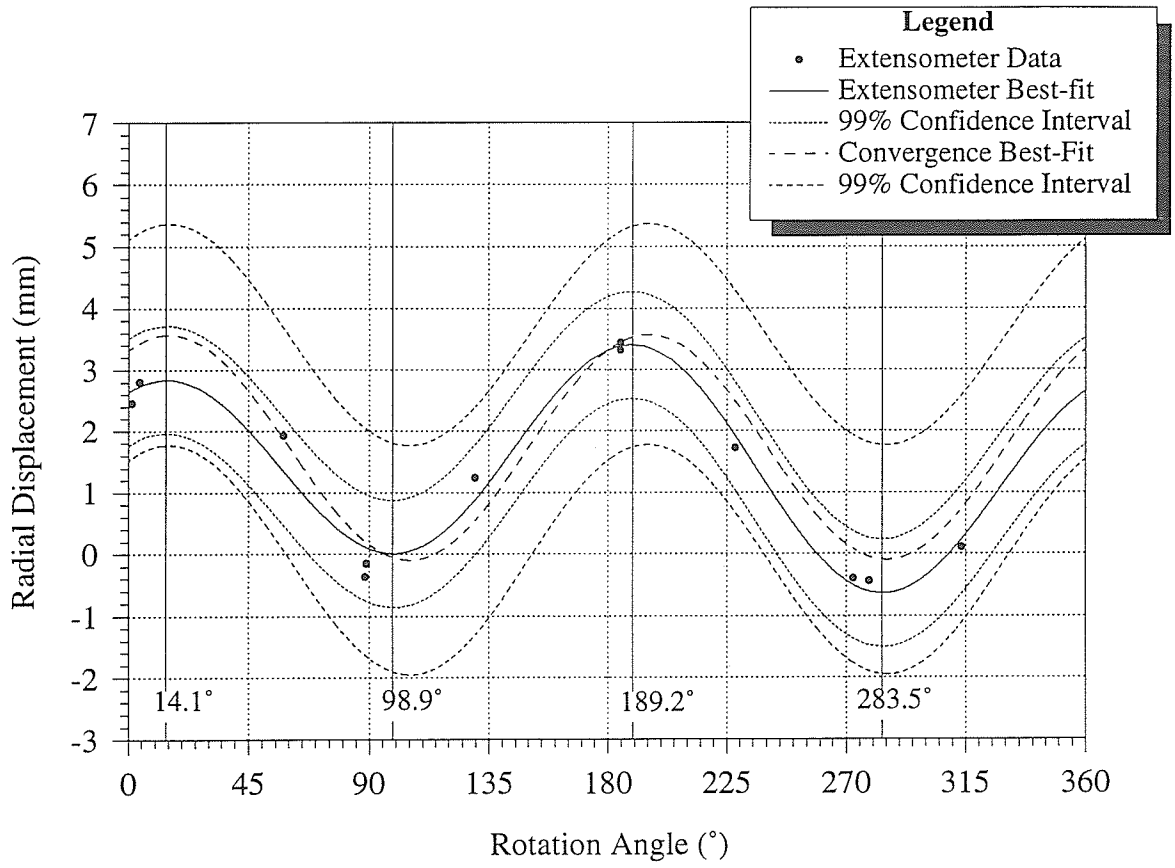

Figure 5.23: Comparison of posterior radial displacement results from extensometers F and convergence arrays. The radial displacement for the convergence arrays is taken as one-half the total convergence. Results from all eight convergence arrays were considered. Note the asymmetry in the magnitude and rotation angle of the maxima and minima.

Table 5.4: Function coefficients for the radial displacement response versus rotation angle measured with extensometers.

Domain	α	β_1	β_2	β_3	β_4	r^2
Anterior	0.205	0.458	0.216	-0.059	0.018	0.9599
Posterior	1.402	1.578	0.667	-0.339	0.261	0.9633

coefficients associated with the best-fit approximation to the extensometer measurements are shown in Table 5.4.

Figure 5.23 illustrates several interesting points. First, the measured results, the best-fit function and the 99% confidence intervals for the extensometers fall completely within the 99% confidence intervals for the convergence response. Furthermore, the convergence best-fit function falls completely within the 99% confidence intervals for the extensometer response. These facts suggest that the two responses have similar mean values, amplitudes and phase constants, and are consistent within the specified confidence interval.

The approximating function chosen to interpolate the extensometer results is composed of an axisymmetric component, two harmonic components with a periodicity of 180°, and two harmonic components with a periodicity of 360°. The resulting best-fit function for the extensometer data has asymmetric maxima and minima for $0 \leq \theta \leq 360°$, suggesting that the antiplane shear stress components, with a periodicity of 360°, are non-zero. The resulting displacement pattern shows the maxima at $\theta = 14.1°$ and 189.2°, and the minima at $\theta = 98.9°$ and 283.5°. Consequently, the zones of maximum divergence far from the tunnel face are located 9.2° and 13.5° counterclockwise of vertical in the roof and floor, respectively.

In order to obtain an estimate of the relative influence of the various components of the partitioned stress tensor that was not biased by the development of large-scale excavation damage, the radial displacement response at $X/D = 0$ from the extensometers (D_l) was plotted versus rotation angle (Figure 5.24). This response represents the anterior portion of

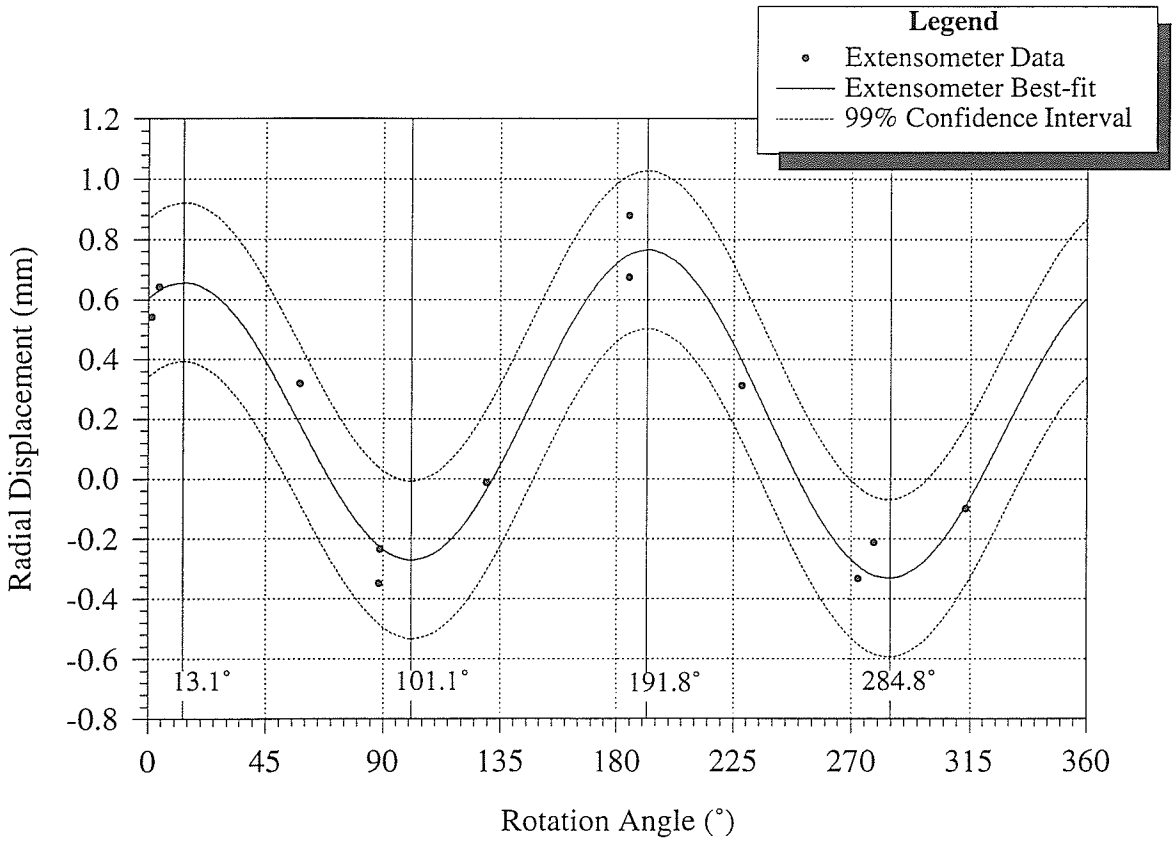

Figure 5.24: Anterior radial displacement response from extensometers D_l measured at $X/D = 0$. Note the asymmetry in magnitude and rotation angle of the maxima and minima.

the total radial displacement response, i.e., the portion that would be missed by posterior-type instruments such as convergence arrays. The radial displacement response is a function of all six stress components, and, therefore, the general approximating function given by Equation 5.6 was fit to the measured data. The coefficients for the best-fit curve to the anterior response are shown in Table 5.4.

The radial displacement response at $X/D = 0$ is asymmetric with regards to the relative positions and magnitudes of the maxima and minima. The maxima occur at $\theta = 13.3°$ and 191.8°, while the minima occur at $\theta = 101.1°$ and 284.8°. Therefore, the antiplane shear stress components account for a 3.7° shift between the two minima, and a 1.5° shift in the maxima. Likewise, the magnitudes of the two maxima are different, as are the magnitudes of the two minima. Like the results from the posterior domain, the maximum on the SE side of the tunnel is larger than that on the NW side. Likewise, the minimum in the floor shows more divergence than that in the roof. These results suggest that, prior to significant progressive failure of the excavation, the radial displacement response associated with the antiplane shear stresses is small, yet significant, illustrating that the tunnel axis is not coincident with a principal stress direction. The development of excavation damage exaggerates the asymmetry in the response, causing additional divergence in the roof and floor, and additional convergence in the sidewalls.

These results also suggest that, in conditions where significant antiplane shear stresses exist owing to a deviation in the orientation of the tunnel axis relative to each of the principal stress directions, the radial displacement response versus rotation angle can potentially be very asymmetric. This asymmetry is reflected in the stress/strain field around a tunnel, and, consequently, in the angular positions of the initiation points of progressive failure. The relationship between displacements, stresses and asymmetrical breakouts is explored in Chapter 6.

The extensometer and convergence measurements were also compared by summing the results from opposing extensometers and overlaying the combined convergence results from

all eight arrays (Figure 5.25). In this case, because all of the measurements are relative in nature, i.e., independent of the effect of antiplane shear stress components, the approximating function given by Equation 5.5 was used for both sets of data. The resulting functions have a periodicity of 180°, so the maxima and minima are symmetric in both rotation angle and magnitude. From the extensometer results, the phase constant ψ was found to be 12.1°, less than the 15.2° estimated from the convergence results. Both of these estimates were influenced by the development of excavation damage within the tunnel, which reduced the reliability of measurements in regions where divergence was observed, and exaggerated the maximum to minimum displacement ratio. As in the previous comparison, the measured

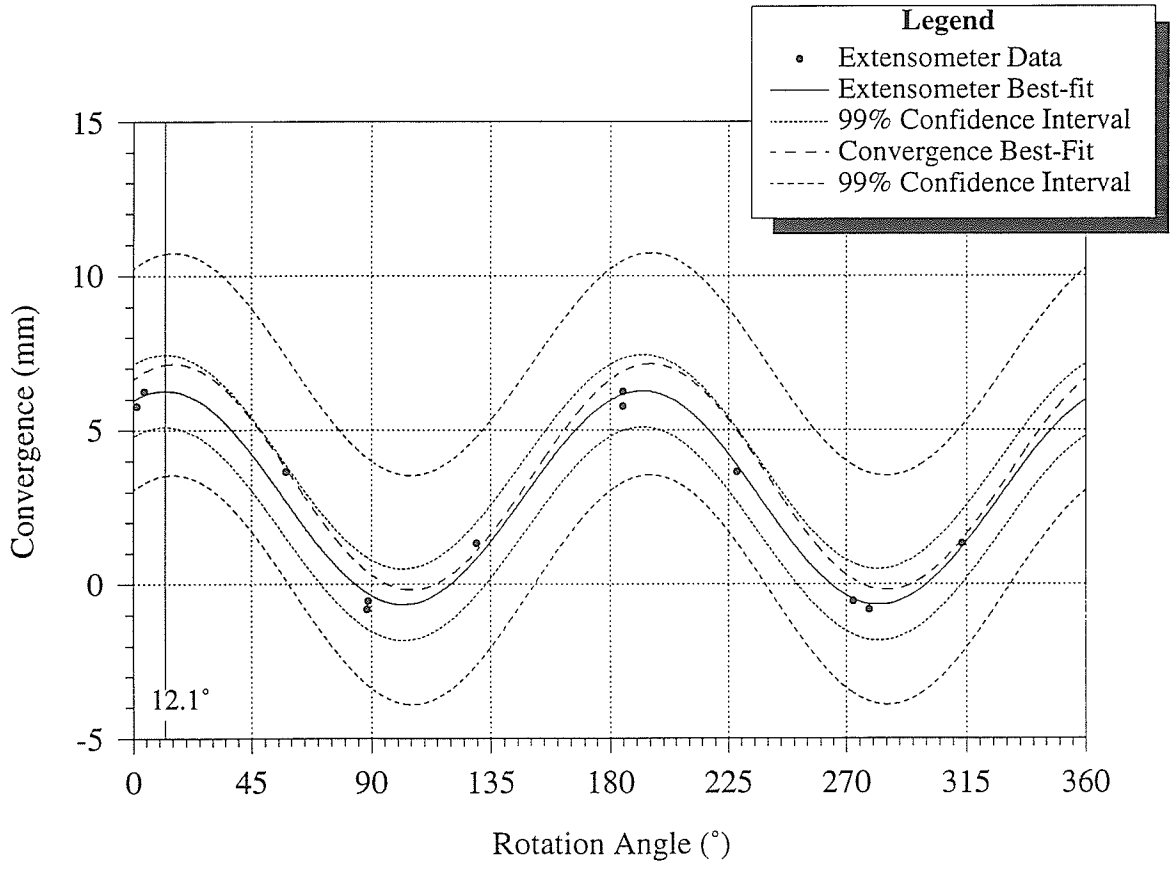

Figure 5.25: Comparison of posterior convergence results from extensometers and convergence arrays. The convergence for the extensometers is taken as the sum of measurements from opposing instruments in the posterior domain.

Table 5.5: Function coefficients for the posterior portion of the convergence response versus rotation angle measured with extensometers.

Instruments	α	β	ψ	r^2
EXT1 to 12	2.799	3.475	12.101	0.9804

results, the best-fit function and the 99% confidence intervals for the extensometers fall completely within the 99% confidence intervals for the convergence array data. Likewise, the best-fit function for the convergence array data falls completely within the confidence intervals for the extensometer data, suggesting that the two measurement types are similar within the specified confidence interval. The coefficients for the best-fit approximating function for the extensometer data versus rotation angle are given in Table 5.5.

A final comparison between the extensometer and convergence responses was conducted to assess the measured convergence response versus face position. For this component of the study, the only reliable measurements with similar orientation were taken with the horizontal extensometers and horizontal diametral measurement lines (Line 1-7) in the convergence arrays. Although both types of instrument measured displacement in the vertical direction, the onset of progressive failure in the tunnel reduced the reliability in the data measured in this direction. The best-fit approximation to the combined convergence data from the first four convergence arrays, and the best-fit convergence responses associated with the two extensometer arrays, are shown in Figure 5.26. The extensometer responses were produced by summing the approximating functions for the posterior radial displacement response (Table E.3) of opposing horizontal extensometers in each array: EXT2 and 4 in the first array, and EXT7A and 11 in the second. As part of the comparison, the curvature κ of each response, given by

$$\kappa = \frac{\left|\frac{d^2y}{dx^2}\right|}{\left[1+\left(\frac{dy}{dx}\right)^2\right]^{3/2}} \tag{5.7}$$

was also determined from the *spliced logistic function* used to approximate the combined

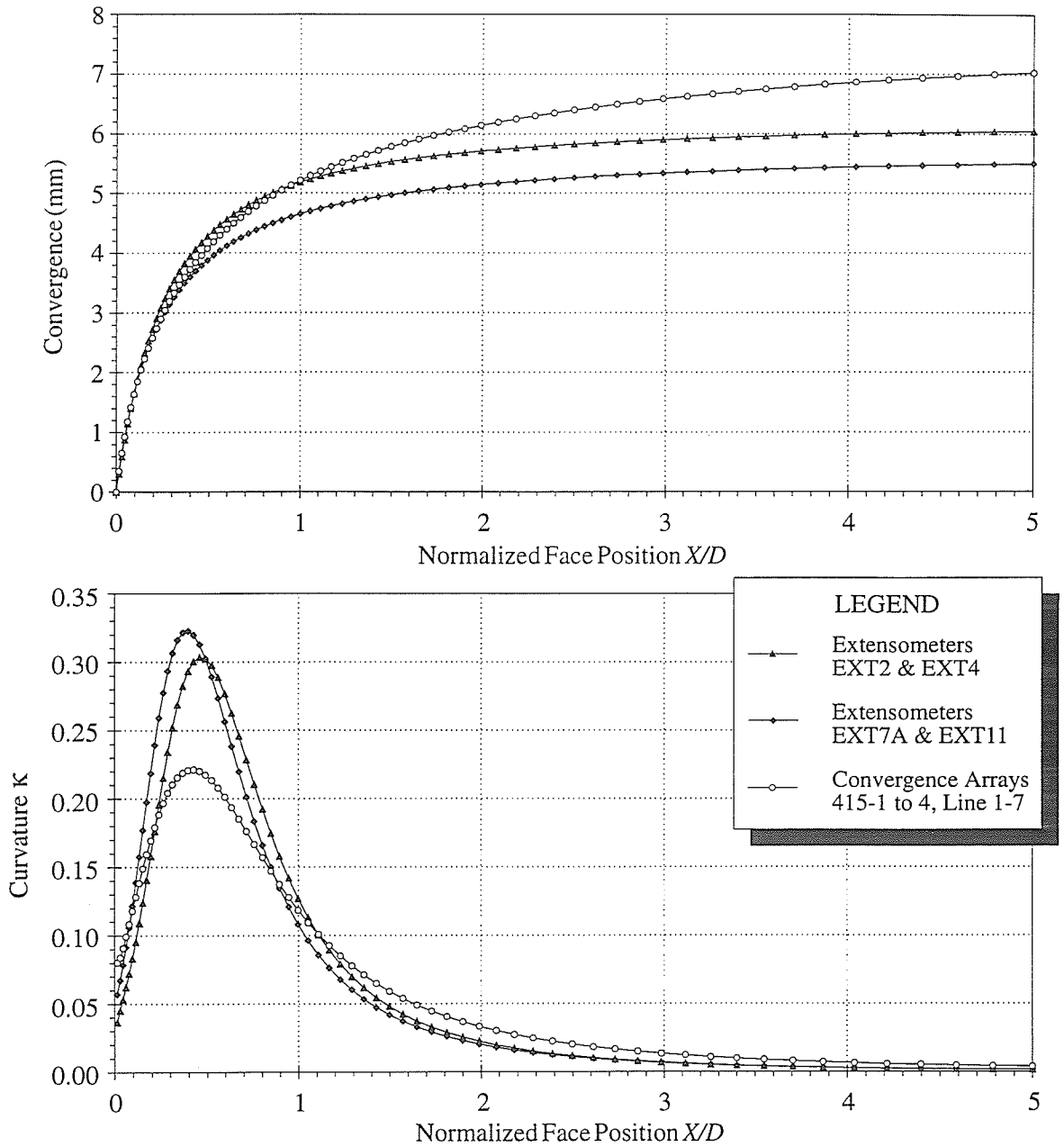

Figure 5.26: Comparison of convergence results for horizontal instruments from extensometer and convergence arrays located in granite. The convergence for the extensometers is taken as the sum of approximating functions for opposing instruments. Note that the peak magnitudes of the curvature functions for the responses differ, but that the x-coordinate of the peaks are similar.

Table 5.6: Function coefficients for the anterior portion of the radial displacement response versus face position measured with extensometers.

Instruments	A	B	F	r^2
EXT2 & 4	0.290	-1.156	6.241	1.0000
EXT7A & 11	0.239	-1.005	5.757	1.0000
Array 415-1 to 4 (Line 1-7)	0.294	-0.745	8.201	0.9750

extensometer results, and the convergence results. The derivation of the curvature function κ for the *spliced logistic function* is given in Appendix C. The coefficients for the approximating function for the combined extensometer results and for the convergence array measurements are given in Table 5.6.

The plot of convergence versus face position illustrates that there is no significant difference between the responses from the extensometers and convergence arrays within the region $0 \leq X/D < 0.1$. However, past this point, the responses show the effects of excavation damage development within the tunnel, and the associated variability it introduces into the displacement responses. Despite the different peak magnitudes for the respective curvature functions, the x-coordinates of the peaks are similar. The point of maximum curvature for the extensometer responses occurs at $X/D = 0.457$ and 0.395 for the horizontal extensometers in the first and second array, repectively. The peak occurs at $X/D = 0.425$ for the combined horizontal diametral measurements from convergence Arrays 415-1 to 4. From Table 5.6 it is obvious that the radial displacement at $X/D = +\infty$, given by F, is significantly greater for the convergence arrays than for the extensometers. This finding is likely related to the progressive deterioration of the convergence pin installations as the tunnel deforms. Overall, the responses from the two instrument types are very similar for $X/D \leq 1$, suggesting that displacement results from each type can be used in combination for stress back analysis.

5.3 Back Analysis of the *In Situ* Stress Tensor

Having applied the first five steps of the back analysis methodology, and having confirmed that extensometers and convergence arrays for the field study produced consistent displacement measurements, the sixth step was to establish the equations relating the measured displacements and the *in situ* stress components. To this end, the corrected results from the Mine-by Experiment were imported into NEARFACE, the spreadsheet used in Chapter 4 (Apendix D). The spreadsheet incorporates the equations and coefficients determined from the partitioned tensor studies, and is set up to handle measurements of convergence, radial displacement at $R = 1$, and radial displacement at $R > 1$. Each of the three measurement types has its own associated set of equations and coefficients. The adjusted data set included 665 measurements of radial displacement at $R > 1$, 442 measurements of radial displacement at $R = 1$, and 138 convergence measurements. Only measurements from convergence array 415-8 were included in the data set because it was the only array that did not experience large-scale geometry changes associated with progressive failure.

Each entry in the data set included the measurement type, the cylindrical coordinates of the measurement point, and the measured displacement. The values of the six functions f_1 to f_6 in Equation 4.32 were calculated from the parametric equations at the coordinates associated with each measurement. The data were then classified according to the performance of each instrument, and those data from instruments that either malfunctioned or that were obviously affected by progressive failure of the tunnel were excluded from the analysis. The plots of radial displacement response versus time were relied upon as the basis for this classification. Data were sorted into subsets by instrument type and location, and incremental analyses were performed to estimate the *in situ* stress tensor. These analyses involved first considering individual subsets of data grouped by measurement type, then combinations of subsets for different types of measurements. The results of these analyses are summarized in Table 5.7 and are discussed in the sections that follow.

Table 5.7: Summary of stress back analysis results from the field study.

Type	X/D Range From	To	Number of Data	σ_{11}	σ_{22}	σ_{33}	σ_{12}	σ_{23}	σ_{13}
Radial Displacement for $R > 1$									
R_1	-0.40	-0.40	132	57.52	44.82	7.52	-4.75	2.72	12.88
R_2	-0.10	-0.10	132	58.03	-6.68	5.41	-3.59	2.75	13.33
R_3	0.00	0.00	132	63.13	106.36	13.37	-3.29	2.59	12.36
R_4	0.10	0.10	124	60.32	1.13	5.60	-5.80	1.75	13.78
R_5	0.40	0.40	119	76.82	173.81	22.73	-7.57	2.26	14.04
R_{1-2}	-0.40	-0.10	264	58.55	42.98	6.60	-4.01	2.79	13.20
R_{1-3}	-0.40	0.00	396	56.75	49.25	5.99	-3.73	2.75	12.73
R_{1-4}	-0.40	0.10	520	60.87	40.16	8.18	-4.19	2.49	13.39
R_{1-5}	-0.40	0.40	639	63.73	45.18	10.29	-4.52	2.44	13.98
r_{1-2}	-0.40	-0.10	220	60.22	39.75	11.02	-4.00	3.32	13.19
r_{1-3}	-0.40	0.00	308	57.95	48.18	10.18	-3.75	3.77	12.74
r_{1-4}	-0.40	0.10	390	62.27	38.63	13.22	-4.29	4.09	13.20
r_{1-5}	-0.40	0.40	467	65.11	42.57	15.38	-4.71	4.72	13.51
Radial Displacement for $R = 1$									
W_1	-1.00	0.00	84	52.99	39.79	1.71	-2.86	2.57	11.46
W_2	-1.00	0.10	103	67.36	35.73	11.33	-3.65	2.33	13.03
W_3	-1.00	0.40	136	71.89	41.84	14.15	-5.00	2.66	13.87
W_4	-1.00	1.00	164	73.57	46.63	14.81	-5.60	2.75	14.10
w_1	-1.00	0.00	56	54.21	42.81	8.20	-2.85	3.08	11.54
Convergence plus Results for $R > 1$									
CR_1	-0.40	1.19	174	56.96	43.34	11.11	-4.51	2.92	10.70
Cr_{1-3}	-0.40	1.19	350	57.01	45.85	10.82	-3.85	3.71	11.16
cR_1	-0.40	1.19	167	57.40	44.26	12.11	-4.96	2.73	9.93
cr_{1-3}	-0.40	1.19	343	57.26	45.70	11.44	-3.87	3.69	10.81
Combined Results									
r_{1-3}	-0.40	0.00	308	57.95	48.18	10.18	-3.75	3.77	12.74
CR_1	-0.40	1.19	174	56.96	43.34	11.11	-4.51	2.92	10.70
cR_1	-0.40	1.19	167	57.40	44.26	12.11	-4.96	2.73	9.93
CW_1	-1.00	1.19	125	56.66	46.42	10.39	-2.79	2.47	10.72
cW_1	-1.00	1.19	118	57.02	46.46	11.31	-2.82	2.48	10.07
cw_1	-1.00	1.19	91	57.15	46.30	12.20	-2.69	2.96	9.82
R_1CW_1	-1.00	1.19	257	56.81	45.29	10.35	-3.47	2.55	10.80
R_1Cw_1	-1.00	1.19	230	56.85	44.92	10.83	-3.39	2.87	10.78
R_1cW_1	-1.00	1.19	250	57.12	45.08	11.08	-3.49	2.56	10.30
R_1cw_1	-1.00	1.19	223	57.29	44.44	11.92	-3.41	2.85	10.08
$r_{1-3}cw_1$	-1.00	1.19	399	57.19	45.38	11.37	-3.56	3.52	10.86
Best Overall Estimate									
R_1cw_1	-1.00	1.19	223	57.29	44.44	11.92	-3.41	2.85	10.08

The conventions used for the measurement types shown in Table 5.7 are as follows:

R	radial displacement for $R > 1$ including all extensometer measurements,
r	radial displacement for $R > 1$ excluding all vertical extensometer measurements for $X/D > -0.4$,
W	radial displacement for $R = 1$ including all extensometer measurements,
w	radial displacement for $R = 1$ excluding all vertical extensometer measurements,
C	convergence measurements at the tunnel wall, and
c	convergence measurements at the tunnel wall excluding diametral line 3-9.

The subscripts identify the individual or combined subsets from which the stress tensor was estimated. Stress components are given with respect to the tunnel coordinate system, where σ_{11} is orthogonal to the tunnel axis at $\theta = 0$ and 180°, σ_{22} is coincident with the tunnel axis, and σ_{33} is orthogonal to the tunnel axis at $\theta = 90$ and 270°.

5.3.1 Radial displacement measurements for $R > 1$

In keeping with the model studies in Chapter 4, the radial displacement data for $R > 1$ were normalized to the maximum radial displacement resulting from a uniaxial far-field compressive stress of 1 MPa applied orthogonal to the axis of a circular tunnel. The normalizing factor $U_{r_{max}}$ is given by

$$U_{r_{max}} = \frac{a_{eff}\,(1-\nu)}{G} \tag{5.8}$$

For this type of measurement, a_{eff} was 1.75 m owing to the development of damage in the tunnel near the extensometer arrays, ν was 0.25, and G was 26 GPa.

The data set included measurements from 11 radial positions and 8 rotation angles at 5 axial locations along the tunnel. These data were sorted by ascending X/D and descending R. At each value of X/D, data were grouped into subsets associated with the 11 anchor positions. These subsets were combined incrementally starting from the outermost ring of anchors, and successive back analyses of the *in situ* stress tensor were performed. Plots of the six stress components and the three stress invariants I_1, I_3 and I_3 were produced to assess the results of the incremental analyses with the addition of each subset. Those

results showing stable invariant plots, i.e., horizontally asymptotic with increasing number of measurements, were considered reliable estimates of the *in situ* stress tensor, and were used as part of the combined analysis described in Section 5.3.4.

The incremental analysis results from $X/D = -0.4$ are shown in Figure 5.27. Analysis of measurements from the outermost ring of anchors (12 measurements) produced unconstrained estimates of σ_{11}, σ_{22} and σ_{33}, but well-constrained estimates of the plane shear component and antiplane components of the tensor. By considering the outer two rings of anchors (24 measurements), the estimates of σ_{11}, σ_{22} and σ_{33} improved, although the

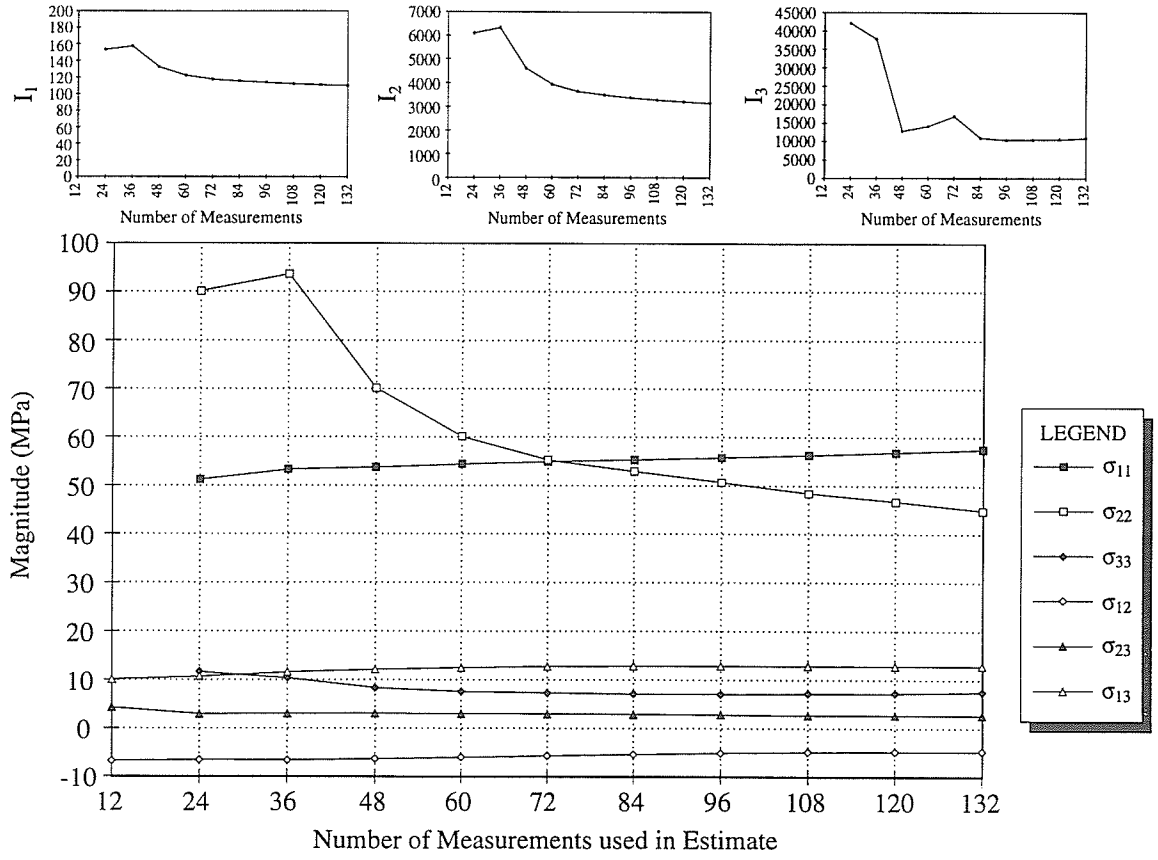

Figure 5.27: Incremental stress back analysis results from radial extensometers for $R > 1$ at $X/D = -0.4$. Note how the invariant plots stabilize as the number of measurements is increased. The estimate of σ_{22}, however, is less stable than for the other components.

estimated value of σ_{22} exceeded that for σ_{11}. With increasing number of measurements, the invariant plots showed a gradually decreasing gradient, with little change once approximately 84 measurements were used in the estimate. The most reliable estimate of the tensor from data at this location, as judged from the invariant plots, included all 132 measurements (Table 5.7).

Incremental analyses of results from $X/D = -0.1$, 0, 0.1 and 0.4 produced unstable invariant plots. The results for $X/D = -0.1$ showed widely varying estimates, and apparent interdependence, of σ_{22} and σ_{33}. Despite poorly constrained estimates of σ_{22} and σ_{33}, estimates of the other components of the stress tensor were relatively stable, particularly the shear components of the stress tensor. For $X/D = 0$, estimates of all three normal stress components varied widely, especially the estimate of σ_{22}. Estimates of the shear components, however, were nearly constant. At $X/D = 0.1$, only the estimate of σ_{22} varied substantially. The estimates of σ_{11} and σ_{33} were affected by the development of excavation damage, with σ_{11} increasing and σ_{33} decreasing as measurements from anchors near the tunnel perimeter were added to the analysis. At $X/D = 0.4$, the development of excavation damage had a large impact on all estimates except those for the antiplane shear stress components. The estimates shown in Table 5.7 for these four axial positions include all the measurements at each position and reflect the effect of progressive failure of the tunnel at positions for $X/D \geq 0$.

Incremental back analysis of stresses was also conducted on the combined data sets from the five axial positions, adding the data for each position sequentially. The incremental predictions for the combined data from $X/D = -0.4$ and -0.1, and from $X/D = -0.4$, -0.1 and 0 produced similar results to those for $X/D = -0.4$, with the most notable difference occurring in the estimate of σ_{22}. Combinations including data from the posterior domain resulted in significantly larger estimates of σ_{11}, and variable estimates of σ_{22}, illustrative of the effect of progressive failure in this region on stress predictions.

As noted in Section 5.1, during the initial interpolation to establish the values of displacement at $X/D = -0.1$ and 0, it was noted that the responses for the vertical extensometers showed very steep gradients near $X/D = 0$. Consequently, the values extrapolated for $X/D = -0.1$ and 0 were highly sensitive to the choice of $X/D = 0$, and have more uncertainty associated with them than for other locations. As part of a sensitivity study, stresses were re-estimated from the combined radial displacement responses for $R > 1$, excluding the data from the vertical extensometers for $-0.1 \leq X/D \leq 0.4$. The resulting estimates (Table 5.7) showed a marked change in the normal stress components, particularly σ_{33}. The most reliable combined estimate was obtained from the data for $X/D = -0.4$, -0.1 and 0, excluding the vertical extensometer results for the last two positions. Based on the invariant plots, the most reliable estimate of the stress tensor from this type of measurement was that given as R_1 in Table 5.7.

5.3.2 Radial displacement measurements for $R = 1$

Radial displacements at the tunnel wall, i.e., $R = 1$, were extrapolated from the measurements at the two innermost anchors. However, in most cases, the innermost anchor was within 10 to 15 cm of the design perimeter of the tunnel, so the extrapolation process introduced only marginal uncertainty into the data set. Only measurements from the region $X/D \geq -1$ were considered because the magnitudes of measurements for $X/D < -1$ were too small to use in the back analysis. Data were normalized to $U_{r_{max}}$ given by Equation 5.8, with $a_{eff} = 1.75$ m, $\nu = 0.25$, and $G = 26$ GPa.

An incremental analysis, adding subsets of measurements sorted by ascending X/D, was attempted for data from $-1 \leq X/D \leq 0$, but the relatively small number of measurements produced widely scattered results for all except the final increment (Table 5.7). Compared to the results obtained in Section 5.3.1, the estimates of σ_{11}, σ_{22} and σ_{33} were smaller in magnitude. By adding results from the posterior domain, the estimated stress magnitudes showed a steady increase in magnitude, reflecting the effect of changing tunnel geometry and

progressive failure on the radial displacement response in this region. Figure 5.28 illustrates the trend in estimated stresses and the associated stress invariant plots.

The stress back analysis for the data from $-1 \leq X/D \leq 0$ in the anterior domain was repeated without the extrapolated results from the vertical extensometers. Although compared to estimate W_1 the magnitudes of the resulting estimates were larger for the normal stress components, in particular the estimate of σ_{33}, the estimates of the antiplane shear stress components were relatively unchanged. Owing to the uncertainty associated

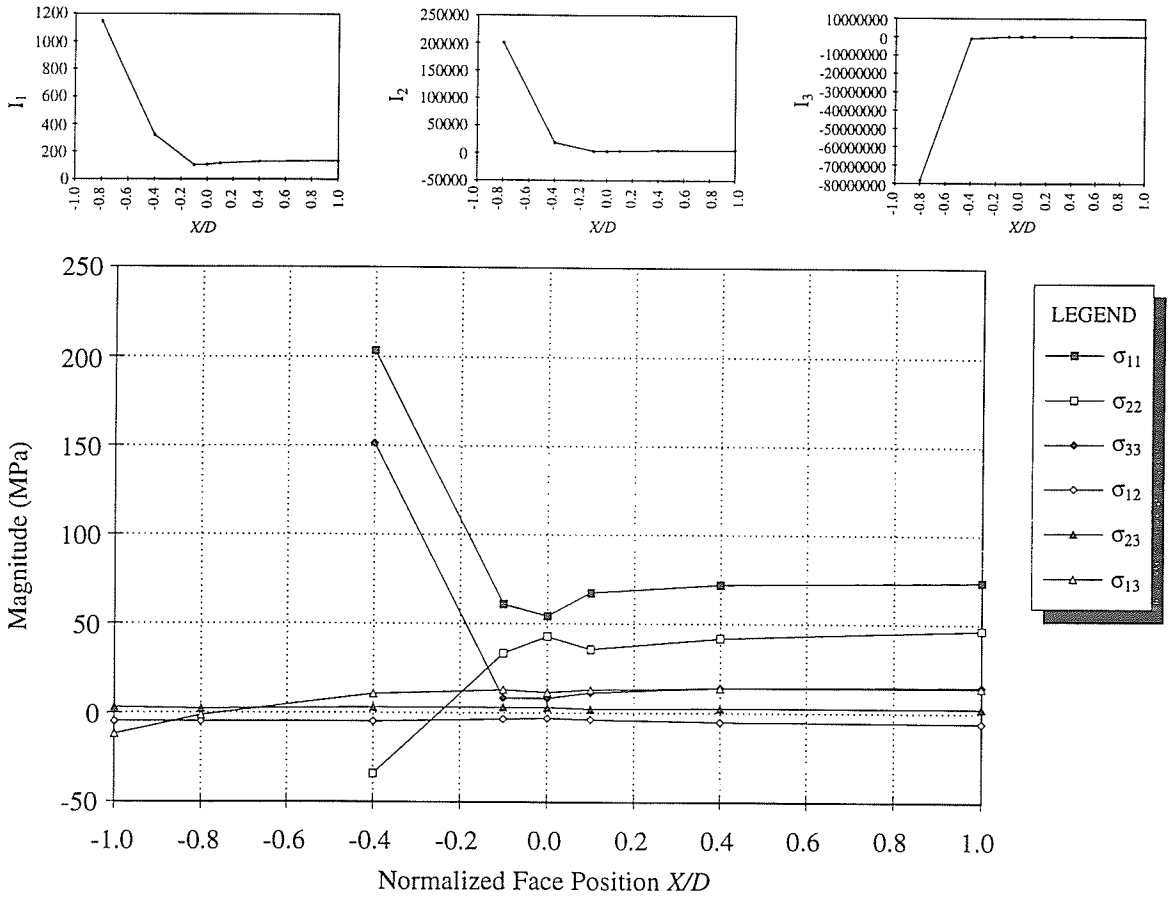

Figure 5.28: Incremental stress back analysis results from radial extensometers at $R = 1$ for $-1 \leq X/D \leq 1$. The invariant plots stabilize near $X/D = -0.1$, then increase in the posterior domain as a result of progressive failure. Note that results for σ_{11}, σ_{22} and σ_{33} in the region $X/D < -0.4$ are not shown.

with the extrapolated results from the vertical extensometers, the best estimate from this type of measurement, as judged from the invariant plots, is given by w_1 in Table 5.7.

5.3.3 Convergence measurements

As mentioned earlier in this chapter, convergence measurements are, by their nature, limited to estimating only the plane components of the *in situ* stress tensor, although they are affected by the antiplane normal component of the tensor. However, in combination with other types of measurements, convergence measurements can be used to constrain the magnitudes of the plane components, providing the convergence array is located in a region where large-scale excavation damage is not an issue. For the Mine-by Experiment, Array 415-8 was located in a region of predominantly granodiorite, which showed only minor changes in tunnel profile over the course of excavation. As noted during excavation, these changes in geometry initiated several tunnel diameters from the advancing face, so measurements within about one tunnel diameter were relatively unaffected by excavation damage, with the possible exception of measurement line 3-9 which was located in the eventual apex of the damaged zone.

The data from Array 415-8 were normalized using Equation 5.8 with an effective radius $a_{eff} = 1.605$ m, based on the model study of a stepped tunnel profile in elastic (undamaged) ground conducted in Chapter 4. The values of ν and G were the same as those used for the other types of measurements. Convergence measurements were sorted by ascending X/D, and were analyzed incrementally by adding them in subsets to the data set for R_1 and r_{1-3} in Table 5.7. In this way, all six components of the stress tensor were estimated rather than just the plane components. Results of the incremental analysis using convergence measurements combined with r_{1-3} are shown in Figure 5.29.

The back analysis results from the convergence measurements in combination with the radial displacement data from the anterior domain produced remarkably consistent estimates of all the components of the stress tensor. However, convergence results past about

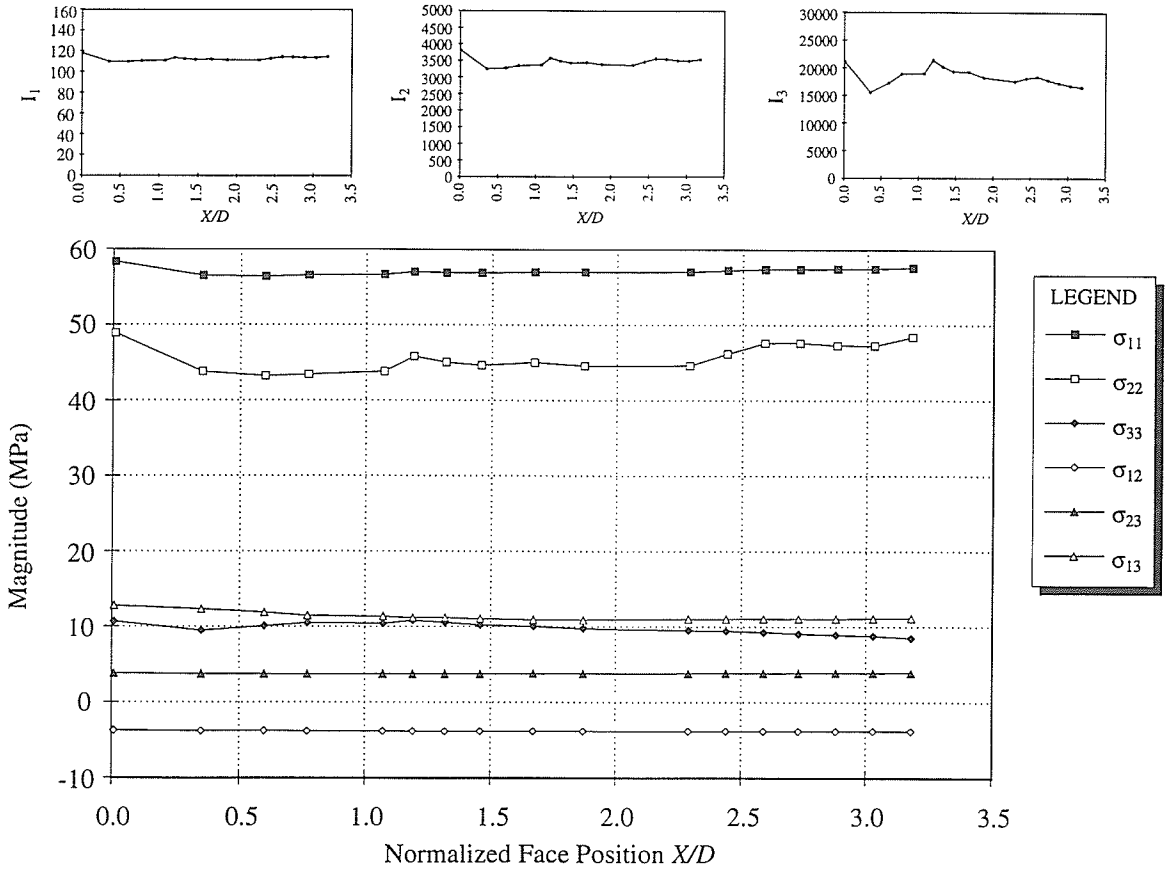

Figure 5.29: Incremental stress back analysis results from combined convergence and radial displacements at $R > 1$ for $-0.4 \leq X/D \leq 0$. Note the stability of the stress components and the invariant plots.

$X/D = 1.2$ appear to show some effect of excavation damage in the estimates of σ_{11} and σ_{33} as evidenced by the gradual change in slope in each response.

To assess the reliability of individual instruments used in the field study, a sensitivity study was undertaken. Measurements from individual extensometers and convergence lines were dropped one at a time from the data set, and the stress tensor was re-estimated. The study showed that the maximum standard deviation for the resulting 18 predictions was only 1.72 MPa on the estimate of σ_{22}. Exclusion of diametral line 3-9 in the convergence array had the biggest influence on the estimate, resulting in a larger estimate of σ_{33}. The estimate from the combined convergence measurements and anterior radial displacements showing the most stable invariant plots is given by cr_{1-3} in Table 5.7.

5.3.4 Combined results

In order to arrive at the best overall estimate of the *in situ* stress tensor and the variability associated with the estimate, eleven combinations of the most reliable data for each measurement type were used in separate back analyses. Subsets of data ranged in size from 91 to 399 measurements. Results from the eleven back analyses are shown in Table 5.7. Using the technique described in Section 5.1.1, the mean and standard deviation tensors were calculated from the eleven predicted tensors, weighting each prediction by the number of measurements upon which it was based. The calculated tensors, expressed in terms of the tunnel coordinate system with values in MPa, are

$$\overline{\sigma} = \begin{bmatrix} 57.18 & -3.60 & 10.81 \\ -3.60 & 45.50 & 3.00 \\ 10.81 & 3.00 & 11.08 \end{bmatrix}$$

$$S_{\overline{\sigma}} = \begin{bmatrix} 0.13 & 0.32 & 0.70 \\ 0.32 & 1.74 & 0.21 \\ 0.70 & 0.21 & 0.42 \end{bmatrix}$$

Although the mean tensor $\overline{\sigma}$ is a good approximation to the best overall estimate of the *in situ* stress tensor, it was difficult to define appropriate weights for the eleven estimates used in its determination given that the estimates were not completely independent i.e.,

individual subsets of data were used in more than one estimate. An alternative to using the mean tensor as the best estimate of the *in situ* stress tensor was to use the most reliable combined estimate of the eleven used to calculate the mean. Based on the results of the individual back analyses, the most reliable estimate incorporates all three types of measurement, and excludes potentially inaccurate extrapolated values. The data set used for the best overall estimate, shown as R_1cw_1 in Table 5.7, comprised 223 measurements, including radial displacement results for $R > 1$ at $X/D = -0.4$, radial displacement results at $R = 1$ for $-1 \leq X/D \leq 0$ (excluding extrapolated data from vertical extensometers) and convergence results from $0 \leq X/D \leq 1.19$ (excluding diametral line 3-9).

The principal stress magnitudes and directions associated with the estimates from the eleven combined data sets used to calculate the mean and standard deviation tensors are shown in Table 5.8. The magnitudes of the principal stress components are very consistent between the eleven estimates, with the most variability noted in the estimate of σ_2. As mentioned previously, the estimates of σ_2 and σ_3 appear to be interdependent, with estimates showing a high value of σ_2 having an associated low value for σ_3.

What is particularly striking about the estimates is the consistency in the orientations of the principal stress components. Results from the eleven estimates using combined data sets, as well as the mean and best overall estimate, show very little variability when plotted on a lower hemisphere stereonet (Figure 5.30). The estimates that did not include radial displacement measurements at $R = 1$ tended to deviate most from the cluster around the mean orientations. The best overall estimate in terms of principal stresses is given in Table 5.8 as R_1cw_1, and is shown in Figure 5.30 not as a point, but as a tabulated value.

5.3.5 Comparison with previous results

As discussed in Chapter 3, the initial estimate of the *in situ* stress tensor at the 420 Level of the URL was based on results from a variety of stress measurement techniques. Traditional small-scale techniques, such as overcoring, were unsuccessful at this level owing to the high

Table 5.8: Summary of principal stresses and directions from back analysis of displacement measurements from the field study. Note the consistency between estimates, both in magnitude and orientation.

Data		σ_1			σ_2			σ_3	
Type	MPa	Trend	Plunge	MPa	Trend	Plunge	MPa	Trend	Plunge
r_{1-3}	61.70	147.00	12.77	48.12	54.98	8.87	6.50	291.07	74.37
CR_1	60.19	148.08	11.25	42.90	56.31	8.86	8.32	288.89	75.61
cR_1	60.63	150.19	10.36	43.51	58.53	9.00	9.63	288.33	76.21
CW_1	59.40	144.93	11.68	46.28	53.60	6.43	7.79	295.30	76.62
cW_1	59.53	145.09	11.13	46.31	53.81	6.51	8.94	294.01	77.07
cw_1	59.52	144.03	11.04	46.31	52.65	7.09	9.82	290.53	76.83
R_1CW_1	59.76	146.46	11.53	45.01	54.99	7.21	7.68	293.58	76.35
R_1Cw_1	59.74	145.65	11.63	44.77	54.07	7.60	8.09	291.58	76.04
R_1cW_1	59.89	146.37	11.12	44.80	54.93	7.26	8.59	292.40	76.67
R_1cw_1	59.93	145.41	11.08	44.29	53.89	7.70	9.43	289.76	76.45
$r_{1-3}cw_1$	60.14	145.85	11.59	45.36	54.06	8.68	8.44	288.06	75.45
Mean Estimate									
	60.16	146.48	11.51	45.30	54.84	7.99	8.30	290.80	75.92
Best Overall Estimate									
R_1cw_1	59.93	145.41	11.08	44.29	53.89	7.70	9.43	289.76	76.45

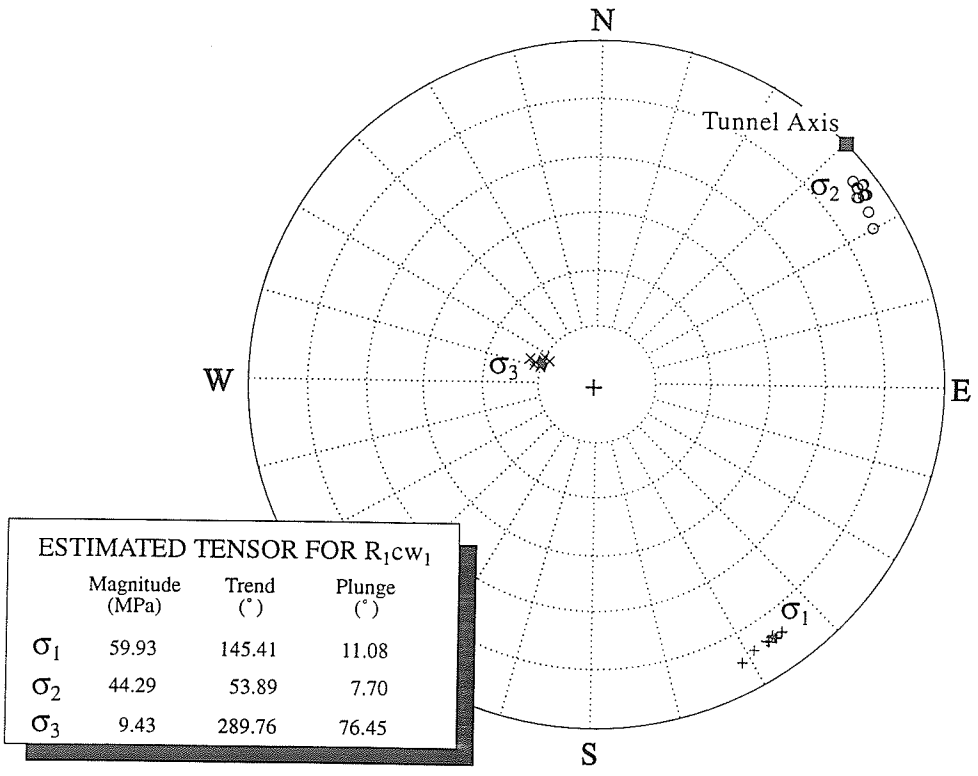

Figure 5.30: Lower hemisphere stereoplot of principal stresses estimated from back analysis of the field study displacement measurements. With the exception of those estimates excluding data at $R = 1$ in the anterior domain, estimates cluster very tightly about the best estimate shown in the legend.

stress magnitudes. Other studies at the URL used convergence measurements to establish or confirm the *in situ* stresses [125], but the effects discussed in Chapter 4 associated with face shape and antiplane stresses were not accounted for in the analysis. In addition, providing these effects could be taken into consideration, convergence measurements give only an estimate of the components of the stress tensor in the measurement plane. An under-excavation study using CSIRO cells around the bored vent raise from the 420 to 240 Level [190] provided an estimate of the complete tensor, but results were affected by uncertainty in the CSIRO cell locations and orientations, small induced strains in the axial direction, and non-linear behaviour around the instrument boreholes once the advancing face was within 1 diameter of the instruments. Of the stress measurement techniques described in Chapter 3, no single method provided a reliable estimate of all six components of the stress tensor, and the resulting tensor was, therefore, a composite of the most reliable components of each technique. The composite nature of the tensor posed some difficulties, however, in constraining the relative magnitudes of the various components, as reflected by the differences in the stress ratios associated with the initial estimate of the tensor in Chapter 3, and associated with that presented in this chapter.

In comparing the best overall estimate from the field study R_1cw_1 to the initial composite estimate, one of the most notable differences is that σ_2 in the new estimate is not parallel to the test tunnel axis. In fact, the tunnel axis deviates 8.9° in trend, and 7.7° in plunge from σ_2. This condition implies that antiplane shear stresses near the tunnel face in the anterior domain are distributed in an asymmetric manner with respect to the tunnel axis, and precludes back analysis techniques based on the assumption of parallelism between the tunnel axis and a principal stress direction. The implications of this difference are explored in Chapter 6.

The other significant difference between the estimates is the magnitude of σ_3. In the initial estimate in Chapter 3, σ_3 was based primarily on results of hydraulic fracturing tests conducted in horizontal boreholes at the 420 Level of the URL. Doe [35] interpreted the

shut-in pressure in tests producing subhorizontal fractures in horizontal boreholes as σ_3, based on the assumption that the fractures formed orthogonal to the minimum principal stress direction. However, Haimson et al. [62] showed that, in a vertical borehole in the same region of the rock mass near the 420 Level, nine hydraulically-produced fractures had dips ranging from 15 to 39° and dip directions ranging from 068 to 245°, illustrating that the induced fractures do not necessarily form orthogonal to σ_3. They further showed that, by assuming the vertical stress to be equal to the calculated lithostatic stress, the best estimate of the maximum horizontal stress near the 420 Level of the URL was approximately 54 MPa.

The calculated lithostatic stress at the 420 Level of the URL is approximately 11 MPa. The magnitudes of the vertical stress σ_{33} in both the best combined estimate and the mean estimate of the *in situ* stress tensor based on results from the field study compare favourably with this value. The fact that no additional constraint equations were required to achieve this value provides a degree of confidence in the estimated tensor and the elastic constants used in the back analysis ($E = 65$ GPa and $\nu = 0.25$). The values of the elastic constants are in keeping with those shown in Chapter 3 from previous laboratory testing, and are believed representative of the portion of the rock mass from which the measurements used in the back analysis were taken, i.e., primarily from the anterior domain and remote from the excavation. The estimated stress components are directly proportional to Young's modulus, and inversely proportional to $(1 - \nu)$.

In addition to predicting a vertical stress component close to lithostatic, the orientation of σ_1 is almost parallel to the average orientation of the fracture zones identified at the URL. The fact that σ_1 is not horizontal can be attributed to a reduction in shear stress parallel to the dip direction of the fracture zones. Observed large-scale shear displacement in the upper portion of the Lac du Bonnet batholith, such as reverse thrusting of up to 7.3 m along Fracture Zone 2 [44], is evidence for this type of stress relief. Using two simple numerical models, Chandler and Martin [16] showed that stress redistribution associated with shearing along the major fracture zones also accounts for perturbations in the stresses

in the upper part of the batholith. This process generates high stresses in the dip direction of the fracture zones, which results in rotation of the azimuth of the maximum principal stress. Further confirmation of the estimated stress tensor is undertaken in Chapter 6.

5.4 Summary

In this chapter, it was shown that by following a structured methodology which incorporates procedures for interpolating and extrapolating from a measured data set, it is possible to use the back analysis method described in Chapter 4 to back analyze the *in situ* stress tensor from measured displacements. It is important, however, to account for displacements that occur beyond the outermost extensometer anchor, as these can be up to about 20% of the total radial displacement response depending on rotation angle. In contrast, missed displacement resulting from the first measurement being taken a finite distance ahead of the advancing face is negligible if the distance between the instrument and the face associated with the first measurement is greater than about 3 tunnel diameters.

Extensometer and convergence measurements from the Mine-by Experiment both indicated convergence in the sidewalls of the tunnel, and divergence in the roof and floor as excavation progressed. Progressive failure of the tunnel tended to exaggerate this displacement pattern, and was evident in the displacement measurements. In particular, instruments located in the areas that eventually failed showed significant convergence (dilation) related to the damage associated with the failure process.

A comparison of extensometer and convergence results revealed that the two instrument types produced similar estimates of the posterior portion of the tunnel convergence response, but that convergence measurements did not capture the asymmetry in the radial displacement response caused by antiplane shear stress components. As noted in Chapter 4, convergence measurements cannot be used on their own to back analyze the complete *in situ* stress tensor. Extensometer results at $X/D = 0$ showed that the amount of the radial displacement response occurring in the anterior domain was not a constant proportion of

the total displacement, suggesting that the antiplane normal stress component contributes significantly to the radial displacement response.

Results from back analysis of the *in situ* stress tensor showed that the tunnel axis is not aligned with a principal stress direction, and that the magnitudes of the principal stress components, particularly σ_3, differ from those in the initial estimate of the tensor shown in Chapter 3. However, the new estimate of the tensor suggests that the vertical stress component is very close to the lithostatic stress at the 420 Level, and that the rotation of σ_1 from horizontal reflects the relief of shear stress along the major fracture zones in the Lac du Bonnet batholith. In addition, the back analysis results provide the only reliable estimate of all six components of the stress tensor at the 420 Level using a single measurement method.

Chapter 6

Characterizing Excavation Damage

Numerical modeling was undertaken to establish the link between displacements, excavation damage, and the material behaviour near the tunnel periphery. To this end, observations of progressive failure during the excavation of the test tunnel were combined with results of *in situ* field characterization and previous work summarized by Martin [125] to develop an understanding of the failure process and its relationship to stress and displacement patterns. Using the measured displacements and estimated *in situ* stresses from the field study as calibration data, and *in situ* characterization data regarding the shape and extent of the damaged zone around the Mine-by Experiment test tunnel, the material behaviour near the tunnel in the posterior domain was investigated through a series of two-dimensional model simulations.

6.1 The Process of Progressive Failure

Progressive failure was observed in the upper SE and lower NW quadrants of the test tunnel during its excavation, resulting in well-developed v-shaped notches typical of borehole breakouts (Figure 6.1). The processes associated with progressive failure in Lac du Bonnet granite have been described by Martin [125]. In general, the steps involved are: 1) crushing at a point on the tunnel periphery approximately 0.5 to 1 m back from the face; 2) dilation

Figure 6.1: Final profile of the Mine-by Experiment test tunnel as of August 1992 showing well-developed v-shaped breakouts in the upper SE and lower NW quadrants.

and small-scale flaking at a localized area resulting in the formation of thin slabs; 3) buckling of long thin slabs on the flanks of the developing notch, becoming shorter and localized near the notch tip as slabbing progresses; 4) further crushing at the notch tip with dilation, resulting in reinitiation of the slabbing process. The process continues until the geometry stabilizes in a convex-in shape. The geometry of the notch re-orients the maximum principal stress trajectory radially outward into the rock mass, which results in high localized values of σ_1 under high confinement conditions at the notch tip [125, 196]. Cook [21] showed through triaxial laboratory tests on Witswaterand quartzite that dilatancy in brittle rocks is a pervasive volumetric property. Likewise, it is clear from observations in the test tunnel and recent constitutive model development (Cundall, pers. comm.) that dilation at the notch tip is a key component of the failure process (Figure 6.2). The process differs slightly in granodiorite, with the initiation of the slabbing process starting more than two tunnel

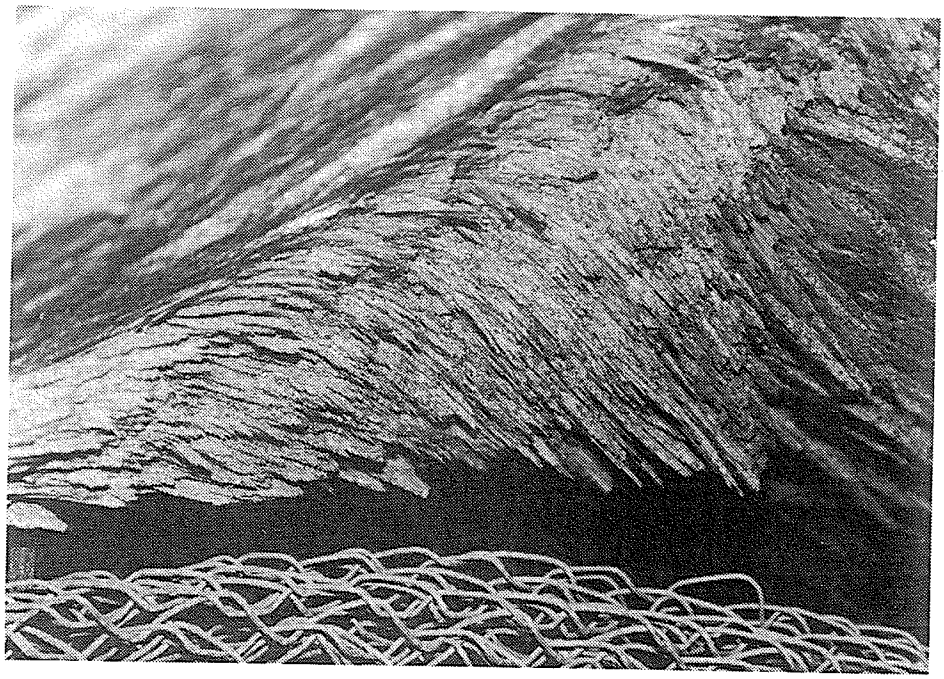

Figure 6.2: Remnants of slabs *in situ* showing dilation near the notch tip. This structure is referred to as having a "deck of cards" appearance.

diameters behind the tunnel face, and the final extent of the notch much diminished.

6.1.1 The role of crack initiation stress

Martin [125] noted that the breakouts in regions of granite in Room 415 of the Mine-by Experiment initiated within 1 m of the tunnel face where the maximum tangential stress at the tunnel wall is about 120 to 130 MPa (using the tensor estimated in Chapter 5). This apparent low *in situ* strength was puzzling given that σ_c, the peak uniaxial compressive strength, of the Lac du Bonnet granite is over 200 MPa [113], and σ_{cd}, the "long term" strength [7] or crack damage stress [114], is approximately 0.7 to 0.8 σ_c [110, 7] or about 160 MPa. Martin [125] showed that, for cylindrical samples, σ_{cd} could be reduced by inducing permanent volumetric strain, i.e., damage, through cyclic loading. However, he found that in order to cause damage significant enough to reduce σ_{cd}, a loading cycle had to exceed the crack damage stress of the rock. *In situ* he found that σ_{cd} was not exceeded in the portion of the rock mass ahead of the breakouts. Based on work by Wu and Pollard [194], Martin [125] attributed the reduction of σ_{cd} *in situ* to damage resulting from stress rotation ahead of the tunnel face in regions where the crack initiation stress σ_{ci} was exceeded. The combination of stress rotation and loading above σ_{ci} resulted in a reduction in the cohesion component of the rock strength [125].

The crack initiation stress σ_{ci} is the start of stable crack growth parallel to the maximum applied load [114]. This point typically occurs at 0.3 to 0.4 σ_c [7], although Lajtai et al. [114] illustrated that σ_{ci} can be quite variable between different constituent minerals in granite. Lajtai [113] showed that σ_{ci} from uniaxial and triaxial laboratory tests on Lac du Bonnet granite was dependent on confining stress σ_3, and could be expressed as a linear relationship given by

$$\sigma_{ci} = 3.24\sigma_3 + 72.8 \text{ MPa} \tag{6.1}$$

Consequently, for unconfined laboratory samples of granite, σ_{ci} is about 73 MPa. Samples of granodiorite from the 420 Level of the URL typically exhibit values of σ_{ci} closer to 100 MPa

in unconfined laboratory tests, as shown in Figure 3.3 in Chapter 3.

Results from acoustic emission/microseismic (AE/MS) monitoring conducted during quiet periods in the excavation cycle of Room 415 showed microseismic activity clustering ahead of the face in the regions where breakouts eventually occurred as the tunnel was advanced (Figure 6.3). These regions correspond to zones of shear stress (or deviatoric stress) concentrations caused by the advancing face, with σ_3 close to zero and rotated to

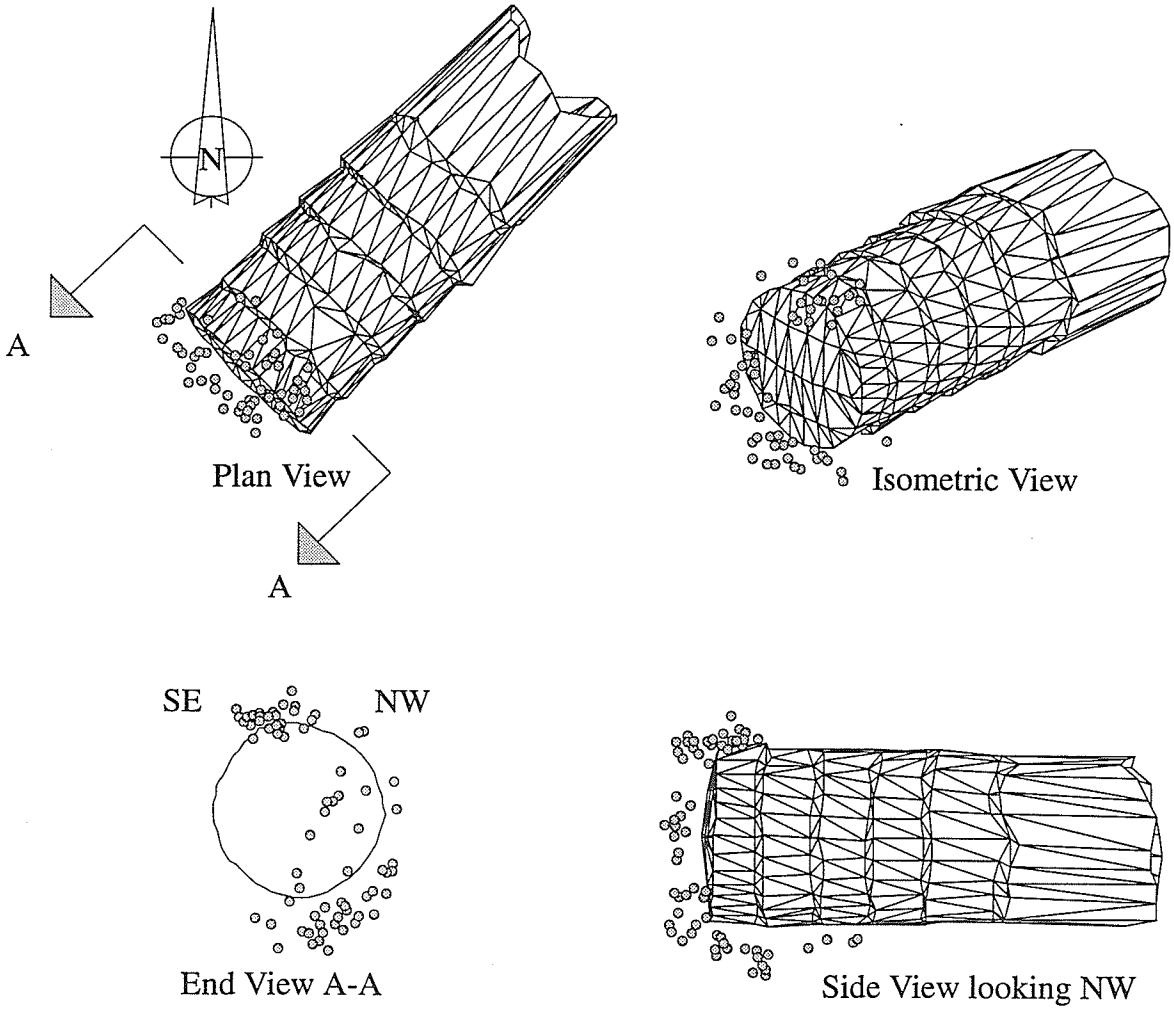

Figure 6.3: Typical pattern of microseismic activity for Round 8 in the Mine-by Experiment test tunnel. Events were monitored over a 12 hour period following completion of the round. Note how they cluster in the upper SE and lower NW quadrants, and occur up to 1 m ahead of the face.

an acute angle with the tunnel axis. Martin [125] showed that the principal stresses at the microseismic sources could be described by a Mohr-Coulomb-type relationship given by

$$\sigma_1 = C \tan\left(45 + \frac{\phi}{2}\right) + \sigma_3 \tan^2\left(45 + \frac{\phi}{2}\right) \tag{6.2}$$

where C is a constant related to crack parameters and ϕ, the mobilized friction angle, is zero. The condition $\phi = 0$ implies that the mode of cracking at the microseismic sources is extensional, and involves reducing cohesion rather than mobilizing friction [125]. Equation 6.2 can be rewritten as a simple linear relationship given by

$$(\sigma_1 - \sigma_3) = C \tag{6.3}$$

At the leading edge of the region of AE/MS activity ahead of the face, $(\sigma_1 - \sigma_3)$ is 73 MPa, suggesting that the microseismic events are indicators of *in situ* crack initiation. Based on the AE/MS results, the *in situ* crack initiation threshold in the 420 Level granite corresponds to a maximum deviatoric stress of 73 MPa.

6.1.2 The influence of geology

Extensive underground mapping [46] and laboratory analyses of drill core samples from representative areas of the test tunnel were conducted as part of the post-excavation characterization. During the excavation of Room 415, six closed fractures were encountered, each with an areal extent on the order of 1 m^2. These types of fractures are interpreted as cooling fractures associated with the margins of a granodiorite dyke, and are tight with minor infillings of chlorite, serecite, hematite and carbonate [46]. They do not constitute paths of increased hydraulic conductivity because they are not connected, and are of very limited size.

As originally expected from exploratory drilling and excavation of the access tunnels for the Mine-by Experiment, the test tunnel was excavated in an area of mixed granite-granodiorite lithology. A typical face photograph is shown in Figure 6.4, illustrating the difference in appearance of grey granite (light) and granodiorite (dark) on the macroscopic

scale. The distribution of grey granite and granodiorite is depicted on an unfolded perimeter map of the tunnel in Figure 6.5. Note that, with increasing chainage, the proportion of granodiorite increases to a maximum of 100% near chainage 30+00, then decreases again towards the end of the tunnel. In comparing the geology perimeter map to similar maps of overbreak contours and of microseismic activity occurring outside the design perimeter of the tunnel, it is clear that there is a correlation between geology, microseismic activity, and breakout development. Regions of predominantly granite showed more microseismic activity during excavation, and developed more pronounced breakouts as the tunnel advanced, than regions of granodiorite.

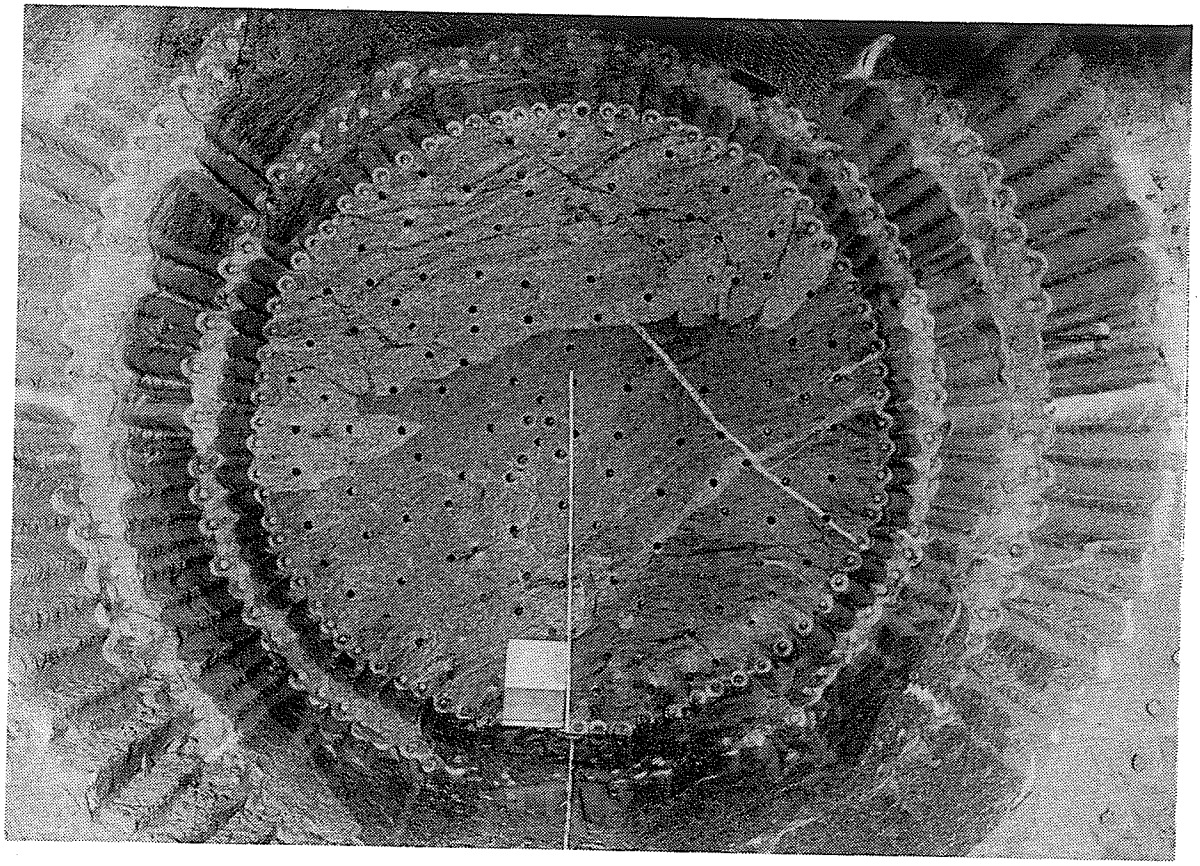

Figure 6.4: Typical tunnel face exposed during excavation of Room 415 showing mixed lithology. The darker material is described as granodiorite, the lighter material as grey granite.

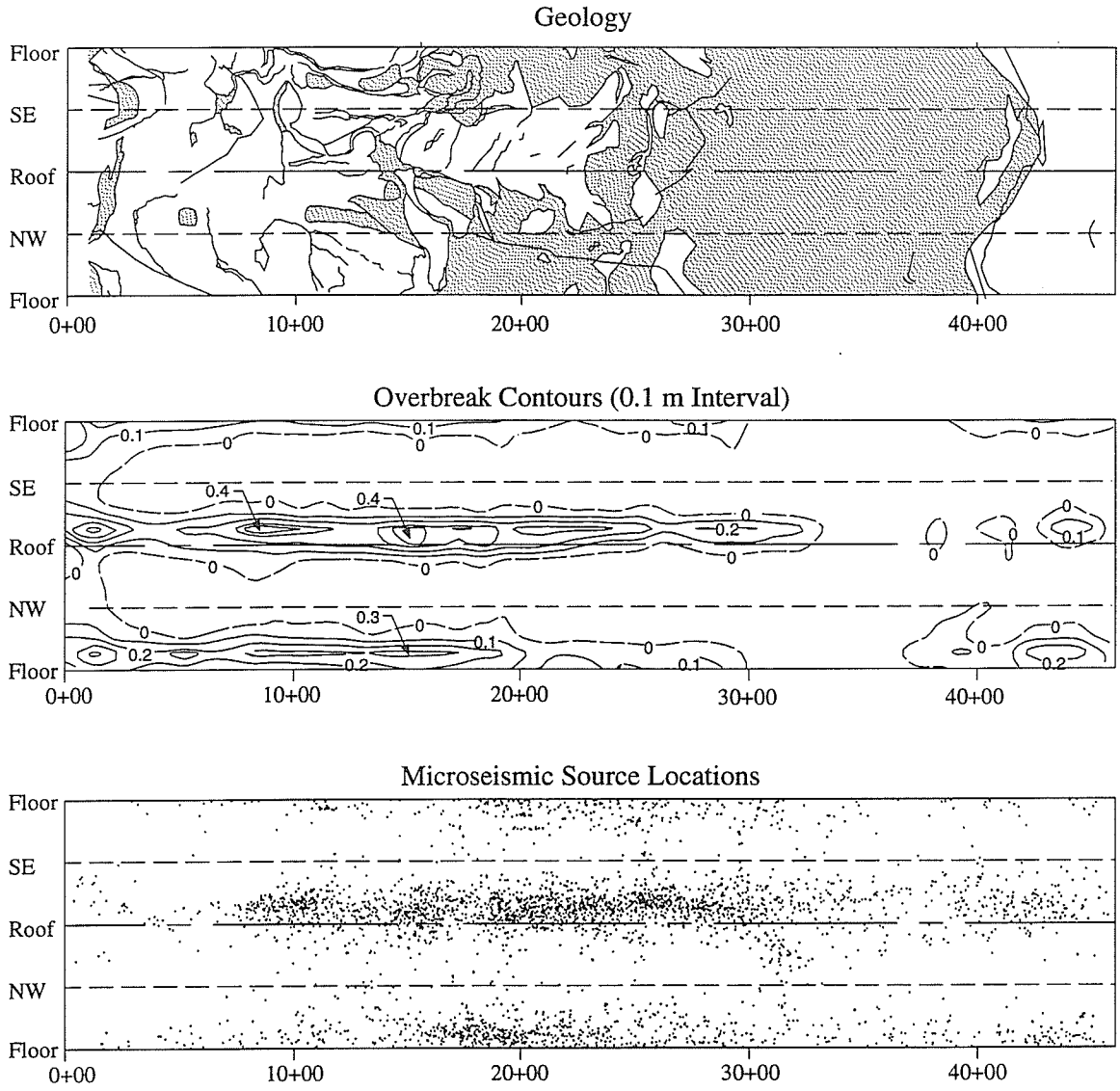

Figure 6.5: Perimeter maps of geology, overbreak and microseismic activity. Granite is shown as the light regions and granodiorite as the dark regions on the geology map. Note the correlation between areas of grey granite, overbreak and concentrated microseismic activity. Distance is shown as chainage (m) from the start of Room 415.

Table 6.1: Mineralogical composition of nine samples from the field study area (after Kelly et al. [96]). Samples AE1, 2, 3, 5 and 9 are grey granite, the others granodiorite.

Mineral	Mineralogic Percentage								
	AE1	AE2	AE3	AE4	AE5	AE6	AE7	AE8	AE9
Alkali Feldspar	48.1	47.6	44.1	29.7	37.5	37.1	40.1	33.9	33.0
Plagioclase	16.6	10.8	20.0	27.1	29.5	20.8	19.2	28.4	35.9
Quartz	28.6	33.1	33.9	30.7	26.2	33.4	29.3	22.6	25.4
Biotite	5.3	7.8	1.8	10.2	6.0	7.6	10.1	13.2	4.7
Muscovite	0.9	0.1	tr.	0.7	0.6	0.3	0.3	0.5	0.1
Chlorite	0.3	-	-	0.2	-	0.1	0.4	0.2	0.2
Opaques	0.2	0.3	0.2	0.5	-	0.4	0.6	0.9	0.7
Apatite	tr.	-	tr.	-	-	tr.	-	tr.	tr.
Sphene	-	0.3	-	0.7	-	tr.	tr.	0.1	-
Zircon	-	-	tr.	0.2	-	0.2	-	0.1	-
Allanite	-	-	-	tr.	-	-	tr.	tr.	tr.
Rutile	-	-	-	tr.	-	-	-	-	-
Epidote	-	-	-	-	-	0.1	-	0.1	-

Petrographic analysis of nine samples carried out at Laurentian University [96] showed that, although the rock types had previously been identified as granite and granodiorite, all rock types within the test tunnel volume fall within the International Union of Geological Sciences (IUGS) granite classification. However, to avoid confusion, the terms granite and granodiorite have been retained. The results of the petrographic analysis are summarized in Table 6.1.

Mineralogically, the samples are similar, with minor variations in mineral proportions. According to Kelly et al. [96], the samples originally described as granodiorite contain between 7.6 and 13.2% biotite, while samples initially classified as grey granite contain between 1.8 and 7.8% biotite. This difference in biotite content accounts for the darker appearance of the granodiorite. Mineralogical alteration was found to be minor, and consistent throughout the sample set. Biotite was faintly to slightly altered to chlorite, and the feldspars were faintly sericitized. Minor abundances of epidote and carbonate were noted in the granodiorite samples.

Table 6.2: Grain sizes of the main minerals in nine samples from the field study area (after Kelly et al. [96]). Samples AE1, 2, 3, 5 and 9 are granite, the others granodiorite.

Mineral	Grain Size (mm)								
	AE1	AE2	AE3	AE4	AE5	AE6	AE7	AE8	AE9
Alkali Feldspar									
Min.	1.0	0.5	1.0	0.25	1.0	0.5	0.5	0.5	1.0
Max.	8.0	3.5	7.0	2.0	7.0	2.5	3.0	2.5	6.0
Mean	4.0	3.0	4.0	1.0	4.5	1.0	1.0	1.0	3.0
Plagioclase									
Min.	0.5	0.5	1.0	0.5	0.5	0.5	0.5	<0.5	2.0
Max.	6.0	6.0	5.0	2.0	4.0	2.0	2.5	1.5	5.0
Mean	4.0	3.5	3.0	1.5	2.0	1.0	1.0	1.0	3.0
Quartz									
Min.	0.5	0.25	0.25	<0.25	<0.25	<0.25	<0.25	<0.5	<0.25
Max.	4.0	3.0	4.0	1.0	4.0	1.5	1.5	1.5	3.0
Mean	2.0	1.5	2.5	0.75	2.0	0.5	0.75	0.75	0.75
Biotite									
Min.	0.25	<0.25	<0.25	<0.25	<0.25	<0.25	<0.25	<0.25	<0.25
Max.	2.0	2.0	2.0	1.0	2.5	0.5	1.5	2.0	2.0
Mean	1.0	0.75	1.0	0.25	1.0	0.5	0.5	1.0	0.75

As shown in the petrofabric analysis conducted by Kelly et al. [96], the main difference between the two lithologic units is related to grain size and texture. The grey granite samples are generally coarsely crystalline, and inequigranular, containing large metamorphosed crystals of both alkali feldspar and plagioclase. The granodiorite, by contrast, is finely crystalline, and equigranular by comparison. Table 6.2 presents the range and average grain sizes for the main minerals in each sample. The analysis further showed that "the existence of strained quartz with undulatory extinction, annealed textures and characteristic cuspate-lobate grain boundaries suggests that all of the samples have undergone metamorphism". The large feldspars characteristic of the grey granite were noted to be often significantly more fractured than finer-grained crystals, indicative of more brittle behaviour. It was concluded that differences in the rock mass characteristics of the two rock

types are probably related to their grain size and textural characteristics rather than compositional differences [96]. Figure 6.6 shows core samples of granite (left) and granodiorite (right), illustrating the obvious differences in their grain structure. The granite shows more visible signs of damage related to cracking of the larger feldspar crystals caused by stress relief during sampling.

In uniaxial tests of Lac du Bonnet granite using 43 strain gauges per sample, Lajtai [113] showed that the crack initiation stress varies for the different constitutive grains of the Lac du Bonnet granite, with bimodal peaks at 75-90 and 105-120 MPa attributed to dilation

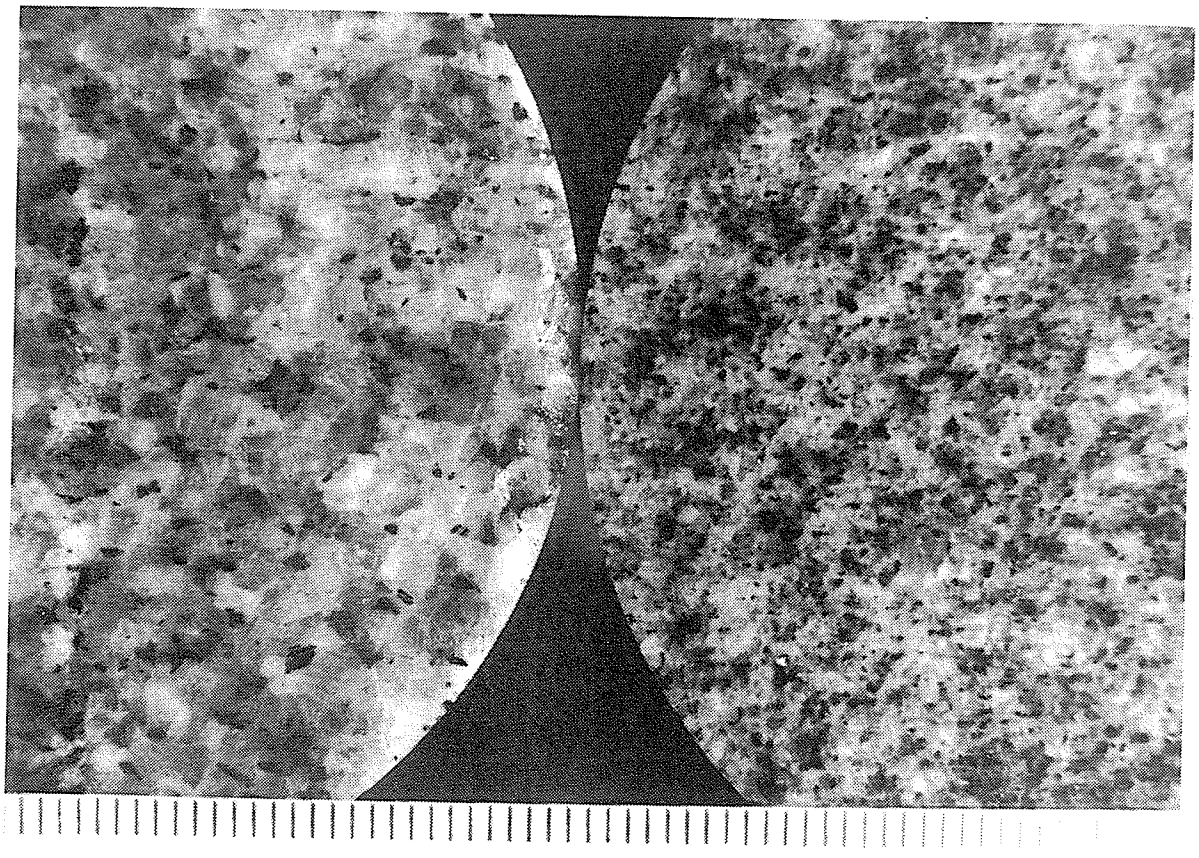

Figure 6.6: Core samples of grey granite (left) and granodiorite (right), illustrating the difference in petrofabric. Note the much larger crystals and inequigranular structure in the granite sample compared to the equigranular granodiorite sample. The small divisions at the bottom of the photograph are millimetres.

along feldspar cleavage (lower peak) and fracturing in quartz (upper peak), respectively (Figure 6.7). Martin [125] showed that the crack damage stress is related to the crack length: longer cracks imply more damage, and result in a greater reduction in the rock strength. He also noted that the crack length was related to the grain size of the granite. Owing to the inequigranular structure of the grey granite and the abundance of large feldspar crystals, the grey granite would be expected to experience more damage closer to the lower peak of about 75 MPa. The threshold for granodiorite, on the other hand, would be higher owing to its smaller grain size and equigranular structure. Laboratory results suggest that the average crack initiation threshold for granodiorite is about 100 MPa. Consequently, regions of granodiorite *in situ* would sustain less initial damage related to shear stress (or deviatoric stress) concentrations ahead of the advancing face, and would therefore develop

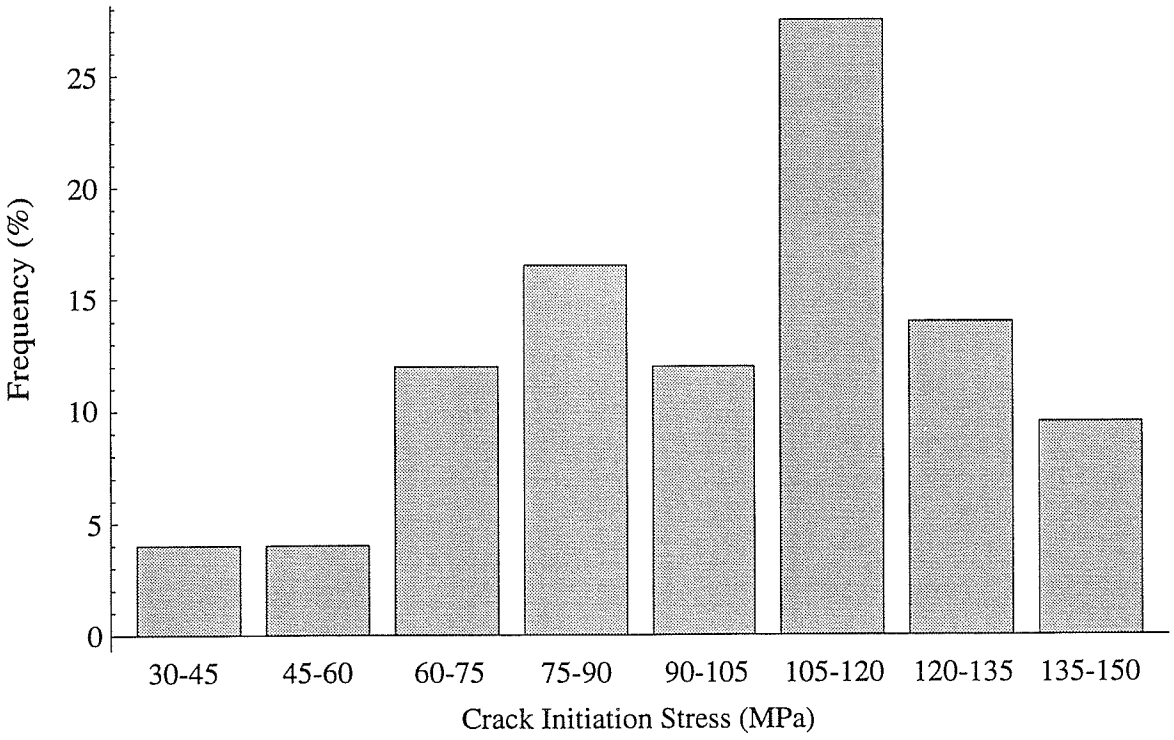

Figure 6.7: Crack initiation stress in Lac du Bonnet granite (after Lajtai [113]). Note the bimodal distribution with peaks corresponding to dilation along feldspar cleavage (75-90 MPa) and fracture in quartz (105-120 MPa).

less pronounced breakouts behind the advancing face, than regions of granite under identical stress conditions.

6.2 Relationship between Stress, Displacement and Excavation Damage

The maximum deviatoric stress ahead of the tunnel face plays an important role in the development of damage, and the subsequent reduction in effective strength near the tunnel wall. Because the patterns of maximum deviatoric stress and radial displacement are related, the radial displacement pattern should reflect the development of excavation damage around the tunnel.

6.2.1 Stress rotation near the tunnel face

The stress history of a point on the design perimeter of a cylindrical tunnel can be complex depending on the *in situ* stress tensor, and the orientation of the tunnel relative to the principal stress directions. Consider, for example, a tunnel in a standard r, θ, z cylindrical coordinate system with its axis parallel to the σ_{zz} principal stress direction as shown in Figure 6.8. Far ahead of the tunnel face (point A), the principal stresses are aligned parallel and orthogonal to the tunnel axis. As the tunnel advances, the principal stress trajectories are perturbed ahead of the face. Close to the tunnel face (point B), the principal stresses have rotated in the $r-z$ plane, creating antiplane shear stress σ_{rz}. The magnitude of the induced shear stress is related, in part, to the magnitude of the axial stress component σ_{zz}. Figure 6.9 shows the antiplane shear stress induced by an axial stress of 1 MPa acting alone, i.e., uniaxial conditions. Note that the pattern is axisymmetric with respect to the tunnel axis. The addition of unequal stress components σ_{rr} and $\sigma_{\theta\theta}$ to the uniaxial case changes the pattern of shear stresses from one of axisymmetry to one of quarter symmetry about the $\sigma_p - z$ and $\sigma_q - z$ planes, where σ_p and σ_q are, respectively, the maximum and minimum stresses in the plane orthogonal to the tunnel axis. Behind the tunnel face in the posterior

domain (points C and D), the principal stress directions are parallel and orthogonal to the tunnel wall.

For a tunnel that is not aligned with a principal stress direction, the symmetric near-field stress distribution around the tunnel is distorted. Ahead of the face (point B), the far-field antiplane shear stresses are superimposed on the induced shear stress pattern caused by stress redistribution near the face. As shown in Chapter 4, the antiplane shear stresses are antisymmetric with respect to a cutting plane through the tunnel axis parallel to the plane in which they act, i.e., they have a periodicity of 360°. Consequently, they affect points on opposite sides of the tunnel in an antisymmetric manner, increasing the shear stress on one side while decreasing it on the other. In the most general case, where the stress tensor defined in the tunnel reference frame has unequal antiplane shear stress components, the

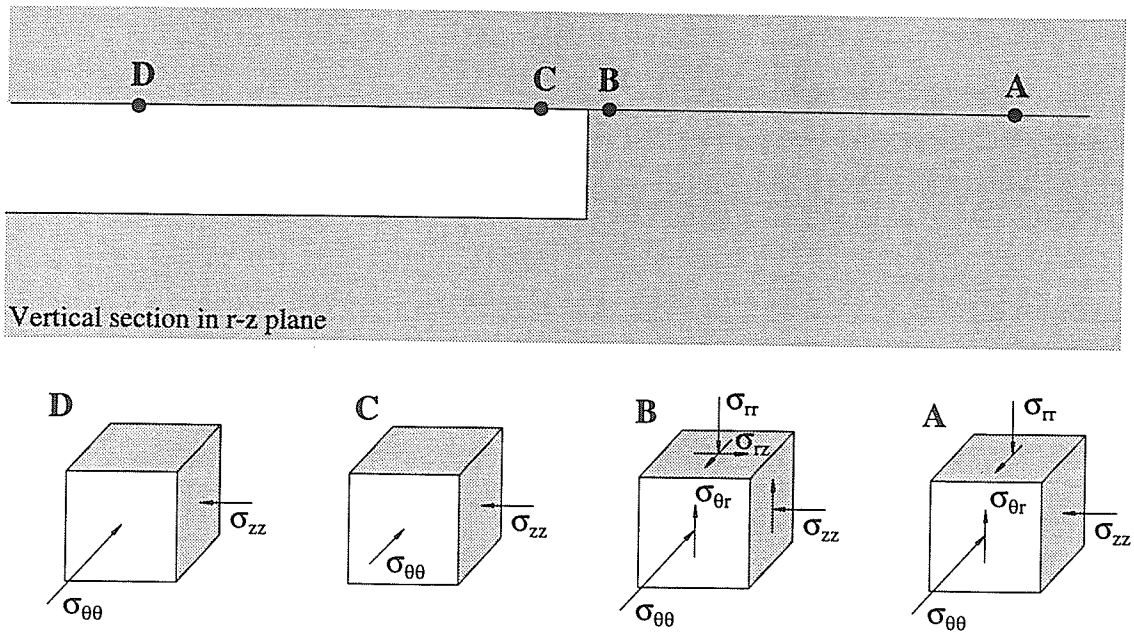

Figure 6.8: Stress rotation occurring ahead of the face, resulting in the development of shear stresses. Note that the tunnel is aligned with the σ_{zz} principal stress direction, and that the far-field principal stresses in the plane orthogonal to the tunnel axis are inclined, i.e., there is a plane shear stress component when considering stresses in a vertical-horizontal reference frame.

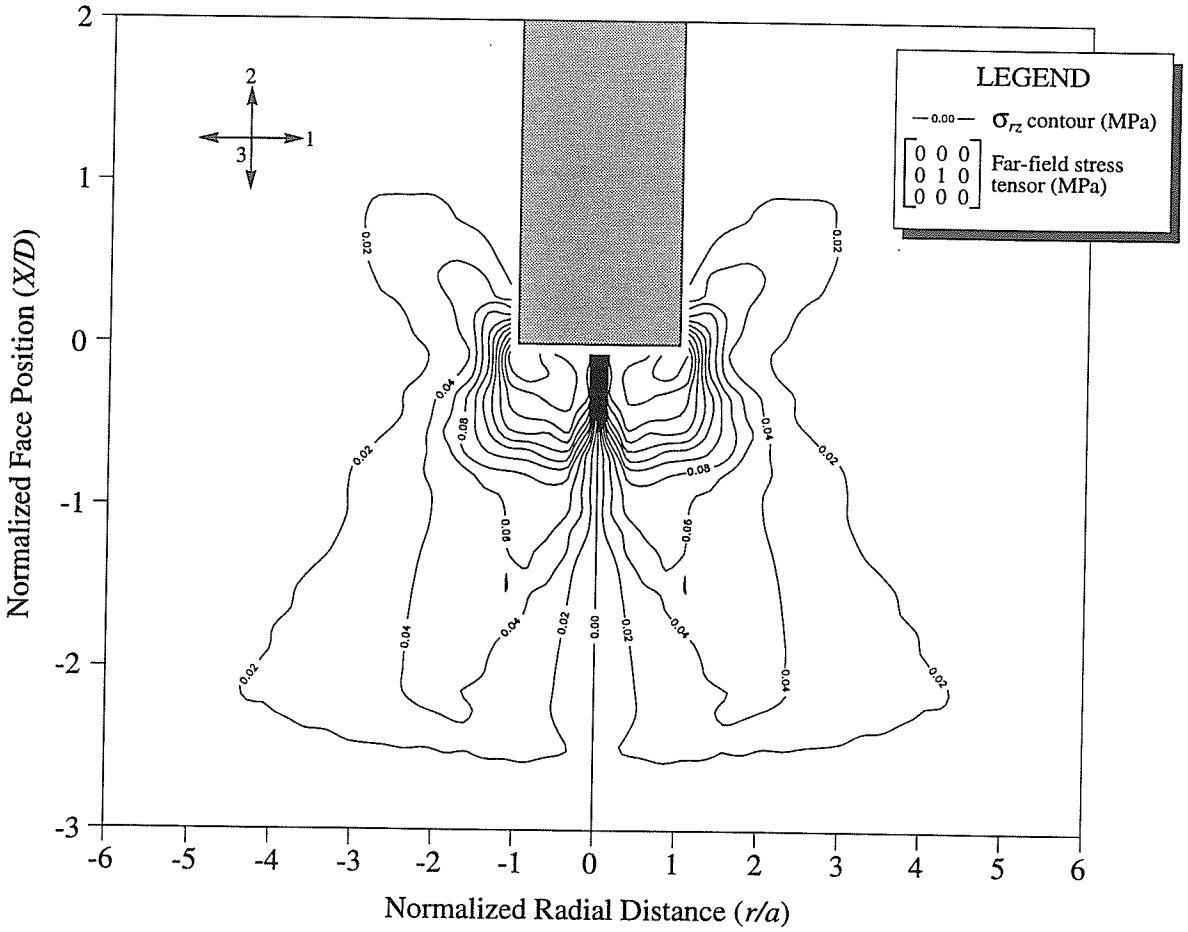

Figure 6.9: Shear stress σ_{rz} induced near the face by application of $\sigma_{zz} = 1$ MPa parallel to the tunnel axis.

shear stress (or deviatoric stress) distribution ahead of the tunnel face can be expected to be asymmetric. If the failure process is influenced by damage associated with crack initiation, as postulated by Martin [125], and this damage is caused by the maximum deviatoric stress ahead of the tunnel face, then the pattern of breakouts inside the tunnel should show evidence of this asymmetric distribution of damage.

6.2.2 Displacement as a diagnostic tool

In linear elasticity, the relationship between stress, strain and displacement can be expressed in terms of twelve equations and two elastic constants, E and ν. In standard cylindrical coordinates r, θ and z, these equations are:

$$\sigma_{rr} = \frac{E}{(1+\nu)(1-2\nu)}\left[(1-\nu)\varepsilon_{rr} + \nu\left(\varepsilon_{\theta\theta} + \varepsilon_{zz}\right)\right] \tag{6.4}$$

$$\sigma_{\theta\theta} = \frac{E}{(1+\nu)(1-2\nu)}\left[(1-\nu)\varepsilon_{\theta\theta} + \nu\left(\varepsilon_{rr} + \varepsilon_{zz}\right)\right] \tag{6.5}$$

$$\sigma_{zz} = \frac{E}{(1+\nu)(1-2\nu)}\left[(1-\nu)\varepsilon_{zz} + \nu\left(\varepsilon_{rr} + \varepsilon_{\theta\theta}\right)\right] \tag{6.6}$$

$$\sigma_{r\theta} = \frac{E}{(1+\nu)}\varepsilon_{r\theta} \tag{6.7}$$

$$\sigma_{rz} = \frac{E}{(1+\nu)}\varepsilon_{rz} \tag{6.8}$$

$$\sigma_{\theta z} = \frac{E}{(1+\nu)}\varepsilon_{\theta z} \tag{6.9}$$

$$\varepsilon_{rr} = \frac{\partial U_r}{\partial r} \tag{6.10}$$

$$\varepsilon_{\theta\theta} = \frac{U_r}{r} + \frac{1}{r}\frac{\partial U_\theta}{\partial \theta} \tag{6.11}$$

$$\varepsilon_{zz} = \frac{\partial U_z}{\partial z} \tag{6.12}$$

$$\varepsilon_{r\theta} = \frac{1}{2}\left(\frac{1}{r}\frac{\partial U_r}{\partial \theta} + \frac{\partial U_\theta}{\partial r} - \frac{U_\theta}{r}\right) \tag{6.13}$$

$$\varepsilon_{rz} = \frac{1}{2}\left(\frac{\partial U_r}{\partial z} + \frac{\partial U_z}{\partial r}\right) \tag{6.14}$$

$$\varepsilon_{\theta z} = \frac{1}{2}\left(\frac{1}{r}\frac{\partial U_z}{\partial \theta} + \frac{\partial U_\theta}{\partial z}\right) \tag{6.15}$$

Substituting for ε_{rz} in Equation 6.8, the antiplane shear component σ_{rz} can be expressed

in terms of displacements as

$$\sigma_{rz} = \frac{E}{(1+\nu)}\left[\frac{1}{2}\left(\frac{\partial U_r}{\partial z} + \frac{\partial U_z}{\partial r}\right)\right] \tag{6.16}$$

The displacement gradients $\frac{\partial U_r}{\partial z}$ and $\frac{\partial U_z}{\partial r}$ are the slopes of the radial displacement response versus face position and the axial displacement response versus radial distance, respectively (Appendix B). Although the component σ_{rz} does not necessarily correspond to the maximum shear stress $\frac{1}{2}(\sigma_1 - \sigma_3)$, the displacement gradients that define it are indicators of regions of antiplane shear stress. Consequently, these types of plots can be used in a qualitative way to identify potentially high antiplane shear stresses. An expression for the maximum deviatoric stress can be derived in terms of displacements by considering the difference in the eigenvalues associated with the near-field stress tensor, but the resulting equations are complex and are difficult to use in a diagnostic sense. A thorough investigation into the relationship between displacement gradients and progressive failure is beyond the scope of this thesis.

Plots of radial displacement response versus rotation angle are also useful in diagnosing the existence of far-field antiplane shear stress components. For example, as shown in Chapter 5 and as demonstrated by Everitt et al. [46], the breakout pattern for the Mine-by Experiment test tunnel was slightly asymmetric, with the apex of the breakout in the roof occurring at 11° counterclockwise of vertical, while the apex of the floor notch averaged 16° counterclockwise of vertical. Far from the tunnel face, the asymmetry diminished, with the orientation of the tips of the roof and floor notches both averaging about 12° counterclockwise from vertical. The radial displacement pattern within the region $-1 \leq X/D \leq 1$ reflects the overall distribution of stresses near the face, and is sensitive to the development of antiplane shear stresses. The points of minimum radial displacement correspond to regions of stress concentrations, and these, in turn, coincide with the eventual locations of large-scale excavation damage. The initial pattern of asymmetry displayed by the breakouts was apparent in the radial displacement plots, affecting the magnitudes and

rotation angles of the minima and maxima.

6.3 Using Excavation Damage to Verify the *In Situ* Stress Tensor

Asymmetry in the development of excavation damage can be influenced by anisotropy and/or heterogeneity of the rock mass, variations in gravitational effects, and the excavation sequence or method. For instance, differences in the development of breakouts in the roof and floor of a horizontal tunnel could be affected in the short term by small confining pressures, as shown by the influence of untensioned roof support in Chapter 5. In order to verify the *in situ* stress tensor, and, in particular, the existence of antiplane shear stresses *in situ*, it is first necessary to rule out other factors that might bias the development of breakouts. The ideal case against which to compare the tensor is a vertical, perfectly cylindrical excavation in homogeneous rock showing breakouts, excavated using an axially symmetric full-face method.

6.3.1 Excavation damage in Room 405

As part of the Mine-by Experiment, a 1.24-m-diameter borehole was diamond drilled vertically to a depth of 5 m in the floor of Room 405, one of the instrumentation galleries for the Mine-by Experiment [46]. The horizontal horse-shoe shaped room was 3.5 m high by 5.0 m wide and aligned with azimuth 225°. Excavation damage related to the development of the room was evident to a depth of 0.76 m below the concrete floor, characterized by multiple subhorizontal fractures. Below this zone of damage, breakouts were evident in the borehole during the drilling process, and followed the advancing face as the hole was deepened. As shown in Figure 6.10, the pattern of breakouts was asymmetrical, with the tips of the breakouts at azimuth 048° and 245° at 1.5 m depth below the damaged floor of Room 405. In addition, the NE breakout extended to a depth of 2.94 m below the damaged zone, while the SW breakout extended only to 2.46 m. The hole was cylindrical and

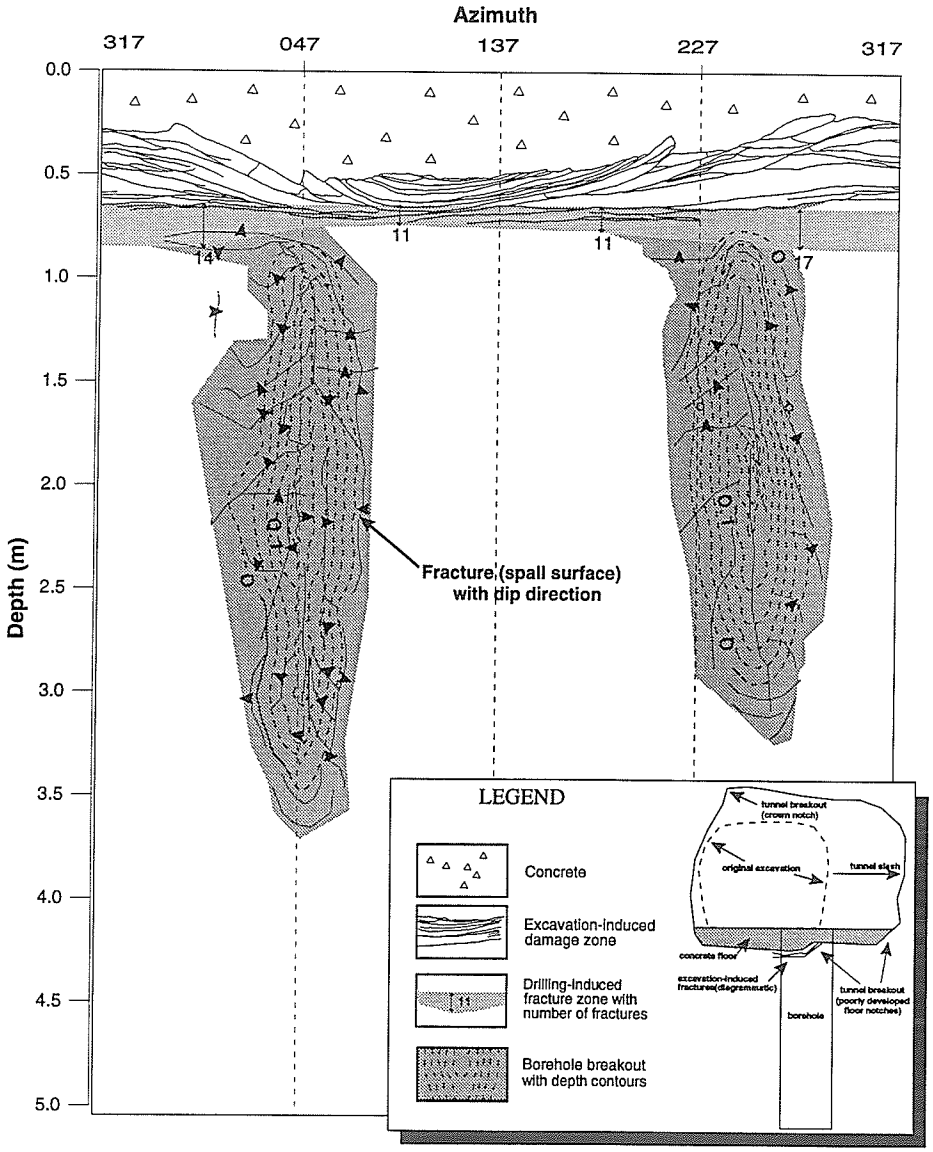

Figure 6.10: Perimeter map showing borehole breakouts in 1.24-m diameter borehole in Room 405 (after Everitt et al. [46]). Note the asymmetry in the azimuth and depth of breakouts on opposite sides of the borehole. The contour interval is 33 mm, and the borehole location relative to Room 405 is shown in the inset.

diamond drilled vertically in homogeneous granite, thus ruling out the effects of gravity and excavation method that might contribute to asymmetry in the development of borehole breakouts. However, the pattern of stresses and displacements around the borehole were affected by the proximity of the borehole to Room 405.

6.3.2 Model description

A three-dimensional boundary element model of Room 405 and the large-diameter borehole was constructed using EXAMINE^{3D}. Three borehole depths (1.5, 2.6 and 4.3 m) were chosen to assess the conditions ahead of the face at: a) a point where the breakouts formed on both sides of the borehole, b) a point where the borehole breakout occurred on one side only, and c) a point where no breakouts were evident. Figure 6.11 shows a typical model, with the floor representing the lower boundary of the zone of excavation-induced damage, and the borehole extending 2.6 m below this boundary. The *in situ* stress tensor estimated in Chapter 5 was used for the model runs.

Despite the zone of excavation damage beneath the floor of Room 405, and the influence of the Room on the stress and displacement fields, the 1.24-m-diameter borehole provides a good field case for verifying the *in situ* stress tensor. If correct, the estimated tensor should produce a pattern of maximum deviatoric stress ahead of the face consistent with the observed pattern of breakouts. In particular, the azimuth of each breakout, the difference in their extent, and their eventual termination points should be explained by the maximum deviatoric stress pattern. To this end, the maximum deviatoric stress ahead of the face at the design perimeter was plotted versus azimuth to determine if the peaks in the response correlated with the apex of each breakout. In addition, the magnitudes of the maximum deviatoric stress concentrations were compared with the crack initiation threshold to determine if they were indeed high enough to initiate damage ahead of the face, and whether or not there was any asymmetry in their values. The relationship between the radial displacement response and the breakout pattern was also considered in a similar

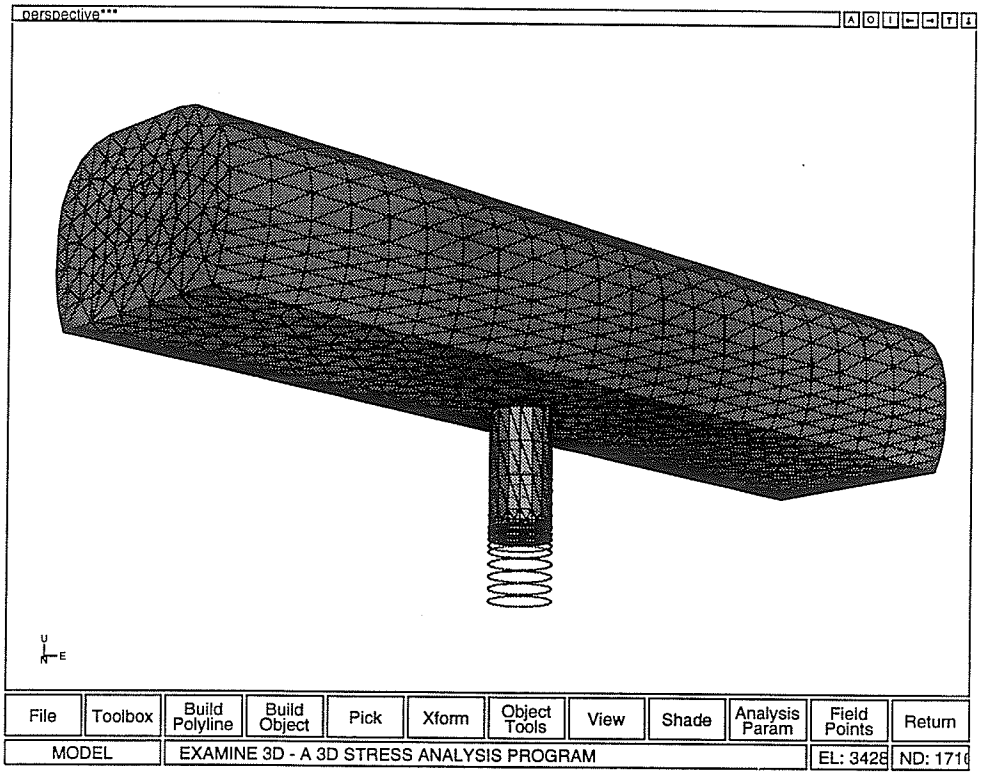

Figure 6.11: Boundary element model of Room 405 and 1.24-m-diameter borehole. The borehole is 2.6 m deep.

manner.

In order to capture the stress and displacement effects associated with advancing the hole, eleven rings of 72 field points each were used at positions 0, 0.1, 0.2, 0.4, 0.6, 0.8 and 1 hole diameter either side of the face at the design radius of 0.62 m. Two additional rings, with depths corresponding to the termination points of each breakout, were added to the model of a 4.3-m-deep borehole. The borehole perimeter was discretized into 64 elements in the region near the field points. As the borehole was deepened in subsequent models, the number of elements varied from 3396 to 6340. The elastic constants E and ν were 65 GPa and 0.25, respectively.

6.3.3 Maximum deviatoric stress pattern

The maximum deviatoric stress pattern ahead of the advancing face at the design perimeter is shown in Figure 6.12. The mean breakout azimuths, 48° and 245° for the NE and SW breakout, respectively, are shown on each of the three plots for reference. Owing to the singularity in stresses at the edge of the face, the closest position to the face in the anterior domain at which the maximum deviatoric stress was calculated was $X/D = -0.1$. As shown in each of the plots, the periodicity of the maximum deviatoric stress response changes from 360° to 180° as X/D goes from -1 to -0.1.

The plot for a 1.5-m-deep hole corresponds to a position in the fully-excavated hole where breakouts were evident on both sides of the borehole. Using $(\sigma_1 - \sigma_3) = 73$ MPa for the crack initiation threshold, it is clear that, at this depth, both peaks in the maximum deviatoric stress response ahead of the face exceed the threshold. In addition, the peak for the NE wall of the tunnel has a larger magnitude than that for the SW side. In terms of azimuth, the peaks in the maximum deviatoric stress response evolve as X/D approaches zero, converging approximately to the positions shown for $X/D = -0.1$. As shown in Figure 6.12, these positions correlate well with those of the borehole breakouts at this depth.

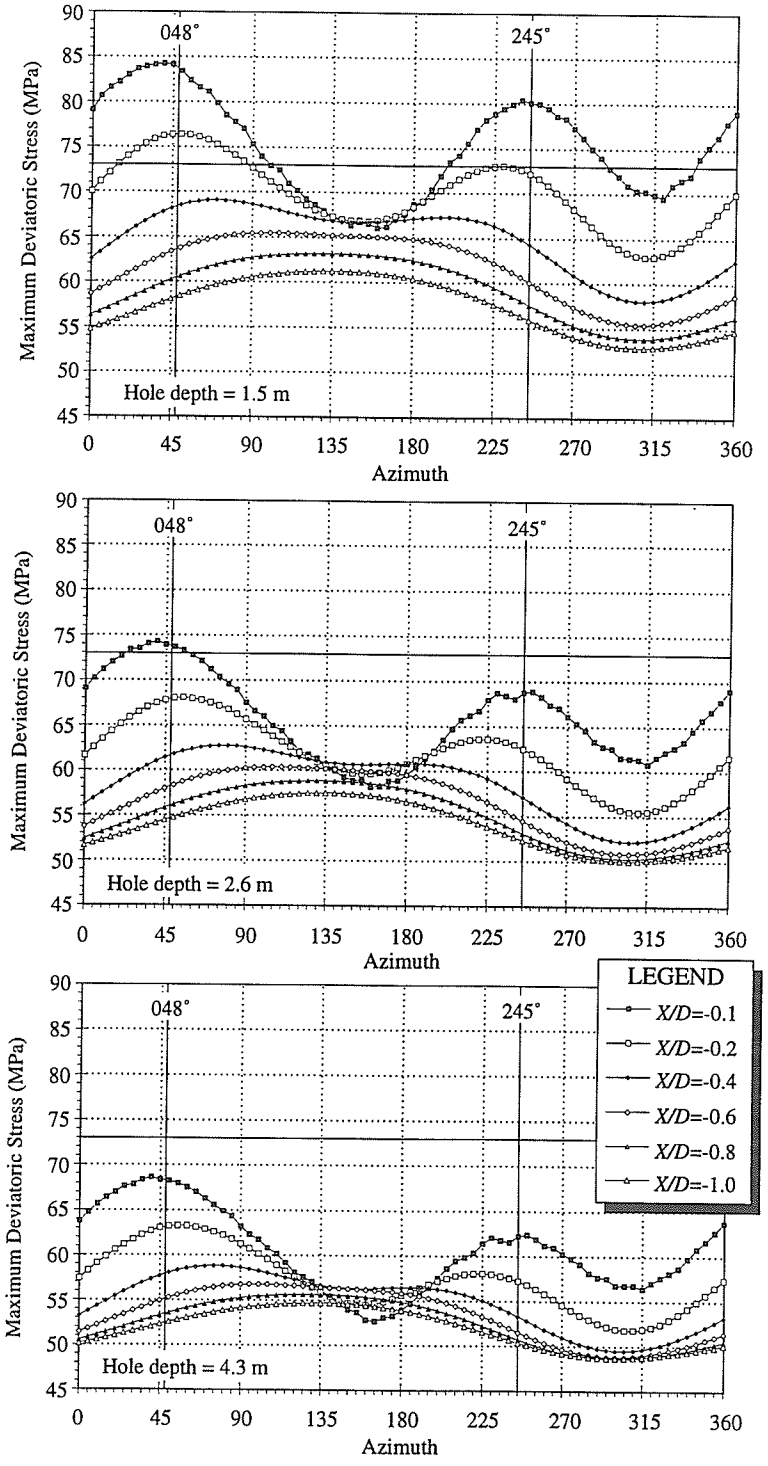

Figure 6.12: Maximum deviatoric stress pattern ahead of the Room 405 borehole face at three depths: 1.5, 2.6 and 4.3 m below the top of intact rock in the tunnel floor. Note the asymmetry of the peaks, both in magnitude and azimuth. The crack initiation threshold $(\sigma_1 - \sigma_3) = 73$ MPa is shown as a horizontal line.

The second plot in Figure 6.12 for a 2.6-m-deep borehole corresponds to a depth in the fully-excavated hole where breakouts were evident on only the NE side of the borehole, i.e., the SW breakout had terminated at 2.46 m. At this depth, the NE peak in the maximum deviatoric stress response exceeds the crack initiation threshold, albeit only marginally, but the SW peak does not. This pattern suggests that strength reduction associated with damage ahead of the face occurs only on the NE side of the borehole at this depth. The positions of the peaks again correlate well with the azimuths of the borehole breakouts.

The third plot in Figure 6.12 for a 4.3-m-deep hole represents the completed borehole. The breakouts in the hole terminated at 2.46 and 2.94 m, so at this depth there were no breakouts near the face. The peaks in the maximum deviatoric stress response ahead of the face confirm that at no point on the tunnel periphery at this depth is the threshold for crack initiation exceeded. In keeping with the results from the other depths, there is a good correlation between the azimuths of the peaks in the maximum deviatoric stress response and of the breakouts further up the borehole.

The maximum deviatoric stress at the borehole wall behind the face in the posterior domain corresponds to the tangential stress, i.e., the radial stress is zero. Figure 6.13 shows the pattern of the maximum deviatoric stress at depths corresponding to the termination points of the breakouts (2.46 and 2.94 m, respectively) and an intermediate depth, with the borehole at 4.3-m depth. Clearly the peaks of each response correspond with the azimuth of Room 405, and do not coincide with the position of the SW breakout. In addition, the magnitudes of the peaks are the same for both the NE and SW sides of hole. The results suggest that, at the termination point of the breakout on the SW side of the tunnel, the maximum tangential stress reaches about 158 MPa. This value corresponds to the initial crack damage stress σ_{cd} of Lac du Bonnet granite [125], and suggests that past this point on the SW side of the borehole, no significant damage has been done to the rock by stresses ahead of the advancing borehole face. On the NE side, the maximum tangential stress at the point of breakout termination is about 150 MPa, slightly below the initial crack damage

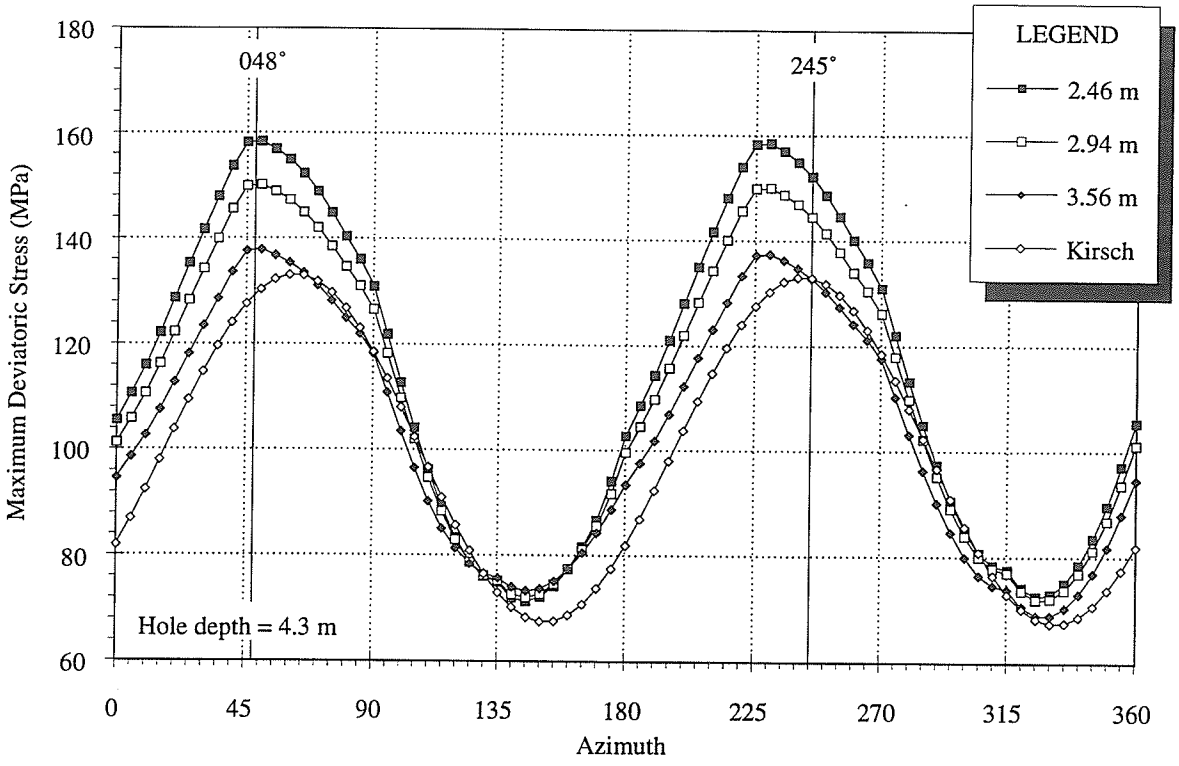

Figure 6.13: Maximum deviatoric stress pattern behind the Room 405 borehole face at depths corresponding to the termination points of the breakouts (2.46 and 2.94 m, respectively) and an intermediate depth with the borehole at 4.3 m depth. The plane strain solution for an infinitely long vertical borehole out of the influence of Room 405 (Kirsch) is shown for reference.

stress. This value suggests that excavation damage ahead of the face has reduced the rock strength at this location by about 10 MPa.

As shown by the intermediate response in Figure 6.13, the maximum tangential stress decreases with distance from Room 405. For an infinitely long vertical borehole, the tangential stress pattern far from the influence of Room 405 would correspond to the plane strain solution of Kirsch [99], given by

$$\sigma_{\theta\theta} = \frac{\sigma_p + \sigma_q}{2}\left(1 + \frac{a^2}{r^2}\right) - \frac{\sigma_p - \sigma_q}{2}\left(1 + \frac{3a^4}{r^4}\right)\cos 2\theta \qquad (6.17)$$

where σ_p and σ_q are the maximum and minimum far-field plane normal stresses, respectively, and θ is the rotation angle measured relative to the σ_p direction. This response, based on the estimated *in situ* tensor from Chapter 5, is also shown in Figure 6.13. Note that the maximum tangential stress for the plane strain case is 133 MPa, oriented towards azimuth 062°. The effect of Room 405 is to distort the pattern of tangential stress at the borehole wall, and the shear stress distribution away from the wall.

6.3.4 Radial displacement pattern

The radial displacement pattern at the design perimeter of the Room 405 borehole in the region $-1 \leq X/D \leq 1$ is shown in Figure 6.14 for hole depths of 1.5, 2.6 and 4.3 m, respectively. As demonstrated in Chapter 4, this pattern can be considered a superposition of the responses associated with the plane and antiplane components of the stress tensor. The radial displacement response resulting from the plane components has a periodicity of 180°, and is related directly to the relative magnitudes of the principal plane components of the stress tensor. The relationship between the principal plane stress ratio σ_p/σ_q and the principal radial displacement ratio $U_{r_{min}}/U_{r_{max}}$ is illustrated in Figure 6.15. In the absence of antiplane stress components, the amount of radial displacement occurring at $X/D = 0$ is 31% of the response at $X/D = +\infty$.

The plot for a hole depth of 1.5 m illustrates that the displacement patterns around the borehole are significantly different from plane strain conditions, with the maxima and

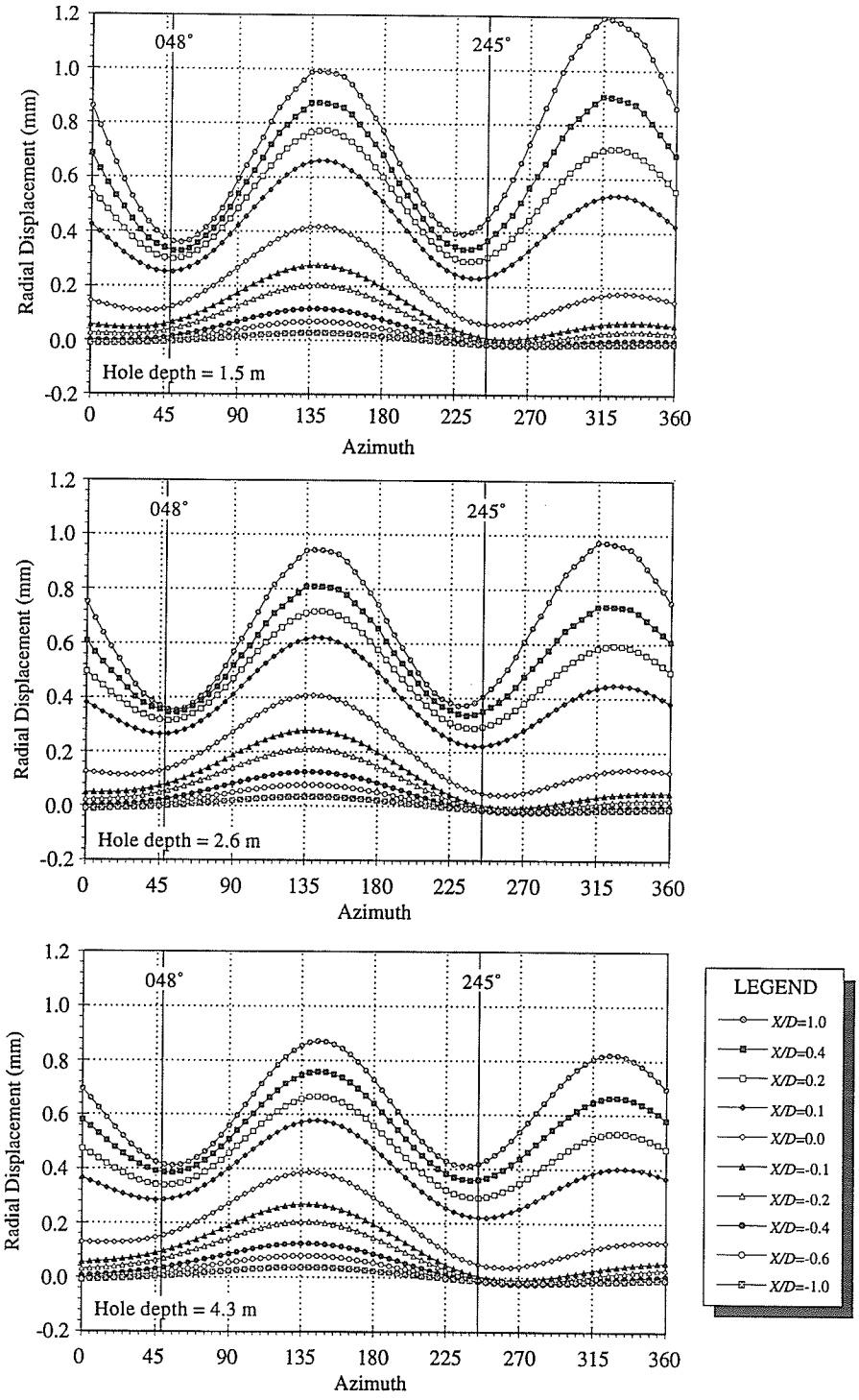

Figure 6.14: Radial displacement pattern near the Room 405 borehole face at depths of 1.5, 2.6 and 4.3 m below the top of intact rock in the tunnel floor. Note the asymmetry of the minima, both in magnitude and azimuth.

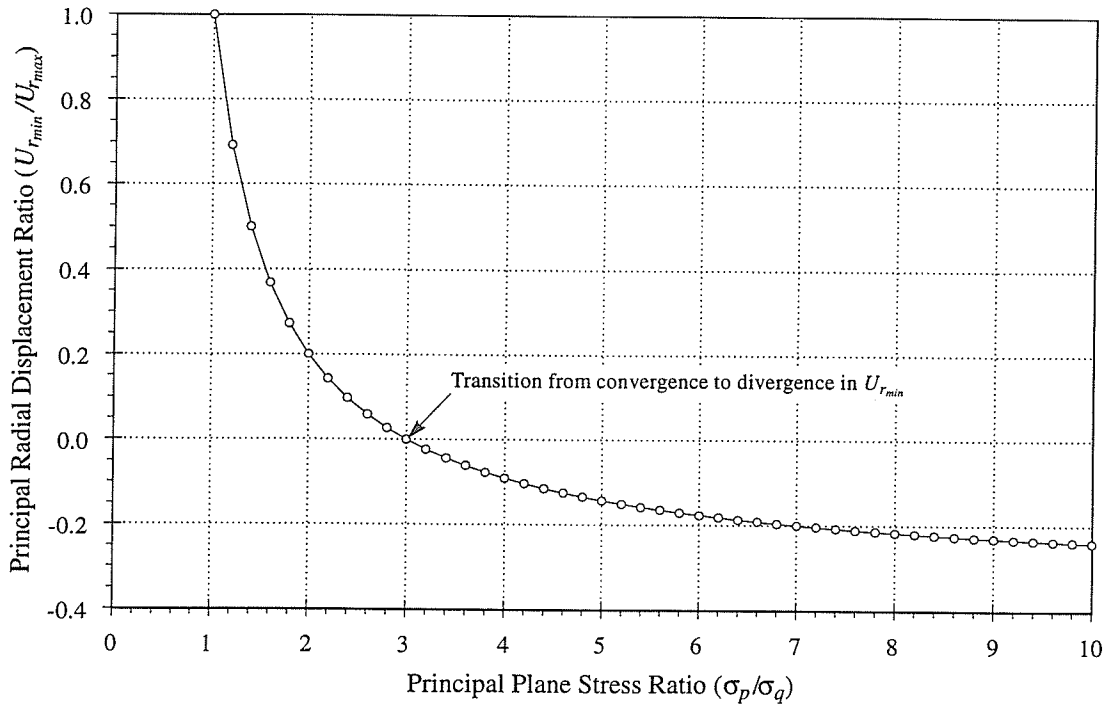

Figure 6.15: Relationship between principal plane stress ratio and principal radial displacement ratio. Note that the transition from convergence to divergence in $U_{r_{min}}$ occurs at a stress ratio of 3.

minima becoming more asymmetric in the posterior domain with distance from the face. This effect complicates the interpretation of the relationship between the displacement gradients and breakouts in the borehole. It is clear, though, that the positions of the minima within the region $0 < X/D < 0.1$ correspond to the positions of the breakout notches. Further from the face in the posterior domain, the position of the minima shift slightly to match the regional stress field near Room 405. At $X/D = 0$, the radial displacement at the NE minimum is greater than that at the SW minimum, suggesting that the maximum deviatoric stress is greater at the NE side of the borehole at this depth.

The second plot shows a similar response to the first, although the magnitudes of the maxima are less, suggesting a less severe stress ratio acting in the plane of the borehole. The tangential stress at the minima is therefore less than in the previous case. The locations of the minima for $0 < X/D < 0.1$ again correspond very well with the locations of the breakouts in the borehole. Further from the face, the maxima and minima tend to align with the regional tensor. The minimum in the radial displacement response corresponding to the NE side of the borehole is greater in magnitude than that on the SW side, again indicating greater maximum deviatoric stress on the NE side of the borehole. The magnitude of the maximum deviatoric stress is, however, less than in the first case owing to the decrease in the tangential stress at this depth. This reduction in tangential stress prevents the occurrence of breakout on the SW side of the borehole.

The third plot shows that the response at $X/D = 1$ is almost symmetric, indicating that the influence of Room 405 on the displacement response is diminished at this depth. The maxima show a reduction in magnitude from those at 2.6-m depth, so the tangential stress at the minima is less than at the previous depths. The NE minimum at $X/D = 0$ has a greater magnitude associated with it than the SW minimum, implying greater maximum deviatoric stresses at this location. However, the reduction in the tangential stress at this location is apparently sufficient to prevent breakouts to occur on both the NE and SW sides of the borehole. The minima at $X/D = 0.1$ coincide with the locations of the breakouts in

the borehole. In the absence of the perturbation caused by the presence of Room 405, it is anticipated that the azimuths of the minima at $X/D = 0$ would correspond to the positions of the breakouts in the borehole. This hypothesis is explored in Section 6.5.1. Figure 6.16 shows the displacement patterns at three depths in the Room 405 borehole compared to the plane strain solution for an infinite borehole unaffected by the presence of Room 405. In the absence of Room 405, the maxima align with the maximum plane stress direction. The effect of Room 405 is to shift the maxima towards an azimuth orthogonal to the room axis.

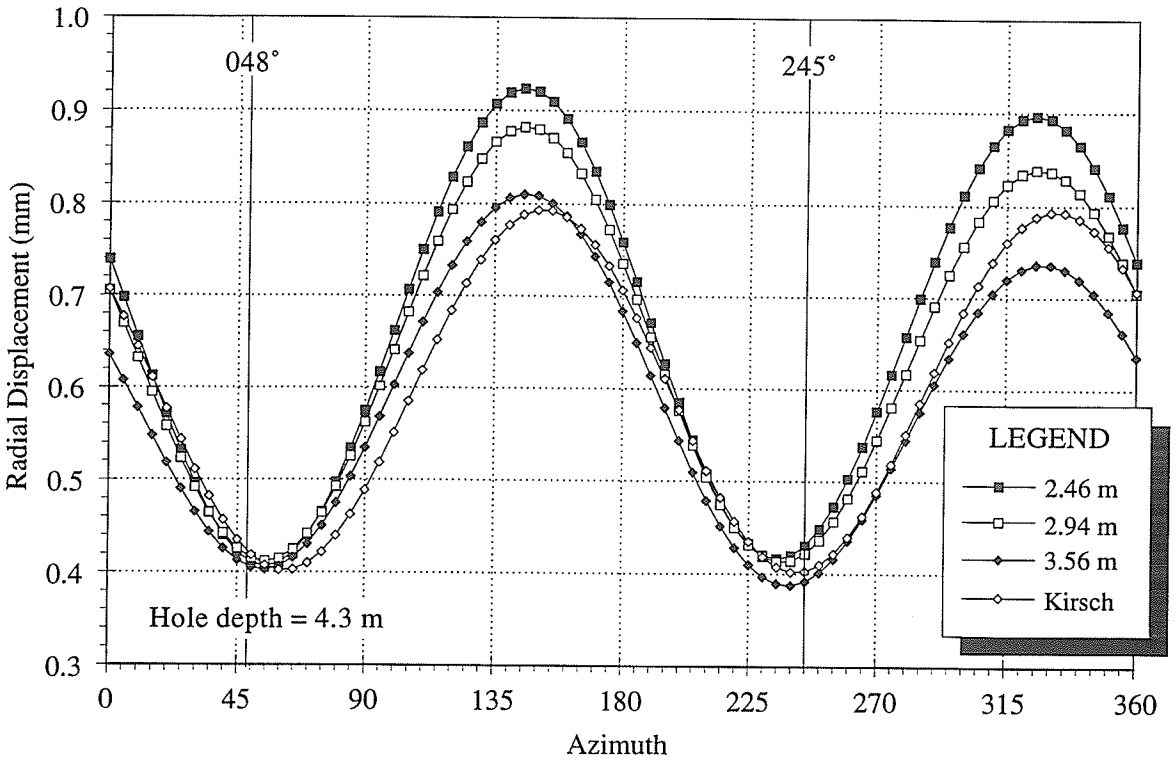

Figure 6.16: Radial displacement pattern behind the Room 405 borehole face at depths corresponding to the termination points of the breakouts (2.46 and 2.94 m, respectively) and an intermediate depth with the borehole at 4.3 m depth. The plane strain solution for an infinitely long vertical borehole out of the influence of Room 405 (Kirsch) is shown for reference.

6.3.5 Conclusions from Room 405

From the Room 405 simulations, it can be concluded that the estimated *in situ* stress tensor is consistent with the observed pattern of excavation damage in the large-diameter borehole. In particular, the pattern of maximum deviatoric stress ahead of the face provides an explanation of the observed asymmetric breakout pattern. The radial displacement pattern reflects the stress distribution around the tunnel, and also provides evidence that the minima in the response display asymmetry in their position and magnitude consistent with the observed breakout pattern.

6.4 *In Situ* Characterization of Excavation Damage in Room 415

Having established that the stress tensor estimated in Chapter 5 is consistent with the breakout patterns observed in the Room 405 borehole, the same approach was planned for Room 415. As a preliminary step, a detailed field investigation was undertaken to determine the visible extent of damage around the tunnel. To this end, a series of trenches, slots and boreholes were completed to provide a cross-sectional view of possible damage beyond the tunnel perimeter.

6.4.1 Connected permeability trench

A large trench was excavated between chainages 31+70 and 35+90 in the test tunnel as part of a connected permeability experiment [155]. The lithology in this area of the test tunnel was predominantly granodiorite, so notch development was not as extensive as in other parts of the tunnel. The trench provided an excellent sectional view of the floor notch in the plane orthogonal to the tunnel axis. The upper photograph in Figure 6.17 shows the shape of the breakout zone in the floor, illustrating the characteristic convex-in geometry observed in all breakouts at the 420 Level of the URL. The flanks of the notch were sounded using a scaling bar, and were found to be drummy within about 300 mm of the notch tip.

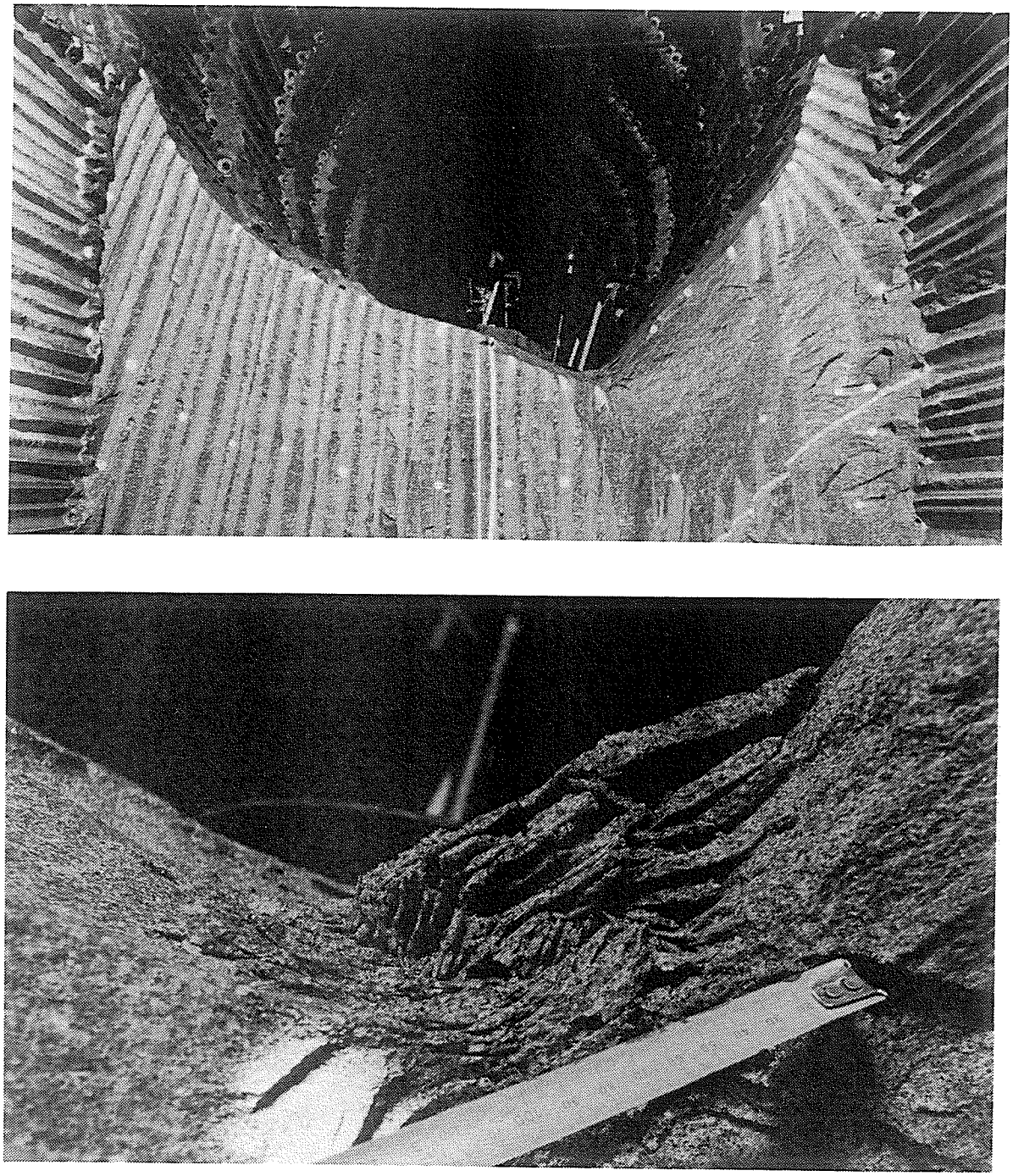

Figure 6.17: Exposure of the floor notch in the connected permeability trench. Note the convex-in shape of the breakout notch in the upper photograph, and the localized dilation at the notch tip in the lower photograph extending less than 100 mm into the rock mass.

A close-up view of the notch tip is shown in the lower photograph illustrating the localized dilation associated with the active process zone, extending less than 100 mm into the rock mass at the notch tip.

6.4.2 Roof and floor observation slots

Two slots of connected 150-mm-diameter boreholes were drilled orthogonal to the tunnel axis at chainage 16+00 in the test tunnel across the notch apex in the roof and floor. The roof slot, shown in the upper photograph in Figure 6.18, was 360 mm long and was located in predominantly grey granite. Remnants of slabs associated with the development of the roof notch showed slickensides up to 380 mm from the notch tip. The exposed walls of the slot showed a crushed, dilated zone at the notch tip approximately 300 mm wide and 110 mm deep (lower photograph, Figure 6.18). Cracks oriented parallel to the notch flanks extended to 180 mm depth, at which point the slot developed significant breakouts. The fact that the breakouts started beyond the observed fracturing suggests that the cracked material carried no load during drilling of the slot, indicating that the damage predates the slot. The start of the breakout at 180 mm, therefore, coincides with the transition from damaged to intact rock.

The floor slot was 960 mm long and crosscut the notch tip in the floor of the tunnel (Figure 6.19). As in the roof, the lithology was predominantly grey granite, and slickensides were noted on the flanks of the notch. Material in the notch tip area had been removed during earlier scaling activities, so much of the dilated material noticeable in the connected permeability slot was removed. However, significant fracturing was still visible in the slot, extending to 200-mm depth at the notch tip, and dying out rapidly on the flanks of the notch. At the extreme NW side of the slot, only two discrete fractures, 60 mm from the wall, were visible. However, when sounded with a scaling bar, the walls were drummy over the entire notch area.

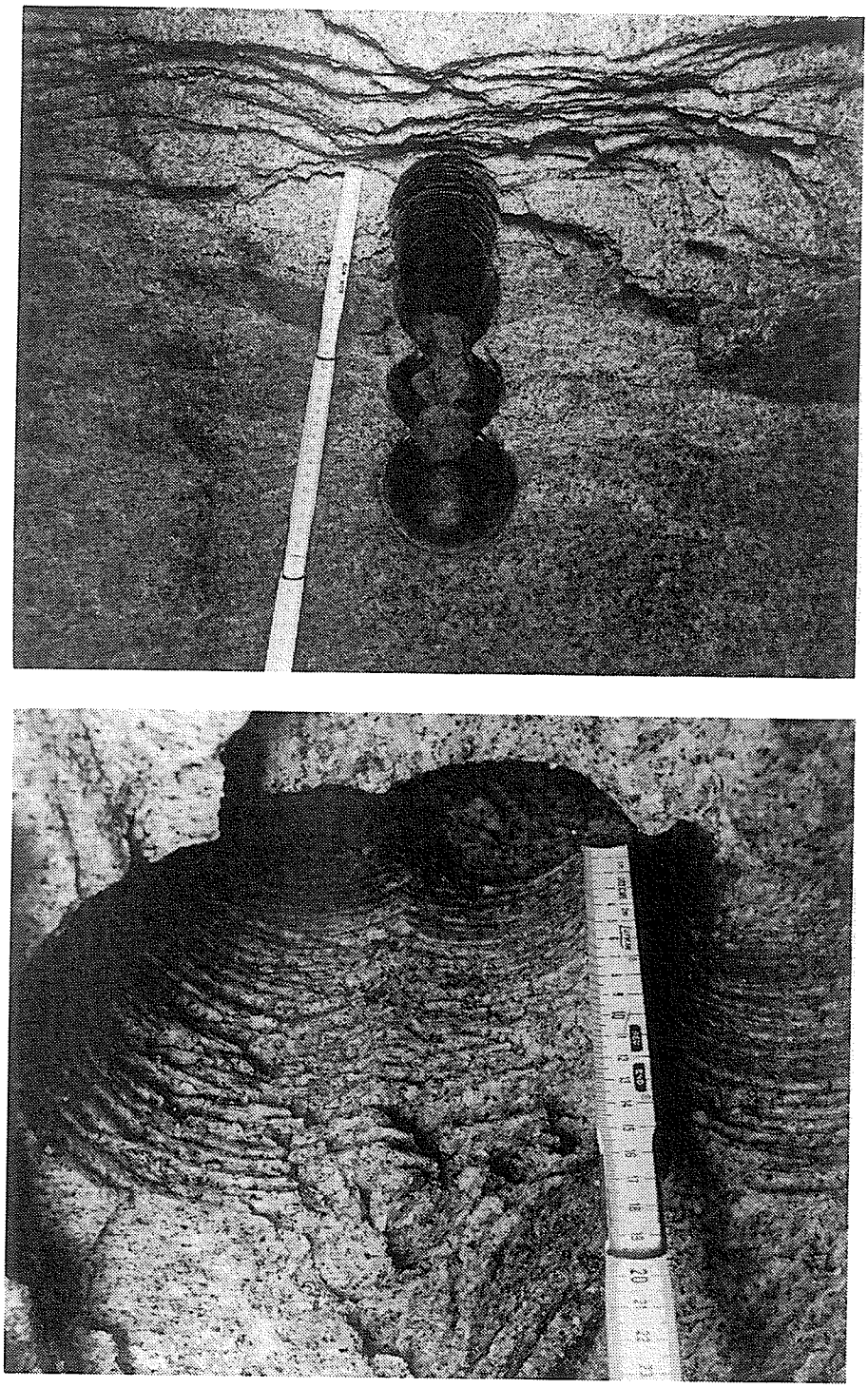

Figure 6.18: Details of damage in the roof slot drilled across the notch tip. The roof slot, shown in the upper photograph, was drilled as a series of connected 150-mm-diameter boreholes. Fracturing extends 180 mm into the rock mass at the notch tip.

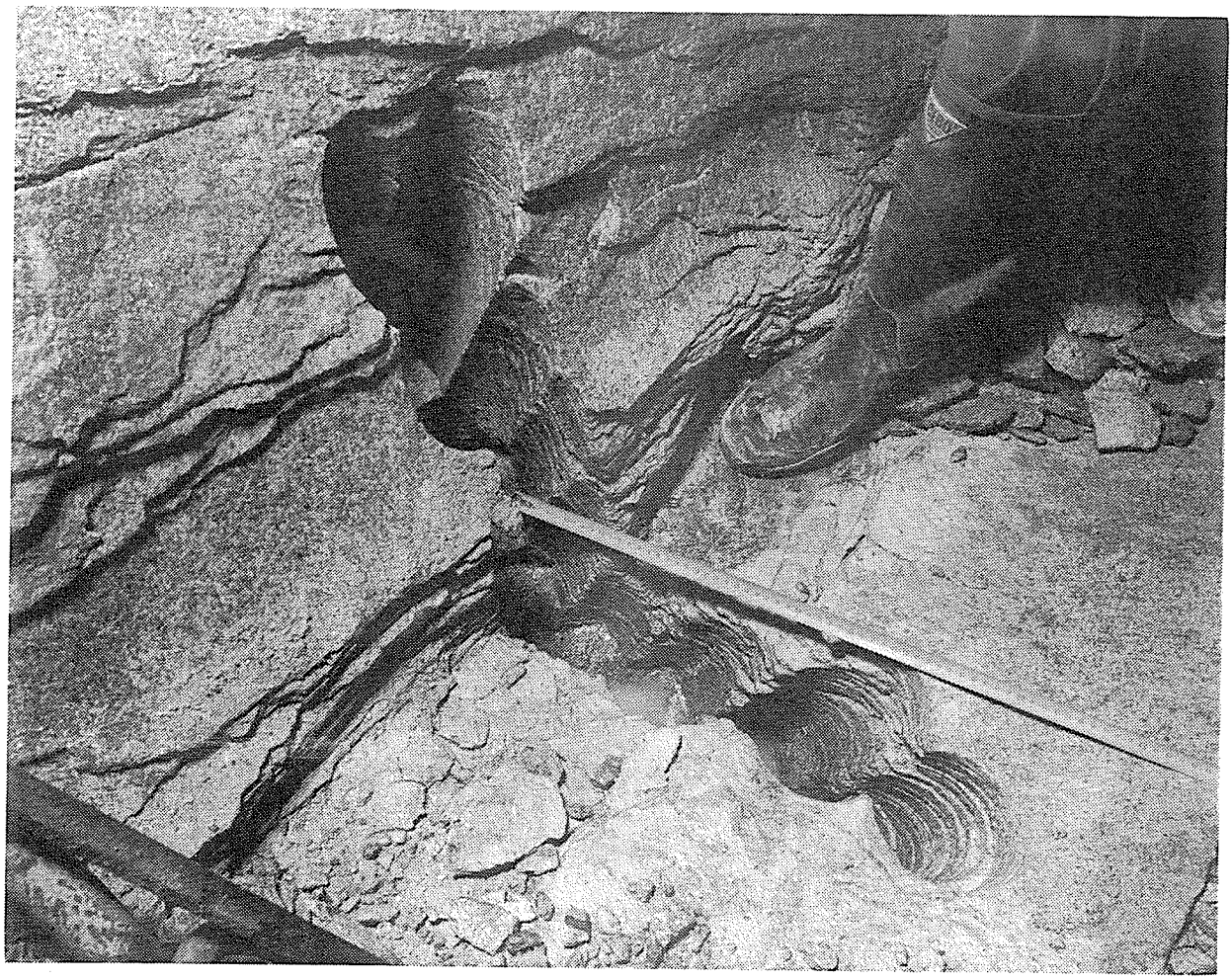

Figure 6.19: Damage in the floor slot drilled across the notch tip. Note that the fractures extend 200 mm into the rock mass, and show significant dilation. Fracturing diminishes on the flanks of the notch away from the apex.

6.4.3 Observation boreholes

In order to assess the extent of the damage, and whether or not it was pervasive along the test tunnel, four 510-mm-deep observation boreholes were drilled along the apex of the floor notch between chainages 16+50 and 22+05. Two of the extensometer boreholes drilled prior to the excavation of the test tunnel provided additional information. A summary of the fracturing found in the observation holes is shown in Figure 6.20. Fracturing was observed in the observation holes parallel to the notch flanks to a maximum depth of 240 mm, and in all cases, borehole breakouts started at the point where the fracturing ended. This finding again suggests that the observed fracturing is independent of the borehole drilling, and is

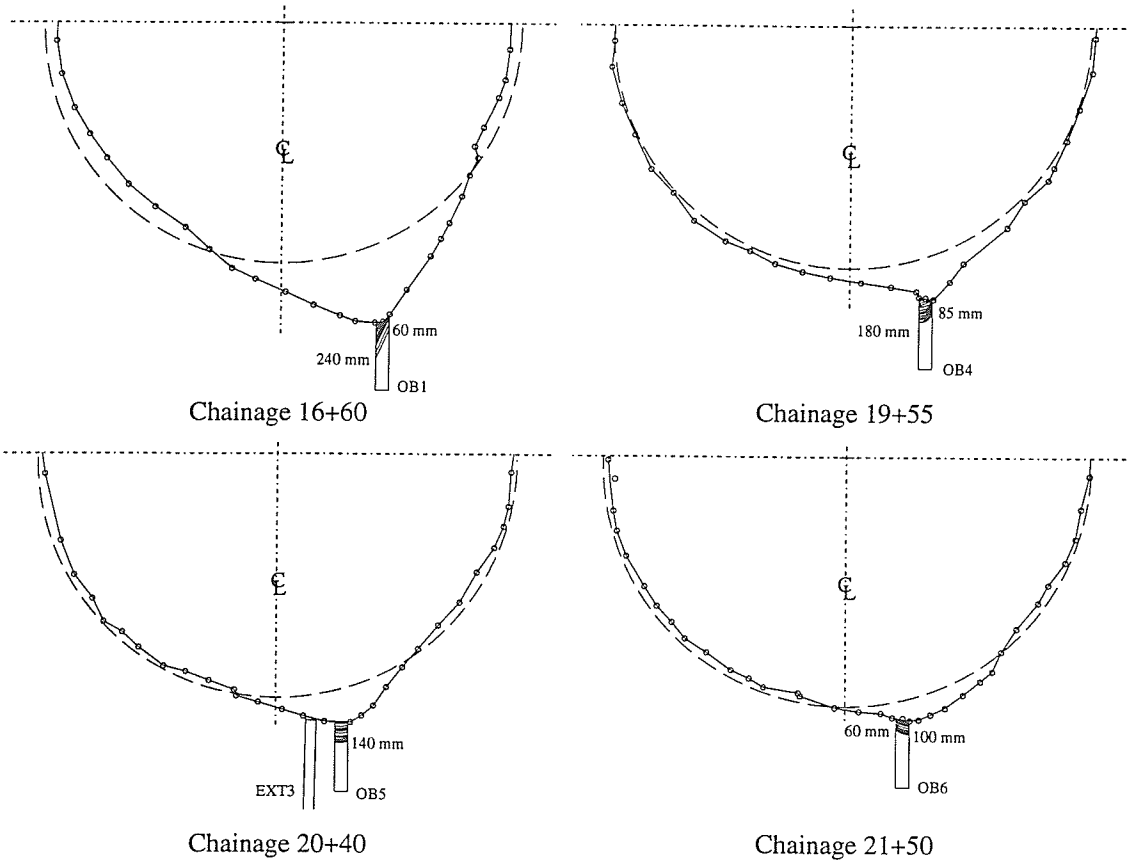

Figure 6.20: Extent of damage in the observation boreholes drilled along the apex of the floor notch. Note how the fractures parallel the free surface in all cases.

related to *in situ* damage at the notch tip. The start of the breakout zone is coincident with the transition from damaged to competent rock around the tunnel.

In the extensometer boreholes, breakouts extended to floor level, suggesting that they formed prior to development of damage around the tunnel. Borehole EXT9 showed two distinct fractures at 40 and 100 mm below, and parallel to, the floor. As shown in Figure 6.21, both fractures showed shear offsets of up to 1.5 mm, indicating movement of the upper slabs towards the notch tip.

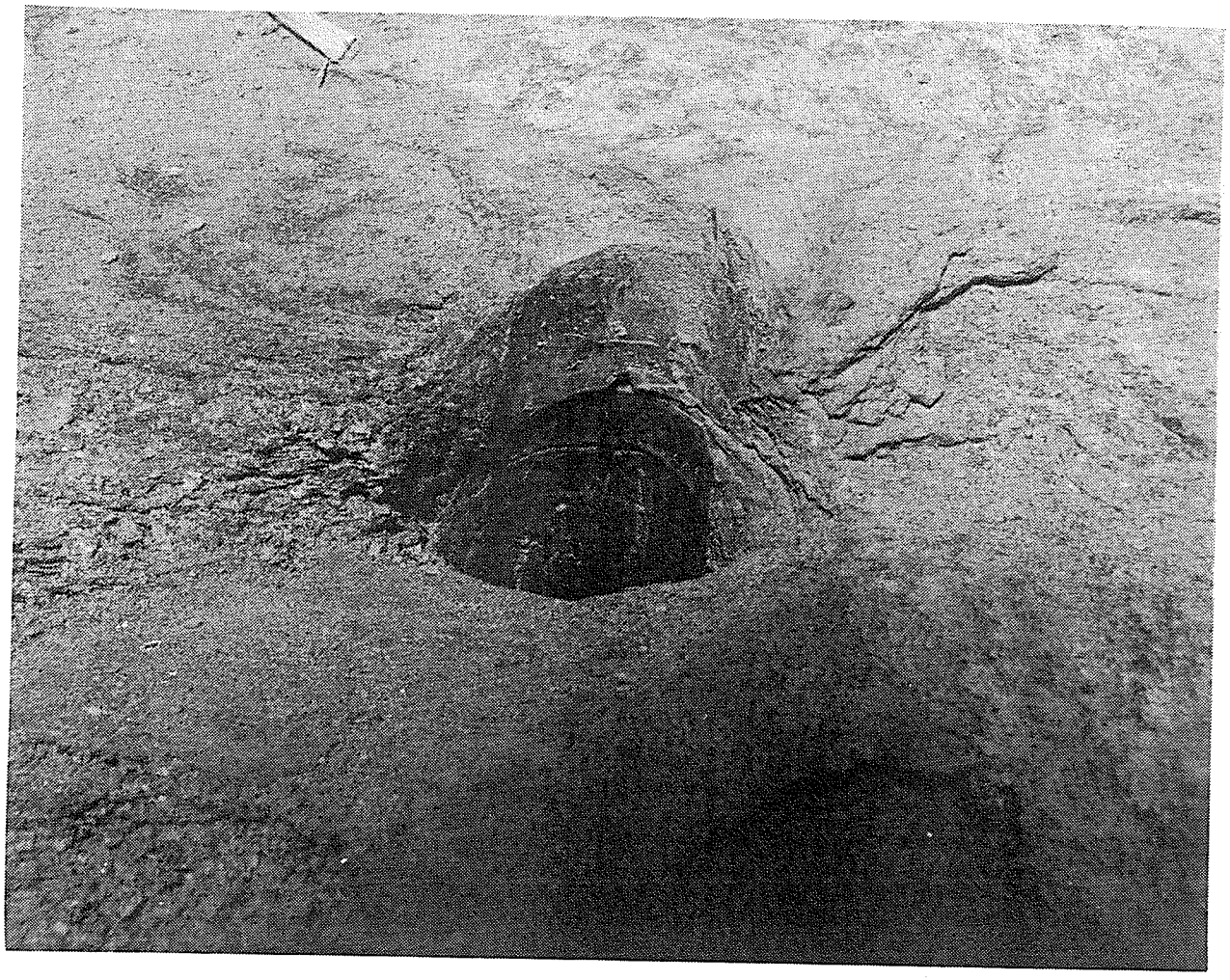

Figure 6.21: Shear offset in extensometer boreholes drilled prior to tunnel excavation. Movement is on the order of 1.5 mm, with the upper slabs moving towards the notch tip.

6.4.4 Observation trench

A wedge-shaped observation trench (Figure 6.22) was excavated between chainages 17+08 and 19+50 by first drilling two longitudinal cut-off slots to reduce the stresses in the area, then line-drilling a wedge from the destressed region. The lithology in this area was mixed granite and granodiorite. On the vertical face of the exposure, large-scale cracking was observed, believed to be related to widening of the first 16 m of Room 415. Like the floor slot, the process zone at the notch tip was disturbed prior to the trench excavation, and only a small remnant of the dilated material was left in place (upper photograph, Figure 6.23). However, the face of the trench that was inclined at 30° provided a good inclined section

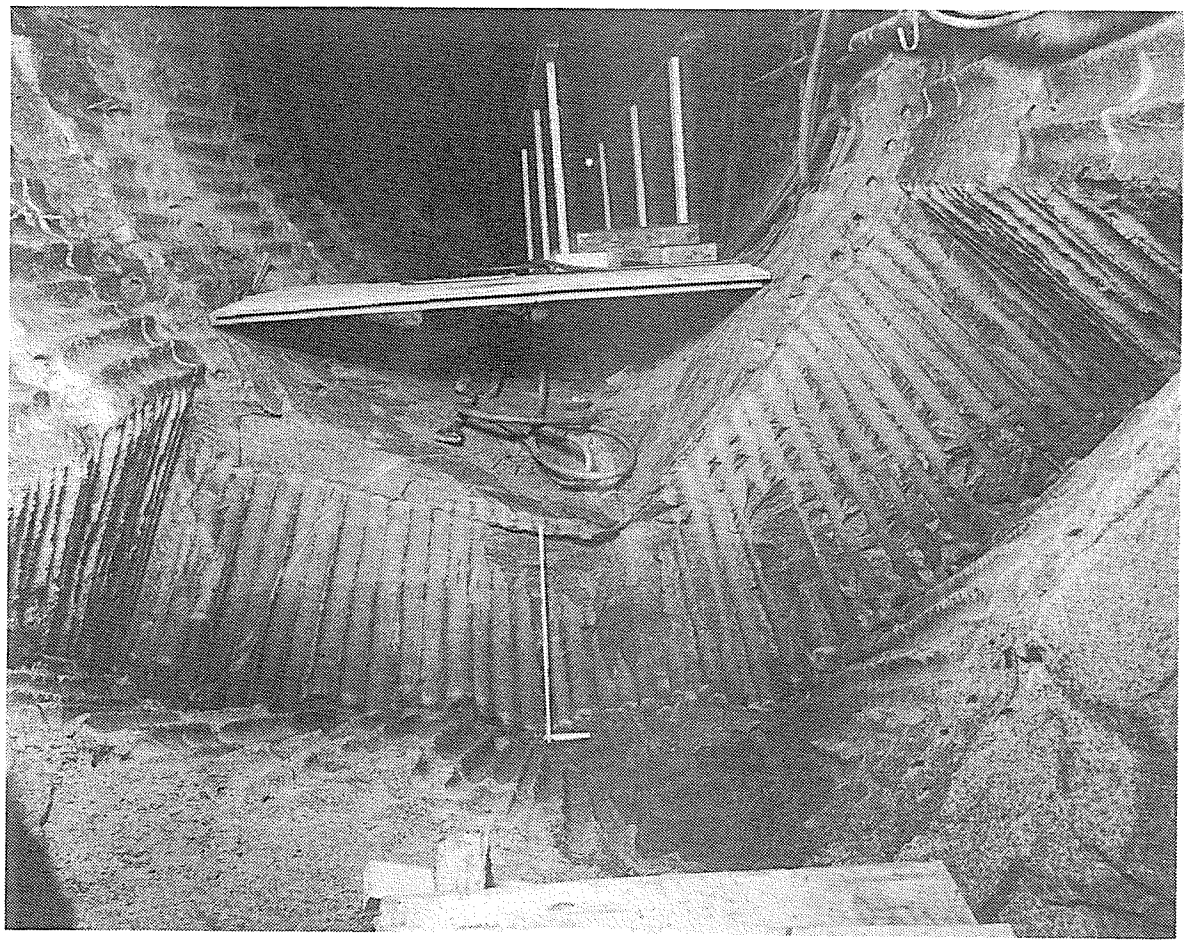

Figure 6.22: Wedge-shaped observation trench in the test tunnel.

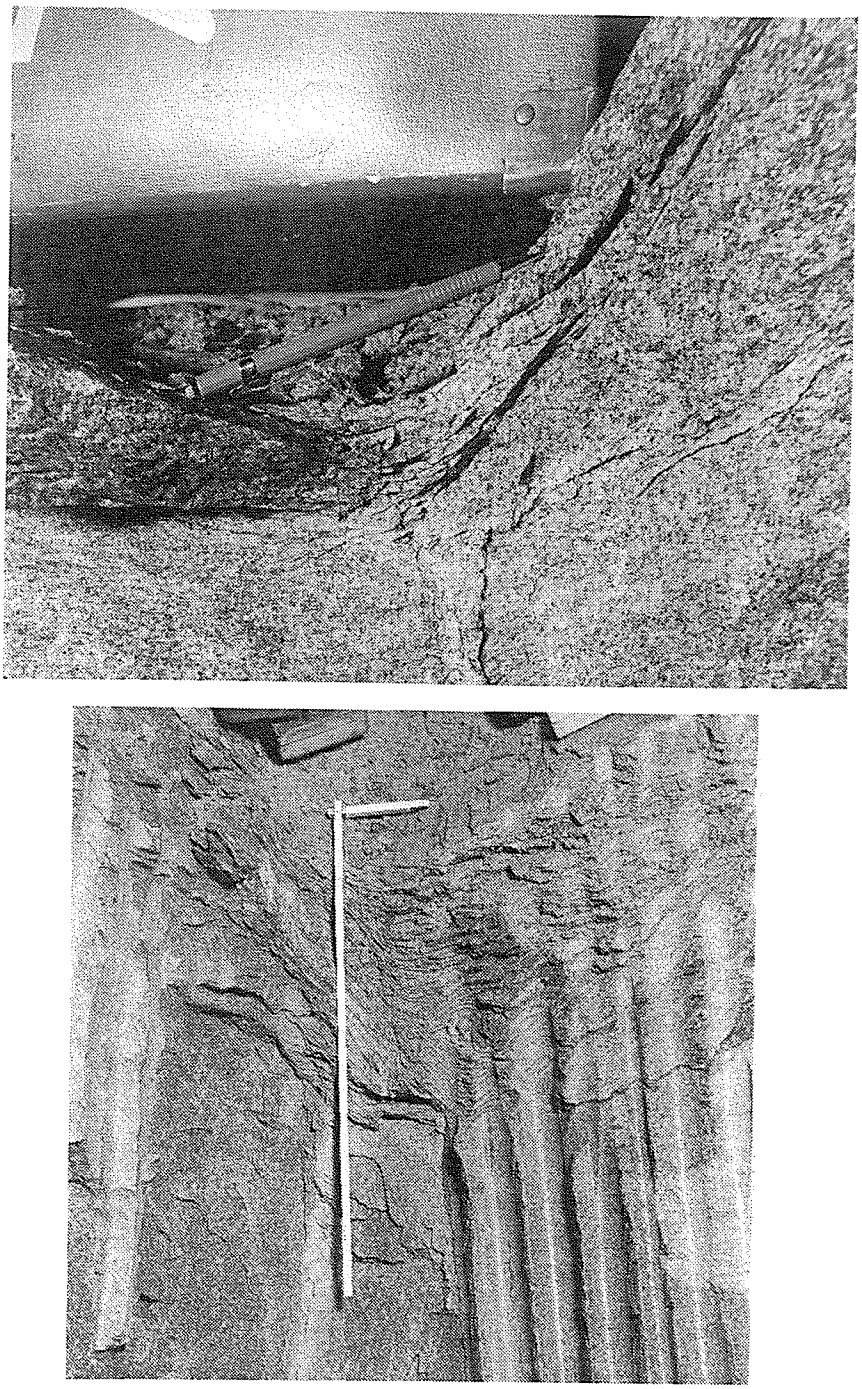

Figure 6.23: Extent of damage in the observation trench. Remnants of the dilated material at the notch tip in the floor of the test tunnel are shown in the upper photograph. Damage in the inclined face of the trench extends 225 mm into the rock mass.

through the damaged zone at the notch tip (lower photograph, Figure 6.23). Measurements of the damage showed that it extended to a maximum depth of 225 mm at the notch tip, and was characterized by fracturing parallel to the free surface.

6.4.5 Summary of observed damage

The observed damage around the test tunnel is concentrated near the notch tip in the roof and floor. In the roof, the damage extends about 180 mm into the rock mass, and occurs up to about 500 mm either side of the notch tip in the flanks of the notch. In the floor, the damage extends to about 240 mm depth, dying out within 500 mm on the NW flank, and within 800 mm on the SE flank. The damaged zone comprises a series of closely spaced fractures that are parallel to the free surface. Consequently, the rock in the damaged zones has a much lower elastic modulus than the intact rock as supported by the fact that breakouts do not occur in sections of boreholes or slots penetrating these regions. Figure 6.24 shows the observable extent of excavation damage on a typical tunnel profile taken at chainage 20+40.

6.5 Modeling of Excavation Damage in Room 415

Numerical modeling was conducted using EXAMINE^{3D} to assess the effect of the change in tunnel geometry associated with progressive failure on the stress and displacement patterns around the test tunnel. FLAC was then used to conduct a series of model simulations to assess the material behaviour in the posterior domain, incorporating the results from *in situ* characterization of excavation damage, and the stress tensor estimated in Chapter 5.

6.5.1 Displacements and stresses without notched geometry

Following the same procedure used to investigate the relationship between the stress and displacement patterns around the borehole in Room 405 and borehole breakouts, the Mine-by Experiment test tunnel was simulated using a cylindrical model constructed using

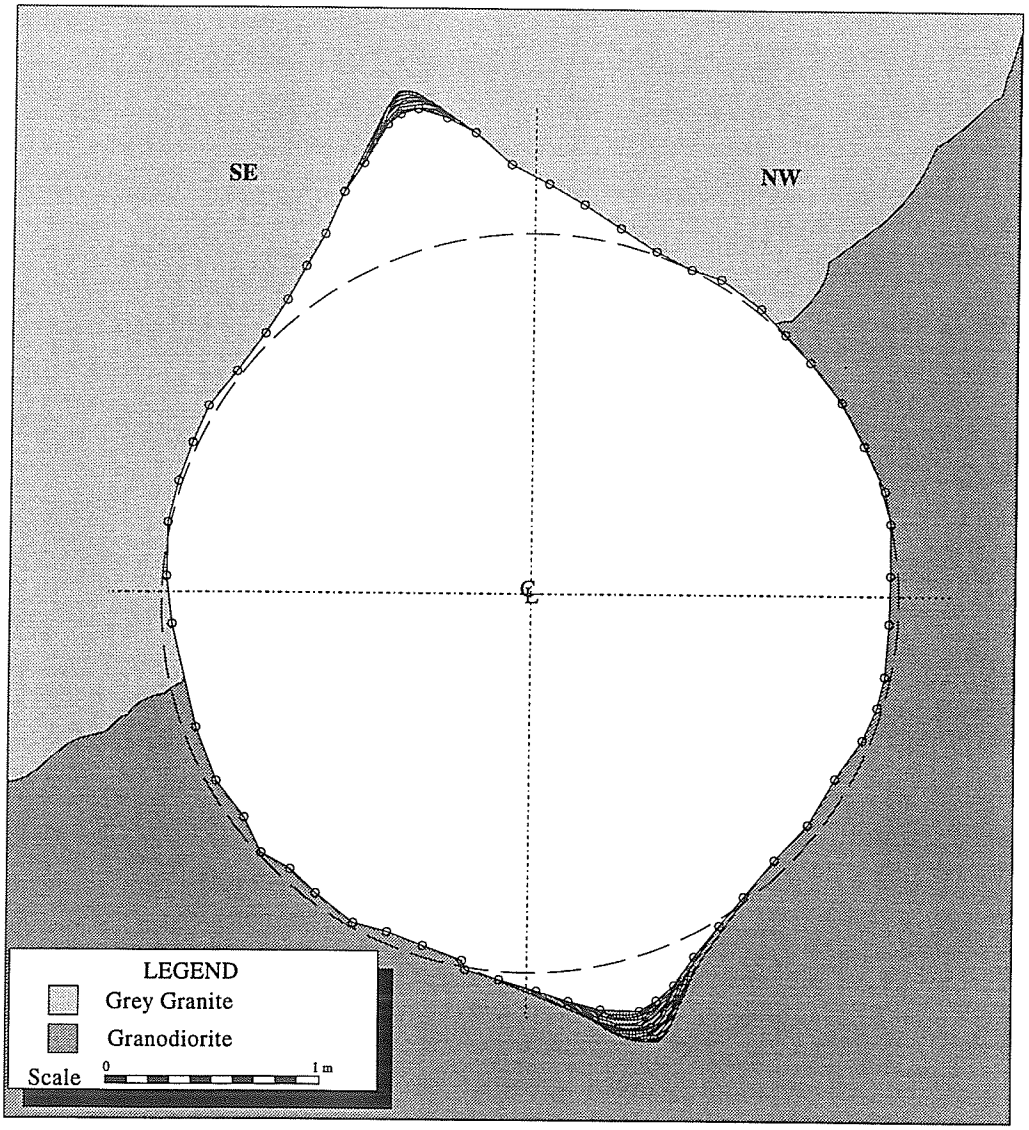

Figure 6.24: Typical profile at chainage 20+40 showing the extent of observable excavation-induced damage around Room 415. The damaged zone in the roof is about 180 mm thick, while that in the floor is 240 mm thick.

EXAMINE^{3D}. The model, shown in Figure 6.25, comprised 3772 elements, and had eleven rings of 72 field points each, positioned at the face and at 1. 0.8, 0.6, 0.4, 0.2, 0.1 tunnel diameters either side of the face. The elastic constants used in the simulation were $E = 65$ GPa and $\nu = 0.25$.

The pattern of maximum deviatoric stress ahead of the tunnel face in the region $-1 \leq X/D \leq -0.1$ is shown in Figure 6.26. The response is slightly asymmetric, both in the magnitudes and positions of the maxima and minima. The response corresponding to $X/D = -0.2$ indicates both maxima are just below the crack initiation threshold. At this location, the rotation angles of the maxima correspond well with the eventual location of the breakouts in the tunnel, shown on the plot as 101° and 286°. Closer to the face, the proximity to the stress singularity at the edge of the tunnel face causes a shift in the positions and a change in the shape of the response. The minimum in the response

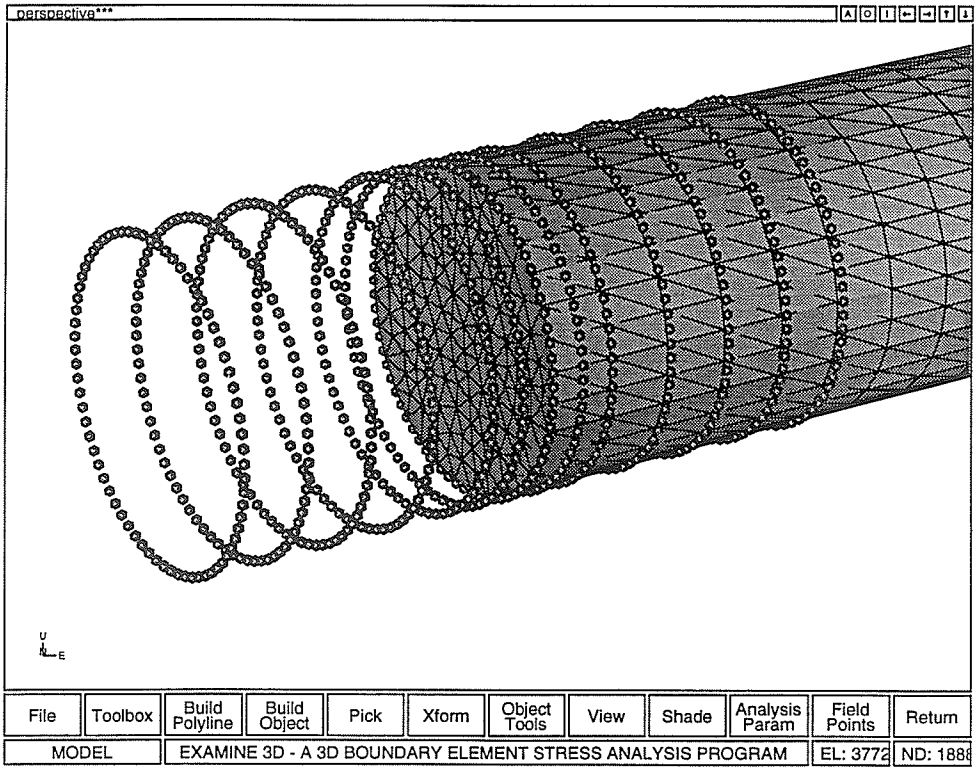

Figure 6.25: Boundary element model of Room 415 without notched geometry.

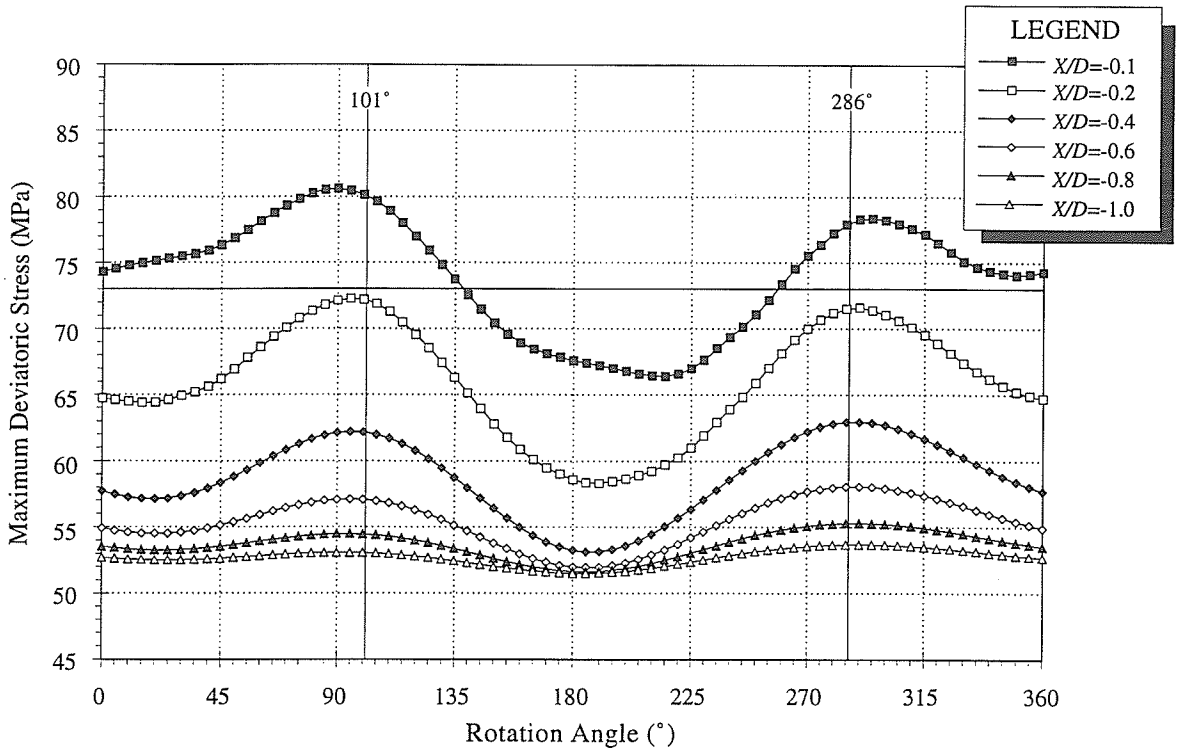

Figure 6.26: Pattern of maximum deviatoric stresses ahead of the face in Room 415. The threshold for crack initiation $(\sigma_1 - \sigma_3) = 73$ MPa is shown as a horizontal line.

corresponding to the roof of the tunnel is larger in magnitude than that corresponding to the floor, suggesting that higher maximum deviatoric stress, and therefore more damage, occurs in the roof ahead of the advancing tunnel face. This observation was confirmed by the patterns of AE/MS activity recorded during the Mine-by Experiment [129] which show more activity in the upper SE quadrant ahead of the face than in the lower NW quadrant.

The radial displacement pattern for the test tunnel is shown in Figure 6.27. The response for $X/D = 1$ is almost symmetric, indicating that the stresses around the tunnel approach plane strain conditions at this location. Closer to the face, however, there is marked asymmetry in the responses, particularly at $X/D = 0$. The rotation angles associated with the

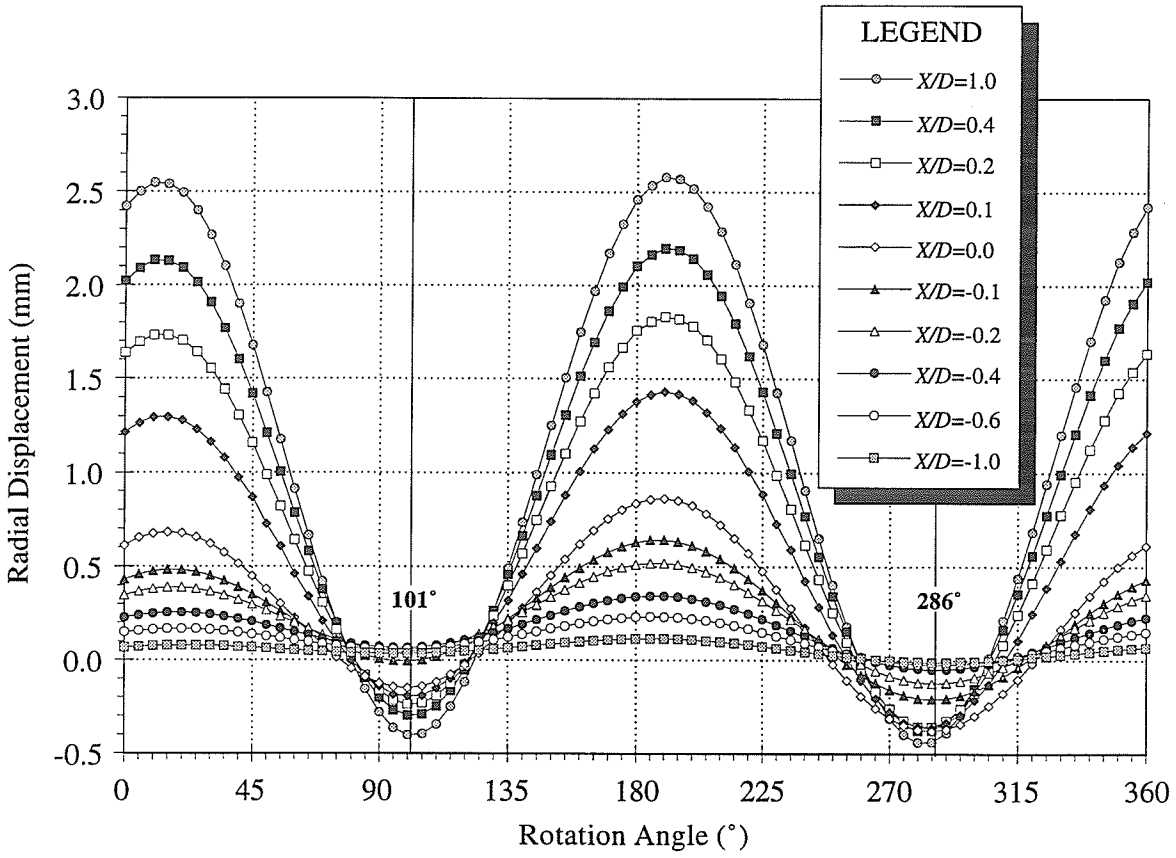

Figure 6.27: Pattern of radial displacement around Room 415 for the region $-1 \leq X/D \leq 1$. Note the asymmetry in the magnitude and positions of the maxima and minima in the response at $X/D = 0$.

minima in the response at this location (i.e., 101° and 286°) correspond exactly with the measured breakout angles observed in the test tunnel. As shown on the plot, the rotation angles of the minima tend to converge to 12° counterclockwise of vertical as the distance from the face increases, corresponding with the plunge of the minimum principal stress component in the plane orthogonal to the tunnel axis. It was noted that, during progressive failure of the tunnel, the positions of the breakouts were initially asymmetric, but tended to converge to 12° counterclockwise of vertical as the tunnel advanced [46]. The magnitude of the radial displacement at the minimum corresponding to the roof is greater than that for the minimum associated with the floor. As shown in the Room 405 investigation, this pattern indicates higher maximum deviatoric stresses in the roof, and lower stresses in the floor, as a result of antiplane components of of the far-field *in situ* stress tensor. Therefore, microseismic activity and notch development in the roof would be expected to be more pronounced in the roof than in the floor.

6.5.2 Displacements and stresses with notched tunnel geometry

The same model simulation was repeated using a cylindrical tunnel incorporating a notched geometry starting 1 m back from the tunnel face (Figure 6.28). The shape of the notches was based on the measured profile for excavation round 13. The model comprised 4058 elements, and 936 field points arranged in the same manner as the cylindrical tunnel simulation. However, only those field points ahead of the notch were considered in the study. An additional ring of 72 points at the start of the notch geometry was interpolated from the surface elements.

The maximum deviatoric stress pattern associated with the notched geometry is shown in Figure 6.29. In comparison to the responses for the cylindrical tunnel, the maximum deviatoric stress responses for the notched geometry are identical in shape and marginally higher in magnitude. For example, the peak at 101° has a magnitude of slightly over 82 MPa as opposed to 81 MPa for the cylindrical geometry. The difference in magnitudes

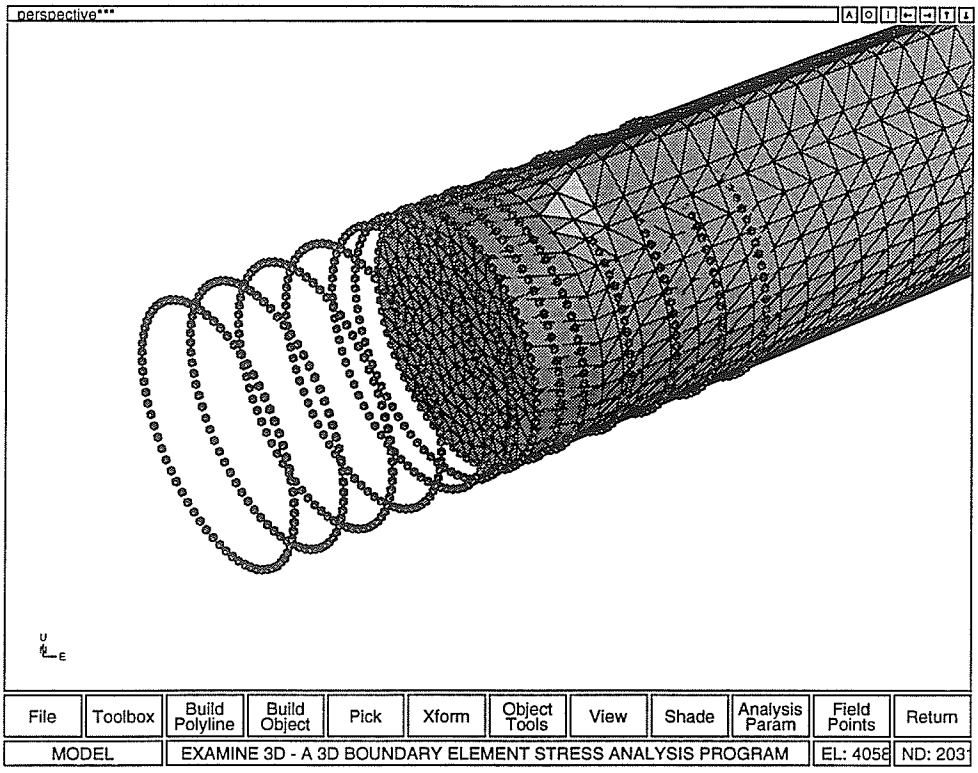

Figure 6.28: Boundary element model of Room 415 with a notch starting 1 m back from the face.

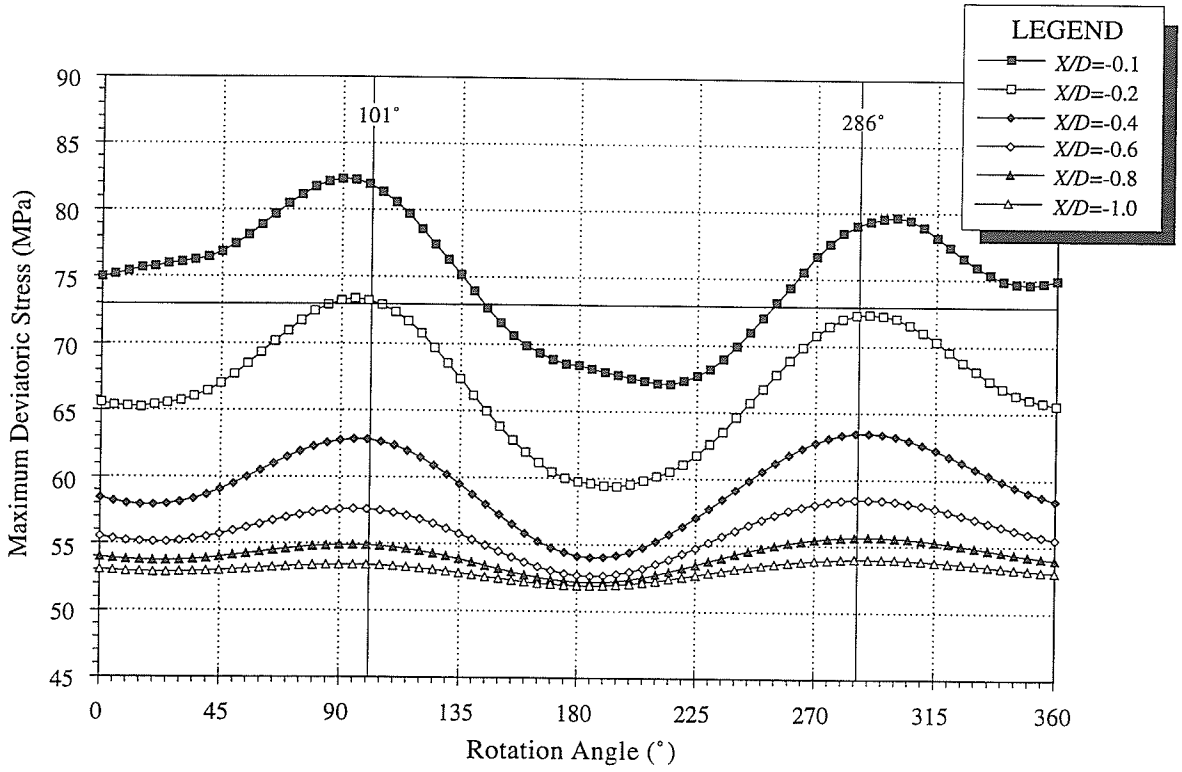

Figure 6.29: Pattern of maximum deviatoric stresses ahead of the face in Room 415, including breakouts 1 m from the face. The threshold for crack initiation $(\sigma_1 - \sigma_3) = 73$ MPa is shown as a horizontal line.

diminishes with distance from the face. The main significance of the difference is that the crack initiation threshold is exceeded in the roof at $X/D = -0.2$. Otherwise, the conclusions are the same as those for the cylindrical tunnel.

The radial displacement pattern for the notched tunnel geometry is shown in Figure 6.30. Like the maximum deviatoric stress response, there is only a marginal difference between the anterior responses for the notched and cylindrical tunnels. However, in the posterior domain, the notch geometry serves to increase the magnitudes of the maxima, and slightly decrease those of the minima, thus increasing the difference in the maximum and minimum displacements. Consequently, if these values were used in a stress back analysis, they would

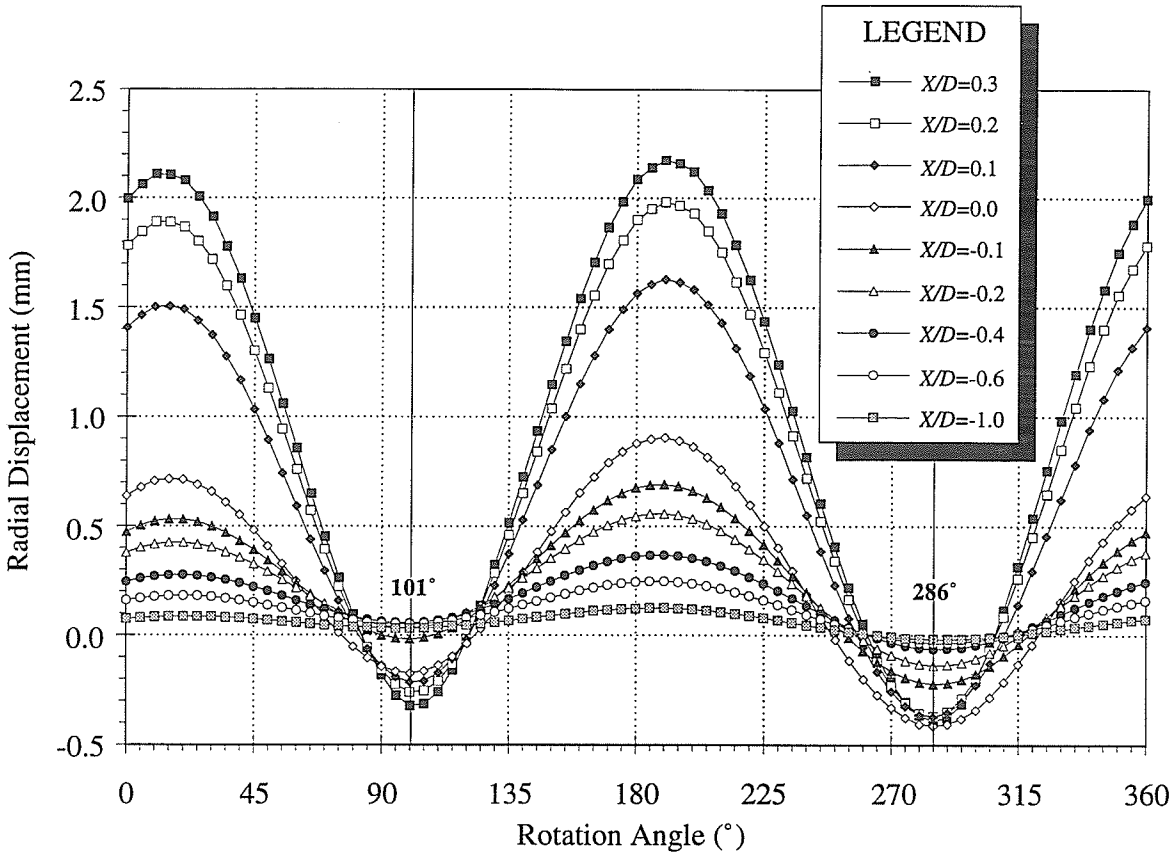

Figure 6.30: Pattern of radial displacement around Room 415 incorporating a notched geometry for the region $-1 \leq X/D \leq 1$. Note the asymmetry in the magnitude and positions of the maxima and minima in the response at $X/D = 0$.

greatly overestimate the *in situ* stress components acting in the plane orthogonal to the tunnel axis. The other observations regarding the coincidence of the breakout locations and the minima, and the relative magnitudes of the minima, are the same as those for the cylindrical tunnel. In short, only in the posterior domain does the existence of a notched geometry significantly affect the radial displacement pattern. Furthermore, it affects only the magnitudes of the displacements, not the orientation of the maxima and minima with respect to the tunnel.

6.5.3 Comparison of measured and modeled displacements

The radial displacement responses measured with the twelve Bof-ex extensometers in the Mine-by Experiment were compared to those from the cylindrical and notched geometry models at four locations: $X/D = -0.4$, -0.1, 0 and 0.1. The model results represent the displacements predicted using the *in situ* tensor estimated in Chapter 5, which was based on measurements taken both close to, and remote from, the design perimeter of the tunnel. Owing to the potential for damage and other nonlinear phenomenon near the tunnel, differences between the measured and modeled results, if present, would be most pronounced at the design perimeter. Consequently, results were compared at a radial distance $r/a = 1$. For $X/D > 0.3$, the tunnel geometry deviated from a cylinder, so results could not be compared at $r/a = 1$ past this location for all rotation angles.

The radial displacement responses versus rotation angle at $X/D = -0.4$ and -0.1 are shown in Figure 6.31. In both cases, the notched geometry model produced slightly more convergence in the sidewalls than the cylindrical model, but similar amounts of divergence in the roof and floor. In comparison to the measured results, the modeled results at both locations fall completely within the 99% confidence (prediction) interval determined for the measured response. At $X/D = -0.4$, however, the modeled results compare more closely to the mean measured response than at $X/D = -0.1$. In addition, the positions and pattern of asymmetry in the minima and maxima of the measured and modeled results coincide in

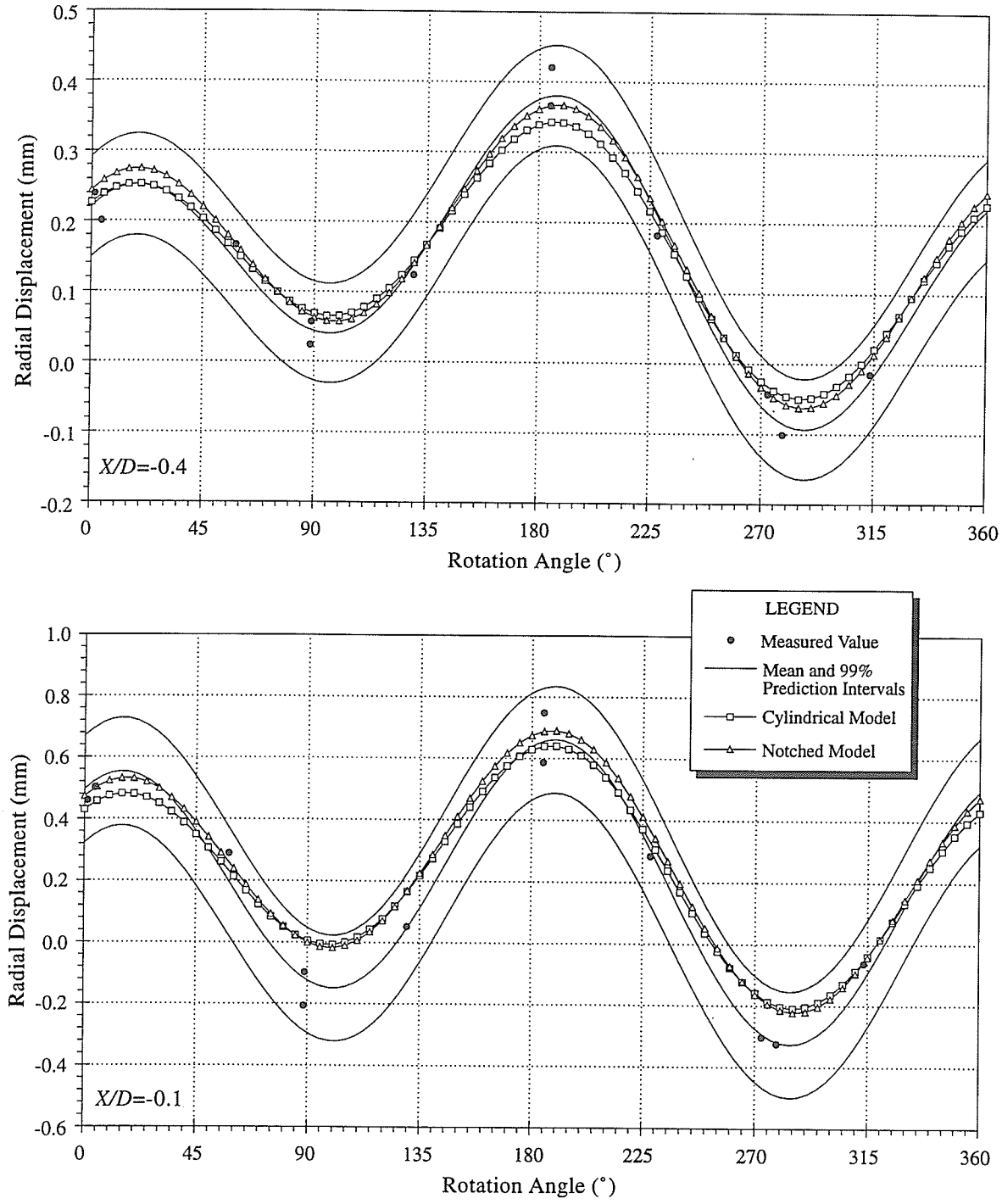

Figure 6.31: Comparison of measured and modeled radial displacements in the anterior domain at $X/D = -0.4$ and -0.1.

both cases.

The radial displacement responses versus rotation angle at $X/D = 0$ and 0.1 are shown in Figure 6.32. At $X/D = 0$, there is only a minor difference in the results from the two numerical models, and both compare favourably with the mean measured response. The modeled responses fall completely within the 99% confidence (prediction) interval for the measured response, and there is very little difference in the positions and pattern of asymmetry of the maxima and minima. At $X/D = 0.1$, however, there are significant differences between the displacement results from the two numerical models, and between the modeled and measured results. In comparing the responses from the two models, the effect of the notched geometry is apparent, causing an increase in convergence of the sidewalls of the tunnel while having relatively little effect on the response in the roof and floor. The measured results indicate that, even accounting for the notched geometry of the tunnel, the radial displacement at the sidewalls is much greater than the models would predict. Although the notched model response falls within the 99% confidence (prediction) interval of the measured response, the pattern of asymmetry of the maxima is different. The measured response at $\theta = 192°$, for instance, deviates more from the model results than at $\theta = 12°$. For the cylindrical tunnel, the response falls outside the 99% confidence (prediction) interval, suggesting that the effect of geometry change in the tunnel is significant at this point.

From these cases, it can be concluded that the results from the cylindrical model compare well with the measured responses in the anterior domain, but deviate significantly for $X/D > 0.1$ in the posterior domain where the tunnel shows a well-developed notch geometry within 1 m of the tunnel face. The notched geometry model captures some of the effects of the geometry change in the actual tunnel, but there are still significant differences between the measured and modeled radial displacement responses that cannot be explained with a simple linear elastic model incorporating the measured tunnel profile. The effect of excavation damage beyond the measured profile, variations in geology, and deviations

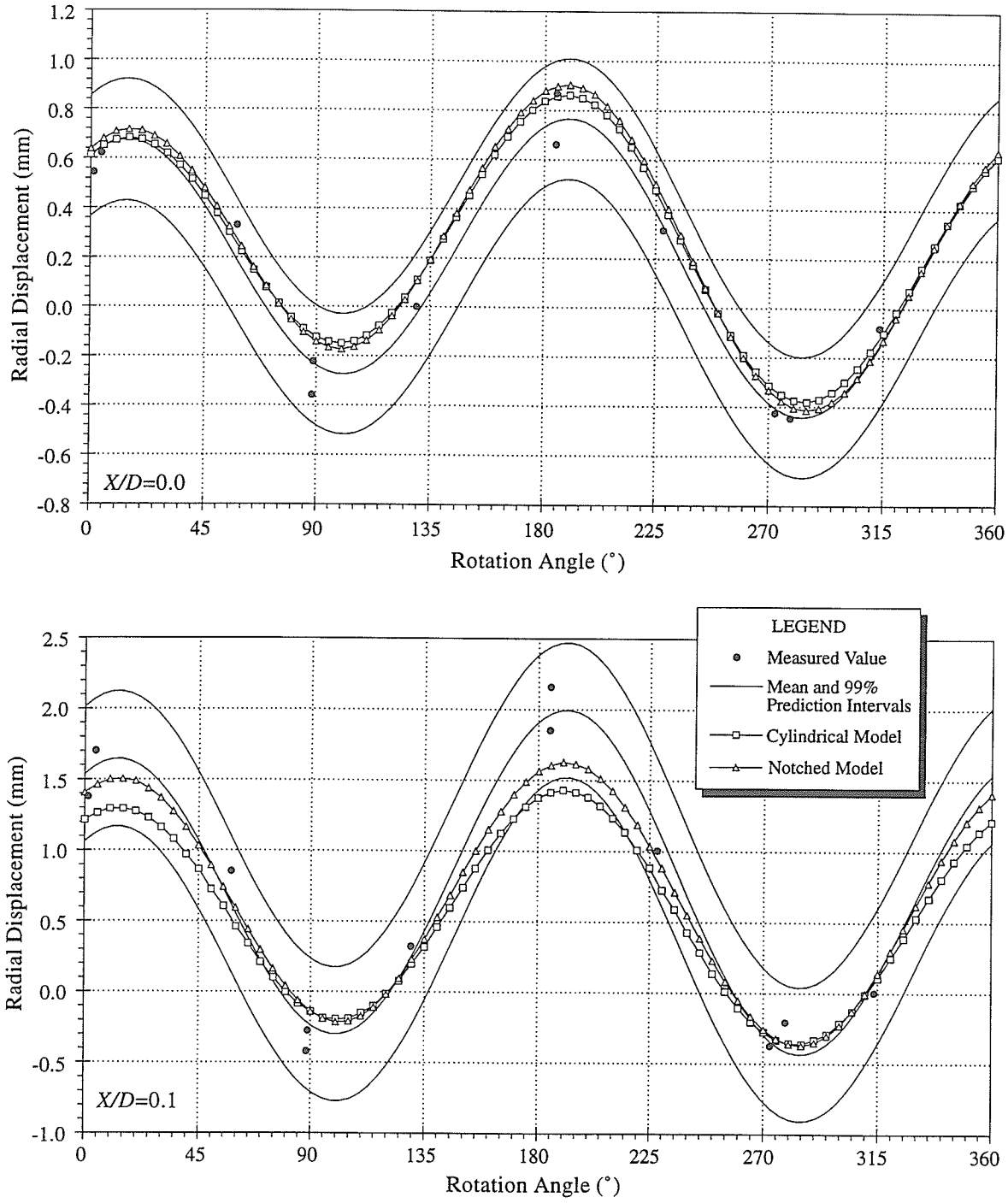

Figure 6.32: Comparison of measured and modeled radial displacements in the posterior domain at $X/D = 0.1$ and at the tunnel face.

from linear elastic material behaviour on the radial displacement response in the posterior domain are considered in the next section.

6.6 Excavation Damage in the Posterior Domain

A series of two-dimensional finite difference model simulations were conducted using FLAC to investigate the observed difference in the measured and modeled radial displacement responses in the posterior domain. A computer routine written by Read [154] was modified to produce control programs containing user-defined algorithms for FLAC for different choices of material properties, constitutive models, and failure criteria. An important feature of these programs is an algorithm that produces a radial finite difference grid with an inner boundary that matches the shape of the actual tunnel profile, and a circular outer boundary. Figure 6.33 is an example of the inner 4 m by 4 m portion of a typical radial

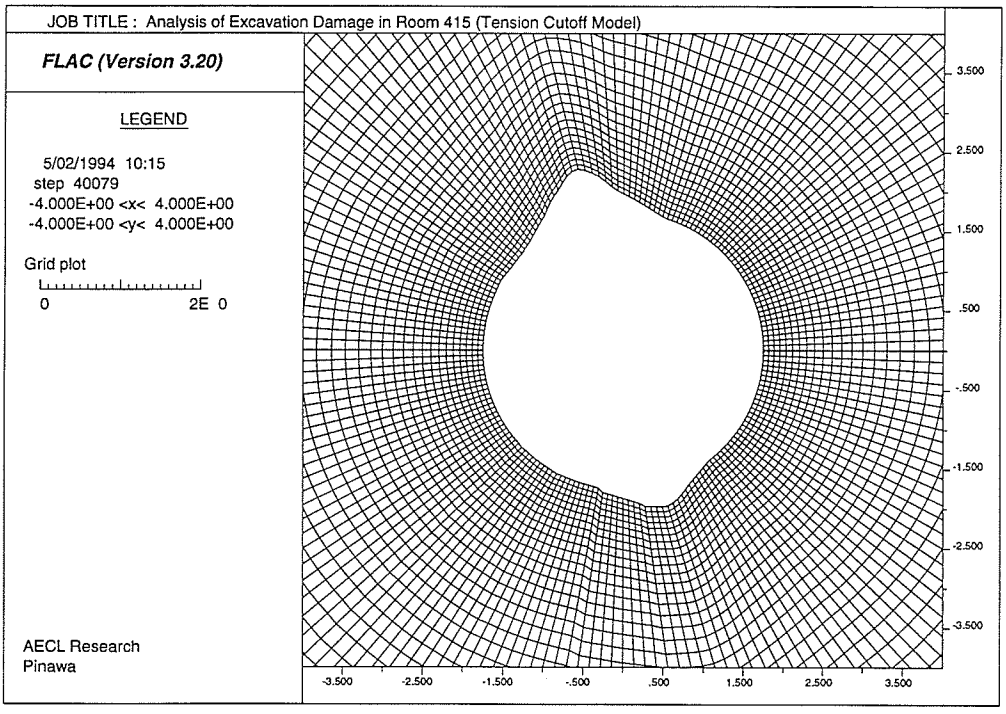

Figure 6.33: FLAC grid used in the analysis of material behaviour in the posterior domain. Note that only the centre portion of the complete grid is shown.

grid based on the tunnel profile at chainage 20+40 in Room 415 (Figure 6.24). The radial geometry facilitates the calculation of radial displacement along individual gridlines, and avoids irregularly-shaped elements near the inner boundary. The complete grid comprised 9720 elements.

A staged approach was used in the numerical modeling exercise, starting with a simple elastic model, then progressively adding details consistent with observations from the *in situ* characterization of the test tunnel. Table 6.3 summarizes the various cases that were considered in the study. The main modifications made to the elastic model included: 1) a low modulus zone beyond the notch tips to account for observed *in situ* cracking in these regions, 2) a uniaxial tensile failure criterion using ubiquitous joints to simulate a unidirectional reduction in tensile strength in regions where $\sigma_3 < \sigma_t$, 3) a softening criterion to account for reduction of the shear modulus for regions where $\sigma_3 < \sigma_t$, and 4) two different material types, each with unique properties and failure characteristics, to account for the variations in geology near the extensometer arrays. A plasticity model, using a Hoek-Brown failure criterion based on long-term strength and non-associated plastic flow, was used to illustrate that a phenomenological approach could produce reasonable agreement between observed and modeled displacements, but because the goal of the modeling study was to determine possible mechanisms responsible for the observed difference in the responses, general plasticity models were avoided.

As a base case, the radial displacement responses versus normalized radial distance for a purely elastic model were generated for eight rotation angles (Figure 6.34). To assess the effect of the damage beyond the notch tip shown in Figure 6.24, zones of reduced elastic modulus were added to the model in these regions. The damaged modulus in these zones was taken as 10% and 1% of the intact modulus in separate simulations. The resulting radial displacement responses using a damaged modulus equal to 10% of the intact modulus, are compared to the base elastic case in Figure 6.34. It is readily apparent from these plots that the damage observed *in situ* in the roof and floor of the tunnel has no significant effect

Table 6.3: Summary of models used to simulate radial displacement patterns observed in the posterior domain of the test tunnel.

Model	Material Model	Yield Criterion	Post-Yield Behaviour	Comments
1	Elastic	None	Elastic	Base case with notch geometry
2	Elastic	None	Elastic	Reduced E at notch tips
3	Elastic/ Ubiq/Mohr	Hoek-Brown	Non-associated plastic flow	Reduced E at notch tips
4	Elastic	Tension Cutoff	Elastic	Reduced E at notch tips, reduced G for $\sigma_3 < \sigma_t$
5	Elastic/ Ubiq	Tension Cutoff	Elastic	Reduced E at notch tips, reduced G for $\sigma_3 < \sigma_t$, uniaxial reduction in tensile strength
6	Elastic/ Ubiq	Tension Cutoff	Elastic	Reduced E at notch tips, reduced G for $\sigma_3 < \sigma_t$, uniaxial reduction in tensile strength, two material types

Note:
UBIQ - Ubiquitous Joint
MOHR - Mohr-Coulomb

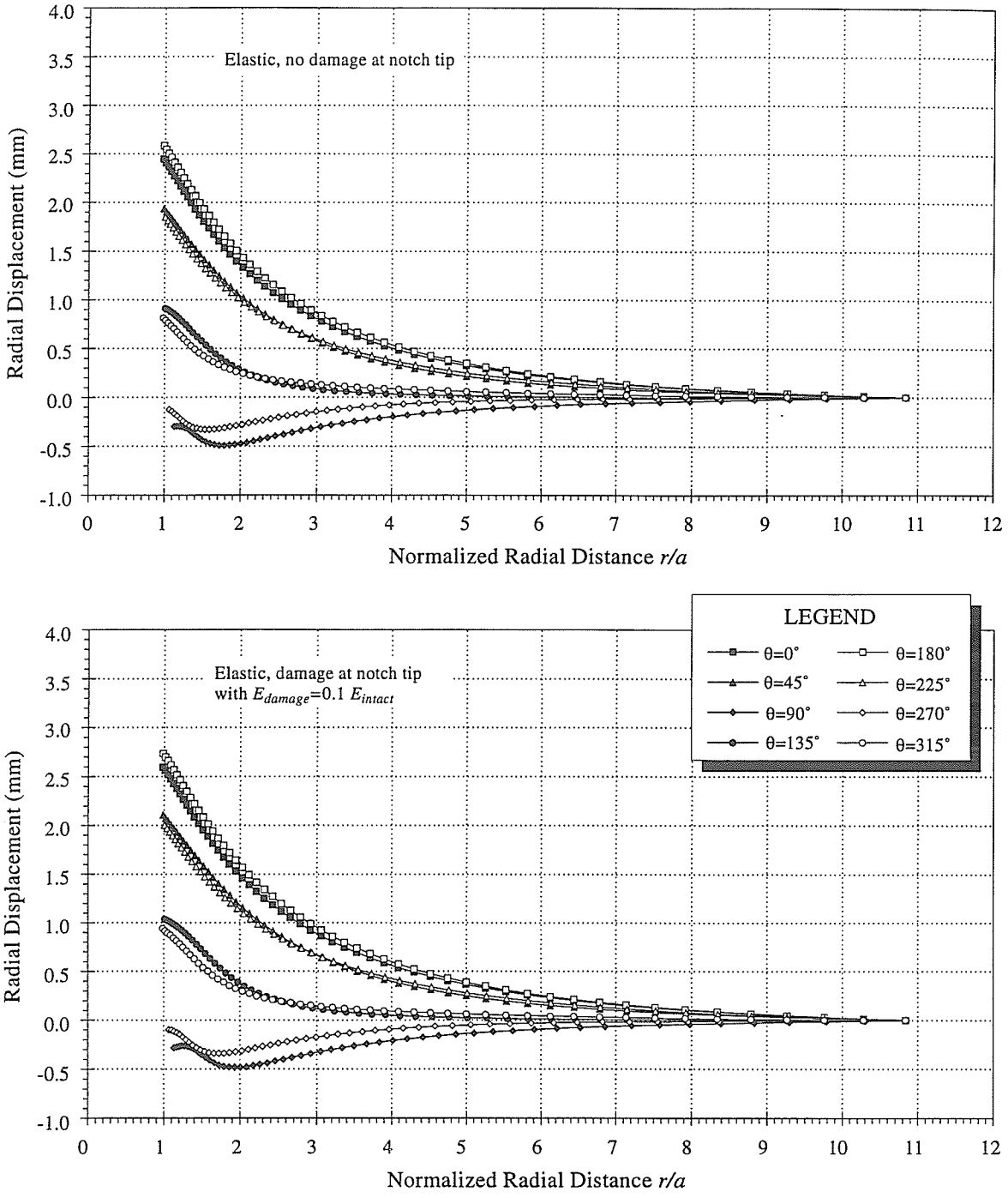

Figure 6.34: Radial displacement responses for elastic models excluding and including damage beyond the notch tip. Note that there is only a marginal difference in the responses resulting from the inclusion of additional damage at the notch tips.

on the radial displacement responses, producing only a marginal increase in displacement in the sidewalls. The same was true of the results using a damaged modulus equal to 1% of the intact modulus. The major role of the damage beyond the notch tip is to drive the point of maximum tangential stress into the rock mass away from the tunnel boundary, thus allowing sufficient confining stress to develop at that point to prevent further failure, i.e., the stresses at the point of maximum tangential stress would fall inside the failure envelope in principal stress space.

The measured radial displacement responses for the two extensometer arrays used in the Mine-by Experiment are shown in Figure 6.35. The responses represent the measured displacements at the end of excavation round 36, when the tunnel face was almost five tunnel diameters past the second instrument array. In comparison to the results in Figure 6.34, the measured displacement responses deviate from the elastic responses starting

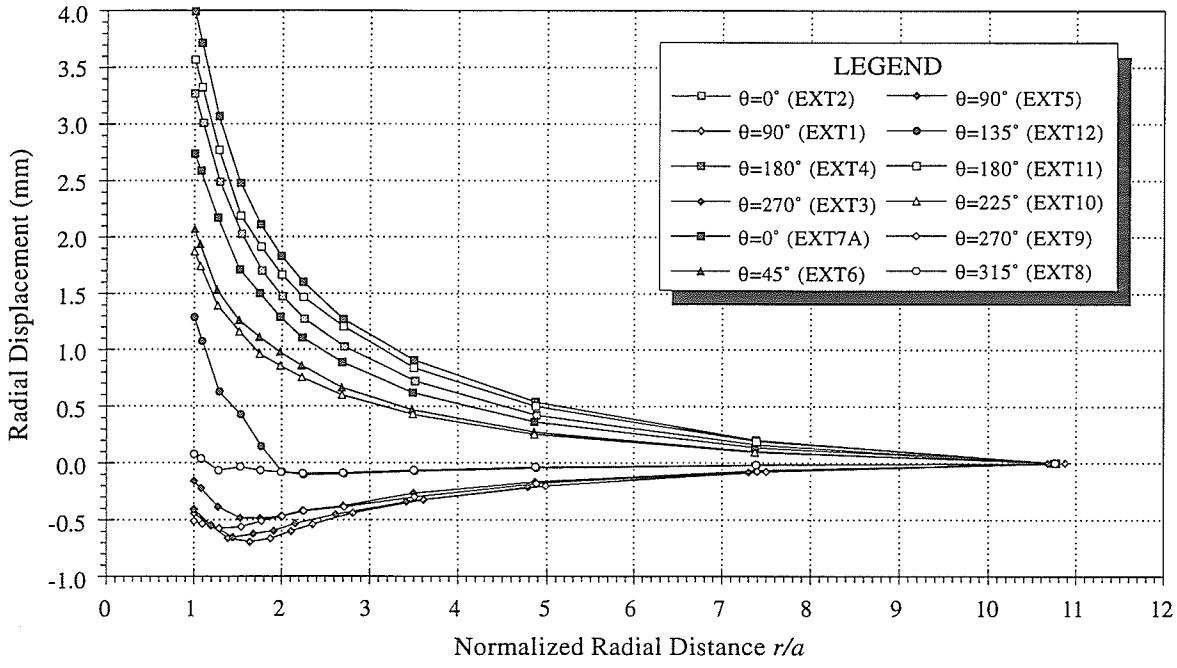

Figure 6.35: Radial displacement responses for the two extensometer arrays in the field study. Results from Array 1 are shaded in grey. Note the differences in these responses within one radius of the tunnel wall compared to the elastic case.

about one tunnel radius from the wall. The most notable differences are for instruments oriented at $\theta = 0$, 135, 180 and 315°. For the horizontal instruments, the gradient of the measured radial displacement responses is much steeper within one radius of the tunnel wall than for the elastic case. In the regions containing these instruments, the tangential stress near the tunnel is highly tensile, exceeding the tensile strength of the rock (approximately 10 MPa [125]) within about 200 mm of the wall. Lajtai [113] and Stimpson and Chen [174] have shown that the elastic behaviour of Lac du Bonnet granite is different under tensile loading than it is for compressive loading. In addition, Martin [125] has shown that the crack damage stress in tension for Lac du Bonnet granite is approximately 7.4 MPa, close to 80% of the Brazilian strength measured in a suite of tests he conducted. He further showed that accumulated damage in the rock results in an increase in Poisson's ratio and a decrease in the Young's modulus, effectively reducing the shear modulus G of the damaged material. Comparing the results from the elastic model and the measured results, the difference in the horizontal responses is consistent with a reduction in the shear modulus in the zone within one radius of the sidewalls. Likewise, the large increase in radial displacement in EXT12 in the upper SE quadrant of the tunnel indicates a similar change in the material properties in this region.

Velocity surveys conducted between the various galleries for the Mine-by Experiment prior to excavation of the test tunnel confirmed that the rock mass is homogeneous, with a compressional velocity of 5880±60 m/s [51]. From cross-hole tomography studies between the extensometer holes in the Mine-by Experiment conducted before and after excavation of Room 415, Hayles et al. [66] have reported a reduction of about 10% in seismic velocities in the sidewalls of the tunnel, and an increase in induced anisotropy in these regions. These low velocity zones are concentrated within 1 m of the tunnel wall, but on the SE side of the tunnel the zone extends further into the rock mass near EXT12. An acoustic emission (AE) study conducted by Carlson and Young [13] in Room 415 showed extensive high frequency, i.e., 1 MHz, activity in the sidewalls close to the extensometer arrays (Figure 6.36). Most

of the AE activity was concentrated 0.3 m into the wall. This study further illustrated that the compressional velocity in this region was strongly anisotropic as a result of induced damage in the tunnel wall. According to Carlson and Young [13], the principal directions of the velocity anisotropy suggest open crack porosity within the first one metre of the wall.

The studies by Hayles et al. [66] and Carlson and Young [13] support the idea of damage development in the tensile regions around the test tunnel, resulting in induced anisotropy, i.e., directional cracking, and reduced shear modulus. Several relatively simple models were used to simulate this process, and the resulting radial displacement responses. A simple elastic model, (case 4 in Table 6.3), using a softening criterion to reduce the shear modulus in zones where $\sigma_3 < \sigma_t$, produced only marginal changes in the radial displacement response, even when the shear modulus was reduced by an order of magnitude. To account for the reduction in tensile load bearing capacity orthogonal to the induced cracking in the damaged material, ubiquitous joint elements were introduced into the zones where $\sigma_3 < \sigma_t$ (case 5). Stress redistribution associated with the reduction in tensile stresses near the tunnel wall was captured by iteratively checking for new zones where $\sigma_3 < \sigma_t$, substituting ubiquitous joint elements for those elastic elements that violated the tensile

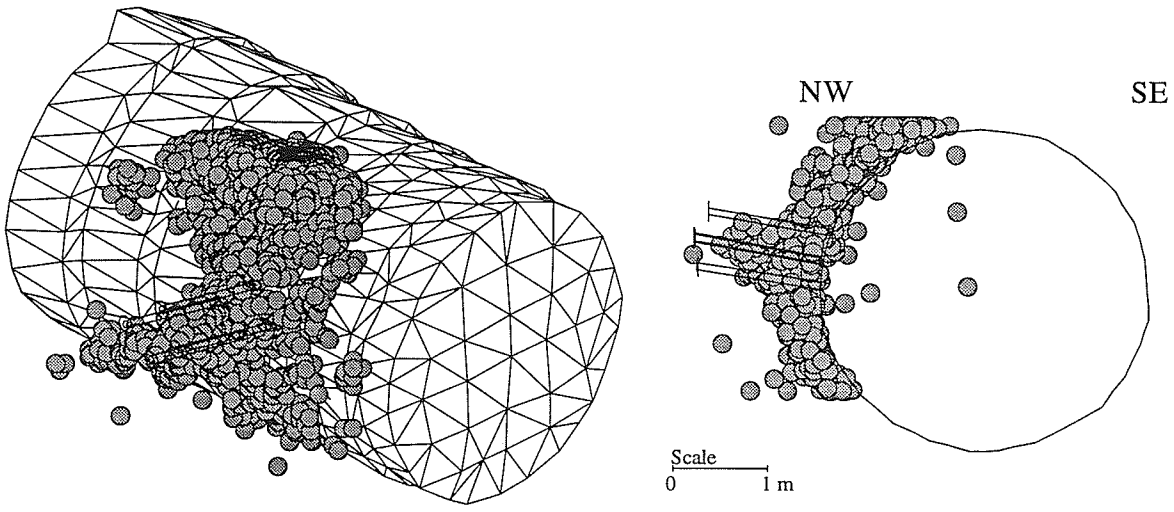

Figure 6.36: AE events in the sidewall of Room 415 (after Carlson and Young [13]).

cutoff criterion, then allowing the model to equilibrate. In this way, the zone of damaged material propagated away from the tunnel wall until equilibrium was reached. Depending on the value selected for σ_t, the final extent of the zone of extensional damage could be significantly larger than the region that initially exceeded the tension cutoff. The redistribution of stresses increased the radial displacement measured near the tunnel wall by the horizontal instruments. By incorporating a reduced shear modulus in the ubiquitous joint elements, the resulting displacement response from the model was very similar to the measured response.

Using this approach, it was found that differences in radial displacements between the two sides of the tunnel were more pronounced in the measured results than in the model results. As determined from *in situ* characterization of the test tunnel near extensometer array 2 [46], the upper SE quadrant and part of the upper NW quadrant are primarily grey granite, while the other quadrants are granodiorite (Figure 6.24). Differences have been noted in the appearance [125] and behaviour [45, 46] of granite and granodiorite from the 420 Level. The granite typically shows more visible signs of cracking along grain boundaries than the granodiorite upon stress-relief, both *in situ* and in laboratory samples. The difference in their behaviour is evident in uniaxial testing of samples from the 420 Level. Compared to samples taken from lower stress domains, samples of granite show a marked reduction in compressive strength, but samples of granodiorite do not.

Lajtai et al. [110] noted that in tension, stresses at fracture nucleation and failure are assumed identical. Although tensile testing was not conducted on samples of granodiorite from the 420 Level, the Hoek-Brown envelope for crack initiation (σ_{ci}), start of unstable crack growth (σ_{cd}), and the peak strength (σ_c) summarized in Chapter 3 predict that the tensile strength is between 8 and 11 MPa. The crack damage stress for granite in tension was measured as 7.4 MPa from Brazilian tests, and as low as 1.5 MPa from direct tension tests on damaged samples from the 420 Level of the URL [125]. The results in Chapter 3 predict values as low as 5.5 MPa.

The elastic/ubiquitous joint model was modified to account for the two material types in the vicinity of the second extensometer array. A sensitivity study was then conducted, considering different tensile cutoff stresses and reduced shear moduli for the two rock types. As shown in Figure 6.37, reasonable agreement with the measured radial displacement response was obtained when tensile cutoff stresses of 6 and 11 MPa, and reduced shear moduli of 5 and 10 GPa, were used respectively for granite and granodiorite. The values of shear moduli represent reductions of 81 and 62% for granite and granodiorite, respectively. The extent of the zone of extensional damage is shown in Figure 6.38.

While this modeling approach appears to capture some of the mechanistic features observed *in situ*, it has several limitations. The most significant of these is that a tension cutoff in FLAC implies that, once a stress component falls below the tensile limit, it is cut to zero and cannot be tensile from that point on. In reality, the reduction in tensile strength related to the development of induced anisotropy as directional cracking along grain boundaries is directly related to the amount of damage sustained by the material [125]. Because the cracking is at the grain scale [13], and the cracks are not necessarily connected, damaged material would still be able to sustain tensile loading, albeit at a reduced level. The tensile limit of the material would therefore increase towards the boundary of the tensile region, and, consequently, the stress redistribution *in situ* would be less extensive than suggested by the model. Nevertheless, the model illustrates that stress redistribution and a reduction in shear modulus resulting from induced cracking in the tensile region can account for the difference between the measured and modeled radial displacement responses.

6.7 Summary

In this chapter, numerical modeling and *in situ* characterization were undertaken to establish the relationship between displacements, excavation damage, and the material behaviour near the tunnel periphery. A review of the work by Martin [125] showed that induced damage ahead of the tunnel face accounts for a reduction in the strength of the rock mass

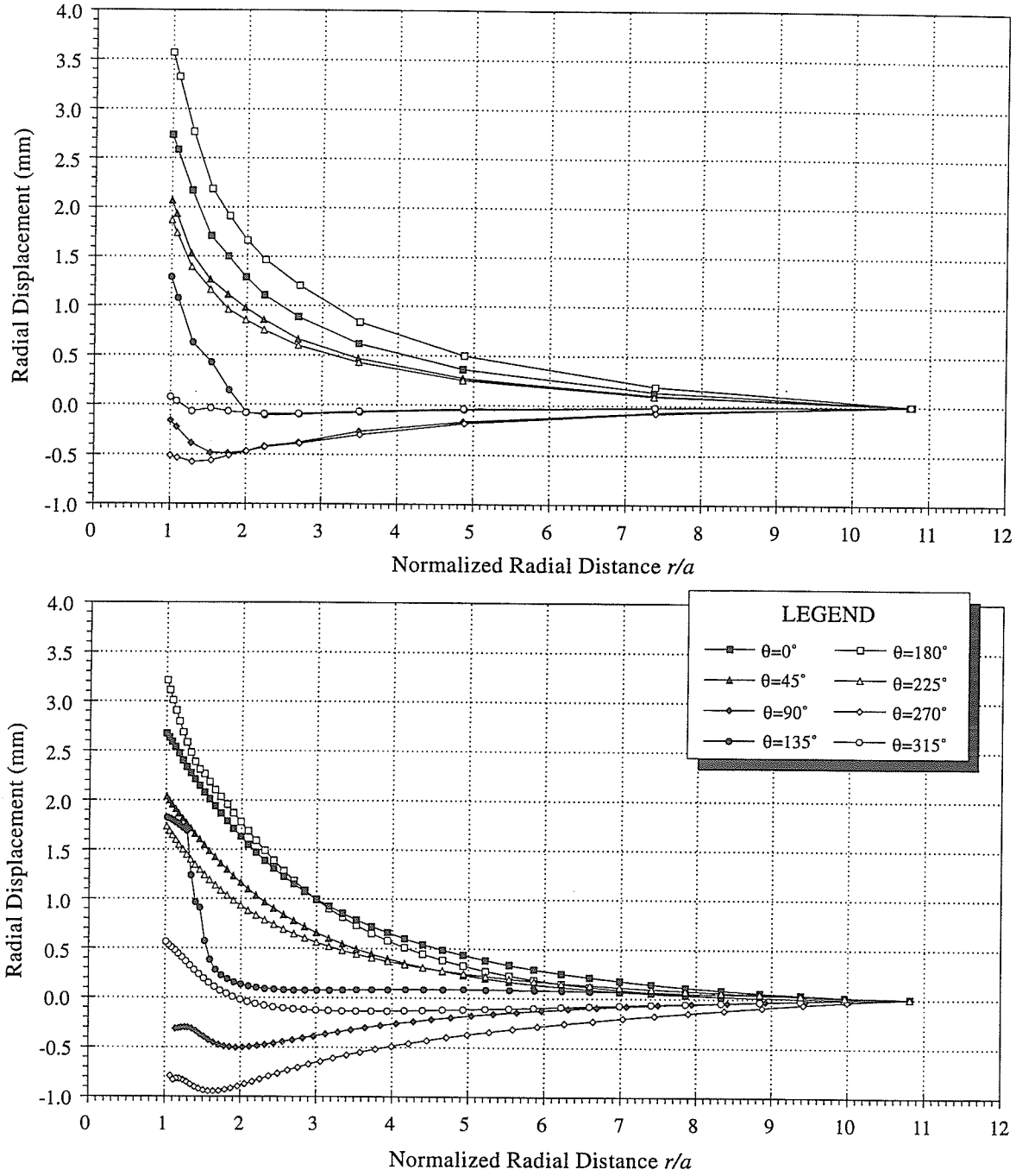

Figure 6.37: Radial displacement responses from the tension cutoff model (bottom) compared to measured results from extensometer array 2 (top).

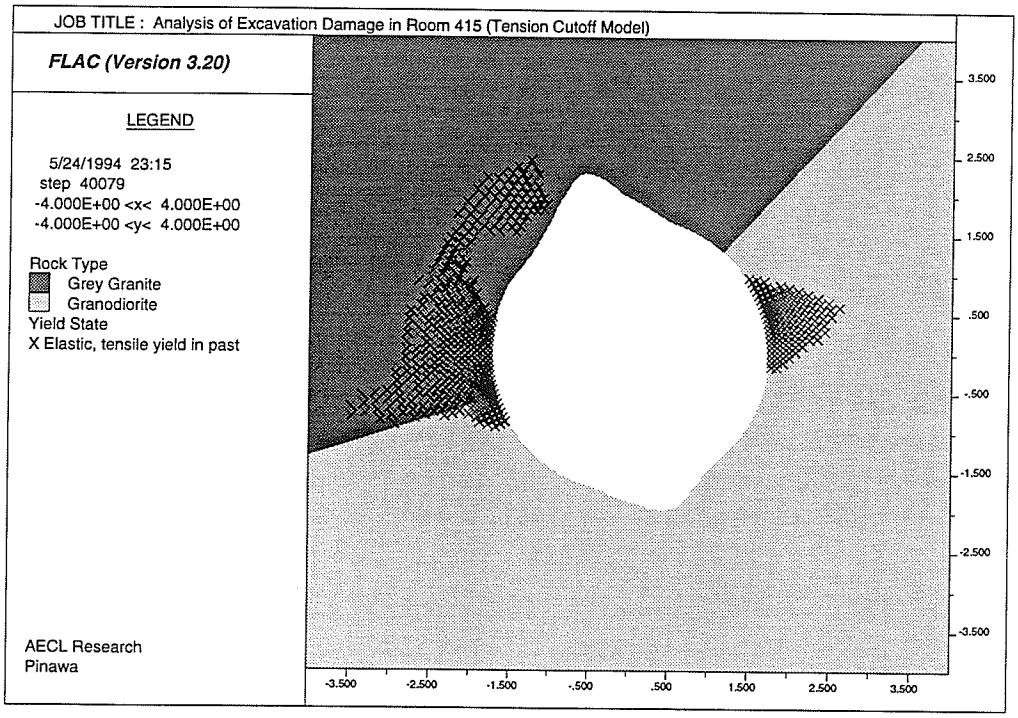

Figure 6.38: Extent of the zone of extensional damage in the tension cutoff model. Because of limitations in the model, the extent of the damaged region is overestimated.

near the tunnel. It was determined that the crack initiation threshold near the face is related to the maximum deviatoric stress. For granite, this threshold is about 73 MPa, and for granodiorite it is about 100 MPa.

Petrographic and petrofabric analysis showed that the granite and granodiorite from the 420 Level have similar compositions, but differ in their grain size and structure. The granite is coarsely crystalline and inequigranular, while the granodiorite is finer-grained and equigranular. The difference in their petrofabric accounts for the higher crack initiation threshold in granodiorite, and results in less damage and less pronounced breakouts in the granodiorite *in situ* compared to the granite. Similar observations were made regarding the crack initiation threshold in tension for the two rock types.

By considering a uniaxial stress component aligned with the tunnel axis, it was demonstrated that stress rotation near the tunnel face induces antiplane shear stress concentrations. In conditions where the tunnel axis is not coincident with a principal stress direction, the combination of far-field antiplane shear stress components and those induced near the face result in an asymmetric distribution of antiplane shear stresses near the face. This asymmetric pattern was evident in plots of maximum deviatoric stress and radial displacement versus rotation angle. Using these types of plots, it was shown that the *in situ* stress tensor estimated in Chapter 5 produced maximum deviatoric stress and radial displacement patterns consistent with the observed asymmetric breakouts in the Room 405 borehole, and those in the test tunnel. In particular, the relative magnitudes and positions of the minima in the radial displacement response versus rotation angle plots reflected the position and intensity of breakouts.

In situ characterization of the extent of damage around the test tunnel showed that zones of intense fracturing exist up to about 240 mm beyond the tips of the breakout notches in Room 415. This damage dies out on the flanks of the notch within 1 m of the notch tip. Numerical modeling showed that the damage in these areas only slightly affects the radial displacement response, but stabilizes the notch area by forcing the maximum

stress concentration away from the tunnel wall into the rock mass where confining stresses are high enough to prevent further progressive failure.

Comparison of radial displacement responses from cylindrical models of Room 415 with and without a notched geometry showed negligible difference for positions in the anterior domain, i.e., $X/D \leq 0$. In addition, the measured displacement responses in this region compared closely to those predicted by elastic theory using the estimated *in situ* stress tensor. In the posterior domain, the notched geometry had the effect of increasing the convergence in the sidewalls of the tunnel, but did not significantly affect the divergence in the roof. In both cases, the patterns of maximum deviatoric stress and radial displacements near the face were consistent with the observed breakouts in Room 415.

In comparing the measured and predicted radial displacement responses for a tunnel profile typical of regions with pronounced breakouts, it was shown that the measured displacements exceeded those predicted in the horizontal and 135° directions within a radius of the tunnel wall. A numerical modeling study of material behaviour in the posterior domain showed that stress redistribution and material softening resulting from induced cracking in the tensile region around Room 415 could account for the difference between the two responses. Tensile strength and reduction in shear modulus resulting from induced damage were found to depend on lithology, and differences in the measured radial displacement responses for opposite sides of the tunnel were attributed to variations in lithology.

Chapter 7

Summary and Conclusions

This thesis was undertaken to investigate the hypothesis that, in an unjointed, highly stressed, brittle rock mass that has sustained significant damage through excavation-induced stress redistribution, it is possible to use displacements measured near the face of a cylindrical tunnel to determine the *in situ* stress tensor, and the extent and characteristics of the excavation-induced damage around the tunnel. Using AECL's Mine-by Experiment as the field study, both objectives were achieved.

7.1 The *In Situ* Stress Tensor

As a result of the highly stressed condition of the rock mass, standard stress measurement techniques were unsuccessful in estimating the complete *in situ* stress tensor at the 420 Level of the Underground Research Laboratory, the field study location for the thesis. The initial estimate of the tensor prior to the field study was a composite of partial results from different techniques. The composite nature of the estimate, however, precluded the use of rigorous statistical methods in determining the mean value and confidence intervals of each of the stress components, and their respective orientations. Consequently, a new method for interpreting stresses from field measurements was required. To this end, functional relationships between the components of the stress tensor and the radial displacement response within the region $-1 \leq X/D \leq 1$ were developed, both for the radial displacement response

versus normalized face position and versus radial distance, and were incorporated into a back analysis method.

The *spliced logistic function* was developed as an approximating function for the radial displacement response versus face position, and it was shown that this type of function could be used to develop general parametric equations for radial displacement at the tunnel wall for all face positions and rotation angles. It was found that the radial displacement response at the tunnel wall can be considered the result of superposition of six *characteristic radial displacement surfaces*, each described by a combination of *spliced logistic functions.* Of these, there are only three unique surfaces, the others being surfaces of the same shape, but with a phase shift associated with them.

Using the same developmental approach, a general approximating function comprising an inverse polynomial series was developed to describe the radial displacement response versus radial distance. This approximating function was, in turn, used to develop general parametric equations describing the relationship between the components of the stress tensor and the radial displacement response versus radial distance for all rotation angles at five axial positions in the tunnel. These equations represent *characteristic radial displacement surfaces* in the $r - \theta$ plane.

Having developed the equations relating the various stress components and their corresponding radial displacement responses, it was shown that a least-squares technique can be used to back calculate the *in situ* stress tensor from measurements of radial displacement in the region $-1 \leq X/D \leq 1$. The method incorporated the parametric equations for measurements taken at the wall, and at increasing radial distance from it, in both the anterior and posterior domains. Using simulated measurements from a numerical model, it was demonstrated that these different types of measurements can be combined to accurately estimate the six components of the stress tensor. The best estimate was obtained when measurements from both the anterior and posterior domains were used, as this tended to

constrain the estimate of the antiplane normal stress component. Nevertheless, good estimates were obtained even when only one type of measurement was used, although anterior measurements produced better results than posterior measurements. Convergence measurements, however, were found to be independent of the antiplane shear components, and therefore required additional measurements of other types to estimate the complete stress tensor. It was also demonstrated that constraint equations could be added to the analysis if additional information regarding the relative magnitudes of the stress components were known. The model simulation clearly showed that radial displacement measurements from the region $-1 \leq X/D \leq 1$ produce accurate estimates of the *in situ* stress tensor providing the rock mass ahead of the face can be considered a homogeneous, linear elastic medium. The estimate can be improved if measurements from portions of the tunnel in the posterior domain unaffected by excavation damage are included in the analysis.

Following development of the back analysis technique, a methodology was established to standardize field measurements of radial displacement in an enhanced dataset, where the values of displacement at specific axial positions were interpolated, and the amount of displacement missed by each instrument was estimated. To illustrate the process, it was applied to results from the field study. It was found that a two-part interpolation method, considering the anterior and posterior domains separately, produced near-perfect matches between the measured displacements and combinations of *spliced logistic functions*. From numerical modeling, an extrapolation procedure, based on an inverse polynomial series function, was also developed to account for displacements occurring beyond the outermost extensometer anchors. It was found that these missed displacements could be a significant proportion of the measured response. Displacements missed ahead of the tunnel face, in contrast, were found to be negligible if the first measurement was taken approximately three tunnel diameters ahead of the face.

As part of the analysis of measurements from the field study, results from extensometers were compared directly to those from convergence arrays. It was found that the two

measurement types produced consistent results, but that convergence measurements were, by their nature, unaffected by antiplane shear components of the stress tensor. Consequently, plots of convergence versus rotation angle have symmetric maxima and minima for $0 \leq \theta \leq 360°$. Extensometer results, on the other hand, were shown to be sensitive to antiplane shear stresses near the tunnel face, resulting in asymmetry in the magnitude and angular positions of the maxima and minima of the radial displacement response versus rotation angle for $0 \leq \theta \leq 360°$. Contrary to previous publications, the amount of radial displacement occurring ahead of the advancing tunnel face is a constant 31% only in the case of a flat face under conditions of zero antiplane stress components. For the general case, the proportion varies with the shape of the tunnel face, and the magnitude of the antiplane components of the stress tensor.

Once the field data from the Mine-by Experiment were standardized, back analysis of the *in situ* stress tensor was conducted. Because of the large number of measurements, data were grouped systematically by measurement type, and incremental predictions of the *in situ* stress tensor were made. Using plots of stress invariants as an indicator of the reliability of the individual estimates, the most reliable data from the different measurement types were combined to refine the stress predictions. The best estimate of the tensor was based on data from three different types of measurements.

Based on results from the stress back analysis described in this thesis, the estimated stress tensor at the 420 Level of the URL is similar, but not identical, to composite tensor estimated prior to the field study. In particular, the orientations of the principal stresses indicate that antiplane shear stress components are an important aspect of the stress tensor, i.e., the test tunnel is not aligned with a principal stress direction. In terms of magnitudes, the only principal component that falls outside the estimated confidence intervals on the composite estimate is σ_3. However, it was shown that the vertical component of the estimated stress tensor compares closely with the lithostatic stress calculated for the 420 Level. In addition, the estimated tensor was shown to be consistent with observed shearing on

Fracture Zone 2, and observations of asymmetric breakouts in the Room 405 borehole and in the test tunnel. In terms of principal stresses, the best estimate of the tensor is

σ_1			σ_2			σ_3		
MPa	Trend	Plunge	MPa	Trend	Plunge	MPa	Trend	Plunge
59.93	145.41	11.08	44.29	53.89	7.70	9.43	289.76	76.45

From comparison of the predicted and measured displacement responses in the anterior domain, the initial estimates of E (65 GPa) and ν (0.25) were found to be satisfactory.

7.2 Characterization of Excavation Damage

Having determined a reliable estimate of all six components of the stress tensor, numerical modeling and *in situ* characterization were undertaken to investigate the extent and characteristics of excavation-induced damage around the test tunnel. The relationship between the measured radial displacement response and the development of damage was investigated using observations of borehole breakouts in a vertical 1.24-m diameter borehole in Room 405, and in the test tunnel. It was shown that conditions where the tunnel or borehole axis is not parallel to a principal stress direction can result in asymmetric breakout patterns. In these conditions, the far-field antiplane shear stresses distort the shear stress (or deviatoric stress) pattern ahead of the face, causing an increase in magnitude on one side of the tunnel, and a decrease on the other. This effect also causes a shift in the rotational position of the maximum deviatoric stress concentration ahead of the face. It was shown that this pattern of asymmetry is evident in the radial displacement response, characterized by asymmetry of the maxima and minima, both in terms of magnitude and rotational position, for $0 \leq \theta \leq 360°$. The minima in the radial displacement response correspond to the locations of maximum deviatoric stress concentration, and were shown to match the locations of breakouts in the test tunnel. The minimum point showing the largest positive distortion in magnitude as a result of the antiplane shear stresses corresponds to the point

of highest maximum deviatoric stress concentration, and consequently represents the region where most damage is incurred during tunnel advance. In both Room 405 and the test tunnel, this minimum point corresponded with the most pronounced breakout.

Field characterization was conducted using a series of trenches, slots and boreholes to determine the extent of observable damage beyond the stable tunnel profile in Room 415. Highly fractured zones were discovered near the apex of each breakout, extending approximately 180 mm into the rock mass in the roof, and 240 mm into the floor. These zones were localized within 1 m of the notch tip. Observations showed that breakouts in the slots and boreholes started at the outer boundary of the highly fractured zone, indicating that the rock outside the damaged zone was intact and highly stressed, and that the damaged material had undergone a reduction in modulus. This finding is consistent with modeling results showing that the damaged material forces the maximum tangential stress concentration into the rock mass where confining stresses develop to prevent further failure.

Using the estimated stress tensor, the displacement patterns predicted from linear elastic models were compared to the measured field results at different locations in the test tunnel. It was found that the results in the anterior domain, and at the tunnel face, compared closely, with the model predictions falling within the 99% confidence (prediction) intervals for the measured data. In the posterior domain, however, it was found that past $X/D = 0.1$, the results from numerical modeling underestimated the magnitude of convergence observed in the sidewalls, even when the damage beyond the notch tip was taken into account. It was concluded that, in areas of the posterior domain exhibiting large-scale excavation-damage, the rock mass behaves non-linearly within about a radius of the tunnel wall in regions where one or more components of the near-field stress tensor are tensile. A series of model studies using FLAC illustrated that stress redistribution and a reduction in shear modulus resulting from induced cracking in the tensile region around Room 415 can account for the difference between the measured radial displacement response and that predicted by linear elasticity.

The tensile crack initiation threshold and reduction in shear modulus resulting from induced damage were found to depend on lithology, with granodiorite being less susceptible to induced damage than granite at the 420 Level. Differences in the radial displacement responses on opposite sides of the tunnel in the posterior domain were attributed, in part, to variations in lithology.

7.3 Factors affecting Displacement Responses

The main factors that were identified in the course of this thesis that affect the displacement response around a tunnel in highly stressed granite are as follows:

- Face shape - the shape of the face affects the definition of the zero reference position, the shape of the displacement responses, and the amount of displacement occurring in the anterior domain. A correction methodology for the zero reference position was developed for faces with $d/D < 0.1$.

- Longitudinal geometry - a stepped tunnel geometry in the longitudinal direction was found to reduce the magnitude of the radial displacement response in the posterior domain, effectively reducing the radius of the tunnel. However, the effect was negligible in the anterior domain. Variations in the response within a given excavation round for a stepped tunnel were also noted within 0.5 radii of the wall. A relationship between the maximum and minimum radii, and the effective radius was developed.

- Geology - differences in the grain size and structure of the granite and granodiorite at the 420 Level of the URL resulted in significant differences in their *in situ* behaviour. In particular, regions of granodiorite exhibited a higher crack initiation threshold in both compression and tension, which resulted in less damage and less pronounced breakouts in these areas compared to regions of granite.

- Antiplane stress components - antiplane components of stress were shown to produce asymmetric radial displacement and maximum deviatoric stress responses versus rotation angle. The antiplane normal component was also shown to significantly affect the shape of the displacement response, and the proportion of the response occurring in the anterior domain.

- Progressive failure - the development of pronounced breakout notches in the test tunnel exaggerated the difference between the maximum and minimum radial displacements. Time-dependent behaviour associated with the progressive failure process also resulted in increased scatter in convergence data measured near the tunnel face.

- Material behaviour - a departure from linear elastic material behaviour in the posterior domain produced significantly more radial displacement within one radius of the tunnel than would be predicted by linear elasticity. Material behaviour ahead of the tunnel face, however, was shown to be linear elastic, and therefore suitable for application of the stress back analysis technique.

7.4 Applicability of Findings

Although the field study for this thesis is unusual in terms of the level of instrumentation and the fact that the instruments were installed in the anterior domain, similar experiments have been undertaken elsewhere [73]. In addition, because the Mine-by Experiment was conducted, in part, to assess its usefulness as a large-scale characterization test in the Canadian concept for nuclear fuel waste disposal, there is the possibility of similar tests in the future. Consequently, the analysis techniques developed in this thesis may be directly applicable to other studies. An important aspect of any such experiment in highly stressed rock, however, is the installation of instruments in the anterior domain.

In a specific context, the estimate of stresses and the extent of excavation damage around the test tunnel are important contributions to the understanding of rock mass behaviour

at the 420 Level of the URL, and sites in similar geological and stress conditions. The findings show that interpretation of convergence measurements are subject to much more uncertainty than was previously recognized, particularly in conditions where the tunnel is not aligned with a principal stress direction, and the antiplane components of the stress tensor are significant. It was observed in the course of the field study that significant differences in the failure characteristics of different rock types may not be obvious from laboratory testing. As shown in the field study, petrofabric i.e., grain size and structure, can affect the crack initiation threshold of a material, and is consequently an important consideration in the design and interpretation of similar experiments. The findings also show that, although the zones of maximum tangential stress around the tunnel experience the most dramatic development of damage, excavation-induced damage is also evident at a smaller scale in other regions around the tunnel, particularly in zones of tension in the sidewalls of the test tunnel.

7.4.1 Practical implications

In most practical situations, it is not possible to achieve the quantity or quality of data that was obtained from the field study. Nonetheless, there are some specific findings from the field study that are applicable to practical tunneling situations.

In terms of *in situ* stress determination, high resolution instruments such as the borehole fracture monitor extensometers (Bof-exs) used for the Mine-by Experiment are essential in hard brittle rock masses. Ahead of the tunnel face, radial displacements may be only a fraction of a millimetre, requiring instruments with a resolution of better than 10 μm. For softer rock masses with potentially larger displacements, other types of extensometers, i.e., sonic probe or rod extensometers, may provide adequate resolution. Eight radially-oriented extensometers installed in the anterior domain are recommended if the measured displacements are to be used in the back analysis technique. These instruments should be installed greater than three tunnel diameters ahead of the tunnel face, and should be

continuously datalogged to obtain as many data points as possible as the face is advanced. The tunnel should be excavated using either a continuous mining method, e.g., a tunnel boring machine (TBM), or a non-explosive step-wise method, such as that described in Chapter 3, employing 0.5-m-long excavation rounds. Although much more costly than other methods, the advantages of using a TBM are a near-perfect cylindrical geometry, a uniformly flat face, and continuous advance of the tunnel. For non-circular tunnels, radial displacements induced by advancing a circular pilot tunnel can be used to back analyze the *in situ* stress tensor.

In strictly elastic ground, three orthogonal tunnels instrumented with convergence arrays can also provide an estimate of the complete *in situ* stress tensor provided the correct parametric functions are used in the back analysis to account for the effect of the axial stress component. These arrays should contain a minimum of six diametral measurement lines, and should be installed as close as possible to the tunnel face using a template to ensure the measurement plane is orthogonal to the tunnel axis. As shown in the field study, posterior measurements of this type cannot be used to back analyze *in situ* stresses if there is evidence of excavation-induced damage or non-linear behaviour in the region of the tunnel where the measurements are taken.

Instrument placement is a major consideration in using this technique, both in terms of surveying accuracy and the high cost of excavating access and instrumentation galleries to install instruments in the anterior domain. For a typical civil engineering tunnel, if the depth of rock cover is less than about 25 m, long instrumentation boreholes could be drilled from surface into the anterior domain ahead of the tunnel face. These boreholes would intersect the design centreline ahead of the tunnel, and extend approximately 25 m beyond the intersection point. Using four such boreholes inclined at different angles in the plane orthogonal to the tunnel axis, eight extensometer strings could be installed, two per borehole on opposite sides of the design centreline. This array would provide radial displacement measurements as the face approached the instruments, but would, by virtue of

the wiring arrangement, require removal prior to being intersected by the advancing tunnel. Hole alignment could be verified once the tunnel had advanced past the array location, exposing the ends of the instrumentation boreholes. In a multi-level mining operation, access development costs could be eliminated by using different production levels to provide drilling access for instrumentation boreholes. If designed properly, the experiment could be incorporated into the overall mine development plan.

Aside from the radial instruments considered in the field study, the tangential and axial displacement responses described in Chapter 4 also have characteristic shapes. Axial or tangential instruments might therefore provide additional information that could be used to characterize damage around a tunnel. In particular, they might help to verify the mechanisms responsible for non-linear behaviour in the posterior domain. However, because the interpretation of tangential and axial displacements was not considered in detail, specific recommendations for these types of instruments are beyond the scope of this thesis.

7.5 Recommendations for Future Research

Several areas of additional research were identified in the course of this thesis. For example, the relationship between displacement gradients and progressive failure was touched on in Chapter 6, but was not explored in detail. Further investigation of this relationship might provide a better understanding of the mechanics of failure around underground openings.

In addition, the behaviour of the granite and granodiorite under conditions where one or more of the applied stresses are tensile was found from numerical modeling to affect the observed displacement responses measured in the sidewalls of the test tunnel. Laboratory tests on the different rock types to refine the estimates of the crack initiation threshold under these types of stress conditions, and the resulting changes in the material properties of the samples, would help characterize the damage in the tensile regions around the tunnel.

It was also noted in the model study of excavation damage in the posterior domain that the numerical models used in the investigation had several limitations. Alternate

methods or models might be better suited for simulating the mechanics of excavation damage development in these regions. Specifically, a general constitutive model that captures all of the observed elements associated with both large- and small-scale excavation-induced damage has not been developed.

Finally, to make the stress determination approach more applicable as a field characterization tool, the parametric equations for the radial displacement response could be expanded to incorporate the axial displacement response. In this way, boreholes could be drilled at 45° to the tunnel axis in the $r - z$ plane from the wall of a large drift, and a large-diameter borehole could be drilled through the centre of the instrument array. This approach would eliminate the need for access drifts to drill the boreholes, and could be done on a smaller scale than the Mine-by Experiment. However, because of the reduced scale of the test, the location and resolution of instrumentation would be of paramount importance to interpreting the results. Nevertheless, this modified approach might prove valuable in characterizing highly stressed, brittle rock masses where standard stress measurement techniques cannot be applied.

Bibliography

[1] W. A. Amberg and G. Lombardi. Une méthode de calcul elasto-plastique de l'état de tension et de déformation autour d'une cavité souterraine. In *Advances in Rock Mechanics, Proc. Third Congress of the Int. Soc. for Rock Mech., Vol. 2, Part B*, pages 1055–1060, 1974.

[2] A. R. Atkins and M. Keen. The measurement of rock deformation about excavations in hard rock mining. In *Proc. South African National Group on Rock Mechanics (ISRM), Monitoring for Safety in Geotechnical Engineering*, pages 47–53, 1984.

[3] G. Barla. A method for the analysis of stress in brittle rock. *Int. J. Rock Mech. Min. Sci.*, 9(1):87–102, 1972.

[4] J. P. Barlow. Interpretation of tunnel convergence measurements. Master's thesis, Department of Civil Engineering, University of Alberta, Edmonton, AB, 1986.

[5] J. P. Barlow and P. K. Kaiser. Interpretation of tunnel convergence measurements. In *Proc. 6th Int. Congress on Rock Mech., Vol. 2, Montreal*, pages 787–792, 1987.

[6] Z. T. Bieniawski. Mechanisms of rock fracture in compression. Technical report, CSIR Report MEG 459, Pretoria, South Africa, 1966.

[7] Z. T. Bieniawski. Stable and unstable fracture propagation in rock. Technical report, CSIR Report MEG 493, Pretoria, South Africa, 1966.

[8] B. H. G. Brady and E. T. Brown. *Rock Mechanics for underground mining.* George Allen and Unwin, London, 1985.

[9] J. W. Bray. A study of jointed and fractured rock. Part II - Theory of limiting equilibrium. *Rock Mechanics and Engineering Geology*, 5(4):197–216, 1967.

[10] A. Brown, N. M. Soonawala, R. A. Everitt, and D. C. Kamineni. Geology and geophysics of the Underground Research Laboratory site, Lac du Bonnet Batholith, Manitoba. *Can. J. Earth Sci.*, 26:404–425, 1989.

[11] E. T. Brown and E. Hoek. Technical Note: Trends in relationships between measured in situ stresses and depth. *Int. J. Rock Mech. Min. Sci. & Geomech. Abstr.*, 15(4):211–215, 1978.

[12] Edwin T. Brown, John W. Bray, Branko Ladanyi, and Evert Hoek. Ground response curves for rock tunnels. *J. Geotech. Engng. Div. ASCE*, 109(1):15–39, 1983.

[13] S. R. Carlson and R. P. Young. Acoustic emission and ultrasonic velocity study of excavation-induced microcrack damage at the Underground Research Laboratory. *Int. J. Rock Mech. Min. Sci. & Geomech. Abstr.*, 30(7):901–907, 1993.

[14] T. Chan, P. Griffiths, and B. Nakka. Finite element modelling of geomechanical and hydrogeological responses to the Room 209 heading extension excavation response experiment: II. Post-excavation analysis of experimental results. Atomic Energy of Canada Limited Interim Report, 1988.

[15] T. Chan, P. A. Lang, and P. M. Thompson. Mechanical response of jointed granite during shaft sinking at the Canadian Underground Research Laboratory. In *Proc. 26th U.S. Symp. Rock Mech., Rapid City, SD*, pages 785–794, 1985. Also Atomic Energy of Canada Limited Reprint, AECL-8690.

[16] N. Chandler and D. Martin. The influence of near surface faults on in situ stresses in the Canadian Shield. In *Accepted for Proc. 1st North American Rock Mech. Symp., Austin, TX*, 1994.

[17] N. A. Chandler. Bored raise overcoring for in situ stress determination at the Underground Research Laboratory. *Int. J. Rock Mech. Min. Sci. & Geomech. Abstr.*, 30(7):989–992, 1993.

[18] T. Chow, S. D. Falls, S. R. Carlson, and R. P. Young. Ultrasonic imaging and acoustic emission monitoring of laboratory hydraulic fracturing experiments in Lac du Bonnet grey granite from AECL's Underground Research Laboratory. Contractor's Report to AECL Research, Contract No. WS-29J-54491 RP008AECL, Queen's University, 1990.

[19] D. F. Coates and Y. S. Yu. A note on stress concentrations at the end of a cylindrical hole. *Int. J. Rock Mech. Min. Sci.*, 7(6):583–588, 1970.

[20] N. G. W. Cook. The basic mechanics of rockbursts. *J. S. Afr. Inst. Min. Metall.*, 64:71–81, 1963.

[21] N. G. W. Cook. An experiment proving that dilatancy is a pervasive volumetric property of brittle rock loaded to failure. *Rock Mechanics*, 2:181–188, 1970.

[22] N. G. W. Cook, E. Hoek, J. P. G. Pretorius, W. D. Ortlepp, and M. D. G. Salamon. Rock mechanics applied to the study of rockbursts. *J. S. Afr. Inst. Min. Metall.*, 66(10):436–528, 1966.

[23] R. Corthesay and D. Gill. Doorstopper stress measurements at the 420 Level of the URL. Final Report to AECL Research, le Centre de Développement Technologique de l'École Polytechnique de Montréal, 1992.

[24] Marc S. Costantino. Statistical variation in stress-volumetric strain behaviour of Westerly granite. *Int. J. Rock Mech. Min. Sci. & Geomech. Abstr.*, 15(3):105–111, 1978.

[25] S. L. Crouch. Experimental determination of volumetric strains in failed rock. *Int. J. Rock Mech. Min. Sci.*, 7(6):589–603, 1970.

[26] Peter Cundall. *FLAC - Fast Lagrangian Analysis of Continua.* ITASCA CONSULTING GROUP, INC., 1991.

[27] J. H. Curran and B. T. Corkum. *EXAMINE^{3D} - Three-Dimensional Excavation Analysis for Mines, Version 2.0.* Data Visualization Laboratory, Department of Civil Engineering, University of Toronto, 1993.

[28] J. J. K. Daemen and C. Fairhurst. Influence of failed rock properties on tunnel stability. In *Dynamic Rock Mechanics, Proc. Twelfth Symp. on Rock Mechanics, AIME*, pages 855–875, 1971.

[29] C. C. Davison, A. Brown, and N. M. Soonawala. Preconstruction site evaluation program at the Canadian Underground Research Laboratory. In *Proc. 14th Information Meeting Nuclear Fuel Waste Management Program (1982 General Meeting)*, 1982. Also Atomic Energy of Canada Limited Technical Record, TR-207, pages 162-187*.

[30] R. V. de la Cruz and Richard E. Goodman. Theoretical basis of the borehole deepening method of absolute stress measurement. In *Rock Mechanics Theory and Practice, Proc. 11th Symp. Rock Mech., Berkeley*, pages 353–374, 1969.

[31] C. S. Desai and T. H. Wu. A general function for stress-strain curves. In *Proc. 2nd Int. Conf. Num. Meth. Geomech., ASCE, Vol. 1, Blacksburg*, pages 306–318, 1976.

[32] E. Detournay and C. Fairhurst. Two-dimensional elastoplastic analysis of a long, cylindrical cavity under non-hydrostatic loading. *Int. J. Rock Mech. Min. Sci. & Geomech. Abstr.*, 24(4):197–212, 1987.

[33] Emmanuel Detournay and Christopher M. St. John. Design charts for a deep circular tunnel under non-uniform loading. *Rock Mech. Rock Engng.*, 21:119–137, 1988.

[34] F. H. Diest. A nonlinear continuum approach to the problem of fracture zones and rockbursts. *J. S. Afr. Inst. Min. Metall.*, 65(10):502–522, 1965.

[35] T. Doe. Hydraulic-fracturing stress measurements in horizontal holes at the 240- and 420-m Levels of the Underground Research Laboratory. Consulting Report to AECL Research 893-1002, Golder Associates, 1989.

[36] H. Duddeck. On the basic requirements for applying the convergence-confinement method. *Underground Space*, 4(4):241–247, 1980.

[37] J. M. Duncan and C. Y. Chang. Nonlinear analysis of stress and strain in soils. *J. Soil Mech. Found. Div. ASCE*, 96(SM5):1629–1653, 1970.

[38] J. M. Edmond and M. S. Paterson. Volume changes during deformation of rocks at high pressures. *Int. J. Rock Mech. Min. Sci.*, 9(2):161–182, 1972.

[39] P. Egger. Gebirgsdruck im tunnelbau und stutzwirkung der ortsburst bei uberschreiten der gebirgsfestigkeit. In *Advances in Rock Mechanics, Proc. of the Third Congress of the Int. Soc. for Rock Mech., Vol. 2, Part B*, pages 1007–1011, 1974.

[40] P. Egger. Deformations at the face of the heading and determination of the rock mass. *Underground Space*, 4(5):313–318, 1980.

[41] Zdenek Eisenstein, Heinrich Heinz, and Arsenio Negro. On three-dimensional ground response to tunnelling. In *Tunnelling in Soil and Rock, Proc. Two Sessions at GEOTECH '84, ASCE, New York, NY*, pages 107–127, 1984.

[42] D. J. Curtis et al. In situ ground and lining studies for the Channel tunnel project. In *Proc. Symp. Tunnelling '76, London*, 1976.

[43] R. A. Everitt and A. Brown. Subsurface geology of the Underground Research Laboratory: An overview of recent developments. In *Proc. 20th Information Meeting Can. Nuclear Fuel Waste Management Program (1985 General Meeting), Vol. 1*, pages 146–181, 1986. Also Atomic Energy of Canada Limited Technical Record, TR-375* .

[44] R. A. Everitt, A. Brown, C. C. Davison, M. Gascoyne, and C. D. Martin. Regional and local setting of the Underground Research Laboratory. In R.S. Sinha, editor, *Proc. Int. Symp. on Unique Underground Structures, Vol. 2, Denver, Colorado*, pages 64:1–23. CSM Press, Denver, 1990.

[45] R. A. Everitt, P. Chernis, D. Good, and A. Grogan. Mapping of the excavation damage zone around the circular access shaft at Atomic Energy of Canada Limited's Underground Research Laboratory. In *Excavation Response in Geological Repositories for Radioactive Waste, Proc. NEA Workshop, Winnipeg, MB, 1988 April*, pages 271–282, 1989.

[46] R. A. Everitt, P. Gann, and D. M. Boychuk. Mine-by Experiment data summary: Part 7 - Geological setting and general geology. Report RC-1080, Atomic Energy of Canada Limited, 1993.

[47] R. A. Everitt, D. Woodcock, P. Gann, and D. Robinson. Geology of the 420 Level of the Underground Research Laboratory. Technical Record TR-529*, Atomic Energy of Canada Limited, 1990.

[48] R. T. Ewy and N. G. W. Cook. Deformation and fracture around cylindrical openings in rock - I. Observations and analysis of deformations. *Int. J. Rock Mech. Min. Sci. & Geomech. Abstr.*, 27(5):387–407, 1990.

[49] R. T. Ewy and N. G. W. Cook. Deformation and fracture around cylindrical openings in rock - II. Initiation, growth and interaction of fractures. *Int. J. Rock Mech. Min. Sci. & Geomech. Abstr.*, 27(5):409–427, 1990.

[50] C. Fairhurst. On the validity of the Brazilian test for brittle materials. *Int. J. Rock Mech. Min. Sci.*, 1(1):535–546, 1964.

[51] B. Feignier and R. P. Young. Moment tensor inversion of induced microseismic events: evidence of non-shear failures in the $-4 < M < -2$ moment magnitude range. *Geophys. Res. Lett.*, 19:1503–1506, 1993.

[52] R. Fenner. Untersuchungen zur erkenntnis des gebirgsdruckes. *Glückauf*, 74:681–695 and 705–715, 1938.

[53] L. N. G. Filon. On antiplane stress in an elastic solid. *Proc. R. Soc. London*, A160:137–154, 1937.

[54] A. L. Florence and L. E. Schwer. Axisymmetric solution of a Mohr-Coulomb medium around a circular hole. *Int. J. Num. Anal. Meth. Geomech.*, 2(4):367–379, 1978.

[55] Y. C. Fung. *Foundations of solid mechanics.* Prentice-Hall, NJ, 1965.

[56] E. M. Galle and J. C. Wilhoit. Stresses around a wellbore due to internal pressure and unequal principal geostatic stresses. *Soc. Pet. Engng. J.*, 2(2):145–155, 1962.

[57] P. Gesta, J. Kerisel, P. Londe, and M. Panet. Tunnel stability by convergence-confinement method. *Underground Space*, 4(4):225–232, 1980.

[58] J. Ghaboussi and G. Gioda. On the time dependent effects in advancing tunnels. *Int. J. Num. Anal. Meth. Geomech.*, 1:249–269, 1977.

[59] Richard E. Goodman. *Introduction to rock mechanics.* John Wiley and Sons, NY, 1989.

[60] Murray W. Grabinsky and John H. Curran. Harmonic finite element analysis of a cylindrical excavation in an infinite medium. Contractor's Report to AECL Research, Contract No. W108113 Publication 93-02, Rock Engineering Group, Department of Civil Engineering, University of Toronto, 1993.

[61] A. Guenot, M. Panet, and J. Sulem. New aspect in tunnel closure interpretation. In *Proc. 26th U.S. Symp. Rock Mech., Rapid City, SD*, pages 455–460, 1985.

[62] B. Haimson, M. Lee, N. Chandler, and D. Martin. Estimating the state of stress from subhorizontal hydraulic fractures at the Underground Research Laboratory, Manitoba. *Int. J. Rock Mech. Min. Sci. & Geomech. Abstr.*, 30(7):959–964, 1993.

[63] B. C. Haimson and C. G. Herrick. In situ stress evaluation from borehole breakout experimental studies. In *Proc. 26th U.S. Symp. Rock Mech., Rapid City, SD*, pages 1207–1218, 1985.

[64] E. A. Hanafy and J. J. Emery. Advancing face simulation of tunnel excavations and lining placement. In *Proc. 2nd Int. Conf. on Ground Movements and Structures, Cardiff, Wales*, pages 377–394, 1981.

[65] E. A. Hanafy and J. J. Emery. Three-dimensional simulation of tunnel excavation in squeezing ground. In *Proc. 4th Int. Conf. on Numerical Methods in Geomechanics, Vol. 3, Edmonton*, pages 1203–1209, 1982.

[66] J. G. Hayles, M. H. Serzu, G. Lodha, P. Street, and D. T. Stedner. Seismic velocity studies for the Mine-by Experiment. Technical report, Atomic Energy of Canada Limited, 1994.

[67] A. J. Hendron and A. K. Aiyer. Stresses and strains around a cylindrical tunnel in an elasto- plastic material with dilatancy. Technical Report 10, Missouri River Division, U.S. Corps of Engineers, Omaha, 1972.

[68] G. Herget. Variation of rock stresses with depth at a Canadian iron mine. *Int. J. Rock Mech. Min. Sci.*, 10(1):37–51, 1973.

[69] G. Herget. Regional stresses in the Canadian Shield. In *Proc. 13th Can. Rock Mech. Symp. (The H.R. Rice Memorial Symposium), CIM Special Volume 22*, pages 9–16. Can. Inst. Min. Metall., 1980.

[70] G. Herget. *Stresses in rock.* A. A. Balkema, Rotterdam, 1988.

[71] G. Herget and B. Arjang. Update on ground stresses in the Canadian Shield. In *Proc. Specialty Conference: Stresses in Underground Structures, Ottawa*, pages 33–47, 1990.

[72] F. E. Heuzé. Sources of errors in rock mechanics field measurements, and related solutions. *Int. J. Rock Mech. Min. Sci.*, 8(4):297–310, 1971.

[73] F. E. Heuzé, W. C. Patrick, T. R. Butkovich, J. C. Peterson, R. V. de la Cruz, and C. F. Voss. Rock mechanics studies of mining in the Climax granite. *Int. J. Rock Mech. Min. Sci. & Geomech. Abstr.*, 19(4):167–183, 1982.

[74] Y. Hiramatsu and Y. Oka. Determination of the stresses in rock unaffected by boreholes or drifts, from measured strains or deformations. *Int. J. Rock Mech. Min. Sci.*, 5(4):337–353, 1968.

[75] D. W. Hobbs. A study of the behaviour of broken rock under triaxial compression and its application to mine roadways. *Int. J. Rock Mech. Min. Sci.*, 3:11–43, 1966.

[76] G. Hocking. Three-dimensional elastic stress distribution around the flat end of a cylindrical cavity. *Int. J. Rock Mech. Min. Sci. & Geomech. Abstr.*, 13(12):331–337, 1976.

[77] E. Hoek and E. T. Brown. Empirical strength criteria for rock masses. *J. Geotech. Engng. Div. ASCE*, 106(GT9):1013–1035, 1980.

[78] E. Hoek and E. T. Brown. *Underground excavations in rock.* Inst. Min. Metall., London, 1980.

[79] E. R. Hoskins. An investigation of strain rosette relief methods of measuring rock stress. *Int. J. Rock Mech. Min. Sci.*, 4(2):155–164, 1967.

[80] E. R. Hoskins. Strain rosette relief measurements in hemispherically ended boreholes. *Int. J. Rock Mech. Min. Sci.*, 5(6):551–559, 1968.

[81] R. Jackson, J. S. O. Lau, and A. Annor. Mechanical, thermo-mechanical and joint properties of rock samples from the site of AECL,s Underground Research Laboratory, Lac du Bonnet, Manitoba. In *Proc. 42nd Canadian Geotechnical Conference, Winnipeg, MB*, pages 41–49, 1989.

[82] Jandel Scientific, 2591 Kerner Blvd., San Rafael, CA 94901. *TableCurve Windows v1.0*, 1992.

[83] P. K. Kaiser. Effect of stress-history on the deformation behaviour of underground openings. In *Underground Rock Engineering: Proc. 13th Canadian Rock Mech. Symp., Montreal*, pages 133–140, 1980.

[84] P. K. Kaiser. A new concept to evaluate tunnel performance - influence of excavation procedure. In *Rock Mechanics from Research to Application, Proc. 22nd U.S. Symp. on Rock Mech., Cambridge*, pages 284–291, 1981.

[85] P. K. Kaiser, D. H. Chan, D. Tannant, F. Pelli, and C. Neville. Numerical simulation of Room 209 instrument ring. Interim Technical Report to Atomic Energy of Canada Limited for Research Period August 1986 to April 1987, University of Alberta, 1987.

[86] P. K. Kaiser, A. Guenot, and N. R. Morgenstern. Deformation of small tunnels - IV. Behaviour during failure. *Int. J. Rock Mech. Min. Sci. & Geomech. Abstr.*, 22(3):141–152, 1985.

[87] P. K. Kaiser and N. R. Morgenstern. Phenomenological model for rock with time-dependent strength. *Int. J. Rock Mech. Min. Sci. & Geomech. Abstr.*, 18(2):153–165, 1981.

[88] P. K. Kaiser and N. R. Morgenstern. Time-dependent deformation of small tunnels - I. Experimental facilities. *Int. J. Rock Mech. Min. Sci. & Geomech. Abstr.*, 18(2):129–140, 1981.

[89] P. K. Kaiser and N. R. Morgenstern. Time-dependent deformation of small tunnels - II. Typical test data. *Int. J. Rock Mech. Min. Sci. & Geomech. Abstr.*, 18(2):141–152, 1981.

[90] P. K. Kaiser and N. R. Morgenstern. Time-independent and time-dependent deformation of small tunnels - III. Prefailure behaviour. *Int. J. Rock Mech. Min. Sci. & Geomech. Abstr.*, 19(6):307–324, 1982.

[91] P. K. Kaiser and T. Wiles. Mine-by Experiment assessment criteria - final report. Report to Atomic Energy of Canada Limited under contract WS-30J-54558, Laurentian University, 1991.

[92] P. K. Kaiser, T. D. Wiles, and D. Zou. Two- and three-dimensional stress back-analysis. Report to Atomic Energy of Canada Limited under contract WS-29J-54460, Laurentian University, 1991.

[93] H. Kastner. Uber den echten gebiergsdruck beim bau tiefliengender tunnel. *Osterreich Bauzeitschrift*, 10(11), 1949.

[94] T. Kawamoto. On the state of stress and deformation around a tunnel in orthotropic, elastic ground. *Memorial of the Faculty of Engineering, Kumamoto University*, 10(1):1–30, 1963.

[95] S. G. Keith and D. P. Onagi. Mine-by Experiment data summary: Part 8 - Construction summary. Report RC-1081, Atomic Energy of Canada Limited, 1993.

[96] Dana Kelly, David C. Peck, and Richard S. James. Petrography of granitic rock samples from the 420 m Level of the Underground Research Laboratory, Pinawa, Manitoba. Contractor's report to aecl research, Laurentian University, 1993.

[97] P. C. Kelsall, J. B. Case, and C. R. Chabannes. Evaluation of excavation-induced changes in rock permeability. *Int. J. Rock Mech. Min. Sci. & Geomech. Abstr.*, 21(3):123–135, 1984.

[98] T. C. Kennedy and H. E. Lindberg. Tunnel closure for nonlinear Mohr-Coulomb functions. *J. Engng. Mech. Div. ASCE*, 104(EM6):1313–1326, 1978.

[99] G. Kirsch. Die theorie der elastizitat und die bedurfnisse der festigkeitslehre. *Veit. Ver. Deut. Ing.*, 42:797–807, 1898.

[100] T. Kitagawa, T. Kumeta, T. Ichizyo, S. Soga, M. Sato, and M. Yasukawa. Application of convergence confinement analysis to the study of preceding displacement of a squeezing rock tunnel. *Rock Mech. Rock Engng.*, 24:31–51, 1991.

[101] S. Kobayashi, N. Nishimura, and K. Matsumoto. Displacements and strains around a non-flat-end borehole. In *Proc. 2nd Int. Symp. on Field Measurements in Geomechanics*, pages 1079–1084, 1988.

[102] G. E. Korbin. Simple procedure for the analysis of deep tunnels in problematic ground. In *Site Characterization, Proc. 17th U.S. Symp. on Rock Mech., Salt Lake City*, pages 1A3–1–1A3–7, 1976.

[103] Fred H. Kulhawy. Stresses and displacements around openings in homogeneous rock. *Int. J. Rock Mech. Min. Sci. & Geomech. Abstr.*, 12(3):43–58, 1975.

[104] Fred H. Kulhawy. Stresses and displacements around openings in rock containing an elastic discontinuity. *Int. J. Rock Mech. Min. Sci. & Geomech. Abstr.*, 12(3):59–72, 1975.

[105] Fred H. Kulhawy. Stresses and displacements around openings in rock containing an inelastic discontinuity. *Int. J. Rock Mech. Min. Sci. & Geomech. Abstr.*, 12(3):73–78, 1975.

[106] H. Labasse. Les pressions de terrains dans les mines de huiles. *Revue Universelle des Mines, Series 9*, 5(3):78–88, 1949.

[107] B. Ladanyi. Use of the long-term strength concept in the determination of ground pressure on tunnel linings. In *Advances in Rock Mechanics, Proc. Third Congress of the Int. Soc. for Rock Mech., Vol. 2, Part B*, pages 1150–1156, 1974.

[108] B. Ladanyi and Don Nguyen. Study of strains in rock associated with brittle failure. In *Proc. Sixth Canadian Rock Mech. Symp., Ottawa*, pages 49–64, 1971.

[109] E. Z. Lajtai and L. P. Bielus. Stress corrosion cracking of Lac du Bonnet granite in tension and compression. *Rock Mech. Rock Engng.*, 19:71–87, 1986.

[110] E. Z. Lajtai, B. J. Carter, and M. L. Ayari. Criteria for brittle fracture in compression. *Eng. Frac. Mech.*, 37(1):59–74, 1990.

[111] E. Z. Lajtai and R. H. Schmidtke. Delayed failure in rock loaded in uniaxial compression. *Rock Mech. Rock Engng.*, 19:11–25, 1986.

[112] Emery Z. Lajtai. The fracture of Lac du Bonnet granite. Office of Industrial Research report TR-M-00007, University of Manitoba, Geological Engineering Department, 1982.

[113] Emery Z. Lajtai. The deformation, fracture and strength of Lac du Bonnet granite. Research report 19, University of Manitoba, Geological Engineering Department, 1988.

[114] Emery Z. Lajtai, Bruce J. Carter, and E. J. Scott Duncan. Mapping the state of fracture around cavities. *Engng. Geol.*, 31:277–289, 1991.

[115] P. A. Lang. Room 209 excavation response test in the Underground Research Laboratory. In *Excavation Response in Geological Repositories for Radioactive Waste, Proc. NEA Workshop, Winnipeg, MB, 1988 April*, pages 295–330, 1989.

[116] P. A. Lang, T. Chan, C. C. Davison, R. A. Everitt, E. T. Kozak, and P. M. Thompson. Near-field mechanical and hydraulic response of a granitic rock mass to shaft excavation. In *Proc. 28th U.S. Symp. Rock Mech., Tucson, AR*, pages 509–516, 1987.

[117] E. R. Leeman. The borehole deformation type of rock stress measuring instrument. *Int. J. Rock Mech. Min. Sci.*, 4(1):23–34, 1967.

[118] R. K. Livesley. *Mathematical methods for engineers.* Ellis Horwood Limited, Chichester, 1st edition, 1989.

[119] G. Loegters. Das raumliche verformungsgeschehen beim vortrieb oberflachennaher tunnel-rohren. *Public. Inst. Boden-und Felsmechanik, Univ. Karlsruhe*, 59, 1974.

[120] G. Lombardi. Influence of rock characteristics on the stability of rock cavities. *Tunn. Tunnlg.*, 2(1 and 2):19–22 and 104–109, 1970.

[121] G. Lombardi. Long-term measurements in underground openings and their interpretation with special consideration to the rheological behaviour of rock. In *Field Measurements in Rock Mechanics, Vol. 2*, pages 839–858, 1977.

[122] G. Lombardi. Some comments on the convergence-confinement method. *Underground Space*, 4(4):249–258, 1980.

[123] J. Marti and P. A. Cundall. Mixed discretization procedure for accurate solution of plasticity problems. *Int. J. Num. Methods Eng.*, 6:129–139, 1982.

[124] C. D. Martin. Characterizing in situ stress domains at the AECL Underground Research Laboratory. *Can. Geotech. J.*, 27:631–646, 1990.

[125] C. D. Martin. *The strength of rock around underground openings.* PhD thesis, Department of Civil Engineering, University of Manitoba, Winnipeg, MB, 1993.

[126] C. D. Martin and R. S. Read. The in situ strength of massive granite around excavations. In *Proc. 16th Can. Rock Mech. Conf., Sudbury*, pages 1–10, 1992.

[127] C. D. Martin, R. S. Read, and P. A. Lang. Seven years of in situ stress measurements at the URL - an overview. In *Proc. 31st U.S. Symp. Rock Mech., Golden, CO*, pages 15–26, 1990.

[128] J. B. Martino. Distometer convergence readings in the shaft extension of Atomic Energy of Canada Limited's Underground Research Laboratory. Technical Record TR-482*, Atomic Energy of Canada Limited, 1989.

[129] J. B. Martino, R. S. Read, and D. Collins. Mine-by Experiment data summary report: Part 6 - Acoustic emission/ microseismic results. Technical Record TR-597, Atomic Energy of Canada Limited, 1993.

[130] J. B. Martino and M. H. Spinney. Stress change results from the 324 and 384 instrument arrays using CSIRO Hollow Inclusion strain cells. Technical Record TR-503*, Atomic Energy of Canada Limited, 1990.

[131] R. D. Mindlin. Stress distribution around a tunnel. In *Transactions ASCE, Vol. 105*, pages 117–153, 1940.

[132] R. G. Morrison and D. F. Coates. Soil mechanics applied to rock failure in mines. *The Canadian Mining and Metallurgical Bulletin*, 48(523):701–711, 1955.

[133] N. I. Muskhelishvili. *Some basic problems of the mathematical theory of elasticity.* Noordhoff Ltd., Holland, 1953.

[134] D. Nguyen Minh and P. Berest. Étude de la stabilité des cavités souteraines avec un modéle de comportement élastoplastique radoucissant. In *Proc. 4th Congress of the Int. Soc. for Rock Mech., Vol. 1*, pages 249–256, 1979.

[135] Y. Niwa, S. Kobayashi, and T. Fukui. Stresses and displacements around an advancing face of a tunnel. In *Proc. 4th Int. Congr. Rock Mech., Vol. 1, Montreux*, pages 703–710, 1979.

[136] D. P. Onagi, S. G. Keith, and G. W. Kuzyk. Non-explosive excavation technique developed for the excavation of AECL's Mine-by Experiment test tunnel at the Underground Research Laboratory. In *Proc. 10th Annual Tunnelling Assoc. of Canada Conf., Banff, AB*, 1992.

[137] W. D. Ortlepp and N. G. W. Cook. The measurement and analysis of the deformation around deep, hard-rock excavations. In *Proc. 4th Int. Conf. on Rock Mech. and Strata Control in Mines*, pages 140–150, 1964.

[138] M. Otsuka and T. Kondoh. On the displacement forecasting methods and their application to tunnelling by NATM. In *Proc. Int. Symp. on Weak Rock, Tokyo*, pages 945–950, 1981.

[139] Frederick L. Paillet and Kunsoo Kim. Character and distribution of borehole breakouts and their relationship to in situ stresses in deep Columbia River basalts. *J. Geophys. Res.*, 92(B7):6223–6234, 1987.

[140] X. D. Pan and J. A. Hudson. Technical note. Plane strain analysis in modelling three-dimensional tunnel excavations. *Int. J. Rock Mech. Min. Sci. & Geomech. Abstr.*, 25(5):331–337, 1988.

[141] Y. W. Pan and J. J. Dong. Time-dependent tunnel convergence - I. Formulation of the model. *Int. J. Rock Mech. Min. Sci. & Geomech. Abstr.*, 28(6):469–476, 1991.

[142] Y. W. Pan and J. J. Dong. Time-dependent tunnel convergence - II. Advance rate and tunnel-support interaction. *Int. J. Rock Mech. Min. Sci. & Geomech. Abstr.*, 28(6):477–488, 1991.

[143] Yii-Wen Pan and Yi-Ming Chen. Plastic zones and characteristic-line families for openings in elasto-plastic rock mass. *Rock Mech. Rock Engng.*, 23:275–292, 1990.

[144] M. Panet. Analyse de la stabilité d'un tunnel creusé dans un massif rocheux en tenant compte du comportement aprés la rupture. *Rock Mechanics*, 8(4):209–223, 1976.

[145] M. Panet. Time dependent deformation in underground works. In *Proc. 4th Int. Congr. on Rock Mech., Vol. 3, Montreux*, pages 279–289, 1979.

[146] M. Panet and P. Guellec. Contribution a l'etude du soutenement d'un tunnel a l'arriere du front de taille. In *Advances in Rock Mechanics, Proc. 3rd Congr. Int. Soc. Rock Mech., Denver, Vol. 2B*, pages 1163–1168, 1974.

[147] M. Panet and A. Guenot. Analysis of convergence behind the face of a tunnel. In *Proc. 3rd Int. Symp. on Tunnelling, Brighton, England*, pages 197–204, 1982.

[148] F. Pelli. *The influence of near face behaviour on monitoring of deep tunnels.* PhD thesis, Department of Civil Engineering, University of Alberta, Edmonton, AB, 1987.

[149] F. Pelli, P. K. Kaiser, and N. R. Morgenstern. The influence of near face behaviour on monitoring of deep tunnels. *Can. Geotech. J.*, 28(2):226–238, 1991.

[150] F. Pelli, P. K. Kaiser, and N. R. Morgenstern. An interpretation of ground movements recorded during construction of the Donkin-Morien tunnel. *Can. Geotech. J.*, 28(2):239–254, 1991.

[151] A. P. Pierce and J. A. Ryder. Extended boundary element methods in the modelling of brittle rock behaviour. In *Proc. 5th Int. Congress on Rock Mechanics, Volume 2, Melbourne*, pages F159–F168, 1983.

[152] R. Pusch and R. Stanfors. The zone of disturbance around blasted tunnels at depth. *Int. J. Rock Mech. Min. Sci. & Geomech. Abstr.*, 29(5):447–456, 1992.

[153] L. Rabcewicz. The new Austrian tunnelling method. *Water Power, Nov./Dec. 1964/Jan. 1965*, pages 453–457, 1964.

[154] R. S. Read. Mine-by Experiment - prediction of excavation-induced rock mass response. Technical Memorandum URL-EXP-022-M048, Atomic Energy of Canada Limited, 1991.

[155] R. S. Read and C. D. Martin. Mine-by Experiment final design report. Report AECL-10430, Atomic Energy of Canada Limited, 1991.

[156] R. S. Read and C. D. Martin. The Underground Research Laboratory Mine-by Experiment - a research perspective on tunnel design. *Canadian Tunnelling*, 7:75–88, 1991.

[157] R. S. Read and C. D. Martin. Monitoring the excavation-induced response of granite. In *Proc. 33rd U.S. Symp. on Rock Mech., Santa Fe*, pages 201–210, 1992.

[158] R. S. Read, J. B. Martino, G. R. Karklin, E. Jacobs, and G. Hiltz. Mine-by Experiment data summary: Part 1 - Survey results. Report RC-1076, Atomic Energy of Canada Limited, 1994.

[159] R. S. Read, J. B. Martino, and J. H. Mitchell. Mine-by Experiment data summary: Part 4 - Convergence results. Technical Record TR-595, Atomic Energy of Canada Limited, 1993.

[160] R. S. Read, J. B. Martino, and J. H. Mitchell. Mine-by Experiment data summary: Part 2 - Triaxial strain cell results. Report RC-1077, Atomic Energy of Canada Limited, 1994.

[161] R. S. Read, J. B. Martino, J. H. Mitchell, and M. H. Spinney. Mine-by Experiment data summary: Part 3 - Extensometer results. Report RC-1078, Atomic Energy of Canada Limited, 1994.

[162] R. M. Richard and B. J. Abbott. Versatile elastic-plastic stress-strain formula. *J. Engng. Mech. Div. ASCE*, 101(EM4):511–515, 1975.

[163] J. A. Ryder and N. C. Officer. An elastic analysis of strata movement observed in the vicinity of inclined excavations. *J. S. Afr. Inst. Min. Metall.*, 64(6):219–244, 1964.

[164] S. Sakurai. Approximate time dependent analysis of tunnel support structure considering progress of tunnel face. *Int. J. Num. Anal. Meth. Geomech.*, 2:159–175, 1978.

[165] M. D. G. Salamon. Elastic analysis of displacements and stresses induced by the mining of seam or reef deposits. *J. S. Afr. Inst. Min. Metall.*, 64:128–149, 1963.

[166] M. D. G. Salamon. Elastic analysis of displacements and stresses induced by the mining of seam or reef deposits - Part IV Inclined reefs. *J. S. Afr. Inst. Min. Metall.*, 65:148–167, 1965.

[167] J. Salençon. Contraction quasistatique d'une cavité à symétrie sphérique ou cylindrique dans un milieu élastoplastique. *Annales des Pontes et Chaussées*, 1(4):231–236, 1969.

[168] F. J. Santarelli and E. T. Brown. Performance of deep wellbores in rock with a confining pressure-dependent modulus. In *Proc. 6th Congr. Int. Soc. Rock Mech., Montreal, Vol. 2*, pages 1217–1222, 1987.

[169] F. J. Santarelli, E. T. Brown, and V. Maury. Technical note. Analysis of borehole stresses using pressure dependent linear elasticity. *Int. J. Rock Mech. Min. Sci. & Geomech. Abstr.*, 23(6):445–449, 1986.

[170] C. W. Schwartz and H. H. Einstein. Simplified analysis for ground-structure interaction in tunnelling. In *The State of the Art in Rock Mechanics, Proc. 21st U.S. Symp. on Rock Mech., Rolla*, pages 787–796, 1980.

[171] F. S. Shuri. Summary of in situ stresses and rock mass response measured during URL shaft sinking from 0 to 255 m depth. Consulting Report to Atomic Energy of Canada Limited 872-1462, Golder Associates, 1989.

[172] Wang Sijing, Yang Zhifa, and Xue Ling. The back-analysis method from displacements for viscoelastic rock mass. In *Proc. 2nd Int. Symp. on Field Measurements in Geomechanics, Rotterdam*, pages 1059–1068, 1988.

[173] G. R. Simmons. Operating Phase experiments planned for Atomic Energy of Canada Limited's Underground Research Laboratory. In *Proc. Int. Symp. on Unique Underground Structures, Denver, CO, Chapter 67*, pages 1–19, 1990.

[174] B. Stimpson and R. Chen. A new technique for measuring the bimodularity of rock. In *Proc. Canadian Conf. on Appl. Mechanics, Winnipeg, MB*, 1991.

[175] K. Sugawara and Y. Obara. Measurement of in-situ rock stress by hemispherical-ended borehole technique. *Min. Sci. Technol.*, 3:287–300, 1986.

[176] J. Sulem, M. Panet, and A. Guenot. An analytical solution for time-dependent displacements in a circular tunnel. *Int. J. Rock Mech. Min. Sci. & Geomech. Abstr.*, 24(3):155–164, 1987.

[177] J. Sulem, M. Panet, and A. Guenot. Closure analysis in deep tunnels. *Int. J. Rock Mech. Min. Sci. & Geomech. Abstr.*, 24(3):145–154, 1987.

[178] S. Talebi and R. P. Young. Design of a microseismic system for the URL Mine-by Experiment. Contractor's Report to AECL Research, Contract No. WS-30J-54474 RP006AECL, Queen's University, 1990.

[179] S. Talebi and R. P. Young. Microseismic monitoring in highly stressed granite: relation between shaft-wall cracking and in situ stress. *Int. J. Rock Mech. Min. Sci. & Geomech. Abstr.*, 29(1):25–34, 1992.

[180] C. Tanimoto, S. Hata, and K. Kariya. Interaction between fully bonded bolts and strain softening rock in tunnelling. In *Rock Mechanics from Research to Application, Proc. 22nd U.S. Symp. on Rock Mech., Cambridge*, pages 367–372, 1981.

[181] K. Terzaghi and F. E. Richart. Stresses in rock about cavities. *Geotechnique*, 2(1):57–90, 1952.

[182] P. M. Thompson, E. T. Kozak, and C. D. Martin. Rock displacement instrumentation and coupled hydraulic pressure/rock displacement instrumentation for use in stiff crystalline rock. In *Excavation Response in Geological Repositories for Radioactive Waste, Proceedings of a NEA Workshop, Winnipeg, MB, 1988 April*, pages 257–270, 1989.

[183] P. M. Thompson and P. A. Lang. Rock displacements measured during URL shaft sinking. In *Proc. Can. Nuclear Soc. 2nd Int. Conf. on Radioactive Waste Management, Winnipeg, MB*, pages 332–340, 1986.

[184] P. M. Thompson, J. B. Martino, and M. H. Spinney. Detailed measurements of deformation in the excavation disturbed zone. In *Proc. 34th U.S. Symposium on Rock Mechanics, 1993 June 27-30, Madison, Vol. 2*, pages 757–760, 1993.

[185] W. L. van Heerden. Potential fracture zones around boreholes with flat and spherical ends. *Int. J. Rock Mech. Min. Sci.*, 6(5):453–463, 1969.

[186] J. R. Walker, C. D. Martin, and E. J. Dzik. Technical note - Confidence intervals for in situ stress measurements. *Int. J. Rock Mech. Min. Sci. & Geomech. Abstr.*, 27(2):139–141, 1990.

[187] J. B. Walsh, E. E. Leyde, A. J. A. White, and B. L. Carragher. Stope closure studies at West Driefontein gold mine. *Int. J. Rock Mech. Min. Sci. & Geomech. Abstr.*, 14(5/6):277–281, 1977.

[188] Joseph B. Walsh. Energy changes due to mining. *Int. J. Rock Mech. Min. Sci. & Geomech. Abstr.*, 14(1):25–33, 1977.

[189] Zhu Weishen, Lin Shisheng, Zhu Jiaqiao, Dai Guanyi, and Zhan Caizhao. Some practical cases of back analysis of underground opening deformability concerning time and space effects. In *Proc. 6th Int. Conf. Rock Mech., Vol. 2, Montreal*, pages 1353–1356, 1987.

[190] T. D. Wiles and P. K. Kaiser. Under excavation method incremental analysis of 420 Level vent raise and Room 209 data. Contractor's report to Atomic Energy of Canada Limited, Laurentian University, 1992.

[191] Terry D. Wiles and Peter K. Kaiser. In situ stress determination using the under-excavation technique – Part 1: Theory. *Int. J. Rock Mech. Min. Sci. & Geomech. Abstr.*, 31:In press, 1994.

[192] Terry D. Wiles and Peter K. Kaiser. In situ stress determination using the under-excavation technique – Part 2: Application. *Int. J. Rock Mech. Min. Sci. & Geomech. Abstr.*, 31:In press, 1994.

[193] G. Worotnicki and R. J. Walton. Triaxial "hollow inclusion" gauges for the determination of rock stresses in situ. In *Proc. Symp. on Investigation of Stresses in Rock and Advances in Stress Measurement, supplement*, page 108, 1976.

[194] H. Wu and D. D. Pollard. Possible secondary fracture patterns due to a change in the direction of loading. In *Preprints Conf. on Fractured and Jointed Rock Masses, Vol. 2, Lake Tahoe*, pages 505–512. U.S. Dept. of Energy, 1992.

[195] H. Yoshimura, T. Yuki, Y. Yamada, and N. Kokubun. Analysis and monitoring of the Miyana railway tunnel constructed using the New Austrian Tunnelling Method. *Int. J. Rock Mech. Min. Sci. & Geomech. Abstr.*, 23(1):67–76, 1986.

[196] Ziqiong Zheng, John Kemeny, and Neville G. W. Cook. Analysis of borehole breakouts. *J. Geophys. Res.*, 94(B6):7171–7182, 1989.

[197] M. D. Zoback, D. Moos, and L. Mastin. Wellbore breakouts and in situ stress. *J. Geophys. Res.*, 90:5523–5530, 1985.

Appendix A

Solutions to the Axisymmetric Tunnel Problem

Table A.1: Summary of solutions to the axisymmetric tunnel problem (modified after Brown et al. [12]).

Author and Year	Strength/Yield Criterion	Stress-Strain Model	Treatment of Plastic Volumetric Strains	Special Features of Analysis
Fenner 1938 [52]	Mohr-Coulomb	elastic-plastic	none	
Kastner 1949 [93]	Mohr-Coulomb	elastic-plastic	none	nonhydrostatic stress field
Labasse 1949 [106]	Mohr-Coulomb with zero cohesion	elastic-plastic	evaluated average volumetric strain in plastic zone	nonhydrostatic stress field
Morrison and Coates 1955 [132]	Mohr-Coulomb peak and residual with constant ϕ, zero residual cohesion	elastic-brittle-plastic	none	corrected errors made by Fenner [52]
Diest 1965 [34]	Mohr-Coulomb with zero residual strength	elastic-strain softening	none	
Hobbs 1966 [75]	nonlinear power law with reduced strength in plastic zone	elastic-brittle-plastic	none, but different E and ν used for plastic zone	
Bray 1967 [9]	Mohr-Coulomb	elastic-plastic	none	slip on log spiral surfaces in plastic zone
Salencon 1969 [167]	Tresca and Mohr-Coulomb	elastic-plastic	used associated flow rule; rate of plastic volume change independent of strain	
Daemen and Fairhurst 1971 [28]	bilinear with different peak and residual strengths	elastic-strain softening	plastic volume change constant or varying linearly with radial strain	closed-form solutions not presented
Lombardi 1970 [120, 1, 121, 122]	Mohr-Coulomb with different peak and residual cohesion and ϕ	elastic-brittle-plastic	average volumetric strain in plastic zone estimated; different E and ν in plastic zone	
Hendron and Aiyer 1972 [67]	Mohr-Coulomb with constant ϕ and either constant, varying or zero cohesion in plastic zone	elastic-plastic, elastic-brittle-plastic, and a special case of elastic-strain softening	associated flow rule applied over entire plastic zone; different E and ν in plastic zone in some solutions	several different cases solved; all features not included in one solution
Ladanyi 1974 [107]	nonlinear Fairhurst criteria [50] for original and broken rock in short and long term	elastic-brittle-plastic	associated flow rule applied over limited range of post-peak strain	
Egger 1974 [39, 40]	Mohr-Coulomb peak and residual with constant ϕ, zero residual cohesion	elastic-strain softening	major and minor principal plastic strains linearly related by variable parameter ϕ	

Table A.1 (continued).

Author and Year	Strength/Yield Criterion	Stress-Strain Model	Treatment of Plastic Volumetric Strains	Special Features of Analysis
Panet 1974 [146, 144]	Mohr-Coulomb peak and residual with constant ϕ, zero residual cohesion	elastic-strain softening	major and minor principal plastic strains linearly related by variable parameter ϕ	allows for influence of tunnel face
Korbin 1976 [102]	piecewise linear Coulomb approximation of nonlinear Mohr envelope	nonlinear strain-softening	uses Hendron and Aiyer's [67] application of the associated flow rule	
Kennedy and Lindberg 1978 [98]	piecewise linear Coulomb approximation of nonlinear Mohr envelope	elastic-plastic	associated flow rule applied over entire plastic zone; an alternative incompressible flow solution presented	
Florence and Schwer 1978 [54]	Mohr-Coulomb	elastic-plastic	associated flow rule applied over entire plastic zone	allows for influence of axial stress resulting in up to three different plastic zones depending on values of ν and ϕ and relative magnitudes of tangential, radial and axial stresses
Nguyen Minh and Berest 1979 [134]	Mohr-Coulomb peak and residual with constant ϕ	elastic-strain softening with possible Class 2 behaviour [180]	major and minor principal plastic strains linearly related by variable parameter β	allows for influence of axial stress resulting in two different plastic zones depending on relative magnitudes of radial, tangential and axial stresses
Schwartz and Einstein 1980 [170]	Mohr-Coulomb	elastic-plastic	zero total volume change in plastic zone (nonassociated flow rule)	allows for influence of tunnel face
Hoek and Brown 1980 [78]	empirical nonlinear peak and residual criteria [77]	elastic-brittle-plastic	associated flow rule applied over a limited range of post-peak strain	calculation steps given for complete ground-support interaction calculations

Table A.1 (continued).

Author and Year	Strength/Yield Criterion	Stress-Strain Model	Treatment of Plastic Volumetric Strains	Special Features of Analysis
Kaiser 1981 [84]	rate-dependent Mohr-Coulomb peak and residual	elastic-brittle-plastic; stiffness and strength loss rate-dependent	major and minor principal plastic strains linearly related by variable parameter β	
Brown et al. 1983 [12]	empirical non-linear peak and residual criteria [77]	elastic-brittle-plastic and elastic-strain softening	post-peak strain increments in two different regimes related by experimental parameters or by the associated flow rule	closed-form solution for simple case; stepwise numerical solution for more complex material behaviour model

Appendix B

Modeling Results for a Cylindrical Tunnel

B.1 Displacement Responses at the Tunnel Wall for Components of the Partitioned Stress Tensor

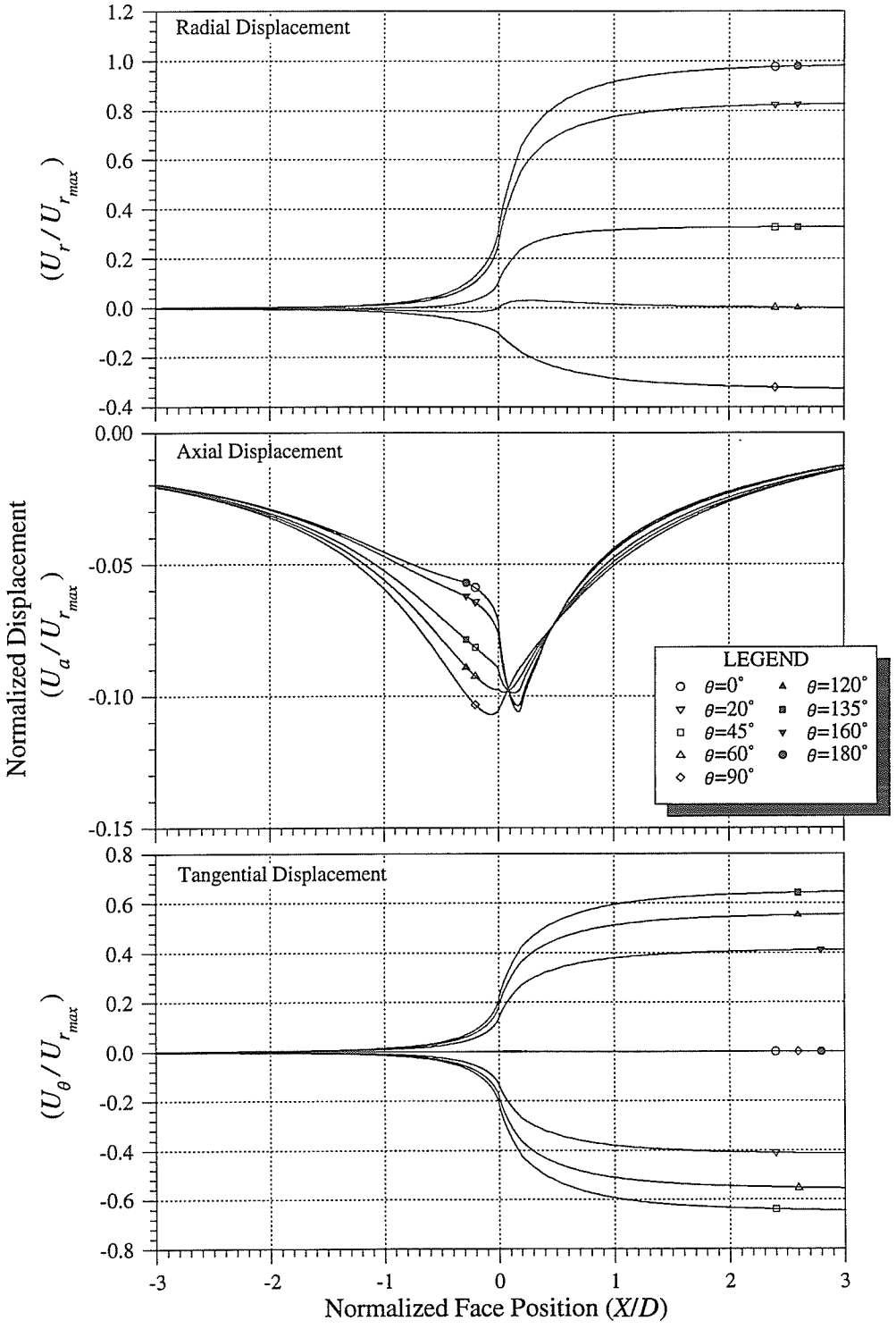

Figure B.1: Displacement response versus face position for σ_{11} tensor.

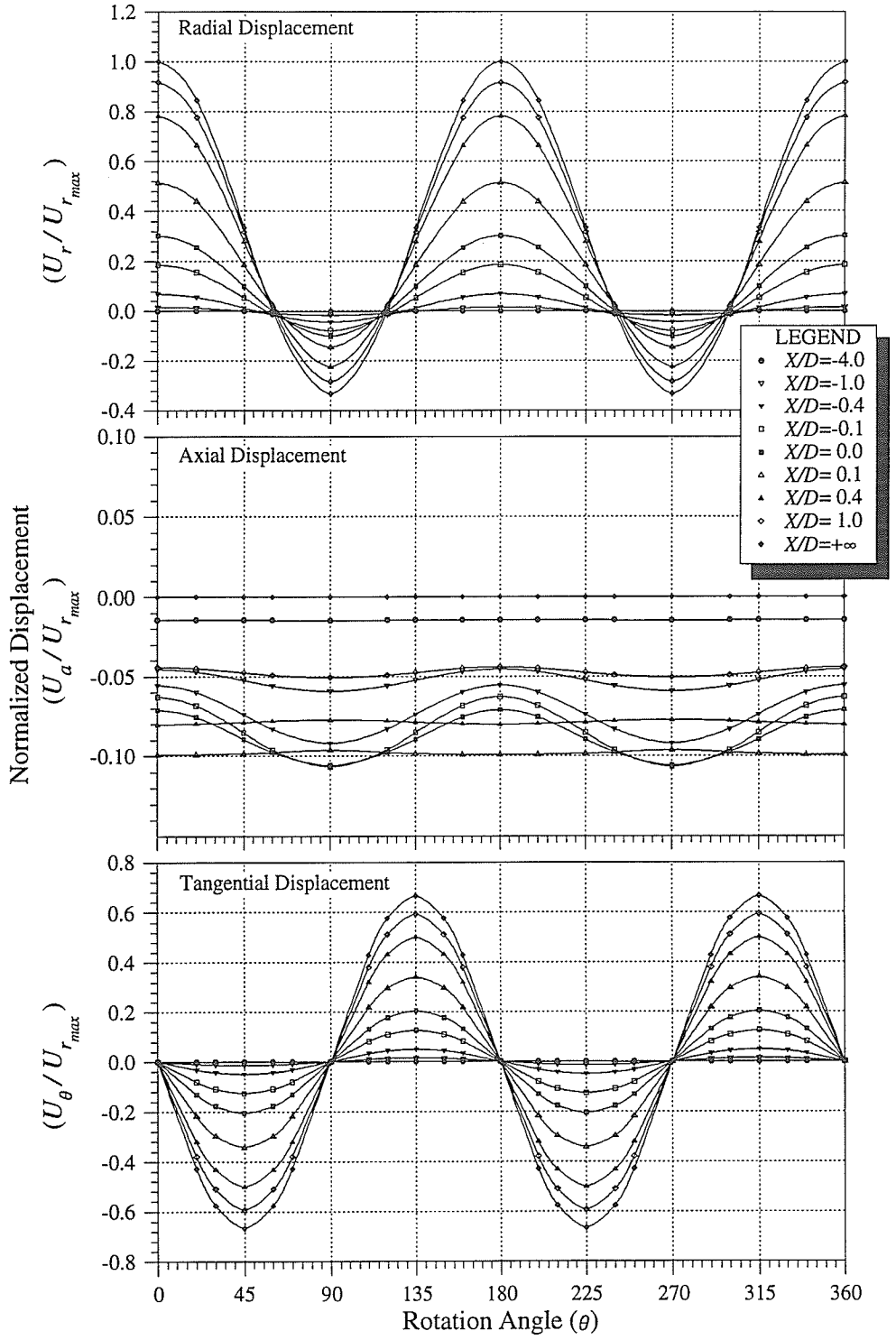

Figure B.2: Displacement response versus rotation angle for σ_{11} tensor.

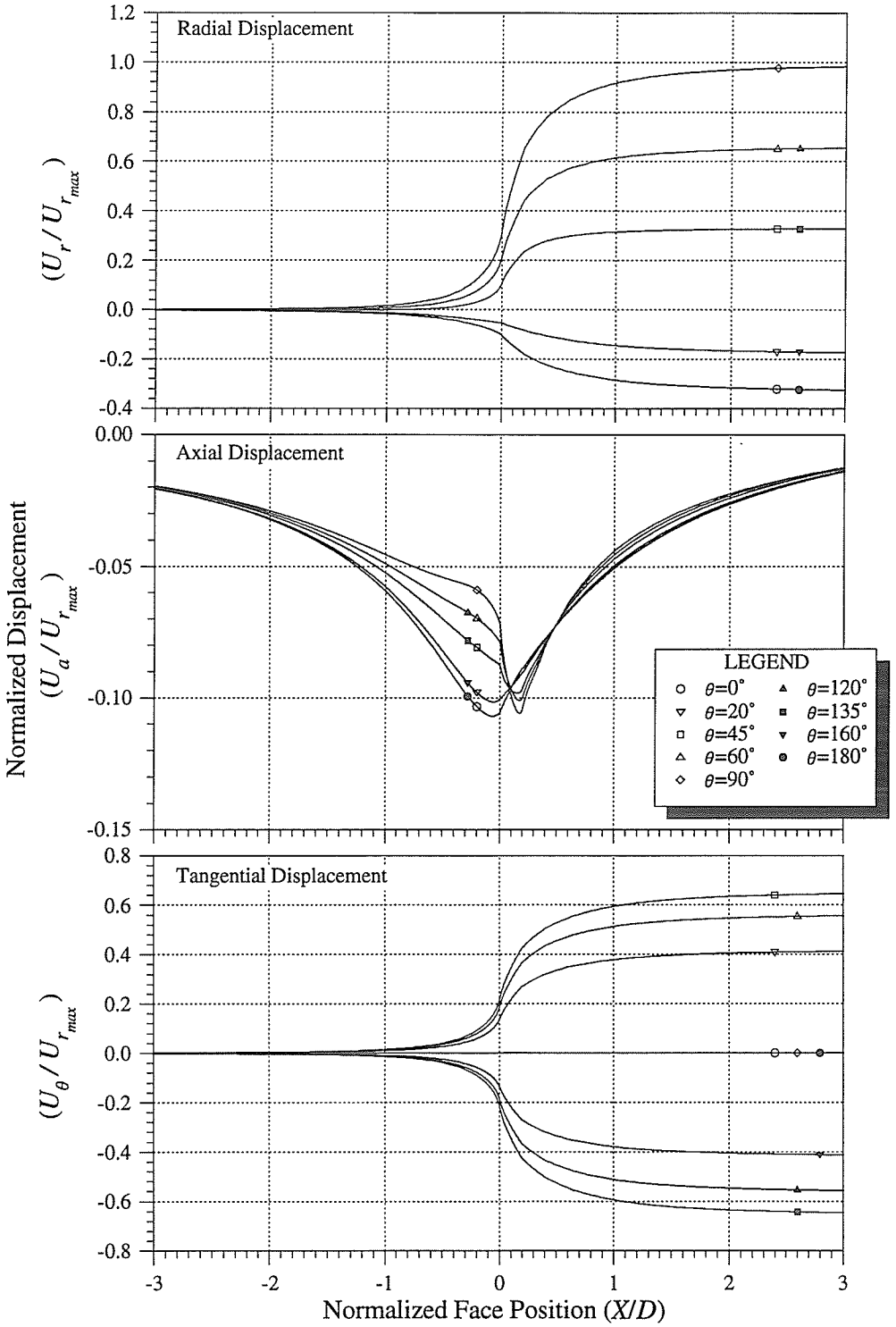

Figure B.3: Displacement response versus face position for σ_{33} tensor.

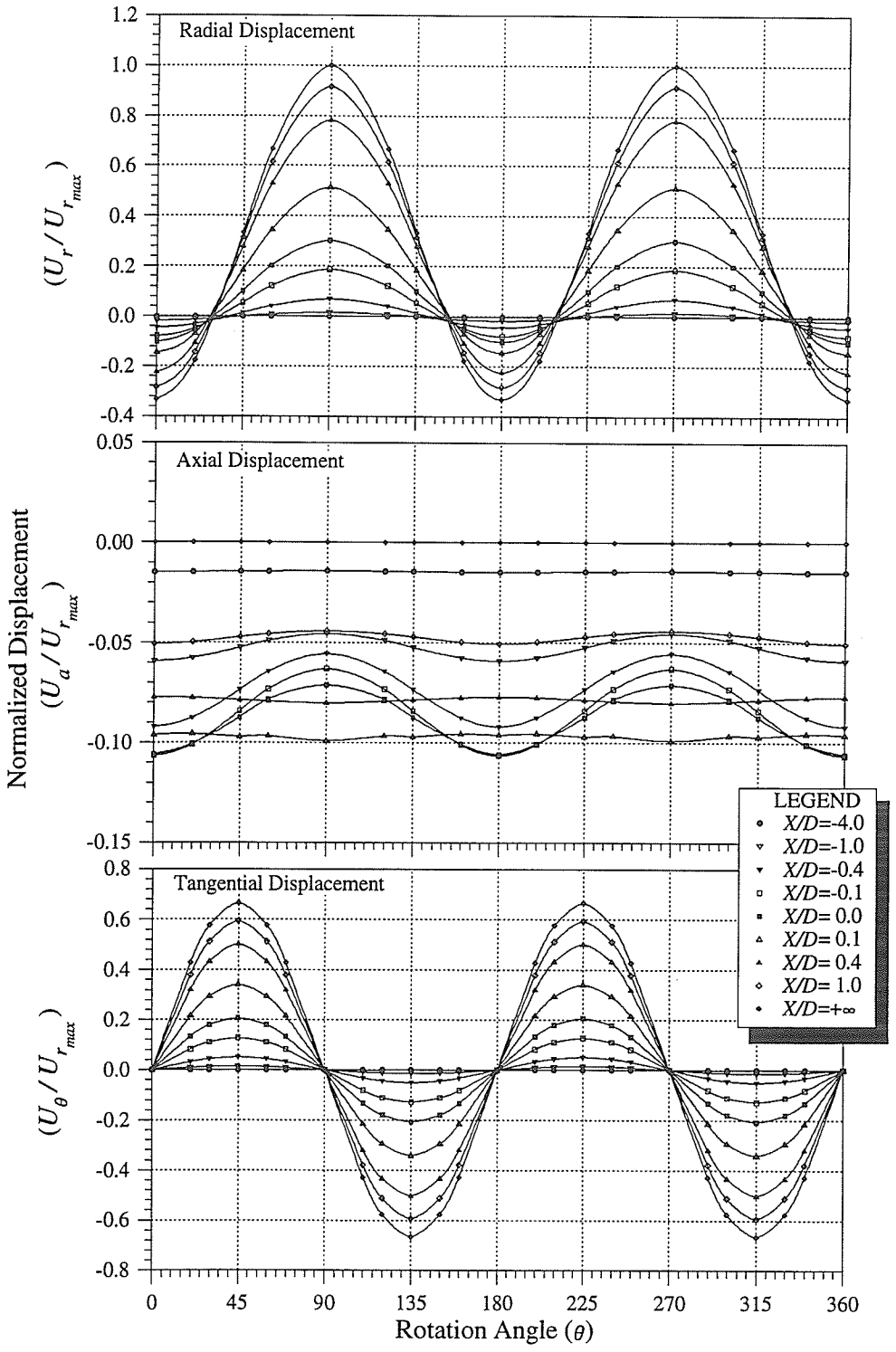

Figure B.4: Displacement response versus rotation angle for σ_{33} tensor.

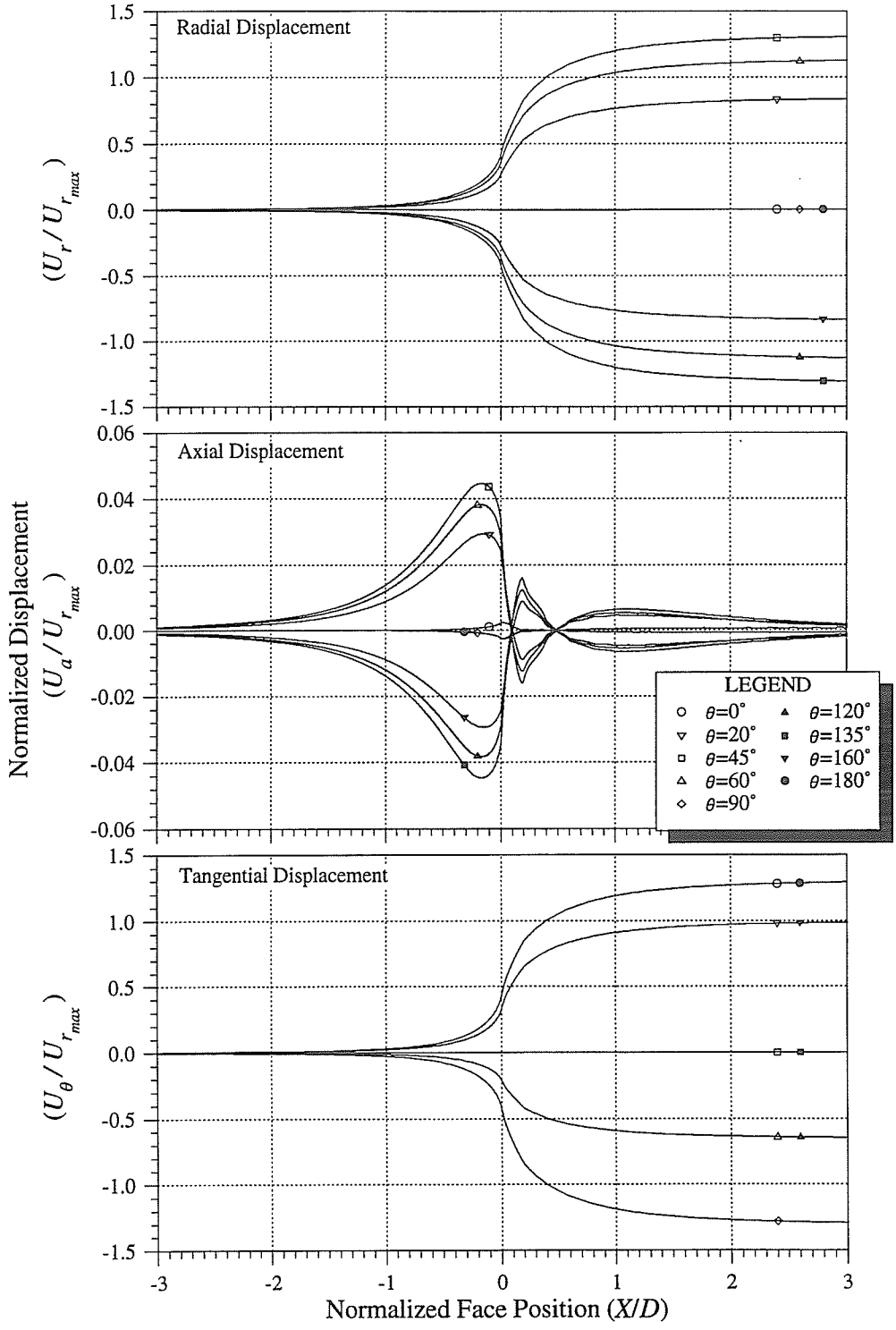

Figure B.5: Displacement response versus face position for σ_{13} tensor.

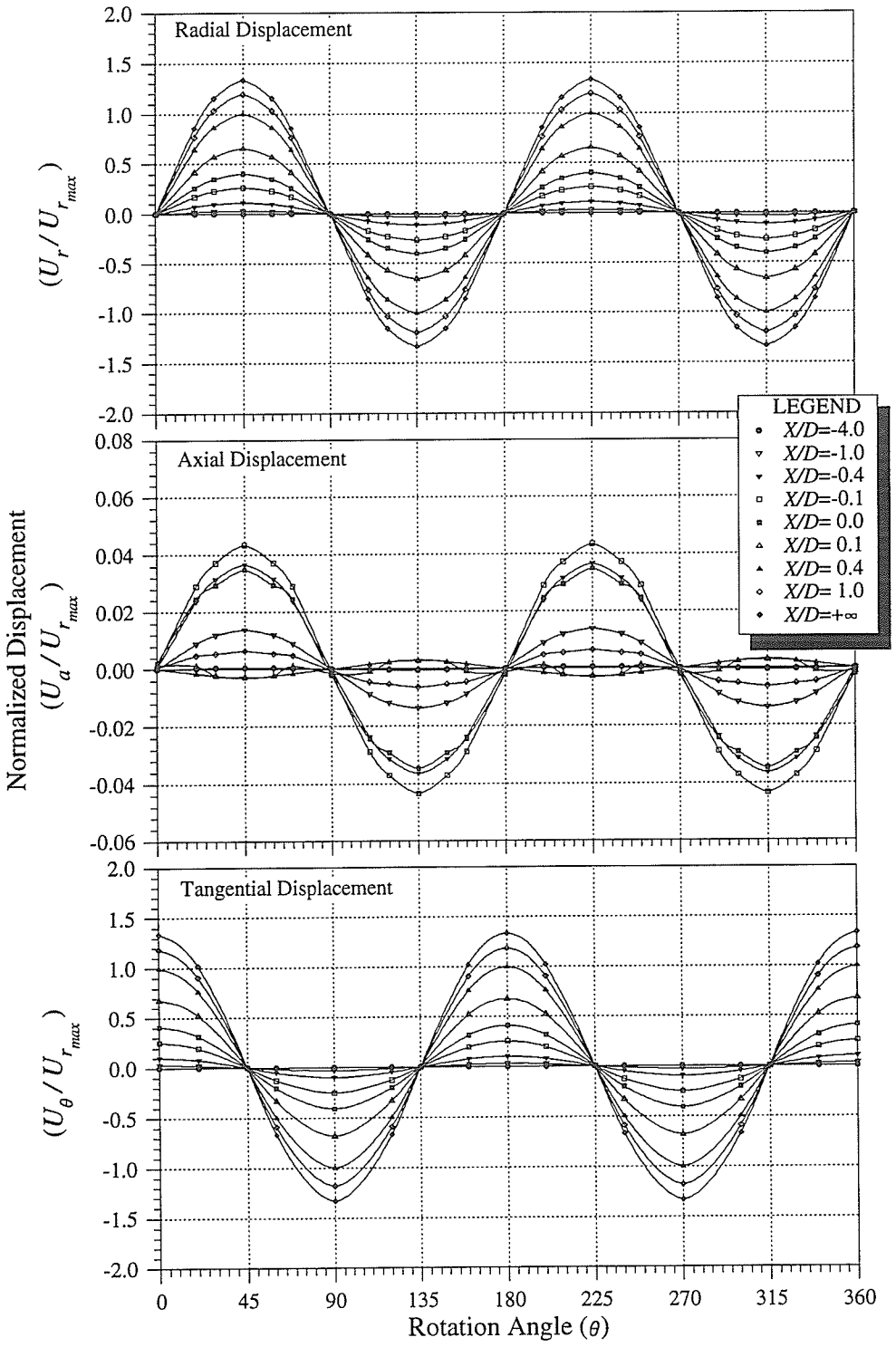

Figure B.6: Displacement response versus rotation angle for σ_{13} tensor.

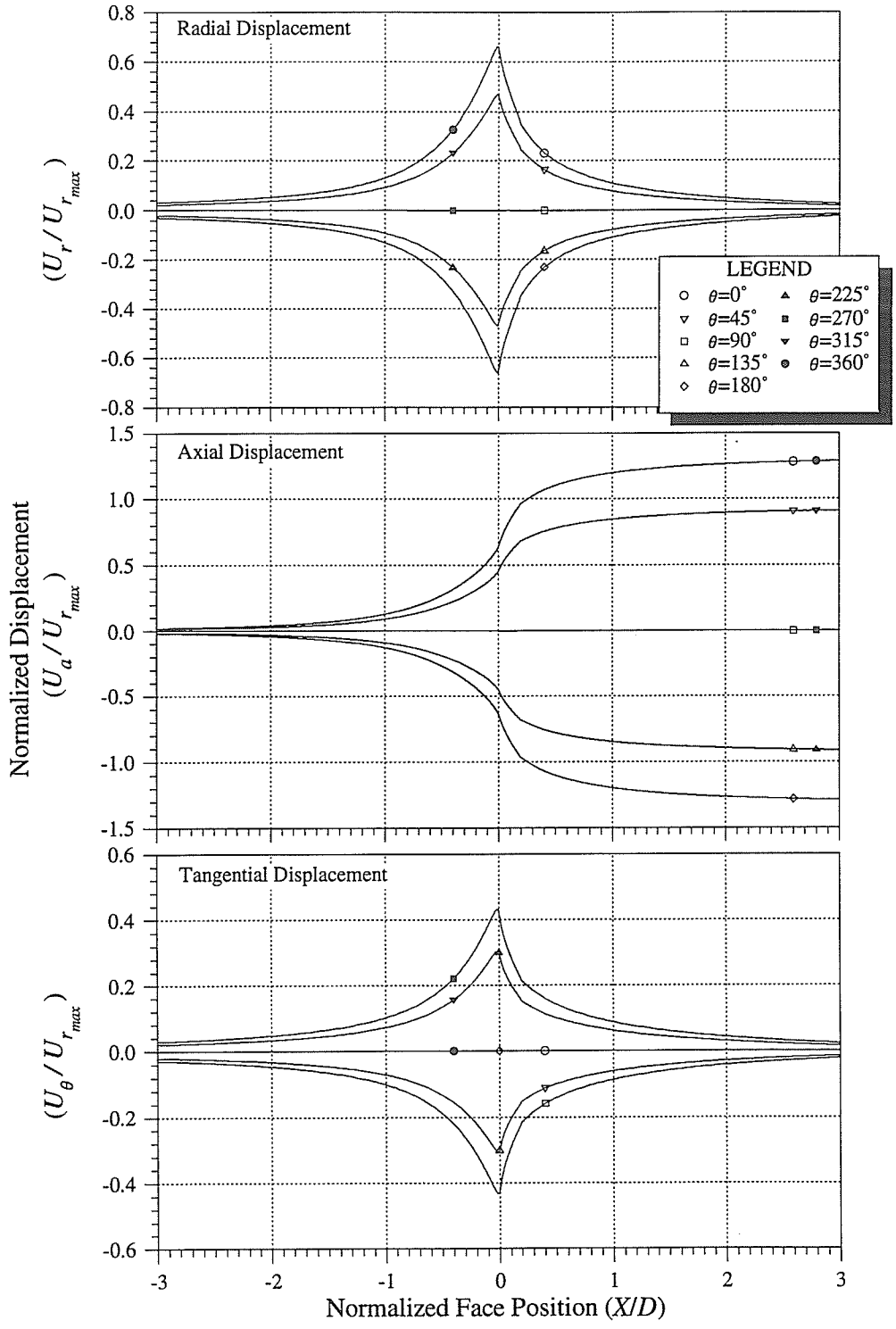

Figure B.7: Displacement response versus face position for σ_{12} tensor.

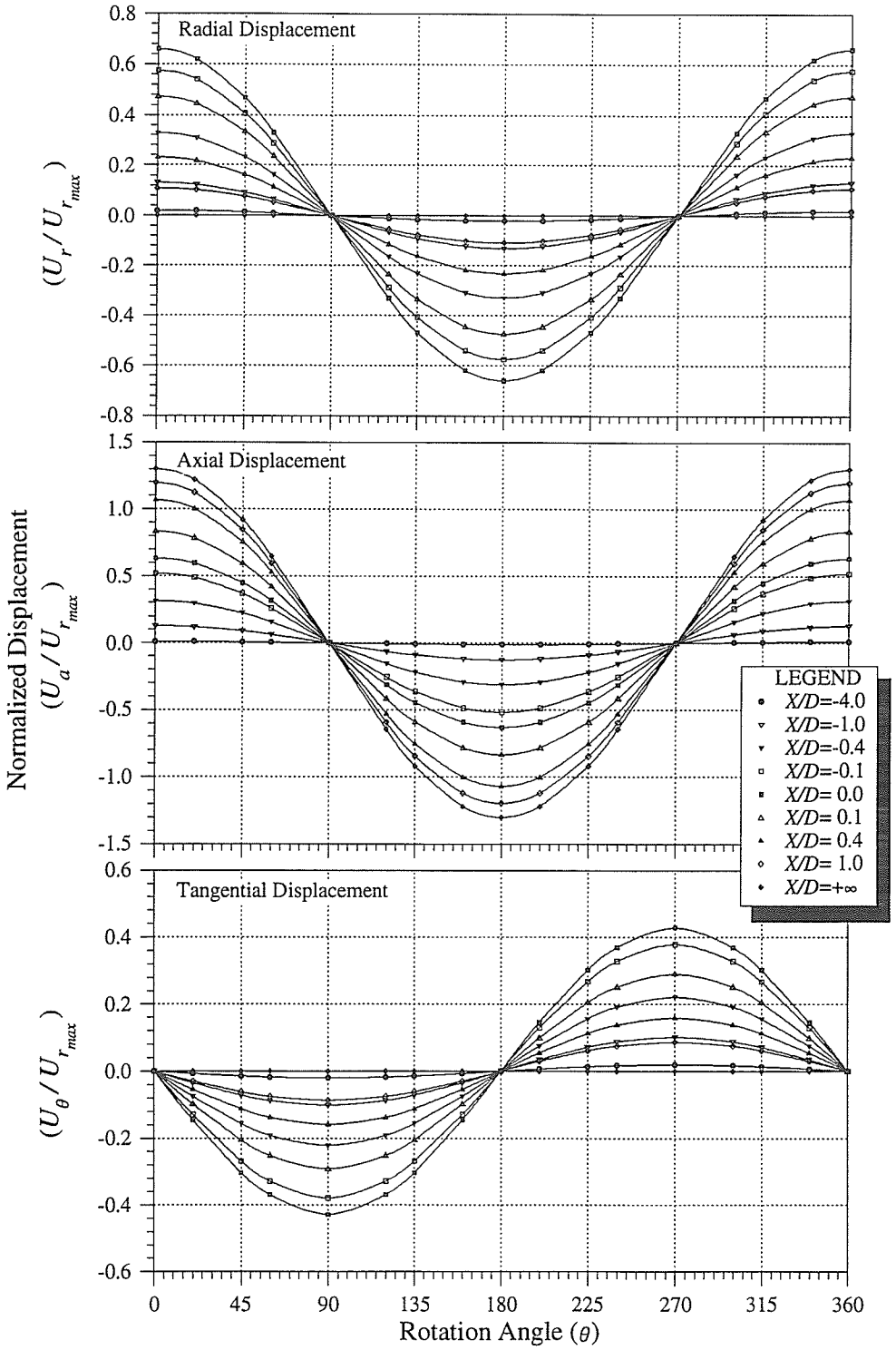

Figure B.8: Displacement response versus rotation angle for σ_{12} tensor.

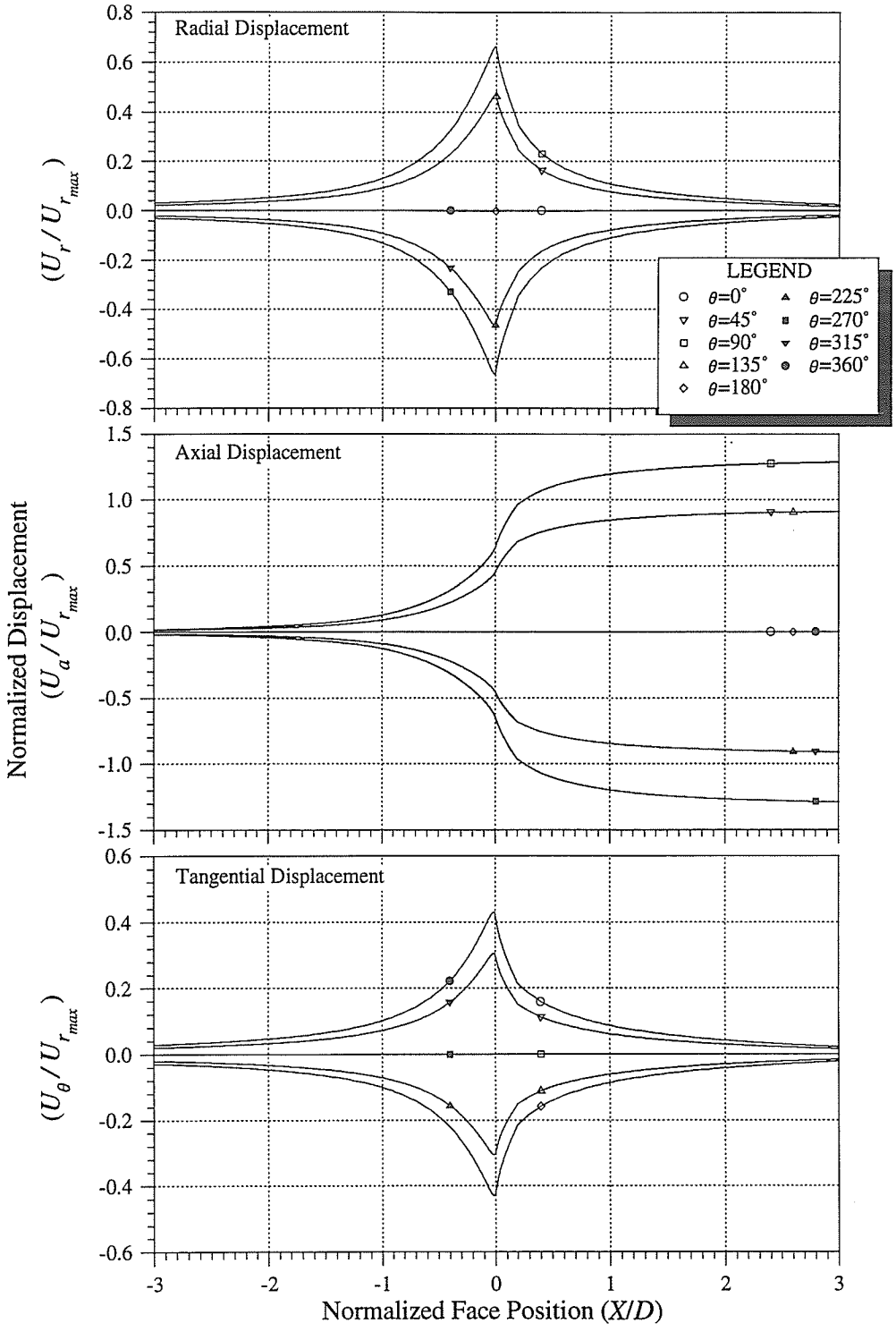

Figure B.9: Displacement response versus face position for σ_{23} tensor.

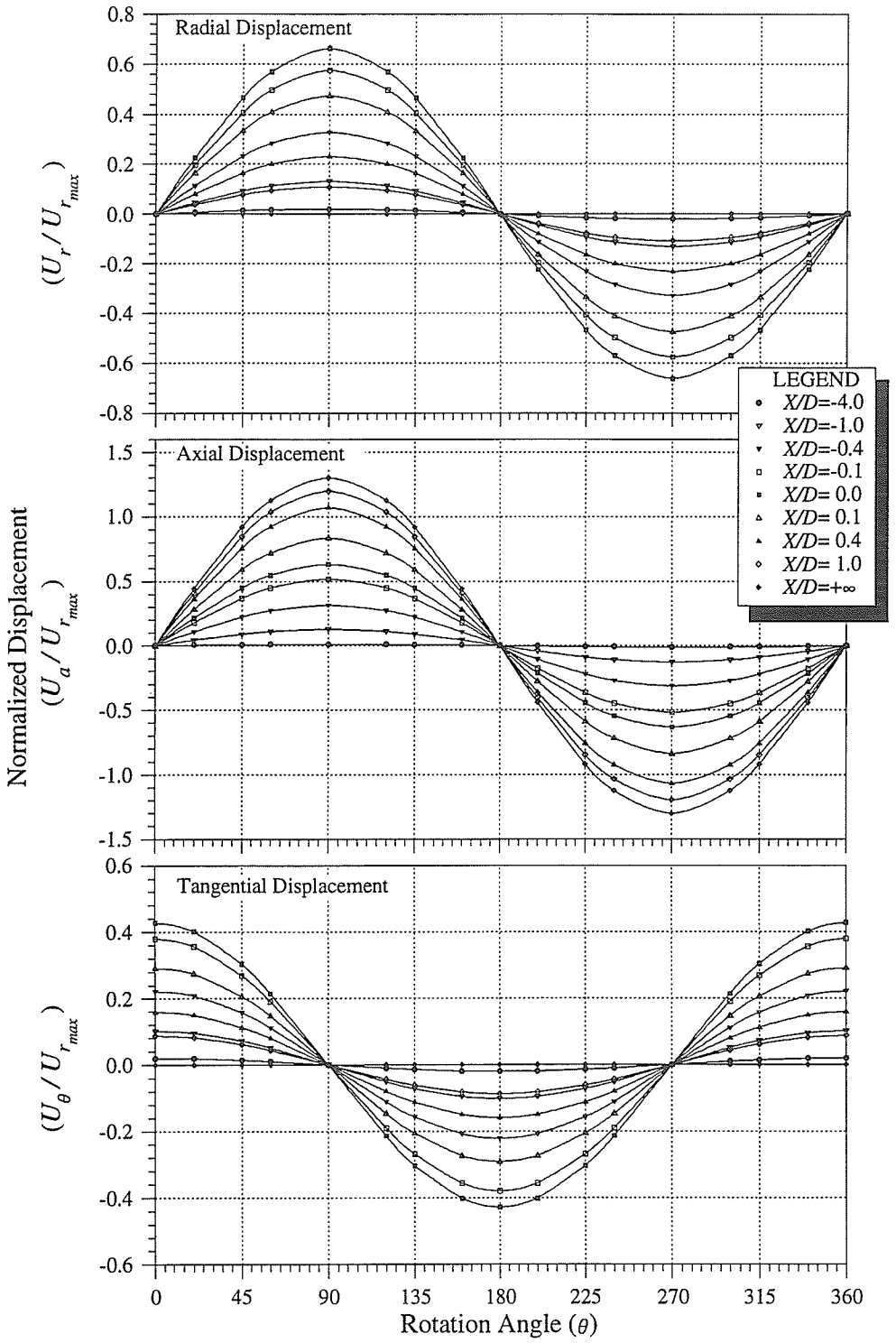

Figure B.10: Displacement response versus rotation angle for σ_{23} tensor.

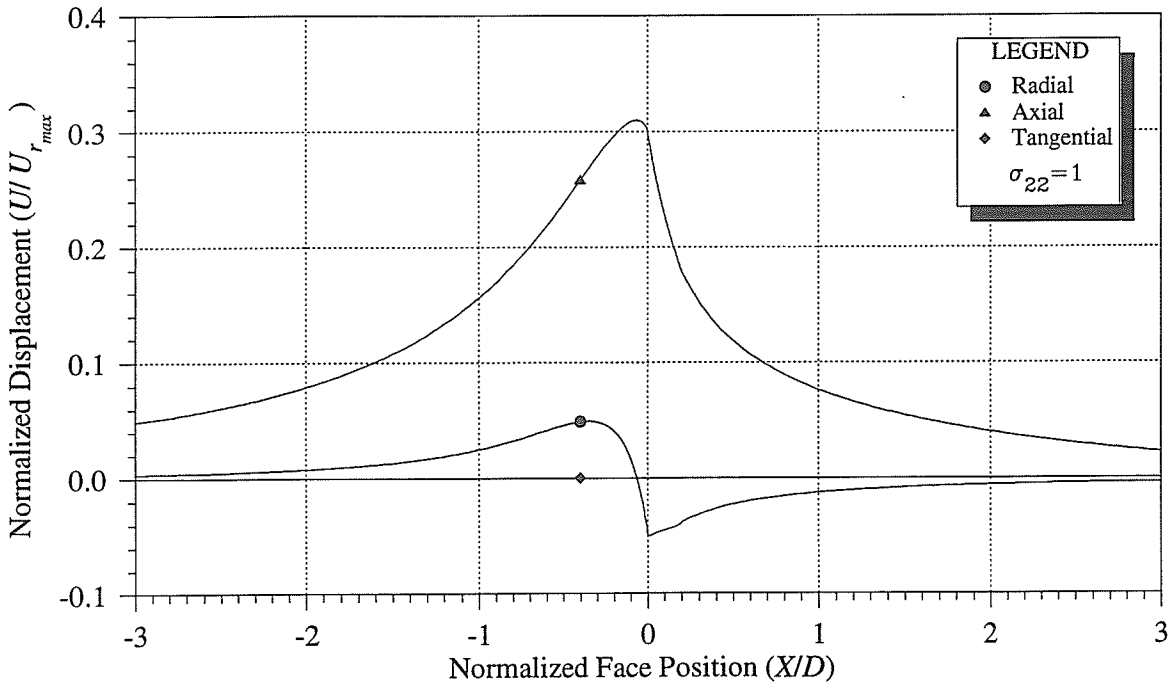

Figure B.11: Displacement response versus face position for σ_{22} tensor.

B.2 Displacement Responses at the Tunnel Wall for Axisymmetric Cases

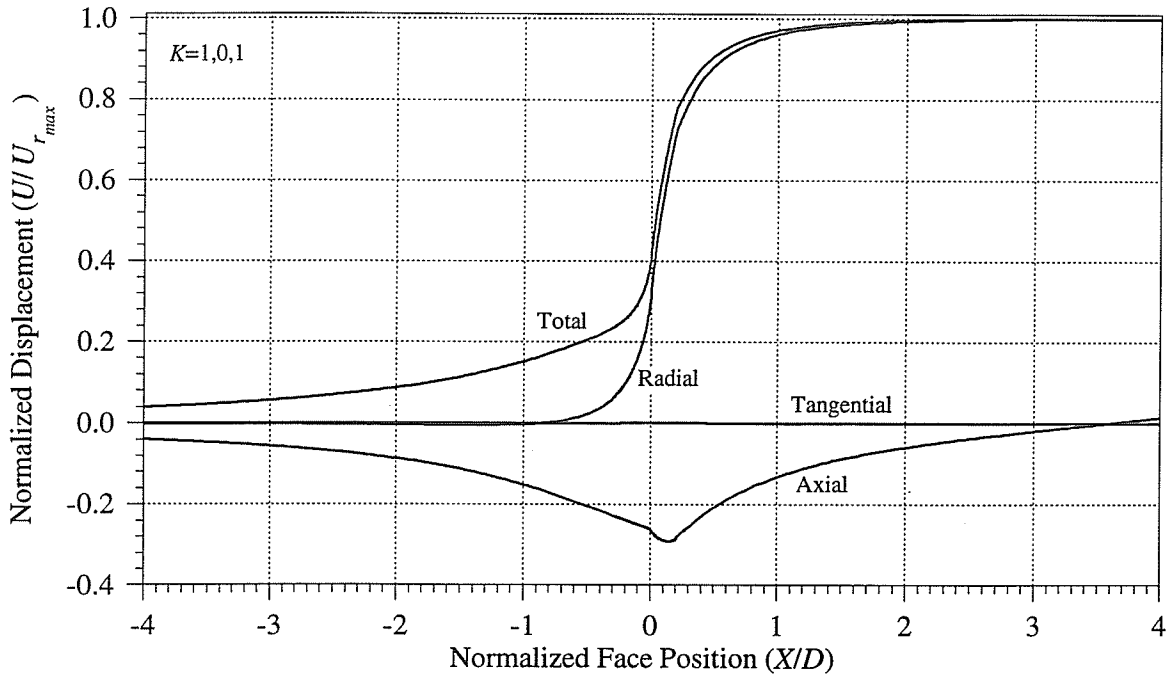

Figure B.12: Components of displacement for $K = 1, 0, 1$.

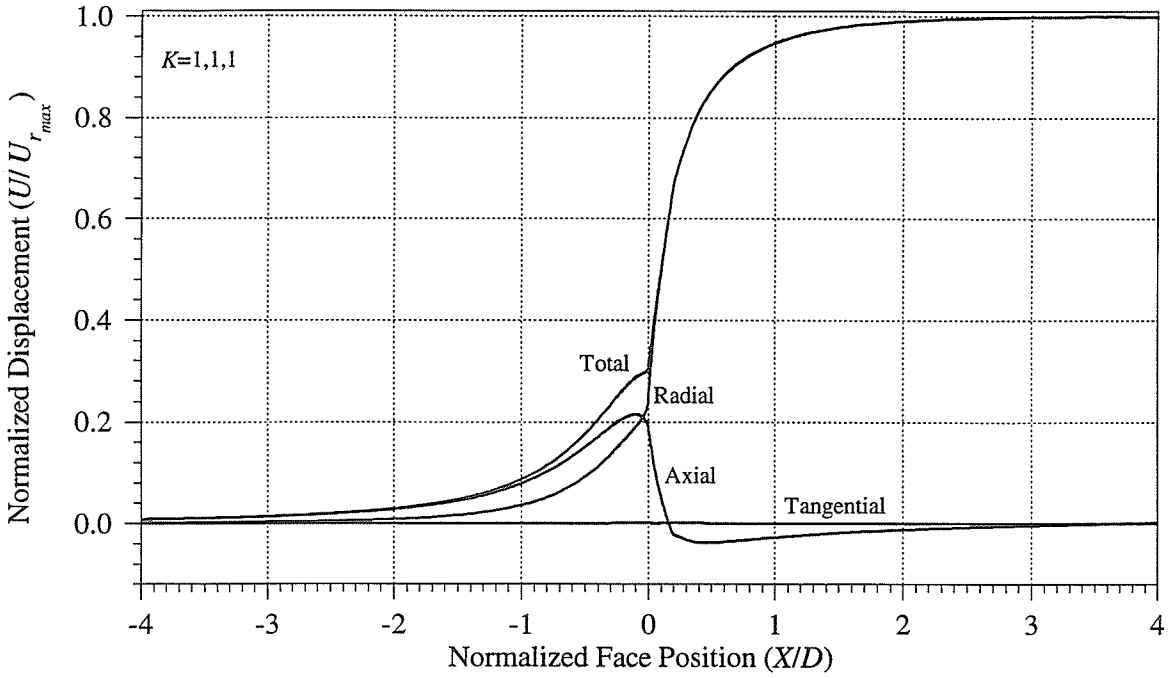

Figure B.13: Components of displacement for $K = 1, 1, 1$.

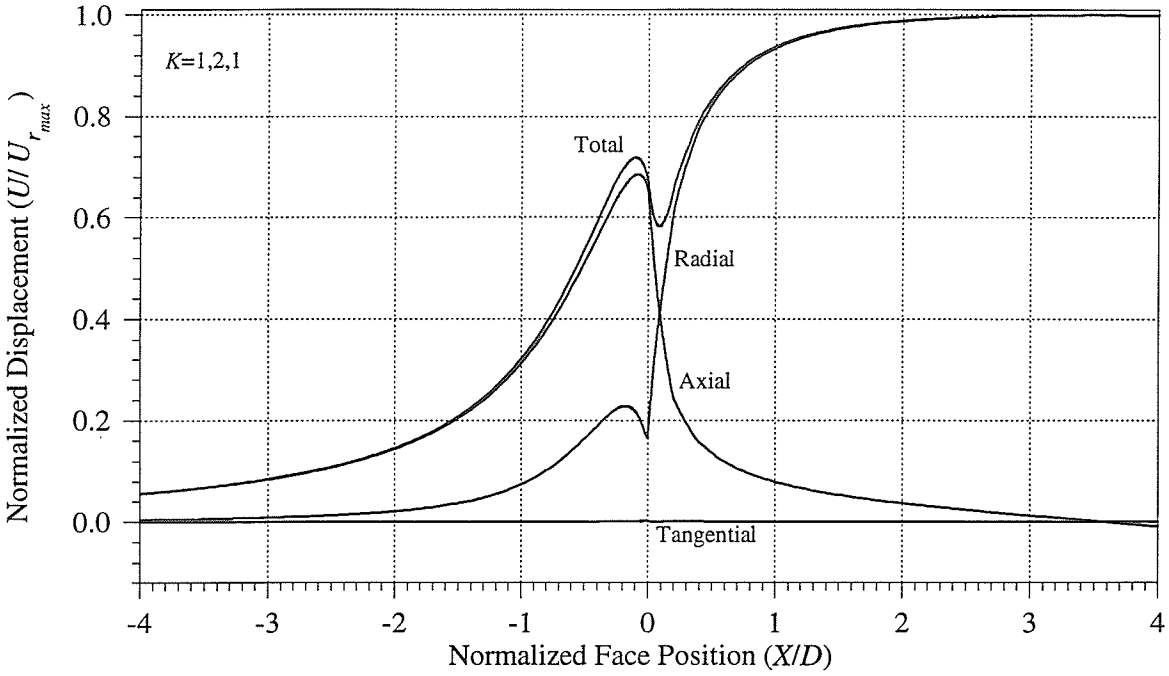

Figure B.14: Components of displacement for $K = 1, 2, 1$.

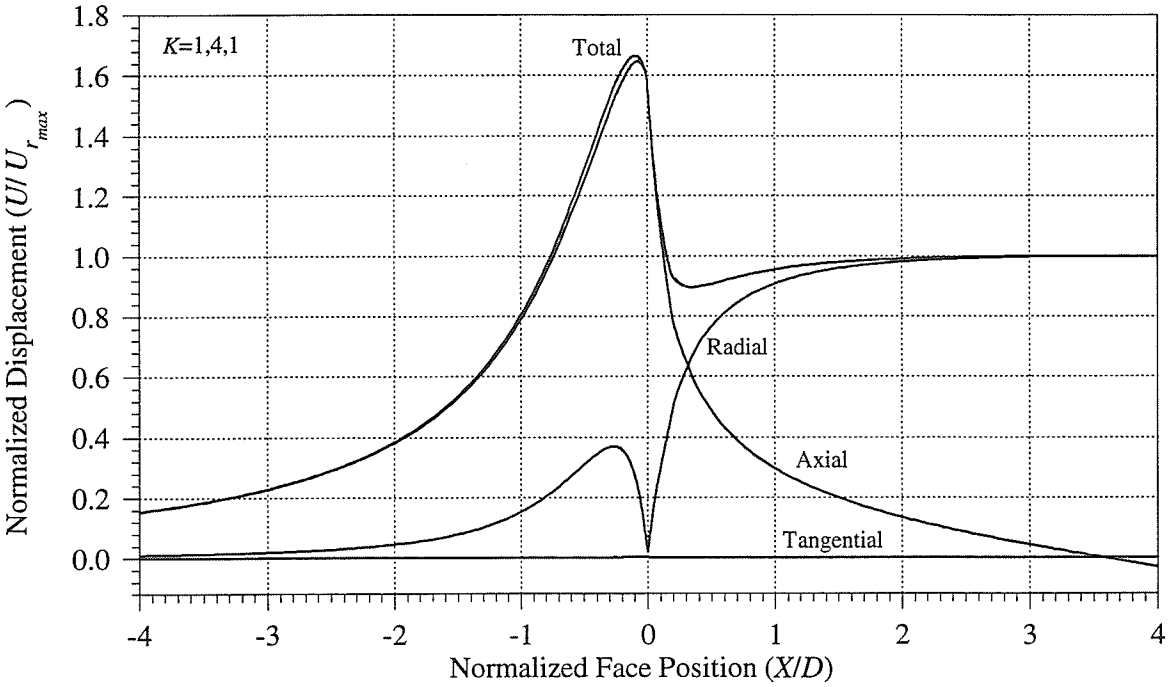

Figure B.15: Components of displacement for $K = 1, 4, 1$.

B.3 Displacement Responses at the Tunnel Wall for Non-axisymmetric Cases

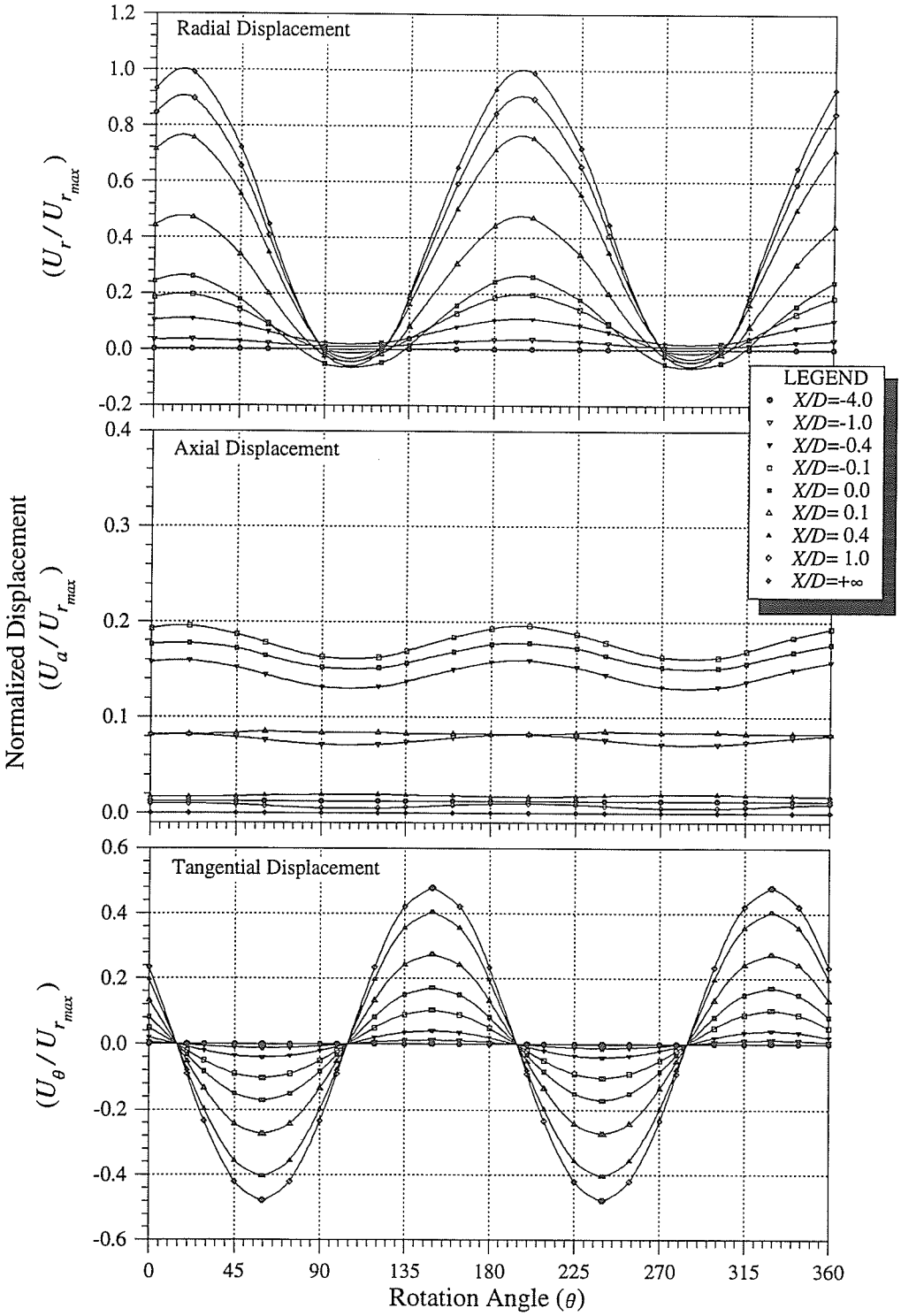

Figure B.16: Displacement responses versus rotation angle for $K = 3.93, 3.43, 1$ with σ_1 at $\theta = 14.5°$.

B.4 Displacement Responses versus Radial Distance for the Partitioned Stress Tensor

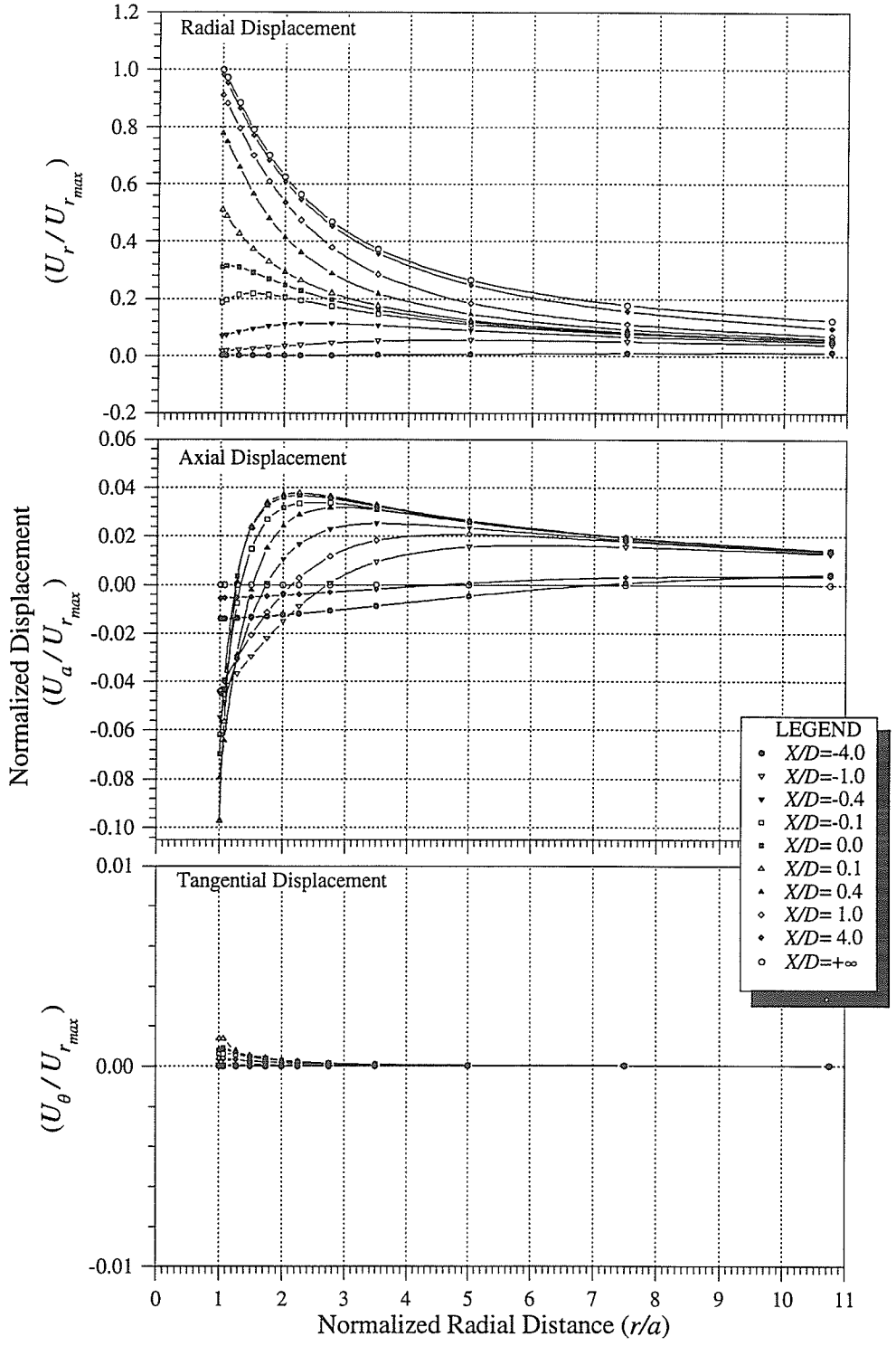

Figure B.17: Displacement response versus radial distance for σ_{11} tensor, $\theta = 0°$.

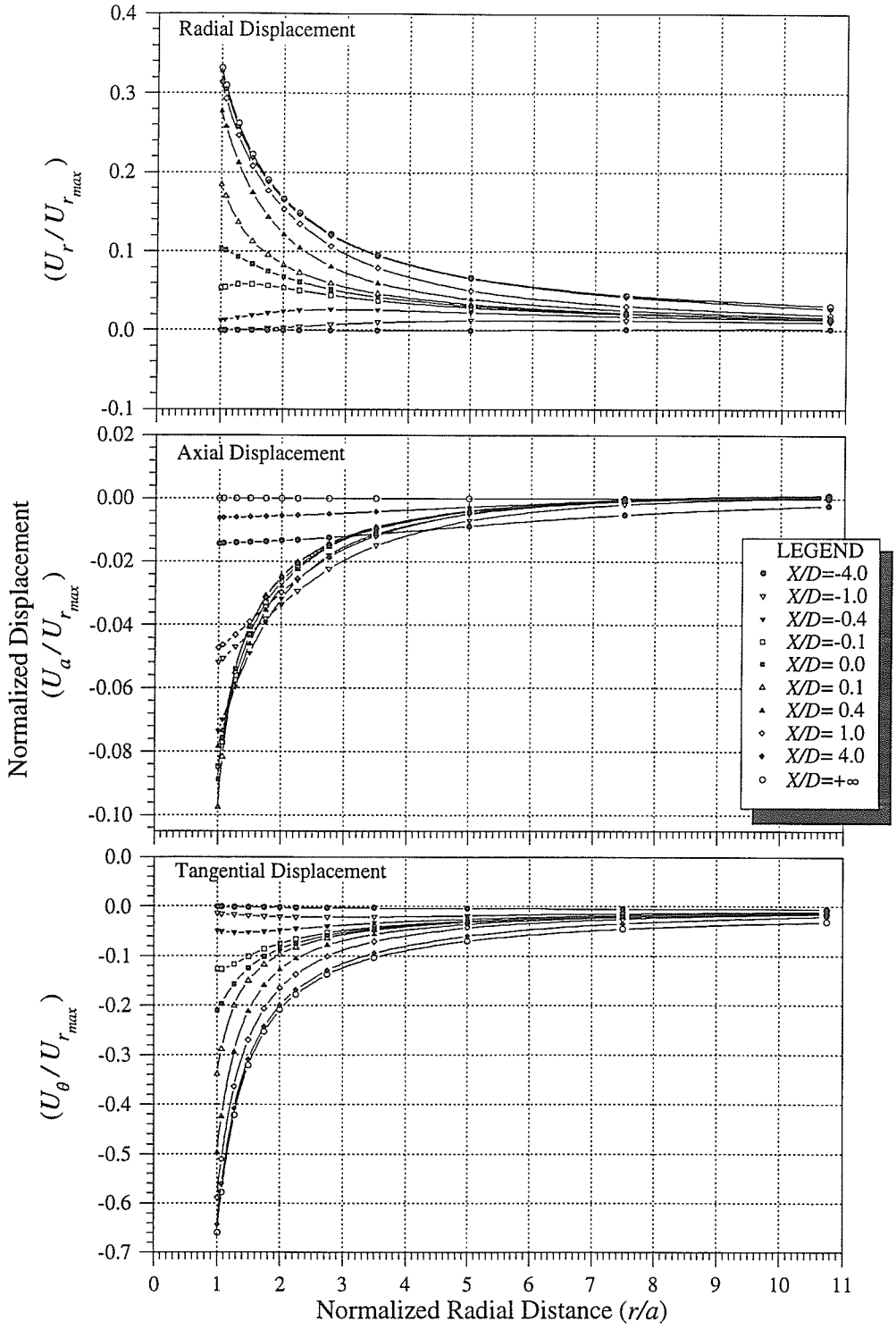

Figure B.18: Displacement response versus radial distance for σ_{11} tensor, $\theta = 45°$.

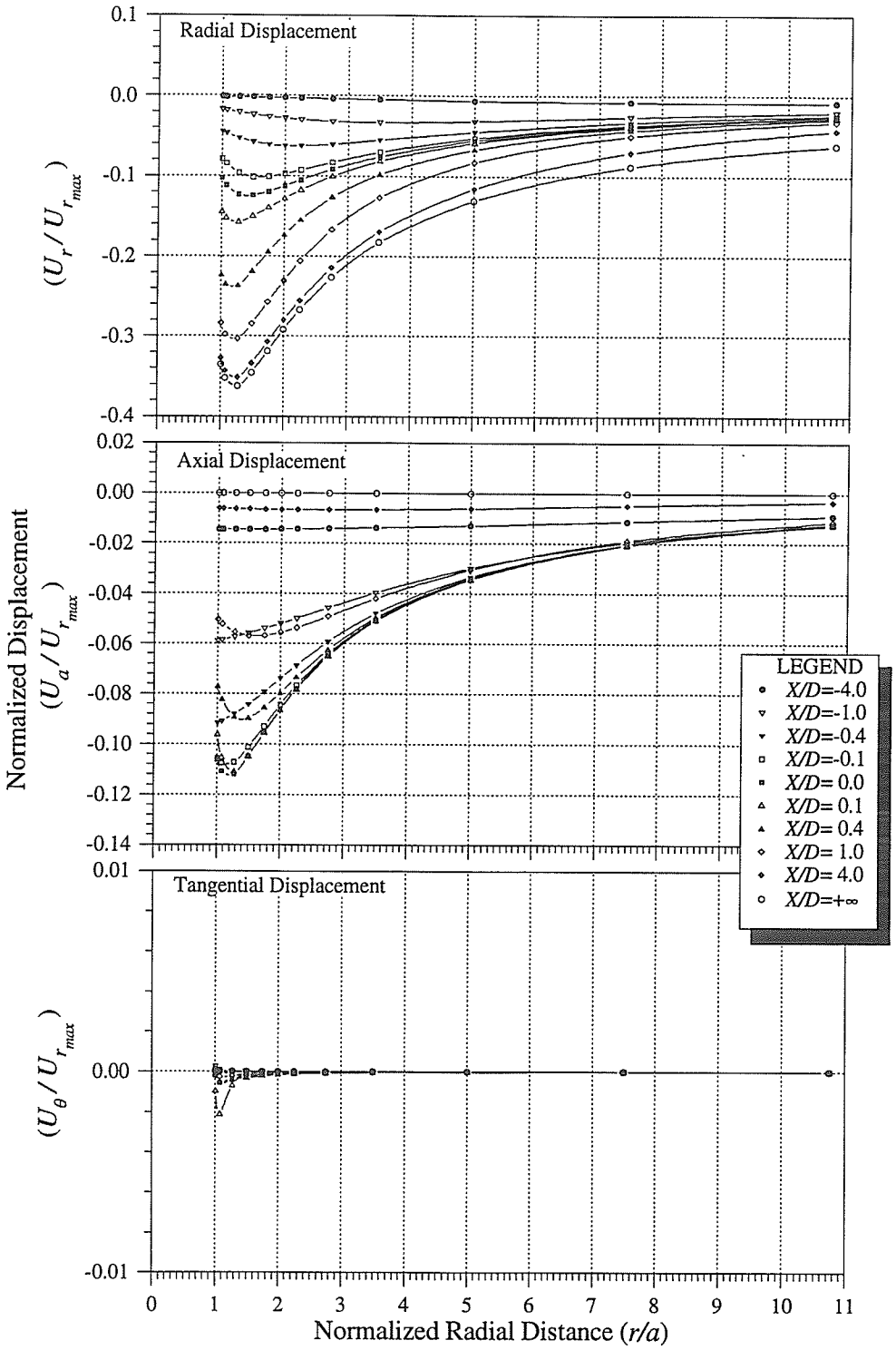

Figure B.19: Displacement response versus radial distance for σ_{11} tensor, $\theta = 90°$.

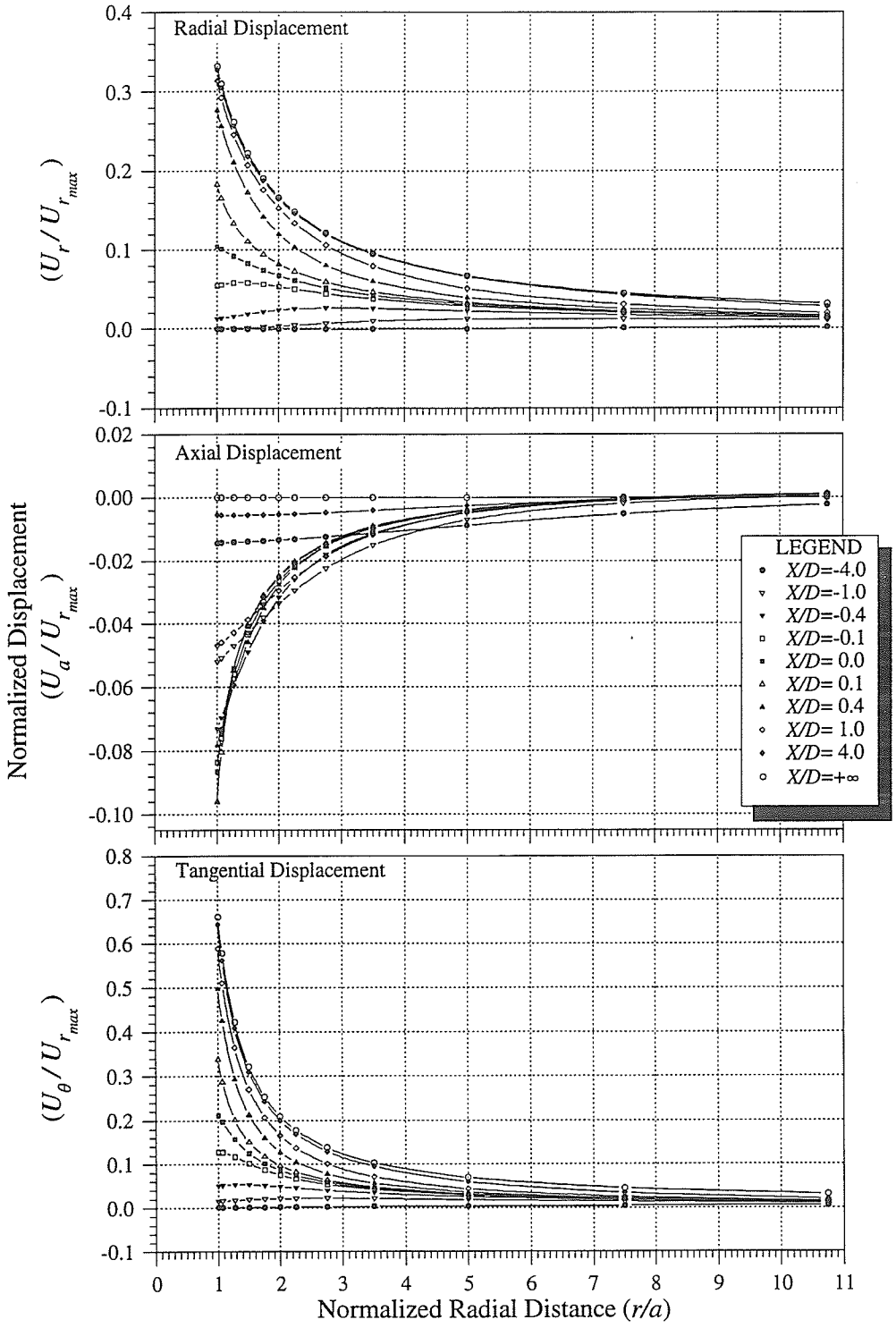

Figure B.20: Displacement response versus radial distance for σ_{11} tensor, $\theta = 135°$.

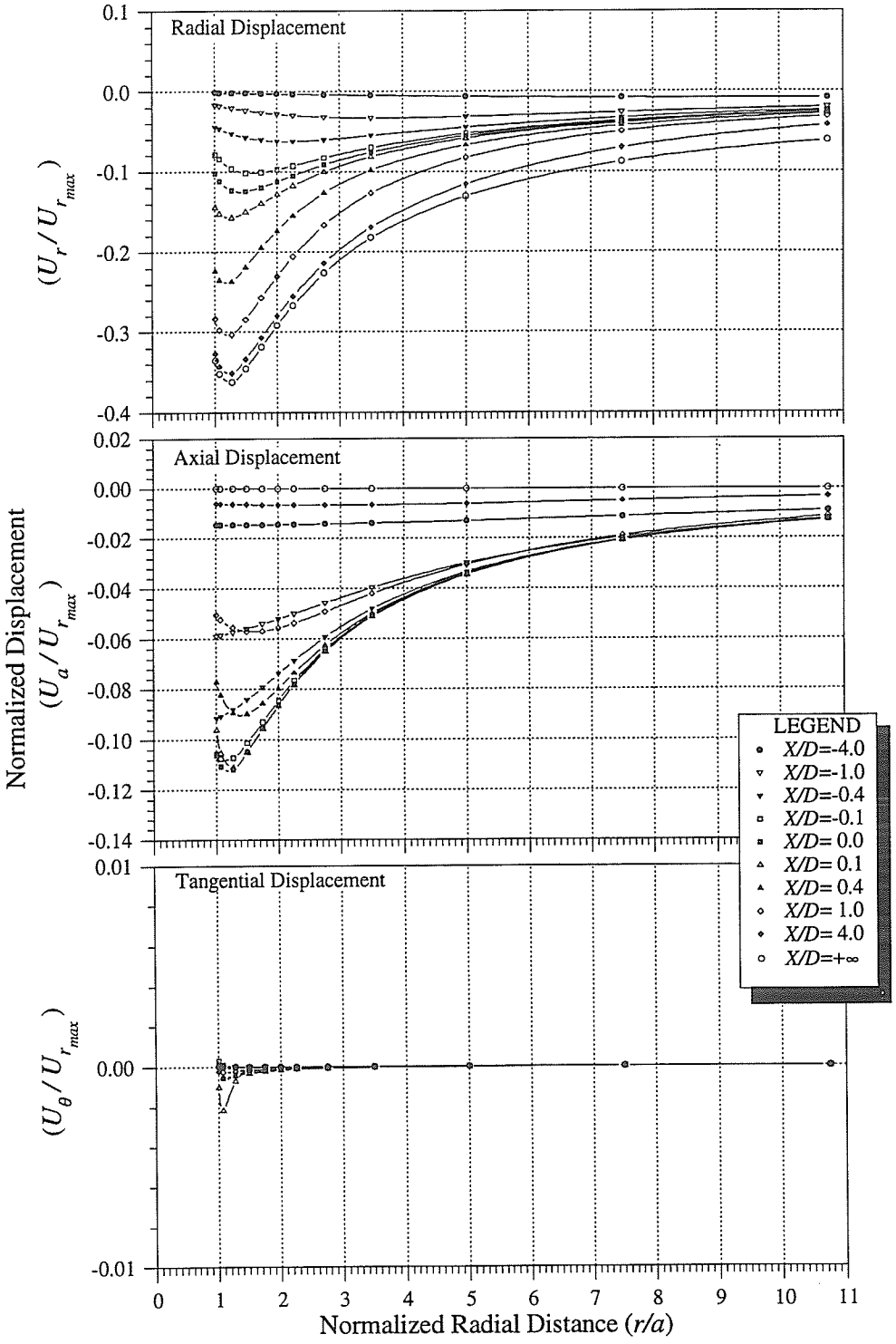

Figure B.21: Displacement response versus radial distance for σ_{33} tensor, $\theta = 0°$.

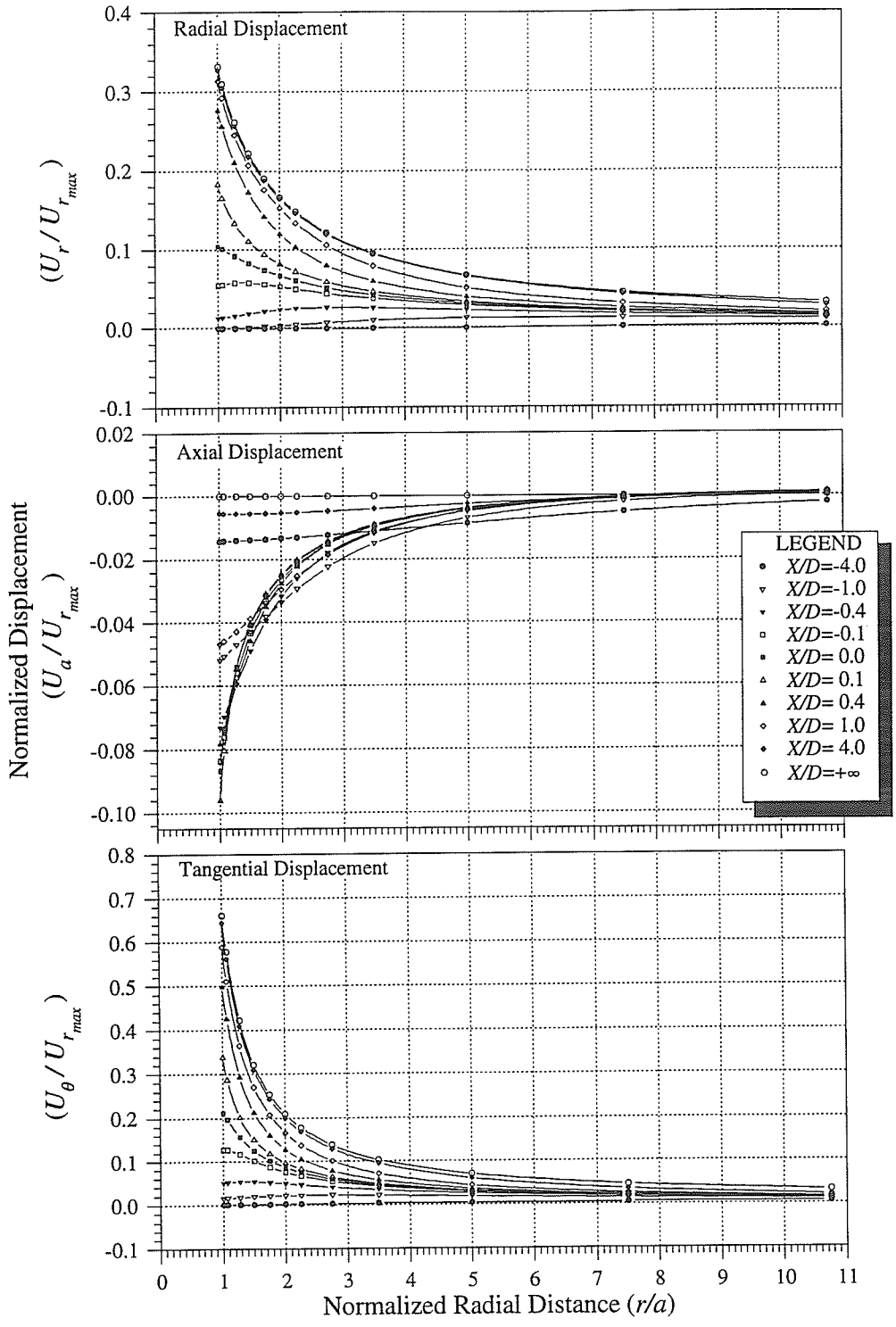

Figure B.22: Displacement response versus radial distance for σ_{33} tensor, $\theta = 45°$.

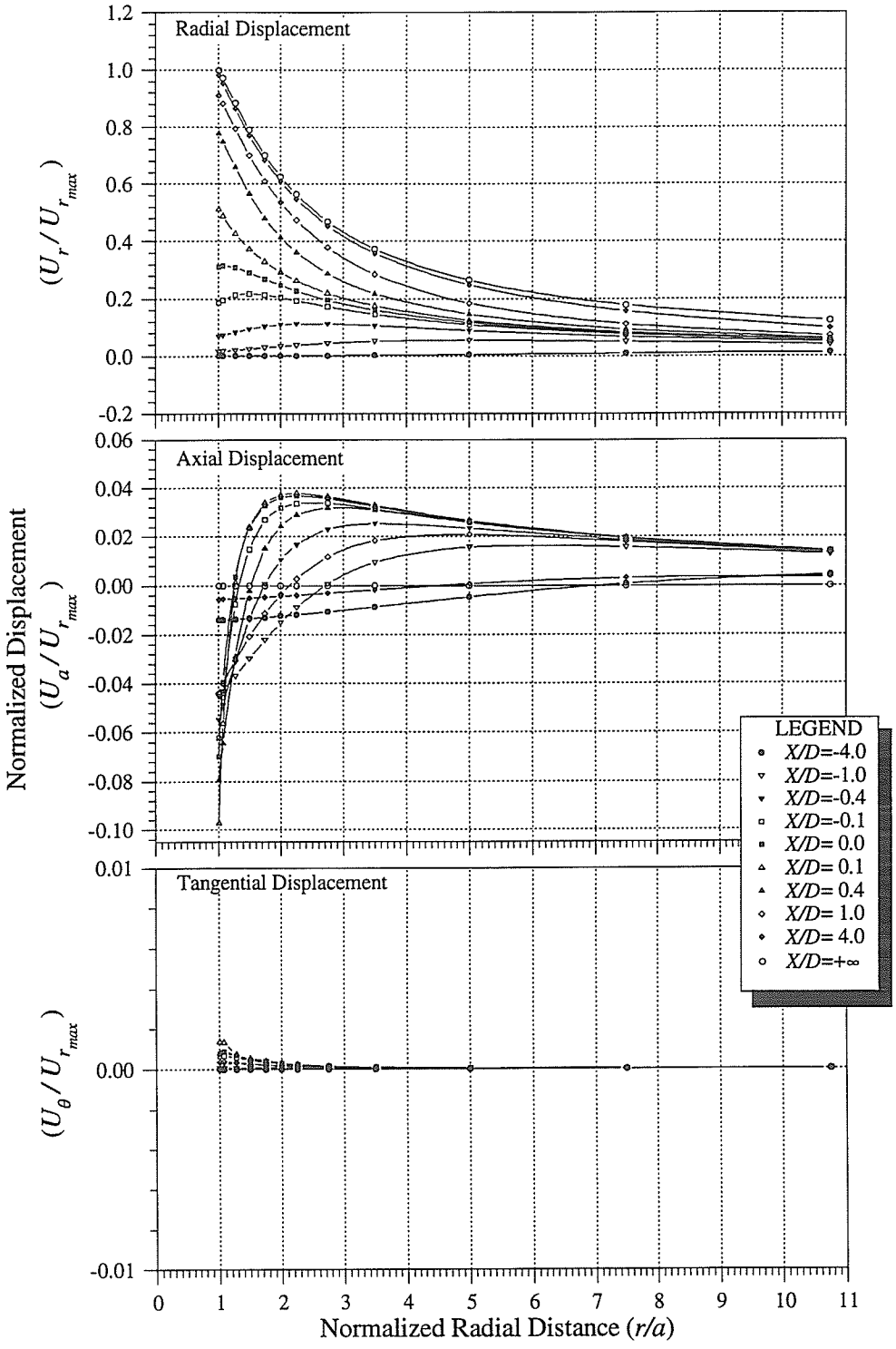

Figure B.23: Displacement response versus radial distance for σ_{33} tensor, $\theta = 90°$.

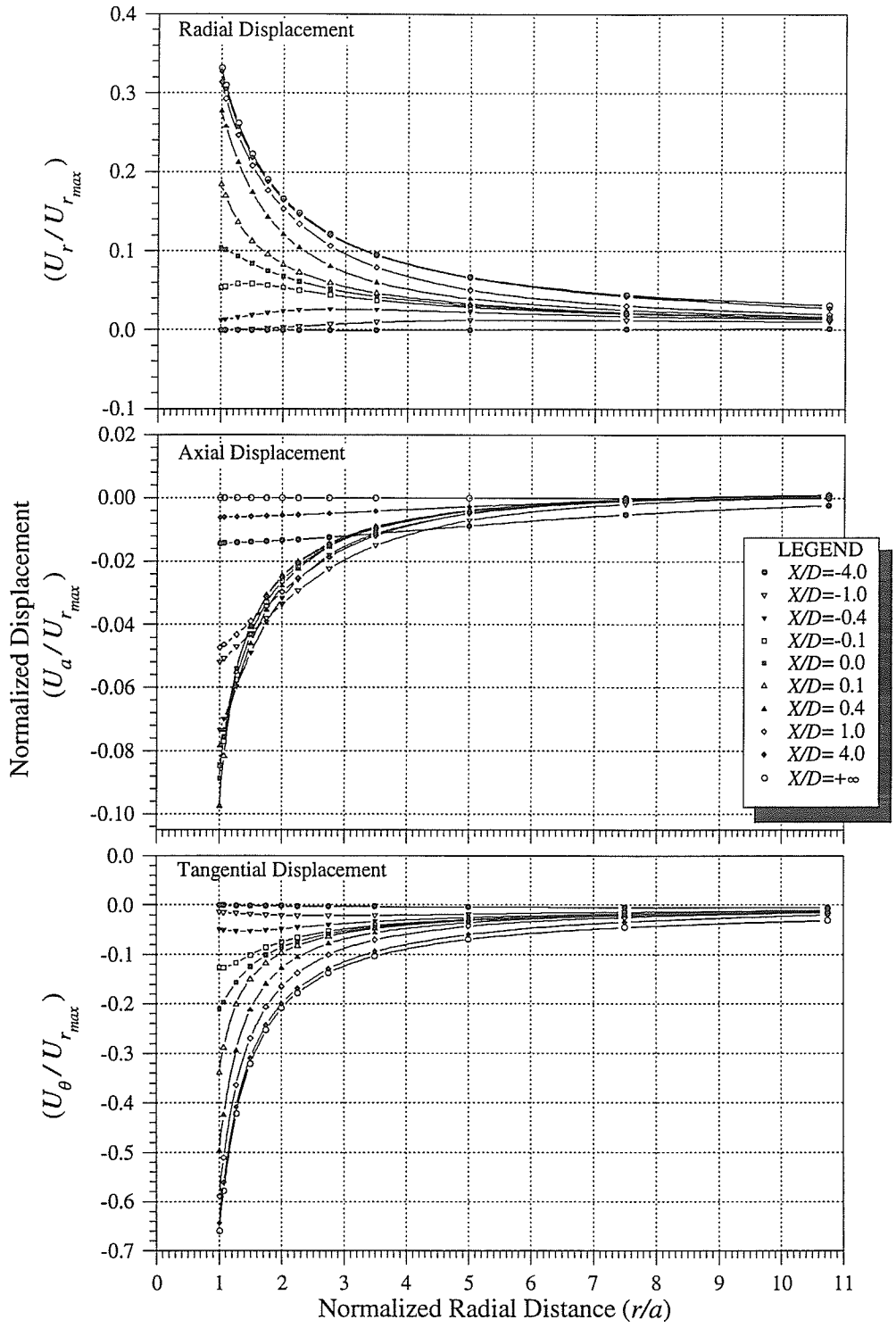

Figure B.24: Displacement response versus radial distance for σ_{33} tensor, $\theta = 135°$.

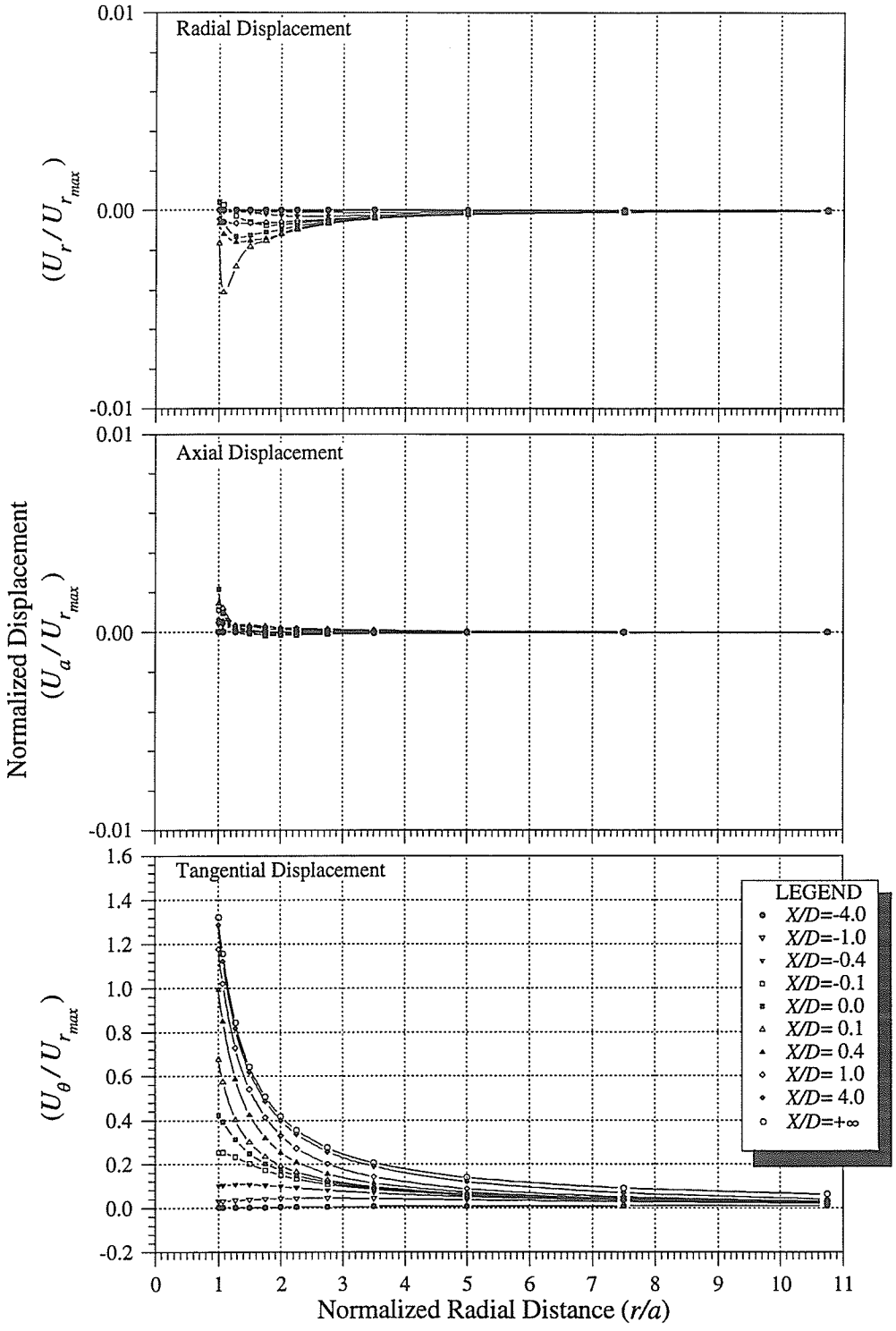

Figure B.25: Displacement response versus radial distance for σ_{13} tensor, $\theta = 0°$.

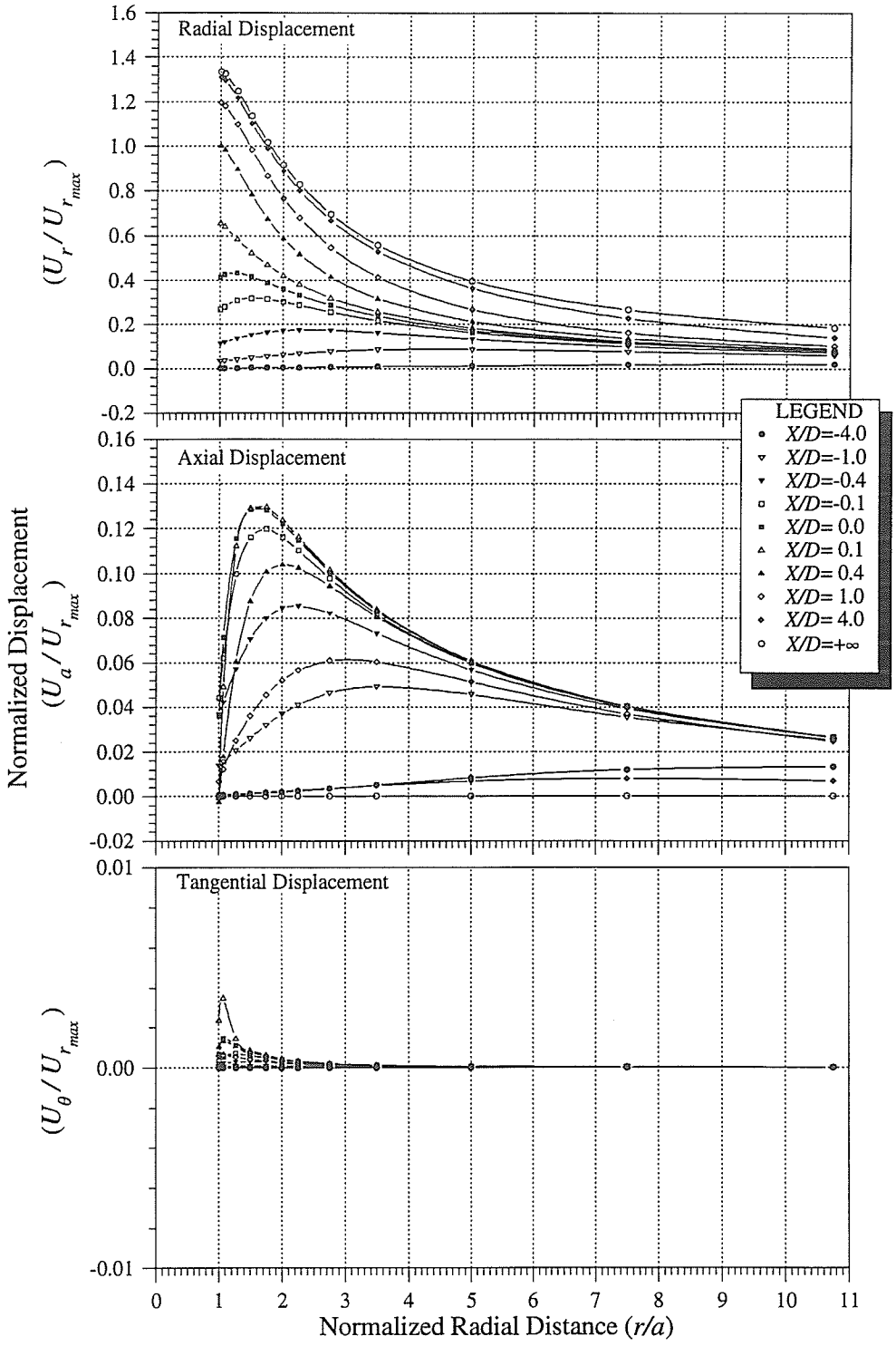

Figure B.26: Displacement response versus radial distance for σ_{13} tensor, $\theta = 45°$.

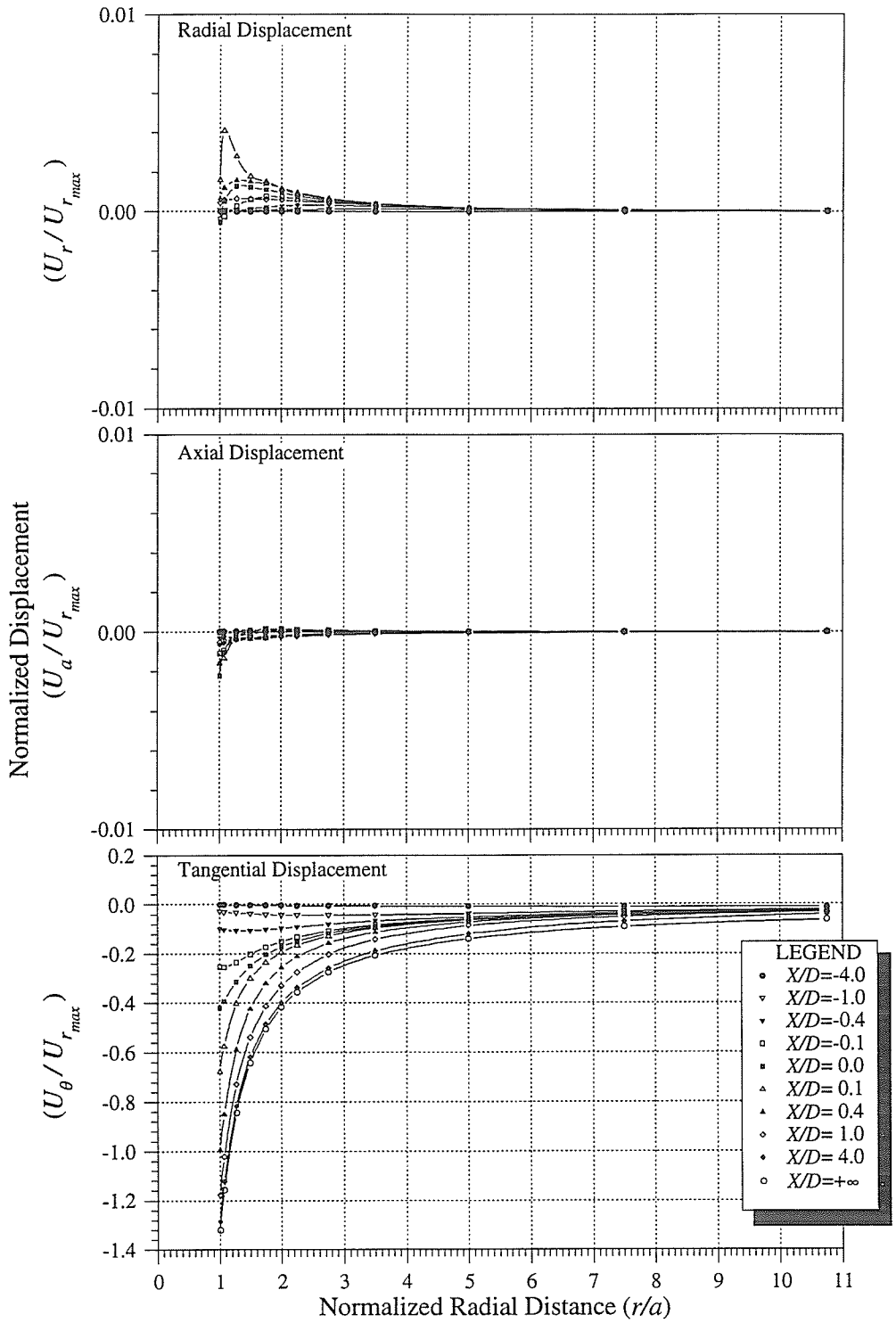

Figure B.27: Displacement response versus radial distance for σ_{13} tensor, $\theta = 90°$.

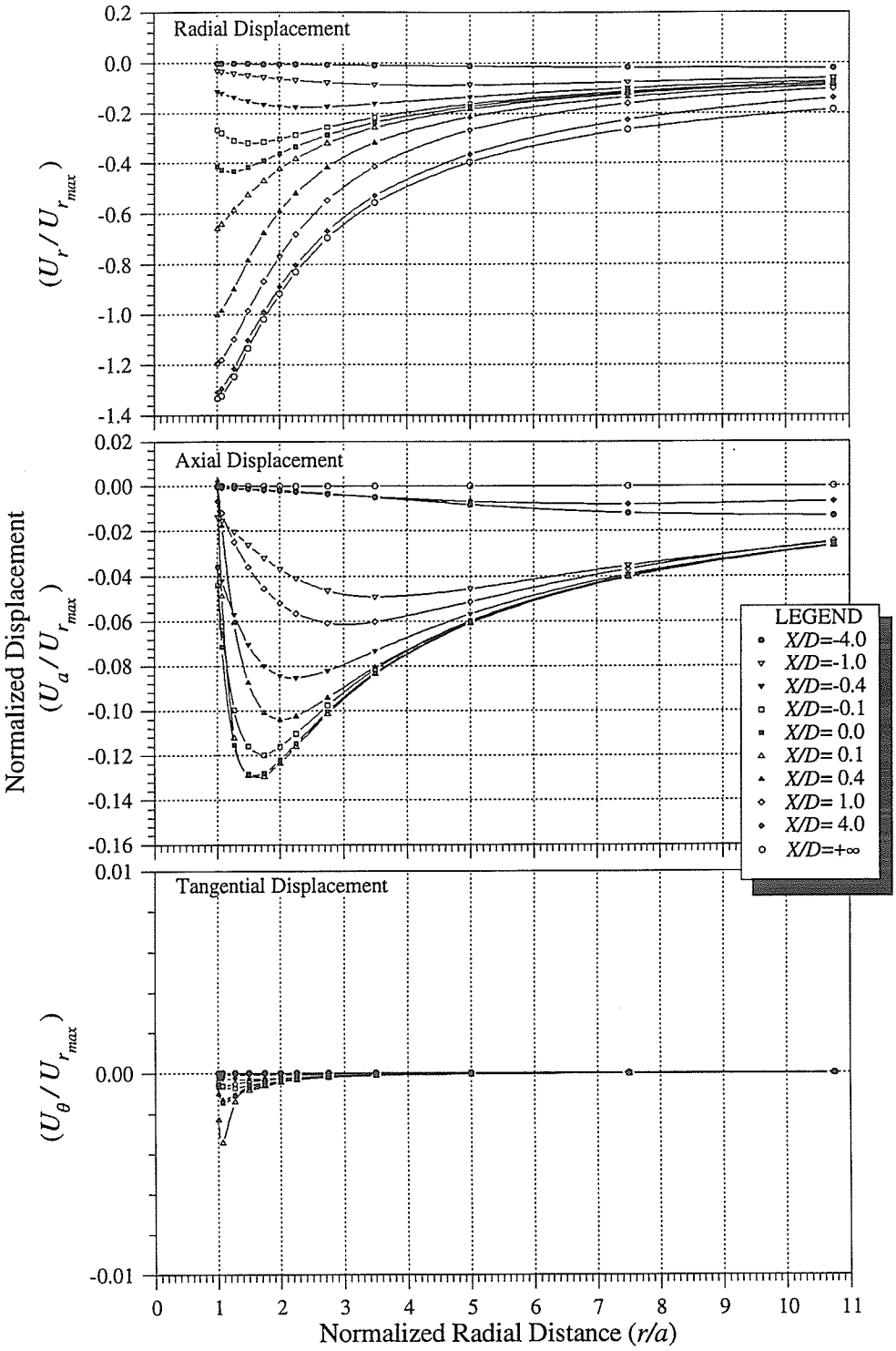

Figure B.28: Displacement response versus radial distance for σ_{13} tensor, $\theta = 135°$.

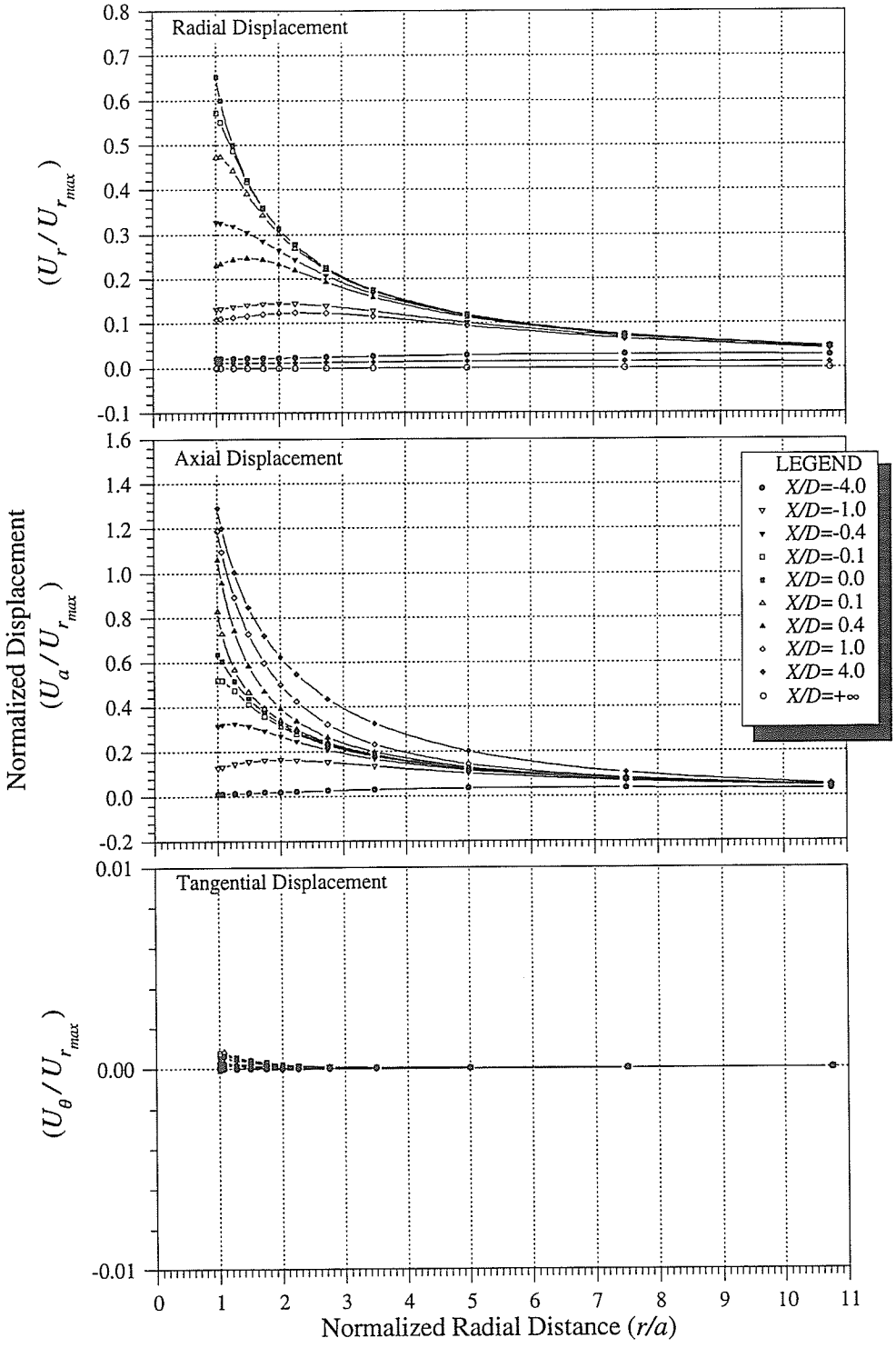

Figure B.29: Displacement response versus radial distance for σ_{12} tensor, $\theta = 0°$.

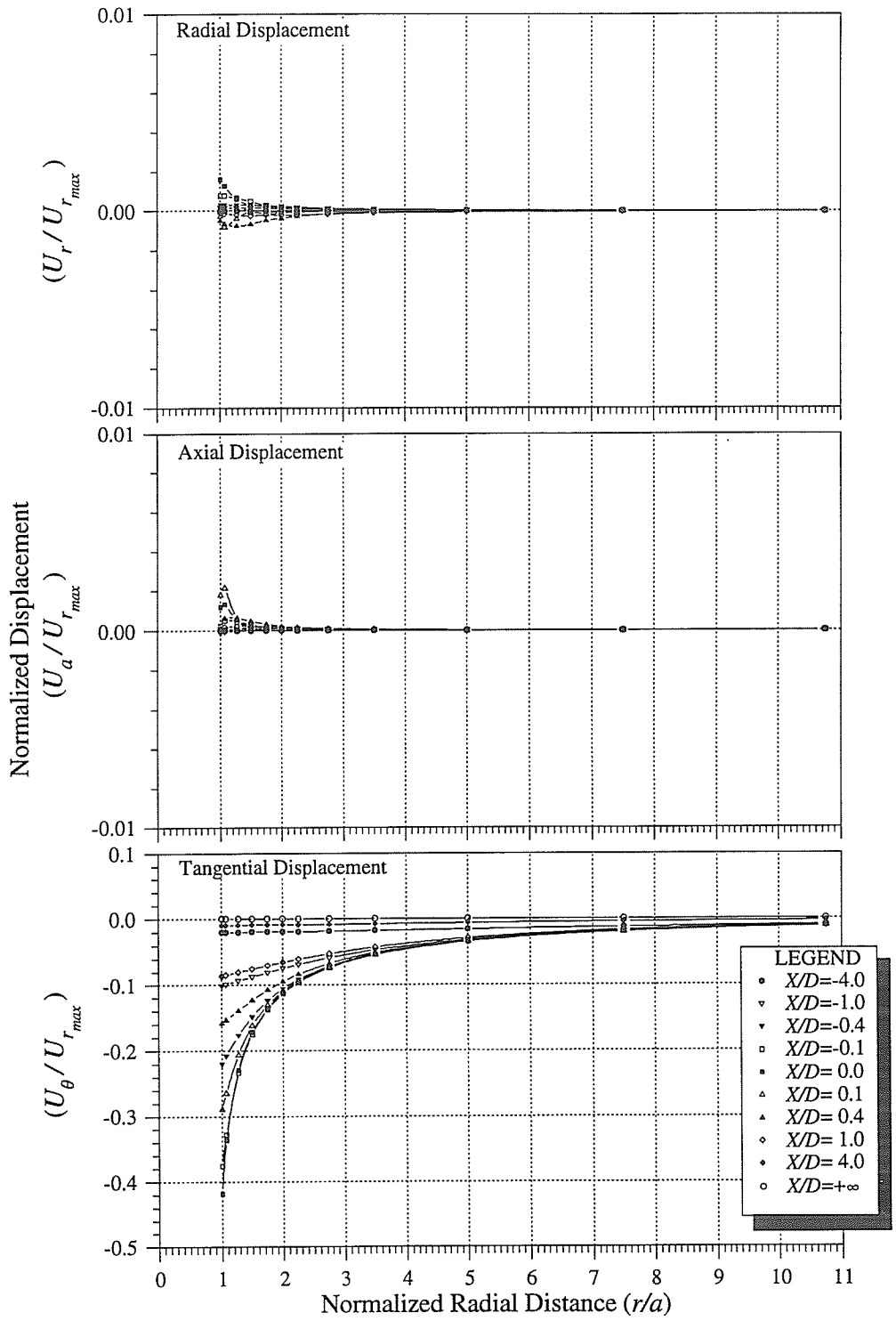

Figure B.30: Displacement response versus radial distance for σ_{12} tensor, $\theta = 90°$.

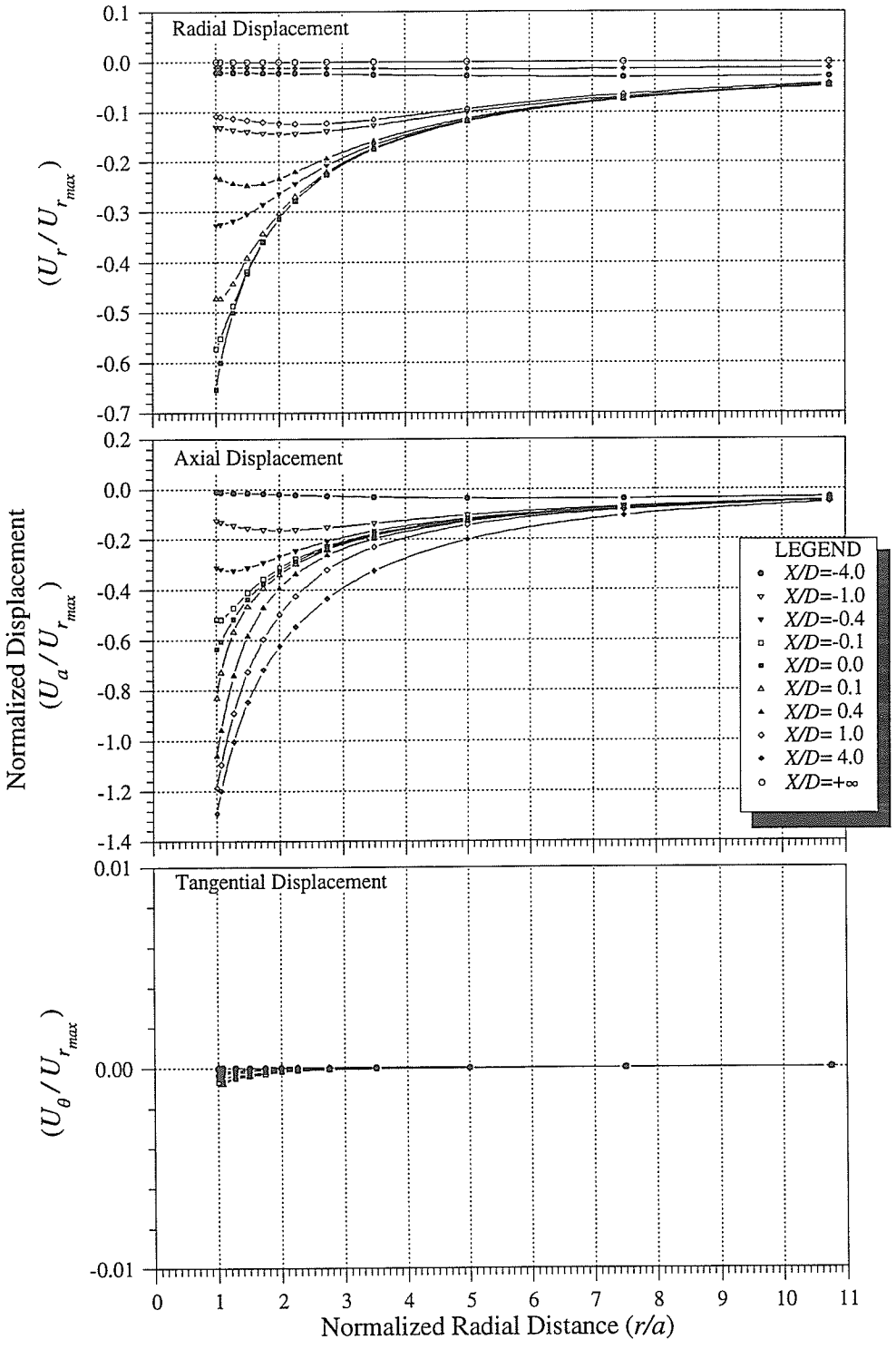

Figure B.31: Displacement response versus radial distance for σ_{12} tensor, $\theta = 180°$.

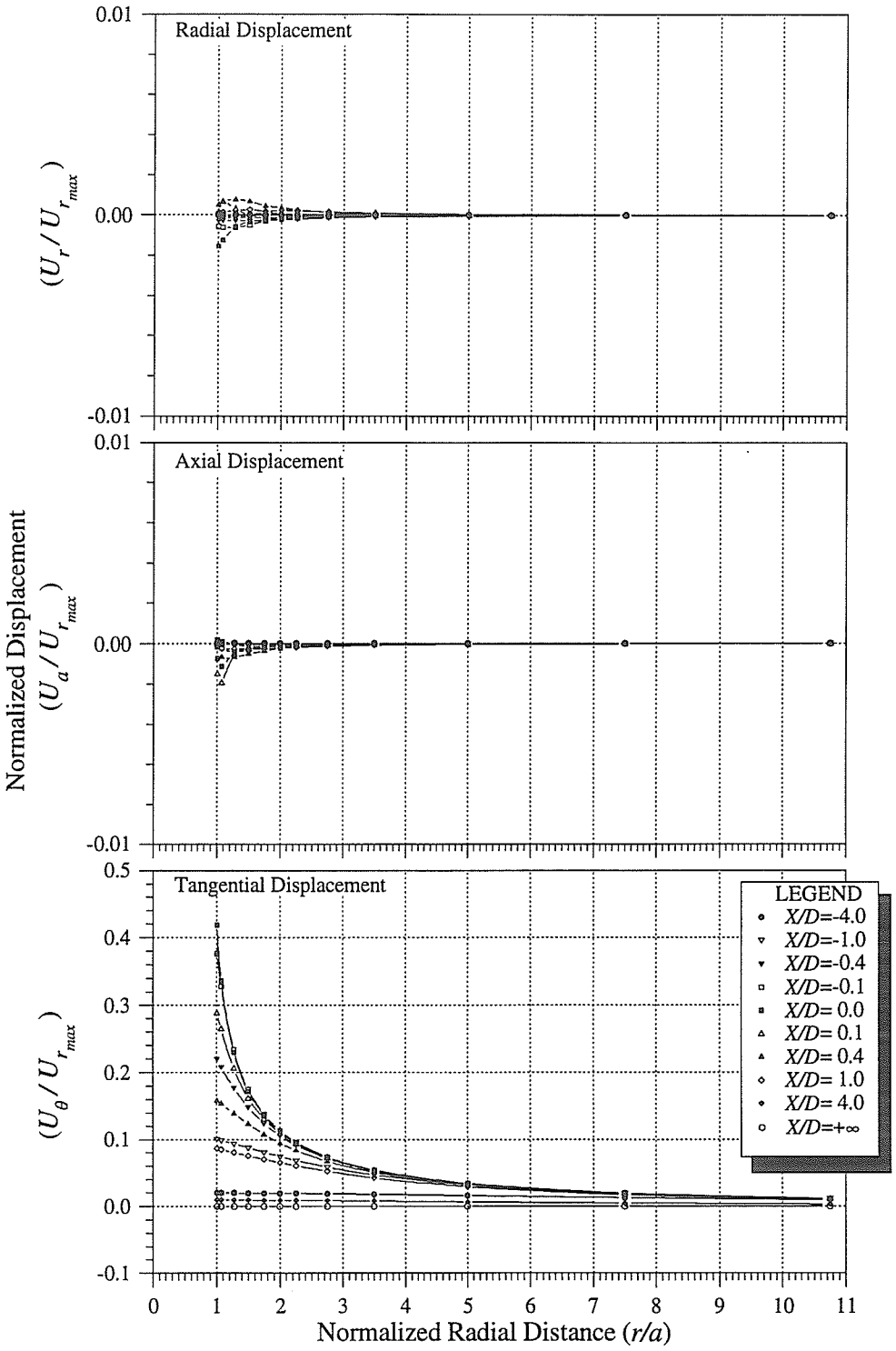

Figure B.32: Displacement response versus radial distance for σ_{12} tensor, $\theta = 270°$.

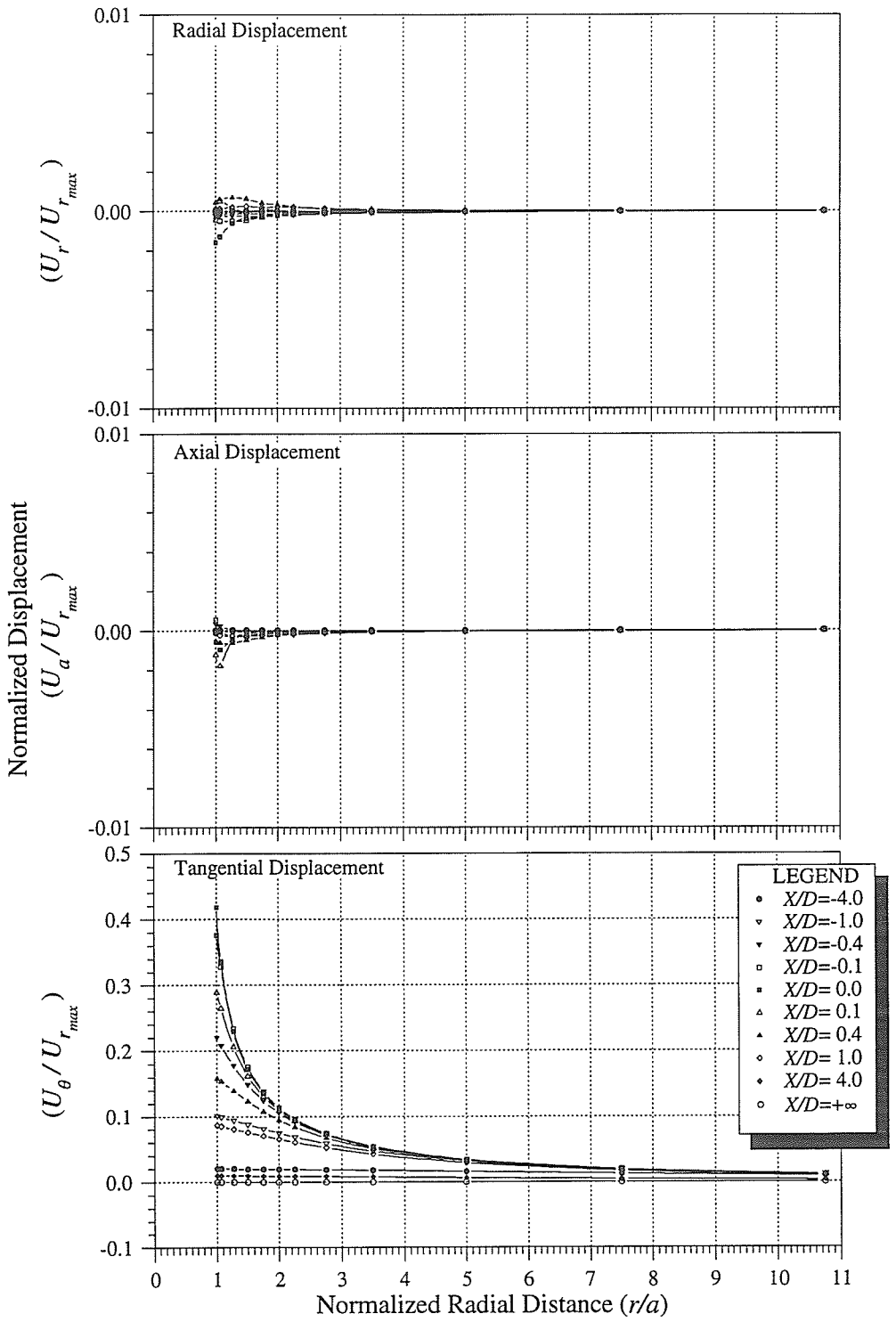

Figure B.33: Displacement response versus radial distance for σ_{23} tensor, $\theta = 0°$.

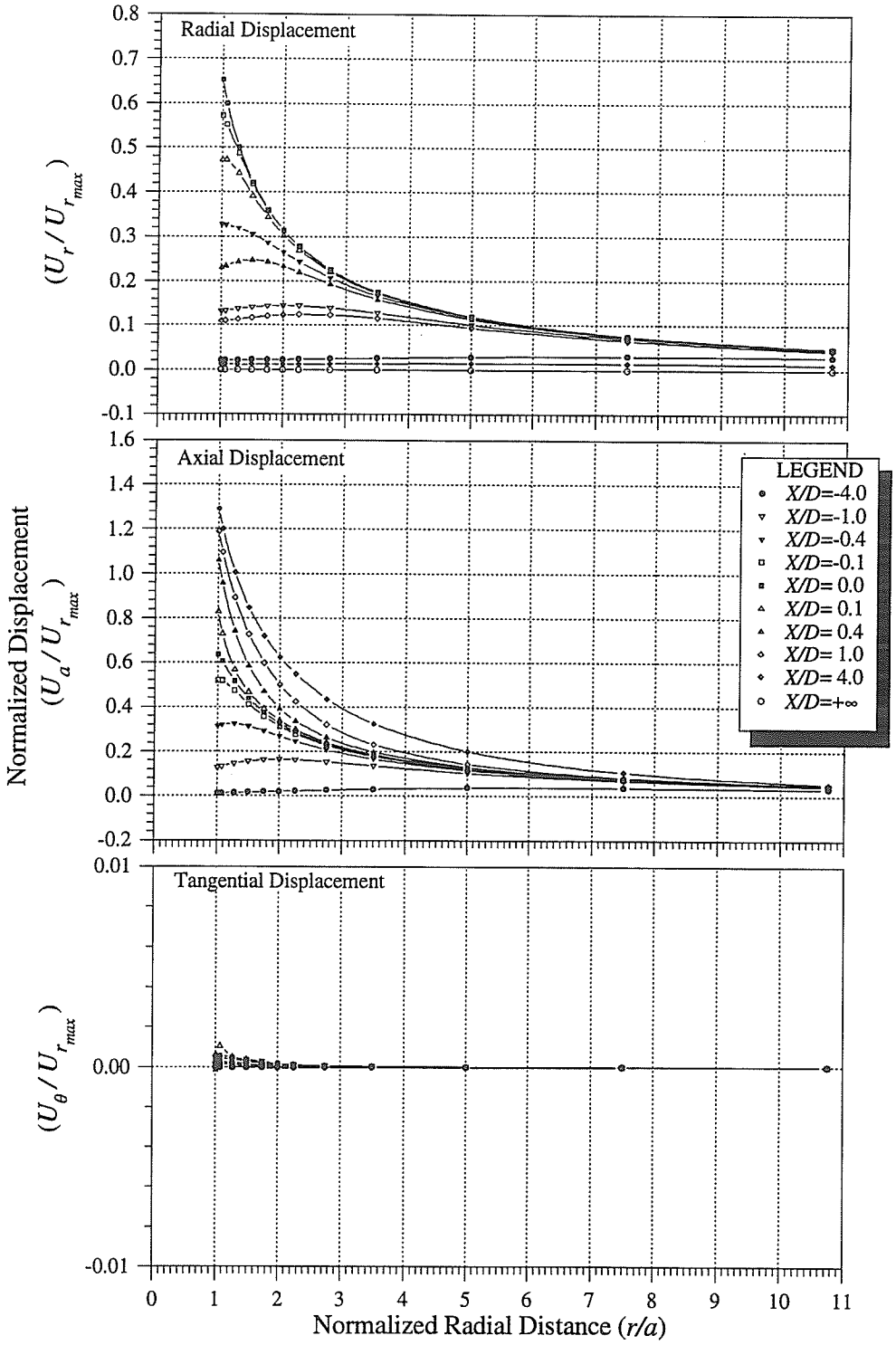

Figure B.34: Displacement response versus radial distance for σ_{23} tensor, $\theta = 90°$.

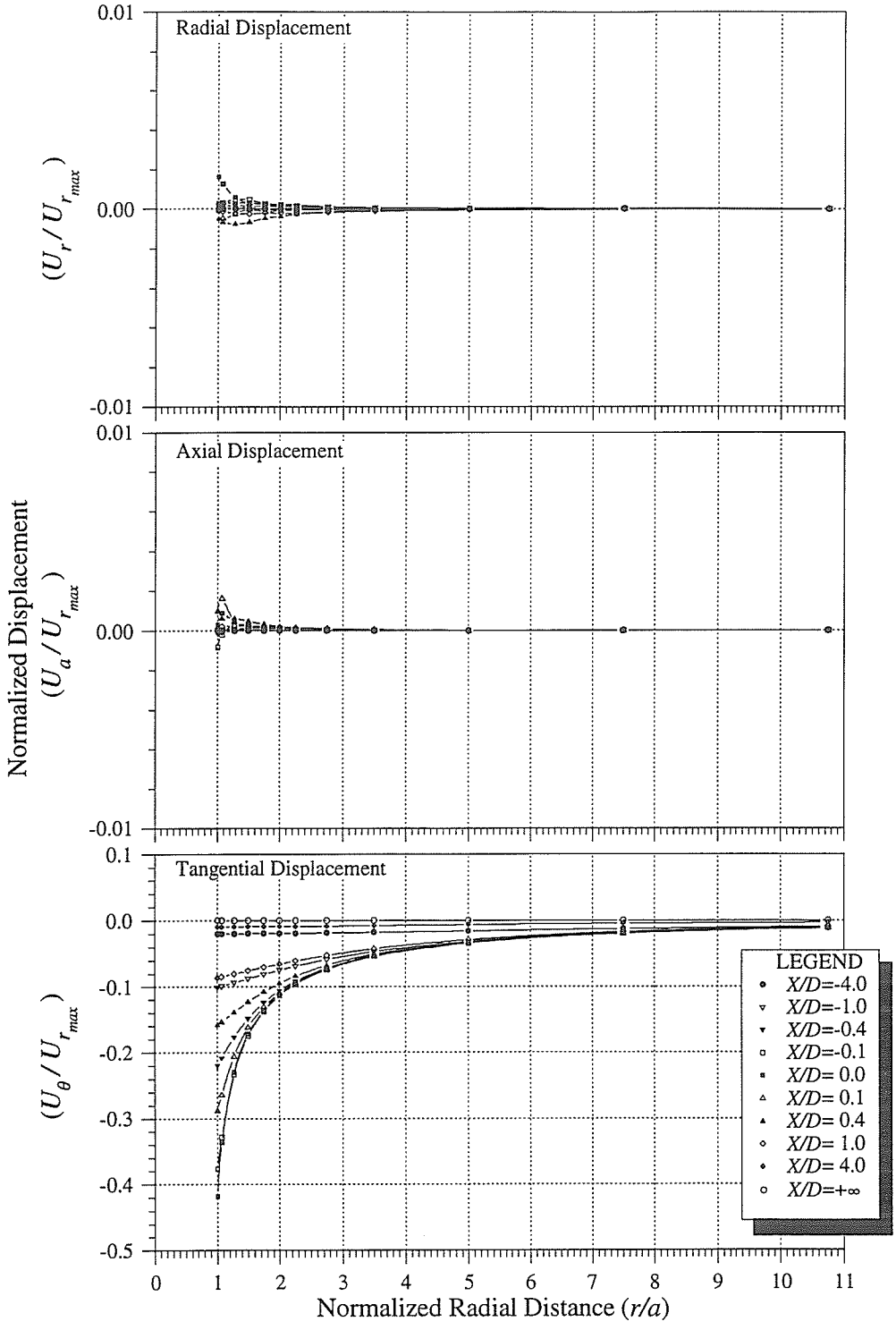

Figure B.35: Displacement response versus radial distance for σ_{23} tensor, $\theta = 180°$.

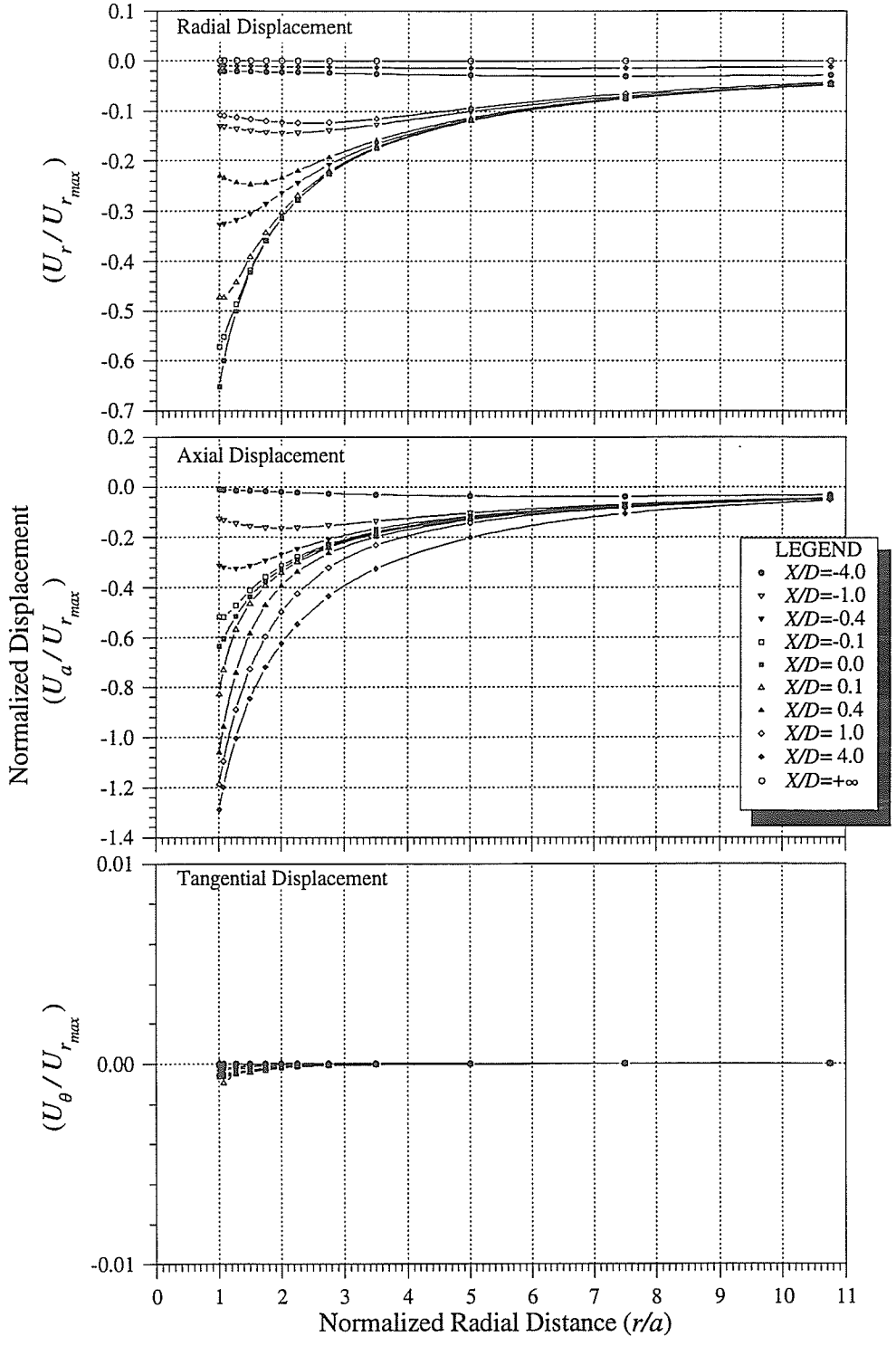

Figure B.36: Displacement response versus radial distance for σ_{23} tensor, $\theta = 270°$.

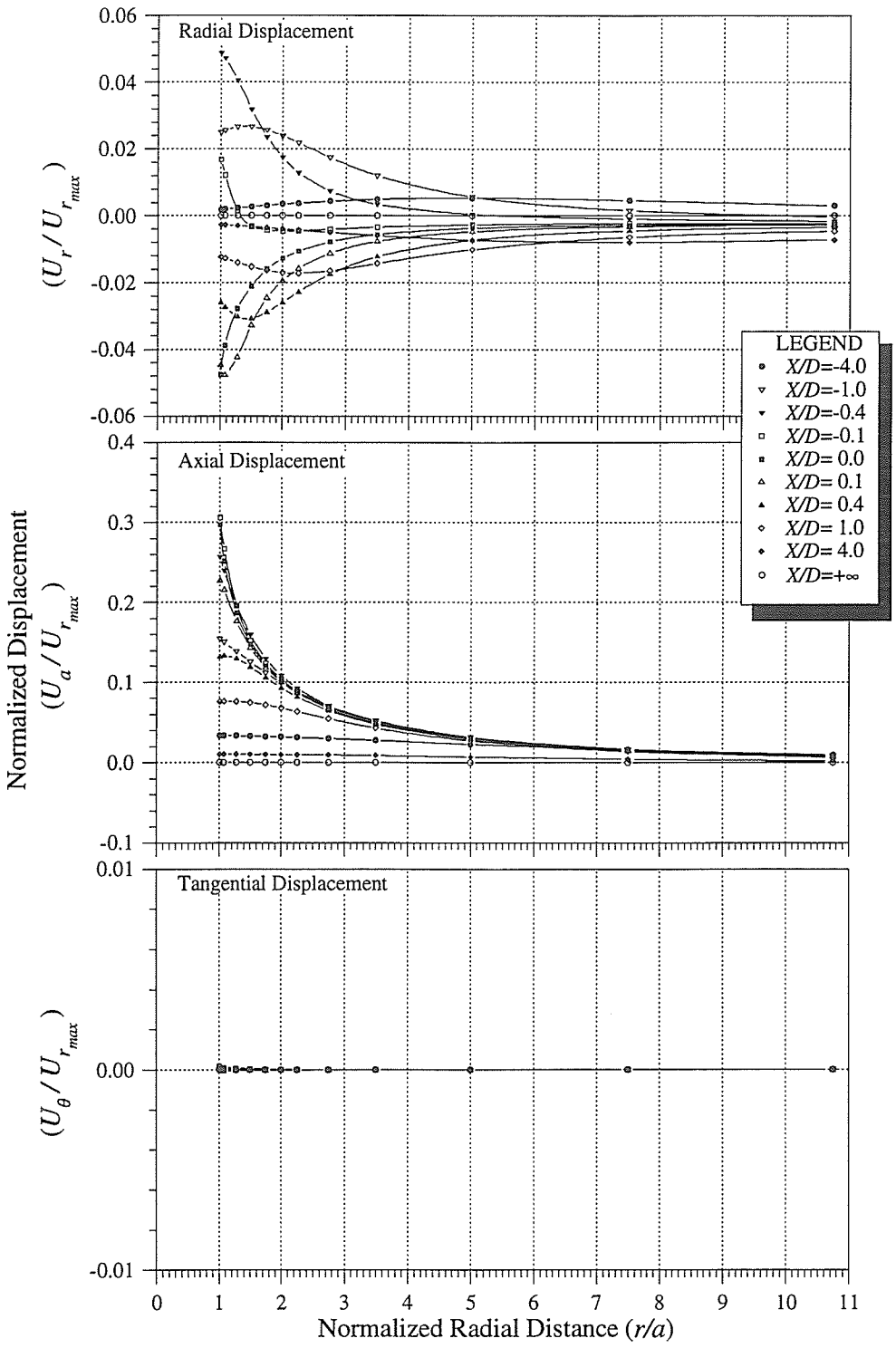

Figure B.37: Displacement response versus radial distance for σ_{22} tensor, all θ.

Appendix C

Derivation of a Radial Displacement Function

The *spliced logistic function*, an approximating function for radial displacement responses at the wall of a cylindrical tunnel, was derived from the general five-parameter logistic function [82]. The general form of the function in the positive x domain is given by

$$U_r(x) = U_r(0) + \frac{[U_r(+\infty) - U_r(0)]}{\left[1 + \left(\frac{x}{A}\right)^B\right]^C}, x \geq 0 \tag{C.1}$$

where $U_r(x)$ is the radial displacement of the tunnel wall when the advancing face is a distance x past the measurement point, $U_r(0)$ is the radial displacement at $x = 0$, $U_r(+\infty)$ is the maximum radial displacement when the tunnel face is an infinite distance past the measurement point, A is the hinge point of the curve (i.e., A is the x-value about which the curve pivots for different values of B), B is a slope parameter, and C is a symmetry parameter. The properties of this function are such that it is easily differentiable, and has an upper asymptote of $U_r(+\infty)$, and a y-intercept of $U_r(0)$.

For the sake of continuity, the function can be extended into the anterior domain, i.e., $x < 0$, by modifying Equation C.1 to

$$U_r(x) = U_r(0) + sign(x) \frac{|U_r(\pm\infty) - U_r(0)|}{\left[1 + \left|\frac{x}{A}\right|^B\right]^C}, \forall x \tag{C.2}$$

where

$$sign\,(x) = \begin{cases} 1 & x > 0 \\ 0 & x = 0 \\ -1 & x < 0 \end{cases}$$

In Equation C.2, $U_r\,(+\infty)$ is used in the numerator for $x \geq 0$, and $U_r\,(-\infty)$ is used for $x < 0$. In all cases, $U_r\,(-\infty) = 0$. Equation C.2 can be rearranged to express the various parameters in dimensionless form by letting

$$y = \frac{U_r\,(x)}{U_{r_{max}}}$$

$$D_l = \frac{U_r\,(0)}{U_{r_{max}}}$$

$$E_l = \frac{U_r\,(+\infty)}{U_{r_{max}}}\,, x \geq 0$$

$$E_l = \frac{U_r\,(-\infty)}{U_{r_{max}}}\,, x < 0$$

$$F = E_l - D_l\,, x \geq 0$$

$$F = D_l - E_l\,, x < 0$$

Consequently,

$$y = D_l + F\left[1 + \left(\frac{x}{A}\right)^B\right]^{-C}\,, x \geq 0 \tag{C.3}$$

The first, second and third derivatives of this function are important in determining the inflection points, the peak in the second derivative curve, and a curvature function κ. The first derivative of Equation C.3 is determined as follows:

$$\frac{dy}{dx} = F\frac{d}{dx}\left\{\left[1 + \left(\frac{x}{A}\right)^B\right]^{-C}\right\}\,, x \geq 0$$

$$Let \qquad \left[1 + \left(\frac{x}{A}\right)^B\right] = u\,, \qquad \frac{du}{dx} = \frac{B}{A^B}\,x^{(B-1)}$$

$$\frac{dy}{dx} = F\left[\frac{d\left(u^{-C}\right)}{du}\,\frac{B}{A^B}\,x^{(B-1)}\right] = \frac{-FBC}{A^B}\left[u^{-(C+1)}\,x^{(B-1)}\right]$$

Consequently, the first derivative is given as

$$\frac{dy}{dx} = \frac{-FBC}{A^B}\left\{\left[1 + \left(\frac{x}{A}\right)^B\right]^{-(C+1)}\,x^{(B-1)}\right\} \tag{C.4}$$

The second derivative of Equation C.3 is determined as follows:

$$\frac{d^2y}{dx^2} = \frac{-FBC}{A^B}\frac{d}{dx}\left\{\left[1+\left(\frac{x}{A}\right)^B\right]^{-(C+1)} x^{(B-1)}\right\}$$

$$Let \qquad \left[1+\left(\frac{x}{A}\right)^B\right]^{-(C+1)} = u\,, \qquad x^{(B-1)} = v$$

$$\frac{duv}{dx} = u\frac{dv}{dx} + v\frac{du}{dx}\,,$$

$$\frac{du}{dx} = \frac{-B\,(C+1)}{A^B}\left\{\left[1+\left(\frac{x}{A}\right)^B\right]^{-(C+2)} x^{(B-1)}\right\}\,,$$

$$\frac{dv}{dx} = (B-1)\,x^{(B-2)}$$

Therefore,

$$\frac{d^2y}{dx^2} = \frac{-FBC\,(B-1)}{A^B}\left\{\left[1+\left(\frac{x}{A}\right)^B\right]^{-(C+1)} x^{(B-2)}\right\} + \frac{FB^2C\,(C+1)}{A^{2B}}\left\{\left[1+\left(\frac{x}{A}\right)^B\right]^{-(C+2)} x^{2(B-1)}\right\} \tag{C.5}$$

To determine the inflection points, Equation C.5 is set to zero, and terms are rearranged as follows:

$$(B-1)\left\{\left[1+\left(\frac{x}{A}\right)^B\right]^{-(C+1)} x^{(B-2)}\right\} = \frac{B\,(C+1)}{A^B}\left\{\left[1+\left(\frac{x}{A}\right)^B\right]^{-(C+2)} x^{2(B-1)}\right\}$$

Rearranging

$$\frac{(B-1)\,A^B}{B\,(C+1)} = x^B\left[1+\left(\frac{x}{A}\right)^B\right]^{-1} = \frac{A^Bx^B}{A^B+x^B}$$

Inverting

$$\frac{B\,(C+1)}{(B-1)\,A^B} = \frac{1}{x^B} + \frac{1}{A^B}$$

Combining terms

$$\frac{BC+1}{(B-1)A^B} = \frac{1}{x^B}$$

Therefore,

$$x = \pm A\left(\frac{B-1}{BC+1}\right)^{\frac{1}{B}} \tag{C.6}$$

From numerical modeling, the inflection point in the radial displacement response versus face position coincides with $x = 0$, which constrains the exponents B and C for $A \neq 0$ such that either $B = 1$, or $C = -\frac{1}{B}$ with $B < 0$. Assuming $B \neq 1$ and $A \neq 0$, Equations C.3, C.4, and C.5 then become, respectively:

$$y = D_l + F\left[1 + \left(\frac{x}{A}\right)^B\right]^{\frac{1}{B}}, x \geq 0 \tag{C.7}$$

$$\frac{dy}{dx} = \frac{F}{A^B}\left\{\left[1 + \left(\frac{x}{A}\right)^B\right]^{\left(\frac{1}{B}-1\right)} x^{(B-1)}\right\}, x \geq 0 \tag{C.8}$$

$$\frac{d^2y}{dx^2} = \frac{F(B-1)}{A^B}\left\{\left[1 + \left(\frac{x}{A}\right)^B\right]^{\left(\frac{1}{B}-1\right)} x^{(B-2)}\right\} - \frac{F(B-1)}{A^{2B}}\left\{\left[1 + \left(\frac{x}{A}\right)^B\right]^{\left(\frac{1}{B}-2\right)} x^{2(B-1)}\right\}, x \geq 0 \tag{C.9}$$

Making these equations continuous functions for all x:

$$y = D_l + sign(x)\, F\left[1 + \left|\frac{x}{A}\right|^B\right]^{\frac{1}{B}}, \forall\, x \tag{C.10}$$

$$\frac{dy}{dx} = \frac{F}{|A|^B}\left\{\left[1 + \left|\frac{x}{A}\right|^B\right]^{\left(\frac{1}{B}-1\right)} |x|^{(B-1)}\right\}, \forall\, x \tag{C.11}$$

$$\frac{d^2y}{dx^2} = sign(x)\frac{F(B-1)}{|A|^B}\left\{\left[1 + \left|\frac{x}{A}\right|^B\right]^{\left(\frac{1}{B}-1\right)} |x|^{(B-2)}\right\} - sign(x)\frac{F(B-1)}{|A|^{2B}}\left\{\left[1 + \left|\frac{x}{A}\right|^B\right]^{\left(\frac{1}{B}-2\right)} |x|^{2(B-1)}\right\}, \forall\, x \tag{C.12}$$

From comparison with responses from numerical modeling, it was found that most radial displacement responses versus face position could be approximated using a function of the form

$$U_r(x) = y + \lambda \frac{d^2y}{dx^2} \tag{C.13}$$

where the function y and its second derivative are given respectively by Equations C.10 and C.12. Equation C.13 is the *spliced logistic function.* An example of such a function, fit to modelling results for an axisymmetric case with stress ratios $K = 1, 2, 1$, is shown in Figure C.1. For more complicated cases, combinations of *spliced logistic functions* with $\lambda = 0$ were found to provide near-perfect matches to the radial displacement response. The curvature function κ was found to be useful in comparing the shapes of different responses. Knowing the first and second derivatives of the original function, the curvature κ of the

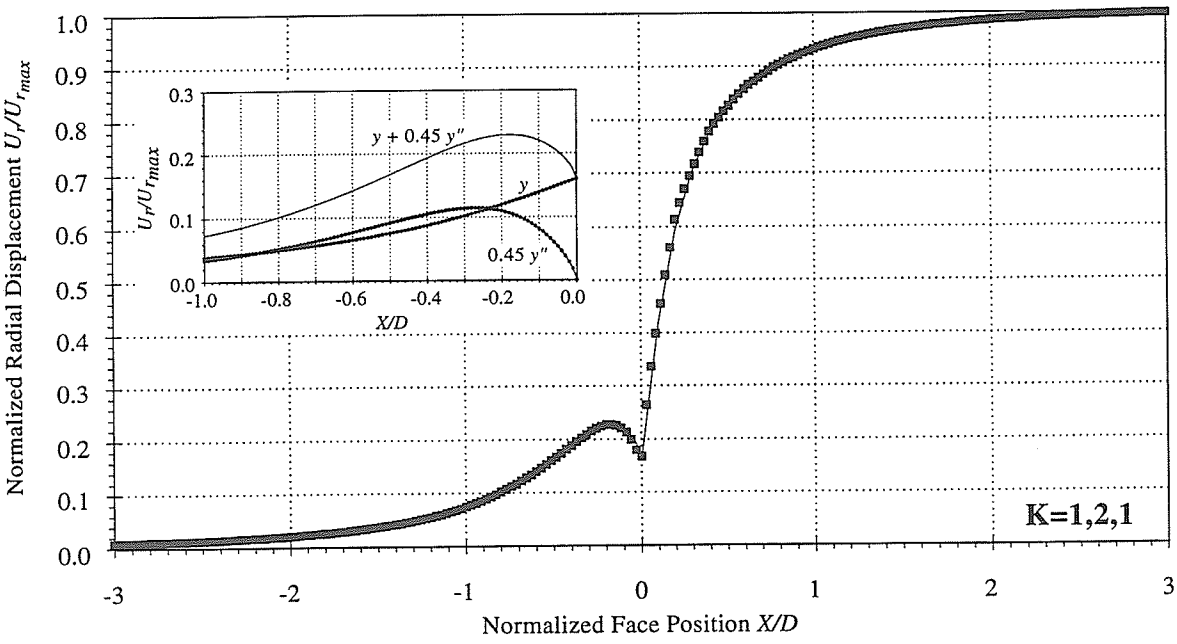

Figure C.1: Comparison of *spliced logistic function* to the radial displacement response for $K = 1, 2, 1$. Note that in the anterior domain, $\lambda = 0.45$, but in the posterior domain, $\lambda = 0$. The responses associated with the function y and its second derivative in the anterior domain are shown in the inset. The coefficient of determination r^2 is 0.99999 for $X/D < 0$ and 0.99941 for $X/D \geq 0$.

function is given by:

$$\kappa = \frac{\left|\frac{d^2y}{dx^2}\right|}{\left[1+\left(\frac{dy}{dx}\right)^2\right]^{\frac{3}{2}}}, \forall\, x \tag{C.14}$$

The peaks in the second derivative curve are also useful for matching responses involving $\lambda \neq 0$. The third derivative of Equation C.3 is determined as follows:

$$\frac{d^3y}{dx^3} = \frac{F(B-1)}{A^B}\frac{d}{dx}\left\{\left[1+\left(\frac{x}{A}\right)^B\right]^{\left(\frac{1}{B}-1\right)} x^{(B-2)}\right\} - \frac{F(B-1)}{A^{2B}}\frac{d}{dx}\left\{\left[1+\left(\frac{x}{A}\right)^B\right]^{\left(\frac{1}{B}-2\right)} x^{2(B-1)}\right\}, x \geq 0$$

For the first part of the equation

Let $\left[1+\left(\frac{x}{A}\right)^B\right]^{\left(\frac{1}{B}-1\right)} = u\,, \qquad x^{(B-2)} = v$

$$\frac{duv}{dx} = u\frac{dv}{dx} + v\frac{du}{dx}\,,$$

$$\frac{du}{dx} = \frac{1-B}{A^B}\left\{\left[1+\left(\frac{x}{A}\right)^B\right]^{\left(\frac{1}{B}-2\right)} x^{(B-1)}\right\}\,,$$

$$\frac{dv}{dx} = (B-2)\,x^{(B-3)}$$

$$\frac{duv}{dx} = (B-2)\left\{\left[1+\left(\frac{x}{A}\right)^B\right]^{\left(\frac{1}{B}-1\right)} x^{(B-3)}\right\} + \frac{(1-B)}{A^B}\left\{\left[1+\left(\frac{x}{A}\right)^B\right]^{\left(\frac{1}{B}-2\right)} x^{(2B-3)}\right\}$$

For the second part of the equation

Let $\left[1+\left(\frac{x}{A}\right)^B\right]^{\left(\frac{1}{B}-2\right)} = f\,, \qquad x^{2(B-1)} = g$

$$\frac{dfg}{dx} = f\frac{dg}{dx} + g\frac{df}{dx},$$

$$\frac{df}{dx} = \frac{1-2B}{A^B}\left\{\left[1+\left(\frac{x}{A}\right)^B\right]^{\left(\frac{1}{B}-3\right)} x^{(B-1)}\right\},$$

$$\frac{dg}{dx} = 2(B-1)\,x^{(2B-3)}$$

$$\frac{dfg}{dx} = 2(B-1)\left\{\left[1+\left(\frac{x}{A}\right)^B\right]^{\left(\frac{1}{B}-2\right)} x^{(2B-3)}\right\} + \frac{(1-2B)}{A^B}\left\{\left[1+\left(\frac{x}{A}\right)^B\right]^{\left(\frac{1}{B}-3\right)} x^{3(B-1)}\right\}$$

Combining the results for two parts of the derivation, the third derivative is given by:

$$\frac{d^3y}{dx^3} = \frac{F(B-1)(B-2)}{A^B}\left\{\left[1+\left(\frac{x}{A}\right)^B\right]^{\left(\frac{1}{B}-1\right)} x^{(B-3)}\right\} - \frac{3F(B-1)^2}{A^{2B}}\left\{\left[1+\left(\frac{x}{A}\right)^B\right]^{\left(\frac{1}{B}-2\right)} x^{(2B-3)}\right\} - \frac{F(B-1)(1-2B)}{A^{3B}}\left\{\left[1+\left(\frac{x}{A}\right)^B\right]^{\left(\frac{1}{B}-3\right)} x^{3(B-1)}\right\},\ x \geq 0 \qquad \text{(C.15)}$$

To find the peaks in the second derivative function, Equation C.15 is set to zero, and terms are rearranged as follows:

$$(B-2)\left\{\left[1+\left(\frac{x}{A}\right)^B\right]^{\left(\frac{1}{B}-1\right)} x^{(B-3)}\right\} - \frac{3(B-1)}{A^B}\left\{\left[1+\left(\frac{x}{A}\right)^B\right]^{\left(\frac{1}{B}-2\right)} x^{(2B-3)}\right\} - \frac{(1-2B}{A^{2B}}\left\{\left[1+\left(\frac{x}{A}\right)^B\right]^{\left(\frac{1}{B}-3\right)} x^{3(B-1)}\right\} = 0$$

Letting $\left[1+\left(\frac{x}{A}\right)^B\right] = j$

$$(B-2)\left\{j^{\left(\frac{1}{B}-1\right)} x^{(B-3)}\right\} - \frac{3(B-1)}{A^B}\left\{j^{\left(\frac{1}{B}-2\right)} x^{(2B-3)}\right\} -$$

$$\frac{(1-2B)}{A^{2B}}\left\{j^{\left(\frac{1}{B}-3\right)}\,x^{3(B-1)}\right\}=0$$

Dividing by $j^{\left(\frac{1}{B}-3\right)}\,x^{(B-3)}$

$$(B-2)j^2-\frac{3\,(B-1)}{A^B}j\,x^B-\frac{(1-2B)}{A^{2B}}x^{2B}=0$$

Substituting for j

$$(B-2)\left[1+\left(\frac{x}{A}\right)^B\right]^2-\frac{3\,(B-1)}{A^B}\left[1+\left(\frac{x}{A}\right)^B\right]\,x^B-\frac{(1-2B)}{A^{2B}}x^{2B}=0$$

Expanding

$$(B-2)\left[1+2\left(\frac{x}{A}\right)^B+\left(\frac{x}{A}\right)^{2B}\right]-3\,(B-1)\left(\frac{x}{A}\right)^B-$$
$$3\,(B-1)\left(\frac{x}{A}\right)^{2B}-(1-2B)\left(\frac{x}{A}\right)^{2B}=0$$

Collecting terms

$$(B-2)-(B+1)\left(\frac{x}{A}\right)^B=0$$

Therefore, the peaks of the second derivative curve are defined by

$$x=\pm A\left[\frac{(B-2)}{(B+1)}\right]^{\frac{1}{B}} \tag{C.16}$$

Appendix D

Least-Squares Matrix Operations

The least-squares matrix operations used in the stress back analysis approach were incorporated into a spreadsheet, NEARFACE. For m equations with known values of F and B, and n unknowns X, i.e.,

$$\underbrace{[F]}_{m\text{x}n}\underbrace{\{X\}}_{n\text{x}1} = \underbrace{\{B\}}_{m\text{x}1} \tag{D.1}$$

the solution for the n values of X is given by

$$\underbrace{\{X\}}_{n\text{x}1} = \underbrace{\left[\underbrace{[F]}_{n\text{x}m}{}^{\mathrm{T}}\underbrace{[F]}_{m\text{x}n}\right]^{-1}}_{n\text{x}n}\underbrace{[F]}_{n\text{x}m}{}^{\mathrm{T}}\underbrace{\{B\}}_{m\text{x}1} \tag{D.2}$$

In the case of the field study, the matrix F corresponds to the parametric functions $f_1 - f_6$, B corresponds to the measured radial displacements normalized to $U_{r_{max}}$, and X is the matrix of unknown stress components. Typical pages generated using NEARFACE are shown in Figures D.1, D.2, D.3 and D.4.

NEARFACE

A routine to use the radial displacement versus face position and versus radial distance data from extensometers and convergence arrays near the face to back calculate in situ stresses. The expressions for each type of measurement are shown below.

U_r vs R

$\sigma_{11} \Rightarrow U_{r_{11}} = \alpha_{11} + \beta_{11}\cos 2\theta$

$\sigma_{33} \Rightarrow U_{r_{33}} = \alpha_{11} - \beta_{11}\cos 2\theta$

$\sigma_{13} \Rightarrow U_{r_{13}} = 2\beta_{11}\sin 2\theta$

$\sigma_{22} \Rightarrow U_{r_{22}} = \alpha_{22}$

$\sigma_{12} \Rightarrow U_{r_{12}} = \beta_{12}\cos\theta$

$\sigma_{23} \Rightarrow U_{r_{23}} = \beta_{12}\sin\theta$

$$\alpha, \beta = \sum_{i=1}^{3} \frac{A_i}{R^i} \qquad R = \frac{r}{a}$$

$1 \le R < +\infty$

$x = -0.4, -0.1, 0.0, 0.1, 0.4$

U_r vs x

$\sigma_{11} \Rightarrow U_{r_{11}} = \alpha_{11} + \beta_{11}\cos 2\theta$

$\sigma_{33} \Rightarrow U_{r_{33}} = \alpha_{11} - \beta_{11}\cos 2\theta$

$\sigma_{13} \Rightarrow U_{r_{13}} = 2\beta_{11}\sin 2\theta$

$\sigma_{22} \Rightarrow U_{r_{22}} = \alpha_1 + \alpha_2 + \alpha_3$

$\sigma_{12} \Rightarrow U_{r_{12}} = \beta_{12}\cos\theta$

$\sigma_{23} \Rightarrow U_{r_{23}} = \beta_{12}\sin\theta$

$$\alpha, \beta = D_l + sign(x) F \left(1 + \left|\frac{x}{A}\right|^B\right)^{\frac{1}{B}}$$

$$x = \frac{X}{D} \qquad -\infty < x < +\infty \qquad R = 1$$

$F = E_l - D_l \qquad x > 0$
$F = D_l - E_l \qquad x < 0$

C vs x

$\sigma_{11} \Rightarrow C_{11} = 2\alpha_{11} + 2\beta_{11}\cos 2\theta$

$\sigma_{33} \Rightarrow C_{33} = 2\alpha_{11} - 2\beta_{11}\cos 2\theta$

$\sigma_{13} \Rightarrow C_{13} = 4\beta_{11}\sin 2\theta$

$\sigma_{22} \Rightarrow C_{22} = 2\alpha_1$

$\sigma_{12} \Rightarrow C_{12} = 0$

$\sigma_{23} \Rightarrow C_{23} = 0$

$$\alpha, \beta = sign(x) F \left(1 + \left|\frac{x}{A}\right|^B\right)^{\frac{1}{B}}$$

$$x = \frac{X}{D} \qquad 0 \le x < +\infty \qquad R = 1$$

Figure D.1: Title page for NEARFACE.

1) Function parameters for Ur vs R at five face positions using anterior extensometers

	X/D=-0.4			X/D=-0.1			X/D=0.0			X/D=0.1			X/D=0.4		
	σ11	σ22	σ12	σ11	σ22	σ12	σ11	σ22	σ12	σ11	σ22	σ12	σ11	σ22	σ12
α1	0.1640	-0.0383	-	0.1694	-0.0098	-	0.1634	-0.0210	-	0.1707	0.0072	-	0.1545	-0.0275	-
α2	-0.3132	0.2089	-	-0.1362	-0.0280	-	-0.0551	0.0101	-	-0.0412	-0.1429	-	0.2234	-0.0909	-
α3	0.1625	-0.1217	-	0.0198	0.0555	-	-0.0039	-0.0373	-	0.0555	0.0884	-	-0.0986	0.0942	-
β1	0.4722	-	0.6298	0.4895	-	0.5186	0.4714	-	0.5708	0.4712	-	0.5071	0.4350	-	0.6707
β2	-0.7808	-	-0.1357	-0.4015	-	0.3830	-0.1840	-	0.1249	-0.0602	-	0.4369	0.5510	-	-0.4218
β3	0.3670	-	-0.1737	0.0417	-	-0.3268	-0.0820	-	-0.0440	-0.0821	-	-0.4706	-0.4840	-	-0.0268

Typical function equations using discrete point data

Type	Name	X/D	Theta	R	f1	f2	f3	f4	f5	f6	**Ur**
A-Radial	EXT1	-0.100	0.00	1.000	0.183	-0.077	0.000	0.018	0.575	0.000	1.000
P-Radial	EXT1	0.100	0.00	1.000	0.514	-0.144	0.000	-0.047	0.473	0.000	1.000

Typical function equations using three-parameter curve-fit data

Type	Name	X/D	Theta	i	f1	f2	f3	f4	f5	f6	**Ai**
A-Radial	EXT1	0.000	45.00	1	0.163	0.163	0.943	-0.021	0.404	0.404	27.180
A-Radial	EXT1	0.000	45.00	2	-0.055	-0.055	-0.368	0.010	0.088	0.088	-9.893
A-Radial	EXT1	0.000	45.00	3	-0.004	-0.004	-0.164	-0.037	-0.031	-0.031	-4.995

Typical function equations using five-parameter curve-fit data

Type	Name	X/D	Theta	R	f1	f2	f3	f4	f5	f6	**ΣAi**
A-Radial	EXT1	0.400	0.00	1.000	0.781	-0.223	0.000	-0.024	0.222	0.000	12.291

Notes: A-Radial - Anterior domain, radial displacement at radial distance R>1 (includes x=-0.4, -0.1 and 0)
P-Radial - Posterior domain, radial displacement at radial distance R>1 (includes x=0, 0.1 and 0.4)

2) Function parameters for Ur and C vs x at the tunnel wall using extensometers and convergence arrays

Anterior Domain							Posterior Domain						
	σ11		σ22			σ12		σ11		σ22			σ12
Anterior	α11	β11	α1	α2	α3	β12	Posterior	α11	β11	α1	α2	α3	β12
A	0.162	0.249	-	0.959	0.162	0.686	A	0.218	0.324	0.703	-	-	0.285
B	-1.560	-1.412	-	-1.933	-1.228	-1.772	B	-1.337	-1.307	-1.566	-	-	-1.196
D	0.104	0.206	-	0.142	-0.192	0.654	D	0.104	0.206	-0.051	-	-	0.654
E	0.000	0.000	-	0.000	0.000	0.000	E	0.333	0.667	0.000	-	-	0.000
F	0.104	0.206	-	0.142	-0.192	0.654	F	0.230	0.460	0.051	-	-	-0.654

Typical function equations for three instrument types/positions

Type	Name	X/D	Theta	R	f1	f2	f3	f4	f5	f6	**Ur, C**
A-Ewall	EXT1	-1.000	45.00	1.000	0.004	0.004	0.037	0.025	0.096	0.096	1.000
P-Ewall	EXT2	1.000	45.00	1.000	0.209	0.209	0.786	0.038	-0.391	-0.391	1.000
P-Cwall	CNV1-1	1.000	45.00	1.000	0.419	0.419	1.572	0.076	0.000	0.000	1.000

Notes: A-Ewall - Anterior extensometer, radial displacement at R=1 (both domains)
P-Ewall - Posterior extensometer, radial displacement at R=1 (posterior domain)
P-Cwall - Posterior convergence array, convergence at radial distance R=1 (posterior domain)

Figure D.2: Parametric equations for different types of measurements.

3) Equations from measured data

						F						B
Weight	Type	Name	X/D	Theta	R, i	f1	f2	f3	f4	f5	f6	Ur, C, Ai
3	A-Ewall	EXT1	-2.764	88.445	1.000	-0.004	0.006	0.001	0.004	0.001	0.029	0.404
3	A-Ewall	EXT1	-2.463	88.445	1.000	-0.005	0.007	0.001	0.005	0.001	0.035	0.461
3	A-Ewall	EXT1	-2.131	88.445	1.000	-0.006	0.008	0.001	0.007	0.001	0.045	0.659
3	A-Ewall	EXT1	-1.843	88.445	1.000	-0.007	0.010	0.001	0.010	0.002	0.056	0.774
3	A-Ewall	EXT1	-1.565	88.445	1.000	-0.008	0.012	0.001	0.013	0.002	0.073	0.957
3	A-Ewall	EXT1	-1.297	88.445	1.000	-0.011	0.016	0.001	0.018	0.003	0.096	1.218
3	A-Ewall	EXT1	-1.037	88.445	1.000	-0.014	0.021	0.002	0.024	0.004	0.130	1.395
3	A-Ewall	EXT1	-0.742	88.445	1.000	-0.021	0.032	0.003	0.035	0.005	0.195	1.440
3	A-Ewall	EXT1	-0.407	88.445	1.000	-0.038	0.065	0.006	0.048	0.009	0.333	0.780
3	A-Ewall	EXT1	-0.400	88.445	1.000	-0.039	0.066	0.006	0.048	0.009	0.336	0.743
3	A-Ewall	EXT1	-0.115	88.445	1.000	-0.080	0.177	0.014	0.023	0.015	0.547	-3.445
3	A-Ewall	EXT1	-0.100	88.445	1.000	-0.083	0.190	0.015	0.017	0.015	0.560	-3.844
3	A-Ewall	EXT1	0.000	88.445	1.000	-0.102	0.310	0.022	-0.051	0.018	0.654	-6.830
3	A-Ewall	EXT1	0.100	88.445	1.000	-0.141	0.516	0.036	-0.044	0.013	0.468	-8.064
1	A-Ewall	EXT1	0.185	88.445	1.000	-0.171	0.629	0.043	-0.038	0.010	0.367	-8.905
1	A-Ewall	EXT1	0.400	88.445	1.000	-0.226	0.782	0.055	-0.028	0.006	0.227	-11.705
0	A-Ewall	EXT1	0.508	88.445	1.000	-0.244	0.824	0.058	-0.024	0.005	0.188	-12.728
0	A-Ewall	EXT1	0.752	88.445	1.000	-0.270	0.880	0.062	-0.017	0.004	0.133	-10.937
0	A-Ewall	EXT1	0.905	88.445	1.000	-0.280	0.902	0.064	-0.014	0.003	0.111	-11.057
0	A-Ewall	EXT1	1.067	88.445	1.000	-0.288	0.918	0.066	-0.012	0.003	0.095	-11.526
0	A-Ewall	EXT1	1.237	88.445	1.000	-0.295	0.930	0.067	-0.010	0.002	0.081	-11.388
0	A-Ewall	EXT1	1.419	88.445	1.000	-0.300	0.941	0.067	-0.009	0.002	0.071	-11.633
0	A-Ewall	EXT1	1.749	88.445	1.000	-0.307	0.954	0.069	-0.007	0.002	0.056	-11.626
0	A-Ewall	EXT1	2.011	88.445	1.000	-0.311	0.961	0.069	-0.005	0.001	0.048	-11.767
0	A-Ewall	EXT1	2.309	88.445	1.000	-0.314	0.967	0.070	-0.004	0.001	0.042	-11.745
0	A-Ewall	EXT1	2.576	88.445	1.000	-0.316	0.971	0.070	-0.004	0.001	0.037	-11.794
0	A-Ewall	EXT1	2.845	88.445	1.000	-0.318	0.974	0.070	-0.003	0.001	0.033	-11.645
0	A-Ewall	EXT1	3.139	88.445	1.000	-0.320	0.977	0.070	-0.003	0.001	0.029	-11.630
0	A-Ewall	EXT1	3.430	88.445	1.000	-0.321	0.979	0.071	-0.003	0.001	0.027	-11.664
0	A-Ewall	EXT1	3.760	88.445	1.000	-0.322	0.981	0.071	-0.002	0.001	0.024	-11.705
0	A-Ewall	EXT1	4.022	88.445	1.000	-0.323	0.983	0.071	-0.002	0.001	0.022	-11.747
0	A-Ewall	EXT1	4.185	88.445	1.000	-0.324	0.984	0.071	-0.002	0.001	0.021	-11.772
0	A-Ewall	EXT1	4.363	88.445	1.000	-0.324	0.985	0.071	-0.002	0.001	0.020	-11.768
0	A-Ewall	EXT1	4.484	88.445	1.000	-0.324	0.985	0.071	-0.002	0.001	0.020	-11.763
0	A-Ewall	EXT1	4.607	88.445	1.000	-0.325	0.985	0.071	-0.002	0.001	0.019	-11.738
0	A-Ewall	EXT1	4.738	88.445	1.000	-0.325	0.986	0.071	-0.002	0.000	0.018	-11.817
0	A-Ewall	EXT1	4.877	88.445	1.000	-0.325	0.986	0.071	-0.002	0.000	0.018	-11.908
3	A-Ewall	EXT2	-2.801	4.171	1.000	0.005	-0.004	0.001	0.004	0.029	0.002	-0.567
3	A-Ewall	EXT2	-2.500	4.171	1.000	0.006	-0.004	0.002	0.005	0.035	0.003	-0.770
3	A-Ewall	EXT2	-2.168	4.171	1.000	0.008	-0.005	0.002	0.007	0.044	0.003	-0.907
3	A-Ewall	EXT2	-1.880	4.171	1.000	0.009	-0.007	0.002	0.009	0.055	0.004	-1.109
3	A-Ewall	EXT2	-1.602	4.171	1.000	0.012	-0.008	0.003	0.012	0.070	0.005	-1.216
3	A-Ewall	EXT2	-1.334	4.171	1.000	0.015	-0.010	0.004	0.017	0.092	0.007	-1.188
3	A-Ewall	EXT2	-1.073	4.171	1.000	0.020	-0.013	0.005	0.023	0.124	0.009	-0.970
3	A-Ewall	EXT2	-0.779	4.171	1.000	0.030	-0.019	0.007	0.033	0.184	0.013	-0.092

Figure D.3: Typical data entries from the field study.

4) Least squares fit to measured data

For m equations and n unknowns, solve for unknown parameter X given coefficients F and measured values B.

$$[F]_{mxn}\{X\}_{nx1} = \{B\}_{mx1}$$

Solution:

$$\{X\}_{nx1} = \left[[F]^T_{nxm}[F]_{mxn}\right]^{-1}[F]^T_{nxm}\{B\}_{mx1}$$

FT F

	1	2	3	4	5	6
1	12.024	-4.422	-3.681	0.660	-0.045	-0.087
2	-4.422	12.750	0.735	0.737	0.060	0.096
3	-3.681	0.735	22.015	-0.246	-0.154	0.160
4	0.660	0.737	-0.246	0.183	0.009	-0.006
5	-0.045	0.060	-0.154	0.009	3.403	0.041
6	-0.087	0.096	0.160	-0.006	0.041	3.858

Inverse FT F

	1	2	3	4	5	6
1	0.228	0.162	0.016	-1.457	0.005	-0.002
2	0.162	0.219	0.003	-1.468	0.003	-0.004
3	0.016	0.003	0.048	-0.009	0.002	-0.002
4	-1.457	-1.468	-0.009	16.657	-0.041	0.031
5	0.005	0.003	0.002	-0.041	0.294	-0.003
6	-0.002	-0.004	-0.002	0.031	-0.003	0.259

Best-fit Coefficients

Coeff's	X	Expected	Δ	Δ 2	X-Mean	X-Mean 2
C1	56.654	52.430	4.224	17.843	35.497	1260.060
C2	11.062	16.570	-5.508	30.340	-10.094	101.895
C3	10.514	9.939	0.576	0.331	-10.642	113.256
C4	43.180	48.000	-4.820	23.230	22.024	485.048
C5	-4.523	0.000	-4.523	20.461	-25.680	659.453
C6	2.915	0.000	2.915	8.500	-18.241	332.734
	Mean	21.156				
	r 2	0.9659				

Estimated 420 Level Tensor

Theta -14.500

Sigma Principal

55.000	0.000	0.000
0.000	48.000	0.000
0.000	0.000	14.000

Sigma XYZ

52.430	0.000	9.939
0.000	48.000	0.000
9.939	0.000	16.570

Alpha

0.968	0.000	-0.250
0.000	1.000	0.000
0.250	0.000	0.968

Alpha Transpose

0.968	0.000	0.250
0.000	1.000	0.000
-0.250	0.000	0.968

Best-fit Stress Tensor

σ	1	2	3
1	56.654	-4.523	10.514
2	-4.523	43.180	2.915
3	10.514	2.915	11.062

Best-fit Principal Stress Tensor

σ	1	2	3
1	59.840	0.000	0.000
2	0.000	42.723	0.000
3	0.000	0.000	8.333

Coefficient of Determination

0.96589

	σ1	σ2	σ3
Trend	148.29	56.53	288.59
Plunge	11.09	8.90	75.71

Invariants

I1	110.8961
I2	3411.189
I3	21302.77

Figure D.4: Typical solution to the least-squares problem.

Appendix E

Mine-by Experiment Monitoring Results

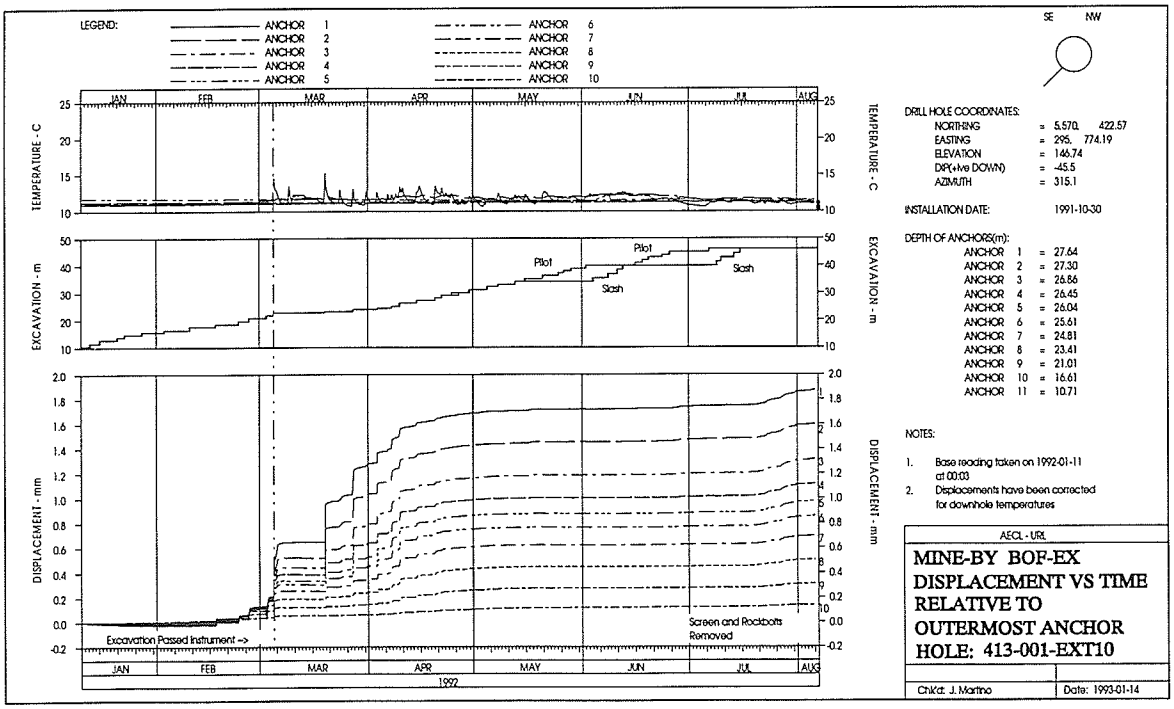

Figure E.1: Radial displacement response versus time for a typical 45-225° inclined extensometer (413-001-EXT10).

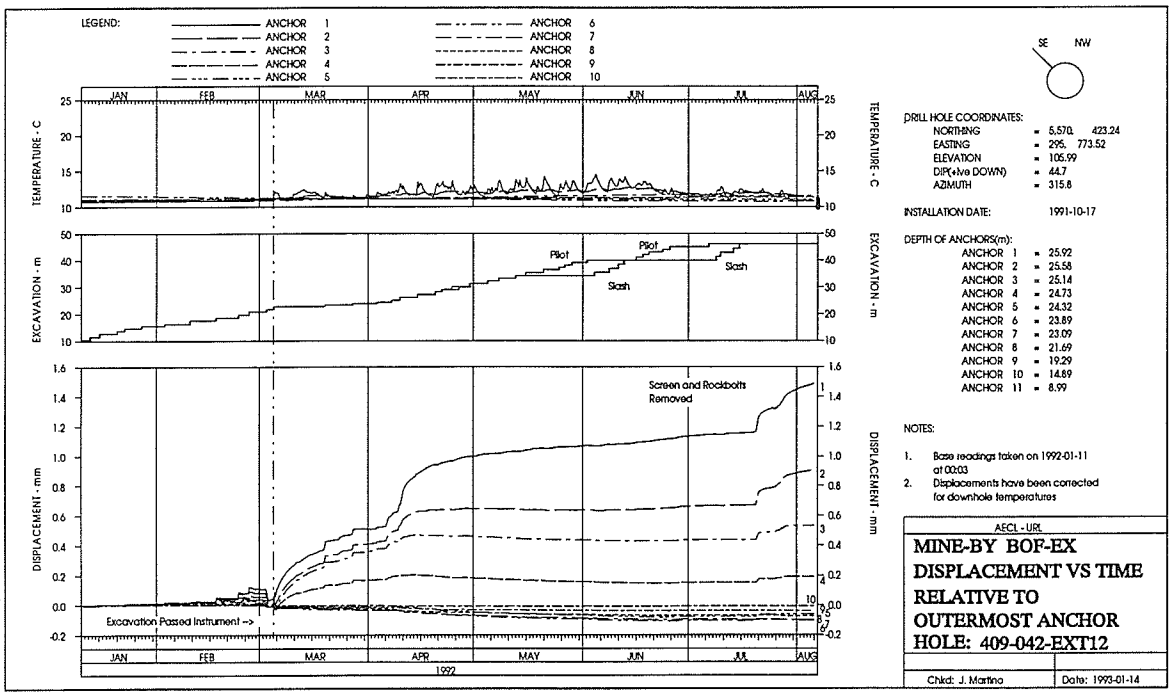

Figure E.2: Radial displacement response versus time for a typical 135-315° inclined extensometer (409-042-EXT12).

Table E.1: Corrected face chainages for the 30 full-face excavation rounds of the Mine-by Experiment.

Face	Excavation Method	Centre Chainage (m)	Edge Chainage (m)	d (m)	d/D	Δx (m)	Face Chainage (m)
1	MF	2.152	1.932	0.220	0.063	-0.200	1.952
2	EF	5.247	4.662	0.585	0.167	-0.532	4.715
3	EF	8.254	7.695	0.559	0.160	-0.508	7.746
4	CF	9.373	9.192	0.181	0.052	-0.164	9.208
5	CF	10.508	10.327	0.181	0.052	-0.164	10.343
6	MF	11.588	11.378	0.210	0.060	-0.191	11.397
7	MF	12.708	12.542	0.166	0.047	-0.151	12.557
8	MF	13.791	13.545	0.247	0.071	-0.225	13.567
9	MF	14.703	14.521	0.182	0.052	-0.165	14.538
10	MF	15.563	15.469	0.093	0.027	-0.085	15.478
11	MF	16.302	16.397	-0.095	-0.027	0.086	16.389
12	MF	17.636	17.398	0.238	0.068	-0.216	17.420
13	MF	18.629	18.589	0.041	0.012	-0.037	18.593
14	MF	19.735	19.602	0.133	0.038	-0.121	19.614
15	MF	20.843	20.645	0.198	0.056	-0.180	20.663
16	MF	21.816	21.793	0.023	0.007	-0.021	21.795
17	MF	22.837	22.629	0.208	0.060	-0.190	22.648
18	MF	23.325	23.172	0.153	0.044	-0.140	23.186
19	MF	23.903	23.735	0.168	0.048	-0.153	23.750
20	MF	24.472	24.333	0.139	0.040	-0.126	24.345
21	MF	25.177	24.963	0.215	0.061	-0.195	24.982
22	MF	26.221	26.130	0.091	0.026	-0.083	26.138
23	MF	27.267	27.035	0.232	0.066	-0.211	27.056
24	MF	28.255	28.085	0.170	0.049	-0.155	28.100
25	MF	29.178	29.019	0.159	0.045	-0.144	29.034
26	MF	30.086	29.962	0.124	0.035	-0.113	29.973
27	MF	31.160	30.988	0.173	0.049	-0.157	31.003
28	MF	32.245	32.000	0.246	0.070	-0.224	32.022
29	MF	33.175	33.175	0.000	0.000	0.000	33.175
30	MF	34.266	34.077	0.189	0.054	-0.172	34.094

Notes: Excavation Method
MF = Mechanical Full-Face
EF = Explosive Full-Face
CF = Combination Full-Face

Table E.2: Parameter values for convergence versus excavation advance (individual measurement lines). Note that F is the difference between E_l and D_l.

Array	Line	A	B	D_l	E_l	F	λ	r^2
415-1	1-7	0.249	-0.679	-0.804	7.842	8.646	0.000	0.996
	2-8	0.577	-0.870	-0.297	5.801	6.098	0.000	0.996
	5-11	0.293	-0.547	-0.424	5.370	5.794	0.000	0.996
	6-12	0.330	-0.757	-0.737	7.672	8.409	0.000	0.998
415-2	1-7	0.469	-0.963	-0.016	7.910	7.926	0.000	0.986
	2-8	0.528	-0.813	0.000	5.635	5.635	0.000	0.977
	5-11	0.727	-1.150	-0.032	5.019	5.051	0.000	0.972
	6-12	0.462	-0.928	-0.022	7.843	7.865	0.000	0.992
415-3	1-7	0.323	-0.814	-0.515	7.592	8.107	0.000	0.987
	2-8	0.357	-0.814	-0.349	5.545	5.894	0.000	0.981
	5-11	0.598	-1.058	-0.198	4.567	4.765	0.000	0.981
	6-12	0.407	-0.940	-0.371	7.690	8.061	0.000	0.989
415-4	1-7	0.296	-0.873	-0.608	6.352	6.960	0.000	0.985
	2-8	0.305	-0.718	-0.407	4.808	5.215	0.000	0.964
	5-11	1.051	-1.331	-0.606	1.994	2.600	0.000	0.896
	6-12	0.271	-0.883	-0.689	6.732	7.421	0.000	0.988
415-5	1-7	0.133	-0.530	-0.634	5.370	6.004	0.000	0.989
	2-8	0.177	-0.617	-0.539	4.203	4.742	0.000	0.984
	5-11	0.015	-0.352	-0.868	3.613	4.481	0.000	0.977
	6-12	0.224	-0.774	-0.591	5.582	6.173	0.000	0.991
415-6	1-7	0.421	-1.029	-0.177	4.910	5.087	0.000	0.981
	2-8	0.225	-0.635	-0.239	3.666	3.905	0.000	0.973
	3-9	1.009	-3.074	0.027	-0.256	-0.283	10.557	0.816
	4-10	6.160	-0.947	0.244	-0.363	-0.607	-61.437	0.174
	5-11	0.001	-0.240	-0.720	3.711	4.431	0.000	0.924
	6-12	0.136	-0.646	-0.620	5.622	6.242	0.000	0.989
415-7	1-7	0.510	-1.343	-0.302	4.122	4.424	0.000	0.945
	5-11	0.009	-0.366	-0.838	2.545	3.383	0.000	0.919
	6-12	0.281	-0.864	-0.456	4.598	5.054	0.000	0.980
415-8	1-7	0.228	-0.777	-0.200	4.073	4.273	0.000	0.985
	2-8	0.122	-0.595	-0.177	3.398	3.575	0.000	0.981
	3-9	3.160	-2.636	-0.004	-0.478	-0.474	0.000	0.790
	4-10	0.959	-1.534	-0.057	-0.443	-0.386	7.897	0.857
	5-11	0.043	-0.545	-0.233	1.684	1.917	0.000	0.950
	6-12	0.155	-0.634	-0.227	4.716	4.943	0.000	0.990

Table E.3: Parameter values for radial displacement versus excavation advance for the twelve extensometers used in the field study. Note that each extensometer has three sets of parameter values: two for the anterior domain and one for the posterior domain. The coefficients of determination r^2 are for the combination of two anterior functions, and for the combination of all three functions, respectively.

Extensometer	Domain	A	B	D_l	E_l	r^2
EXT1	Anterior	1.431	-1.796	0.326	0.001	0.9997
		0.430	-1.793	-0.674	-0.029	
	Posterior	0.484	-1.710	-0.348	-0.716	0.9989
EXT2	Anterior	0.643	-2.022	0.890	-0.019	1.0000
		2.578	-2.329	-0.248	0.067	
	Posterior	0.313	-1.264	0.642	3.452	0.9997
EXT3	Anterior	2.542	-1.166	0.460	-0.128	0.9997
		1.103	-1.551	-0.670	-0.041	
	Posterior	1.522	-1.256	-0.211	-0.651	0.9950
EXT4	Anterior	0.902	-2.025	1.310	0.042	1.0000
		3.193	-2.033	-0.430	0.084	
	Posterior	0.271	-1.072	0.880	4.318	0.9998
EXT5	Anterior	0.926	-1.374	0.443	-0.022	0.9985
		0.369	-1.547	-0.679	-0.008	
	Posterior	0.401	-9.995	-0.235	-0.382	0.9815
EXT6	Anterior	1.114	-3.202	0.796	-0.023	0.9951
		1.465	-3.138	-0.478	0.022	
	Posterior	0.459	-1.337	0.318	2.243	0.9996
EXT7A	Anterior	0.947	-1.974	0.845	-0.030	0.9997
		2.538	-5.642	-0.304	0.010	
	Posterior	0.264	-1.133	0.541	3.000	0.9999
EXT8	Anterior	1.058	-2.228	0.485	0.000	0.9981
		0.844	-2.130	-0.584	-0.002	
	Posterior	3.588	-1.963	0.689	0.204	0.9331
		0.219	-0.215	-0.788	2.563	
EXT9	Anterior	0.548	-1.322	0.350	-0.006	0.9998
		0.509	-2.762	-0.682	-0.013	
	Posterior	1.522	-1.822	-0.332	-0.726	0.9998
EXT10	Anterior	1.105	-3.756	0.602	0.088	0.9986
		1.772	-0.809	-0.289	0.060	
	Posterior	0.177	-0.967	0.313	2.040	0.9993
EXT11	Anterior	1.041	-2.959	0.868	0.000	0.9999
		3.670	-2.517	-0.193	0.067	
	Posterior	0.219	-0.913	0.674	3.989	0.9996
EXT12	Anterior	0.730	-2.203	0.553	-0.006	0.9996
		0.450	-2.351	-0.566	0.004	
	Posterior	0.440	-0.857	-0.013	1.226	0.9971